

Alma Mater Studiorum – Università di Bologna

DOTTORATO DI RICERCA IN  
SCIENZE VETERINARIE  
Ciclo 34

**Settore Concorsuale:** 05/E1-BIOCHIMICA GENERALE

**Settore Scientifico Disciplinare:** BIO/10-BIOCHIMICA

IONS AND SMALL MOLECULES AS MODULATORS OF  $F_1F_0$ -ATPase,  
MITOCHONDRIAL BIOENERGETICS AND CELL METABOLISM

**Presentata da:** Dott.ssa Cristina Algieri

**Coordinatore Dottorato:**

Prof.ssa Carolina Castagnetti

**Supervisore**

Prof. Salvatore Nesci

**Esame finale anno 2022**

## ***Abstract***

The properties of the mitochondrial  $F_1F_0$ -ATPase activated by the natural cofactor  $Mg^{2+}$  or by  $Ca^{2+}$ , were studied, mainly on heart mitochondria from swine, widely used in translational medicine. The  $Ca^{2+}$  driven conformational changes in the  $F_1F_0$ -ATPase form the mitochondrial permeability transition pore (mPTP), which triggers regulated cell death and is involved in severe pathologies. The  $Ca^{2+}$ -activated  $F_1F_0$ -ATPase hydrolyzes ATP with kinetics slightly different from those of the  $Mg^{2+}$ -ATPase. Known  $F_1$ -ATPase inhibitors inhibit both the  $Ca^{2+}$ -activated  $F_1F_0$ -ATPase and the mPTP formation strengthening the molecular link between them. The different  $Gd^{3+}$  effects on the  $Ca^{2+}$ - and  $Mg^{2+}$ -activated  $F_1F_0$ -ATPases confirm their difference as also phenylglyoxal which preferentially inhibits the  $Ca^{2+}$ -activated  $F_1F_0$ -ATPase. The effects of phenylarsine and dibromobimane, which interact with differently distant Cys thiols, show that mPTP opening is ruled by nearby or distant dithiols. Bergamot polyphenols and melatonin inhibit the mPTP and ROS formation.  $H_2S$ , a known cardiovascular protector, unaffected the  $F_1F_0$ -ATPase, but inhibits  $Ca^{2+}$  absorption and indirectly the mPTP, both in swine heart and mussel midgut gland mitochondria. New generation triazoles inhibit the  $Ca^{2+}$ -activated  $F_1F_0$ -ATPase and the mPTP, but unaffected the  $Mg^{2+}$ -activated  $F_1F_0$ -ATPase.

In parallel, the energy metabolism was investigated in mammalian cells. In boar sperm ATP is mainly produced by mitochondrial oxidative phosphorylation (OXPHOS), even if it decreases over time because of less active mitochondria. Insufficient ATP may induce sperm dysfunction. Also, canine mesenchymal stem cells rely on OXPHOS; those from umbilical cord which produce more ATP than those from adipose tissue, seem preferable for transplant studies. The intestinal porcine enterocyte cell line IPEC-J2, used for human gut research, responds to different fetal bovine serum concentrations by remodeling OXPHOS without altering the bioenergetic parameters. The IPEC-J2 bioenergetics is modulated by Vitamin K vitamers. These data-shoulder cell bioenergetics as precious tool for medical research.

# Contents

<b><i>Introduction</i></b>	4
<b><i>1. Cell metabolism and role of the mitochondrion</i></b>	5
1.1. Cell metabolism	5
1.2. Glycolysis	9
1.3. The mitochondrial respiration	12
<b><i>2. The <math>F_1F_0</math>-ATPase and implication for new drugs</i></b>	18
2.1. Structure and function of the $F_1F_0$ -ATPase	18
2.2. Correlation between the $F_1F_0$ -ATPase and the permeability transition pore	23
2.3. Pathologies related to the uncontrolled regulation of permeability transition pore	26
2.4. $F_1F_0$ -ATPase as a pharmacological target	27
<b><i>3. Ions and small molecules as hypothetical therapeutic agents</i></b>	32
3.1. Polyphenols	33
3.2. Gadolinium	34
3.3. Phenylglyoxal	35
3.4. Dithiol reagents	36
3.5. Melatonin	37
3.6. $H_2S$	38
3.7. Triazole derivatives	40
3.8. Vitamins K	41
<b><i>4. Animal models</i></b>	43
4.1. Swine as a model animal in translational medicine	43
4.2. Mollusks as a model for the study of biochemical mechanisms	44
<b><i>Materials and methods</i></b>	46

<b>5. Evaluation of mitochondrial energy parameters and activity of the transition pore (section I)</b>	47
5.1. Preparation of the mitochondrial fractions	47
5.1.1. Extraction of mitochondria from swine heart	47
5.1.2. Extraction of mitochondria from mussel digestive gland	48
5.2. F <sub>1</sub> domain purification	49
5.3. Swine and mussel mitochondrial F-ATPase activity assays	50
5.4. F <sub>1</sub> -ATPase activity assays	51
5.5. Kinetic analysis	52
5.6. Mitochondrial respiration assay	53
5.7. Evaluation of mPTP, membrane potential and ROS production	54
5.8. Evaluation of oxidative phosphorylation	55
5.9. Mitochondrial substrate oxidation	56
<b>6. Cell metabolism analysis (section II)</b>	58
6.1. Evaluation of ATP production	58
6.2. Measurement of the parameters of mitochondrial function	59
6.3. Cell Energy Phenotype	60
6.4. Oxidation of substrates	60
<b>7. Statistic analysis</b>	61
<b>Results</b>	62
<b>8. Evaluation of the effect of ions and small molecules on F<sub>1</sub>F<sub>0</sub>-ATPase activity and correlation with mPTP opening (section I)</b>	63
Mitochondrial Ca <sup>2+</sup> -activated F <sub>1</sub> F <sub>0</sub> -ATPase hydrolyzes ATP and promotes the permeability transition pore	65
The inhibition of gadolinium ion (Gd <sup>3+</sup> ) on the mitochondrial F <sub>1</sub> F <sub>0</sub> -ATPase is linked to the modulation of the mitochondrial permeability transition pore	81
Phenylglyoxal inhibition of the mitochondrial F <sub>1</sub> F <sub>0</sub> -ATPase activated by Mg <sup>2+</sup> or by Ca <sup>2+</sup> provides clues on the mitochondrial permeability transition pore	90
The mitochondrial F <sub>1</sub> F <sub>0</sub> -ATPase exploits the dithiol redox state to modulate the permeability transition pore	97
The effect of polyphenolic fraction of bergamot (BPF) on isolate mitochondria	102

The effect of melatonin on the mitochondrial F <sub>1</sub> F <sub>0</sub> -ATPase activity, mPTP formation and ROS production	105
Sulfide affects the mitochondrial respiration, the Ca <sup>2+</sup> -activated F <sub>1</sub> F <sub>0</sub> -ATPase activity and the permeability transition pore but does not change the Mg <sup>2+</sup> -activated F <sub>1</sub> F <sub>0</sub> -ATPase activity in swine heart mitochondria	114
Mitochondrial F <sub>1</sub> F <sub>0</sub> -ATPase and permeability transition pore response to sulfide in the midgut gland of <i>Mytilus galloprovincialis</i>	124
1,5-Disubstituted-1,2,3-triazoles as inhibitors of the mitochondrial Ca <sup>2+</sup> -activated F <sub>1</sub> F <sub>0</sub> -ATP(hydrol)ase and the permeability transition pore	131
<b><i>9. Characterization of cell metabolism (section II)</i></b>	144
Sperm function and mitochondrial activity: An insight on boar sperm metabolism	148
Studies on sperm energy metabolism and time dependance after collection	155
Biological characteristics and metabolic profile of canine mesenchymal stem cells isolated from adipose tissue and umbilical cord matrix	159
Relationship between serum concentration, functional parameters and cell bioenergetics in IPEC-J2 cell line	178
Vitamin K vitamers differently affect energy metabolism in IPEC-J2 cells	187
<b><i>Discussion</i></b>	199
<b>Section I</b>	200
<b>Section II</b>	213
<b><i>Conclusion</i></b>	217
<b>Section I</b>	218
<b>Section II</b>	221
<b><i>Publication list</i></b>	223
<b><i>References</i></b>	225

## *Introduction*

# 1. Cell metabolism and role of the mitochondrion

## 1.1. Cell metabolism

Metabolism is the set of all chemical reactions that take place in the cell and are essential for life.

These chemical reactions are divided into *catabolism* and *anabolism* (figure1):

- *catabolism*, or degradation, in which nutrients are degraded to make energy available or to be reused;
- *anabolism*, or biosynthesis, in which biological macromolecules are synthesized starting from simple compounds<sup>1</sup>.

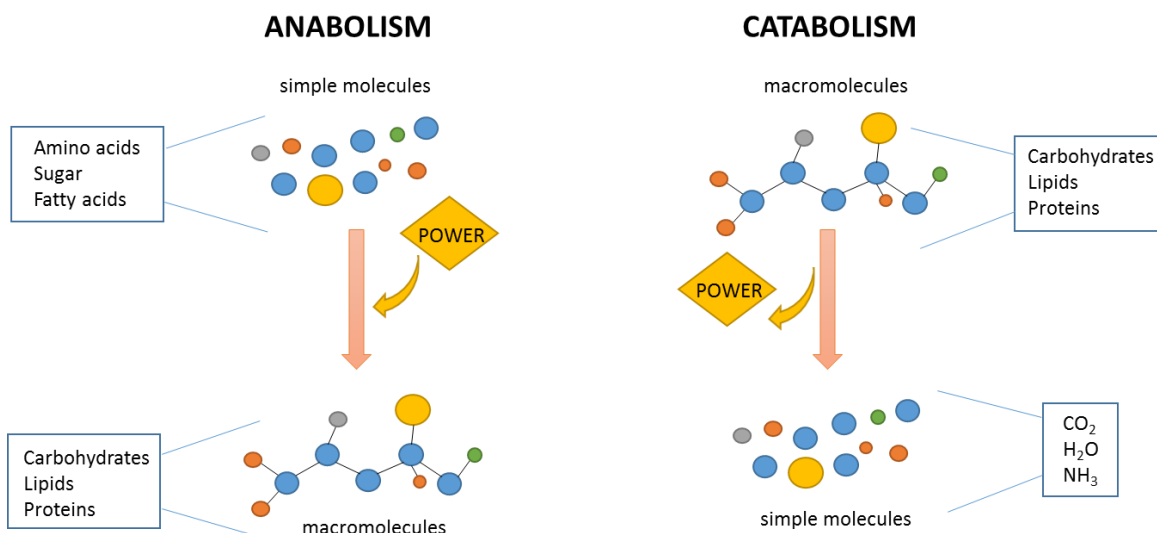


**Figure 1. Catabolism and Anabolism.** Catabolism releases energy when macromolecules are broken down into simpler molecules. Anabolism utilizes energy to make macromolecules and biomolecular polymers.

The catabolic reactions carry out the exergonic oxidation of the nutrient molecules and the energy released by this reaction is used to carry out endergonic reactions of anabolism, but also the active transport of molecules against a concentration gradient or mechanical work. The metabolism maximizes the capture of energy and minimizes its use<sup>2</sup>.

The nutritional needs of organisms concern the source of energy necessary to carry out their metabolism. Therefore, it is possible to divide the organisms into:

- *autotrophs* which synthesize all their cellular constituents starting from simple molecules ( $\text{H}_2\text{O}$ ,  $\text{CO}_2$ ,  $\text{H}_2\text{S}$  and  $\text{NH}_3$ ); the two sources of free energy to carry out this process allow us to distinguish the organisms in *chemolithotrophs*, which oxidize inorganic compounds and *photoautotrophs*, which obtain energy through photosynthesis by exploiting light energy;

- *heterotrophs* which obtain free energy from the oxidation of organic compounds. Metabolic reactions are supported by specific enzymes and lead to the production of specific products starting from reagents and passing through specific intermediates (metabolites). In the degradative pathways, the cleavage of macromolecules implies the release of free energy which is used for the synthesis of molecules with a high energy content such as adenosine triphosphate (ATP) or by reducing coenzymes nicotinamide adenine dinucleotide ( $\text{NAD}^+$ ) and nicotinamide adenine dinucleotide phosphate ( $\text{NADP}^+$ ) to NADH and NADPH, respectively<sup>3</sup>. Therefore, ATP and NADPH are energy sources for biosynthetic reactions. Almost all the biosynthesis and degradation reactions are catalyzed by *enzymes* without which such reactions would not take place except in very long times. These enzymes specifically ensure the efficiency of the reactions, they provide a mechanism for coupling endergonic reactions (which do not react spontaneously) with exergonic reactions (energetically favorable reactions). These reactions can be classified into:

- *redox*, catalyzed by oxidoreductases;
- *transfer of chemical groups*, catalyzed by transferases and hydrolases;
- *synthesis or hydrolysis of carbon-carbon (C-C) bonds*, catalyzed by hydrolase, lyase and ligase;
- *molecular elimination, isomerization, and redistribution*, catalyzed by isomerase and mutase<sup>4</sup>.

The specificity of the enzymes together with the cellular compartmentalization guarantee the carrying out of hundreds of metabolic reactions that occur simultaneously.

It is also important to be able to evaluate the rate with which a reaction occurs and how the metabolic pathway is regulated according to the cellular needs. The laws of thermodynamics also help us predict whether a reaction is possible and how much energy is required or released in the process.

If the change in free energy  $\Delta G$  (constant energy change during the standard state pH 7.0 at 25°C 1 atm, when the concentration of substrates is 1.0 M) of a reaction is negative, a reaction proceeds spontaneously and with a loss of free energy. This reaction is called *exergonic*, or if it gives off heat, exothermic. On the other hand, if the  $\Delta G$  is positive, the reaction is unfavored or non-spontaneous, *i.e.* the reaction is *endergonic*, or in the case of heat absorption, endothermic<sup>5</sup>. When the reactants are present at concentrations close to those of equilibrium,  $\Delta G = 0$  as is the case with many metabolic reactions, by modifying the ratios between reactants and products, it is possible to reverse the direction of the reaction. Many reactions with a positive  $\Delta G$ , and therefore in theory not spontaneous, can occur if coupled to other reactions. Accordingly, the product of one becomes the substrate for the next, therefore, the substrates can accumulate and the products can be removed quickly, changing their equilibrium and making the  $\Delta G$  negative<sup>6</sup>. Exergonic reactions are often associated with endergonic reactions to aid completion as the free energy of coupled processes can be summed. However, biological reactions do not take place at standard conditions of 25 °C, therefore their thermodynamics is expressed by the standard free energy variation  $\Delta G^\circ$ .

In the oxidation of metabolic fuels, there is the release of free energy which accumulates in some high-energy intermediates such as ATP or reduced coenzymes such as NADH or NADPH. These molecules represent a form of storage of energy that the cell uses to do work such as the biosynthesis of biomolecules. The ATP molecule, adenosine (adenine + ribose) bound to three phosphoric groups by one phosphoester bond and two phosphoanhydride bonds (*figure 2*), releases a large amount of free energy when the phosphoric groups are transferred to an acceptor and the

phosphoanhydride bonds are cleaved. High-energy bonds are defined as such by the very negative value of  $\Delta G^\circ$ , of the reaction of their cleavage<sup>7</sup>.

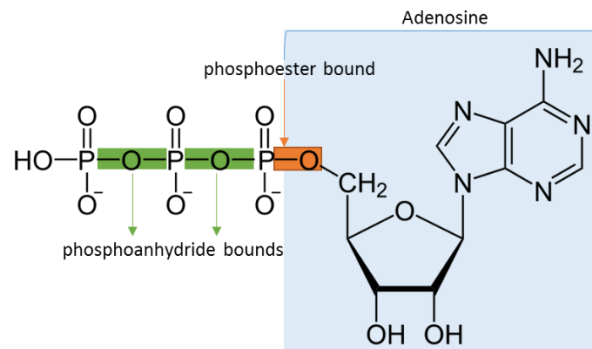


**Figure 2. ATP structure.** Adenosine triphosphate is made up of one molecule of adenine and one of ribose (Adenosine) to which three phosphoric groups are linked, by means one phosphoester bound (orange) and two phosphoanhydride bounds (green).

Along with ATP,  $NAD^+$  also acts as an energy reserve in its reduced form  $NADH + H^+$ . It acts as a universal electron carrier in the cell, carrying electrons from the catabolism site to the electron transport chain (ETC).

Along with  $NAD^+$ , flavin adenine dinucleotide (FAD) and flavin adenin mononucleotide (FMN) are also coenzymes involved in electron transport. The acquisition of the electron by  $NAD^+$  and  $NADP^+$  occurs in the form of hydride ion (a proton with two electrons) which one at a time will then be transferred to the final acceptor, which in aerobic organisms is  $O_2$ . The FAD can accept one or two electrons producing the semiquinone  $FADH$  or the totally reduced form  $FADH_2$ , respectively. The reductions of  $NAD^+$  and FAD are reversible so that the electrons can be passed on to other donors and reused for further reductions<sup>8</sup>.

## 1.2. Glycolysis

Glucose obtained from the degradation of dietary polysaccharides, through its carrier (belonging to the family of GLUT transporters) enters the cells where, in the cytosol of eukaryotic cells, the enzymes involved in its catabolism are found. The latter process is called *glycolysis*. The reactions that characterize glycolysis are 10, divided into two main phases:

*PHASE I*: in which there is the hydrolysis of two ATP molecules and the glucose is converted into two glyceraldehyde-3-phosphate molecules;

*PHASE II*: the energy is recovered with the production of four ATP molecules and each glyceraldehyde-3-phosphate is converted in pyruvate.

**Glucose** is phosphorylated to **glucose 6-phosphate (G6P)** by *hexokinase* or *glucokinase* in liver cells, consuming a first molecule of ATP. G6P, by the action of *phosphoglucose isomerase*, is converted into **fructose-6-phosphate (F6P)** which as a substrate for the *phosphofructokinase* which phosphorylates it, consuming a second molecule of ATP, to obtain **fructose-1,6-bisphosphate (FBP)**. FBP, by *aldolase*, is split into **glyceraldehyde-3-phosphate (GAP)** and **dihydroxyacetone phosphate (DHAP)** of which only GAP continues in the glycolytic path, therefore DHAP by the *triose phosphate isomerase* is converted into another molecule of GAP. The phase II of glycolysis provides that the two molecules of GAP are oxidized and phosphorylated by *glyceraldehyde-3-phosphate dehydrogenase* with the formation of the final product **1,3-bisphosphoglycerate (1,3-BPG)** and  $\text{NADH} + \text{H}^+$ . In presence of ADP, 1,3-BPG is converted into **3-phosphoglycerate (3PG)** releasing an ATP molecule, reaction catalyzed by *phosphoglycerate kinase*. *Phosphoglycerate mutase* catalyzes the conversion reaction of 3PG into **2-phosphoglycerate (2PG)** which is dehydrated to **phosphoenolpyruvate (PEP)** in a reaction catalyzed by *enolase*. The final reaction of glycolysis is catalyzed by *pyruvate kinase* with final production of **pyruvate** and release of another molecule of ATP<sup>9</sup> (*figure 3*).

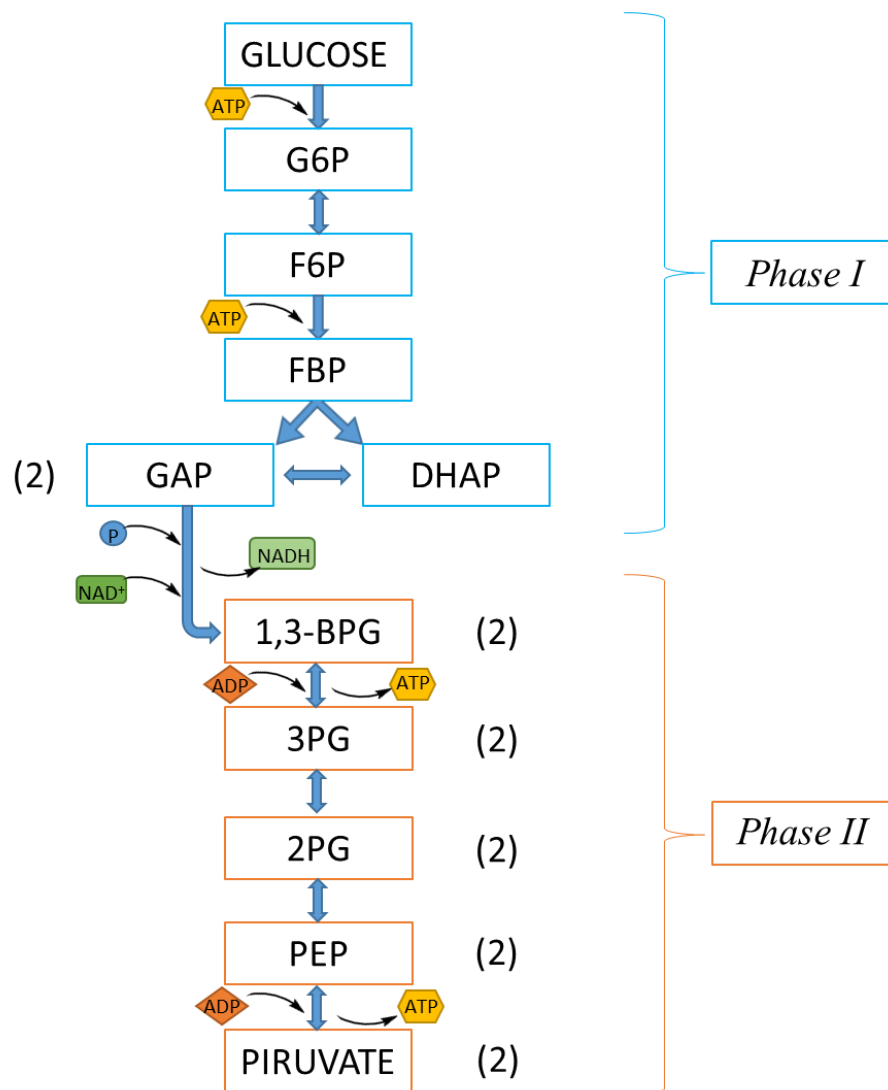
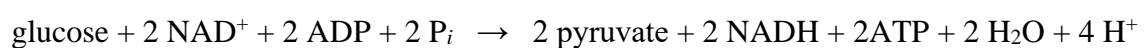


**Figure 3. Graphical representation of glycolysis divided into the energy investment phase (phase I) and energy payoff phase (phase II).**

The overall reaction describing glycolysis:



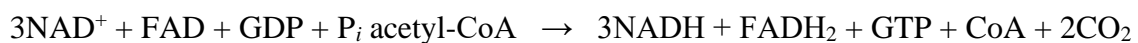
From one molecule of glucose, the consumption of 2 ATP in *phase I* is rewarded by the production of 4 ATP in *phase II*, with the final net production of 2 ATP. NADH represents the source of free energy recoverable by subsequent oxidation. Pyruvate, under aerobic conditions, is completely

oxidized to CO<sub>2</sub> and H<sub>2</sub>O in the tricarboxylic acid cycle (TCA) and the electron transport chain while under anaerobic conditions, pyruvate is converted into a reduced final product, the lactate, which forms NAD<sup>+</sup> to sustain the glycolysis. This occurs through *lactic fermentation* in the muscles, where pyruvate is reduced to lactate to regenerate NAD<sup>+</sup> or through *alcoholic fermentation*, in yeasts, where pyruvate is decarboxylated to CO<sub>2</sub> and acetaldehyde which, in turn reduced by NADH, restores d NAD<sup>+</sup> and ethanol<sup>8</sup>. The process of glycolysis according to cellular needs is finely regulated by activation or inhibition of three specific enzymes:

- hexokinase (and glucokinase)
- phosphofructokinase
- pyruvate kinase <sup>10</sup>.

When the pyruvate obtained from glycolysis is transformed into lactate by *lactate dehydrogenase*, the cell eliminates a product that is still reduced, while if it is further oxidized, a greater amount of energy is recovered. The oxidation of an organic compound requires a final electron acceptor which, in aerobic organisms, is O<sub>2</sub>. The oxidation of pyruvate continues in the TCA to CO<sub>2</sub> and the released electrons are stored as free energy in compounds such as NAD<sup>+</sup> and the prosthetic group of succinate dehydrogenase FAD which reduce to NADH and FADH<sub>2</sub> respectively.

The overall reaction of the TCA cycle is:



The electrons released by glucose oxidation process are initially transferred to the NAD<sup>+</sup> and FAD coenzymes which are reduced (for each glucose molecule 10NADH and 2FADH<sub>2</sub>) (*figure 4*). Next, the reduced coenzymes will transfer the electrons to the mitochondrial electron transport chain where will reach final O<sub>2</sub> acceptor.

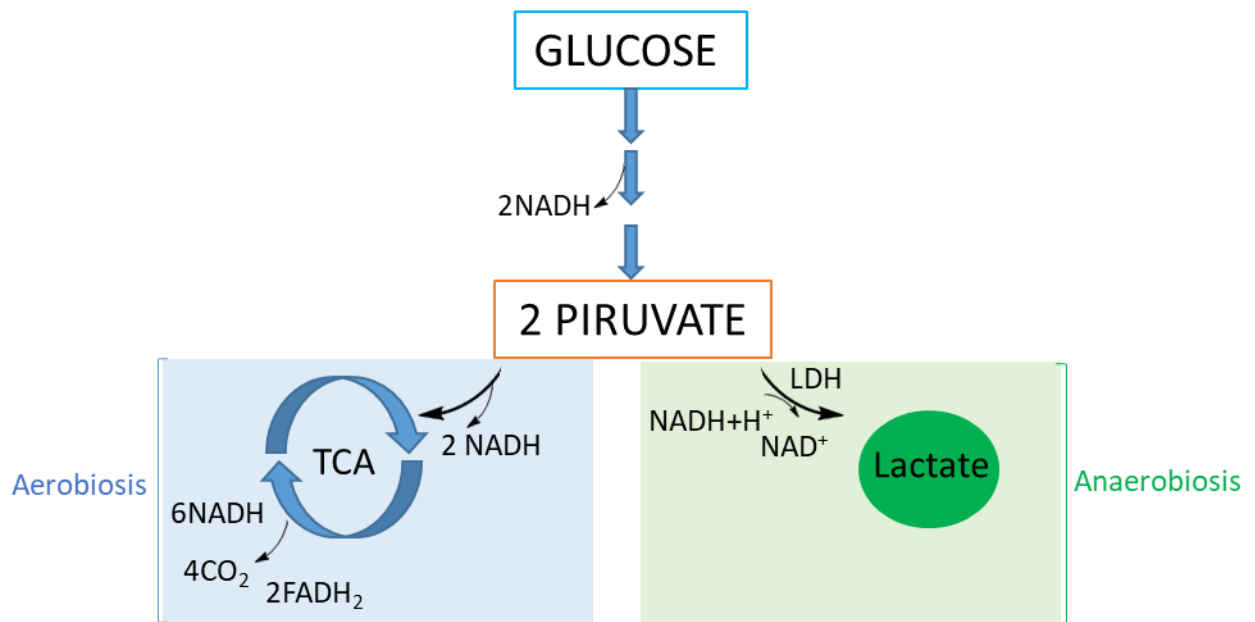


**Figure 4.** Graphical representation of the fate of pyruvate under aerobic and anaerobic conditions and yield of the reduced coenzymes obtained from the complete oxidation of one glucose molecule.

### 1.3. The mitochondrial respiration

The electrons obtained from the catabolic processes and acquired by the  $\text{NAD}^+$  coenzymes and by the prosthetic group of the succinate dehydrogenase FAD, are destined for the molecular  $\text{O}_2$  present in the mitochondria. The reduced coenzymes produced in the cytosol are transported in the mitochondria by *the malate-aspartate shuttle system*, as the inner mitochondrial membrane is impermeable to small molecules and ions. In this system, the NADH produced in the cytosol and present in the mitochondrial intermembrane space, transfers its two reducing equivalents to oxaloacetate forming malate. In the inner mitochondrial membrane, there is the malate- $\alpha$ -ketoglutarate transporter through which the malate enters in the mitochondrial matrix where it is reconverted into oxaloacetate by transferring the reducing equivalents to  $\text{NAD}^+$  with final formation of NADH destined for reoxidation by the ETC. The resulting oxaloacetate from this process is transaminated into aspartate which returns into the intermembrane space through the glutamate-malate transporter. The aspartate in the cytosol is converted back to oxaloacetate and

the cycle can begin again<sup>8</sup>. An alternative system for transferring reducing equivalents from the cytosol to the mitochondrion is the *glycerol-3-phosphate shuttle system*. The dihydroxyacetone phosphate in the cytosol accepts two reducing equivalents from NADH forming glycerol-3-phosphate. The *glycerol-3-phosphate dehydrogenase* bound on the outer face of the inner mitochondrial membrane, transfers the two reducing equivalents from glycerol-3-phosphate in the intermembrane space to ubiquinone, restoring the dihydroxyacetone phosphate<sup>11</sup>.

The electrons are transferred to the ETC consisting of a series of electron carriers in the intermembrane respiratory complexes. Complex I (CI) and Complex II (CII) transfer electrons from NADH and succinate respectively to ubiquinone. Complex III (CIII) transfers electrons from the reduced ubiquinone to the cytochrome *c* and Complex IV (CIV) oxidizes cytochrome *c* by transferring electrons to O<sub>2</sub> completing the process. As already mentioned in part, other transporters such as *ubiquinone*, *cytochromes* and *iron-sulfur proteins* operate in the respiratory chain. The ubiquinone, coenzyme Q (Q) is a fat-soluble benzoquinone with a long isoprenoid side chain and being small and hydrophobic it can diffuse through the inner mitochondrial membrane. When it accepts a single electron it becomes a semiquinone radical ( $\bullet\text{QH}^-$ ) while, when it accepts two electrons, it is completely reduced to ubiquinol (QH<sub>2</sub>)<sup>12</sup>.

In mitochondria, there are three distinct classes of cytochromes: *a*, *b* and *c*, which in their structure they have a heme prosthetic group, containing iron. Cytochrome *a*, *b* and some *c* are integral proteins of the inner mitochondrial membrane with the exception of the mitochondrial cytochrome *c*, a soluble protein that binds the outer surface of the inner mitochondrial membrane by electrostatic interactions<sup>13</sup>. In iron-sulfur (Fe-S) proteins, iron is associated with inorganic sulfur atoms or with sulfur atoms of Cys residues of proteins. These iron-sulfur (Fe-S) clusters can have a single iron atom coordinated with 4 Cys sulfur atoms or be more complex and have 2 to 4 iron atoms. Rieske's iron-sulfur proteins differ in that the iron atom is coordinated with 2 His and not with Cys<sup>14</sup>.

*CI*, or NADH dehydrogenase, has an L-shape with a peripheral arm immersed in the matrix and an inner membrane arm. It contains a flavoprotein (FMN) and 6 Fe-S clusters involved in the transfer of a hydride ion from NADH to Q in the peripheral arm. The NADH electrons pass through the FMN and Fe-S clusters to reach the Q on the arm that extends into the membrane forming QH<sub>2</sub>. Its catalysis also involves the transfer of 4H<sup>+</sup> from the matrix to the intermembrane space, in the membrane arm, guided by the energy that derives from the transfer of electrons. Some compounds such as rotenone or barbiturates inhibit this process by preventing the flow of electrons from the Fe-S centres to the Q<sup>15</sup>.

*CII*, or succinate dehydrogenase, is the only TCA enzyme bound to the inner mitochondrial membrane. Consists of 4 protein subunits (SDH) which SDHC and SDHD are integral membrane proteins and contain a *heme b* and the binding site for Q. SDHA and SDHB are in the mitochondrial matrix and contain three Fe-S clusters, one FAD and the site of succinate binding. The two electrons generated by the conversion of succinate to fumarate in SDHA pass on to the FAD and the three Fe-S clusters in SDHB reaching the Q. The *heme b* helps to stabilize the electrons adjacent to Q to promote the formation of QH<sub>2</sub><sup>16,17</sup>.

*CIII*, called ubiquinol cytochrome *c* oxidoreductase, receives the electrons of QH<sub>2</sub> coming from *CI* and *CII*, and transfers them to cytochrome *c*. Furthermore, its catalysis involves the vector transfer of 4H<sup>+</sup> from the matrix to the intermembrane space taking up 2H<sup>+</sup> from the matrix. *CIII* is a dimer with three catalytic subunits per monomers conserved from bacteria to eukaryotes: cytochrome *b*, with its two heme *b* groups (*b<sub>H</sub>* and *b<sub>L</sub>*), cytochrome *c1*, with heme *c1* and Rieske's Fe-S protein, protruding from the side of the intermembrane space and contacting cytochrome *c*. Antimycin A is an electron transfer inhibitor that binds the Q site of heme *b<sub>H</sub>* near the mitochondrial matrix (Q<sub>N</sub>). Myxothiazole acts as an inhibitor by binding instead to the Q binding site of heme *b<sub>L</sub>* near the intermembrane space (Q<sub>P</sub>). The interface between the two monomers forms two "caverns" placed in the middle of the membrane where Q can diffuse from the side of

the matrix to the side of the intermembrane space<sup>18</sup>. The Q during its transfer of electrons and protons through the CIII performs the so-called *Q cycle*. The QH<sub>2</sub> produced by CI reaches the Q<sub>P</sub> site and releases an electron which is acquired by Rieske's Fe-S protein. From here, through the cytochrome *c1*, the electron is acquired by the cytochrome *c*, which is reduced. The other electron of QH<sub>2</sub> then, through the heme *b<sub>H</sub>* and *b<sub>L</sub>*, reaches the Q at the Q<sub>N</sub> site where a •QH<sup>-</sup> semiquinone radical is generated. At the same time, the 2H<sup>+</sup> of QH<sub>2</sub> are transferred from the matrix to the intermembrane space. When a second QH<sub>2</sub> reaches CIII in the same way it transfers an electron to cytochrome *c* while the other reaches the Q<sub>N</sub> site where the semiquinone will be present which, accepting the second electron, will become QH<sub>2</sub> taking 2H<sup>+</sup> from the mitochondrial matrix. In synthesis for two oxidized QH<sub>2</sub> two reduced cytochrome *c* and one QH<sub>2</sub> are formed with simultaneous transfer of 4H<sup>+</sup> into the intermembrane space<sup>19-21</sup>.

*CIV* or cytochrome oxidase transfers electrons from reduced cytochrome *c* to O<sub>2</sub> forming H<sub>2</sub>O. It is formed by 13 subunits of which three membrane-embedded subunits are the catalytic core. The subunit I contains two heme groups, *a* and *a<sub>3</sub>*, next to a Cu<sub>B</sub> ion which, together with heme *a<sub>3</sub>*, constitute a Fe-Cu center. Subunit II contains 2Cu complexed with the SH- of the Cys forming the Cu<sub>A</sub> binucleated center. The binding site of cyt *c* is in a domain of this subunit in the projection of the intermembrane space. Subunit III, on the other hand, is indispensable for the rapid transfer of H<sup>+</sup> through subunit II. The electron transfer proceeds from cyt *c* to the Cu<sub>A</sub> center, the heme *a* group, the *a<sub>3</sub>*-Cu<sub>B</sub> center and the O<sub>2</sub>. For every four electrons following this path, *CIV* transfers 4H<sup>+</sup> from the matrix to the intermembrane space and 4H<sup>+</sup> of matrix are used to convert O<sub>2</sub> into 2H<sub>2</sub>O<sup>22,23</sup> (*figure 5*).

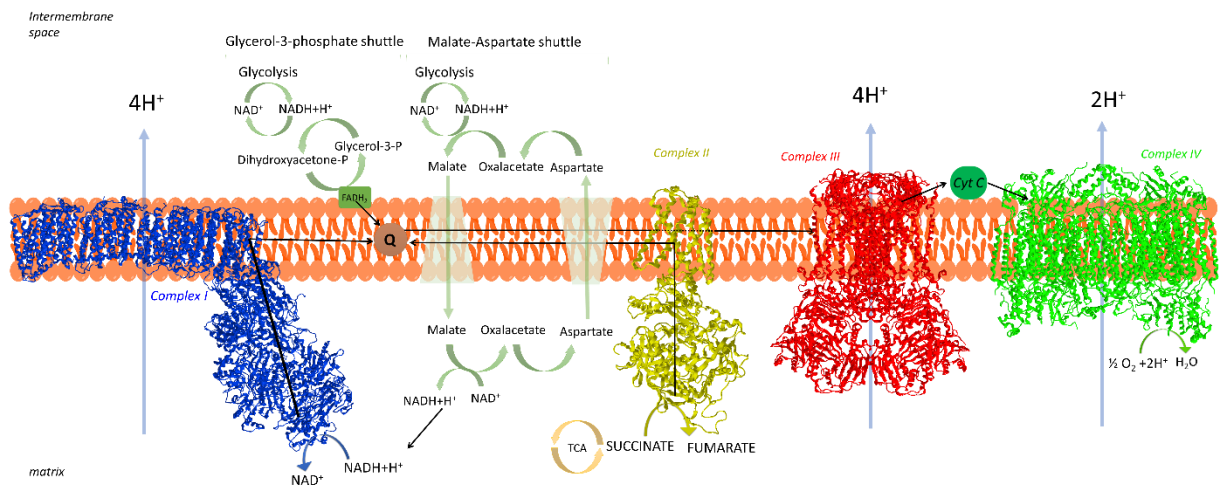


**Figure 5. Electron Transport Chain.** Representation of the transport of electrons (black arrow) originating from cell catabolism, through the complexes of the electron transport chain. The represented  $H^+$  ions (for each pair of electrons) are pumped from the matrix to the intermembrane space.

Respiratory complexes associate with each other to form supercomplexes. Many studies confirm the presence of higher-order assemblies of complexes which contain the three respiratory complexes, CI, CIII and CIV. The supercomplex known as respirasome is composed of  $CI_1CIII_2CIV_1$  and other supercomplexes are obtained from the assembly of  $CI_1CIII_2$  or  $CIII_2CIV_1$ <sup>24</sup>. Probably these aggregates are formed to improve the substrate channeling, reduce excessive ROS production, enhance catalysis in inter-complex electron transfer<sup>25</sup> to boost the respiratory efficiency or maintain the mitochondrial structure and function, but no consensus has been reached yet on their functional significance.

The electron transfer along the ETC is a strongly exergonic reaction and much of the released energy is used by CI, CIII and CIV to pump protons from the matrix to the intermembrane space generating an *electrochemical gradient*. In this gradient, the energy, also called *proton-motive force* ( $\Delta p$ ), consists of two components: the difference in concentration of the  $H^+$  ions across the membrane (*chemical potential energy*  $\Delta pH$ ) and the separation of the charges on the two sides of the membrane (*electrical energy potential energy*  $\Delta\Phi$ ). This proton flux is associated with the

synthesis of ATP in a process called oxidative phosphorylation (OXPHOS). In accordance with the *chemiosmotic model*, the  $\Delta p$  allows the synthesis of ATP when the proton flow is reversed and returns to the mitochondrial matrix through a proton channel associated with the ATP synthase. The transfer of electrons along the ETC accompanied by the simultaneous  $H^+$  pumping in the intermembrane space and the synthesis of ATP are matched processes, namely the inhibition of one also leads to the inhibition of the other. When, for example, the flow of protons towards the matrix is inhibited by the known inhibitor of the ATP synthase oligomycin, the protons do not have an alternative path, therefore the  $\Delta p$  accumulates across the membrane, thus blocking the electron flow along the ETC<sup>26</sup>. Some known decouplers, such as carbonyl cyanide-p-(trifluoromethoxy)phenylhydrazone (FCCP), diffuse across the membrane and release  $H^+$  in the matrix by dissipating the gradient.

## 2. The F<sub>1</sub>F<sub>0</sub>-ATPase and implication for new drugs

### 2.1. Structure and function of the F<sub>1</sub>F<sub>0</sub>-ATPase

Mitochondrial ATP synthase is an F-type ATPase, a membrane-bound enzyme complex which uses a proton gradient to drive ATP synthesis and, conversely, harnesses the energy obtained from ATP hydrolysis to restore the proton gradient across the membrane. The mitochondrial F<sub>1</sub>F<sub>0</sub>-ATPase is composed by a peripheral F<sub>1</sub> domain and an integral portion of F<sub>0</sub> membrane, so called because it gives the complex the sensitivity to the well-known oligomycin inhibitor. The two domains, F<sub>1</sub> and F<sub>0</sub>, are joined by a central and a lateral stalk. The hydrophilic F<sub>1</sub> domain consists of a spherical extrinsic hexamer formed by three catalytic  $\beta$  subunits alternating with three non-catalytic  $\alpha$  subunits. At the center of the hexamer there is the asymmetrical central stalk (composed of the subunits  $\gamma$ ,  $\delta$  and  $\epsilon$ ). The central stalk is joined to the F<sub>0</sub> on the subunits  $c$ , at the loop of each subunit, where the number of these subunits is species dependent (from 8 to 15) and are arranged to form a ring ( $c$ -ring). The higher the number of these subunits, the larger is the rotor, but the bioenergetic efficiency decrease as more H<sup>+</sup> are needed to synthesize an ATP molecule. The ATP produced is in fact obtained from the ratio between the number of protons translocated through the membrane and the 3 molecules of ATP that are produced during a complete (360°) rotation of the rotor. Mammals have a small  $c$ -ring, but a very efficient rotor since fewer translocated protons synthesize an ATP molecule. In these small rotors, the  $\Delta\Phi$  prevails over the  $\Delta p$ H in the composition of the  $\Delta p$ , because of an evolutionary adaptation. Conversely, large rotors, such as those present in the F-ATPase of chloroplasts and some bacteria, are less efficient from a bioenergetic point of view and associated with a  $\Delta p$ H prevalent over  $\Delta\Phi$  in the composition of  $\Delta p$ .

The  $a$  subunit embedded in the membrane with two hairpin helices named H5-H6, has the H<sup>+</sup> sites and adapts perfectly to the size of the  $c$ -ring to create the H<sup>+</sup> translocation pathway. The peripheral stalk acts as a stator to prevent rotation of the hexamer  $\alpha_3\beta_3$  of the central stalk. It is composed of

various subunits, namely the hydrophilic protein that confers sensitivity to oligomycin (*OSCP*), *F6*, *b*, *d*, bound to the  $F_1$  catalytic domain and incorporated into the inner mitochondrial membrane by the hydrophobic portion of the *A6L* subunits and the hydrophobic part of *b* subunit. The peripheral stalk is also associated with the supernumerary membrane subunits *e*, *f*, *g*, the 6.8-kDa proteolipid (6.8PL), and the diabetes-associated protein in insulin-sensitive tissue (*DAPIT*). These supernumerary subunits seem to play an essential role in the super-molecular organization of  $F_1F_0$ -ATPase, that is, in the formation of dimers or tetramers, typical of mammals<sup>27</sup> (*figure 6*).

The synthesis of ATP is based on the coupling of the rotary mechanisms of  $F_0$  and  $F_1$ <sup>28</sup>. The proton-motive force drives the  $H^+$  translocation through the  $F_0$  domain generating a rotation and allowing the conformational changes in  $F_1$  where the phosphorylation of  $ADP + P_i$  takes place producing ATP. In mitochondria,  $F_1F_0$ -ATPase can also function in reverse when the proton motive force fails. In this case, the hydrolysis of ATP provides the energy necessary for the pumping of  $H^+$  by  $F_0$  to the intermembrane space<sup>29</sup>. In both the forward and reverse reactions, the translocation of  $H^+$  across the inner mitochondrial membrane is due to the reversible protonation/deprotonation of the carboxyl sites, which also converts the flow of  $H^+$  into a rotation of  $F_0$ . The sensitivity of the enzyme to the antibiotic oligomycin, which acts by covering the  $H^+$  binding sites and blocking the rotation of the *c*-ring and enzyme catalysis in both directions<sup>30</sup>, is considered a parameter of the efficient coupling between the two domains. Each *c* subunit has a glutamate residue in the protonated form, but which can release  $H^+$  thanks to the hydrophilic environment created by the half-channels of the *a* subunit. The protons pass from the *c*-ring to the subunit *a*, which forms two discontinuous hydrophilic half-channels, the ends of which open one in the matrix and one in the intermembrane space. Specifically, the protons pass from *aHis*-168 and *aHis*-172 on the H5 helix and terminate at the *aGlu*-203 on the H6 helix of the *a* subunit, which acts as an intermediate donor of  $H^+$  to the *cGlu*-58 of the *c*-ring<sup>31,32</sup>. Through reversible protonations, such as carboxylations/decarboxylations of glutamate, the protons are transferred

one after the other from one side of the membrane to the other. The positive charge of an arginine of  $a$  subunit, Arg-159, acts as an electrostatic barrier between two half-channels, attracting the  $c$ Glu-58 carboxylate and promoting proton transfer between  $a$  and  $c$  subunits<sup>33</sup>. In the catalysis process, the three  $\beta$  catalytic sites adopt three conformations: open ( $\beta_E$ ), which is empty, closed ( $\beta_{TP}$ ), which contains Mg-ATP and semi-closed ( $\beta_{DP}$ ) which hosts Mg-ADP. Each of the three non-catalytic  $\alpha$  subunits binds Mg-ATP<sup>34</sup>. The synthesis of ATP is driven by the rotation of the  $c$ -ring and consequently of the  $\gamma$  subunit which, coming into contact with the  $\beta$  catalytic subunits, induces a conformational change favoring the reversible interconversion of the 3 conformations<sup>35</sup>, which change their affinity for ADP and ATP. During a complete revolution ( $360^\circ$ ) of the  $c$ -ring each catalytic site undergoes all three different conformations that lead to synthesis/hydrolysis of three ATP molecules. Furthermore, Mg-ATP bound to the non-catalytic sites allows the release of ADP from the  $\beta_{DP}$  site and the synthesis of ATP<sup>36</sup>.

During ATP hydrolysis, the transition between the  $\beta_E$ ,  $\beta_{TP}$  and  $\beta_{DP}$  conformations in  $F_1$  drives the rotation of the  $\gamma$  subunit and of the  $c$ -ring clockwise (viewed from the matrix), following the opposite direction for ATP synthesis (counterclockwise viewed from the matrix), and favoring the formation of the  $H^+$  gradient across the inner mitochondrial membrane by pushing  $H^+$  against the gradient<sup>37</sup>. Instead, when ATP is synthesized,  $H^+$  flow from the intermembrane space to the mitochondrial matrix according to their gradient. The direction of rotation and catalysis is imposed by the  $\Delta p$  (*figure 6*).

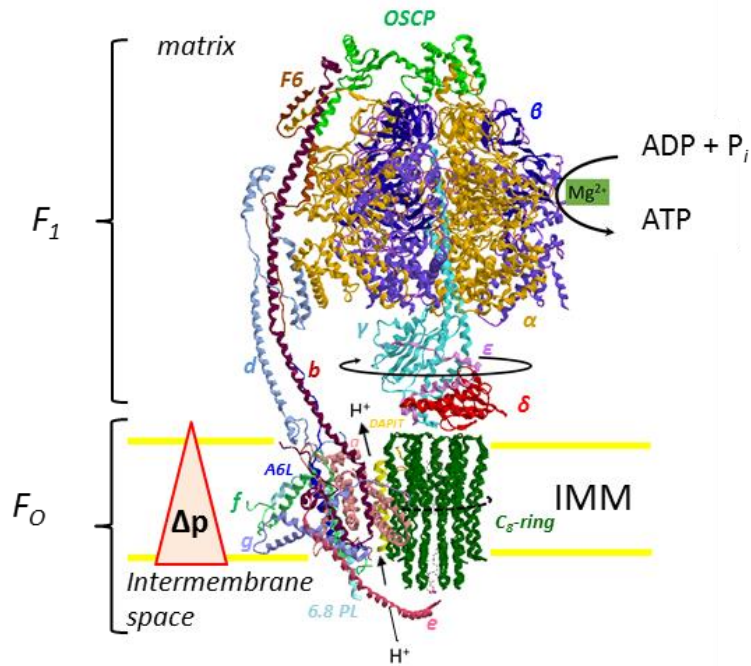


**Figure 6. Ribbon representation of the  $F_1F_0$ -ATPase monomers in mammalian mitochondria** obtained from modified PDB ID code: 6TT7. The letter colors are the same as those of the subunit to which they belong.

In eukaryotes, the function of  $F_1F_0$ -ATPase and the maintenance of its structure are related to the supermolecular organization, that is the association of monomers in dimers and tetramers<sup>38</sup> in which the supernumerary subunits intervene, absent in bacteria and chloroplasts that do not form dimers<sup>39</sup>. In mammals *a*, *e*, *f*, *DAPIT* and *6.8PL*, are needed to join the monomers, whereas *b*, *e* and *g* subunits fold the membrane.

The monomers joining two by two form the dimers which are positioned in long rows on the inner mitochondrial membrane using contact regions in different subunits in the different species<sup>28</sup>. The sites of the MICOS complex (mitochondrial contact site and cristae organization system) at the junction of the cristae form the curved edges of the cristae<sup>40</sup>. The dimers are linked together by the mitochondrial ATPase inhibition factor 1 (IF1), which by binding to the catalytic interface between the  $\alpha$  and  $\beta$  subunits and interacting with a region of the  $\gamma$  subunit, plays the main role of inhibitor

of the enzyme rotation and hydrolytic activity<sup>38</sup> also contributes to the formation of dimers and to the maintenance of the mitochondrial morphology<sup>41-43</sup>.

The dimers associate antiparallel to each other to form H-shaped tetramers, held together by interactions between subunits *e-e* and *g-g*<sup>44</sup>. Furthermore, the monomers are held together on the side in a row by the DAPIT which interacts with the subunit *a* from the side of the matrix and with the subunit *g* from the two sides, that is from the side of the matrix and the *intracristae* space. The dimers are linked together through the *6.8PL* of a monomer that interacts with the subunits *f* and *e* of another monomer and *vice versa*, on both sides. Two *a* subunits bind to the middle of the membrane, while on the matrix side the *f-f* subunits and towards the *intracristae* space and the *e-e* subunits form many contact<sup>27</sup>. The union of two  $F_0$  is reinforced by the GXXXG dimerization motif in the  $\alpha$  helices of the two subunits *e* and *g*<sup>45,46</sup>.

The single  $\alpha$  helices of subunit *e* and the H3 helix of subunit *g* interact with the respective GXXXG motifs and with the H2 of subunit *b* form a triple transmembrane helix assembly (TTMHB), U-folded thanks to the H2 and H3 helices of the *b* subunit, which creates a sort of BAR domain that folds the membrane forming the apex of the *cristae*<sup>47</sup>, while the *e* and *g* subunits stabilize the tetramer (*figure 7*).

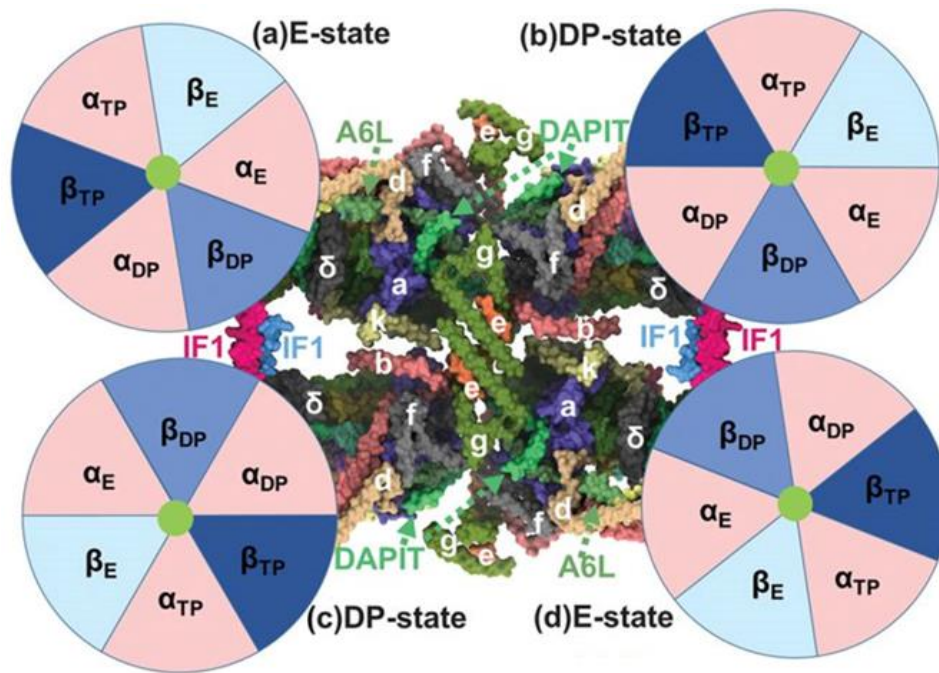


**Figure 7. Tetramer of  $F_1F_0$ -ATPase.** Schema of the swine ATP synthase tetramer bound to IF1<sup>42</sup>.

## 2.2. Correlation between the $F_1F_0$ -ATPase and the permeability transition pore

Recently,  $F_1F_0$ -ATPase has been a candidate as a major player in the formation of the mitochondrial permeability transition pore (mPTP), a pore in the inner mitochondrial membrane that makes the membrane permeable to water and other solutes<sup>48,49</sup>.

If the openings of the mPTP are short-lived, this process is reversible, but if the mPTP remains open for a long time it becomes irreversible and causes permeabilization of the membrane with a massive entry of water, swelling and bursting of the mitochondrion. These events are followed by the release of cytochrome *c* and other pro-apoptotic factors into the cytosol that drive programmed cell death<sup>50</sup>.

The formation of mPTP is a feature of mammalian and yeast mitochondria but has recently also been found in sea urchin oocytes<sup>51</sup>, in the nematode *Caenorhabditis elegans*<sup>52</sup>, in plathelminths<sup>53</sup> and insects<sup>54,55</sup> still being discussed in crustaceans<sup>56,57</sup>.

The formation of mPTP is stimulated by some factors such as the increase in the concentration of reactive oxygen species (ROS) and  $\text{Ca}^{2+}$ , by the binding of the mitochondrial protein cyclophilin D (CyPD) and instead inhibited by  $\text{H}^+$ ,  $\text{Mg}^{2+}$ , adenyly nucleotides and cyclosporine A (CsA) which displaces the CyPD and makes mPTP less sensitive to the increase of  $\text{Ca}^{2+}$ <sup>58</sup>. The involvement of  $\text{F}_1\text{F}_0$ -ATPase in the formation of mPTP makes it an enzyme complex responsible for cell life or death. Current hypotheses hold that  $\text{F}_1\text{F}_0$ -ATPase is involved in the formation of mPTP through the *c*-ring<sup>49,59</sup> or the monomer-monomer interface of the dimer<sup>48</sup>.

It is known that the increase in  $\text{Ca}^{2+}$  concentration in the mitochondrial matrix initiates a cascade of events that lead to cell death. In fact,  $\text{Ca}^{2+}$  can bind  $\text{F}_1\text{F}_0$ -ATPase in the sites of divalent cations in place of the natural cofactor  $\text{Mg}^{2+}$ , to support only the hydrolysis activity of the enzymatic complex<sup>60,61</sup>. This event, which occurs in the presence of high  $\text{Ca}^{2+}$  concentrations in the mitochondria, since the enzymatic affinity for  $\text{Ca}^{2+}$  is lower than  $\text{Mg}^{2+}$ <sup>62</sup> has been associated with the mPTP opening. Recent investigations that make use of cryo-electron microscopy in mammals have clarified that, when  $\text{F}_1\text{F}_0$ -ATPase is bound to  $\text{Ca}^{2+}$ , the enzyme presents unusual and different states from those shown in the presence of  $\text{Mg}^{2+}$ , in direct relation to mPTP opening. In Sazanov's laboratory, a model was developed, called “bent-pull”, that is “bend and pull”, in which the role of the *c*-ring and some supernumerary subunits of  $\text{F}_0$  in the formation of the mPTP is defined. In fact, when  $\text{Ca}^{2+}$  replaces  $\text{Mg}^{2+}$  in the catalytic site, being more voluminous, it causes conformational changes in the enzyme and especially in the  $\text{F}_1$  domain, which gradually propagate through the peripheral stalk<sup>63</sup> to the  $\text{F}_0$  subunits that form the mPTP. In support of this model, when the  $\text{Ca}^{2+}$ -activated  $\text{F}_1\text{F}_0$ -ATPase is inhibited, the formation of mPTP also appears delayed or even prevented.

The cavity of the *c*-ring contains phosphatidylserine on the side of the matrix, anchored by ionic bonds to the positive charge of Arg-38 of the *c* subunits. In correspondence with the space inside the *cristae*, there is instead a lysophosphatidyl-serine, which interacts with the Lys-71 of the *e* subunit. The two different phospholipids are separated within the *c*-ring by the hydrophobic amino

acid valine, *c*Val-168. Phosphatidylserine has a double acyl chain, so it doesn't have much space around the *c*-ring lipid plug and rotates with it. On the contrary, lysophosphatidyl-serine has only one acyl chain, which can play the role of a lubricated plug. It is likely that the binding of  $\text{Ca}^{2+}$  causes the inclination and distortion of the enzyme causing a cascade of conformational changes that cause the mPTP opening. The transmission of the conformational variation from  $F_1$  to  $F_0$  most likely exploits the long helix of the *b* subunit, which modifies the position of the *e* subunits, pushes the lysophosphatidylserine out of the central hole of the *c*-ring and opens the pore on the positive side of the internal mitochondrial membrane<sup>59</sup>, flattening the edges of the *cristae* and moving away from the dimer monomers of the enzyme<sup>64,65</sup>. According to Sazanov's hypothesis, the water molecules inside the *c*-ring destabilize the phosphatidylserine which pushes out the lipid plug and forms the pore inside the *c*-ring<sup>66</sup>. These conformational changes detach the  $F_1$  domain from  $F_0$  (figure 8).

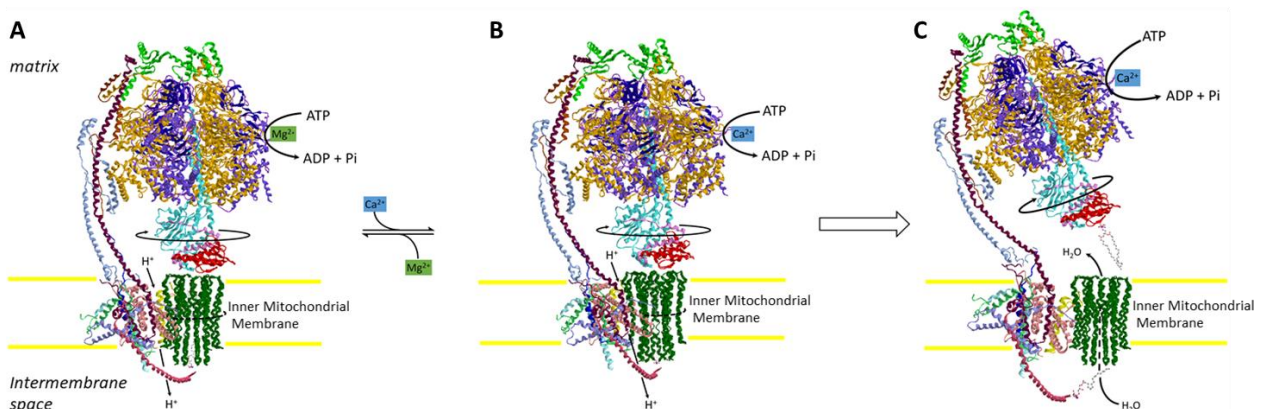


**Figure 8. mPTP opening model.** The hydrolysis of ATP sustained by  $\text{Mg}^{2+}$  (A) or  $\text{Ca}^{2+}$  (B) is coupled to the translocation of  $\text{H}^+$ . The different size of the two cofactors modifies the  $F_1F_0$ -ATPase conformation. The transition of the  $\text{Ca}^{2+}$ -dependent  $F_1F_0$ -ATPase from the assembled state (B) to the disassembled state (C) could induce the loss of the  $\text{H}^+$  translocation. Consequently, the mPTP opens when a retracted *e* subunit extracts the lyso-phosphatidylserine plug from the *c*-ring on the side of the inner mitochondrial membrane, while the  $F_1F_0$  destabilization extracts the phosphatidylserine from the matrix side<sup>61</sup>.

However, other evidence has been reported that appears to exclude *c*-ring and other F<sub>1</sub>F<sub>0</sub>-ATPase components from mPTP formation. One possible situation is the formation of pores of different sizes in the inner mitochondrial membrane. The membrane can be depolarized by an increase in conductance correlated to the increase in the concentration of Ca<sup>2+</sup>, thanks to ion channels and/or transporters<sup>67</sup>. Therefore, the F<sub>1</sub>F<sub>0</sub>-ATPase when activated by Ca<sup>2+</sup> would intervene in the formation of the largest pore, responsible for the greater depolarization of the membrane, while it is not excluded that other transporters or channels may lead to lower depolarizations. Taken together, these mechanisms would contribute to mPTP, highlighted as an increase in conductance<sup>68</sup>. However, it seems very likely that F<sub>1</sub>F<sub>0</sub>-ATPase is directly involved in the formation of the largest, or main pore, which ends up identifying itself with mPTP, inhibited by CsA, but not by bongkreikic acid (BKA), which instead inhibits the translocator of adenyl nucleotides (ANT)<sup>69</sup>. The latter, present in various isoforms and for some time involved in the formation of mPTP, could instead form a secondary pore, inhibited by both CsA and BKA<sup>70</sup>. mPTP is stimulated by Ca<sup>2+</sup> and regulated by selective inhibitors of the F<sub>1</sub> and F<sub>0</sub><sup>71,72</sup> domains to support the involvement of F<sub>1</sub>F<sub>0</sub>-ATPase in the formation of mPTP. It has also been shown that purified monomers and dimers<sup>73,74</sup> of F<sub>1</sub>F<sub>0</sub>-ATPase function as voltage-regulated ion channels and show properties like mPTP.

### 2.3. Pathologies related to the uncontrolled regulation of permeability transition pore

Under normal conditions, the regulated opening of the mPTP is a physiological event involved in the efflux of Ca<sup>2+</sup> from the mitochondrion to mitigate its overload in the matrix<sup>75</sup>, as well as taking part in the development of cardiomyocytes and the maturation of mitochondria<sup>76-78</sup>. However, a lack of or insufficient regulation of mPTP causes an uncontrolled increase in cell mortality or, on the contrary, a lower sensitivity or refractoriness to apoptotic signals and the onset of very serious

pathological conditions. As knowledge about mPTP and the mechanism of regulation of its opening increases, the list of diseases related to mPTP is constantly increasing. As far as it is known, diseases related to the malfunctioning of mPTP regulation are varied and affect various districts: neurological diseases (Parkinson's, Alzheimer's), cardiovascular diseases<sup>77</sup>, type 1-diabetes<sup>79</sup>, some types of cancer<sup>80</sup> inflammatory bone diseases<sup>81</sup> and diseases caused by exposure to contaminants<sup>82</sup>. In general, diseases associated with conditions of oxidative stress, which stimulates the mPTP opening, are also characterized by defects in the regulation of the mPTP<sup>58</sup>. The latter has also been called into question in determining the length of life of an organism<sup>83</sup>, as ageing itself involves insufficient regulation of mPTP, and in the repair of bone tissue<sup>84</sup>.

#### 2.4. F<sub>1</sub>F<sub>0</sub>-ATPase as a pharmacological target

On considering the dual role as a life supporter in ATP synthesis and cell death involved in the formation of mPTP, this enzyme complex has excellent prospects of being exploited as a pharmacological target<sup>85</sup>. The use of the enzyme as a drug target was considered above all for the purpose of selectively eliminating harmful cells<sup>86-88</sup>, due to the direct link between ATP deficiency and cell death, but also for diseases of mitochondrial origin. Several diseases of genetic origin, caused by point mutations that is a substitution of one or more amino acids in the *a* subunit, or in other subunits of the F<sub>1</sub>F<sub>0</sub>-ATPase, such as MLASA (mitochondrial myopathy-lactic acidosis-sideroblastic anemia) and hereditary Leigh syndrome, characterized by mitochondrial dysfunction, lead to very severe symptoms. It was therefore considered the possibility of reducing symptoms by inducing post-translational modifications on the mutated amino acid through chemical agents, in order to restore the full functionality of the F<sub>1</sub>F<sub>0</sub>-ATPase. The modulators of mPTP and Ca<sup>2+</sup>-activated F<sub>1</sub>F<sub>0</sub>-ATPase are carefully considered as possible therapeutic agents to restore the correct regulation of mPTP and treat diseases related to mPTP, given the connection between F-ATPase and mPTP. Most mitochondrial F-ATPase inhibitors are directed towards the F<sub>1</sub> catalytic

domain and block all or part of its catalytic activity<sup>89</sup> such as many phytochemicals with antibacterial properties that have polycyclic polyphenolic structures (safranal, baicalein, thymoquinone, piceatannol). Indeed, these can bind F<sub>1</sub> in a common region called of phytochemicals. Their inhibiting power on ATP synthesis varies greatly depending on the type and location of the functional groups. Some insect venom peptides (wasps, spiders, scorpions)<sup>90</sup> that bind to the F<sub>1</sub> domain of the enzyme in the  $\beta$ DELSEED motif have also shown antibacterial properties. These peptides exhibit a varying degree of hydrophobicity and hydrophilicity and interact with different amino acids in a common region of F<sub>1</sub>. The F<sub>0</sub> membrane domain is also considered as a possible target for lipophilic drugs<sup>91-93</sup>, such as some natural compounds with a structure similar to oligomycin, the antibiotic that inhibits both the synthesis and hydrolysis of ATP. Some cysteines present in F<sub>0</sub> appear to be essential for oligomycin inhibitory effect; oxidation of the thiol groups of these cysteines causes the enzyme to lose sensitivity not only to oligomycin, but also to other macrolide compounds with similar structures, such as venturicidin, bafilomycin and apoptolidin<sup>94</sup>. Depending on the different structures, these macrolides interact with F<sub>0</sub> in a common binding region but bind to different amino acids depending on their specific functional groups. On this basis, the hypothesis of desensitizing the mammalian enzyme through post-translational modifications of these cysteines, to leave the inhibitor only active on the pathogen's enzyme, was also considered. Among other differences, the prokaryote enzyme does not have these cysteines in the *c*-ring and bacterial proteins are not subject to post-translational modifications<sup>95</sup>. However, the problem of using non-toxic substances to induce these post-translational modifications remains, as so far only very toxic organotin compounds have been found to be able to oxidize these thiols and desensitize the enzyme to macrolides<sup>96</sup>.

In cardiovascular therapy the drugs used exert cardioprotective action due to chemical modifications induced on the F-ATPase. During a heart attack, post-translational modifications are induced in the  $\alpha$  subunit of F<sub>1</sub> and in the  $\gamma$  subunit, namely the establishment of disulfide bridges

between two cysteines or even *S*-glutathionylations and *S*-nitrosylations which inhibit the catalytic activity by altering the conformation of proteins<sup>86</sup>. The therapy, which consists of an electrical stimulation implemented to counteract heart failure, modifies some proteins involved in redox homeostasis and mitochondrial OXPHOS while the disulfide bridges are replaced by *S*-nitrosylations, compatible with the catalytic activity of the enzyme. Most likely this therapy stimulates the antioxidant defenses and creates a more reducing environment. If the oxidation of thiols of cysteines during a cardiac pathology may initially represent a strategy to counteract oxidative stress, the inhibition of ATPase activity would have the meaning of limiting the consumption of ATP, reducing the membrane potential and therefore the driving force for  $\text{Ca}^{2+}$  intake<sup>97</sup>. Many therapeutic compounds for the cardiovascular system could act by inducing post-translational modifications on the enzyme such as nitrite, the intake of which is recommended to prevent cardiovascular diseases. Nitrite was shown to induce post-translational modifications of tyrosines in  $F_1$  with the formation of dityrosines with a radical mechanism, producing an incompetitive inhibition of the hydrolytic activity of the  $F_1F_0$ -ATPase<sup>98</sup> and thus avoiding the dissipation of ATP<sup>99</sup>.

It is essential to find effective anti-tuberculous drugs due to the spread of numerous strains of antibiotic-resistant mycobacteria. Mycobacteria and related strains of the pathogen *Mycobacterium tuberculosis*, have a *c*-ring with a peculiar structure such that F-ATPase can only synthesize ATP. A new antituberculosis drug, bedaquiline, with a diarylquinoline structure binds the *c*-ring<sup>100</sup> and seven bedaquiline molecules are bound to seven of the nine *c* subunits; the other two potential *c* subunit binding sites were obstructed by the adjacent *a* subunit<sup>101</sup>. The bedaquiline also interacts with the  $\epsilon$  subunit of mycobacterium<sup>102</sup>, blocking the synthesis of ATP and consequently also the growth of mycobacterium. However, strains resistant to bedaquiline are increasing, so new compounds are being studied<sup>103</sup>, which interact with other *c*-subunit amino

acids than bedaquiline and appear to have good bactericidal activity and minimal toxic effects on mammals.

The antiproliferative effect induced by the inhibition of ATP synthesis may represent a strategy to counteract the uncontrolled growth of cells typical of cancer. The problem that remains, however, is to selectively eliminate the harmful cells, leaving the "normal" ones unchanged. Most of the phytochemicals that inhibit F<sub>1</sub>-ATPase by binding F<sub>1</sub>, have shown anticancer properties in *in vitro* tests<sup>104</sup>. Antitumor and antibacterial properties have been associated with the action of some peptides extracted from insects, yeasts, amphibians which bind F<sub>1</sub> by inhibiting the catalytic activity<sup>105</sup>. Recent assumptions about the involvement of F<sub>1</sub>F<sub>0</sub>-ATPase in the formation of the mPTP make it an excellent pharmacological target by those compounds capable of preventing the mitochondrial permeability transition<sup>48</sup>. On the contrary, the so-called "pore shutters", which prevent or slow down the opening of the pore, could be used to counteract a whole series of pathologies in which the mPTP is poorly or insufficiently or nil regulated, resulting in an increase in cell mortality.

Some benzodiazepines (1,4-benzodiazepines) bind to OSCP at the same site as cyclophilin D, the only mPTP protein modulator known so far. This benzodiazepine induces apoptosis by sensitizing the mPTP to Ca<sup>2+</sup><sup>106</sup>. On the contrary, cyclosporin A, known for some time as being able to inhibit the formation of mPTP, increases the Mg<sup>2+</sup>-dependent F<sub>1</sub>F<sub>0</sub>-ATPase activity by displacing cyclophilin D from its binding site<sup>107</sup>. Other known inhibitors of mPTP related to cardioprotective action in conditions of ischemia/reperfusion, in which the opening of mPTP causes the death of cardiomyocytes, are some drugs of a triazolic nature such as 1,3,4-triazaspiro(4,5)decane which interacts on the subunit *c* of F-ATPase inhibiting the formation of mPTP and thus reducing the mortality of cardiomyocytes due to apoptosis at reperfusion<sup>72</sup>.

The formation of mPTP is one of the molecular mechanisms also related to ageing, which leads to an increase in the incidence of degenerative diseases. The so-called "pore shutters" in this case could have multiple therapeutic roles and counteract the effects of ageing.

The anti-apoptotic protein Bcl-XL acts on the outer mitochondrial membrane<sup>108</sup> but can also affect the inner mitochondrial membrane. When Bcl-XL is co-localized with the  $\beta$  subunit of F<sub>1</sub>F<sub>0</sub>-ATP synthase<sup>109</sup>, acts as an anti-apoptotic regulator by blocking the opening of mPTP. The chemotherapeutic agent ABT-737, which mimics the BH3 domain, the only protein that binds to Bcl-XL, reverses the binding of Bcl-XL to the subunit and increases the escape conductance of the membrane<sup>110</sup>.

The connection between the mitochondrial F-ATPase and mPTP strongly stimulates the development of new drugs that act as modulators of F-ATPase activity and, at the same time of the mPTP. These compounds can be used for therapies to correct the biochemical defect at the mitochondrial level, assumed that they can distinguish the mutated/pathological enzyme complexes from normal ones and only act on the former.

### **3. Ions and small molecules as hypothetical therapeutic agents**

Small molecule drugs, which development involves very simple production, characterization, and regulation processes, are compounds capable of modulating biochemical processes to diagnose, treat or prevent diseases. They are very interesting due to their relatively low molecular weight and simple chemical structures, which give them more predictable pharmacokinetics and pharmacodynamics than those of biologics. Most of the drugs on the market such as aspirin and diphenhydramine are small molecules<sup>111</sup>, highly selective molecules able to bind their specific target with high affinity, with a very small dissociation constant of the drug-target complex, preferably of the nanomolar order, conditions obtained only if the target protein envelops the drug in a cavity. In the protein targets of many drugs on the market, such as many enzymes, for example, they present a specific domain in which the drug binds by acting mostly as enzyme inhibitors. Very often, however, they do not act on a single target, therefore they can cause possible side effects. The effectiveness of small molecules, as well as being able to be amplified in the laboratory by adding groups that enhance their effects, is found above all in the development of antimicrobial drugs which are directed against a target of the pathogen that often differs from that of the host, minimizing side effects<sup>112</sup>. Equally interesting is exploring the use of metal ions as therapeutic agents most of which are essential cofactors of enzymes, including cobalt (Co), copper (Cu), gallium (Ga), iron (Fe), manganese (Mn), silver (Ag), strontium (Sr), vanadium (V), and zinc (Zn). The use of metal ions has the advantage of not involving any risk of decomposition or instability, which is intrinsic to organic molecules. Furthermore, the unique properties of ions with therapeutic significance such as redox and hydrolytic activity, Lewis acidity, electrophilicity, valence, geometry, magnetic effect, spectroscopy and radiochemical properties, indicate the ability of these ions to interact with other ions that can alter functions and cellular metabolism by binding also to macromolecules such as enzymes and nucleic acids and/or by activating ion channels or secondary signals<sup>113</sup>.

Many recent studies have shown the main role played by metal ions in the modification of the folding and/or aggregation of proteins leading to serious pathologies. An example is Alzheimer's disease, in which  $\beta$ -amyloid peptides aggregate in the brain, leading to the formation of amyloid plaques. The accumulation of redox-active metal ions in these amyloid plaques is probably responsible for the oxidative stress that induces neuronal lesions in the brain that cause the irreversible loss of intellectual faculties. In this case, the therapeutic use of a metal-ligand has led to improvements in patients suffering from Alzheimer's disease and indicated that therapeutic approaches with metal chelating ions are possible in neurodegenerative diseases<sup>114,115</sup>.

In the search for therapeutic molecules that can act on mPTP by binding to the  $F_1F_0$ -ATPase, particular attention has been paid to small and mainly lipophilic compounds, able to cross the plasma membrane and the mitochondrial double membrane without difficulty, without the need to be conveyed. It is essential that these molecules, in view of their use as therapeutic agents, are not toxic at the cellular and organism level and can bind to the protein structures of the enzyme, especially when it is activated by  $Ca^{2+}$ . Indeed, a very important requirement is that these molecules acting as  $Ca^{2+}$ -activated  $F_1F_0$ -ATPase inhibitors without inducing a negative effect on the  $Mg^{2+}$ -activated enzyme. The selected molecules should not produce heavy side effects by decreasing cellular energy reserves.

### 3.1. Polyphenols

Phenolic compounds, whose simplest molecule is phenol, derive from shikimic acid and have one or more hydroxyl groups linked to an aromatic ring. Compounds containing multiple hydroxyl groups are named *polyphenols*. The delocalization of the negative charge of the phenoxide ion, the formation of stable radicals after the donation of an electron of the phenoxide ion and the formation of hydrogen bridges with other molecules characterize phenols. Thanks to their structure, they play

a scavenger role against free radicals by chelating metals and acting as reducing agents. The main source of polyphenols is fruits and drinks such as red wine. Flavonoids belong to the polyphenol family and have a beneficial effect on humans, on heart disease by inhibiting the oxidation of low-density proteins, reducing platelet aggregation and capillary permeability and fragility. Some act as natural antibiotics and have antibacterial, antiviral, anti-inflammatory and vasodilator activity<sup>116</sup>. Thanks to these characteristics, polyphenols modulate the mitochondrial function<sup>117</sup>. Some of them, such as resveratrol, quercetin and piceatannol, were shown to interact with F<sub>1</sub>-ATPase, causing enzyme inhibition by hydrogen bonding with a common site in F<sub>1</sub> domain where a bearing is present, which allows rotation of the  $\gamma$  subunit tip within the ring during catalysis. Their inhibitory role could be useful in cancer cells where inhibition of ATP synthesis could cause cell death by apoptosis<sup>118</sup>. Bergamot (*Citrus bergamia* Risso et Poiteau) is an endemic plant that grows in Calabria (southern Italy). It has a profile of flavonoids and glycosides, such as neoeriocitrin, neohesperidin, naringin, rutin and melitidin. Recent studies demonstrate the strong antioxidant and anti-inflammatory effects of bergamot, as well as interesting hypolipidemic and hypocholesterolemic properties that shed new light on its use as a nutraceutical<sup>119</sup>. Due to these characteristics, the beneficial effect of bergamot extract (BPF) was evaluated on isolated mitochondria and on the mPTP opening, with a view to the protective effect of bergamot against regulated cell death, driven by mPTP formation and opening and induced by ROS.

### 3.2. Gadolinium

Gadolinium, a lanthanide element, became commonplace in medical diagnostics. Like platinum in cancer therapeutics and technetium in cardiac scanning, the unique magnetic properties of the gadolinium (III) ion placed it right in the middle of a revolutionary development in medicine: magnetic resonance imaging (MRI)<sup>120</sup>. In fact, it is the main ingredient in most MRI contrast agents. Lanthanide salts inhibit ion channels in animals and plants and have been used

extensively as plasma membrane calcium channel antagonists<sup>121</sup>. The ionic radius of gadolinium is almost equal to that of  $\text{Ca}^{2+}$ , and  $\text{Gd}^{3+}$  can compete with  $\text{Ca}^{2+}$  interfering with multiple  $\text{Ca}^{2+}$ -dependent processes, including membrane fusion<sup>122</sup> becoming toxic in biological systems. To reduce the toxicity of  $\text{Gd}^{3+}$ , it must be administered to humans in chelated forms to avoid the presence of free gadolinium<sup>123–125</sup>, therefore, several types of gadolinium-based contrast agents have been developed to satisfy these conditions.

Regarding the possible toxic effects, it appears that  $\text{Gd}^{3+}$  induced an increase in reactive oxygen species and the onset of cell death that could be caused by mitochondrial dysfunction<sup>126</sup>, related to the mPTP opening, an important factor in the pathogenesis of regulated cell death<sup>127</sup>. It has been shown that at high concentrations  $\text{Gd}^{3+}$  could induce a series of phenomena that indicate the mPTP opening such as swelling, collapsed transmembrane potential and reduced membrane fluidity interacting with proteins but also with anionic lipids<sup>128</sup>. Due to its wide use in medicine, it is important to broaden the knowledge of the molecular mechanisms through which gadolinium exerts any cytotoxic effects, particularly on the mitochondria and on the components of mPTP, which are mainly responsible for cell death.

### 3.3. Phenylglyoxal

Phenylglyoxal may be useful for modifying accessible arginine residues in proteins but when proteins are treated with a large excess of the reagent over a long period, a reaction with lysine residues may also occur. Selective chemical modification of arginine residues in proteins is desirable especially in correspondence with the active sites of enzymes to explore functional mechanisms. Reagents for arginine residues are scarce but glyoxal can be used under mild conditions for this purpose phenylglyoxal (PGO) reacts with arginine residues in proteins under mild conditions quickly and selectively and can be reversibly removed at neutral or slightly

alkaline pHs<sup>129</sup>. PGO, which contains both an aldehyde and a ketone group, is chemically reactive, while its phenyl head allows for incorporation into hydrophobic environments. The guanidino group of arginine, which makes it the most basic amino acid in proteins and a poor nucleophile, can react with PGO to produce more products. PGO is widely exploited as a chemical tool, not only to explore the role of arginine residues in mitochondrial F<sub>1</sub>F<sub>0</sub>-ATPase function, but also to shed light on the mechanisms of mPTP formation. The effects of phenylglyoxal on mPTP are related to the different adducts established within the enzyme structure<sup>130</sup>. In fact, it seems that mPTP is inhibited on intact rat liver mitochondria treated with PGO, indicating that the covalent modification of arginine residues directly affects the probability of pore opening, suggesting that arginine residues play a crucial role in pore regulation<sup>131</sup>. In this regard, it is interesting to exploit the PGO to verify if the probable formation of stable adducts with the Arg residues of F<sub>1</sub>F<sub>0</sub>-ATPase influences the mPTP opening in swine mitochondria.

### 3.4. Dithiol reagents

The side chain of cysteine residues, the thiol groups (-SH) are susceptible to reaction with ROS species, giving rise to a series of post-translational oxidative modifications, which in some cases can functionally regulate the protein<sup>132</sup>.

The reversible oxidations of cysteine (Cys) are versatile regulators of the structure and function of F<sub>1</sub>F<sub>0</sub>-ATPase and it has been shown that the altered function of F<sub>1</sub>F<sub>0</sub>-ATPase in patients with heart failure is due to the oxidation of Cys. Increased oxidative stress in heart disease favors the oxidative modification of Cys on the  $\alpha$  subunits of F<sub>1</sub>F<sub>0</sub>-ATPase<sup>133</sup>. In particular, disulfide bonds are formed between cysteines of two  $\alpha$  subunits ( $\alpha$ Cys-251) or Cys of  $\alpha$  and  $\gamma$  subunits ( $\alpha$ Cys-251  $\gamma$ Cys-78)<sup>86</sup>, associated with loss of F<sub>1</sub>F<sub>0</sub>-ATPase function in patients with heart failure.

The formation of mPTP is particularly influenced by oxidative stress which can oxidize and/or reticulate the protein thiols, therefore, the redox state of the Cys residues can favour or prevent the opening of mPTP. The mechanisms by which thiol oxidation promotes mPTP formation could have biological implications in unravelling the mechanism of cell damage under oxidative stress<sup>134</sup>.

Phenylarsine oxide (PAO) and dibromobimane (DBrB) are the modifying agents of the -SH used for the study of the structure-function correlation of Mg<sup>2+</sup>- and Ca<sup>2+</sup> activated F<sub>1</sub>F<sub>0</sub>-ATPase and related to the opening of mPTP. These compounds have been selected because they cause intramolecular cross-linking between two -SH of neighbouring cysteines<sup>132</sup>. PAO selectively binds vicinal thiols (3.8 Å) forming a stable dithioarsin ring<sup>135</sup>, and also reacts directly with -SH groups of mPTP which are inaccessible to hydrophilic reagents in the absence of Ca<sup>2+</sup><sup>136</sup>. DBrB, unlike PAO, crosslinks distant cysteine residues (6.6 Å), in fact, the ability of the compound to bind the dithiols depends on its molecular structure which establishes sulfur bridges (-S-X-S-) of different length<sup>137</sup> between disulfides, which depend on the distance between the two thiols (the -S-S-distance).

### 3.5. Melatonin

Melatonin is a multifaceted molecule with direct antiradical, indirect antioxidant<sup>138</sup> and anti-inflammatory activity. Due to its presence in bacteria<sup>139,140</sup>, which evolved several billion years ago, it is hypothesized that it is the oldest existing antioxidant<sup>141</sup>. Therefore, it has had many opportunities during evolution to refine and diversify its functions against toxic oxygen derivatives<sup>142,143</sup>.

Recent studies show that melatonin is found in particularly high concentrations in the mitochondria, the main seat of the production of ROS<sup>144,145</sup>. Therefore, it may have a positional

advantage that improves its ability to eliminate toxic radicals and reduce associated oxidative stress<sup>146</sup>. The antioxidant action of melatonin can be exerted directly, by releasing one of its delocalized electrons to neutralize a free radical<sup>147,148</sup>, or indirectly by interacting with membrane receptors<sup>149,150</sup> present on the cell membrane or intracellular organelles<sup>151,152</sup>. In the latter case, the antioxidant effect is obtained even at much lower concentrations than those required when it functions as a direct scavenger of free radicals, probably because the signal transduction pathways associated with the receptors amplify the response<sup>142</sup>.

The effects of melatonin at the mitochondrial level are also exerted on the formation of the mPTP that is inhibited<sup>153</sup>. Conversely, melatonin improves the mitochondrial functions of various organs and tissues such as liver, kidneys and inguinal white adipose tissue, under conditions of diabetes in Zucker diabetic fatty (ZDF) animals<sup>154</sup>. Due to these characteristics, melatonin was selected to evaluate its effects at the mitochondrial level on F<sub>1</sub>F<sub>0</sub>-ATPase activity, mPTP formation and its antioxidant role on ROS production.

### 3.6. H<sub>2</sub>S

Hydrogen sulfide (H<sub>2</sub>S) is an endogenous gaseous transmitter, long considered a powerful respiratory and mitochondrial poison and now instead considered for its beneficial properties<sup>155</sup>. Numerous biological functions are regulated by H<sub>2</sub>S: its modulatory role is carried out in cytoprotection, inflammation, neuromodulation and on the cardiovascular system. Moreover, it mediates vascular remodelling and angiogenesis, sharing some of the signaling pathways with other gases endogenously produced<sup>156</sup>. Currently, H<sub>2</sub>S, together with NO and CO, is considered a gas modulator whose action is mainly expressed in cell signalling, through various proposed mechanisms. The most obvious mechanism concerns the action on the respiratory chain: low concentrations stimulate cellular respiration and the production of ATP, while high concentrations

block cytochrome oxidase. A second mechanism is based on the redox properties acting as a reducing agent and contributing to the formation of disulfides and post-translational modifications of proteins. A third mechanism concerns the modulation of hemoproteins binding to heme with an irreversible coordination bond and forming sulfohemoglobin unable to transport oxygen, or they reduce Fe by blocking it in the  $\text{Fe}^{2+}$  form. One of the best known and most immediate mechanisms of  $\text{H}_2\text{S}$  action is to induce post-translational modifications in the cysteines, acting on the -SH inducing the formation of hydro-persulfide (-SSH).

In mammals, the enzymes cystathionine- $\beta$  synthase (CBS), cystathionine  $\gamma$  lyase (CSE) and 3-mercaptopyruvate sulfotransferase (STD), expressed in vascular cells<sup>157</sup>, are involved in the synthesis of  $\text{H}_2\text{S}$  which, if present in excess, in vertebrates is mostly broken down in the mitochondria through a sulfoquinone oxidoreductase (SQR)<sup>158</sup>. Due to its gaseous state and its instability,  $\text{H}_2\text{S}$  donors are often used in the study of its effects, such as NaHS sulfide salt and  $\text{Na}_2\text{S}$  sodium sulfide. On considering its beneficial effects,  $\text{H}_2\text{S}$  donors have also been synthesized in the form of organic sulfur compounds and natural products extracted from plants for use in basic and pre-clinical studies<sup>159</sup>. In aqueous solutions,  $\text{H}_2\text{S}$  reversibly dissociates into hydrosulfide ( $\text{HS}^-$ ) and disulfide ( $\text{S}^{2-}$ ) anions, the proportion of which depends on pH and temperature. As the pH increases, as in sea water, the level of  $\text{H}_2\text{S}$  decreases, while the concentrations of  $\text{HS}^-$  and  $\text{S}^{2-}$  increase and can somehow contribute to the bioactivity of the sulfides, which have as main target the mitochondria, which in turn provide the main defense against environmental sulfide<sup>160</sup>. Among the three forms of sulfides that coexist in aqueous solutions in pH-dependent equilibria, *i.e.*  $\text{H}_2\text{S}$ ,  $\text{HS}^-$  and  $\text{S}^{2-}$  at physiological pHs,  $\text{H}_2\text{S}$  is the most likely candidate to directly affect mitochondrial proteins, as it can easily cross biomembranes due to its lipophilicity and lack of electrical charge. The  $\text{F}_1\text{F}_0$ -ATPase contains numerous cysteines susceptible to post-translational modifications induced by  $\text{H}_2\text{S}$ , which can function as redox sensors of the microenvironment, and can undergo persulfidation, favouring changes in cellular bioenergetics<sup>86,161</sup>. The post-translational

modifications induced by H<sub>2</sub>S on F<sub>1</sub>F<sub>0</sub>-ATPase seem to be linked to its beneficial effects in the cardiovascular field, in fact, post-translational modifications occur during heart failure such as the formation of disulfide bridges between two cysteines. Studies on the effects of sulfides have mainly focused on mammals, due to the emerging role of sulfide as a physiological gas modulator and its involvement in cardiovascular protection. However, sulfide toxicology has common characteristics in the aquatic biota, especially at the biochemical level, which affects the health, survival, productivity and distribution of aquatic species<sup>162</sup>.

### 3.7. Triazole derivatives

Azoles are a class of nitrogen-containing heterocycles with different biological activities such as antimalarial, antifungal, antibacterial, anti-HIV and anti-inflammatory properties. In particular, 1,2,3-triazole and its derivatives have aroused a continuous interest in pharmaceutical chemistry and some drugs currently in use are based on triazoles, in particular the 1,2,3-triazole fraction as the agent anti-HIV TSAO, the antibiotic Cefatrizine and the antibacterial agent Tazobactam<sup>163</sup>. Some properties of the triazole ring, such as moderate dipole character, hydrogen bonding capacity, stiffness and stability under *in vivo* conditions, are responsible for their enhanced biological activities<sup>164</sup>. Triazole derivatives are also considered a new class of effective anti-tuberculous candidates such as isoniazid, which acts by inhibiting the growth of bacteria by blocking lipid biosynthesis, one of the most interesting strategies for the development of effective anti-tuberculous agents<sup>165</sup>. The 1,2,3-substituted triazoles consist of three vicinal nitrogen atoms in the aromatic ring, characteristics that make them resistant to many reactions such as oxidation, acid reduction and reduction or basic hydrolysis<sup>166</sup>. They can form hydrogen bonds with different biological targets, interactions that can be expanded when different substituents are present on the skeleton of these molecules<sup>167</sup>. Thanks to these features, the effects of metabolically stable triazole compounds appear to induce inhibition of mPTP causing the recovery of muscle structure and

function in a severe model of Duchenne muscular dystrophy in *sapje zebrafish*. Inhibition of mPTP by triazole compounds induces *in vivo* restoration of otherwise defective myoblasts and myotubes, allowing normal development of *sapje* individuals despite the lack of dystrophin, supporting the use of triazole derivatives as therapeutic agents for muscular dystrophy of Duchenne in which the opening phenomenon of the mPTP seems to be involved<sup>168</sup>. In light of the effects exerted on mPTP regulation, new generation of small molecules such as the substituted 1,2,3-triazoles, obtained from a 1,3-dipolar Huisgen cycloaddition reaction catalyzed by copper or ruthenium salts, represent interesting compounds for the evaluation of the structure-activity relationship of the activity of F<sub>1</sub>F<sub>0</sub>-ATPase, the main responsible for the formation of mPTP.

### 3.8. Vitamins K

Vitamin K (VK) is a component in blood coagulation, being a cofactor for vitamin K-dependent carboxylase, which facilitates the post-translational modification of glutamic acid in  $\gamma$ -carboxy-glutamic acid residues in selected proteins<sup>169</sup>, a role that makes it a micronutrient. Although partially supplied by the intestinal microbiota, VK requires dietary absorption by a typical lipid mechanism<sup>170</sup>. It belongs to a family consisting of structurally similar and lipophilic naphthoquinones, therefore, they can easily cross cell membranes. In nature, we find two forms: phylloquinone (VK1), which carries a phytyl side chain, comes mainly from plants and constitutes over 90% of dietary VKs, and menaquinones (VK2), which exist in multiple structures, come mainly from bacterial synthesis in the intestine. The VK2 menaquinone-4 form can be synthesized from VK1, which is absorbed in the small intestine and represents the most abundant VK form in tissues<sup>171</sup>. In VK2 vitamers the side chain varies both in length and in saturation degree<sup>172</sup>. The basic structure VK2, which has a side chain with four double bonds, is like Q, involved as an electron carrier in mitochondrial respiration, but has a shorter hydrophobic side chain whose four prenyl units confer greater hydrophilicity. This structural similarity has raised hopes of exploiting

VK2 to treat some mitochondrial defects<sup>173</sup>. On the other hand, menadione, or VK3, lacks the hydrocarbon side chain and is considered a metabolite or a provitamin. VK plays relevant roles in energy metabolism<sup>172</sup>, in counteracting inflammation and colorectal cancer and other types of cancer<sup>174</sup>, in this case by inhibiting cell proliferation and inducing apoptosis<sup>175</sup>. Some of these emerging roles are mediated by their interaction with transcription factors or other enzymes. At the intestinal level, absorption occurs by the enterocytes, which the mitochondrial activity is essential for their function. Indeed, mitochondrial uncoupling increases intestinal permeability, generating local and systemic inflammation, which is associated with the development of inflammatory bowel diseases<sup>176</sup>. For this reason, the effects of VKs were tested on the bioenergetics of the IPEC-J2 cell line, as biological representative of enterocytes, the main responsible for intestinal absorption.

## 4. Animal models

Mammals are complex organisms in which organs perform highly regulated physiological functions. Research very often interrogates organisms at multiple levels: molecules, cells, organs in physiological or pathological conditions. *In vitro* approaches, such as cell cultures, are often used to better understand the molecular mechanisms. On the other hand, in many cases no *in vitro* model is available to fully recapitulate specific interactions, therefore, investigations on humans and animals are necessary. Hypotheses and models may emerge from *in vitro* studies, but they must be tested and validated in an entire organism, otherwise, they remain speculative. Animal models were used to tackle a variety of scientific issues, from basic science to the development and evaluation of new vaccines or therapies. The use of animals is not only based on the broad commonalities of the physiology of most mammals, but also on the fact that human diseases often affect other animal species. It is true for most infectious diseases but also very common conditions such as type I diabetes, hypertension, allergies, cancer, epilepsy, myopathies and so on. Not only are these diseases shared, but also often the mechanisms are so similar that 90% of veterinary drugs used to treat animals are identical or very similar to those used to treat humans. However, all the results obtained on animals are not necessarily confirmed by further human studies because, despite the great similarities, there are differences between a given animal and human species. For example, over 95% of the genes are homologous between mice and humans, but there are also differences in members of gene families, which result in physiological differences<sup>177</sup>.

### 4.1. Swine as a model animal in translational medicine

The swine, in addition to having similar dimensions and homology with humans, is an appropriate medical model in many research fields for the anatomical and physiological similarity of the organs, physiology and progression of the disease, the availability of genomic and transcriptomic

tools, proteomics and the presence of stable cell lines<sup>178</sup>. The domestic swine (*Sus scrofa domestica*) is a phylogenetically similar mammal to primates, scientific evidence supports this similarity that most systems and organs have between swines and humans including the digestive, urinary, cardiovascular and nervous system, together with the skin and dental structure. It is a farmed animal, easy and inexpensive to maintain, characterized by high fertility and fecundity, available in a variety of natural, selected and transgenic breeds and, like humans, omnivorous. The porcine genome involves 18 autosomal chromosomes and 2 sex chromosomes with dimensions like that of humans. Some studies<sup>179</sup> reveal that they are genetically more like humans than mice. Knowledge of swine genetics and physiology allows the study of complex diseases and the understanding of the genetic predisposition of important pathologies. The swine has been widely used as a model animal in numerous diseases: cardiovascular, infectious, neurological, obesity and diabetes<sup>180</sup>. In the field of biomedicine, the swine model is widely used in pharmacology and, specifically, in pharmacokinetics, pharmacodynamics, in toxicological studies and disease models, in surgery to study new surgical techniques, transplants and to test and validate medical devices, thanks to human like organs and structures, making it a very suitable model<sup>181</sup>.

#### 4.2. Mollusks as a model for the study of biochemical mechanisms

Usually, the drug discovery process in research begins with the identification of one or more targets, potentially implicated in a specific human disease, on which specific molecules that modify their function are tested. Identifying a single promising compound from thousands of candidates can be time-consuming, costly, and have no guarantee of success. The high costs of these studies and the numerous difficulties in obtaining permits for animal testing have prompted researchers to seek other strategies. In addition to *in vitro* models, there has been a need to identify alternative and reliable models that have fewer ethical restrictions. The evolutionary process has led to diversity between species, however, favoring the conservation of numerous physiological

processes between species, including humans<sup>182</sup>. Unlike mammals, invertebrates often have short generation times and can be more easily manipulated experimentally. Detailed genetic knowledge can be a powerful tool that allows a fine dissection of metabolic pathways, favoring the understanding of the basic mechanisms of physiology and pathology in the analyzed organism. To this end, some of the most advanced research on invertebrates<sup>183</sup> in the biomedical field provide a fast and efficient way to develop treatments for human diseases<sup>184</sup>. For example, the tumor suppressor gene p53 is one of the most studied genes in human cancer research<sup>185</sup>. The bivalve mollusk *Mya arenaria* is an excellent model of interest in the study of human cancer thanks to the discovery of human homologs for the p53 (Map53) and p73 (Map73) genes. Invertebrates represent a valid alternative model in the study and characterization of pathological processes in humans and in the discovery and development of new drug therapies, thanks to the great advances in comparative genomics that have made possible the use of inexpensive animal models, simple and easy to handle, but in some situations as effective as mammalian models. Compared to mammalian models, mollusks have a remarkable experimental efficiency due to the reduced time required for experiments and the low costs for their care. Furthermore, the conservation of fundamental genetic information in invertebrate models allows researchers to benefit from it to draw conclusions about humans<sup>186</sup>.

## *Materials and methods*

## **5. Evaluation of mitochondrial energy parameters and activity of the transition pore (section I)**

### 5.1. Preparation of the mitochondrial fractions

#### 5.1.1. Extraction of mitochondria from swine heart

The swine heart was taken after slaughtering the animal in a local abattoir and transported to the laboratory within 2 hours on ice at 0-4 °C. After removing the blood clots, approximately 30-40 g of heart tissue, particularly taken from the left ventricle, was immersed in medium A (0.25 M sucrose, 10 mM Tris (hydroxymethyl) aminomethane (Tris), pH 7.4) and cut in small pieces with scissors. Subsequently, the tissues were gently dried on absorbent paper, weighed, and homogenized in medium B (0.25 M sucrose, 10 mM Tris, 1 mM EDTA (free acid), 0.5 mg / mL BSA free of fatty acids, pH 7.4 with HCl) in a ratio of 10 mL of medium B for each g of tissue. After a preliminary homogenization using Ultraturrax T25, the tissue was carefully homogenized at 650 rpm with a Braun Melsungen Type 853202 homogenizer using a Teflon pestle. The mitochondrial fraction was then obtained by differential centrifugation (Sorvall RC2-B, rotor SS34). The homogenate was subjected to a first centrifugation at 1,000xg for 5 minutes, from which a supernatant and a pellet were obtained. The latter was re-homogenized in the previous conditions and re-centrifuged at 1,000xg for 5 min. The supernatants collected from these two centrifugations were filtered through four layers of cotton gauze and then centrifuged at 10,500xg for 10 minutes to obtain the raw mitochondrial pellet. The latter was re-suspended in medium A and further centrifuged at 10,500xg for 10 min to obtain the mitochondrial pellet, which in turn was re-suspended in a small volume of medium A using a Teflon Potter Elvehjem homogenizer, thus obtaining a suspension with protein concentration, approximately 30 mg/mL<sup>187</sup>. The entire extraction procedure was carried out maintaining a temperature of about 0-4 °C. Protein concentration was determined using the Bradford<sup>188</sup> method of Bio-Rad Protein Assay kit II using

bovine serum albumin (BSA) for the preparation of standards with known protein content. The mitochondrial preparations were then stored in liquid nitrogen until the time of analysis.

### 5.1.2. Extraction of mitochondria from mussel digestive gland

Samples of mussel *Mytilus galloprovincialis Lamarck* were obtained from coastal culture facilities in the northern Adriatic Sea and transported alive in laboratory-ventilated seawater tanks. Approximately 60 commercial sized adult mussels (average weight 20 g, shell length > 20 mm) were used for each extraction, subdivided into pools of 10-15 animals. After dissection, the digestive gland (hepatopancreas) was rapidly removed from each animal, immediately deprived of the crystalline stylus and immersed for washing in medium A (0.25 M sucrose, 5 mM Tris (hydroxymethyl) -aminomethane (Tris), 5 mM ethylenediamine tetra acetic acid (EDTA), pH 7.4) and subsequently dried with absorbent paper. The tissues were then weighed and homogenized in medium B (0.25 mM sucrose, 0.5 g/L fatty acid-free bovine serum albumin (BSA), Tris 24 mM, pH 7.4), in the proportion 11 mL of medium B for each g of tissue, using a homogenizer (Braun Melsungen Type 853202) at 450 rpm for 1 min. By differential centrifugation (Sorvall RC2-B, SS34 rotor) the homogenate was centrifuged at 1,100xg for 8 min. The obtained supernatant was filtered through four layers of gauze and further centrifuged at 16,800xg for 10 min to produce the raw mitochondrial pellet. The latter was re-suspended in medium B and further centrifuged at the same speed for 10 minutes to obtain the final mitochondrial pellet which was re-suspended in a small volume of medium B using a Potter Elvehjem homogenizer, until a protein concentration of 10-12 mg/mL was obtained. The entire extraction procedure was carried out maintaining a temperature of about 0-4 °C. Protein concentration was determined by the Bradford<sup>188</sup> Bio-Rad Protein Assay kit II colorimetric method with BSA as standard. The mitochondrial preparations were then stored in liquid nitrogen until the time of analysis.

## 5.2. F<sub>1</sub> domain purification

After thawing, the swine heart mitochondria suspensions were diluted with 50 ml of medium A until a concentration of 20 mg/mL of protein, sonicated on ice with MSE Soniprep 150 Sonicator at 210  $\mu$ m amplitude for 3 min for three times with 30 s intervals, centrifuged at 10,000xg for 10 minutes. The supernatant of this first centrifugation was further centrifuged at 100,000xg for 2 hours. All the centrifugation steps were carried out at 4 °C. The pellet was resuspended in medium A plus 4 mM Na<sub>2</sub>ATP, the pH was adjusted to 9.2 by addition of small aliquots of 20% (w/w) NH<sub>4</sub>OH solution, and stored overnight at 4 °C. Then, the suspension, in which the pH was brought back to 8.0 by adding small aliquots of 2N HCl aqueous solution, was sonicated at an amplitude of 210  $\mu$ m for 5 minutes. The sonicated suspension was centrifuged a 300,000xg for 1 h and the resulting pellet was resuspended in 9 mL of medium A plus 2 mM EDTA, pH 7.6. Then, after the addition of 4.5 mL of chloroform, the resulting mixture was vigorously vortexed for 15 s and centrifuged at 600xg for 10 min allowing the separation of the two phases. The upper part the aqueous phase was collected and further centrifuged at 100,000xg for 1 hour. The pale yellow the supernatant obtained was supplemented with adequate aliquots of freshly prepared ATP solution to obtain a final concentration of 4 mM ATP and with 2 N NaOH solution to adjust the pH to 8.0. After dropwise addition of saturated solution (NH<sub>4</sub>)<sub>2</sub>SO<sub>4</sub> plus 5 mM EDTA under continuous stirring to obtain 37% saturation and pH adjustment to 8.0 with 1 N KOH solution, the suspension was centrifuged at 10,000xg for 15 minutes. The pellet was discarded, and the collected supernatant was brought to 60% saturation with solid (NH<sub>4</sub>)<sub>2</sub>SO<sub>4</sub>; the mixture was then brought to pH 8.0 with 1N KOH solution and stored overnight at 4 °C. Finally, the pellet of the last centrifugation at 150,000xg for 90 min, resuspended by mixing gently with a Potter Elvehjem Teflon Homogenizer in a small volume of medium containing 100 mM Tris/H<sub>2</sub>SO<sub>4</sub>, 1 mM EDTA and 50% glycerol, pH 8.0, made up the partially purified F<sub>1</sub> fraction<sup>189</sup>. The protein concentration

was determined according to the Bio-Rad Protein Assay kit II colorimetric method using BSA as standard<sup>188</sup>.

### 5.3. Swine and mussel mitochondrial F-ATPase activity assays

Swine heart mitochondrial preparations thawed at room temperature were used for the analysis of F-ATPase activity. The hydrolysis capacity of ATP was evaluated in a reaction medium (1 mL) containing 0.15 mg of mitochondrial protein and ethanolamine-HCl buffer 75 mM pH 9.0, 6.0 mM Na<sub>2</sub>ATP and 2.0 mM MgCl<sub>2</sub> for the Mg<sup>2+</sup>-activated F<sub>1</sub>F<sub>0</sub>-ATPase assay and the same buffer at pH 8.8 plus 3.0 mM Na<sub>2</sub>ATP and 2.0 mM CaCl<sub>2</sub> for the Ca<sup>2+</sup>-activated F<sub>1</sub>F<sub>0</sub>-ATPase assay. Preliminary tests showed that under these slightly different assay conditions for Mg<sup>2+</sup>- and Ca<sup>2+</sup>-activated F<sub>1</sub>F<sub>0</sub>-ATPases, maximum enzymatic activities were detected. To evaluate the oligomycin insensitive enzyme activity, 1.0 μL of 3.0 mg/mL oligomycin solution solubilized in dimethyl sulfoxide (DMSO) in some tubes in each set of experiments was added directly to the reaction system before initiate the enzymatic reaction. After 5 min of pre-incubation at 37 °C, the reaction was carried out at the same temperature, with the initial addition of the Na<sub>2</sub>ATP substrate and stopped after 5 min by the addition of 1 mL of aqueous solution of ice-cold 15% trichloroacetic acid (w/w). To evaluate the F<sub>1</sub>F<sub>0</sub>-ATPase activities of mussel mitochondria, mitochondrial preparations of mussel digestive gland were used immediately after thawing. The ATP hydrolysis reaction was carried out in a reaction medium (1 mL) containing 0.15 mg of mitochondrial protein, 75 mM of ethanolamine/HCl buffer pH 8.9, 5.0 mM Na<sub>2</sub>ATP and 2.0 mM MgCl<sub>2</sub> to evaluate the Mg<sup>2+</sup>-activated F<sub>1</sub>F<sub>0</sub>-ATPase activity, while 2.0 mM CaCl<sub>2</sub> instead of MgCl<sub>2</sub> were used to evaluate Ca<sup>2+</sup>-activated F<sub>1</sub>F<sub>0</sub>-ATPase activity. To evaluate the oligomycin insensitive enzyme activity, 1.0 μL of 4.0 mg/mL oligomycin solution solubilized in dimethyl sulfoxide (DMSO) in some tubes in each set of experiments was added directly to the reaction system before initiate the enzymatic reaction. After 5 minutes of pre-incubation at 30 °C, the reaction was always carried out at 30 °C,

starting it from the addition of the  $\text{Na}_2\text{ATP}$  substrate and blocking it after 5 minutes with 1 mL of ice-cold aqueous solution of 15% trichloroacetic acid (w/w). Subsequently, the procedure for swine and mussel mitochondria is common. Once the reaction was stopped, the vials were centrifuged for 15 min at 3500 rpm (Eppendorf Centrifuge 5202). In the supernatant, the concentration of inorganic phosphate ( $\text{P}_i$ ) hydrolyzed by known amounts of mitochondrial protein, which is an indirect measure of F-ATPase activity, was evaluated spectrophotometrically<sup>62</sup>. Total ATPase activity was calculated by detecting  $\text{P}_i$  in control tubes run in parallel and containing 1  $\mu\text{L}$  of DMSO per mL of reaction system. The dose employed of oligomycin, a specific inhibitor of F-ATPase which selectively blocks the  $\text{F}_0$  subunit, ensured maximum inhibition of the enzymatic activity and has been currently used in F-ATPase assays. The  $\text{F}_1\text{F}_0$ -ATPase activity was measured by subtracting the hydrolyzed  $\text{P}_i$  from the total ATPase activity, the hydrolyzed  $\text{P}_i$  in the presence of oligomycin. In all experiments, the F-ATPase activity was expressed as  $\mu\text{mol P}_i \text{ mg protein}^{-1} \text{ min}^{-1}$ .

#### 5.4. $\text{F}_1$ -ATPase activity assays

Partially purified  $\text{F}_1$  domains were used for  $\text{F}_1$ -ATPase activity assays without and with compounds under study. The capability of ATP hydrolysis was assayed in a reaction medium (1 mL) containing 0.15 mg  $\text{F}_1$  purified protein and 75 mM ethanolamine-HCl buffer pH 9.0, 6.0 mM  $\text{Na}_2\text{ATP}$ , and 2.0 mM  $\text{MgCl}_2$  for the  $\text{Mg}^{2+}$ -activated  $\text{F}_1\text{F}_0$ -ATPase or 2.0 mM  $\text{CaCl}_2$  for  $\text{Ca}^{2+}$ -activated  $\text{F}_1\text{F}_0$ -ATPase assays. The methods and parameters of ATP hydrolysis and  $\text{P}_i$  detection were the same as those used for the mitochondrial F-ATPase activity assays. The sensitivity to 3  $\mu\text{g/mL}$  oligomycin was tested to verify the detachment of  $\text{F}_0$  domain.

## 5.5. Kinetic analysis

To calculate the IC<sub>50</sub> values, *i.e.* the inhibitor concentration that causes half of the maximal inhibition of enzyme activity, the enzyme activity data obtained in the absence of the specific inhibitor and in the presence of increasing concentrations of it were used to calculate enzyme inhibition which, after background correction, have been adapted to a 3-parameter equation (i), where the lower limit of the data (no enzyme inhibition) is 0. In equation (i) the enzymatic activity (y) is a function of the inhibitor concentration (x), "Interval" is the uninhibited enzyme activity (in the absence of inhibitor) and s is a slope factor. Since x is in the denominator, y decreases as x values increase.

$$y = \frac{\text{Range}}{1 + \left(\frac{x}{IC_{50}}\right)^s} \quad (i)$$

The graphical methods of the Dixon and Cornish-Bowden graphs, which complement each other<sup>190</sup>, were used to detect the inhibition mechanism of specific inhibitors on Ca<sup>2+</sup>- or Mg<sup>2+</sup>-activated F<sub>1</sub>F<sub>0</sub>-ATPase. The 1/v (reciprocal of enzymatic activity) in the Dixon diagram or the S/v ratio in the Cornish-Bowden diagram were plotted as a function of the concentration of each specific inhibitor. To build these graphs, several experimental sets were designed in which the activity of F-ATPase was evaluated in the presence of increasing concentrations of inhibitor at two concentrations of ATP, keeping the concentration of the metal cofactor constant or the other way around. The values of *K<sub>i</sub>* and *K'<sub>i</sub>*, which represent the dissociation constant of the *EI* and *ESI* complex respectively, were calculated as the *abscissa* (transformed into positive) of the intercept of the lines obtained in the Dixon and Cornish-Bowden graphs respectively. In all the graphs, the specific enzymatic activity was assumed as an expression of v.

Kinetic studies on the mutual exclusion of different inhibitors on the same F-ATPase activity are useful to understand the possible interaction on the F<sub>1</sub> or F<sub>0</sub> domain between inhibitors under examination and inhibitors known for their binding site on the enzyme. To construct graphs similar

to Dixon, in which the reciprocal data of enzymatic activity ( $1/v$ ) (y axis) with respect to the concentration of the inhibitor under examination (x axis) were plotted, the F-ATPase activity was assayed in presence of increasing concentrations of the latter at fixed values concentrations of known inhibitors and constant concentration of substrate ATP. According to the graphical method employed<sup>191</sup>, when the lines show different slopes and intersection points, the enzymatic inhibition reflects the combined effect of the two inhibitors. When F-ATPase is inhibited by two compounds that are not mutually exclusive, the enzyme can combine with both inhibitors to produce the  $ESI_1I_2$  quaternary complex. The value of  $-\alpha K'i$ , which represents the dissociation constant of the quaternary complex  $ESI_1I_2$ , was calculated from the abscissa (transformed into positive) of the intersection point of the two lines obtained in the presence and absence of the known inhibitors. The interaction constant  $\alpha$  was calculated from the ratio between  $\alpha K'i$  and  $K'i$ <sup>94</sup>.

## 5.6. Mitochondrial respiration assay

The thawed mitochondrial fractions were used to evaluate the effects of the tested compounds on mitochondrial respiration on the enzymatic activity of the respiratory chain complexes. To do this, oxygen consumption rates were polarographically assessed using Clark-type electrodes using a thermostatted Oxytherm system (Hansatech Instruments) equipped with a 1 mL polarographic chamber. The reaction mixture (120 mM KCl, 10 mM Tris-HCl buffer, pH 7.2), kept under control of the Peltier thermostat at 37 °C and under continuous stirring, contained 0.25 mg of mitochondrial protein<sup>192</sup>. To evaluate NADH-O<sub>2</sub> oxidase activity, mitochondrial oxidation was performed under substrate saturating conditions (75  $\mu$ M NADH) after 2 minutes of oxygen signal stabilization. Preliminary tests showed that, under these conditions, O<sub>2</sub> consumption was suppressed by 2.5  $\mu$ M of rotenone, a known inhibitor of CI<sup>193</sup>. Succinate-O<sub>2</sub> oxidase activity was determined by the oxidation of succinate in the presence of 2.5  $\mu$ M of rotenone. The reaction was started by adding 10 mM of succinate after 2 min of stabilization of the oxygen signal. Again,

preliminary tests showed that, under the conditions applied, the oxidation of succinate was suppressed by 1  $\mu\text{g}/\text{mL}$  of antimycin A, a selective inhibitor of CIII<sup>193</sup>. To evaluate the effects of the compounds under study, mitochondrial suspensions were added concurrently with the test molecules at the appropriate concentrations in the polarographic chamber before starting. The mitochondrial respiratory rate was automatically evaluated by the O<sub>2</sub>view software and expressed as nmoles O<sub>2</sub> mg of protein<sup>-1</sup> min<sup>-1</sup>. Polarographic assays were performed at least in triplicate on different mitochondrial preparations.

### 5.7. Evaluation of mPTP, membrane potential and ROS production

Determining the formation and opening of mPTP, which permeabilizes the mitochondrial membrane, requires the use of intact mitochondria. Freshly extracted mitochondrial preparations were immersed in a buffer solution (130 mM KCl, 1 mM KH<sub>2</sub>PO<sub>4</sub>, 20 mM HEPES, pH 7.2 with TRIS), and incubated at 37 °C (swine heart) or 30 °C (mussel digestive gland) with 1  $\mu\text{g}/\text{mL}$  of rotenone (CI inhibitor) and 5 mM succinate (CII respiratory substrate). These incubation temperatures were selected based on preliminary tests in which, under these experimental conditions, the most reproducible response was obtained. In all cases, the concentrations of the compounds to be tested were added to the mitochondrial suspensions before the evaluation of the mPTP.

mPTP opening was induced by the addition of low concentrations of Ca<sup>2+</sup> (10  $\mu\text{M}$ ) at 1-minute intervals, using an aqueous solution of CaCl<sub>2</sub>. The calcium retention capacity (CRC), the lowering of which indicates the opening of mPTP, was evaluated spectrofluorometrically in the presence of 0.8  $\mu\text{M}$  Fura-FF. This probe has different properties in the absence and in the presence of Ca<sup>2+</sup>, that is it has excitation/emission spectra of 365/514 nm in the absence of Ca<sup>2+</sup> (Fura-FF low Ca<sup>2+</sup>) and passes to 339/507 nm in the presence of high concentrations of Ca<sup>2+</sup> (Fura-FF high

Ca<sup>2+</sup>). The opening of the mPTP was then evaluated by the increase in the ratio between the fluorescence intensities (Fura-FF high Ca<sup>2+</sup>)/(Fura-FF low Ca<sup>2+</sup>), which indicates a decrease in CRC. The opening of the pore causes a loss of membrane potential ( $\Delta\phi$ ) evaluated using the JC-10 0.5  $\mu$ M probe. In polarized mitochondrial membranes, this probe generates an orange JC-10 aggregate (excitation/emission spectra of 540/590 nm), but when the  $\Delta\phi$  decreases, JC-10 monomers are generated causing a shift in the spectrum towards green (spectra of excitation/emission of 490/525 nm). Depolarization of the membrane (decrease in  $\Delta\phi$ ) is attributed to the formation of mPTP. This depolarization was detected by the increase in the fluorescence intensity ratio which corresponds to an increase in the aggregate JC-10/JC-10 monomer ratio. ROS production was evaluated on freshly isolated mitochondria, starting from CI (with 5mM of pyruvate/malate) and CII (with 5mM of succinate), induced by the addition of Antimycin A (1 $\mu$ M). The ROS production was carried out spectrofluorometrically in the presence of 5  $\mu$ M of the MitoSox probe (excitation/emission spectrum at 510/580 nm) pre-incubated with mitochondria for 5 minutes before reading. All the assessments carried out were processed by the RF LabSolutions software.

## 5.8. Evaluation of oxidative phosphorylation

To evaluate the OXPHOS, the freshly extracted and therefore intact mitochondria were added to the reaction mixture, maintained under constant temperature and continuous stirring, containing 0.25 mg/mL mitochondrial suspension, 40 mM KCl, 75 mM sucrose, 0.5 mM EDTA, 30 mM Tris-HCl, pH 7.4, 5 mM KH<sub>2</sub>PO<sub>4</sub> plus 3 mM MgCl<sub>2</sub>. The rate of oxygen consumption was evaluated in the presence of specific substrates, namely glutamate/malate (1:1), for CI and succinate for CII with 1  $\mu$ g/mL of rotenone, to inhibit CI, and 1  $\mu$ M of antimycin A to inhibit CIII. The oxidation of glutamate/malate was taken as a measure of the activity of NADH: ubiquinone oxidoreductase; oxidation of succinate mirrored the multicomponent succinoxidase pathway, which represents the

flow of electrons in the respiratory chain through CII. To assess mitochondrial integrity, since intact mitochondrial membranes are not permeable to NADH, 75  $\mu\text{M}$  of NADH was added to the reaction mixture during the polarographic assay in the presence of glutamate/malate as substrate. The coupling of respiratory activity to phosphorylation was evaluated by adding 150 nmol of ADP to state 2 of breathing mitochondria. The compounds under study were added in small aliquots to the reaction mixture. Respiratory activities were evaluated as nmoles  $\text{O}_2 \cdot \text{mg protein}^{-1} \cdot \text{min}^{-1}$ . In the routine experimental protocol, the reagents were injected with a syringe into the polarographic cell containing the mitochondrial protein suspensions in the presence and absence of the compounds to be tested in the following order: inhibitors of the previous phases of the respiratory chain, when required, substrate, ADP, inhibitor (rotenone for glutamate/malate-stimulated respiration and antimycin A for succinate-stimulated respiration). Respiratory activities of state 3 and 4, the respiratory control ratio (RCR), that is the ratio of activities of state 3 and 4, were determined as defined by Chance and Williams<sup>194,195</sup>. Polarographic assays were performed at least in triplicate on three mitochondrial preparations from different animals.

## 5.9. Mitochondrial substrate oxidation

To evaluate the oxidation capacity of the substrate into the boar spermatozoa, a reaction medium (2 mL) containing  $10^6$  cells in Androhep at 38 °C was used. The oxidation of NADH and  $\text{FADH}_2$ , which transfer electrons to CI and CII respectively, was detected by exploiting the autofluorescence of the reduced form of these coenzymes<sup>196</sup>. The autofluorescence intensity of NADH (excitation 360 nm, emission 455 nm) and  $\text{FADH}_2$  (excitation 450 nm, emission 520 nm) were monitored by the Shimadzu RF-6000 spectrophotometer. The oxidation of NADH and  $\text{FADH}_2$  was measured as a decrease in the intensity of autofluorescence after the addition of the following inhibitors: 2  $\mu\text{M}$  rotenone, 5 mM DDM (only in  $\text{FADH}_2$  autofluorescence) to inhibit complexes I and II respectively; 1  $\mu\text{g/mL}$  oligomycin, which blocks the ATP generation, to verify

the coupling between substrate oxidation and ATP synthesis and 0.5  $\mu\text{M}$  FCCP, which makes the mitochondrial membrane permeable to protons, to maximize the oxidation of NADH or  $\text{FADH}_2$  at the minimum concentration of these substrates the intensity, expressed as NADH or  $\text{FADH}_2$  arbitrary units/min/ $10^6$  cells, was evaluated by the LabSolutions RF software.

## 6. Cell metabolism analysis (section II)

The study of cellular metabolism was carried out by simultaneously measuring the rate of oxygen consumption (OCR), a cellular respiration index (pmol/min) and the rate of extracellular acidification (ECAR), a glycolysis index (mpH/min), using the Seahorse XFp analyzer (Agilent). The cells under study were cultured in XFp (Agilent) cell culture microplates for 24 hours. On the day of the experiment, the cells were transferred to Seahorse XF DMEM medium at pH 7.4 supplemented with 10 mM glucose, 1 mM sodium pyruvate and 2 mM L-glutamine, without (control) and with specific molecules under study. Plates were incubated at 37 °C in air for 45 minutes before measuring OCR and ECAR by the appropriate programs (ATP Rate Assay, Cell Mito Stress Test, Cell Energy Phenotype Test and Mito Fuel Flex Test). The injection ports of the XFp sensor cartridges, which were hydrated overnight with the XF calibrant at 37 °C, were loaded with a 10-fold concentration of inhibitors according to instructions provided by Seahorse XFp ATP Rate Assay, Cell Mito Stress Test, Cell Energy Phenotype Test and Mito Fuel Flex Test. All analyzes were performed at 37 °C. All data were analyzed by the WAVE software and the OCR and ECAR values were normalized to the total number of cells per well. All tests were performed three times in independent experiments.

### 6.1. Evaluation of ATP production

Cellular metabolic regulation allows cells to adapt to changes in ATP demand by responding with changes in ATP production to maintain total intracellular levels. A highly informative measure to describe cellular metabolism is the rate of ATP production, as it is the main dominant high-energy molecule in cells. Agilent Seahorse XFp Real-time ATP Rate assay measures the total rate of ATP production in living cells by distinguishing between ATP fractions produced by mitochondrial

OXPHOS (mitoATP Production Rate) and glycolysis related to the conversion of glucose to lactate (glycoATP Production Rate), the two main metabolic pathways responsible to produce ATP in mammalian cells. The relationship between the mitoATP production rate and the glycoATP production rate (ATP Rate Index) allows us to detect changes in the metabolic phenotype (a ratio  $> 1$  mainly indicates the OXPHOS pathway; a ratio  $< 1$  means mainly glycolytic pathway). The assay consists in the use of metabolic modulators such as 1.5  $\mu\text{M}$  oligomycin and a mixture of 0.5  $\mu\text{M}$  rotenone and antimycin A, which, when injected in series, allow the calculation of the production rates of mitochondrial and glycolytic ATP providing a real-time measurement of the rates of cellular ATP production and a quantitative phenotype of cellular energy balance<sup>197</sup>.

## 6.2. Measurement of the parameters of mitochondrial function

Mitochondrial parameters were evaluated using the Mito Stress Test which consists in the use of metabolic modulators such as 1.5  $\mu\text{M}$  oligomycin, the desired concentration of Carbonyl cyanide-4 (trifluoromethoxy) phenylhydrazone (FCCP) and a mixture of 0.5  $\mu\text{M}$  rotenone and antimycin A, which are injected in series. The detected parameters are basal respiration (basal OCR before adding oligomycin), minimal respiration (OCR in the presence of oligomycin), maximal respiration (OCR after adding FCCP), proton leak (difference between basal respiration and respiration in the presence of oligomycin) indicating the translocation of  $\text{H}^+$  into the intermembrane space independently of  $\text{F}_1\text{F}_0$ -ATP synthase. All parameters were subtracted from non-mitochondrial respiration, evaluated as OCR in the presence of rotenone and antimycin A. The difference between maximal and basal respiration provides reserve capacity, *i.e.* the cell's ability to respond to an increase in energy demand, considered a measure of the flexibility of the OXPHOS<sup>198</sup>.

### 6.3. Cell Energy Phenotype

The cellular energy phenotype test rapidly measures mitochondrial respiration and glycolysis under basal and stressful conditions, to reveal the three key parameters of cellular energy metabolism: basal phenotype, stressed phenotype, and metabolic potential. By injecting 1  $\mu\text{M}$  oligomycin and desired concentration of FCCP at the same time, the tool allows us to evaluate two main parameters of cellular energy metabolism, known as metabolic phenotypes (basal and stressed phenotype) and metabolic potential. The basal phenotype is characterized by the OCR and ECAR values in the cells in the initial condition in the presence of substrates. The stressed phenotype is shown by the OCR and ECAR values in the cells after the addition of stressful compounds (oligomycin and FCCP). The metabolic potential is the ability to increase energy production through respiration and glycolysis and is defined as the % increase in the stressed phenotype over the baseline phenotype of OCR and ECAR<sup>199</sup>.

### 6.4. Oxidation of substrates

The Fuel Flex Test is a method of measuring mitochondrial fuel consumption in living cells in which a decrease in oxygen consumption mirrors the decrease in fuel oxidation. Specifically, it determines the oxidation rate of glucose, fatty acids and glutamine by measuring the OCR. The parameters of cell dependency, capacity, and flexibility to oxidize the three mitochondrial fuels are evaluated by blocking the oxidation pathways of nutrients with specific inhibitors. By sequentially inhibiting the path of interest, followed by the two alternative pathways, it is shown how cells exploit the path of interest to satisfy their energy demand. The modulators used are: 3  $\mu\text{M}$  BPTES (bis-2-(5-phenylacetamido-1,3,4-thiadiazol-2-yl) ethyl sulfide), an allosteric inhibitor of glutamine oxidase, which blocks the oxidation pathway of glutamine, 4  $\mu\text{M}$  etomoxir, the long-chain fatty acid pathway inhibitor, which inhibits the gene encoding carnitine palmitoyl-

transferase 1A and 2  $\mu$ M UK5099, which inhibits glucose oxidation by blocking the mitochondrial vector of pyruvate. Fuel dependency represents the dependence of cells on a claimed oxidative pathway to maintain basic respiration. It is calculated by adding the specific inhibitor to block the pathway of interest followed by the inhibitors of two alternative pathways. Conversely, fuel capacity is shown by OCR driven by the specific oxidation of the substrate, achieved by blocking other fuel pathways. Fuel flexibility was achieved by subtracting fuel dependence from fuel capacity, for each path studied; this parameter describes the mitochondrial ability to switch from one oxidative pathway to another to allow the maintenance of OCR when a specific pathway is inhibited<sup>200</sup>.

## **7. Statistic analysis**

All data were reported as the mean  $\pm$  SD (standard deviation) of at least three determinations performed on separate mitochondrial preparations. The statistical analysis, using the SIGMASTAT software, was carried out by subjecting the average values obtained to the analysis of variance (ANOVA) followed by the Student's-Newman-Keuls test when the F values indicated significance ( $P \leq 0.05$ ).

## *Results*

## **8. Evaluation of the effect of ions and small molecules on F<sub>1</sub>F<sub>0</sub>-ATPase activity and correlation with mPTP opening (section I)**

On considering the most recent acquisitions, the mitochondrial F<sub>1</sub>F<sub>0</sub>-ATPase represents the main enzyme complex related to the phenomenon of the mPTP opening. As the formation of mPTP leads to cell death and its dysregulation is increasingly involved in serious human diseases, once the main macromolecular target responsible for the mPTP formation has been identified, several compounds have been considered and studied as its potential modulators. The changes in the kinetic mechanism produced by the binding of Ca<sup>2+</sup> instead of Mg<sup>2+</sup> to the catalytic sites are relevant for the putative role of F<sub>1</sub>F<sub>0</sub>-ATPase in the formation of mPTP<sup>27,60</sup>. In this regard, F<sub>1</sub>-ATPase inhibitors (Is-F<sub>1</sub>) have been used as tools to highlight some characteristics of the cation binding site in the presence of Ca<sup>2+</sup> or Mg<sup>2+</sup> and to study the impact of these cations on the catalytic mechanism of enzyme and mPTP formation<sup>61</sup>.

Similarly, trivalent Gd<sup>3+</sup>, which has biophysical characteristics such as bivalent Ca<sup>2+</sup>, and which therefore can replace Ca<sup>2+</sup> in its biological and biochemical mechanisms, has been evaluated as a modulator of Ca<sup>2+</sup>-activated F<sub>1</sub>F<sub>0</sub>-ATPase and of mPTP.

The amino acid residues play a crucial role in the regulation of enzymatic functions, in particular, the role of the arginine residues of F<sub>1</sub>F<sub>0</sub>-ATPase was evaluated using phenylglyoxal (PGO), known to cause post-translational modifications while, the thiol crosslinking reagents such as PAO and DBrB were used to evaluate how (ir)reversible post-translational modifications of di-thiols on F<sub>1</sub>F<sub>0</sub>-ATPase<sup>86</sup> affect mPTP formation and regulation.

It is known that oxygen free radicals are also inducers of the mPTP opening, therefore the use of antioxidant agents such as BPF and melatonin, allows to confirm the possible correlation between the Ca<sup>2+</sup>-activated F<sub>1</sub>F<sub>0</sub>-ATPase activity, the formation of mPTP and ROS production.

The involvement of the enzymatic complex under study in the onset of multiple pathologies such as cardiovascular diseases raised interest in the application of NaHS as an enzyme modulator, especially in view of the use of sulfur donors to combat these diseases<sup>201</sup>. The investigations, carried out in parallel on the mitochondrial preparations of the digestive gland of mussels, aim to verify how much the mitochondrial mechanisms of response to H<sub>2</sub>S are conserved in phylogenetically very distant organisms, and therefore universal, and how many adaptations they undergo during evolution.

Due to the promising role of F<sub>1</sub>F<sub>0</sub>-ATPase as a pharmacological target, its activity supported by Ca<sup>2+</sup> and compared with that supported by Mg<sup>2+</sup>, was studied in the presence of 1,5-disubstituted derivatives of 1,2,3-triazole, *i.e.* compound 3a and 3b, new generation molecules known for their high biological activity and for interacting with cellular proteins<sup>168</sup>, having antiviral and antitumor effects, in order to research new hypothetical therapeutic agents that can be used in pathologies in which the dysregulation of mPTP seems to be involved.

To sum up, the following ions and compounds were tested (*figure 9*):

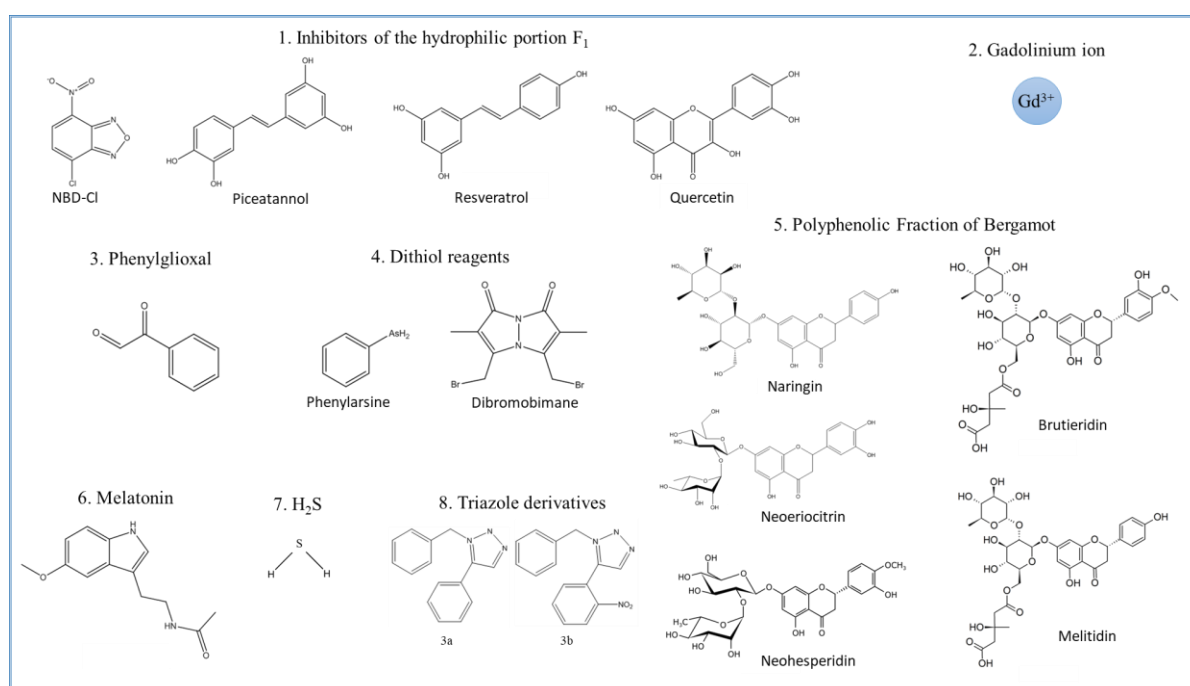


**Figure 9.** Structures of ions and small molecules used in assays on isolated mitochondria.

## ANNALS OF THE NEW YORK ACADEMY OF SCIENCES

Special Issue: *Annals Reports*

ORIGINAL ARTICLE

**Mitochondrial  $\text{Ca}^{2+}$ -activated  $\text{F}_1\text{F}_0$ -ATPase hydrolyzes ATP and promotes the permeability transition pore**Cristina Algieri, Fabiana Trombetti, Alessandra Pagliarani, Vittoria Ventrella, Chiara Bernardini, Micaela Fabbri, Monica Forni, and Salvatore Nesci 

Department of Veterinary Medical Sciences, University of Bologna, Bologna, Italy

Address for correspondence: Alessandra Pagliarani, Department of Veterinary Medical Sciences, University of Bologna, Ozzano Emilia Via Tolara di Sopra 50, Bologna 40064, Italy. alessandra.pagliarani@unibo.it

The properties of the mitochondrial  $\text{F}_1\text{F}_0$ -ATPase catalytic site, which can bind  $\text{Mg}^{2+}$ ,  $\text{Mn}^{2+}$ , or  $\text{Ca}^{2+}$  and hydrolyze ATP, were explored by inhibition kinetic analyses to cast light on the  $\text{Ca}^{2+}$ -activated  $\text{F}_1\text{F}_0$ -ATPase connection with the permeability transition pore (PTP) that initiates cascade events leading to cell death. While the natural cofactor  $\text{Mg}^{2+}$  activates the  $\text{F}_1\text{F}_0$ -ATPase in competition with  $\text{Mn}^{2+}$ ,  $\text{Ca}^{2+}$  is a noncompetitive inhibitor in the presence of  $\text{Mg}^{2+}$ . Selective  $\text{F}_1$  inhibitors (Is- $\text{F}_1$ ), namely NBD-Cl, piceatannol, resveratrol, and quercetin, exerted different mechanisms (mixed and uncompetitive inhibition) on either  $\text{Ca}^{2+}$ - or  $\text{Mg}^{2+}$ -activated  $\text{F}_1\text{F}_0$ -ATPase, consistent with the conclusion that the catalytic mechanism changes when  $\text{Mg}^{2+}$  is replaced by  $\text{Ca}^{2+}$ . In a partially purified  $\text{F}_1$  domain preparation,  $\text{Ca}^{2+}$ -activated  $\text{F}_1$ -ATPase maintained Is- $\text{F}_1$  sensitivity, and enzyme inhibition was accompanied by the maintenance of the mitochondrial calcium retention capacity and membrane potential. The data strengthen the structural relationship between  $\text{Ca}^{2+}$ -activated  $\text{F}_1\text{F}_0$ -ATPase and the PTP, and, in turn, on consequences, such as physiopathological cellular changes.

**Keywords:** mitochondrial permeability transition pore;  $\text{F}_1\text{F}_0$ -ATPase; inhibition kinetics; ATP hydrolysis; divalent cofactors; partially purified  $\text{F}_1$  fraction

**Introduction**

Mitochondria are core to many vital and lethal cell events. Recently, the mitochondrial  $\text{F}_1\text{F}_0$ -ATPase—the molecular engine embedded in the inner mitochondrial membrane (IMM)—has been involved as key enzyme in the start of cascade events, which lead to cell death. The molecular changes that trigger the IMM permeabilization, which initiates the death mechanisms, are still a matter of debate and constitute a common feature both in pathological and normal cells undergoing physiological modifications. The mitochondrial  $\text{F}_1\text{F}_0$ -ATPase role in cell life is well known: the enzyme exploits the proton-motive force ( $\Delta p$ ) across the IMM, generated by the respiratory complexes, to build ATP. The  $\text{H}^+$  flux through the IMM-embedded  $\text{F}_0$  domain, driven by  $\Delta p$  dissipation, rotates the enzyme rotor, which consists of the *c*-ring joined to the central stalk (formed by  $\epsilon$ ,  $\delta$ , and  $\gamma$  subunits in mitochondria).<sup>1</sup>

The  $\gamma$  subunit protrudes in the hydrophilic  $\text{F}_1$  globular hexamer ( $\alpha\beta$ )<sub>3</sub> and transmits the rotation; in turn, the torsion drives ATP synthesis by a binding change mechanism, which involves three catalytic sites<sup>2</sup> at the interface between  $\alpha$  and  $\beta$  subunits of  $\text{F}_1$ .<sup>3</sup> Under pathophysiological conditions, when  $\Delta p$  becomes lower than Gibbs free energy of ATP hydrolysis, the enzyme activity reverses, namely it rotates in the opposite direction, hydrolyzes ATP, and reenergizes the IMM by pumping  $\text{H}^+$  into the intermembrane space.<sup>4</sup> The latter function is emerging as tightly linked to the cascade of events associated with cell death.

Metal divalent cations can bind to the  $\text{F}_1\text{F}_0$ -ATPase catalytic ( $\beta$  subunit) and noncatalytic ( $\alpha$  subunit) sites in the different conformations.<sup>5</sup> The asymmetry of the ( $\alpha\beta$ )<sub>3</sub> globular domain implies that the different conformational states of these sites show different affinities for adenine nucleotides.<sup>6</sup> The binding-change model is based

on the peculiar structure of the F<sub>1</sub> domain, which hosts catalytic and noncatalytic sites. Three nonequivalent adenine nucleotide binding sites lie on the β subunit at the interface with the α subunit, namely the open (empty) conformation β<sub>E</sub> without nucleotides and the closed β<sub>DP</sub> and β<sub>TP</sub> states that bind Mg-ADP or Mg-ATP, respectively.<sup>2</sup> Conversely, the three equivalent adenine nucleotide-binding sites on the noncatalytic α subunit occur in closed conformations at the α-β interface, that is, α<sub>E</sub>, α<sub>DP</sub>, and α<sub>TP</sub>, and only bind Mg-ATP<sup>5</sup> to remove ADP from the β<sub>DP</sub> site and the related ADP-driven enzyme inhibition.<sup>7,8</sup> The natural cofactor Mg<sup>2+</sup> allows ATP synthesis/hydrolysis and forms six coordination bonds in the catalytic site. Mg<sup>2+</sup> can be replaced by other divalent cations, including Ca<sup>2+</sup>.<sup>9</sup> However, Ca<sup>2+</sup> insertion into the catalytic sites may lead to relevant conformational changes that affect catalytic cooperativity. Accordingly, Ca<sup>2+</sup>, which is larger than Mg<sup>2+</sup>, can coordinate up to eight ligands and shows a less rigid geometry with irregular bond distances and angles.<sup>10</sup> Ca<sup>2+</sup>-activated F<sub>1</sub>F<sub>0</sub>-ATPase is known to support ATP hydrolysis, but not ATP synthesis.

The F<sub>1</sub>F<sub>0</sub>-ATPase of *Escherichia coli* hydrolyzes ATP in the presence of Ca<sup>2+</sup> and forms a pH gradient with nearly the same effectiveness as Mg<sup>2+</sup>.<sup>11</sup> In most bacteria,<sup>12</sup> chloroplasts,<sup>13</sup> and beef heart submitochondrial particles,<sup>9</sup> Ca<sup>2+</sup>-activated F<sub>1</sub>F<sub>0</sub>-ATPase has been reported to be unable to translocate H<sup>+</sup>; however, in swine heart mitochondria, the inhibition of Ca<sup>2+</sup>-activated F<sub>1</sub>F<sub>0</sub>-ATPase by oligomycin and DCCD (both blockers of H<sup>+</sup> translocation within F<sub>0</sub>) is of the same extent as inhibition of Mg<sup>2+</sup>-activated F<sub>1</sub>F<sub>0</sub>-ATPase.<sup>14</sup> In inside-out submitochondrial particles, torque generation by the central stalk driven by Ca-ATP hydrolysis in F<sub>1</sub><sup>15</sup> is coupled to the membrane F<sub>0</sub> sector and is sensitive to the transmembrane electrochemical H<sup>+</sup> gradient.<sup>14</sup> Moreover, failed mitochondrial ATP synthesis when the enzyme is stimulated by Ca<sup>2+</sup> is associated with an increase in IMM permeability to ions and solutes, and to Δ*p* disruption. Membrane permeation is ascribed to the formation and opening in the IMM of a regulated channel known as permeability transition pore (PTP).<sup>16,17</sup> Cyclophilin D (CypD) is the only identified positive modulator of PTP opening. Accordingly, cyclosporin A (CsA) binding to CypD inhibits the PTP.<sup>18</sup>

The PTP is involved in some types of regulated cell death that feature in severe human pathologies, including cardiac/neurological ischemia, cancer, and neurodegenerative diseases.<sup>19,20</sup> Moreover, the PTP physiologically drives mitochondrial functions, cell differentiation, and development.<sup>21</sup> The nature and structural composition of the PTP are controversial, even if recent advances strongly support its origin from the F<sub>1</sub>F<sub>0</sub>-ATPase.<sup>22,23</sup> The Ca<sup>2+</sup> coordination chemistry in the β subunits is consistent with PTP formation from the F<sub>1</sub>F<sub>0</sub>-ATPase dimeric form;<sup>24</sup> Ca<sup>2+</sup> insertion would trigger conformational changes that would be transmitted from F<sub>1</sub> to the F<sub>0</sub> membrane subunits.<sup>25</sup> Accordingly, changes in IMM curvature would make the *cristae* disappear,<sup>26,27</sup> while the PTP would form between the two detached F<sub>0</sub> monomers.<sup>28</sup>

Different kinds of inhibitors of the F<sub>1</sub> domain, which bind covalently and noncovalently, can be helpful to enlighten the F<sub>1</sub>F<sub>0</sub>-ATPase catalytic mechanism. Changes in the kinetic mechanism produced by the binding of Ca<sup>2+</sup> instead of Mg<sup>2+</sup> in the catalytic sites may be relevant for the enzyme putative role in the PTP. Covalent inhibitors, such as 4-chloro-7-nitro-1,2,3-benzoxadiazole (NBD-Cl), modify the amino acid residues near the nucleotide-binding site in the catalytic β subunits, while noncovalent inhibitors inhibit enzyme catalysis through weak interactions and do not directly interact with the catalytic sites. Noncovalent inhibitors, namely piceatannol, resveratrol, and quercetin, were selected among polyphenolic phytochemicals that abundantly occur in the Mediterranean diet and are known as beneficial in the treatment and prevention of human pathologies, such as cancer and cardiovascular diseases.<sup>29</sup> These polyphenolic compounds are known to inhibit ATP hydrolysis by F<sub>1</sub> without binding to the catalytic sites by interacting with the enzyme in a common binding region on F<sub>1</sub>.<sup>30</sup> These F<sub>1</sub> inhibitors, collectively referred to here as Is-F<sub>1</sub>, are exploited as tools to point out some features of the cation binding site when Ca<sup>2+</sup> or Mg<sup>2+</sup> is inserted, and to investigate the impact of these cations on the enzyme catalytic mechanism and PTP formation.

By combining different biochemical strategies, we provide results obtained from experiments carried out in swine heart mitochondria and in partially purified F<sub>1</sub> fractions that may contribute to either solving or rejecting the hypothesis that

$\text{Ca}^{2+}$ -ATP hydrolysis, supported by the  $\text{F}_1\text{F}_0$ -ATPase, is required to open the PTP.

## Materials and methods

### Chemicals

NBD-Cl was obtained from Acros Organics. Resveratrol, piceatannol, cyclosporine A, JC-10, Fura-FF, and oligomycin were purchased from Vinci-Biochem (Vinci, Italy).  $\text{Na}_2\text{ATP}$ , quercetin, sodium succinate, rotenone, myxothiazol, and FCCP (carbonyl cyanide 4-(trifluoromethoxy)phenylhydrazine) were obtained from Sigma-Aldrich (Milan, Italy). Rabbit polyclonal anti-ATP5B antibody was from Aviva Systems Biology Corporation (San Diego, CA). All other chemicals were reagent grade. Quartz double-distilled water was used for all reagent solutions, except when differently stated.

### Preparation of the mitochondrial fractions

Swine hearts (*Sus scrofa domesticus*) were collected at a local abattoir and transported to the laboratory within 2 h in ice buckets at 0–4 °C. After the removal of fat and blood clots as much as possible, approximately 30–40 g of heart tissue was rinsed in ice-cold washing Tris-HCl buffer (medium A) consisting of 0.25 M sucrose, 10 mM Tris(hydroxymethyl)aminomethane (Tris), pH 7.4, and finely chopped into fine pieces with scissors. Each preparation was made from one heart. Once rinsed, tissues were gently dried on blotting paper and weighed. Then, tissues were homogenized in a buffer (medium B) consisting of 0.25 M sucrose, 10 mM Tris, 1 mM EDTA (free acid), 0.5 mg/mL BSA, and pH 7.4 with HCl at a ratio of 10 mL medium B per 1 g of fresh tissue. After a preliminary gentle break up by Ultra-Turrax® T25, the tissue was carefully homogenized by a motor-driven teflon pestle homogenizer (Braun Melsungen Type 853202) at 650 rpm with three up-and-down strokes. The mitochondrial fraction was then obtained by stepwise centrifugation (Sorvall RC2-B, rotor SS34). Briefly, the homogenate was centrifuged at  $1000 \times g$  for 5 min, thus yielding a supernatant and a pellet. The pellet was rehomogenized under the same conditions of the first homogenization and recentrifuged at  $1000 \times g$  for 5 minutes. The gathered supernatants from these two centrifugations, filtered through four cotton gauze layers, were centrifuged at  $10,500 \times g$  for 10 min to yield the raw mitochondrial pellet.

The raw pellet was resuspended in medium A and further centrifuged at  $10,500 \times g$  for 10 min to obtain the final mitochondrial pellet. The latter was resuspended by gentle stirring using a Teflon Potter Elvehjem homogenizer in a small volume of medium A, thus obtaining a protein concentration of 30 mg/mL.<sup>31</sup> All steps were carried out at 0–4 °C. The protein concentration was determined according to the colorimetric method of Bradford.<sup>32</sup> by Bio-Rad Protein Assay kit II with bovine serum albumin (BSA) as standard. The mitochondrial preparations were then stored in liquid nitrogen until the evaluation of F-ATPase activities.

### $\text{F}_1$ domain preparation

Immediately after thawing, swine heart mitochondrial suspensions were diluted with 50 mL of medium A up to obtain a concentration of 20 mg/mL protein, sonicated on ice with MSE Soniprep 150 Sonicator at 210  $\mu\text{m}$  amplitude for 3 min for three times with 30-s intervals, and centrifuged at  $10,000 \times g$  for 10 minutes. The supernatant from this first centrifugation was further centrifuged at  $100,000 \times g$  for 2 hours. All these centrifugation steps were performed at 4 °C. The pellet was resuspended in medium A plus 4 mM  $\text{Na}_2\text{ATP}$ , the pH was adjusted to 9.2 by addition of small aliquots of 20% (w/w)  $\text{NH}_4\text{OH}$  solution, and stored overnight at 4 °C. Then, the suspension, in which the pH was brought back to 8.0 by adding small aliquots of 2 N HCl aqueous solution, was sonicated at 210  $\mu\text{m}$  amplitude for 5 minutes. The sonicated suspension was centrifuged at  $300,000 \times g$  for 1 h and the resulting pellet was resuspended in 9 mL medium A plus 2 mM EDTA, pH 7.6. Then, after the addition of 4.5 mL chloroform, the resulting mixture was vigorously vortexed for 15 s and centrifuged at  $600 \times g$  for 10 min to allow the separation of the two phases. The upper aqueous phase was collected and further centrifuged at  $100,000 \times g$  for 1 hour. The pale-yellow supernatant obtained was supplemented with adequate aliquots of freshly prepared ATP solution to obtain a final concentration of 4 mM ATP and with 2N NaOH solution to adjust the pH to 8.0. After the dropwise addition of saturated  $(\text{NH}_4)_2\text{SO}_4$  solution plus 5 mM EDTA under continuous stirring to obtain 37% saturation and pH adjustment to 8.0 with 1N KOH solution, the suspension was centrifuged at  $10,000 \times g$  for 15 minutes. The pellet

was discarded, and the collected supernatant was brought to 60% saturation with solid  $(\text{NH}_4)_2\text{SO}_4$ ; the mixture was then adjusted to pH 8.0 with 1N KOH solution and kept overnight at 4 °C. Finally, the pellet from the last centrifugation at 150,000 g for 90 min, resuspended by gentle stirring using a Teflon Potter Elvehjem homogenizer in a small volume of medium containing 100 mM Tris/ $\text{H}_2\text{SO}_4$ , 1 mM EDTA, and 50% glycerol, pH 8.0, constituted the partially purified  $\text{F}_1$  fraction.<sup>33</sup> The protein concentration was determined according to the colorimetric method of Bradford<sup>32</sup> by Bio-Rad Protein Assay kit II by using BSA as standard. Once verified that in the partially purified  $\text{F}_1$  fraction, the ATPase activity, either sustained by  $\text{Ca}^{2+}$  or  $\text{Mg}^{2+}$ , was completely insensitive to 1  $\mu\text{g}/\text{mL}$  oligomycin, thus proving the detachment of the  $\text{F}_0$  sector, and no further purification was carried out. The partially purified  $\text{F}_1$  fraction was then stored in liquid nitrogen until the evaluation of  $\text{F}_1$ -ATPase activities.

#### Mitochondrial F-ATPase activity assays

Thawed mitochondrial preparations were immediately used for F-ATPase activity assays. The capability of ATP hydrolysis was assayed in a reaction medium (1 mL) containing 0.15 mg mitochondrial protein and 75 mM ethanolamine-HCl buffer pH 9.0, 6.0 mM  $\text{Na}_2\text{ATP}$ , and 2.0 mM  $\text{MgCl}_2$  for the  $\text{Mg}^{2+}$ -activated  $\text{F}_1\text{F}_0$ -ATPase assay, and the same buffer at pH 8.8 plus 3.0 mM  $\text{Na}_2\text{ATP}$  and 2.0 mM  $\text{CaCl}_2$  for the  $\text{Ca}^{2+}$ -activated  $\text{F}_1\text{F}_0$ -ATPase assay. Preliminary assays showed that under these slightly different assay conditions for the  $\text{Mg}^{2+}$ -activated and  $\text{Ca}^{2+}$ -activated F-ATPases, the maximal enzyme activities were detected. After 5 min preincubation at 37 °C, the reaction, carried out at the same temperature, was started by the addition of the substrate  $\text{Na}_2\text{ATP}$  and stopped after 5 min by the addition of 1 mL of ice-cold 15% (w/w) trichloroacetic acid aqueous solution. Once the reaction was stopped, vials were centrifuged for 15 min at 3500 rpm (Eppendorf Centrifuge 5202). In the supernatant, the concentration of inorganic phosphate (Pi) hydrolyzed by known amounts of mitochondrial protein, which is an indirect measure of F-ATPase activity, was spectrophotometrically evaluated.<sup>14</sup> For this aim, 1  $\mu\text{L}$  from a mother solution of 3 mg/mL oligomycin in dimethylsulfoxide (DMSO) was directly added to the reaction mix-

ture before starting the reaction. The total ATPase activity was calculated by detecting the Pi in control tubes run in parallel and containing 1  $\mu\text{L}$  DMSO per mL reaction system. In each experimental set, control tubes were alternated to the condition to be tested. The employed dose of oligomycin, specific inhibitor of F-ATPases that selectively blocks the  $\text{F}_0$  subunit,<sup>34</sup> ensured maximal enzyme activity inhibition and was currently used in F-ATPase assays. The  $\text{F}_1\text{F}_0$ -ATPase activity was routinely measured by subtracting, from the Pi hydrolyzed by total ATPase activity, the Pi hydrolyzed in the presence of 1  $\mu\text{g}/\text{mL}$  oligomycin.<sup>35</sup> In all experiments, the F-ATPase activity was expressed as  $\mu\text{mol Pi}\cdot\text{mg protein}^{-1}\cdot\text{min}^{-1}$ .

#### $\text{F}_1$ -ATPase activity assays

Immediately after thawing, partially purified  $\text{F}_1$  domains were used for  $\text{F}_1$ -ATPase activity assays. The capability of ATP hydrolysis was assayed in a reaction medium (1 mL) containing 0.15 mg  $\text{F}_1$  purified protein and 75 mM ethanolamine-HCl buffer pH 9.0, 6.0 mM  $\text{Na}_2\text{ATP}$ , and 2.0 mM  $\text{MgCl}_2$  or 2.0 mM  $\text{CaCl}_2$  for the  $\text{Mg}^{2+}$ -activated  $\text{F}_1\text{F}_0$ -ATPase and  $\text{Ca}^{2+}$ -activated  $\text{F}_1\text{F}_0$ -ATPase assays, respectively. The methods and parameters of ATP hydrolysis and Pi detection were the same as those used for the mitochondrial F-ATPase activity assays. The sensitivity to 1  $\mu\text{g}/\text{mL}$  oligomycin was tested to verify the detachment of  $\text{F}_0$  domain.

#### Kinetic analyses

To calculate the kinetic parameters ( $V_{\text{max}}$  and  $K_{\text{m}}$ ), enzyme activity data were fitted to the Michaelis-Menten Eq. (1) in which the enzyme reaction rate ( $v$ ), namely the F-ATPase activity, is plotted as a function of the concentration of substrate  $[\text{S}]$ . The mutual relationship between different metal cofactors and the ATP substrate (S) was also explored by building Hanes plots, which follow Eq. (2), a rearrangement of Michaelis-Menten equation, in which the  $[\text{S}]/v$  ratio is plotted against  $[\text{S}]$ .  $K_{\text{m}}$  and  $V_{\text{max}}$  values were calculated from the intercept with  $x$  axis (changed to positive) and the reciprocal of the slope of the straight lines obtained, respectively. The  $\text{IC}_{50}$  values, namely the inhibitor concentration that causes half maximal inhibition of the enzyme activity, were calculated by fitting the enzyme activity data without inhibitor and in the presence of increasing inhibitor concentrations to the four-parameter Eq. (3). In the latter, the enzyme

activity ( $y$ ) is a function of the inhibitor concentration ( $i$ ); *range* is the difference between the maximal enzyme activity recorded (without inhibitor) and the residual enzyme activity not inhibited by any inhibitor concentration, defined as *background*.

$$v = \frac{V_{\max} \cdot [S]}{K_m + [S]} \quad (1)$$

$$\frac{[S]}{v} = \frac{1}{V_{\max}} [S] + \frac{K_m}{V_{\max}} \quad (2)$$

$$y = \frac{\text{Range}}{1 + \left(\frac{x}{IC_{50}}\right)^i} + \text{Background} \quad (3)$$

The graphical methods of Dixon and Cornish-Bowden plots, which complement one another,<sup>36</sup> were used to detect the inhibition mechanism of Is-F<sub>1</sub> on either Ca<sup>2+</sup>- or Mg<sup>2+</sup>-activated F<sub>1</sub>F<sub>0</sub>-ATPase. The reciprocal of the enzyme activity (Dixon plot) or the  $S/v$  ratio (Cornish-Bowden plot) was plotted as a function of the inhibitor concentration. To build these plots, different experimental sets were designed in which the F-ATPase activity was evaluated in the presence of increasing inhibitor concentrations at two concentrations of the Me<sup>2+</sup> cofactor and constant ATP concentration or at two ATP concentrations, keeping the metal cofactor concentration constant. Therefore, in these experiments and plots, alternatively the Me<sup>2+</sup> cofactor or ATP played the  $S$  role. The values of  $K_i$ , which corresponds to the dissociation constant of the EI complex, were calculated from the abscissa of the intercept of the straight lines obtained in the Dixon plots. The  $K_i$  values, which represent the dissociation constant of the ternary ESI complex, were calculated by the abscissa of the intercept of the straight lines obtained in the Cornish-Bowden plots. In all plots, the enzyme-specific activity was taken as the expression of  $v$ . The correlation coefficients of all the straight lines obtained in Hanes, Dixon, and Cornish-Bowden plots were never lower than 0.95, thus confirming the linearity of these plots.<sup>37</sup> All data were processed by GraFit software (version 7.0.3).

#### SDS-PAGE and western blot assays

For SDS-PAGE assay, aliquots containing 5  $\mu$ g of F<sub>1</sub> domain partially purified proteins were separated on Bolt<sup>TM</sup> 4–12% bis-Tris Plus (Life Technologies

Ltd., Paisley, UK) for 55 min at 165 volts. Upon the completion of electrophoresis, the gel was washed three times at ambient temperature with deionized water for 5 min each wash. The gels were then stained with SAFE BLUE (Coomassie blue) for 1 h with gentle shaking, and destained according to the manufacturer's instruction.

For western blot assay, SDS-PAGE separated proteins were electrophoretically transferred onto a nitrocellulose membrane by semidry Turbo<sup>TM</sup> Blot System (Bio-Rad Laboratories Inc., Berkeley, CA). The blot was washed in PBS and protein transfer was checked by staining the nitrocellulose membranes with 0.2% Ponceau Red. Nonspecific binding on nitrocellulose membranes was blocked with 5% milk powder in PBS-T20 (phosphate buffer saline + 0.1% Tween-20) for 1 h at room temperature. The membrane was then incubated overnight at 4 °C with a 1:1000 dilution of rabbit polyclonal anti-ATP5B antibody (Aviva Systems Biology) in PBS-T20. After several washings with PBS-T20, the membrane was incubated with the secondary biotin-conjugate antibody (goat anti-rabbit IgG antibody) and then with a 1:1000 dilution of an anti-biotin horseradish peroxidase-linked antibody. Western blots were developed using chemiluminescent substrate (Clarity Western ECL Substrate) according to the manufacturer's instructions. The intensity of the chemiluminescent signal of the resultant bands was acquired by a Fluor-ST MultiImager using Quantity One Software (Bio-Rad Laboratories Inc.).

#### PTP and membrane potential evaluation

Swine heart mitochondria (1 mg/mL) were suspended and energized in assay buffer (130 mM KCl, 1 mM KH<sub>2</sub>PO<sub>4</sub>, 20 mM HEPES, pH 7.2 with Tris) incubated at 37 °C with 1  $\mu$ g/mL rotenone and 5 mM succinate as respiratory substrate. PTP opening was induced by the addition of low concentrations of Ca<sup>2+</sup> (20  $\mu$ M) at fixed interval of time (1 min). The calcium retention capacity (CRC) was spectrofluorophotometrically evaluated in the presence of 0.5  $\mu$ M Fura-FF. The probe has different spectral properties in the absence and presence of Ca<sup>2+</sup>, namely it displays excitation/emission spectra of 365/514 nm in the absence of calcium (Fura-FF low Ca<sup>2+</sup>) and shifts to 339/507 nm in the presence of high calcium concentrations (Fura-FF high Ca<sup>2+</sup>). PTP opening, which implies a decrease in

CRC, was detected by the increase in fluorescence intensity ratio (Fura-FF high Ca<sup>2+</sup>)/(Fura-FF low Ca<sup>2+</sup>). The membrane potential ( $\Delta\phi$ ) was evaluated in the presence of 0.5  $\mu$ M JC-10. In polarized mitochondrial membranes, this probe selectively generates an orange JC-10 aggregate (excitation/emission spectra of 540/590 nm). The JC-10 monomers, generated when  $\Delta\phi$  decreases, cause a green shift (excitation/emission spectra of 490/525 nm). Accordingly, the membrane depolarization (decrease in  $\Delta\phi$ ) ascribed to PTP formation was detected by the increase in the fluorescence intensity ratio, which corresponds to an increased JC-10 aggregate/JC-10 monomers ratio. All measurements were processed by LabSolutions RF software.

#### Assay of the mitochondrial respiration

Frozen and thawed mitochondrial fractions were used to evaluate the mitochondrial respiration. The oxygen consumption rates were polarographically evaluated by Clark-type electrode using a thermostated Oxytherm System (Hansatech Instruments) equipped with a 1-mL polarographic chamber. The reaction mixture (120 mM KCl, 10 mM Tris-HCl buffer, pH 7.2), maintained under Peltier thermostataion at 37 °C and continuous stirring, contained 0.25 mg mitochondrial protein. The succinate-O<sub>2</sub> oxidase activity by Complex II was determined by the oxidation of succinate in the presence of 1  $\mu$ g/mL rotenone. The reaction was started by the addition of 10 mM succinate after 2 min of stabilization of oxygen signal and preliminary tests assessed that, under the conditions applied, succinate oxidation was suppressed by 1  $\mu$ g/mL myxothiazol, selective inhibitor of Complex III.<sup>38</sup> The effect of succinate-O<sub>2</sub> oxidase activity was evaluated at Is-F<sub>1</sub> concentrations corresponding to the IC<sub>50</sub> values and at the concentration which induces the maximal inhibition of Ca<sup>2+</sup>-activated F<sub>1</sub>F<sub>0</sub>-ATPase. The protonophore FCCP (0.1  $\mu$ M) was added in order to verify the Is-F<sub>1</sub> effect on the maximal mitochondrial respiratory activity. The rate of succinate-O<sub>2</sub> oxidase activities was automatically detected by O<sub>2</sub>view software as nmoles O<sub>2</sub>·mg protein<sup>-1</sup>·min<sup>-1</sup>.

#### Quantification and statistical analysis

All data are expressed as mean  $\pm$  SD. The number of replicates is reported in the figure legends. Data were subjected to one-way ANOVA followed by Dunnett's test when *F* values indicated signifi-

cance ( $P \leq 0.05$ ). Statistical analyses were carried out by SigmaStat software (version 4).

## Results

### Divalent cations in the F<sub>1</sub>F<sub>0</sub>-ATPase kinetic mechanism of catalysis

In the presence of Mg<sup>2+</sup>, Mn<sup>2+</sup>, and Ca<sup>2+</sup>, F<sub>1</sub>F<sub>0</sub>-ATPase supports ATP hydrolysis with different efficiencies. The ATPase activity sustained by Mg<sup>2+</sup> or Mn<sup>2+</sup> exhibits similar *V*<sub>max</sub> and *K*<sub>m</sub> values; in contrast, Ca<sup>2+</sup>-activated F<sub>1</sub>F<sub>0</sub>-ATPase showed a 10-fold higher *K*<sub>m</sub> value than Mg<sup>2+</sup>-activated enzyme, while the *V*<sub>max</sub> was approximately halved (Fig. 1A). These data are consistent with the reported values for Me<sup>2+</sup> dependence of ATP hydrolysis in both coupled submitochondrial particles<sup>9</sup> and isolated F<sub>1</sub> domain.<sup>39</sup> Moreover, kinetic analyses were carried out in the presence of Mg<sup>2+</sup>, Mn<sup>2+</sup>, and Ca<sup>2+</sup> to obtain information on the mutual interactions between these cations. Mn<sup>2+</sup> has an atomic radius similar to that of Mg<sup>2+</sup> (1.61 Å Mn<sup>2+</sup> versus 1.45 Å Mg<sup>2+</sup>) and lower than that of Ca<sup>2+</sup> (1.94 Å). Since the *K*<sub>m</sub> of Mg<sup>2+</sup>-activated F<sub>1</sub>F<sub>0</sub>-ATPase decreased as Mn<sup>2+</sup> concentration increased, while *V*<sub>max</sub> was unaffected, the results indicate a competitive synergistic activation of Mn<sup>2+</sup> with respect to Mg<sup>2+</sup> (Fig. 1B), namely the two cations compete for the same site on the free enzyme. Conversely, the addition of Ca<sup>2+</sup> to the reaction system of Mg<sup>2+</sup>-activated F<sub>1</sub>F<sub>0</sub>-ATPases inhibited the F-ATPase activity by a noncompetitive inhibition mechanism (i.e., *V*<sub>max</sub> decreased, while *K*<sub>m</sub> was unaffected) (Fig. 1C). The noncompetitive inhibition mechanism indicated that Ca<sup>2+</sup> can bind either to the enzyme—Mg-ATP complex or the free enzyme.

### Mechanism of F<sub>1</sub>-ATPase inhibitors

Selective inhibitors of the catalytic F<sub>1</sub> domain (Is-F<sub>1</sub>) known to bind to F<sub>1</sub> covalently (NBD-Cl) or noncovalently (piceatannol, resveratrol, and quercetin) were tested to cast light on the F<sub>1</sub>F<sub>0</sub>-ATPase response when ATP hydrolysis was sustained either by Mg<sup>2+</sup> or Ca<sup>2+</sup>. NBD-Cl (Fig. 2), piceatannol (Fig. 3), resveratrol (Fig. 4), and quercetin (Fig. 5) were tested under different experimental conditions, namely at different concentrations of ATP substrate and cation cofactor to evaluate their inhibition potency (estimated as IC<sub>50</sub>

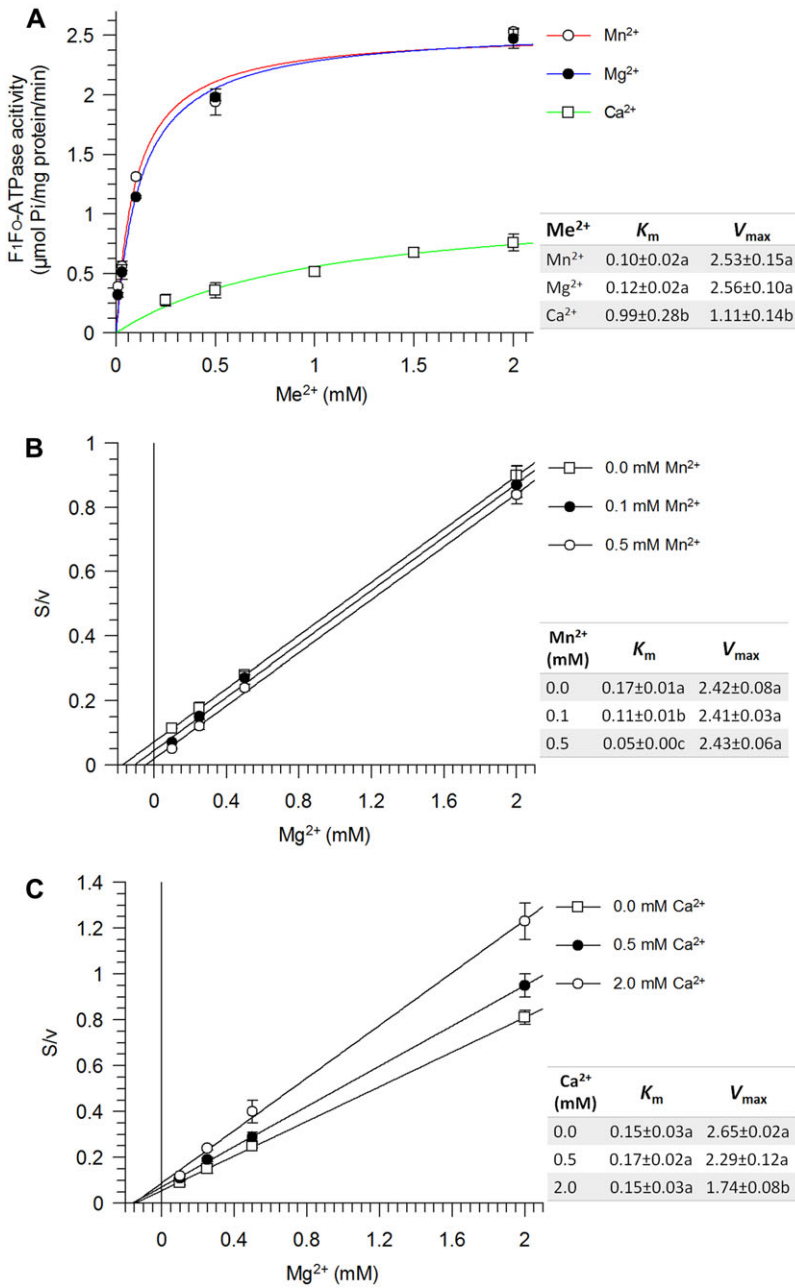


**Figure 1.** Mitochondrial  $\text{F}_1\text{F}_0$ -ATPase activities activated by divalent cations. (A) Michealis–Menten plot of ATP hydrolysis sustained by  $\text{Mn}^{2+}$ ,  $\text{Mg}^{2+}$ , or  $\text{Ca}^{2+}$ . (B and C) Hanes plots of  $\text{Mg}^{2+}$ -activated  $\text{F}_1\text{F}_0$ -ATPase activity in the absence ( $\square$ ) or presence of 0.1 mM ( $\bullet$ ) and 0.5 mM ( $\circ$ )  $\text{Mn}^{2+}$ , B; in the absence ( $\square$ ) or presence of 0.5 mM ( $\bullet$ ) and 2.0 mM ( $\circ$ )  $\text{Ca}^{2+}$ , C.  $K_m$  and  $V_{\max}$  are expressed in mM and  $\mu\text{mol Pi} \cdot \text{mg protein}^{-1} \cdot \text{min}^{-1}$ , respectively. Data represent the mean  $\pm$  SD from three independent experiments carried out on distinct mitochondrial preparations. Different letters indicate significantly different values within each treatment ( $P \leq 0.05$ ).

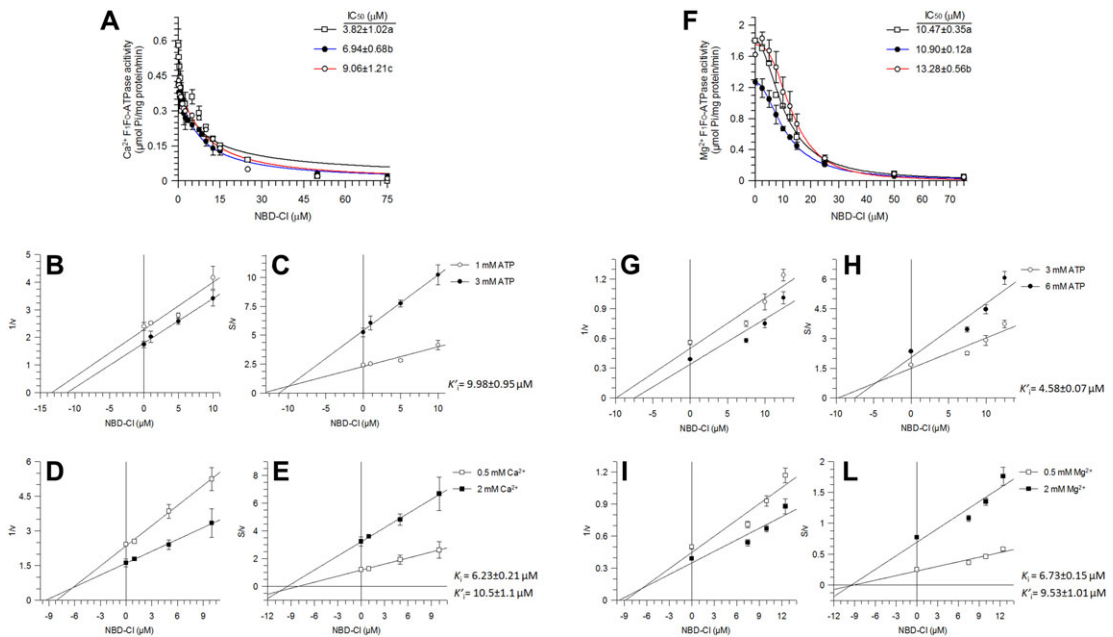


**Figure 2.** NBD-Cl inhibition of Ca<sup>2+</sup>- (A–E) and Mg<sup>2+</sup>-activated (F–L) F<sub>1</sub>F<sub>0</sub>-ATPase. (A) Dose–response curve at: 3 mM ATP + 2 (□) or 0.5 mM Ca<sup>2+</sup> (●); 1 mM ATP + 2 mM Ca<sup>2+</sup> (○). Dixon (B and D) and Cornish-Bowden (C and E) plots at 2 mM Ca<sup>2+</sup> + 1 (○) or 3 mM ATP (●); 3 mM ATP + 0.5 (□) or 2 mM (■) Ca<sup>2+</sup>. (F) Dose–response curve at: 6 mM ATP + 2 (□) or 0.5 mM Mg<sup>2+</sup> (●); 3 mM ATP + 2 mM Mg<sup>2+</sup> (○). Dixon (G and I) and Cornish-Bowden (H and L) plots at 2 mM Mg<sup>2+</sup> + 3 (○) or 6 mM ATP (●); 6 mM ATP + 0.5 (□) or 2 mM Mg<sup>2+</sup> (■). K<sub>i</sub> and K<sub>i</sub>' values were obtained as detailed in the kinetic analyses section of Materials and Methods. Each point represents the mean ± SD from three experiments on distinct mitochondrial preparations. Different letters indicate significantly different values within each treatment ( $P \leq 0.05$ ).

values) and kinetic mechanism as reported in the section on kinetic analyses.

NBD-Cl displayed a higher inhibition efficiency on Ca<sup>2+</sup>-activated F<sub>1</sub>F<sub>0</sub>-ATPase than on Mg<sup>2+</sup>-activated F<sub>1</sub>F<sub>0</sub>-ATPase, as shown by the lower IC<sub>50</sub> value for Ca<sup>2+</sup>-ATPase (Fig. 2A and F). Moreover, Ca<sup>2+</sup>-activated F<sub>1</sub>F<sub>0</sub>-ATPase inhibition decreased when the ATP substrate or Ca<sup>2+</sup> concentration was reduced (Fig. 2A). Conversely, the inhibition of Mg<sup>2+</sup>-activated F<sub>1</sub>F<sub>0</sub>-ATPase decreased only when ATP concentration decreased (Fig. 2F). The inhibition exerted by NBD-Cl on both Ca<sup>2+</sup>- and Mg<sup>2+</sup>-activated F<sub>1</sub>F<sub>0</sub>-ATPase showed an uncompetitive mechanism with respect to the ATP substrate (Fig. 2B and C, and G and H) and a mixed-type mechanism with respect to the cation cofactor (Fig. 2D and E, and I and L). The uncompetitive inhibition indicated that the inhibitor only binds to the enzyme–ATP complex, while the mixed-type inhibition indicated that the inhibitor can also bind to the free enzyme. However, on considering the dissociation constants of the enzyme–inhibitor

complex (K<sub>i</sub>) and the enzyme–substrate–inhibitor complex (K<sub>i</sub>'), since both Ca<sup>2+</sup>- and Mg<sup>2+</sup>-activated F<sub>1</sub>F<sub>0</sub>-ATPases showed K<sub>i</sub> values slightly lower than K<sub>i</sub>' values, the formation of the binary complex (enzyme–NBD) was preferred. Moreover, the K<sub>i</sub>' values (Fig. 2C and H) were lower in the presence of Mg<sup>2+</sup> than in the presence of Ca<sup>2+</sup>, thus pointing out that NDB preferably binds to Mg<sup>2+</sup>-activated F<sub>1</sub>F<sub>0</sub>-ATPase.

Piceatannol more efficiently inhibited F<sub>1</sub>F<sub>0</sub>-ATPase when activated by Ca<sup>2+</sup> than when activated by Mg<sup>2+</sup>. Moreover, the inhibition kinetics revealed that the two differently activated F-ATPase activities showed different responsiveness to the inhibitor. Ca<sup>2+</sup>-activated F<sub>1</sub>F<sub>0</sub>-ATPase inhibition was unaffected when the substrate or cofactor concentration decreased (Fig. 3A); in contrast, Mg<sup>2+</sup>-activated F<sub>1</sub>F<sub>0</sub>-ATPase was less sensitive to piceatannol when ATP concentration decreased (Fig. 3F). Piceatannol exerted a mixed-type inhibition mechanism on Ca<sup>2+</sup>-activated F<sub>1</sub>F<sub>0</sub>-ATPase with respect to ATP substrate (Fig. 3B and C).

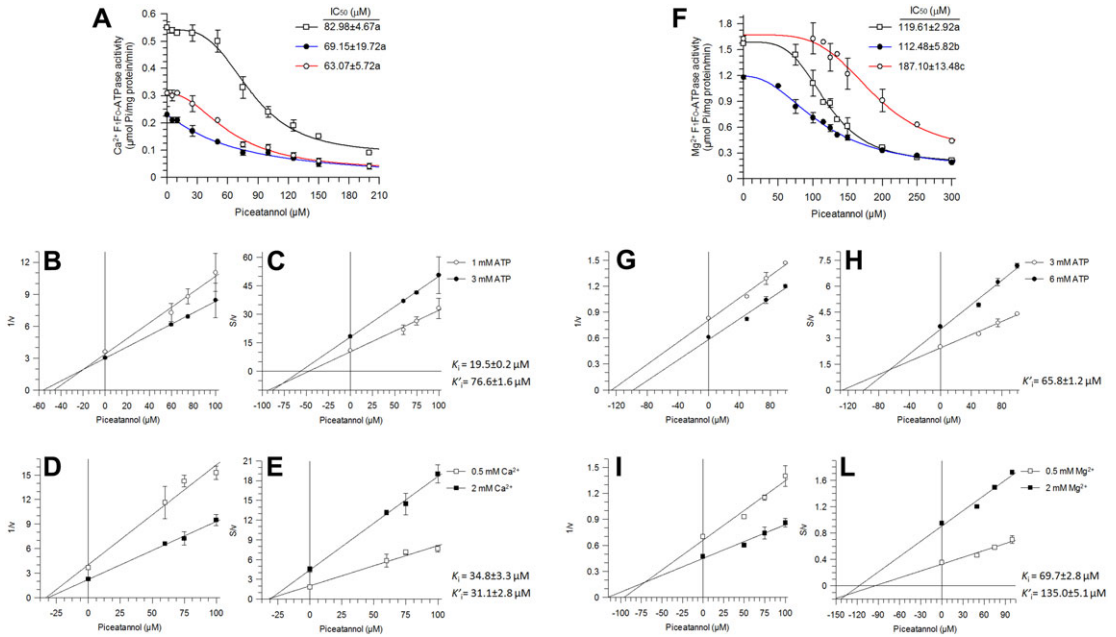


**Figure 3.** Picetannol inhibition of Ca<sup>2+</sup>- (A–E) and Mg<sup>2+</sup>-activated (F–L) F<sub>1</sub>F<sub>0</sub>-ATPase. (A) Dose–response curve at: 3 mM ATP + 2 (□) or 0.5 mM Ca<sup>2+</sup> (●); 1 mM ATP + 2 mM Ca<sup>2+</sup> (○). Dixon (B and D) and Cornish-Bowden (C and E) plots at 2 mM Ca<sup>2+</sup> + 1 (○) or 3 mM ATP (●); 3 mM ATP + 0.5 (□) or 2 mM (■) Ca<sup>2+</sup>. (F) Dose–response curve at: 6 mM ATP + 2 (□) or 0.5 mM Mg<sup>2+</sup> (●); 3 mM ATP + 2 mM Mg<sup>2+</sup> (○). Dixon (G and I) and Cornish-Bowden (H and L) plots at 2 mM Mg<sup>2+</sup> + 3 (○) or 6 mM ATP (●); 6 mM ATP + 0.5 (□) or 2 mM Mg<sup>2+</sup> (■). K<sub>1</sub> and K<sub>1</sub>' values were obtained as detailed in the kinetic analyses section of Materials and Methods. Each point represents the mean ± SD from three experiments on distinct mitochondrial preparations. Different letters indicate significantly different values within each treatment (P ≤ 0.05).

The far lower K<sub>i</sub> value with respect to the K<sub>i</sub>' clearly indicated that the formation of the binary complex (enzyme–picetannol) is favored with respect to that of the tertiary complex (enzyme–ATP–picetannol). Picetannol inhibition of Ca<sup>2+</sup>-activated F<sub>1</sub>F<sub>0</sub>-ATPase was noncompetitive with respect to Ca<sup>2+</sup> (Fig. 3D and E). When the enzyme is activated by Mg<sup>2+</sup>, picetannol acted as an uncompetitive inhibitor with respect to the ATP substrate (Fig. 3G and H). The plots drawn in Figure 3I and L indicated a mixed-type inhibition mechanism with respect to Mg<sup>2+</sup>, namely picetannol can bind either to the free enzyme or to the enzyme–Mg<sup>2+</sup> complex. Nevertheless, picetannol bound to Mg<sup>2+</sup>-activated F<sub>1</sub>F<sub>0</sub>-ATPase with nearly doubled affinity (halved K<sub>i</sub>) to the free enzyme, forming the enzyme–picetannol complex rather than the ternary Mg<sup>2+</sup>–enzyme–picetannol complex (Fig. 3I and L). Picetannol more tightly bound to Ca<sup>2+</sup>-activated F<sub>1</sub>F<sub>0</sub>-ATPase than to Mg<sup>2+</sup>-activated F<sub>1</sub>F<sub>0</sub>-ATPase, as shown by the K<sub>i</sub> and K<sub>i</sub>' values for Mg<sup>2+</sup>-activated F<sub>1</sub>F<sub>0</sub>-ATPase, which

were higher than those for Ca<sup>2+</sup>-activated F<sub>1</sub>F<sub>0</sub>-ATPase. Moreover, the inhibition extent apparently depended on the Ca<sup>2+</sup> concentration (Fig. 3A).

Resveratrol showed lower IC<sub>50</sub> values for Ca<sup>2+</sup>- than for Mg<sup>2+</sup>-activated F<sub>1</sub>F<sub>0</sub>-ATPase. In both cases, the affinity for resveratrol decreased as the substrate concentration decreased (Fig. 4A and F). The inhibition of both the Ca<sup>2+</sup>- and Mg<sup>2+</sup>-activated F<sub>1</sub>F<sub>0</sub>-ATPases was uncompetitive with respect to ATP (Fig. 4B and C, and G and H) and to the divalent cation (Fig. 4D and L, and I and L). The K<sub>i</sub>' values of Ca<sup>2+</sup>-activated F<sub>1</sub>F<sub>0</sub>-ATPase with respect to ATP and cation cofactor were lower than those of Mg<sup>2+</sup>-activated F<sub>1</sub>F<sub>0</sub>-ATPase. The data indicated that the uncompetitive inhibitor resveratrol more easily forms the tertiary complex (i.e., enzyme–substrate/cofactor–resveratrol) with Ca<sup>2+</sup>-activated F<sub>1</sub>F<sub>0</sub>-ATPase than with Mg<sup>2+</sup>-activated F<sub>1</sub>F<sub>0</sub>-ATPase.

Quercetin differently inhibited Ca<sup>2+</sup>- and Mg<sup>2+</sup>-activated F<sub>1</sub>F<sub>0</sub>-ATPase. The IC<sub>50</sub> values of Ca<sup>2+</sup>- and Mg<sup>2+</sup>-activated F<sub>1</sub>F<sub>0</sub>-ATPase were unaffected

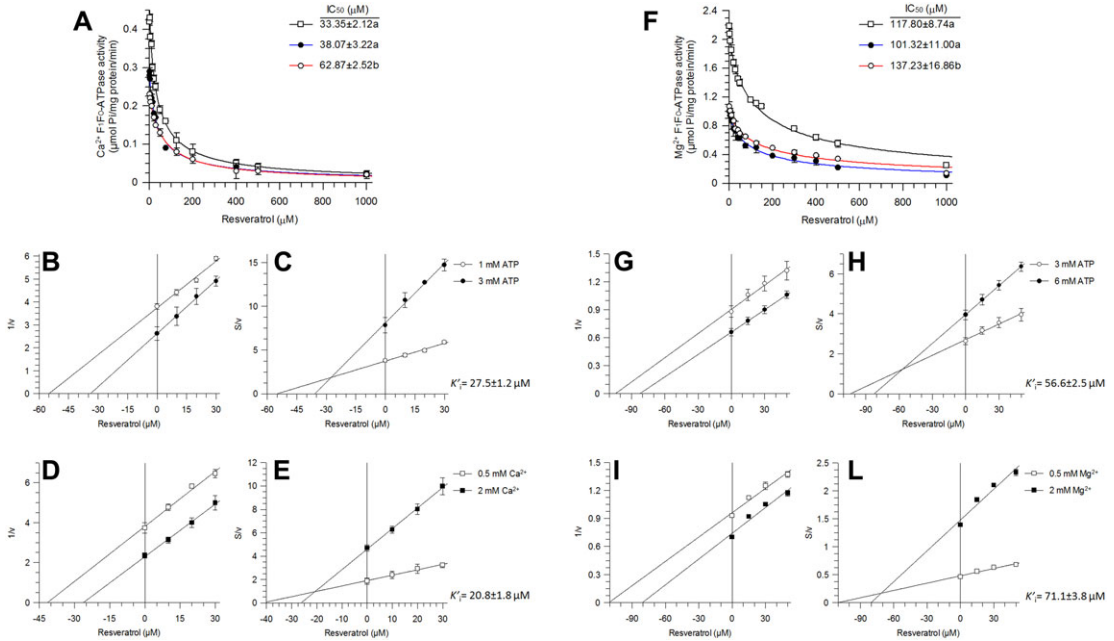


**Figure 4.** Resveratrol inhibition of Ca<sup>2+</sup>- (A–E) and Mg<sup>2+</sup>-activated (F–L) F<sub>1</sub>F<sub>0</sub>-ATPases. (A) Dose–response curve at: 3 mM ATP + 2 (□) or 0.5 mM Ca<sup>2+</sup> (●); 1 mM ATP + 2 mM Ca<sup>2+</sup> (○). Dixon (B and D) and Cornish-Bowden (C and E) plots at 2 mM Ca<sup>2+</sup> + 1 (○) or 3 mM ATP (●); 3 mM ATP + 0.5 (□) or 2 mM (■) Ca<sup>2+</sup>. (F) Dose–response curve at: 6 mM ATP + 2 (□) or 0.5 mM Mg<sup>2+</sup> (●); 3 mM ATP + 2 mM Mg<sup>2+</sup> (○). Dixon (G and I) and Cornish-Bowden (H and L) plots at 2 mM Mg<sup>2+</sup> + 3 (○) or 6 mM ATP (●); 6 mM ATP + 0.5 (□) or 2 mM Mg<sup>2+</sup> (■). K<sub>i</sub> and K<sub>i</sub>' values were obtained as detailed in the kinetic analyses section. Each point represents the mean ± SD from three experiments on distinct mitochondrial preparations. Different letters indicate significantly different values within each treatment ( $P \leq 0.05$ ).

by the substrate and/or cofactor concentrations (Fig. 5A and F). The inhibition mechanism exerted by quercetin on both Ca<sup>2+</sup>- and Mg<sup>2+</sup>-activated F<sub>1</sub>F<sub>0</sub>-ATPase activities was uncompetitive with respect to ATP (Fig. 5B and C, and G and H) and the cation cofactors (Fig. 5D and E, and I and L). However, the K<sub>i</sub>' value obtained for Ca<sup>2+</sup>-activated F<sub>1</sub>F<sub>0</sub>-ATPase with respect to ATP (Fig. 5C) was approximately doubled with respect to that for the cation cofactor (Fig. 5E). In the case of Mg<sup>2+</sup>-activated F<sub>1</sub>F<sub>0</sub>-ATPase, the K<sub>i</sub>' on ATP (Fig. 5H) and on the cofactor (Fig. 5L) attained similar values. Moreover, since Ca<sup>2+</sup>-activated F<sub>1</sub>F<sub>0</sub>-ATPase showed lower IC<sub>50</sub> and K<sub>i</sub>' values for quercetin than Mg<sup>2+</sup>-activated F<sub>1</sub>F<sub>0</sub>-ATPase, quercetin more tightly bound to Ca<sup>2+</sup>-activated F<sub>1</sub>F<sub>0</sub>-ATPase than to Mg<sup>2+</sup>-activated F<sub>1</sub>F<sub>0</sub>-ATPase.

#### Ca<sup>2+</sup>-dependent ATP hydrolysis by the F<sub>1</sub> domain is essential for opening the PTP

Partially purified F<sub>1</sub> domain obtained from swine heart mitochondria and analyzed by SDS-PAGE

showed nine bands corresponding to the enzyme subunits (α, β, γ, δ, ε, b, OSCP, d, and F6). The catalytic β subunit (MW 51.7 kDa) was identified by western blot analyses (Fig. 6A), confirming that the partially purified F<sub>1</sub> fraction contained the known subunits of the hydrophilic sector F<sub>1</sub>.

The partially purified swine F<sub>1</sub> domain was tested for both the capability to hydrolyze ATP in the presence of either Mg<sup>2+</sup> or Ca<sup>2+</sup> and to sensitivity to F<sub>1</sub>F<sub>0</sub>-ATPase inhibitors. In addition to the Is-F<sub>1</sub> described above, the selective inhibitor oligomycin was tested. Oligomycin, a macrolide antibiotic, blocks ATP synthesis/hydrolysis only when the membrane F<sub>0</sub> domain is functionally and structurally linked to the F<sub>1</sub> portion;<sup>40</sup> it binds to two adjacent c subunits, covers the H<sup>+</sup> binding site, and prevents c-ring rotation.<sup>41</sup> As in the mitochondrial preparations (Fig. 1A), F<sub>1</sub>-ATPase activity activated by Ca<sup>2+</sup> (Fig. 6B) was lower than that activated by Mg<sup>2+</sup> (Fig. 6C), even if the F<sub>1</sub>-ATPase/F<sub>1</sub>F<sub>0</sub>-ATPase activity ratio was higher when the F<sub>1</sub>-ATPase activity was sustained by Ca<sup>2+</sup>

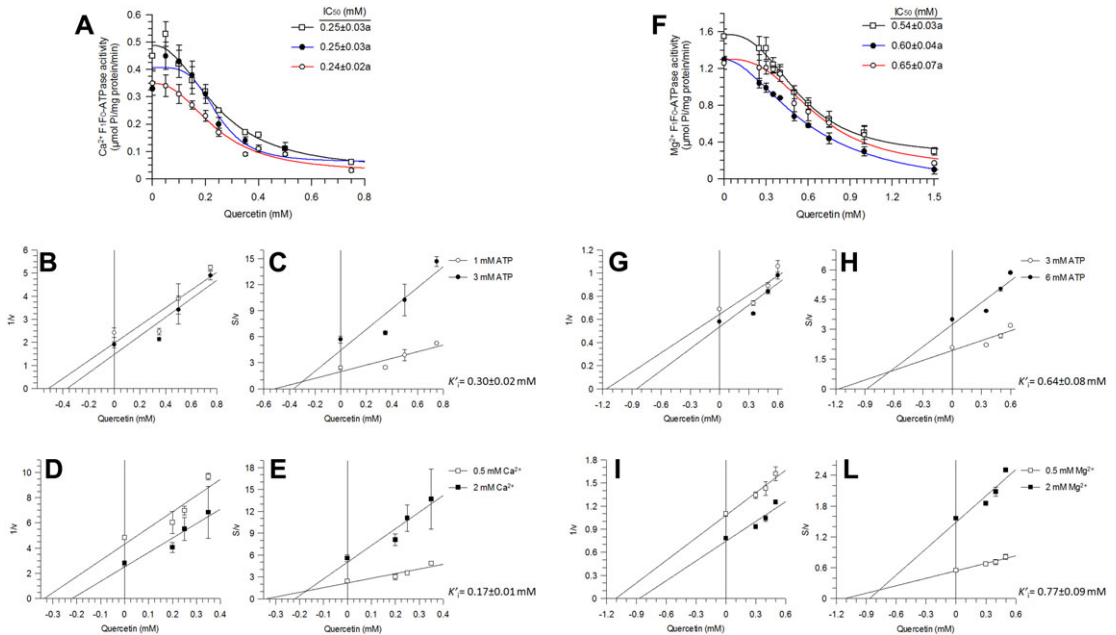


**Figure 5.** Quercetin inhibition of Ca<sup>2+</sup>- (A–E) and Mg<sup>2+</sup>-activated (F–L) F<sub>1</sub>F<sub>0</sub>-ATPases. (A) Dose–response curve at: 3 mM ATP + 2 (□) or 0.5 mM Ca<sup>2+</sup> (●); 1 mM ATP + 2 mM Ca<sup>2+</sup> (○). Dixon (B and D) and Cornish–Bowden (C and E) plots at 2 mM Ca<sup>2+</sup> + 1 (○) or 3 mM ATP (●); 3 mM ATP + 0.5 (□) or 2 mM (■) Ca<sup>2+</sup>. (F) Dose–response curve at: 6 mM ATP + 2 (□) or 0.5 mM Mg<sup>2+</sup> (●); 3 mM ATP + 2 mM Mg<sup>2+</sup> (○). Dixon (G and I) and Cornish–Bowden (H and L) plots at 2 mM Mg<sup>2+</sup> + 3 (○) or 6 mM ATP (●); 6 mM ATP + 0.5 (□) or 2 mM Mg<sup>2+</sup> (■). K<sub>i</sub> and K<sub>i</sub>' values were obtained as detailed in the kinetic analyses section of Materials and Methods. Each point represents the mean ± SD from three experiments on distinct mitochondrial preparations. Different letters indicate significantly different values within each treatment (P ≤ 0.05).

than by Mg<sup>2+</sup> (892.2 versus 644.2). Moreover, irrespective of the activating cation, F<sub>1</sub>-ATPase activity was insensitive to oligomycin and inhibited by Is-F<sub>1</sub> (Fig. 6B and C), confirming that the fraction obtained, even if only partially purified, contained the F<sub>1</sub> domain detached from the membrane-embedded F<sub>0</sub> domain. Interestingly, Ca<sup>2+</sup> sustained ATP hydrolysis in the purified F<sub>1</sub> domain, as in mitochondria.

When Ca<sup>2+</sup> levels in mitochondria attain a threshold value, an uncontrolled Ca<sup>2+</sup> release from mitochondria, associated with the collapse of the membrane potential (Δφ)—known as the electrical component of the Δp—occurs and the PTP opens.<sup>16,42</sup> On considering these related events, PTP activity can be detected by adding Ca<sup>2+</sup> and measuring changes in the CRC and Δφ. The increase in CRC in control mitochondria, stimulated by subsequent 20 μM Ca<sup>2+</sup> additions at fixed time intervals, was abolished by CsA, a known PTP blocker. Similarly, PTP is inhibited by NBD-Cl, while the

other F<sub>1</sub> inhibitors (piceatannol, resveratrol, and quercetin) tested at concentrations corresponding to their respective IC<sub>50</sub> values on Ca<sup>2+</sup>-dependent F<sub>1</sub>F<sub>0</sub>-ATPase apparently desensitized PTP opening to Ca<sup>2+</sup> (Fig. 7A). Accordingly, the increase in fluorescence intensity after Ca<sup>2+</sup> pulses revealed that mitochondrial Δφ collapses, while both CsA and NBD-Cl prevented this event. Conversely, piceatannol and resveratrol apparently polarized the mitochondrial membrane. In the presence of quercetin, Ca<sup>2+</sup> induces hormesis—that is, initially, it promoted an increase in fluorescence intensity, which would suggest Δφ collapse, while subsequent Ca<sup>2+</sup> addition resulted in fluorescence intensity decrease, suggesting membrane repolarization (Fig. 7B).

The inhibitors tested also differently affected mitochondrial respiration. In succinate-energized mitochondria, while NBD-Cl and piceatannol did not significantly affect the succinate-O<sub>2</sub> oxidase activity, the latter was stimulated by resveratrol and inhibited by quercetin (Fig. S1, online only).

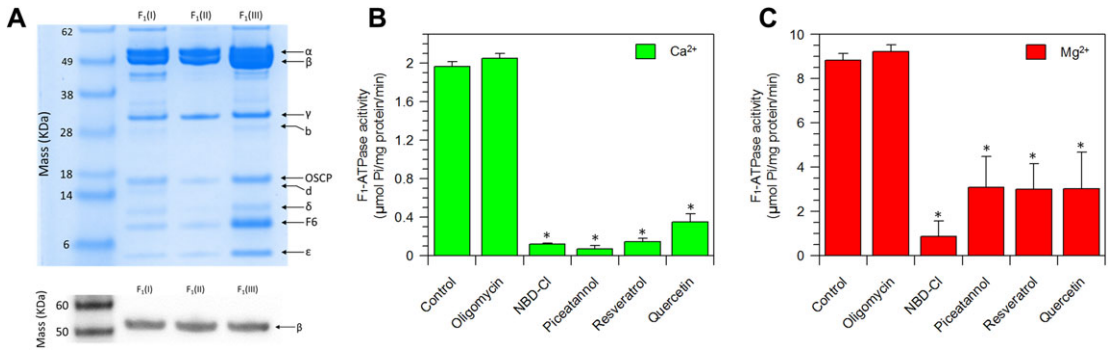


**Figure 6.** Features of the partially purified F<sub>1</sub> domain and F-ATPase responses to inhibitors (Is-F<sub>1</sub>). (A) Upper panel: the (I), (II), and (III) SDS-PAGE lanes are biological replicates of partially purified F<sub>1</sub> domain. On the left-hand lane, broad-range molecular mass markers are shown. On the right-hand side, the F<sub>1</sub> subunit migration positions are shown. Lower panel: the catalytic β subunit band identified by western blot assay. (B) Ca<sup>2+</sup>- and (C) Mg<sup>2+</sup>-dependent F<sub>1</sub>-ATPase activities were evaluated in the absence and presence of the inhibitors: 3 μg/mL oligomycin; 75 μM NBD-Cl; 204 μM piceatannol; 0.8 mM resveratrol; and 0.75 mM quercetin. Each value represents the mean ± SD from three independent experiments carried out on distinct F<sub>1</sub> preparations. The asterisk (\*) indicates significantly different enzyme activity values ( $P \leq 0.05$ ) in the absence and presence of inhibitors.

## Discussion

A combination of different experimental approaches described herein has resulted a realistic model of the intriguing and still poorly explored relationship between Ca<sup>2+</sup> and PTP formation. Most likely, the F<sub>1</sub>F<sub>0</sub>-ATPase catalytic sites undergo different conformational states, not only according to the binding-change mechanism<sup>2</sup> but also promoted by the binding of different cation cofactors. Accordingly, differently sized divalent cations Mg<sup>2+</sup>, Mn<sup>2+</sup>, and Ca<sup>2+</sup> lead to a different

F-ATPase activation (Fig. 1A). The synergistic competitive activation of Mn<sup>2+</sup> on Mg<sup>2+</sup>-activated F<sub>1</sub>F<sub>0</sub>-ATPase is consistent with enzyme-Me<sup>2+</sup> complex formation, which can host either Mg<sup>2+</sup> or Mn<sup>2+</sup> during catalysis. In general, Me<sup>2+</sup>-activated F<sub>1</sub>F<sub>0</sub>-ATPases can sustain ATP hydrolysis; but Mg<sup>2+</sup>- or Mn<sup>2+</sup>-activated F<sub>1</sub>F<sub>0</sub>-ATPases especially can link ATP hydrolysis to an efficient H<sup>+</sup> pumping activity.<sup>9</sup> On the other hand,  $K_m$  and  $V_{max}$  values indicate that Ca<sup>2+</sup>-activated F<sub>1</sub>F<sub>0</sub>-ATPase has lower catalytic efficiency than Mg<sup>2+</sup>-activated F<sub>1</sub>F<sub>0</sub>-ATPase.

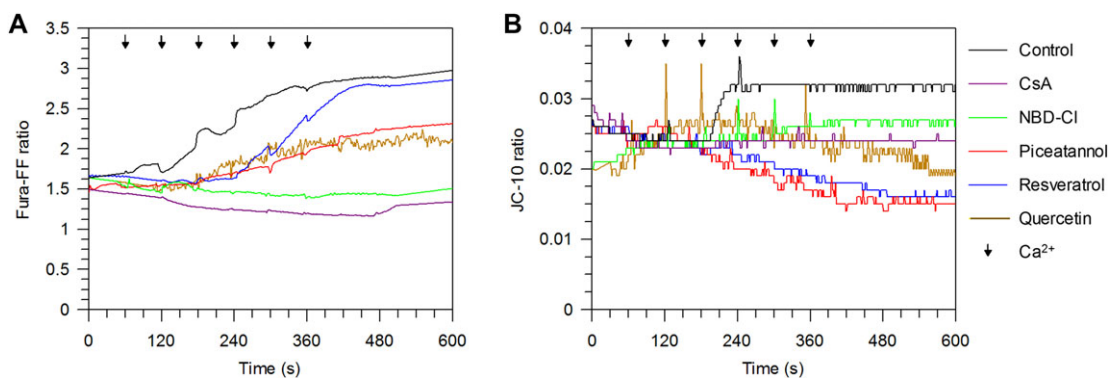


**Figure 7.** Evaluation of PTP opening. Representative curves (A) of the calcium retention capacity (CRC) and (B) of the membrane potential ( $\Delta\phi$ ) in mitochondrial preparations. CRC and  $\Delta\phi$  were monitored in response to subsequent 20 μM CaCl<sub>2</sub> pulses (shown by the arrows), as detailed in the Materials and Methods section, in the absence (control) and presence of the inhibitors 1 μM CsA, 4 μM NBD-Cl, 80 μM piceatannol, 30 μM resveratrol, and 200 μM quercetin. The concentrations of Is-F<sub>1</sub> inhibitors were selected on the basis of their respective IC<sub>50</sub> values on Ca<sup>2+</sup>-activated F<sub>1</sub>F<sub>0</sub>-ATPase. The experiments were carried out in triplicate on three distinct mitochondrial preparations.

Further information is provided by inhibition kinetic analyses. The noncompetitive inhibition of  $\text{Ca}^{2+}$  on  $\text{Mg}^{2+}$ -activated  $\text{F}_1\text{F}_0$ -ATPase suggests that  $\text{Ca}^{2+}$  and  $\text{Mg}^{2+}$  bind to distinct sites in the catalytic subunits of  $\text{F}_1$ . Therefore,  $\text{Ca}^{2+}$  binds either to  $\text{F}_1\text{F}_0$ -ATPase without cofactor or to  $\text{Mg}^{2+}$ -bound  $\text{F}_1\text{F}_0$ -ATPase, that is, to the enzyme–Mg complex.  $\text{Mg}^{2+}$  and  $\text{Mn}^{2+}$  may bind to the same site; in other words, they compete for the same binding site (Fig. 1B and C).  $\text{Mg}^{2+}$  is known to form six bonds in the catalytic site of  $\beta$  subunits: one bond with  $\beta$ -Thr-163 of the P-loop (phosphate-binding loop), three bonds with  $\beta$ -Asp-256,  $\beta$ -Glu-192, and  $\beta$ -Arg-189 residues through three water molecules that build a bridge, and the last two bonds with the  $\gamma$  and  $\beta$  phosphate oxygens of ATP or ADP.<sup>5</sup> Most likely, the higher steric hindrance of  $\text{Ca}^{2+}$  with respect to  $\text{Mg}^{2+}$  and  $\text{Mn}^{2+}$  prevents its insertion into the catalytic sites with the hexacoordinated geometry of  $\text{Mg}^{2+}$ .<sup>10</sup>  $\text{Ca}^{2+}$  would display a different coordination chemistry in the  $\text{F}_1$  hexamer, promoting a spatial rearrangement of the catalytic and noncatalytic sites, both of which can bind divalent cations.<sup>5,43</sup> Interestingly, within  $\text{F}_1$ ,  $\beta$ -Thr-163 is required to sustain  $\text{Ca}^{2+}$ -dependent ATP hydrolysis and confers resistance to PTP opening.<sup>12,24</sup>

The response to  $\text{F}_1$  inhibitors, which act by different mechanisms, provides other clues that help to discriminate between  $\text{Ca}^{2+}$ - and  $\text{Mg}^{2+}$ -activated  $\text{F}_1\text{F}_0$ -ATPases. The  $\text{F}_1$  domain can bind covalent inhibitors that modify amino acid residues near the nucleotide-binding site in  $\beta$  subunits or non-covalent inhibitors, such as polyphenolic phytochemicals. The covalent inhibitor NBD-Cl mainly reacts with  $\beta$ -Tyr-311 and modifies its phenolic oxygen only when the catalytic site is in the  $\beta_E$  conformation.<sup>44</sup> Moreover, the NBD group can move from Tyr to  $\beta$ -Lys-162 of the P-loop within the same  $\beta_E$  subunit at  $\text{pH} \geq 9.0$ .<sup>45</sup> The NBD-Cl shift occurs when the amino acid residue is exposed at the  $\alpha_E$ - $\beta_E$  interface; the NBD group, by making unfavorable steric clashes with the enzyme side chain atoms, prevents the conversion to  $\beta_{TP}$  and blocks ATP hydrolysis<sup>46</sup> (Fig. S2, online only). The similar inhibition mechanism exerted by NBD-Cl on  $\text{Ca}^{2+}$ - and  $\text{Mg}^{2+}$ -activated  $\text{F}_1\text{F}_0$ -ATPases with respect to cation cofactors or substrate (Fig. 2B, C–E, G–I, and L) is consistent with the failed occlusion of the nucleotide pocket by the inhibitor. However,  $\text{Ca}^{2+}$  binding to  $\text{F}_1$  domain can favor inhibitor

interaction with the enzyme. Accordingly, conformational changes promoted by a larger  $\text{Ca}^{2+}$  van der Waals radius, compared with  $\text{Mg}^{2+}$ , may make the binding site more prone to accommodate the inhibitor. Consistently, NBD-Cl enzyme inhibition was more effective on  $\text{Ca}^{2+}$ -activated  $\text{F}_1\text{F}_0$ -ATPase than on  $\text{Mg}^{2+}$ -activated  $\text{F}_1\text{F}_0$ -ATPase (Fig. 2A and B).

The phenolic phytochemicals tested (piceatannol, resveratrol, and quercetin) are known to inhibit ATP hydrolysis by  $\text{F}_1$  without interfering with the catalytic sites. They block the rotary mechanism by binding to individual and mutually independent sites in the hydrophobic region, where the  $\gamma$  subunit C-terminal tip interacts with the “bearing,” a loops region below the “crown region” of  $\alpha$  and  $\beta$  subunits<sup>47</sup> (Fig. S3, online only). Consistently with their individual binding sites, piceatannol, resveratrol, and quercetin exert different inhibition types on the  $\text{Ca}^{2+}$ - and  $\text{Mg}^{2+}$ -activated  $\text{F}_1\text{F}_0$ -ATPases (Figs. 3–5). Furthermore, since their inhibition mechanism is never competitive under the different experimental conditions tested, each phytochemical binds to a distinct site than do ATP,  $\text{Mg}^{2+}$ , and  $\text{Ca}^{2+}$ . Consequently,  $\text{Ca}^{2+}$ , whose binding site is still unknown, most likely inserts into the nucleotide-binding pocket or close to it. Moreover, the inhibitory efficiency of each phytochemical is higher on  $\text{Ca}^{2+}$ -activated  $\text{F}_1\text{F}_0$ -ATPase than  $\text{Mg}^{2+}$ -activated  $\text{F}_1\text{F}_0$ -ATPase under all the study conditions. Evidently, the  $\text{Ca}^{2+}$  size in the  $(\alpha\beta)_3$  globular hexamer implies a higher impact of the cation on the torsional mechanism of the rotor.

Assuming that piceatannol, resveratrol, and quercetin act on the annular sleeve of the bearing and block the rotary mechanism driven by ATP hydrolysis, this loop region on the nucleotide-binding domain of  $\beta$  subunit may transmit the conformational change undergone during enzyme catalysis through the long connecting loop to the crown region (Fig. S3, online only). Accordingly, molecular dynamics simulations suggest that the mechanical energy of  $\text{Ca}^{2+}$  insertion into  $\beta$  subunits is transmitted from the catalytic sites to the crown region and attains the OSCP subunit of the  $\text{F}_1\text{F}_0$ -ATPase lateral stalk, which, in turn, transfers it to the IMM  $\text{F}_0$  subunits, leading to PTP opening.<sup>24,25</sup>

Testing of the partially purified  $\text{F}_1$  domain (Fig. 6A), detached from  $\text{F}_0$  with Is- $\text{F}_1$ , confirmed their higher inhibition of  $\text{Ca}^{2+}$ -activated

F<sub>1</sub>F<sub>0</sub>-ATPase (Fig. 6B and C), even if ATP hydrolysis is still preferentially sustained by Mg<sup>2+</sup>, as in mitochondria. Thus, Is-F<sub>1</sub> selectively inhibits F<sub>1</sub>-ATPase activity and, consequently, its Ca<sup>2+</sup>-dependent ATP hydrolysis. Recent studies on the PTP, aiming at shedding light on the F<sub>1</sub>F<sub>0</sub>-ATPase subunit(s) involved in its formation, lead to two main hypotheses, namely that the PTP would form either inside the *c*-ring or between F<sub>1</sub>F<sub>0</sub>-ATPase monomers of a dimer.<sup>22,23,48–51</sup> However, the molecular mechanism that triggers PTP formation is still enigmatic.<sup>27</sup> Ca<sup>2+</sup>-induced PTP opening is inhibited by CsA, a known PTP blocker, in a similar way as by NBD-Cl (Fig. 7A and B), while the polyphenolic phytochemicals increase the Ca<sup>2+</sup> threshold required for PTP formation. Consistently, the  $\Delta\phi$  decrease linked to PTP opening is similarly inhibited by either CsA or NBD-Cl, while the polyphenolic phytochemicals block the sudden  $\Delta\phi$  dissipation due to PTP formation. The phytochemical effects on  $\Delta\phi$  could also be affected by some concomitant changes in the activities of the mitochondrial respiratory chain complexes, as hinted by the succinate-O<sub>2</sub> activation by resveratrol and inhibition by quercetin in succinate-energized mitochondria (Fig. S1, online only).

The data provided herein indicate that the differences between Mg<sup>2+</sup> and Ca<sup>2+</sup> in their coordination properties and the consequent adoption of different conformations within F<sub>1</sub>, even if not relevant to affect the catalytic mechanism of ATP hydrolysis, are functionally selective. Accordingly, only Ca<sup>2+</sup> can drive the conformational transmission mechanism that leads to PTP opening.

## Conclusion

In summary, Ca<sup>2+</sup> promotes ATP hydrolysis by the mitochondrial F<sub>1</sub>F<sub>0</sub> complex through a different kinetic mechanism from that of the natural cofactor Mg<sup>2+</sup>, probably because of its larger dimensions and different chemical nature, which prevent Ca<sup>2+</sup> insertion into the Mg<sup>2+</sup>-site. However, Ca<sup>2+</sup> binding close to the nucleotide site allows a conformational transmission mechanism that forms and opens the PTP. When the Ca<sup>2+</sup> concentration in mitochondria abruptly increases, F<sub>1</sub>F<sub>0</sub>-ATPase binds Ca<sup>2+</sup> and thereby becomes an energy dissipation molecular engine, which leads to cell death.

Even if recent evidence on the PTP persistence in the presence of defective F<sub>1</sub>F<sub>0</sub>-ATPases appar-

ently rules out any involvement of the enzyme in the PTP,<sup>52</sup> the question is still open. Carroll *et al.*<sup>52</sup> report that in the presence of defective F<sub>1</sub>F<sub>0</sub>-ATPases, the PTP forms and may deeply affect mitochondrial morphology and the structure of the cristae. On the other hand, the intact enzyme would maintain the curvature at the edge of the cristae.<sup>53</sup> Most likely, the PTP forms when the enzyme is absent or defective in some subunits, or Ca<sup>2+</sup> insertion alters the F<sub>1</sub>F<sub>0</sub>-ATPase supercomplex organization.

The evidence that compounds targeting the F<sub>1</sub> domain inhibit both the Ca<sup>2+</sup>-dependent ATP hydrolysis and PTP opening suggests that the two mutually dependent cellular events are linked by a molecular mechanism. Therefore, the model in which the F<sub>1</sub>F<sub>0</sub>-ATPase is the key engine of cell life and death is substantiated. Since PTP opening is involved in a variety of physiopathological events, the results should stimulate research on discovery/design of selective drugs targeting Ca<sup>2+</sup>-activated F<sub>1</sub>F<sub>0</sub>-ATPase to modulate the PTP.

## Acknowledgments

Danilo Matteuzzi (Department of Veterinary Medical Sciences, University of Bologna) is gratefully acknowledged for kindly conferring swine hearts from a local abattoir to our laboratory. This work was supported by CARISBO Foundation grants to S.N. (2017/0313).

## Author contributions

C.A. and S.N. designed and conducted the experiments. C.B. performed gel electrophoresis and western blotting analysis. M.F. and M.F. contributed to experimental design. F.T., V.V., A.P., and S.N. conceived, designed, and directed the experiments. S.N. wrote the manuscript with assistance from A.P. and with input from all authors. The final version was approved by all authors.

## Supporting information

Additional supporting information may be found in the online version of this article.

**Figure S1.** Is-F<sub>1</sub> effect on mitochondrial succinate-O<sub>2</sub> oxidase activity.

**Figure S2.** F<sub>1</sub>-ATPase  $\alpha_E$ - $\beta_E$  structure covalently bound to NBD.

**Figure S3.** Polyphenolic phytochemicals bound to the  $\gamma$ - $\beta$ <sub>TP</sub> structure of the F<sub>1</sub>-ATPase.

## Competing interests

The authors declare no competing interests.

## References

- Kühlbrandt, W. 2019. Structure and mechanisms of F-type ATP synthases. *Annu. Rev. Biochem.* **88**: 515–549.
- Boyer, P.D. 2002. Catalytic site occupancy during ATP synthase catalysis. *FEBS Lett.* **512**: 29–32.
- Abrahams, J.P., A.G. Leslie, R. Lutter, *et al.* 1994. Structure at 2.8 Å resolution of F<sub>1</sub>-ATPase from bovine heart mitochondria. *Nature* **370**: 621–628.
- Nicholls, D.G. & S.J. Ferguson. 2013. 3—Quantitative bioenergetics: the measurement of driving forces. In *Bioenergetics*. 4th ed. D.G. Nicholls & S.J. Ferguson, Eds.: 27–51. Boston, MA: Academic Press.
- Hahn, A., K. Parey, M. Bublitz, *et al.* 2016. Structure of a complete ATP synthase dimer reveals the molecular basis of inner mitochondrial membrane morphology. *Mol. Cell* **63**: 445–456.
- Frasch, W.D. 2000. The participation of metals in the mechanism of the F(1)-ATPase. *Biochim. Biophys. Acta* **1458**: 310–325.
- Bald, D., T. Amano, E. Muneyuki, *et al.* 1998. ATP synthesis by F<sub>0</sub>F<sub>1</sub>-ATP synthase independent of noncatalytic nucleotide binding sites and insensitive to azide inhibition. *J. Biol. Chem.* **273**: 865–870.
- Weber, J., C. Bowman, S. Wilke-Mounts, *et al.* 1995. alpha-Aspartate 261 is a key residue in noncatalytic sites of *Escherichia coli* F<sub>1</sub>-ATPase. *J. Biol. Chem.* **270**: 21045–21049.
- Papageorgiou, S., A.B. Melandri & G. Solaini. 1998. Relevance of divalent cations to ATP-driven proton pumping in beef heart mitochondrial F<sub>0</sub>F<sub>1</sub>-ATPase. *J. Bioenerg. Biomembr.* **30**: 533–541.
- Casadio, R. & B.A. Melandri. 1996. CaATP inhibition of the MgATP-dependent proton pump (H<sup>+</sup>-ATPase) in bacterial photosynthetic membranes with a mechanism of alternative substrate inhibition. *J. Biol. Inorgan. Chem.* **1**: 284–291.
- Perlin, D.S., L.R. Latchney, J.G. Wise, *et al.* 1984. Specificity of the proton adenosinetriphosphatase of *Escherichia coli* for adenine, guanine, and inosine nucleotides in catalysis and binding. *Biochemistry* **23**: 4998–5003.
- Nathanson, L. & Z. Gromet-Elhanan. 2000. Mutations in the  $\beta$ -subunit Thr159 and Glu184 of the *Rhodospirillum rubrum* F<sub>0</sub>F<sub>1</sub> ATP synthase reveal differences in ligands for the coupled Mg<sup>2+</sup>- and decoupled Ca<sup>2+</sup>-dependent F<sub>0</sub>F<sub>1</sub> activities. *J. Biol. Chem.* **275**: 901–905.
- Pick, U. & M. Weiss. 1988. A light-dependent dicyclohexylcarbodiimide-sensitive Ca-ATPase activity in chloroplasts which is not coupled to proton translocation. *Eur. J. Biochem.* **173**: 623–628.
- Nesci, S., F. Trombetti, V. Ventrella, *et al.* 2017. Kinetic properties of the mitochondrial F<sub>1</sub>F<sub>0</sub>-ATPase activity elicited by Ca(2<sup>+</sup>) in replacement of Mg(2<sup>+</sup>). *Biochimie* **140**: 73–81.
- Tucker, W.C., A. Schwarz, T. Levine, *et al.* 2004. Observation of calcium-dependent unidirectional rotational motion in recombinant photosynthetic F<sub>1</sub>-ATPase molecules. *J. Biol. Chem.* **279**: 47415–47418.
- Hunter, D.R. & R.A. Haworth. 1979. The Ca<sup>2+</sup>-induced membrane transition in mitochondria. III. Transitional Ca<sup>2+</sup> release. *Arch. Biochem. Biophys.* **195**: 468–477.
- Hunter, D.R., R.A. Haworth & J.H. Southard. 1976. Relationship between configuration, function, and permeability in calcium-treated mitochondria. *J. Biol. Chem.* **251**: 5069–5077.
- Baines, C.P., R.A. Kaiser, N.H. Purcell, *et al.* 2005. Loss of cyclophilin D reveals a critical role for mitochondrial permeability transition in cell death. *Nature* **434**: 658–662.
- Bernardi, P., A. Rasola, M. Forte, *et al.* 2015. The mitochondrial permeability transition pore: channel formation by F<sub>1</sub>-ATP synthase, integration in signal transduction, and role in pathophysiology. *Physiol. Rev.* **95**: 1111–1155.
- Izzo, V., J.M. Bravo-San Pedro, V. Sica, *et al.* 2016. Mitochondrial permeability transition: new findings and persisting uncertainties. *Trends Cell Biol.* **26**: 655–667.
- Pérez, M.J. & R.A. Quintanilla. 2017. Development or disease: duality of the mitochondrial permeability transition pore. *Dev. Biol.* **426**: 1–7.
- Bonora, M., A. Bononi, E. De Marchi, *et al.* 2013. Role of the c subunit of the F<sub>0</sub> ATP synthase in mitochondrial permeability transition. *Cell Cycle* **12**: 674–683.
- Giorgio, V., S. von Stockum, M. Antoniel, *et al.* 2013. Dimers of mitochondrial ATP synthase form the permeability transition pore. *Proc. Natl. Acad. Sci. USA* **110**: 5887–5892.
- Giorgio, V., V. Burchell, M. Schiavone, *et al.* 2017. Ca(2<sup>+</sup>) binding to F-ATP synthase  $\beta$  subunit triggers the mitochondrial permeability transition. *EMBO Rep.* **18**: 1065–1076.
- Nesci, S., F. Trombetti, V. Ventrella, *et al.* 2018. From the Ca<sup>2+</sup>-activated F<sub>1</sub>F<sub>0</sub>-ATPase to the mitochondrial permeability transition pore: an overview. *Biochimie* **152**: 85–93.
- Baev, A.Y., P.A. Elustondo, A. Negoda & E.V. Pavlov. 2018. Osmotic regulation of the mitochondrial permeability transition pore investigated by light scattering, fluorescence and electron microscopy techniques. *Anal. Biochem.* **552**: 38–44.
- Nesci, S. 2017. Mitochondrial permeability transition, F<sub>1</sub>F<sub>0</sub>-ATPase and calcium: an enigmatic triangle. *EMBO Rep.* **18**: 1265–1267.
- Nesci, S. 2018. A lethal channel between the ATP synthase monomers. *Trends Biochem. Sci.* **43**: 311–313.
- Schwingshackl, L., J. Morze & G. Hoffmann. 2019. Mediterranean diet and health status: active ingredients and pharmacological mechanisms. *Br. J. Pharmacol.* <https://doi.org/10.1111/bph.14778>.
- Ahmad, Z., S.S. Hassan & S. Azim. 2017. A therapeutic connection between dietary phytochemicals and ATP synthase. *Curr. Med. Chem.* **24**: 3894–3906.
- Nesci, S., V. Ventrella, F. Trombetti, *et al.* 2016. Preferential nitrite inhibition of the mitochondrial F<sub>1</sub>F<sub>0</sub>-ATPase activities when activated by Ca(2<sup>+</sup>) in replacement of the natural cofactor Mg(2<sup>+</sup>). *Biochim. Biophys. Acta* **1860**: 345–353.
- Bradford, M.M. 1976. A rapid and sensitive method for the quantitation of microgram quantities of protein utilizing the principle of protein-dye binding. *Anal. Biochem.* **72**: 248–254.
- Penin, F., C. Godinot & D.C. Gautheron. 1979. Optimization of the purification of mitochondrial

- F<sub>1</sub>-adenosine triphosphatase. *Biochim. Biophys. Acta* **548**: 63–71.
34. Nicholls, D.G. & S.J. Ferguson. 2013. 7—ATP synthases and bacterial flagella rotary motors. In *Bioenergetics*. 4th ed. D.G. Nicholls & S.J. Ferguson, Eds.: 197–220. Boston, MA: Academic Press.
  35. Nesci, S., V. Ventrella, F. Trombetti, *et al.* 2013. Mussel and mammalian ATP synthase share the same bioenergetic cost of ATP. *J. Bioenerg. Biomembr.* **45**: 289–300.
  36. Cornish-Bowden, A. 1974. A simple graphical method for determining the inhibition constants of mixed, uncompetitive and non-competitive inhibitors. *Biochem. J.* **137**: 143–144.
  37. Nesci, S., V. Ventrella, F. Trombetti, *et al.* 2011. Tributyltin (TBT) and dibutyltin (DBT) differently inhibit the mitochondrial Mg-ATPase activity in mussel digestive gland. *Toxicol. In Vitro* **25**: 117–124.
  38. Nesci, S., F. Trombetti, M. Pirini, *et al.* 2016. Mercury and protein thiols: stimulation of mitochondrial F<sub>1</sub>F<sub>0</sub>-ATPase and inhibition of respiration. *Chem. Biol. Interact.* **260**: 42–49.
  39. Dorgan, L.J., J.L. Urbauer & S.M. Schuster. 1984. Metal dependence and thermodynamic characteristics of the beef heart mitochondrial adenosine triphosphatase. *J. Biol. Chem.* **259**: 2816–2821.
  40. Devenish, R.J., M. Prescott, G.M. Boyle, *et al.* 2000. The oligomycin axis of mitochondrial ATP synthase: OSCP and the proton channel. *J. Bioenerg. Biomembr.* **32**: 507–515.
  41. Symersky, J., D. Osowski, D.E. Walters, *et al.* 2012. Oligomycin frames a common drug-binding site in the ATP synthase. *Proc. Natl. Acad. Sci. USA* **109**: 13961–13965.
  42. Haworth, R.A. & D.R. Hunter. 1979. The Ca<sup>2+</sup>-induced membrane transition in mitochondria. II. Nature of the Ca<sup>2+</sup> trigger site. *Arch. Biochem. Biophys.* **195**: 460–467.
  43. Hiller, R. & C. Carmeli. 1985. Cooperativity among manganese-binding sites in the H<sup>+</sup>-ATPase of chloroplasts. *J. Biol. Chem.* **260**: 1614–1617.
  44. Andrews, W.W., F.C. Hill & W.S. Allison. 1984. Identification of the essential tyrosine residue in the beta subunit of bovine heart mitochondrial F<sub>1</sub>-ATPase that is modified by 7-chloro-4-nitro[14C]benzofurazan. *J. Biol. Chem.* **259**: 8219–8225.
  45. Andrews, W.W., F.C. Hill & W.S. Allison. 1984. Identification of the lysine residue to which the 4-nitrobenzofurazan group migrates after the bovine mitochondrial F<sub>1</sub>-ATPase is inactivated with 7-chloro-4-nitro[14C]benzofurazan. *J. Biol. Chem.* **259**: 14378–14382.
  46. Orriss, G.L., A.G. Leslie, K. Braig, *et al.* 1998. Bovine F<sub>1</sub>-ATPase covalently inhibited with 4-chloro-7-nitrobenzofurazan: the structure provides further support for a rotary catalytic mechanism. *Structure* **6**: 831–837.
  47. Gledhill, J.R., M.G. Montgomery, A.G.W. Leslie, *et al.* 2007. Mechanism of inhibition of bovine F<sub>1</sub>-ATPase by resveratrol and related polyphenols. *Proc. Natl. Acad. Sci. USA* **104**: 13632–13637.
  48. Alavian, K.N., G. Beutner, E. Lazrove, *et al.* 2014. An uncoupling channel within the c-subunit ring of the F<sub>1</sub>F<sub>0</sub> ATP synthase is the mitochondrial permeability transition pore. *Proc. Natl. Acad. Sci. USA* **111**: 10580–10585.
  49. Carraro, M., V. Checchetto, G. Sartori, *et al.* 2018. High-conductance channel formation in yeast mitochondria is mediated by F-ATP synthase e and g subunits. *Cell. Physiol. Biochem.* **50**: 1840–1855.
  50. Guo, L., M. Carraro, G. Sartori, *et al.* 2018. Arginine 107 of yeast ATP synthase subunit g mediates sensitivity of the mitochondrial permeability transition to phenylglyoxal. *J. Biol. Chem.* **293**: 14632–14645.
  51. Neginskaya, M.A., M.E. Solesio, E.V. Berezhnaya, *et al.* 2019. ATP synthase C-subunit-deficient mitochondria have a small cyclosporine A-sensitive channel, but lack the permeability transition pore. *Cell Rep.* **26**: 11–17.e2.
  52. Carroll, J., J. He, S. Ding, *et al.* 2019. Persistence of the permeability transition pore in human mitochondria devoid of an assembled ATP synthase. *Proc. Natl. Acad. Sci. USA* **116**: 12816–12821.
  53. Paumard, P., J. Vaillier, B. Coulary, *et al.* 2002. The ATP synthase is involved in generating mitochondrial cristae morphology. *EMBO J.* **21**: 221–230.



# The inhibition of gadolinium ion ( $Gd^{3+}$ ) on the mitochondrial $F_1F_0$ -ATPase is linked to the modulation of the mitochondrial permeability transition pore

Cristina Algeri, Fabiana Trombetti, Alessandra Pagliarani<sup>\*</sup>, Micaela Fabbri, Salvatore Nesci<sup>\*</sup>

Department of Veterinary Medical Sciences (DIMEVET), University of Bologna, via Tolara di Sopra, 50, 40064, Ozzano Emilia, Bologna, Italy

## ARTICLE INFO

### Keywords:

Gadolinium ion  
Mitochondria  
 $F_1F_0$ -ATPase  
Permeability transition pore  
Metal cofactors  
Enzyme kinetics

## ABSTRACT

The mitochondrial permeability transition pore (PTP), which drives regulated cell death when  $Ca^{2+}$  concentration suddenly increases in mitochondria, was related to changes in the  $Ca^{2+}$ -activated  $F_1F_0$ -ATPase. The effects of the gadolinium cation ( $Gd^{3+}$ ), widely used for diagnosis and therapy, and reported as PTP blocker, were evaluated on the  $F_1F_0$ -ATPase activated by  $Mg^{2+}$  or  $Ca^{2+}$  and on the PTP.  $Gd^{3+}$  more effectively inhibits the  $Ca^{2+}$ -activated  $F_1F_0$ -ATPase than the  $Mg^{2+}$ -activated  $F_1F_0$ -ATPase by a mixed-type inhibition on the former and by uncompetitive mechanism on the latter. Most likely  $Gd^{3+}$  binding to  $F_1$ , is favoured by  $Ca^{2+}$  insertion. The maximal inactivation rates ( $k_{inact}$ ) of pseudo-first order inactivation are similar either when the  $F_1F_0$ -ATPase is activated by  $Ca^{2+}$  or by  $Mg^{2+}$ . The half-maximal inactivator concentrations ( $K_I$ ) are  $2.35 \pm 0.35$  mM and  $0.72 \pm 0.11$  mM, respectively. The potency of a mechanism-based inhibitor ( $k_{inact}/K_I$ ) also highlights a higher inhibition efficiency of  $Gd^{3+}$  on the  $Ca^{2+}$ -activated  $F_1F_0$ -ATPase ( $0.59 \pm 0.09$   $mM^{-1} \cdot s^{-1}$ ) than on the  $Mg^{2+}$ -activated  $F_1F_0$ -ATPase ( $0.13 \pm 0.02$   $mM^{-1} \cdot s^{-1}$ ). Consistently, the PTP is desensitized in presence of  $Gd^{3+}$ . The  $Gd^{3+}$  inhibition on both the mitochondrial  $Ca^{2+}$ -activated  $F_1F_0$ -ATPase and the PTP strengthens the link between the PTP and the  $F_1F_0$ -ATPase when activated by  $Ca^{2+}$  and provides insights on the biological effects of  $Gd^{3+}$ .

## 1. Introduction

The  $F_1F_0$ -ATPase, an oligomeric complex of the inner mitochondrial membrane (IMM) ubiquitous in mammals, is an energy-transducing machine characterized by a reversible working mode of ATP synthesis/hydrolysis [1]. According to the chemiosmotic theory, the  $H^+$  transfer from the mitochondrial matrix to the intermembrane space by the respiratory complexes, pushed by substrate oxidation, creates the protonmotive force ( $\Delta p$ ) that is converted into a useful chemical form, ATP [2]. Contrary, in the reverse-mode, the hydrolysis of the high-energy phosphoanhydride bonds of ATP drives  $H^+$  pumping in the intermembrane space and energizes the IMM. The bi-functional catalysis of the  $F_1F_0$ -ATPase is a unique energy transmission mechanism sustained by the structural enzyme arrangement in two molecular motors, a hydrolytic  $F_1$  sector and a hydrophobic  $F_0$  sector. The two sectors are coupled by a reversible torque generation [3,4] (Fig. 1). The catalytic domain  $F_1$  is a globular hexamer in which three  $\alpha$  subunits and three  $\beta$  subunits alternate.  $F_1$  contains three catalytic and three non-catalytic sites which bind adenine nucleotides. The catalytic sites are each  $\beta$

subunit at the interface with the adjacent  $\alpha$  subunit, whereas the non-catalytic sites are on each  $\alpha$  subunit at the interface with the adjacent  $\beta$  subunit [5]. During the ATP synthesis/hydrolysis, according to the “binding change model” [6], the conformational change in the  $(\alpha\beta)_3$  assembly occurs during the rotor rotation. During a  $360^\circ$  rotation the catalytic and non-catalytic site conformations change in TP (binding ATP), DP (binding ADP), and E (empty) conformations, driven by the rotation of the central stalk. The  $\beta$  subunits undergo a decrease in affinity for nucleotides with the sequential transition  $\beta_{TP} \rightarrow \beta_{DP} \rightarrow \beta_E$ , while the  $\alpha$  subunits only undergo the conformational changes during the rotor rotation. This mechanochemical mechanism of the  $F_1$  domain is driven by the  $H^+$  flow through  $F_0$  which generates the torsional movement. The  $H^+$  translocation from one side to the opposite side of the IMM occurs within two asymmetrical half-channels on a subunit at the interface with the c-ring which hosts the  $H^+$  binding sites [7]. Differently from the bacterial enzyme, the mitochondrial  $F_0$  domain contains supernumerary subunits which intervene during the enzyme dimerization and oligomerization, which in turn play a morphological role in mitochondrial *crista* formation [8,9]. Moreover, the

<sup>\*</sup> Corresponding authors.

E-mail addresses: [alessandra.pagliarani@unibo.it](mailto:alessandra.pagliarani@unibo.it) (A. Pagliarani), [salvatore.nesci@unibo.it](mailto:salvatore.nesci@unibo.it) (S. Nesci).

<https://doi.org/10.1016/j.ijbiomac.2021.06.065>

Received 10 April 2021; Received in revised form 7 June 2021; Accepted 9 June 2021

Available online 11 June 2021

0141-8130/© 2021 Published by Elsevier B.V.

supernumerary subunits are important to form and open the permeability transition pore (PTP) inside the *c*-ring [10].

Accordingly, the IMM becomes permeable to solutes up to 1.5 kDa in a process defined permeability transition (PT) when the PTP, a  $\text{Ca}^{2+}$ -activated channel with high conductance, opens. It seems ascertained that the  $\text{F}_1\text{F}_0$ -ATPase is the main playmaker which triggers the PTP formation and opening. Additionally, a low conductance channel inhibited by both CsA and BKA could be formed by the adenine nucleotide translocase isoforms [11,12]. After about 50 years of debate, the arcane molecular mechanism of PTP was revealed by Sazanov's group [10]. When  $\text{Ca}^{2+}$  concentration increases in the mitochondrial matrix, the  $\text{F}_1\text{F}_0$ -ATPase can replace the natural cofactor  $\text{Mg}^{2+}$  with  $\text{Ca}^{2+}$  on  $\beta$  subunits [13]. The  $\text{Ca}^{2+}$ -activated enzyme can sustain ATP hydrolysis [14]. Since  $\text{Ca}^{2+}$  has a larger atomic radius than  $\text{Mg}^{2+}$ , it induces conformational changes in the  $\text{F}_1$  domain which are transmitted to the membrane-embedded subunits [15]. Under physiological and pathological conditions, according to the “bent-pull” model of the  $\text{Ca}^{2+}$ -activated  $\text{F}_1\text{F}_0$ -ATPase [16], the PTP opens within the *c*-ring. In detail, the lipid plug anchored to *e* subunit, a lyso-phosphatidylserine which penetrates and fills the hole of the *c*-ring at the intermembrane space, is pulled out by *e* subunit displacement. The different conformational states of the  $\text{F}_1\text{F}_0$ -ATPase when activated by  $\text{Ca}^{2+}$ , which apparently cannot occur when  $\text{Mg}^{2+}$  plays the cofactor role, permit the detachment of the  $\text{F}_1$  domain by pushing the phosphatidylserine that fills the hole at the matrix side when water molecules enter the *c*-ring [10]. The  $\text{F}_1\text{F}_0$ -ATPase activated by  $\text{Ca}^{2+}$  as cofactor undergoes conformational changes which open the PTP [17]. Since PTP opening leads to cell death [18] and

PTP dysregulation is increasingly involved in severe human diseases [2], once identified the main macromolecular target responsible for PTP formation, several compounds have been considered and investigated as potential pore inhibitors [19].

The rare earth transition metals known as Lanthanides are widely used in medicine due to their physicochemical characteristics [20]. They play an increasingly recognized role in diagnosis and therapy, other than being widely exploited in research. Gadolinium (Gd)-based compounds belonging to organometals are widely used in Magnetic Resonance Imaging (MRI) as a contrast medium [21] as well as putative anticancer drugs [22]. Although for clinical use Gd ion ( $\text{Gd}^{3+}$ ) is always chelated with specific ligands due to its high toxicity, it seems to accumulate in the tissues, especially in the brain, therefore its long-term use has raised emerging concern [23]. Interestingly, the trivalent  $\text{Gd}^{3+}$  has biophysical characteristics similar to the divalent  $\text{Ca}^{2+}$  (radius of  $\text{Gd}^{3+}$  1.05–1.11 Å vs  $\text{Ca}^{2+}$  1.00–1.06 Å), which allow it to replace  $\text{Ca}^{2+}$  in its biological and biochemical mechanisms. Accordingly, the biological effects are currently ascribed to the cationic form  $\text{Gd}^{3+}$ . Most likely,  $\text{Gd}^{3+}$  acts at the cellular level by directly interfering with the  $\text{Ca}^{2+}$  entry pathways.  $\text{Gd}^{3+}$  is also used in experimental tests as an inhibitor of  $\text{Ca}^{2+}$  channels activated by stretching [24]. The  $\text{Gd}^{3+}$ -based compounds used in MRI seem to have negative effects on the mitochondrial activity by altering ATP production, reducing mitochondrial oxidative capacities and also promoting cellular apoptosis [25] and other forms of cell death [26]. These effects were also related to the  $\text{Gd}^{3+}$  capability to promote PTP opening [27]. Conversely, the cation was also reported to act as a PTP blocker in mammalian mitochondria [16].

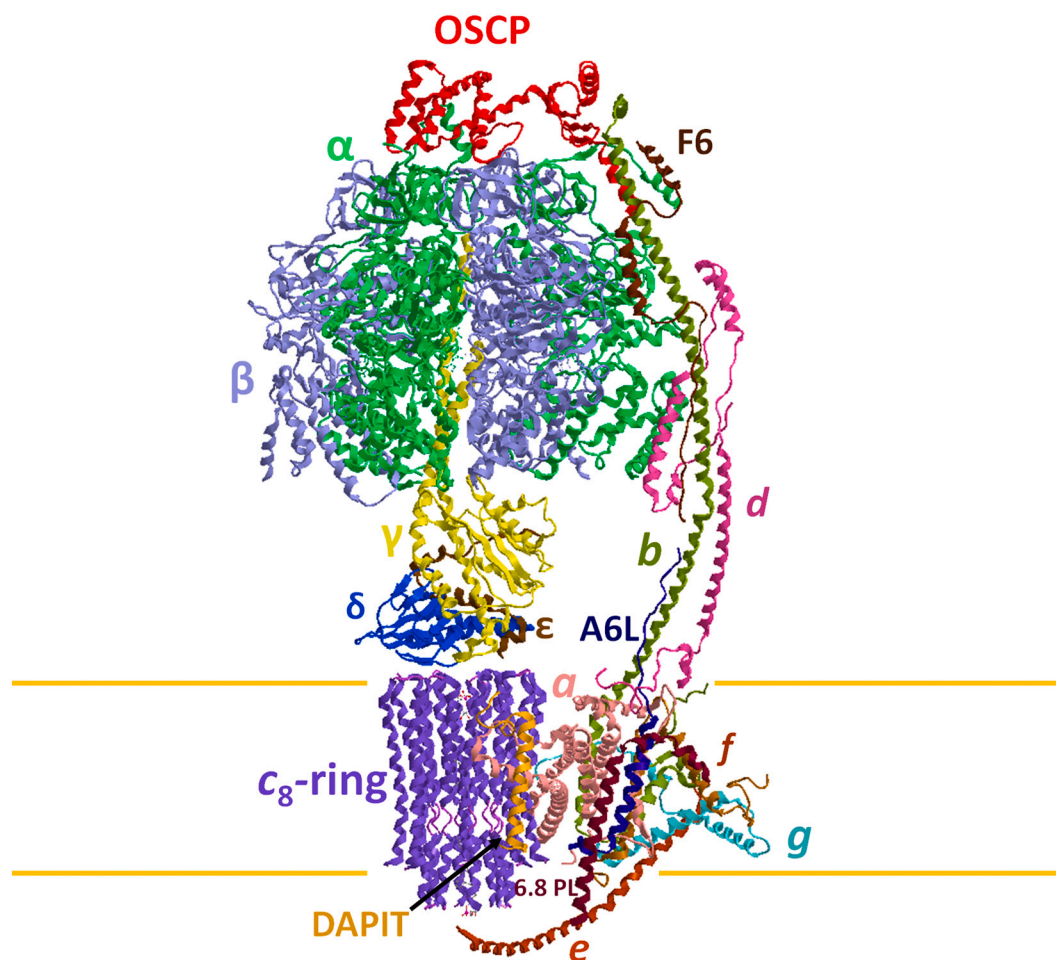


**Fig. 1.** Subunit composition of mammalian mitochondrial  $\text{F}_1\text{F}_0$ -ATPase. The enzyme subunits are drawn as ribbon representations obtained from modified PDB ID code: 6TT7. The letter colors are the same as those of the subunits to which the structures belong.

The possibility that  $Gd^{3+}$  may act on the mammalian  $F_1F_0$ -ATPase activated by  $Ca^{2+}$  differently from the  $Mg^{2+}$ -activated enzyme was investigated and compared with the effects on PTP opening. The results may not only contribute to casting light on some still unexplored molecular mechanisms of  $Gd^{3+}$  toxicity [26], but also may improve the knowledge on the mechanism of PTP formation and opening and broaden the spectrum of exogenous PTP modulators. Moreover, since membrane permeabilization often results in a cellular catastrophe and  $Gd^{3+}$  is widely employed in medical fields, such as research, diagnosis and therapy, the assessment of the  $Gd^{3+}$  action mechanism on the key enzyme in bioenergetics may be extremely useful to adequately exploit  $Gd^{3+}$  properties for medical purposes.

## 2. Materials and methods

### 2.1. Chemicals

Oligomycin (a mixture of oligomycins A, B and C), and Fura-FF were purchased from Vinci-Biochem (Vinci, Italy).  $Na_2ATP$  and gadolinium trichloride ( $GdCl_3$ ) were obtained from Sigma–Aldrich (Milan, Italy). Quartz double distilled water was used for all reagent solutions.

### 2.2. Preparation of the mitochondrial fractions

Swine hearts (*Sus scrofa domestica*) were collected at a local abattoir and transported to the lab within 2 h in ice buckets at 0–4 °C. After removal of fat and blood clots as much as possible, approximately 30–40 g of heart tissue was rinsed in ice-cold washing Tris-HCl buffer (medium A) consisting of 0.25 M sucrose, 10 mM Tris(hydroxymethyl)aminomethane (Tris), pH 7.4 and finely chopped into fine pieces with scissors. Each preparation was made from one heart. Once rinsed, tissues were gently dried on blotting paper and weighted. Then tissues were homogenized in medium B consisting of 0.25 M sucrose, 10 mM Tris, 1 mM EDTA (free acid), 0.5 mg/ml BSA fatty acid free, pH 7.4 with HCl at a ratio of 10 ml medium B per 1 g of fresh tissue. After a preliminary gentle break up by Ultraturrax T25, the tissue was carefully homogenized by a motor-driven teflon pestle homogenizer (Braun Melsungen Type 853202) at 650 rpm with 3 up-and-down strokes. The mitochondrial fraction was then obtained by stepwise centrifugation (Sorvall RC2-B, rotor SS34). Briefly, the homogenate was centrifuged at 1000 ×g for 5 min, thus yielding a supernatant and a pellet. The pellet was re-homogenized under the same conditions of the first homogenization and re-centrifuged at 1000 ×g for 5 min. The gathered supernatants from these two centrifugations, filtered through four cotton gauze layers, were centrifuged at 10,500 ×g for 10 min to yield the raw mitochondrial pellet. The raw pellet was resuspended in medium A and further centrifuged at 10,500 ×g for 10 min to obtain the final mitochondrial pellet. The latter was resuspended by gentle stirring using a Teflon Potter Elvehjem homogenizer in a small volume of medium A, thus obtaining a protein concentration of 30 mg/ml [28]. All steps were carried out at 0–4 °C. The protein concentration was determined according to the colorimetric method of Bradford [29] by Bio-Rad Protein Assay kit II with BSA as standard. The mitochondrial preparations were then stored in liquid nitrogen until the evaluation of  $F_1F_0$ -ATPase activities.

### 2.3. Mitochondrial F-ATPase activity assays

Thawed mitochondrial preparations were immediately used for F-ATPase activity assays. The capability of ATP hydrolysis was assayed in a reaction medium (1 ml). The optimal conditions to obtain the maximal activity of the  $F_1F_0$ -ATPase, which depend on substrates concentration and pH values, are at 0.15 mg mitochondrial protein and 75 mM ethanolamine–HCl buffer pH 9.0, 6.0 mM  $Na_2ATP$  and 2.0 mM  $MgCl_2$  for the  $Mg^{2+}$ -activated  $F_1F_0$ -ATPase assay, and 75 mM ethanolamine–HCl buffer pH 8.8, 3.0 mM  $Na_2ATP$  and 2.0 mM  $CaCl_2$  for the  $Ca^{2+}$ -activated

$F_1F_0$ -ATPase assay [14,30]. These assay conditions were previously proven to elicit the maximal enzyme activities either stimulated by  $Mg^{2+}$  or by  $Ca^{2+}$  in swine heart mitochondria [31]. After 5 min preincubation at 37 °C, the reaction, carried out at the same temperature, was started by the addition of the substrate  $Na_2ATP$  and stopped after 5 min by the addition of 1 ml of ice-cold 15% (w/w) trichloroacetic acid (TCA) aqueous solution. Once the reaction was stopped, vials were centrifuged for 15 min at 3500 rpm (Eppendorf Centrifuge 5202). In the supernatant, the concentration of inorganic phosphate (Pi) hydrolyzed by known amounts of mitochondrial protein, which is an indirect measure of F-ATPase activity, was spectrophotometrically evaluated [32]. According to the method employed, to detect the Pi release by the enzymatic reaction, the Pi released independently of the  $F_1F_0$ -ATPase activity should be quantified. To this aim, 1 µl from a stock solution of 3 mg/ml oligomycin in dimethylsulfoxide was directly added to the reaction mixture before starting the reaction. The total ATPase activity was calculated by detecting the Pi in control tubes run in parallel and containing 1 µl dimethylsulfoxide per ml reaction system. In each experimental set, control tubes were alternated to the condition to be tested. The employed dose of oligomycin, specific inhibitor of F-ATPases which selectively blocks the  $F_0$  subunit ensured maximal enzyme activity inhibition and was currently used in F-ATPase assays [30].

To test the effect of  $Gd^{3+}$  on the differently activated  $F_1F_0$ -ATPase activities, aqueous solutions of  $GdCl_3$  at different standard concentrations were prepared immediately before each experimental set. Small aliquots (10 µl) of these solutions were added to the reaction system and incubated at 37 °C before starting the  $F_1F_0$ -ATPase reaction. Control tubes contained the same final volume, adjusted with 10 µl of the reaction buffer.

In all experiments, the  $F_1F_0$ -ATPase activity was routinely measured by subtracting, from the Pi hydrolyzed by total ATPase activity, the Pi hydrolyzed in the presence of oligomycin [28]. In all experiments the F-ATPase activity, either activated by  $Ca^{2+}$  as cofactor or by  $Mg^{2+}$ , was expressed as  $\mu\text{mol Pi} \cdot \text{mg protein}^{-1} \cdot \text{min}^{-1}$ .

### 2.4. Kinetic analyses

The inhibition mechanism of  $Gd^{3+}$  on the  $Ca^{2+}$ - or  $Mg^{2+}$ -activated  $F_1F_0$ -ATPases was explored by the graphical methods of Dixon and Cornish-Bowden plots, which complement one another. [33] To this aim, the  $1/v$  (reciprocal of the enzyme activity  $v$ ) in Dixon plot or the  $S/v$  ratio in Cornish-Bowden plot were plotted as a function of  $GdCl_3$  concentration. In all plots the enzyme specific activity was taken as the expression of  $v$ . To build these plots, different experimental sets were designed in which the F-ATPase activity was evaluated in the presence of increasing  $GdCl_3$  concentrations at two ATP concentrations, keeping the divalent cofactor ( $Mg^{2+}$  or  $Ca^{2+}$ ) concentration constant. In these plots and in the definition of the binary or ternary complexes  $S$  indicates the ATP substrate. The values of  $K_i$ , which corresponds to the dissociation constant of the  $EI$  complex were calculated from the abscissa (changed to positive) of the intercept of the straight lines obtained in the Dixon plots. The values of  $K'_i$ , which represent the dissociation constant of the ternary  $ESI$  complex, were calculated as the abscissa (changed to positive) of the intercept of the straight lines obtained in the Cornish-Bowden plots.

The inactivation kinetics was investigated by incubating the mitochondrial suspensions in the presence of various  $GdCl_3$  concentrations (1.0–2.0–4.0 mM  $GdCl_3$  when the  $F_1F_0$ -ATPase was activated by  $Mg^{2+}$  as cofactor, and 1.0–1.5–2.0 mM  $GdCl_3$  when the  $F_1F_0$ -ATPase was activated by  $Ca^{2+}$ ). The  $F_1F_0$ -ATPase reaction activated by either  $Mg^{2+}$  or  $Ca^{2+}$  as cofactor was stopped after different time intervals (1–7 min) by 1 ml TCA 15% (w/w) addition. The pseudo first-order rate constants ( $k_{obs}$ ) for the enzyme inactivation were determined in both cases by plotting the natural logarithm of the residual activity vs time and extracting the rate constant from the slope [34].

A double-reciprocal plot is created by plotting the  $1/k_{obs}$  (x axis) as a

function of the inverse of the  $\text{GdCl}_3$  concentrations ( $1/[\text{GdCl}_3]$ ) (y axis). The maximal inactivation rate ( $k_{\text{inact}}$ ) can be accurately determined and thus the inhibitor concentration at  $1/2k_{\text{inact}}$  ( $K_i$ ) can also be determined with accuracy because a straight line is formed. The y-intercept is  $1/k_{\text{inact}}$ , and the x-intercept is  $-1/K_i$ . The ratio  $k_{\text{inact}}/K_i$  is used to calculate the inhibitor efficiency, a rate constant for the potency of a mechanism-based inhibitor [35].

### 2.5. Evaluation of PTP

Immediately after the preparation of swine heart mitochondrial fractions, fresh mitochondrial suspensions (1 mg/ml) were energized in the assay buffer (130 mM KCl, 1 mM  $\text{KH}_2\text{PO}_4$ , 20 mM HEPES, pH 7.2 with TRIS), incubated at 25 °C with 1  $\mu\text{g}/\text{ml}$  rotenone and 5 mM succinate as respiratory substrate. To evaluate  $\text{Gd}^{3+}$  effect, selected  $\text{Gd}^{3+}$  concentrations, obtained by sampling small aliquots from standard  $\text{GdCl}_3$  aqueous solutions, as described in Section 2.3, were added to the mitochondrial suspensions before PTP evaluation. PTP opening was induced by the addition of low concentrations of  $\text{Ca}^{2+}$  (10  $\mu\text{M}$ ) as  $\text{CaCl}_2$  aqueous solution at fixed time intervals (1 min). The  $\text{Ca}^{2+}$  retention capacity (CRC), whose lowering indicates mPTP opening, was spectrofluorometrically evaluated in the presence of 0.8  $\mu\text{M}$  Fura-FF. The probe has different spectral properties in the absence and in the presence of  $\text{Ca}^{2+}$ , namely it displays excitation/emission spectra of 365/514 nm in the absence of  $\text{Ca}^{2+}$  (Fura-FF low  $\text{Ca}^{2+}$ ) and shifts to 339/507 nm in the presence of high  $\text{Ca}^{2+}$  concentrations (Fura-FF high  $\text{Ca}^{2+}$ ). PTP opening, was evaluated by the increase in the fluorescence intensity ratio (Fura-FF high  $\text{Ca}^{2+}$ )/(Fura-FF low  $\text{Ca}^{2+}$ ), which indicates a decrease in CRC [36]. All measurements were processed by LabSolutions RF software.

### 2.6. Calculations and statistics

The data represent the mean  $\pm$  SD (shown as vertical bars in the figures) of the number of experiments reported in the figure captions. In each experimental set, the analyses were carried out on different pools of animals. Statistical analyses were performed by SIGMASTAT software. The analysis of variance followed by Students–Newman–Keuls' test when F values indicated significance ( $P \leq 0.05$ ) was applied. Percentage data were arcsin-transformed before statistical analyses to ensure normality.

## 3. Results and discussion

The mPTP opening and the mitochondrial  $\text{F}_1\text{F}_0$ -ATPase participation in the mPTP are both linked to an abrupt  $\text{Ca}^{2+}$  increase in mitochondria. In detail, the substitution of the natural cofactor  $\text{Mg}^{2+}$  by  $\text{Ca}^{2+}$  as cofactor in the  $\beta$  subunits of the  $\text{F}_1\text{F}_0$ -ATPase [13] has been involved in the mechanism of mPTP formation [9,30]. The mitochondrial  $\text{F}_1\text{F}_0$ -ATPase can be activated by either  $\text{Mg}^{2+}$  or  $\text{Ca}^{2+}$ , which can both act as cofactor, even if by displaying different kinetic features [14,17]. The rare earth metal cation  $\text{Gd}^{3+}$ , whose effects on the mPTP are still partially known, offers the opportunity to verify the effect on the  $\text{F}_1\text{F}_0$ -ATPase and to explore its putative connection with the mPTP. Accordingly,  $\text{Gd}^{3+}$  was reported to induce mitochondrial dysfunction, probably due to PTP opening [27]. Acute toxicity of the intraperitoneally injected salt of all the stable rare earth compounds in mice at level of 300 to 500 mg/Kg were produced [37]. In erythrocyte membranes  $\text{Gd}^{3+}$ , which is able to interact with membrane phospholipids [38], would act as pore former [39]. Conversely,  $\text{Gd}^{3+}$  was shown to inhibit membrane permeabilization by physically modifying the membrane structure in a model system [40]. In this paper all the mitochondrial effects of  $\text{Gd}^{3+}$  were tested by adding selected concentrations of the chloride salt  $\text{GdCl}_3$  which in aqueous media dissociates yielding  $\text{Gd}^{3+}$  and  $\text{Cl}^-$ . We tried to exploit the  $\text{Gd}^{3+}$  inhibition mechanism to understand its modulatory role of  $\text{Gd}^{3+}$  on the  $\text{Ca}^{2+}$ -activated  $\text{F}_1\text{F}_0$ -ATPase when the PTP forms. So

the observed effects are currently ascribed to  $\text{Gd}^{3+}$ , known to interact with proteins.

### 3.1. $\text{Gd}^{3+}$ affects the $\text{F}_1\text{F}_0$ -ATPase activity either activated by $\text{Mg}^{2+}$ or by $\text{Ca}^{2+}$

The effect of  $\text{GdCl}_3$ , in the range of 0.01–5.0 mM, was evaluated on the  $\text{F}_1\text{F}_0$ -ATPase either activated by  $\text{Mg}^{2+}$  or by  $\text{Ca}^{2+}$  as cofactor (Fig. 2). Increasing  $\text{GdCl}_3$  concentrations promote an exponential  $\text{F}_1\text{F}_0$ -ATPase activity decay independently of the divalent cofactors that sustain ATP hydrolysis. Both the differently activated  $\text{F}_1\text{F}_0$ -ATPase activities are increasingly inhibited by increasing  $\text{GdCl}_3$  concentrations. However, the main difference between the  $\text{F}_1\text{F}_0$ -ATPase activities when activated by  $\text{Mg}^{2+}$  or by  $\text{Ca}^{2+}$  as cofactor is that the  $\text{F}_1\text{F}_0$ -ATPase when activated by  $\text{Mg}^{2+}$  only attains a maximal 40% inhibition at the highest concentration tested (5 mM  $\text{GdCl}_3$ ) (Fig. 2A), while when activated by  $\text{Ca}^{2+}$  the enzyme is progressively inhibited up to attain a value close to zero at 5 mM  $\text{GdCl}_3$  (Fig. 2B).

### 3.2. The Inhibition mechanism is revealed by inhibition kinetics analyses

Kinetic studies, based on the building of Dixon and Cornish-Bowden plots, can lead to define the features of the enzyme–inhibitor complex in the presence or in the absence of the ATP substrate or cation cofactors. These kinetic analyses were carried out to understand the  $\text{GdCl}_3$  inhibition mechanism, most likely exerted by  $\text{Gd}^{3+}$ , on the  $\text{F}_1\text{F}_0$ -ATPase. The inhibition exerted by  $\text{Gd}^{3+}$  on the  $\text{Mg}^{2+}$ -activated  $\text{F}_1\text{F}_0$ -ATPase shows a competitive mechanism with respect to the ATP substrate (Fig. 3A, B) and an uncompetitive type mechanism with respect to the  $\text{Mg}^{2+}$  cofactor (Fig. 3C, D). The competitive inhibition indicates that the inhibitor only binds to the free enzyme, while the uncompetitive inhibition indicates that  $\text{Gd}^{3+}$  only binds to the enzyme- $\text{Mg}^{2+}$  complex. According to the mechanism of uncompetitive inhibition, usually observed when the enzyme has two or more binding sites [41],  $\text{Gd}^{3+}$  binds to a different site than that of the  $\text{Mg}^{2+}$  cofactor, but only when the enzyme–substrate (ES) complex is already formed, to yield the enzyme–substrate-inhibitor (ESI) complex.

The competitive inhibition mechanism is also exerted by  $\text{Gd}^{3+}$  on the  $\text{Ca}^{2+}$ -activated  $\text{F}_1\text{F}_0$ -ATPase with respect to the ATP substrate (Fig. 4A, B).  $\text{Gd}^{3+}$  blocks the ATP binding to the enzyme by inhibiting the ATPase activity irrespective of the cation cofactor. The  $K_i$  value of the  $\text{F}_1\text{F}_0$ -ATPase is about three times lower than that of the  $\text{Mg}^{2+}$ -activated  $\text{F}_1\text{F}_0$ -ATPase ( $0.5 \pm 0.4$  mM vs  $1.4 \pm 0.1$  mM) (Table 1). These  $K_i$  values indicate that  $\text{Gd}^{3+}$  more efficiently competes with ATP in the substrate binding site to form the binary complex (EI) when the  $\text{F}_1\text{F}_0$ -ATPase is activated by  $\text{Ca}^{2+}$  as cofactor than when the enzyme is activated by  $\text{Mg}^{2+}$ . Moreover, when the natural cofactor  $\text{Mg}^{2+}$  is substituted by  $\text{Ca}^{2+}$ , the  $\text{F}_1\text{F}_0$ -ATPase undergoes a mixed type inhibition mechanism on the cofactor (Fig. 4C, D). This inhibition type indicates that the inhibitor  $\text{Gd}^{3+}$  can bind either to the free enzyme or to the enzyme  $\text{Ca}^{2+}$ -complex. These results prove that  $\text{Gd}^{3+}$  and  $\text{Ca}^{2+}$  bind to distinct enzyme sites. Since the  $\text{Gd}^{3+}$  binding site does not overlap with the  $\text{Ca}^{2+}$  binding site on  $\beta$  subunits [13], the  $\text{Ca}^{2+}$ -activated  $\text{F}_1\text{F}_0$ -ATPase can form either a binary (enzyme- $\text{Gd}^{3+}$ ) or a ternary ( $\text{Ca}^{2+}$ -enzyme- $\text{Gd}^{3+}$ ) complex with the inhibitor. However, on considering the dissociation constants of the enzyme-inhibitor complex ( $K_i$ ) and of the enzyme-substrate-inhibitor complex ( $K'_i$ ), since the  $K_i$  value is three times lower than the  $K'_i$  value, the formation of the binary complex (enzyme- $\text{Gd}^{3+}$ ) is preferred with respect to that of the ternary complex (enzyme-cofactor-inhibitor). Moreover, the  $K'_i$  values in the presence of  $\text{Mg}^{2+}$  or  $\text{Ca}^{2+}$  as cofactor are similar (Table 1), thus pointing out that the ternary complex is independent of the activating cation. In other words, even if  $\text{Gd}^{3+}$  preferentially binds to the enzyme before the cofactor binding to form the binary complex, it binds to the enzyme-cofactor complex to form the ternary complex with the same strength when the cofactor is  $\text{Mg}^{2+}$  or  $\text{Ca}^{2+}$ .

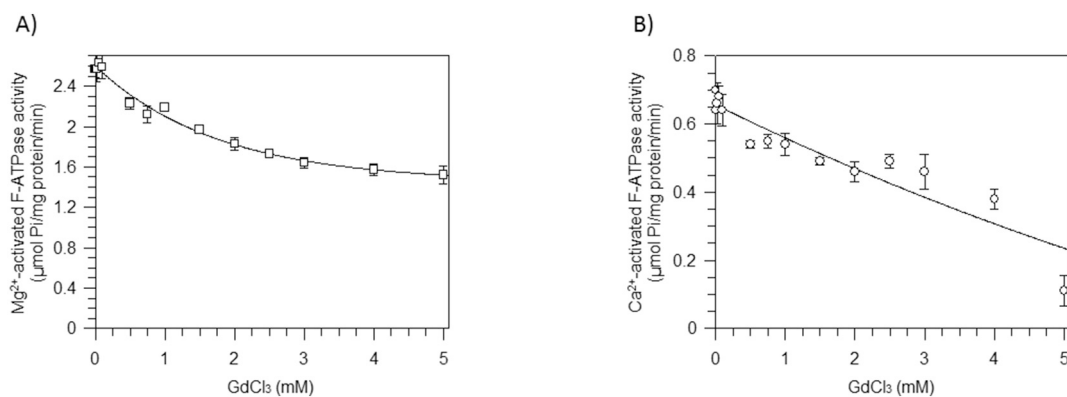


**Fig. 2.** Dose-response curve of  $\text{GdCl}_3$  inhibition of the  $\text{F}_1\text{F}_0$ -ATPase activity. A)  $\text{F}_1\text{F}_0$ -ATPase activated by  $\text{Mg}^{2+}$  ( $\text{Mg}^{2+}$ -activated  $\text{F}_1\text{F}_0$ -ATPase) ( $\square$ ) and by  $\text{Ca}^{2+}$  ( $\text{Ca}^{2+}$ -activated  $\text{F}_1\text{F}_0$ -ATPase) ( $\circ$ ) activities in the presence of increasing  $\text{GdCl}_3$  concentrations. Data represent the mean  $\pm$  SD from three independent experiments carried out on different mitochondrial preparations.

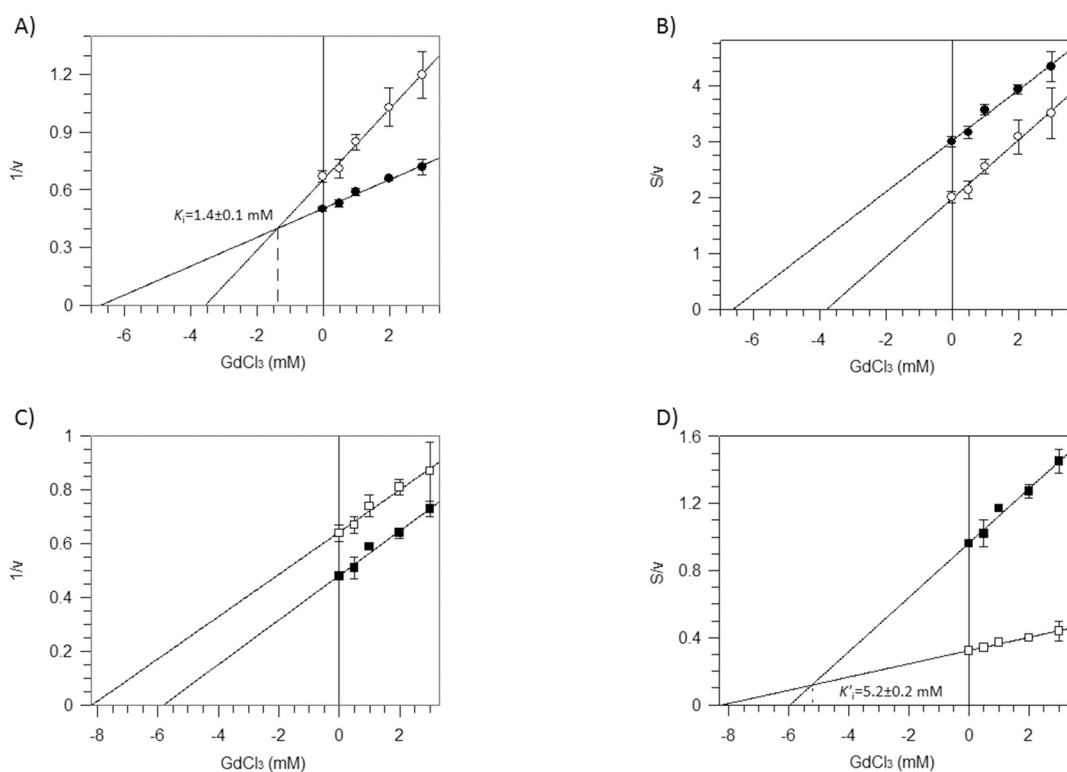


**Fig. 3.** Inhibition kinetics of the mitochondrial  $\text{Mg}^{2+}$ -activated  $\text{F}_1\text{F}_0$ -ATPase by  $\text{GdCl}_3$ . Dixon (A, C) and Cornish–Bowden (B, D) plots at 2 mM  $\text{MgCl}_2$  plus 3 mM ( $\circ$ ) or 6 mM ( $\bullet$ ) ATP (A, B); at 6 mM ATP plus 0.5 mM ( $\square$ ) or 2 mM ( $\blacksquare$ )  $\text{Mg}^{2+}$  (C, D). The experimental design to build these plots is detailed in Section 2.4. All points represent the mean  $\pm$  SD (vertical bars) of four distinct experiments carried out on different mitochondrial preparations.

### 3.3. How the cofactor may affect the $\text{F}_1\text{F}_0$ -ATPase function

The different size of cations with a larger radius than  $\text{Mg}^{2+}$  (1.45 Å) such as  $\text{Ca}^{2+}$  (1.94 Å) would promote a different coordination chemistry in the catalytic sites of the  $\text{F}_1$  hexamer. The hypothesized more flexible coordination geometry, characterized by irregular bond distances and angles in the  $\beta$  subunits induced by  $\text{Ca}^{2+}$ , allows the accommodation of up to eight bonds while  $\text{Mg}^{2+}$  forms hexacoordinated octahedral complexes [42]. The nucleotide-binding to the catalytic and non-catalytic  $\text{F}_1\text{F}_0$ -ATPase subunits requires the coordination of the essential cofactor  $\text{Mg}^{2+}$  which contributes to yield the binding site asymmetry and generation of the different affinities for nucleotides [43]. The presence of  $\text{Ca}^{2+}$  as cofactor modifies the enzyme kinetic parameters [14] and ascribes to the  $\text{F}_1\text{F}_0$ -ATPase a new role in mitochondrial

biology [9,17]. Indeed, the new cryo-EM structure of the  $\text{F}_1\text{F}_0$ -ATPase [10] highlights a thorough conformational change in the enzyme structure when the  $\text{Ca}^{2+}$  replaces  $\text{Mg}^{2+}$  in the catalytic site and triggers the PTP formation according to the “bent-pull” model of the c-ring-gated channel [16]. The role of  $\text{Ca}^{2+}$  in the catalytic sites of the enzyme is corroborated by mutagenesis studies carried out by Bernardi’s group [15]. Among the six bonds that coordinate the  $\text{Mg}^{2+}$  cofactor, only the  $\beta\text{Thr163}$  of P-loop is directly linked to the cation. The Thr-Ser substitution promotes a selective decrease in mitochondrial  $\text{Ca}^{2+}$ -ATPase hydrolysis of ATP [15,44] associated with a resistance to the  $\text{Ca}^{2+}$ -induced PTP opening [15].

The reduction in the  $\text{F}_1\text{F}_0$ -ATPase catalytic efficiency of upon exposure to  $\text{Gd}^{3+}$  helps to correlate the enzyme structure and function in a selected domain, and to understand the enzyme involvement in PTP

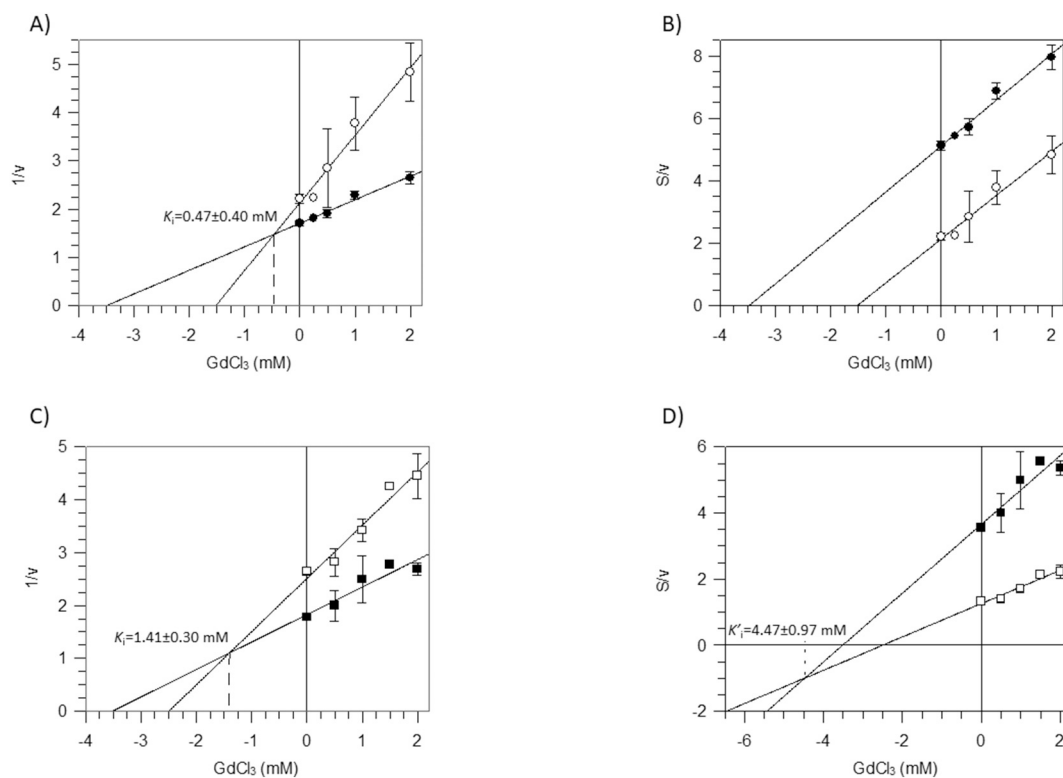


**Fig. 4.** Inhibition kinetics of the mitochondrial  $\text{Ca}^{2+}$ -activated  $\text{F}_1\text{F}_0$ -ATPase by  $\text{GdCl}_3$ . Dixon (A, C) and Cornish–Bowden (B, D) plots at 2 mM  $\text{CaCl}_2$  plus 1 mM (○) or 3 mM (●) ATP (A, B); at 3 mM ATP plus 0.5 mM (□) or 2 mM (■)  $\text{Ca}^{2+}$  (C, D). The experimental design to build these plots is detailed in Section 2.4. All points represent the mean  $\pm$  SD (vertical bars) of four distinct experiments carried out on different mitochondrial preparations.

**Table 1**

Kinetic constants of  $\text{Gd}^{3+}$  inhibition on the  $\text{F}_1\text{F}_0$ -ATPase activated by the cofactors  $\text{Mg}^{2+}$  or  $\text{Ca}^{2+}$ .

	ATP substrate		Cofactor		$K_i$ (mM)	$k_{\text{inact}}$ ( $\text{s}^{-1}$ )	$k_{\text{inact}}/K_i$ ( $\text{mM}^{-1}\cdot\text{s}^{-1}$ )
	$K_i$ (mM)	$K'_i$ (mM)	$K_i$ (mM)	$K'_i$ (mM)			
$\text{Mg}^{2+}$ -ATPase	$1.4 \pm 0.1\text{A}$	$\infty$	$\infty$	$5.2 \pm 0.2\text{A}$	$2.35 \pm 0.35\text{A}$	$0.30 \pm 0.04\text{A}$	$0.13 \pm 0.02\text{A}$
$\text{Ca}^{2+}$ -ATPase	$0.5 \pm 0.4\text{B}$	$\infty$	$1.4 \pm 0.3\text{a}$	$4.5 \pm 1.0\text{Ab}$	$0.72 \pm 0.11\text{B}$	$0.42 \pm 0.06\text{B}$	$0.59 \pm 0.09\text{B}$

$\text{F}_1\text{F}_0$ -ATPase activated by  $\text{Mg}^{2+}$  ( $\text{Mg}^{2+}$ -ATPase);  $\text{F}_1\text{F}_0$ -ATPase activated by  $\text{Ca}^{2+}$  ( $\text{Ca}^{2+}$ -ATPase); Substrate (ATP); Cofactor ( $\text{Mg}^{2+}$  or  $\text{Ca}^{2+}$ ).  $K_i$  and  $K'_i$  values were graphically obtained from the Dixon and Cornish–Bowden plots, respectively reported in Fig. 3 for  $\text{Mg}^{2+}$ -activated  $\text{F}_1\text{F}_0$ -ATPase and in Fig. 5 for the  $\text{Ca}^{2+}$ -activated  $\text{F}_1\text{F}_0$ -ATPase.  $K_i$  and  $k_{\text{inact}}$  values of  $\text{Mg}^{2+}$ -activated  $\text{F}_1\text{F}_0$ -ATPase or  $\text{Ca}^{2+}$ -activated  $\text{F}_1\text{F}_0$ -ATPase were graphically obtained from the double reciprocal plots of Figs. 4B and 5B, respectively. Details are reported in the Section 2.4. Data are the mean  $\pm$  SD of three different experiments carried out on distinct mitochondrial pools. Different upper case letters indicate significantly different values ( $P \leq 0.05$ ) between different activated  $\text{F}_1\text{F}_0$ -ATPases; different lower case letters indicate different values ( $P \leq 0.05$ ) within the same treatment.  $\infty$  = not detectable.

formation. The natural logarithm of the residual activity (uninhibited rate minus inhibited rate) vs time provides the observed first-order rate constants calculated from the slopes of the straight lines obtained at different  $\text{GdCl}_3$  concentrations when either  $\text{Mg}^{2+}$  or  $\text{Ca}^{2+}$  act as cofactor of the  $\text{F}_1\text{F}_0$ -ATPase activity. The plots in Figs. 5A and 6A show the typical time course of  $\text{Gd}^{3+}$ -mediated inhibition on the activity of the  $\text{F}_1\text{F}_0$ -ATPase when activated either by  $\text{Mg}^{2+}$  or by  $\text{Ca}^{2+}$  as cofactor, respectively. In both cases, the time course of the  $\text{Gd}^{3+}$ -mediated inhibition is well fitted to an exponential function. The  $k_{\text{obs}}$ , which is obtained from the slope of each straight line, displays a gradual  $\text{GdCl}_3$  concentration-dependent increase only when the  $\text{F}_1\text{F}_0$ -ATPase is activated by  $\text{Mg}^{2+}$  (Fig. 5A). The inhibition mechanism of  $\text{Gd}^{3+}$  on the  $\text{Mg}^{2+}$ - or the  $\text{Ca}^{2+}$ -activated  $\text{F}_1\text{F}_0$ -ATPase, depicted in Fig. 5B and 5B, respectively, shows the  $\text{GdCl}_3$  concentrations which promote the half-maximal enzyme inactivation in the presence of different cofactors. The  $\text{F}_1\text{F}_0$ -ATPase when activated by  $\text{Ca}^{2+}$  as cofactor shows a three times lower  $K_i$  value than when it is activated by  $\text{Mg}^{2+}$ -activated  $\text{F}_1\text{F}_0$ -ATPase (Table 1), suggesting that  $\text{Gd}^{3+}$  bound to the catalytic region

affects the kinetics of cofactor-mediated ATP hydrolysis. The higher propensity of  $\text{Gd}^{3+}$  to react with the  $\text{F}_1\text{F}_0$ -ATPase when activated by  $\text{Ca}^{2+}$  than when activated by  $\text{Mg}^{2+}$  is also confirmed by a significantly higher  $k_{\text{inact}}$  value for the  $\text{Ca}^{2+}$ -activated  $\text{F}_1\text{F}_0$ -ATPase (Table 1). The inhibition potency of  $\text{Gd}^{3+}$ , which indicates the  $\text{Gd}^{3+}$  inhibition efficiency on the  $\text{Mg}^{2+}$ - and the  $\text{Ca}^{2+}$ -activated  $\text{F}_1\text{F}_0$ -ATPases, is shown by the  $k_{\text{inact}}/K_i$  ratio (Table 1).  $\text{Gd}^{3+}$  shows a  $k_{\text{inact}}/K_i$  ratio for the  $\text{Ca}^{2+}$ -activated  $\text{F}_1\text{F}_0$ -ATPase, which is 4.5 times higher than the ratio for the  $\text{Mg}^{2+}$ -activated  $\text{F}_1\text{F}_0$ -ATPase (Table 1). Therefore,  $\text{Gd}^{3+}$  more quickly reacts with the enzyme in the presence of  $\text{Ca}^{2+}$  as cofactor, resulting in a prompt and stronger inhibition of the  $\text{F}_1\text{F}_0$ -ATPase activity when activated by  $\text{Ca}^{2+}$  as cofactor. To sum up, all data indicate that when  $\text{Ca}^{2+}$  replaces the natural cofactor  $\text{Mg}^{2+}$  in the enzyme binding site, the  $\text{F}_1\text{F}_0$ -ATPase becomes more prone to the inhibition by  $\text{Gd}^{3+}$ .

### 3.4. PTP desensitization to $\text{Ca}^{2+}$

$\text{Ca}^{2+}$  pulses accumulate in the mitochondrial matrix and are released

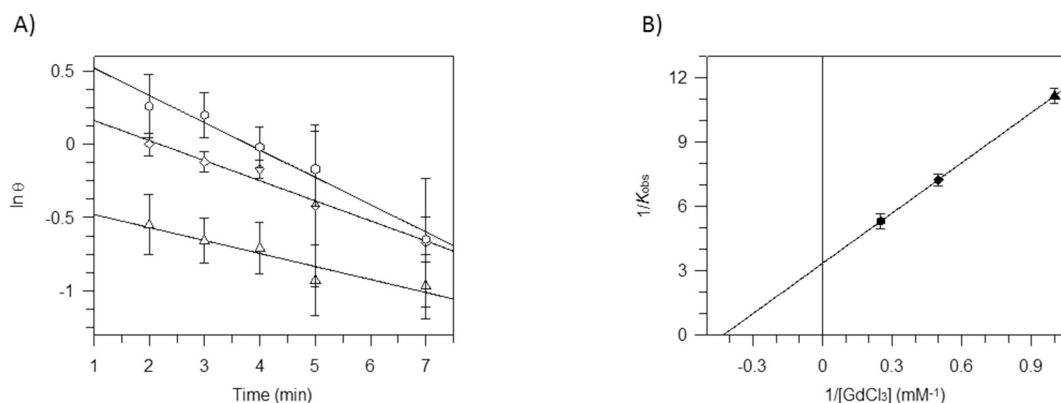


**Fig. 5.** Inactivation kinetics of the  $\text{Mg}^{2+}$ -activated  $\text{F}_1\text{F}_0$ -ATPase by increasing  $\text{GdCl}_3$  concentrations. (A) Semilogarithmic plot of the residual activity ( $\Theta$ ) vs time at fixed concentrations of  $\text{GdCl}_3$  ( $\Delta$ ) 1.0 mM, ( $\diamond$ ) 2.0 mM, ( $\square$ ) 4.0 mM. (B) Replot of the reciprocal of first-order rate constant ( $k_{\text{obs}}$ ) from the straight lines of (A). Each point corresponds to  $\text{GdCl}_3$  ( $\blacktriangle$ ) 1.0 mM, ( $\blacklozenge$ ) 2.0 mM, and ( $\blacksquare$ ) 4.0 mM. The experimental design to build these plots is detailed in Section 2.4. All points represent the mean  $\pm$  SD (vertical bars) of four distinct experiments carried out on different mitochondrial preparations.

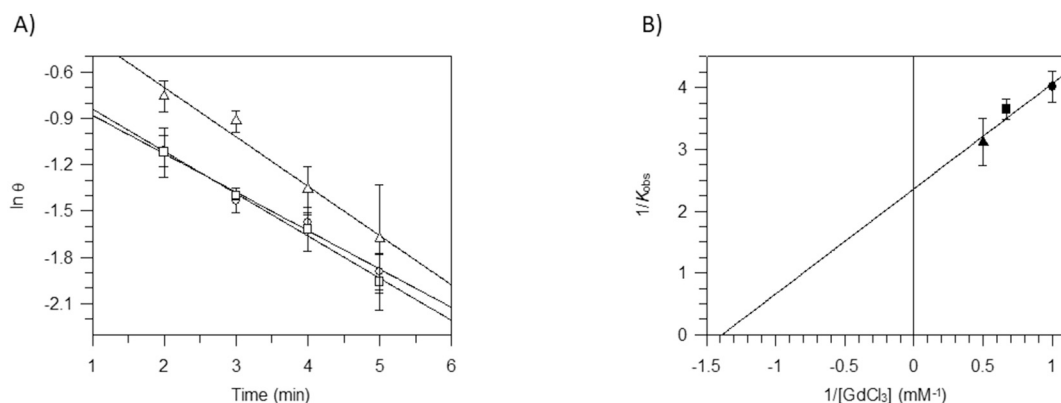


**Fig. 6.** Inactivation kinetics of the  $\text{Ca}^{2+}$ -activated  $\text{F}_1\text{F}_0$ -ATPase by increasing  $\text{GdCl}_3$  concentrations. (A) Semilogarithmic plot of the residual activity ( $\Theta$ ) versus time at fixed concentrations of  $\text{GdCl}_3$  ( $\circ$ ) 1.0 mM, ( $\square$ ) 1.5 mM, ( $\diamond$ ) 2.0 mM. (B) Replot of the reciprocal of first-order rate constant ( $k_{\text{obs}}$ ) from the straight lines of (A). Each point corresponds to 1.0 mM  $\text{GdCl}_3$  ( $\bullet$ ), 1.5 mM  $\text{GdCl}_3$  ( $\blacksquare$ ) and 2 mM ( $\blacktriangle$ ). The experiments were carried out as detailed in Section 2.4. All points represent the mean  $\pm$  SD (vertical bars) of four distinct experiments carried out on different mitochondrial preparations.

when the PTP opens. Mitochondria retain calcium and do not form the PTP until the IMM remains intact. The CRC, represents the capability of intact mitochondria to accumulate  $\text{Ca}^{2+}$ . According to the method

adopted, the CRC decrease in  $\text{GdCl}_3$  treated mitochondria, revealed by an increase in fluorescence intensity, points out the  $\text{Gd}^{3+}$  ability to desensitize the PTP opening (Fig. 7A). In control mitochondria, the CRC

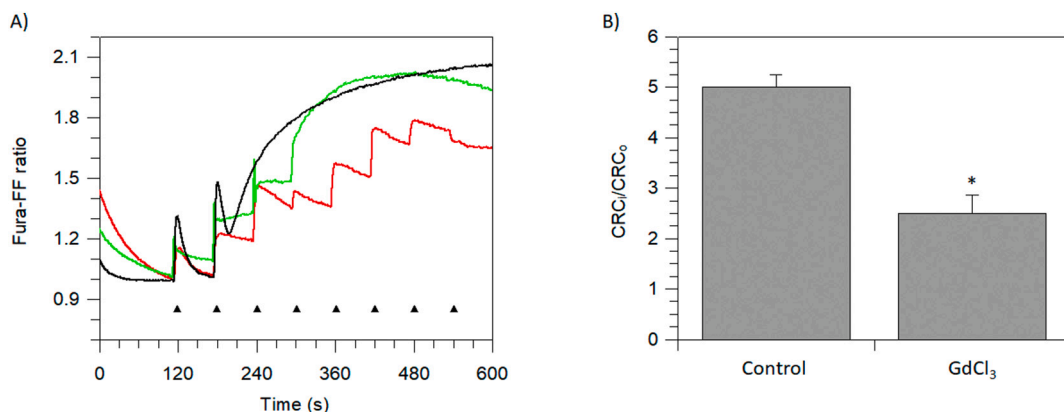


**Fig. 7.** Evaluation of mPTP opening. Representative curves (A) of the calcium retention capacity (CRC). CRC was monitored in response to subsequent  $10 \mu\text{M}$   $\text{CaCl}_2$  pulses (shown by the arrows), as detailed in the Section 2.5, in the absence (Control-black line) and in the presence of the inhibitors 2 mM  $\text{MgADP}$  (red line), and 1 mM  $\text{GdCl}_3$  (green line). (B) Quantitation of the mPTP displayed as the ratio of the number of calcium pulses required to induce the mPTP opening in  $\text{MgADP}$ -inhibited ( $\text{CRC}_i$ ) and uninhibited ( $\text{CRC}_o$ ) mitochondria. Data represent the mean  $\pm$  SD from three independent experiments carried out on distinct mitochondrial preparations. \* indicates significant differences with respect to the control ( $P \leq 0.05$ ). (For interpretation of the references to colour in this figure legend, the reader is referred to the web version of this article.)

decrease is revealed after 210 s upon a two-train  $\text{Ca}^{2+}$  pulses, as shown by the rise in the (Fura-FF high  $\text{Ca}^{2+}$ )/(Fura-FF low  $\text{Ca}^{2+}$ ) ratio. Accordingly, the increase in CRC upon subsequent 10  $\mu\text{M}$   $\text{Ca}^{2+}$  additions at 1 min intervals, indicates that mitochondria in the presence of  $\text{Gd}^{3+}$  must attain a higher threshold value of  $\text{Ca}^{2+}$  concentration in the matrix to trigger PTP formation, with respect to control mitochondria. This phenomenon, known as PTP desensitization to  $\text{Ca}^{2+}$ , is shown by a delayed rise in the Fura-FF ratio, which indicates a decreased CRC (Fig. 7A). Consistently, the PTP formation extent, expressed as the ratio of the number of  $\text{Ca}^{2+}$  pulses required to induce the PTP in MgADP inhibited ( $\text{CRC}_i$ ) and untreated ( $\text{CRC}_o$ ) mitochondria [31], is doubled in the presence of 1.0 mM  $\text{GdCl}_3$  (Fig. 7B).

### 3.5. The $\text{Gd}^{3+}$ inhibition of the $\text{F}_1\text{F}_0$ -ATPase activity when $\text{Ca}^{2+}$ acts as cofactor is consistent with the PTP desensitization

We can speculate that the  $\text{GdCl}_3$  effects on the PTP are due to the interactions of  $\text{Gd}^{3+}$  in the  $\text{F}_1$  region of the  $\text{F}_1\text{F}_0$ -ATPase, which hamper the PTP formation. The  $\text{GdCl}_3$  preferential inhibition on the  $\text{F}_1\text{F}_0$ -ATPase when the cofactor is  $\text{Ca}^{2+}$  corroborates the link between the  $\text{Ca}^{2+}$ -activated  $\text{F}_1\text{F}_0$ -ATPase and the PTP and points out  $\text{Gd}^{3+}$  as a PTP inhibitor, consistently with other reports in swine mitochondria [44]. On the other hand, Lanthanide ions are long known as blockers of membrane permeabilization [40], even if this topic is still controversial [45]. Under the experimental conditions adopted, the strong binding of  $\text{Gd}^{3+}$  to the  $\text{F}_1\text{F}_0$ -ATPase catalytic domain when the enzyme activity is activated by  $\text{Ca}^{2+}$  hampers both ATP hydrolysis and PTP formation.

## 4. Conclusion

The results add further information on the mitochondrial effects of  $\text{Gd}^{3+}$ , which from a literature overview, are still controversial. Lanthanide ions including  $\text{Gd}^{3+}$  were shown to increase mitochondrial fluidity and to promote mitochondrial swelling and apoptosis in mice liver, thus strongly suggesting the induction of PTP opening [45].  $\text{Gd}^{3+}$  promoted PTP opening in rat liver mitochondria at 500  $\mu\text{M}$  concentration [27] and induced mitochondrial impairment and neuronal cell apoptosis [46]. On the contrary, recently  $\text{Gd}^{3+}$  was reported as known PTP blocker in mammalian mitochondria [16]. These reports open intriguing questions on the PTP modulation by exogenous compounds. Most likely the  $\text{Gd}^{3+}$  effect and action mechanism on the membrane permeabilization mainly depend on the dose and on the experimental conditions. The concentration-dependent effects of  $\text{Gd}^{3+}$  on mitochondria were already pointed out [47].

On these bases, the mitochondrial membrane composition and the  $\text{Gd}^{3+}$  concentration may be crucial in determining the accessibility of  $\text{Gd}^{3+}$  to the  $\text{F}_1\text{F}_0$ -ATPase, especially on considering that  $\text{Gd}^{3+}$  by interacting with membrane phospholipids can modify the membrane structure [45].

The inhibition kinetic analyses confirm that in swine heart mitochondria the  $\text{F}_1\text{F}_0$ -ATPase is a molecular target of  $\text{Gd}^{3+}$  which directly interacts with the enzyme proteins. The  $\text{Gd}^{3+}$  effect on the  $\text{F}_1\text{F}_0$ -ATPase catalytic activity reinforces the link between PTP formation and the  $\text{F}_1\text{F}_0$ -ATPase activation in the presence of  $\text{Ca}^{2+}$  as cofactor. Indeed,  $\text{Gd}^{3+}$ , not only blocks PTP opening, but exerts a more efficient  $\text{F}_1\text{F}_0$ -ATPase inhibition when the natural  $\text{Mg}^{2+}$  cofactor is replaced by  $\text{Ca}^{2+}$ . Assuming that the enzyme has different conformations when it binds  $\text{Mg}^{2+}$  or  $\text{Ca}^{2+}$  [10] the molecular model that ascribes to  $\text{Ca}^{2+}$  insertion in the catalytic  $\text{F}_1\text{F}_0$ -ATPase sites the event which triggers the  $\text{F}_1\text{F}_0$ -ATPase conformational changes which open the PTP [9,15,17] is strongly corroborated. The role of  $\text{Gd}^{3+}$  as PTP blocker opens new perspectives in the putative protective role of this cation to prevent mitochondrial decay and cell death. Accordingly,  $\text{GdCl}_3$  administration to counteract ischemia/riperfusion injury was reported to attenuate the mitochondrial damage in liver cells [48] as well as cardiomyocyte apoptosis in rats [49].  $\text{Gd}^{3+}$  derivatives inhibited the mitochondrial pathway of apoptosis

in human hepatocytes [50]. However, since the mitochondrial effects of  $\text{Gd}^{3+}$  are still poorly investigated, any extrapolation should be taken with caution and further studies are required.

## CRedit authorship contribution statement

CA, investigation and methodology; FT and AP, writing - review & editing; MF, resources; AP and SN, visualization; FT, AP and SN, validation; SN, supervision and writing original draft.

## Acknowledgements

Danilo Matteuzzi and Roberto Giusti (Department of Veterinary Medical Sciences, University of Bologna) are gratefully acknowledged for kindly conferring swine hearts from a local abattoir to Biochemistry laboratories.

## Funding

This work was supported by a RFO grant from the University of Bologna, Italy.

## References

- [1] W. Junge, H. Sielaff, S. Engelbrecht, Torque generation and elastic power transmission in the rotary F(O)F(1)-ATPase, *Nature* 459 (2009) 364–370, <https://doi.org/10.1038/nature08145>.
- [2] S. Nesci, F. Trombetti, A. Pagliarani, V. Ventrella, C. Algieri, G. Tioli, G. Lenaz, Molecular and supramolecular structure of the mitochondrial oxidative phosphorylation system: implications for pathology, *Life* 11 (2021) 242, <https://doi.org/10.3390/life11030242>.
- [3] W. Kühlbrandt, Structure and mechanisms of F-type ATP synthases, *Annu. Rev. Biochem.* 88 (2019) 515–549, <https://doi.org/10.1146/annurev-biochem-013118-110903>.
- [4] S. Nesci, A. Pagliarani, C. Algieri, F. Trombetti, Mitochondrial F-type ATP synthase: multiple enzyme functions revealed by the membrane-embedded FO structure, *Crit. Rev. Biochem. Mol. Biol.* 55 (2020) 309–321, <https://doi.org/10.1080/10409238.2020.1784084>.
- [5] A. Hahn, K. Parey, M. Bublitz, D.J. Mills, V. Zickermann, J. Vonck, W. Kühlbrandt, T. Meier, Structure of a complete ATP synthase dimer reveals the molecular basis of inner mitochondrial membrane morphology, *Mol. Cell* 63 (2016) 445–456, <https://doi.org/10.1016/j.molcel.2016.05.037>.
- [6] P.D. Boyer, Catalytic site occupancy during ATP synthase catalysis, *FEBS Lett.* 512 (2002) 29–32, [https://doi.org/10.1016/S0014-5793\(02\)02293-7](https://doi.org/10.1016/S0014-5793(02)02293-7).
- [7] S. Nesci, F. Trombetti, V. Ventrella, A. Pagliarani, Opposite rotation directions in the synthesis and hydrolysis of ATP by the ATP synthase: hints from a subunit asymmetry, *J. Membr. Biol.* 248 (2015) 163–169, <https://doi.org/10.1007/s00232-014-9760-y>.
- [8] M. Strauss, G. Hofhaus, R.R. Schröder, W. Kühlbrandt, Dimer ribbons of ATP synthase shape the inner mitochondrial membrane, *EMBO J.* 27 (2008) 1154–1160, <https://doi.org/10.1038/emboj.2008.35>.
- [9] S. Nesci, A. Pagliarani, Incoming news on the F-type ATPase structure and functions in mammalian mitochondria, *BBA Adv.* 1 (2021), 100001, <https://doi.org/10.1016/j.bbadv.2020.100001>.
- [10] G. Pinke, L. Zhou, L.A. Sazanov, Cryo-EM structure of the entire mammalian F-type ATP synthase, *Nat. Struct. Mol. Biol.* 27 (2020) 1077–1085, <https://doi.org/10.1038/s41594-020-0503-8>.
- [11] J. Karch, M.J. Bround, H. Khalil, M.A. Sargent, N. Latchman, N. Terada, P. M. Peixoto, J.D. Molkenin, Inhibition of mitochondrial permeability transition by deletion of the ANT family and CypD, *Sci. Adv.* 5 (2019) eaaw4597, <https://doi.org/10.1126/sciadv.aaw4597>.
- [12] M.A. Neginskaya, M.E. Solesio, E.V. Berezhnaya, G.F. Amodeo, N. Mnatsakanyan, E.A. Jonas, E.V. Pavlov, ATP synthase C-subunit-deficient mitochondria have a small cyclosporine a-sensitive channel, but lack the permeability transition pore, *Cell Rep.* 26 (2019) 11–17.e2, <https://doi.org/10.1016/j.celrep.2018.12.033>.
- [13] M.J. Hubbard, N.J. McHugh, Mitochondrial ATP synthase F1-beta-subunit is a calcium-binding protein, *FEBS Lett.* 391 (1996) 323–329.
- [14] S. Nesci, F. Trombetti, V. Ventrella, M. Pirini, A. Pagliarani, Kinetic properties of the mitochondrial F1FO-ATPase activity elicited by  $\text{Ca}^{2+}$  in replacement of  $\text{Mg}^{2+}$ , *Biochimie* 140 (2017) 73–81, <https://doi.org/10.1016/j.biochi.2017.06.013>.
- [15] V. Giorgio, V. Burchell, M. Schiavone, C. Bassot, G. Minervini, V. Petronilli, F. Argenton, M. Forte, S. Tosatto, G. Lippe, P. Bernardi,  $\text{Ca}^{2+}$  binding to F-ATP synthase  $\beta$  subunit triggers the mitochondrial permeability transition, *EMBO Rep.* 18 (2017) 1065–1076, <https://doi.org/10.15252/embr.201643354>.
- [16] N. Mnatsakanyan, E.A. Jonas, ATP synthase c-subunit ring as the channel of mitochondrial permeability transition: regulator of metabolism in development and degeneration, *J. Mol. Cell. Cardiol.* 144 (2020) 109–118, <https://doi.org/10.1016/j.yjmcc.2020.05.013>.

- [17] S. Nesci, A. Pagliarani, Ca2 as cofactor of the mitochondrial H<sup>+</sup>-translocating F1FO-ATPase, *Proteins: Struct. Funct. Bioinf.* 89 (2021) 477–482, <https://doi.org/10.1002/prot.26040>.
- [18] T.M. Bauer, E. Murphy, Role of mitochondrial calcium and the permeability transition pore in regulating cell death, *Circ. Res.* 126 (2020) 280–293, <https://doi.org/10.1161/CIRCRESAHA.119.316306>.
- [19] S. Nesci, The mitochondrial permeability transition pore in cell death: a promising drug binding bioarchitecture, *Med. Res. Rev.* 40 (2020) 811–817, <https://doi.org/10.1002/med.21635>.
- [20] G. Wang, Q. Peng, Y. Li, Lanthanide-doped nanocrystals: synthesis, optical-magnetic properties, and applications, *Acc. Chem. Res.* 44 (2011) 322–332, <https://doi.org/10.1021/ar100129p>.
- [21] G. Strijkers, W.M. Mulder, G.F. van Tilborg, K. Nicolay, MRI contrast agents: current status and future perspectives, *Anti Cancer Agents Med. Chem.* 7 (2007) 291–305, <https://doi.org/10.2174/187152007780618135>.
- [22] J. Chen, J. Ramos, M. Sirisawad, R. Miller, L. Naumovski, Motexafin gadolinium induces mitochondrially mediated caspase-dependent apoptosis, *Apoptosis* 10 (2005) 1131–1142, <https://doi.org/10.1007/s10495-005-0887-2>.
- [23] L. Pasquini, A. Napolitano, E. Visconti, D. Longo, A. Romano, P. Tomà, M.C. R. Espagnet, Gadolinium-based contrast agent-related toxicities, *CNS Drugs*. 32 (2018) 229–240, <https://doi.org/10.1007/s40263-018-0500-1>.
- [24] L.C. Adding, G.L. Bannenberg, L.E. Gustafsson, Basic experimental studies and clinical aspects of gadolinium salts and shelles, *Cardiovasc. Drug Rev.* 19 (2006) 41–56, <https://doi.org/10.1111/j.1527-3466.2001.tb00182.x>.
- [25] D.V. Bower, J.K. Richter, H. von Tengell-Koblick, J.T. Heverhagen, V.M. Runge, Gadolinium-based MRI contrast agents induce mitochondrial toxicity and cell death in human neurons, and toxicity increases with reduced kinetic stability of the agent, *Investig. Radiol.* 54 (2019) 453–463, <https://doi.org/10.1097/RLL.0000000000000567>.
- [26] M.J. Akhtar, M. Ahamed, H. Alhadlaq, S. Alokayan, Toxicity mechanism of gadolinium oxide nanoparticles and gadolinium ions in human breast cancer cells, *Curr. Drug Metab.* 20 (2019) 907–917, <https://doi.org/10.2174/1389200220666191105113754>.
- [27] J. Zhao, Z.-Q. Zhou, J.-C. Jin, L. Yuan, H. He, F.-L. Jiang, X.-G. Yang, J. Dai, Y. Liu, Mitochondrial dysfunction induced by different concentrations of gadolinium ion, *Chemosphere* 100 (2014) 194–199, <https://doi.org/10.1016/j.chemosphere.2013.11.031>.
- [28] S. Nesci, V. Ventrella, F. Trombetti, M. Pirini, A. Pagliarani, The mitochondrial F1FO-ATPase desensitization to oligomycin by tributyltin is due to thiol oxidation, *Biochimie* 97 (2014) 128–137, <https://doi.org/10.1016/j.biochi.2013.10.002>.
- [29] M.M. Bradford, A rapid and sensitive method for the quantitation of microgram quantities of protein utilizing the principle of protein-dye binding, *Anal. Biochem.* 72 (1976) 248–254, <https://doi.org/10.1006/abio.1976.9999>.
- [30] C. Algieri, F. Trombetti, A. Pagliarani, V. Ventrella, C. Bernardini, M. Fabbri, M. Forni, S. Nesci, Mitochondrial Ca<sup>2+</sup>-activated F1FO-ATPase hydrolyzes ATP and promotes the permeability transition pore, *Ann. N. Y. Acad. Sci.* 1457 (2019) 142–157, <https://doi.org/10.1111/nyas.14218>.
- [31] C. Algieri, F. Trombetti, A. Pagliarani, V. Ventrella, S. Nesci, Phenylglyoxal inhibition of the mitochondrial F1FO-ATPase activated by Mg<sup>2+</sup> or by Ca<sup>2+</sup> provides clues on the mitochondrial permeability transition pore, *Arch. Biochem. Biophys.* 681 (2020), 108258, <https://doi.org/10.1016/j.abb.2020.108258>.
- [32] V. Ventrella, S. Nesci, F. Trombetti, P. Bandiera, M. Pirini, A.R. Borgatti, A. Pagliarani, Tributyltin inhibits the oligomycin-sensitive Mg-ATPase activity in *Mytilus galloprovincialis* digestive gland mitochondria, *Comp. Biochem. Physiol. C Toxicol. Pharmacol.* 153 (2011) 75–81, <https://doi.org/10.1016/j.cbpc.2010.08.007>.
- [33] A. Cornish-Bowden, A simple graphical method for determining the inhibition constants of mixed, uncompetitive and non-competitive inhibitors, *Biochem. J.* 137 (1974) 143–144.
- [34] V. Algieri, C. Algieri, L. Maiuolo, A. De Nino, A. Pagliarani, M.A. Tallarida, F. Trombetti, S. Nesci, 1,5-Disubstituted-1,2,3-triazoles as inhibitors of the mitochondrial Ca<sup>2+</sup>-activated F1FO-ATPase and the permeability transition pore, *Ann. N. Y. Acad. Sci.* 1485 (2021) 43–55, <https://doi.org/10.1111/nyas.14474>.
- [35] F. Ghanbari, K. Rowland-Yeo, J.C. Bloomer, S.E. Clarke, M.S. Lennard, G.T. Tucker, A. Rostami-Hodjegan, A critical evaluation of the experimental design of studies of mechanism based enzyme inhibition, with implications for in vitro-in vivo extrapolation, *Curr. Drug Metab.* 7 (2006) 315–334, <https://doi.org/10.2174/138920006776359293>.
- [36] S. Nesci, C. Algieri, F. Trombetti, V. Ventrella, M. Fabbri, A. Pagliarani, Sulfide affects the mitochondrial respiration, the Ca<sup>2+</sup>-activated F1FO-ATPase activity and the permeability transition pore but does not change the Mg<sup>2+</sup>-activated F1FO-ATPase activity in swine heart mitochondria, *Pharmacol. Res.* 166 (2021), 105495, <https://doi.org/10.1016/j.phrs.2021.105495>.
- [37] J.G. Graca, F.C. Davison, J.B. Feavel, Comparative toxicity of stable rare earth compounds. II. Effect of citrate and edetate complexing on acute toxicity in mice and Guinea pigs, *Arch. Environ. Health* 5 (1962) 437–444, <https://doi.org/10.1080/00039896.1962.10663310>.
- [38] Null Ermakov YuA, A.Z. Averbakh, A.B. Arbuзова, S.I. Sukharev, Lipid and cell membranes in the presence of gadolinium and other ions with high affinity to lipids. 2. A dipole component of the boundary potential on membranes with different surface charge, *Membr. Cell Biol.* 12 (1998) 411–426.
- [39] Y. Cheng, M. Liu, R. Li, C. Wang, C. Bai, K. Wang, Gadolinium induces domain and pore formation of human erythrocyte membrane: an atomic force microscopic study, *Biochim. Biophys. Acta* 1421 (1999) 249–260, [https://doi.org/10.1016/s0005-2736\(99\)00125-x](https://doi.org/10.1016/s0005-2736(99)00125-x).
- [40] E.C. Gianulis, A.G. Pakhomov, Gadolinium modifies the cell membrane to inhibit permeabilization by nanosecond electric pulses, *Arch. Biochem. Biophys.* 570 (2015) 1–7, <https://doi.org/10.1016/j.abb.2015.02.013>.
- [41] I.H. Segel, Enzyme kinetics, in: W.J. Lennarz, M.D. Lane (Eds.), *Encyclopedia of Biological Chemistry*, Academic Press, Waltham, 2013, pp. 216–220, <https://doi.org/10.1016/B978-0-12-378630-2.00012-8>.
- [42] R. Casadio, B.A. Melandri, CaATP inhibition of the MgATP-dependent proton pump (H<sup>+</sup>-ATPase) in bacterial photosynthetic membranes with a mechanism of alternative substrate inhibition, *JBIC*. 1 (1996) 284–291, <https://doi.org/10.1007/s007750050055>.
- [43] W.D. Frasch, The participation of metals in the mechanism of the F<sub>1</sub>-ATPase, *Biochim. Biophys. Acta* 1458 (2000) 310–325.
- [44] L. Nathanson, Z. Gromet-Elhanan, Mutations in the β-subunit Thr159 and Glu184 of the Rhodospirillum rubrum F<sub>0</sub>F<sub>1</sub> ATP synthase reveal differences in ligands for the coupled Mg<sup>2+</sup>- and decoupled Ca<sup>2+</sup>-dependent F<sub>0</sub>F<sub>1</sub> activities, *J. Biol. Chem.* 275 (2000) 901–905, <https://doi.org/10.1074/jbc.275.2.901>.
- [45] H. Liu, L. Yuan, X. Yang, K. Wang, La(3<sup>+</sup>), Gd(3<sup>+</sup>) and Yb(3<sup>+</sup>) induced changes in mitochondrial structure, membrane permeability, cytochrome c release and intracellular ROS level, *Chem. Biol. Interact.* 146 (2003) 27–37, [https://doi.org/10.1016/s0009-2797\(03\)00072-3](https://doi.org/10.1016/s0009-2797(03)00072-3).
- [46] X. Feng, Q. Xia, L. Yuan, X. Yang, K. Wang, Impaired mitochondrial function and oxidative stress in rat cortical neurons: implications for gadolinium-induced neurotoxicity, *Neurotoxicology*. 31 (2010) 391–398, <https://doi.org/10.1016/j.neuro.2010.04.003>.
- [47] J. Zhao, L. Ma, X. Xiang, Q.-L. Guo, F.-L. Jiang, Y. Liu, Microcalorimetric studies on the energy release of isolated rat mitochondria under different concentrations of gadolinium (III), *Chemosphere* 153 (2016) 414–418, <https://doi.org/10.1016/j.chemosphere.2016.03.082>.
- [48] W.-H. Zhang, J.-S. Wang, Y. Zhou, J.-Y. Li, Gadolinium chloride and salvia miltiorrhiza compound ameliorate reperfusion injury in hepatocellular mitochondria, *World J. Gastroenterol.* 9 (2003) 2040–2044, <https://doi.org/10.3748/wjg.v9.i9.2040>.
- [49] M. Chen, Y. Zheng, Y. Song, J. Xue, Z. Liang, X. Yan, D. Luo, Pretreatment with low-dose gadolinium chloride attenuates myocardial ischemia/reperfusion injury in rats, *Acta Pharmacol. Sin.* 37 (2016) 453–462, <https://doi.org/10.1038/aps.2015.156>.
- [50] T. Yu, M. Zhen, J. Li, Y. Zhou, H. Ma, W. Jia, C. Wang, Anti-apoptosis effect of amino acid modified gadofullerene via a mitochondria mediated pathway, *Dalton Trans.* 48 (2019) 7884–7890, <https://doi.org/10.1039/c9dt00800d>.



# Phenylglyoxal inhibition of the mitochondrial $F_1F_0$ -ATPase activated by $Mg^{2+}$ or by $Ca^{2+}$ provides clues on the mitochondrial permeability transition pore

Cristina Algieri, Fabiana Trombetti, Alessandra Pagliarani\*, Vittoria Ventrella, Salvatore Nesci

Department of Veterinary Medical Sciences, University of Bologna, Ozzano Emilia Via Tolara di Sopra 50, Bologna, 40064, Italy

## ARTICLE INFO

### Keywords:

Phenylglyoxal  
 $F_1F_0$ -ATPase  
 Mitochondria  
 Permeability transition pore  
 Inhibition kinetics  
 Divalent cations

## ABSTRACT

Phenylglyoxal (PGO), known to cause post-translational modifications of Arg residues, was used to highlight the role of arginine residues of the  $F_1F_0$ -ATPase, which may be crucial to yield the mitochondrial permeability transition pore (mPTP). In swine heart mitochondria PGO inhibits ATP hydrolysis by the  $F_1F_0$ -ATPase either sustained by the natural cofactor  $Mg^{2+}$  or by  $Ca^{2+}$  by a similar uncompetitive inhibition mechanism, namely the tertiary complex (*ESI*) only forms when the ATP substrate is already bound to the enzyme, and with similar strength, as shown by the similar  $K_i$  values ( $0.82 \pm 0.07$  mM in presence of  $Mg^{2+}$  and  $0.64 \pm 0.05$  mM in the presence of  $Ca^{2+}$ ). Multiple inhibitor analysis indicates that features of the  $F_1$  catalytic sites and/or the  $F_0$  proton binding sites are apparently unaffected by PGO. However, PGO and  $F_1$  or  $F_0$  inhibitors can bind the enzyme combine simultaneously. However they mutually hinder to bind the  $Mg^{2+}$ -activated  $F_1F_0$ -ATPase, whereas they do not mutually exclude to bind the  $Ca^{2+}$ -activated  $F_1F_0$ -ATPase. The putative formation of PGO-arginine adducts, and the consequent spatial rearrangement in the enzyme structure, inhibits the  $F_1F_0$ -ATPase activity but, as shown by the calcium retention capacity evaluation in intact mitochondria, apparently favours the mPTP formation.

## 1. Introduction

Chemical modifications in the side chain of critical amino acids often cause substantial changes in enzyme structure and function. The basic amino acid arginine has a crucial role in the functioning of bacterial and eukaryotic  $F_1F_0$ -ATPase [1,2], the enzyme complex which builds and hydrolyzes ATP. Other than in the enzymatic catalysis driven by the electrochemical transmembrane gradient of  $H^+$  ( $\Delta\mu_{H^+}$ ) [3] and in the morphology of the *cristae* [4], most likely the enzyme complex is also involved in the formation of the mitochondrial permeability transition pore (mPTP) [10–12], which leads to mitochondrial membrane permeabilization, mitochondrial dysfunction and cell death. Interestingly, distinct arginine residues seem to be crucial to allow both the vital enzyme role as ATP builder and its lethal function in mPTP formation [1,5,6].

The  $F_1F_0$ -ATPase complex works by matching two rotary motors featured by different roles and structures. The hydrophilic  $F_1$  domain, formed by  $\alpha_3$ ,  $\beta_3$ ,  $\gamma$ ,  $\delta$ , and  $\epsilon$  subunits, sustains catalysis, namely it synthesizes or hydrolyzes ATP by its  $\alpha_3\beta_3$  globular hexamer. The hydrophobic  $F_0$  domain, embedded in the IMM and hosting the  $H^+$

channel, consists of *a* subunit, the transmembrane  $\alpha$ -helices of *b* subunit and the  $c_8$  subunits which form the *c*-ring. Mammalian  $F_1F_0$ -ATPases also contain the supernumerary subunits *e*, *f*, *g*, *k*, DAPIT, 6.8 kDa proteolipid, and A6L subunits. The two domains are joined by a central stalk (composed by  $\gamma$ ,  $\delta$ ,  $\epsilon$  subunits) and a peripheral stalk, consisting of *d*, OSCP, F6 and the extrinsic  $\alpha$ -helices of A6L and *b* subunits, which prevents the  $\alpha_3\beta_3$  head rotation with  $F_0$  [7]. The bi-functional  $F_1F_0$ -ATPase can synthesize ATP by dissipating the  $\Delta\mu_{H^+}$  or act *in reverse* by hydrolysing ATP and re-energize the IMM [8]. Each  $\alpha/\beta$  subunit interface forms a catalytic site which undergoes one of the three conformations  $\beta_{TP}$ ,  $\beta_{DP}$  (which bind ATP with decreasing affinity) and  $\beta_E$  (empty), which interconvert each other when the central stalk rotates [9]. The  $F_0$  domain can channel  $H^+$  across the IMM in two opposite directions, namely from the intermembrane space to the IMM and *vice versa*. Two discontinuous and asymmetric half-channels separated by a conserved Arg on *a* subunit [1] match  $H^+$  flow to rotation: counter-clockwise (viewed from the mitochondrial matrix side) leading to ATP synthesis, driven by downhill  $H^+$  flux, and clockwise leading to ATP hydrolysis, which sustains  $H^+$  pumping in the intermembrane space [10].

\* Corresponding author. Department of Veterinary Medical Sciences, University of Bologna, via Tolara di Sopra 50, Ozzano Emilia, 40064, Bologna, Italy.  
 E-mail address: [alessandra.pagliarani@unibo.it](mailto:alessandra.pagliarani@unibo.it) (A. Pagliarani).

Mammalian  $F_1F_0$ -ATPases can dimerize by joining two adjacent  $F_0$  domains. The *g/f* subunit on one side and the DAPIT/*k* subunit on the other side of the  $F_1F_0$ -ATPase monomer establish two dimerization contact sites with the *k/DAPIT* and *f/g* pairs of adjacent monomers. Moreover, two specific “curved domains” composed by the *e*, *g* subunits and the membrane N-terminal helix of *b* subunits from the two monomers form the V-shaped dimer [7,11]. These membrane subunits are involved in the  $F_1F_0$ -ATPase dimerization, in the formation of the *cristae* [12] and also in the  $Ca^{2+}$ -dependent high-conductance mPTP formation in the IMM [13], all events most likely interconnected [12].

The recent  $F_1F_0$ -ATPase involvement in the mPTP [14–16], in spite of some controversies [17], is especially attractive, since the mPTP dysregulation is involved in severe pathologies [18] and in aging [19]. By making the IMM unselective to small solutes (less than 1.5 kDa), the mPTP and its long-lasting openings can trigger cell death. The mPTP channel would form between the  $F_1F_0$ -ATPase monomers of the dimer [14] or alternatively within the *c*-ring [15,16], as *c* subunit ablation reduced the mPTP conductance [20]. Recently, a tight connection between the mPTP and the mitochondrial  $Ca^{2+}$ -activated  $F_1F_0$ -ATPase activity was proven in our lab [21], which sustains the hypothesis that the  $Ca^{2+}$ -dependent F-ATPase activity would open the mPTP through a conformational mechanism [21].

Phenylglyoxal (PGO), long known to react preferentially with the guanidino group of arginine [22], is widely exploited as chemical tool, not only to explore the role of arginine residues in the mitochondrial  $F_1F_0$ -ATPase function, but also to cast light in the mechanisms of mPTP formation in which arginine is thought to be involved [6]. PGO, which contains both an aldehyde and a ketone group, is chemically reactive, while its phenyl head allows incorporation in hydrophobic environments. The guanidino group of arginine, which makes it the most basic amino acid in proteins and a poor nucleophile, can react with PGO to produce multiple products whose identification is still a challenge. Consistently, the species-dependent PGO effects on the mPTP were related to the different adducts established within the enzyme structure [6,23–25].

On these bases, the present study exploits PGO to verify if the likely formation of stable adducts with the  $F_1F_0$ -ATPase Arg residues modifies the F-ATPase activity, stimulated by either the natural cofactor  $Mg^{2+}$  or by  $Ca^{2+}$ , and affects PTP opening. The mechanisms yielding mPTP formation, investigated in this work, may hopefully be exploited to counteract the deleterious effects of mPTP dysregulation.

## 2. Material and methods

### 2.1. Chemicals

Sodium azide, dicyclohexylcarbodiimide (DCCD) and oligomycin were purchased by Vinci-Biochem (Vinci, Italy).  $Na_2ATP$  and phenylglyoxal were obtained from Sigma–Aldrich (Milan, Italy). All other chemicals were reagent grade. Quartz double distilled water was used for all reagent solutions except when differently stated.

### 2.2. Preparation of the mitochondrial fractions

Swine hearts (*Sus scrofa domestica*) were collected at a local abattoir and transported to the lab within 2 h in ice buckets at 0–4 °C. After removal of fat and blood clots as much as possible, approximately 30–40 g of heart tissue were rinsed in ice-cold washing Tris-HCl buffer (medium A) consisting of 0.25 M sucrose, 10 mM Tris(hydroxymethyl)aminomethane (Tris), pH 7.4 and finely chopped into fine pieces with scissors. Each preparation was made from one heart. Once rinsed, tissues were gently dried on blotting paper and weighted. Then tissues were homogenized in a buffer (medium B) consisting of 0.25 M sucrose, 10 mM Tris, 1 mM EDTA (free acid), 0.5 mg/mL BSA fatty acid free, pH 7.4 with HCl at a ratio of 10 mL medium B per 1 g of fresh tissue. After a preliminary gentle break up by Ultraturax T25, the tissue was carefully

homogenized by a motor-driven teflon pestle homogenizer (Braun Melsungen Type 853202) at 650 rpm with 3 up-and-down strokes. The mitochondrial fraction was then obtained by stepwise centrifugation (Sorvall RC2-B, rotor SS34). Briefly, the homogenate was centrifuged at 1000 g for 5 min, thus yielding a supernatant and a pellet. The pellet was re-homogenized under the same conditions of the first homogenization and re-centrifuged at 1000 g for 5 min. The gathered supernatants from these two centrifugations, filtered through four cotton gauze layers, were centrifuged at 10,500 g for 10 min to yield the raw mitochondrial pellet. The raw pellet was resuspended in medium A and further centrifuged at 10,500 g for 10 min to obtain the final mitochondrial pellet. The latter was resuspended by gentle stirring using a Teflon Potter Elvehjem homogenizer in a small volume of medium A, thus obtaining a protein concentration of 30 mg/mL [26]. All steps were carried out at 0–4 °C. The protein concentration was determined according to the colorimetric method of Bradford [27] by Bio-Rad Protein Assay kit II with BSA as standard. The mitochondrial preparations were then stored in liquid nitrogen until the evaluation of F-ATPase activities.

### 2.3. Mitochondrial F-ATPase activity assays

Immediately after thawing, mitochondrial preparations were used for F-ATPase activity assays. The capability of ATP hydrolysis was assayed in a reaction medium (1 mL) containing 0.15 mg mitochondrial protein and 75 mM ethanolamine-HCl buffer pH 9.0, 6.0 mM  $Na_2ATP$  and 2.0 mM  $MgCl_2$  for the  $Mg^{2+}$ -activated  $F_1F_0$ -ATPase assay, and a the same buffer at pH 8.8 plus 3.0 mM  $Na_2ATP$  and 2.0 mM  $CaCl_2$  for the  $Ca^{2+}$ -activated  $F_1F_0$ -ATPase assay. After 5 min preincubation at 37 °C, the reaction, carried out at the same temperature, was started by the addition of the substrate  $Na_2ATP$  and stopped after 5 min by the addition of 1 mL of ice-cold 15% (w/w) trichloroacetic acid aqueous solution. Once the reaction was stopped, vials were centrifuged for 15 min at 3500 rpm (Eppendorf Centrifuge 5202). In the supernatant, the concentration of inorganic phosphate (Pi) hydrolyzed by known amounts of mitochondrial protein, which is an indirect measure of F-ATPase activity, was spectrophotometrically evaluated [28]. To this aim, 1  $\mu$ L from a mother solution of 3 mg/mL oligomycin in dimethylsulfoxide was directly added to the reaction mixture before starting the reaction. The total ATPase activity was calculated by detecting the Pi in control tubes run in parallel and containing 1  $\mu$ L dimethylsulfoxide per mL reaction system. In each experimental set, control tubes were alternated to the condition to be tested. The employed dose of oligomycin, specific inhibitor of F-ATPase which selectively blocks the  $F_0$  subunit ensured maximal enzyme activity inhibition and was currently used in F-ATPase assays [21]. The  $F_1F_0$ -ATPase activity was routinely measured by subtracting, from the Pi hydrolyzed by total ATPase activity, the Pi hydrolyzed in the presence of oligomycin [26]. In all experiments the F-ATPase activity was expressed as  $\mu$ mol Pi·mg protein<sup>-1</sup> min<sup>-1</sup>.

### 2.4. Kinetic analyses

To calculate the  $IC_{50}$  values, namely the inhibitor concentration which causes half maximal inhibition of the enzyme activity, the enzyme activity data obtained in the absence of PGO and in the presence of increasing PGO concentrations were used to calculate the enzyme inhibition that, after background correction, were fitted to a 3 parameter equation (i), where the lower data limit (no enzyme inhibition) is 0. In equation (i) the enzyme activity (*y*) is a function of the inhibitor concentration (*x*), “Range” is the uninhibited enzyme activity (in absence of inhibitor), and *s* is a slope factor. As *x* is at the denominator, *y* falls at increasing *x* values.

$$y = \frac{\text{Range}}{1 + \left(\frac{x}{IC_{50}}\right)^s} \quad (i)$$

The graphical methods of Dixon and Cornish-Bowden plots, which complement one another [29], were used to detect the inhibition mechanism of PGO on the  $Ca^{2+}$ - or  $Mg^{2+}$ -activated  $F_1F_0$ -ATPase. The  $1/v$  (reciprocal of the enzyme activity) in Dixon plot or the  $S/v$  ratio in Cornish-Bowden plot were plotted as a function of the PGO concentration. To build these plots, different experimental sets were designed in which the F-ATPase activity was evaluated in the presence of increasing PGO concentrations at two ATP concentrations, keeping the metal cofactor concentration constant. The values of  $K'_i$ , which represent the dissociation constant of the ternary  $ESI$  complex, were calculated as the abscissa (changed to positive) of the intercept of the straight lines obtained in the Cornish-Bowden plots. In all plots the enzyme specific activity was taken as the expression of  $v$ .

Kinetic studies on the mutual exclusion of different inhibitors on the same F-ATPase activity were carried out. These analyses aimed at casting light on the possible interaction on  $F_1$  domain between PGO and azide, a known  $F_1$  inhibitor and on  $F_0$  domain between PGO and either oligomycin or DCCD, both known  $F_0$  inhibitors. To build Dixon-like plots, in which the reciprocal of enzyme activity data ( $1/v$ ) (y axis) were plotted versus PGO concentration (x axis), the F-ATPase activity was assayed in the presence of increasing PGO concentrations at fixed concentrations of  $F_1$  or  $F_0$  inhibitor and at constant ATP substrate concentration. According to the graphical method employed [30], when the straight lines show different slopes and intersection points, the enzyme inhibition mirrors the combined effect of the two inhibitors. When the F-ATPase is inhibited by two not mutually exclusive compounds, for instance PGO ( $I_1$ ) plus  $F_1$  inhibitor ( $I_2$ ) or PGO ( $I_1$ ) plus  $F_0$  inhibitor ( $I_2$ ), the enzyme can combine with both inhibitors yielding the quaternary complex  $ESI_1I_2$  [31]. The value of  $-\alpha K'_i$ , which represents the dissociation constant of the quaternary  $ESI_1I_2$  complex, was calculated from the abscissa (changed to positive) of the point of intersection of the two straight lines obtained in the presence and absence of  $F_1$  or  $F_0$  inhibitor. The interaction constant  $\alpha$  was then calculated from the ratio of  $\alpha K'_i$  to  $K'_i$  [31].

All data were processed by GraFit Data Analysis Software (version 7.0.3). The correlation coefficients of all the straight lines obtained in Dixon and Cornish Bowden plots were never lower than 0.95, thus confirming the linearity of these plots.

## 2.5. mPTP evaluation

Immediately after the preparation of swine heart mitochondrial fractions, mitochondria (1 mg/mL) were suspended and energized in the assay buffer (130 mM KCl, 1 mM  $KH_2PO_4$ , 20 mM HEPES, pH 7.2 with TRIS), incubated at 25 °C with 1  $\mu$ g/mL rotenone and 5 mM succinate as respiratory substrate. To evaluate PGO effect, selected PGO doses were added to mitochondrial suspensions prior to PTP evaluation. PTP opening was induced by the addition of low concentrations of  $Ca^{2+}$  (10  $\mu$ M) as  $CaCl_2$  solution at fixed time intervals (1 min). The calcium retention capacity (CRC) was spectrofluorometrically evaluated in the presence of 0.8  $\mu$ M Fura-FF. The probe has different spectral properties in the absence and in the presence of  $Ca^{2+}$ , namely it displays excitation/emission spectra of 365/514 nm in the absence of  $Ca^{2+}$  (Fura-FF low  $Ca^{2+}$ ) and shifts to 339/507 nm in the presence of high  $Ca^{2+}$  concentrations (Fura-FF high  $Ca^{2+}$ ). mPTP opening, which implies a decrease in CRC, was detected by the increase in the fluorescence intensity ratio (Fura-FF high  $Ca^{2+}$ )/(Fura-FF low  $Ca^{2+}$ ). All measurements were processed by LabSolutions RF software [21].

## 2.6. Statistical analysis

The data represent the mean  $\pm$  SD (shown as vertical bars in the

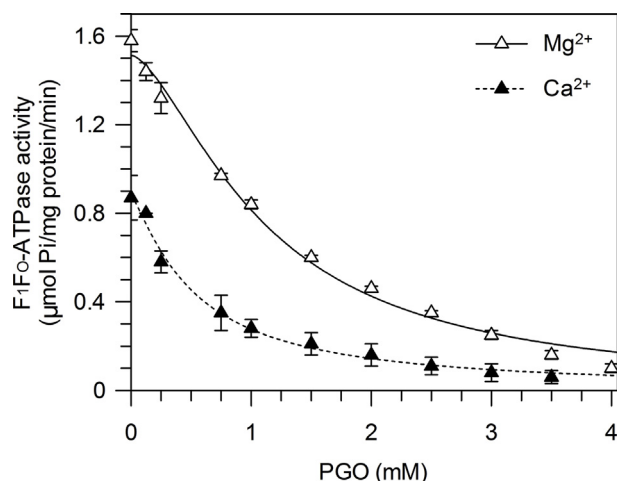


**Fig. 1.** Dose-response curve of PGO on the  $F_1F_0$ -ATPase activity.  $Ca^{2+}$ -activated  $F_1F_0$ -ATPase ( $\blacktriangle$ ) and  $Mg^{2+}$ -activated  $F_1F_0$ -ATPase activities ( $\Delta$ ) in the presence of increasing PGO concentrations. Data represent the mean  $\pm$  SD from three independent experiments carried out on distinct mitochondrial preparations.

figures) of the number of experiments reported in the figure captions and table legends. In each experimental set, the analyses were carried out on different pools of animals. The differences between the enzyme activity data in differently treated mitochondria were evaluated by one way ANOVA followed by Dunnett test when  $F$  values indicated significance ( $P \leq 0.05$ ).

## 3. Results

### 3.1. PGO effect on the $Ca^{2+}$ - and $Mg^{2+}$ -activated $F_1F_0$ -ATPase activities

Apparently, the  $Ca^{2+}$ - and  $Mg^{2+}$ -activated  $F_1F_0$ -ATPases are similarly inhibited by PGO, which exerts the same magnitude order of the inhibition extent, being the maximal enzyme inhibition attained at approximately 4 mM PGO in both cases (Fig. 1). However, on considering the  $IC_{50}$  values, PGO inhibits much more strikingly the  $Ca^{2+}$ -dependent F-ATPase ( $IC_{50} = 0.52 \pm 0.05$  mM) that the  $Mg^{2+}$ -dependent F-ATPase ( $IC_{50} = 1.10 \pm 0.07$  mM) (Fig. 1). The inhibition mechanism of PGO on both the  $Ca^{2+}$ - and  $Mg^{2+}$ -activated  $F_1F_0$ -ATPases is uncompetitive with respect to the ATP substrate (Fig. 2A and B,C-D), namely PGO can only bind to the enzyme-ATP ( $ES$ ) complex forming the tertiary complex ( $ESI$ ), irrespective of the divalent cation which acts as cofactor. Moreover, the Cornish-Bowden plots show that the dissociation constant of the  $ESI$  complex ( $K'_i$ ) of the  $Ca^{2+}$ -activated  $F_1F_0$ -ATPase is lower ( $0.64 \pm 0.05$  mM) (Fig. 2B) than that of the  $Mg^{2+}$ -activated  $F_1F_0$ -ATPase ( $0.82 \pm 0.07$  mM) (Fig. 2D), thus indicating that in the presence of  $Ca^{2+}$  the formation of the ternary complex is easier and stronger than in the presence of  $Mg^{2+}$ .

### 3.2. PGO and inhibitors of $F_1$ and $F_0$ domain in multiple inhibition analysis

Mutual exclusion analyses, carried out by incorporating binary mixtures of  $F_1$  and  $F_0$  inhibitors to the F-ATPase reaction media, aimed at verifying the possible interaction of PGO with the catalytic sites of the hydrophilic  $F_1$  domain (azide plus PGO) or with the transmembrane  $H^+$  pathway within the  $F_0$  portion (oligomycin plus PGO or DCCD plus PGO). Briefly, these experiments aimed at clarifying if PGO can combine with the ternary  $ESI_1$  complex to form the quaternary  $ESI_1I_2$  complex or if the binding of the first inhibitor prevents the binding of the other inhibitor, in other words if the two inhibitors of the  $F_1F_0$ -ATPase are mutually exclusive. The reciprocal of  $Ca^{2+}$ - and  $Mg^{2+}$ -activated  $F_1F_0$ -ATPase activity in the presence and in the absence of fixed

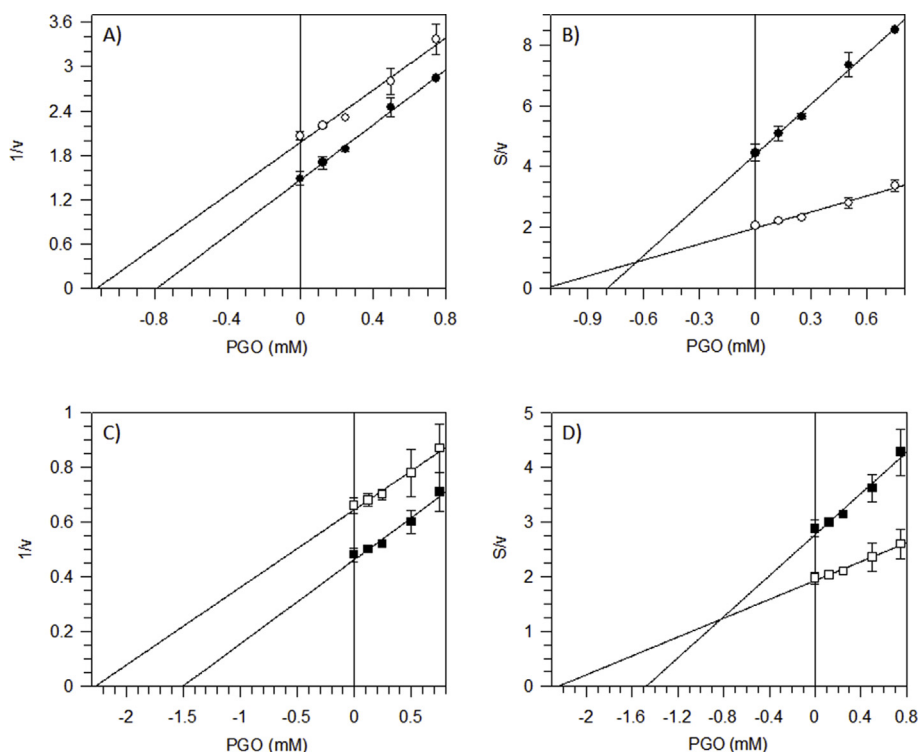


**Fig. 2.** Mitochondrial  $F_1F_0$ -ATPase inhibition by PGO. Dixon (A, C) and Cornish-Bowden (B, D) plots obtained at 1 mM (○) or 3 mM (●) ATP for the  $Ca^{2+}$ -activated  $F_1F_0$ -ATPase (A,B); 3 mM (□) or 6 mM (■) ATP for the  $Mg^{2+}$ - $F_1F_0$ -activated ATPase (C, D) and designing the experiments as detailed in Section 2.4. All points represent the mean  $\pm$  SD (vertical bars) of four distinct experiments carried out on distinct mitochondrial preparations.

azide concentrations was plotted as a function of increasing PGO concentrations. Two straight lines intersecting above the x axis in presence of  $Ca^{2+}$  (Fig. 3A) and  $Mg^{2+}$  (Fig. 3B) were obtained. This result depicts a simultaneous interaction of PGO and azide with the enzyme. The graphically obtained  $\alpha K'_{12}$  value is the dissociation constant of PGO from the enzyme-substrate-azide complex ( $ES$ :azide). Similarly, by employing adequate binary mixtures of PGO plus one of the two  $F_0$  inhibitors, namely increasing [PGO] and constant [oligomycin] (Fig. 3C and D), and increasing [PGO] and constant [DCCD] (Fig. 3E and F) and evaluating the  $Ca^{2+}$ - and  $Mg^{2+}$ -activated  $F_1F_0$ -ATPase activities, the graphically obtained  $\alpha K'_i$  values represent the dissociation constants of the  $ES$ -oligo-PGO complex and of the  $ES$ -DCCD-PGO complex, respectively. The  $\alpha K'_i$  values of the three binary mixtures tested on the  $Ca^{2+}$ - and  $Mg^{2+}$ -activated  $F_1F_0$ -ATPase are reported in Table 1. The interaction constant ( $\alpha$ ) between two different compounds bound to the enzyme obtained from the  $\alpha K'_i$  to  $K'_i$  ratio indicates if the binding of one inhibitor (azide, oligomycin or DCCD) affects ( $\alpha \neq 1$ ) or does not affect ( $\alpha = 1$ ) PGO binding to  $ES$  (Table 2). Since for the  $Ca^{2+}$ -activated  $F_1F_0$ -ATPase all the  $F_1$  and  $F_0$  inhibitors tested in binary mixtures with PGO  $\alpha = 1$  is obtained, the two inhibitors bind independently of each other to yield the  $ES_{11}I_2$  complex. A different situation is pointed out in the case of the  $Mg^{2+}$ -activated  $F_1F_0$ -ATPase. All the calculated  $\alpha$  values are  $> 1$ , thus indicating that in the presence of inhibitors of  $F_1$  or  $F_0$  domain PGO binding to the enzyme is somehow hindered.

### 3.3. mPTP sensitivity to PGO

The mPTP activity can be detected by adding  $Ca^{2+}$  at subsequent steps to the mitochondrial suspensions and by evaluating the CRC, which represents the capability of intact mitochondria to accumulate  $Ca^{2+}$ . According to the method employed, the  $Ca^{2+}$  release from mitochondria ascribed to mPTP opening is revealed by an increase in fluorescence intensity. In control mitochondria CRC increases upon subsequent 10  $\mu$ M  $Ca^{2+}$  additions at fixed time intervals, as shown by the rise in the (Fura-FF high  $Ca^{2+}$ )/(Fura-FF low  $Ca^{2+}$ ) ratio, indicated in Fig. 4A as Fura-FF ratio. In the presence of MgADP, mPTP opening is delayed and a higher CRC is detected. Mitochondrial suspensions were

treated with 0.5 and 1.0 mM PGO, which correspond to the  $IC_{50}$  values for the  $Ca^{2+}$ - and  $Mg^{2+}$ -activated  $F_1F_0$ -ATPases respectively, and with 3.5 mM PGO, namely the concentration that produces the maximal inhibition on the  $Ca^{2+}$ -activated  $F_1F_0$ -ATPase. The mPTP opening sensitization to  $Ca^{2+}$  can be appreciated by the decrease in CRC, as the rise in fluorescence intensity appears earlier (Fig. 4A), namely at lower PGO concentrations. Consistently, the mPTP formation extent, expressed as ratio of the number of  $Ca^{2+}$  pulses required to induce the mPTP in MgADP inhibited ( $CRC_i$ ) and untreated ( $CRC_o$ ) mitochondria, is doubled in the presence of 0.5 and 1.0 mM PGO, while it is apparently unaffected by 3.5 mM PGO (Fig. 4B). Therefore, the ability of PGO to modulate the mPTP in swine heart mitochondria is apparently concentration dependent.

## 4. Discussion

When the  $F_1F_0$ -ATPase functions as  $H^+$  pump by exploiting the free energy of ATP hydrolysis it can use different divalent cations as cofactor [32]. The present findings, obtained on freeze-thawed mitochondria which are clearly permeable to substrates, cofactors and inhibitors, show that PGO more efficiently inhibits the  $Ca^{2+}$ -activated  $F_1F_0$ -ATPase than the  $Mg^{2+}$ -activated  $F_1F_0$ -ATPase, even if both the differently activated enzyme activities are PGO-susceptible (Fig. 1). Recently, a new role in mitochondrial bioenergetics was ascribed to the  $F_1F_0$ -ATPase: an energy-dissipating mechanism [33] that, when activated by  $Ca^{2+}$ , triggers the mPTP formation [21] and is responsible for the reversible mPTP opening. PGO was shown to modulate the mPTP in a species-dependent manner by post-translational modifications of an Arg residue of  $g$  subunit [6]. The uncompetitive inhibition mechanism of the  $F_1F_0$ -ATPase with respect to the ATP substrate in presence of either  $Ca^{2+}$  or  $Mg^{2+}$  shows that PGO does not interact with the enzyme cofactor sites and binds to a different site from that of ATP. Accordingly, the  $ES$ -PGO complex only forms when the  $ES$  complex has already been formed (Fig. 2). Multiple inhibition analyses with binary mixtures of PGO and azide, known to block ATP hydrolysis when Pi leaves the catalytic site [34], indicate that PGO and azide do not mutually exclude and can form the quaternary  $ES$ :azide-PGO complex (Fig. 3A and B). Therefore,

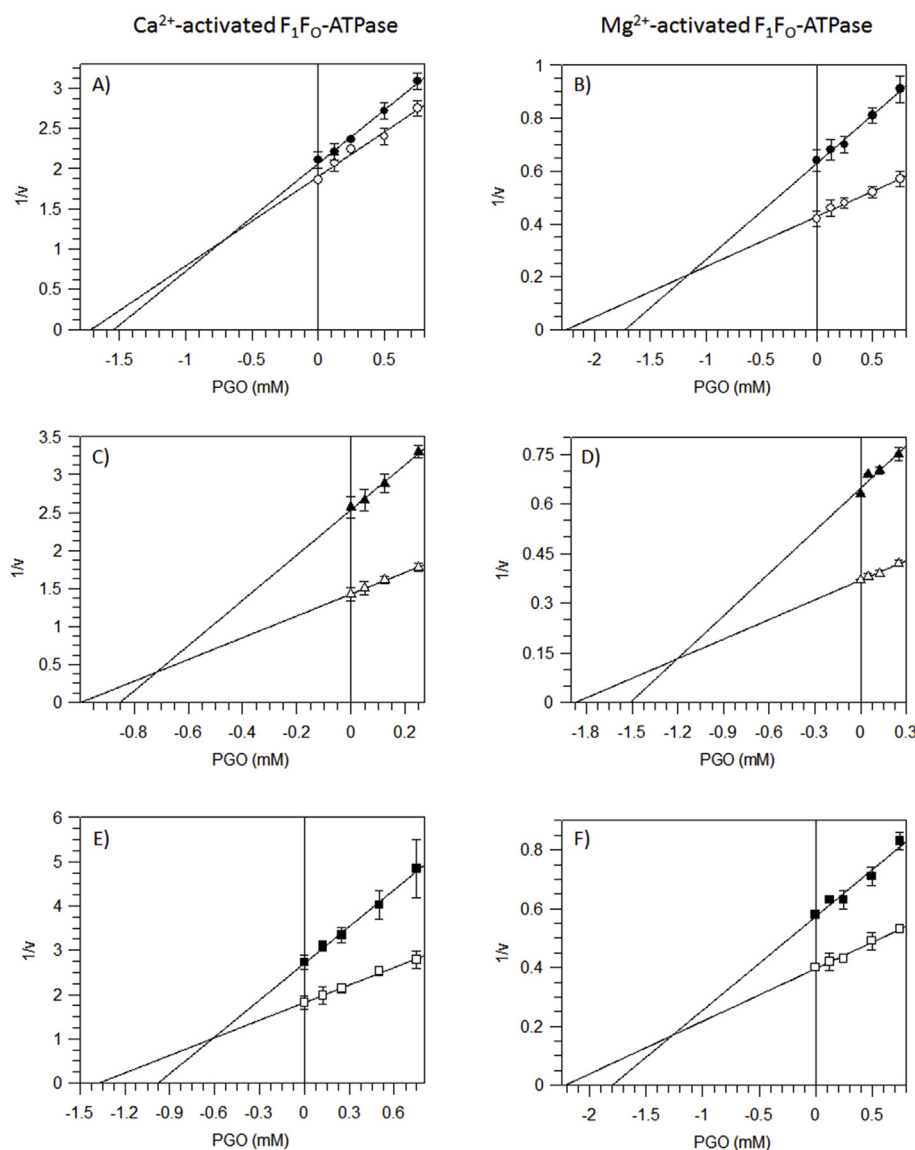


**Fig. 3.** Multiple inhibitor analysis by Dixon plots for the mitochondrial  $F_1F_0$ -ATPase inhibition by PGO. The  $F_1F_0$ -ATPase assay, in the presence of 2 mM  $Ca^{2+}$  plus 3 mM ATP (A, C, E) and in presence of 2 mM  $Mg^{2+}$  plus 6 mM ATP (B, D, F) were carried out in the absence (○) or in the presence of 25  $\mu$ M azide (●); in the absence (△) or in the presence of 3  $\mu$ g/mL oligomycin (▲); in the absence (□) or in the presence of 0.25  $\mu$ M DCCD (■), as detailed in Section 2.4. Each point represents the mean value  $\pm$  SD (vertical bars) of at least three experiments carried out on distinct mitochondrial preparations.

**Table 1**

Dissociation constant ( $\alpha K'_{i2}$ ) of the quaternary complex  $ESI_1I_2$  of PGO ( $I_1$ ) with each of the inhibitors ( $I_2$ ): azide ( $F_1$  inhibitor) and oligomycin (oligo) or DCCD ( $F_0$  inhibitors).

$ESI_1 + I_2$	$\alpha K'_{i2}$ (mM)					
	$Ca^{2+}$ -ATPase		$Mg^{2+}$ -ATPase			
ES azide + PGO	0.69	$\pm$ 0.04	1.17	$\pm$ 0.09		
ES oligo + PGO	0.70	$\pm$ 0.05	1.21	$\pm$ 0.11		
ES DCCD + PGO	0.61	$\pm$ 0.06	1.26	$\pm$ 0.10		

$\alpha K'_{i2}$  values were graphically obtained from the Dixon plots of Fig. 3 as detailed in the section 2.4. Data are the mean  $\pm$  SD of three different experiments carried out on different mitochondrial pools.

PGO binds to a different site from the azide binding site in the catalytic sites of  $F_1$  domain.

In the structurally and functionally coupled  $F_1F_0$ -ATPase complex the blockage of  $H^+$  translocation inhibits ATP hydrolysis. The experiments with the binary mixtures tested, namely oligomycin plus PGO and DCCD plus PGO, show that PGO does not prevent the transmembrane  $H^+$  flow within  $F_0$ . Oligomycin and DCCD bind to the  $H^+$  binding sites of  $c$ -ring and inhibit the  $F_1F_0$ -ATPase. Differently, PGO binds to the  $F_1F_0$ -ATPase complex to form the  $ESI_1$ -PGO complex, without interfering with the binding sites of  $F_0$  inhibitors (Fig. 3C and D

and 3E,F).

Therefore, PGO binds to the enzyme without interfering in the catalytic mechanism of the  $F_1$  domain and in the  $H^+$  translocation mechanism of  $F_0$  domain. However, the results point out some differences in the response of the two differently activated  $F_1F_0$ -ATPase activities. On considering the lower  $\alpha K'_i$  values of the  $Ca^{2+}$ -activated  $F_1F_0$ -ATPase than that of the  $Mg^{2+}$ -activated  $F_1F_0$ -ATPase, it is clear that the PGO has a greater propensity to form the quaternary complex ( $ESI_1I_2$ ) in the presence of  $Ca^{2+}$  than in the presence of  $Mg^{2+}$ . Moreover, the  $\alpha$  value  $> 1$  obtained for the  $Mg^{2+}$ -activated  $F_1F_0$ -ATPase with all the inhibitors under study (Table 2) indicates that the inhibitors of  $F_1/F_0$  domain and PGO mutually hinder. On the contrary all the  $\alpha$  values obtained for the  $Ca^{2+}$ -activated  $F_1F_0$ -ATPase are around 1.0, which indicates no interference between the distinct inhibitor binding sites. Since  $Mg^{2+}$  and  $Ca^{2+}$  insertions are expected to promote different conformational changes on the  $F_1F_0$ -ATPase [35,36], the more striking PGO inhibition on the  $Ca^{2+}$ -activated  $F_1F_0$ -ATPase could be explained by a modification of the enzyme structure caused by Arg adducts. These adducts do not alter ATP binding and  $H^+$  translocation mechanism, but apparently make the enzyme more prone to form the mPTP.

In rat mitochondria 1 mM PGO was reported to inhibit the mPTP and to marginally affect the transmembrane potential generation by

**Table 2**

Interaction constants ( $\alpha$ ) between PGO ( $I_2$ ) and the inhibitors ( $I_1$ ): azide on the  $F_1$  domain and oligomycin or DCCD on the  $F_0$  domain in the  $ESI_1I_2$  complex formation.

	Azide	Oligomycin	DCCD	
PGO	1.08	1.09	0.95	$Ca^{2+}$ -activated $F_1F_0$ -ATPase
	1.43	1.48	1.54	$Mg^{2+}$ -activated $F_1F_0$ -ATPase

$\alpha$  values were obtained as detailed in Section 3.2. Data are the mean  $\pm$  SD of three different experiments carried out on different mitochondrial pools.

Abbreviations: PGO, phenylglyoxal; PTP, permeability transition pore; DCCD, dicyclohexylcarbodiimide; IMM, inner mitochondrial membrane;  $\Delta\mu_{H^+}$ , electrochemical gradient of  $H^+$ ; CRC, calcium retention capacity; mPTP, mitochondrial permeability transition pore.

exploiting ATP hydrolysis in the presence of rotenone [24]. In our experiments, since the  $F_1F_0$ -ATPase activity rate is only almost halved by a similar PGO concentration ( $IC_{50} = 1.10 \pm 0.07$  mM), the  $F_1F_0$ -ATPase may still be able to re-energize the IMM to some extent. Furthermore, the same 1 mM PGO treatment which was reported to 90% inhibit the mPTP in rat liver mitochondria activates the mPTP in swine heart mitochondria (Fig. 4). The  $Ca^{2+}$ -activated  $F_1F_0$ -ATPase activity was proven as essential to trigger mPTP opening [21]. However, the  $Ca^{2+}$ -activated  $F_1F_0$ -ATPase inhibition by PGO apparently contrasts with the concomitant PGO-driven facilitation of the mPTP (Fig. 4). This enigma can be tentatively solved on considering a putative structural role of the PGO-modified Arg. Among the many Arg residues of the  $F_1F_0$ -ATPase, located in  $\alpha$ ,  $\beta$ ,  $\gamma$ ,  $\epsilon$  subunit of  $F_1$  domain, and in  $a$ ,  $c$  and  $g$  subunits of  $F_0$  domain, apparently the only Arg candidate to form an adduct with PGO responsible of mPTP formation is the conserved Arg-107 of  $g$  subunit in yeast, which corresponds to Arg-96 in the human sequence [6]. Therefore, the Arg of  $g$  subunit could represent the PGO modified amino acid residue. Apparently, such chemical change results in the  $F_1F_0$ -ATPase inhibition but does not affect either the  $F_1$  catalytic mechanism or  $H^+$  translocation within  $F_0$  (Fig. 3). Accordingly, the  $g$  subunit is involved in one of the dimerization sites by combining with the  $k$  subunit of the adjacent monomer. Moreover it joins the  $e$  subunit and the N-terminal helix of  $b$  subunits of each monomer to set up a “BAR-like domain” in the dimer that bends the IMM [7]. It seems likely that the PGO adduct on the  $g$  subunit may promote a conformational rearrangement in the transmembrane portion of  $F_1F_0$ -ATPase super-complex which mimics the oligomeric  $Ca^{2+}$ -activated  $F_1F_0$ -ATPase conformation which forms the mPTP. This structural re-arrangement would prevent the chemo-mechanical coupling of ATP hydrolysis, alter the IMM curvature and the formation of the *cristae* so as to favour the

mPTP formation [35].

## 5. Conclusion

Some interesting clues emerge from the present findings. The  $F_1F_0$ -ATPase catalytic mechanism and the  $H^+$  translocation, both activated by  $Mg^{2+}$  or by  $Ca^{2+}$ , even if to a different extent, are indirectly inhibited by PGO, namely the inhibitor, without directly targeting the catalytic sites or the  $H^+$  channel, affects the enzyme function. Interestingly, when the  $F_1F_0$ -ATPase activity is sustained by  $Ca^{2+}$  instead of by  $Mg^{2+}$ , the enzyme activity is more strongly inhibited and mPTP formation is facilitated. Since the enzyme is assumed to have a different conformation when it binds  $Ca^{2+}$  or  $Mg^{2+}$  [37], PGO binding slightly differs due to the different properties of the activating cation. The apparent discrepancy in the PGO-driven mPTP facilitation accompanied by the inhibition of the  $Ca^{2+}$ -activated  $F_1F_0$ -ATPase activity, strongly implicated in mPTP formation, can be overwhelmed on considering that the Arg adduct may change the  $F_1F_0$ -ATPase conformation/structure so as to mimic the enzyme steric arrangement involved in the mPTP. Future studies, aiming at enlightening the supra-molecular  $F_1F_0$ -ATPase organization, are expected to add further details to shed light on the structural changes in the enzyme complex and on its relationship with the mPTP. On these bases, the multi-tasking  $F_1F_0$ -ATPase may emerge as a promising drug binding bioarchitecture to counteract mPTP-related diseases [38].

## CRedit authorship contribution statement

**Cristina Algeri:** Investigation, Formal analysis. **Fabiana Trombetti:** Writing - review & editing. **Alessandra Pagliarani:** Writing - review & editing, Funding acquisition. **Vittoria Ventrella:** Supervision. **Salvatore Nesci:** Conceptualization, Supervision, Writing - original draft.

## Declaration of competing interest

No competing interests declared.

## Acknowledgements and funding information

Danilo Matteuzzi (Department of Veterinary Medical Sciences, University of Bologna) is gratefully acknowledged for kindly conferring swine hearts from a local abattoir to our laboratory.

This work was financed by a RFO grant from the University of Bologna, Italy and from the Carisbo Foundation (2018/0375), Bologna,

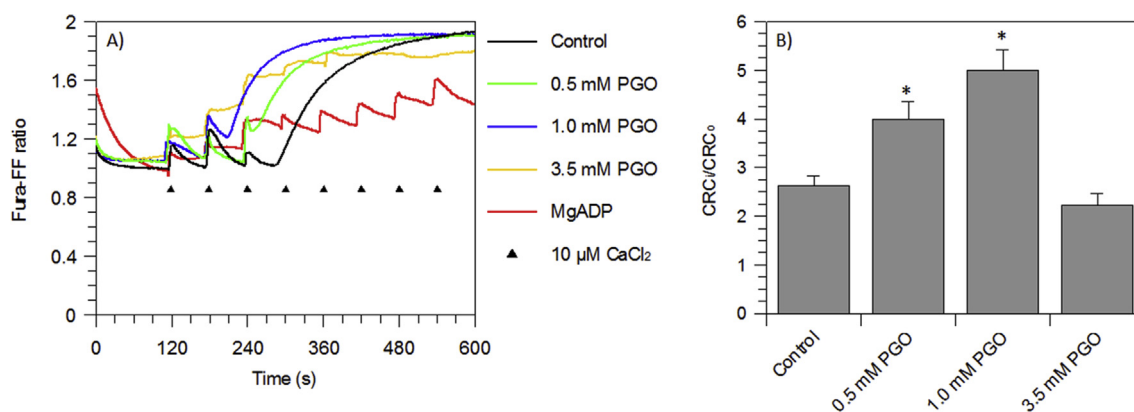


**Fig. 4.** Evaluation of mPTP opening. Representative curves (A) of the calcium retention capacity (CRC) expressed as Fura-FF ratio, monitored in response to subsequent 10  $\mu$ M  $CaCl_2$  pulses (shown by the triangles), as detailed in Section 2.5, in untreated mitochondria (Control), and in the presence of 2 mM MgADP, 0.5, 1.0 or 3.5 mM PGO. B) Quantitation of the mPTP is expressed as the ratio of the number of calcium pulses required to induce the mPTP in MgADP inhibited ( $CRC_i$ ) and untreated ( $CRC_0$ ) mitochondria. Data represent the mean  $\pm$  SD from three independent experiments carried out on distinct mitochondrial preparations. \* indicates significant differences with respect to the control ( $P \leq 0.05$ ).

Italy.

## Appendix A. Supplementary data

Supplementary data to this article can be found online at <https://doi.org/10.1016/j.abb.2020.108258>.

## References

- N. Mitome, S. Ono, H. Sato, T. Suzuki, N. Sone, M. Yoshida, Essential arginine residue of the F(o)-a subunit in F(o)F1-ATP synthase has a role to prevent the proton shortcut without c-ring rotation in the F(o) proton channel, *Biochem. J.* 430 (2010) 171–177, <https://doi.org/10.1042/BJ20100621>.
- L. Langemeyer, S. Engelbrecht, Essential arginine in subunit a and aspartate in subunit c of FoF1 ATP synthase: effect of repositioning within helix 4 of subunit a and helix 2 of subunit c, *Biochim. Biophys. Acta* 1767 (2007) 998–1005, <https://doi.org/10.1016/j.bbabi.2007.05.007>.
- W. Junge, H. Lill, S. Engelbrecht, ATP synthase: an electrochemical transducer with rotary mechanics, *Trends Biochem. Sci.* 22 (1997) 420–423, [https://doi.org/10.1016/S0968-0004\(97\)01129-8](https://doi.org/10.1016/S0968-0004(97)01129-8).
- P. Paumard, J. Vaillier, B. Coulary, J. Schaeffer, V. Soubannier, D.M. Mueller, D. Brèthes, J.-P. di Rago, J. Velours, The ATP synthase is involved in generating mitochondrial cristae morphology, *EMBO J.* 21 (2002) 221–230, <https://doi.org/10.1093/emboj/21.3.221>.
- L. Guo, M. Carraro, A. Carrer, G. Minervini, A. Urbani, I. Masgras, S.C.E. Tosatto, I. Szabò, P. Bernardi, G. Lippe, Arg-8 of yeast subunit e contributes to the stability of F-ATP synthase dimers and to the generation of the full-conductance mitochondrial megachannel, *J. Biol. Chem.* 294 (2019) 10987–10997, <https://doi.org/10.1074/jbc.RA119.008775>.
- L. Guo, M. Carraro, G. Sartori, G. Minervini, O. Eriksson, V. Petronilli, P. Bernardi, Arginine 107 of yeast ATP synthase subunit g mediates sensitivity of the mitochondrial permeability transition to phenylglyoxal, *J. Biol. Chem.* 293 (2018) 14632–14645, <https://doi.org/10.1074/jbc.RA118.004495>.
- J. Gu, L. Zhang, S. Zong, R. Guo, T. Liu, J. Yi, P. Wang, W. Zhuo, M. Yang, Cryo-EM structure of the mammalian ATP synthase tetramer bound with inhibitory protein IF1, *Science* 364 (2019) 1068–1075, <https://doi.org/10.1126/science.aaw4852>.
- P.D. Boyer, The ATP synthase—a splendid molecular machine, *Annu. Rev. Biochem.* 66 (1997) 717–749, <https://doi.org/10.1146/annurev.biochem.66.1.717>.
- P.D. Boyer, Catalytic site occupancy during ATP synthase catalysis, *FEBS Lett.* 512 (2002) 29–32, [https://doi.org/10.1016/S0014-5793\(02\)02293-7](https://doi.org/10.1016/S0014-5793(02)02293-7).
- S. Nesci, F. Trombetti, V. Ventrella, A. Pagliarani, Opposite rotation directions in the synthesis and hydrolysis of ATP by the ATP synthase: hints from a subunit asymmetry, *J. Membr. Biol.* 248 (2015) 163–169, <https://doi.org/10.1007/s00232-014-9760-y>.
- H. Guo, S.A. Bueler, J.L. Rubinstein, Atomic model for the dimeric FO region of mitochondrial ATP synthase, *Science* 358 (2017) 936–940, <https://doi.org/10.1126/science.aao4815>.
- S. Nesci, A. Pagliarani, Emerging roles for the mitochondrial ATP synthase super-complexes, *Trends Biochem. Sci.* 44 (2019) 821–823, <https://doi.org/10.1016/j.tibs.2019.07.002>.
- M. Carraro, V. Checchetto, G. Sartori, R. Kucharczyk, J.-P. di Rago, G. Minervini, C. Franchin, G. Arrigoni, V. Giorgio, V. Petronilli, S.C.E. Tosatto, G. Lippe, I. Szabò, P. Bernardi, High-Conductance Channel Formation in Yeast Mitochondria is Mediated by F-ATP Synthase e and g Subunits, *Cell. Physiol. Biochem.* 50 (2018) 1840–1855, <https://doi.org/10.1159/000494864>.
- V. Giorgio, S. von Stockom, M. Antoniel, A. Fabbro, F. Fogolari, M. Forte, G.D. Glick, V. Petronilli, M. Zoratti, I. Szabò, G. Lippe, P. Bernardi, Dimers of mitochondrial ATP synthase form the permeability transition pore, *Proc. Natl. Acad. Sci. U.S.A.* 110 (2013) 5887–5892, <https://doi.org/10.1073/pnas.1217823110>.
- M. Bonora, A. Bononi, E. De Marchi, C. Giorgi, M. Lebedzinska, S. Marchi, S. Patergnani, A. Rimessi, J.M. Suski, A. Wojtala, M.R. Wieckowski, G. Kroemer, L. Galluzzi, P. Pinton, Role of the c subunit of the FO ATP synthase in mitochondrial permeability transition, *Cell Cycle* 12 (2013) 674–683, <https://doi.org/10.4161/cc.23599>.
- K.N. Alavian, G. Beutner, E. Lazrove, S. Sacchetti, H.-A. Park, P. Licznarski, H. Li, P. Nabili, K. Hockensmith, M. Graham, G.A. Porter, E.A. Jonas, An uncoupling channel within the c-subunit ring of the F1FO ATP synthase is the mitochondrial permeability transition pore, *Proc. Natl. Acad. Sci. U.S.A.* 111 (2014) 10580–10585, <https://doi.org/10.1073/pnas.1401591111>.
- J. Carroll, J. He, S. Ding, I.M. Fearnley, J.E. Walker, Persistence of the permeability transition pore in human mitochondria devoid of an assembled ATP synthase, *Proc. Natl. Acad. Sci. U.S.A.* 116 (2019) 12816–12821, <https://doi.org/10.1073/pnas.1904005116>.
- S. Nesci, F. Trombetti, C. Algieri, A. Pagliarani, A therapeutic role for the F1FO-ATP synthase, *SLAS Discov.* 24 (2019) 893–903, <https://doi.org/10.1177/2472555219860448>.
- N. Jiang, H. Bo, C. Song, J. Guo, F. Zhao, H. Feng, H. Ding, L. Ji, Y. Zhang, Increased vulnerability with aging to MPTP: the mechanisms underlying mitochondrial dynamics, *Neurol. Res.* 36 (2014) 722–732, <https://doi.org/10.1179/1743132813Y.0000000296>.
- M.A. Neginskaya, M.E. Solesio, E.V. Berezhnaya, G.F. Amodeo, N. Mnatsakanyan, E.A. Jonas, E.V. Pavlov, ATP synthase C-Subunit-Deficient mitochondria have a small cyclosporin A-sensitive channel, but lack the permeability transition pore, *Cell Rep.* 26 (2019) 11–17, <https://doi.org/10.1016/j.celrep.2018.12.033> e2.
- C. Algieri, F. Trobetti, A. Pagliarani, V. Ventrella, C. Bernardini, M. Fabbri, M. Forni, S. Nesci, The mitochondrial Ca<sup>2+</sup>-activated F<sub>1</sub>F<sub>o</sub>-ATPase hydrolyses ATP and promotes the permeability transition pore, *Ann. N. Y. Acad. Sci.* (2019), <https://doi.org/10.1111/nyas.14218>.
- K. Takahashi, The reactions of phenylglyoxal and related reagents with amino acids, *J. Biochem.* 81 (1977) 395–402, <https://doi.org/10.1093/oxfordjournals.jbchem.a131471>.
- M.D. Linder, S. Morkunaite-Haimi, P.K.J. Kinnunen, P. Bernardi, O. Eriksson, Ligand-selective modulation of the permeability transition pore by arginine modification. Opposing effects of p-hydroxyphenylglyoxal and phenylglyoxal, *J. Biol. Chem.* 277 (2002) 937–942, <https://doi.org/10.1074/jbc.M107610200>.
- O. Eriksson, E. Fontaine, P. Bernardi, Chemical modification of arginines by 2,3-butanedione and phenylglyoxal causes closure of the mitochondrial permeability transition pore, *J. Biol. Chem.* 273 (1998) 12669–12674, <https://doi.org/10.1074/jbc.273.20.12669>.
- M. Johans, E. Milanese, M. Franck, C. Johans, J. Liobikas, M. Panagiotaki, L. Greci, G. Principato, P.K.J. Kinnunen, P. Bernardi, P. Costantini, O. Eriksson, Modification of permeability transition pore arginine(s) by phenylglyoxal derivatives in isolated mitochondria and mammalian cells. Structure-function relationship of arginine ligands, *J. Biol. Chem.* 280 (2005) 12130–12136, <https://doi.org/10.1074/jbc.M413454200>.
- S. Nesci, V. Ventrella, F. Trombetti, M. Pirini, A. Pagliarani, The mitochondrial F1FO-ATPase desensitization to oligomycin by tributyltin is due to thiol oxidation, *Biochimie* 97 (2014) 128–137, <https://doi.org/10.1016/j.biochi.2013.10.002>.
- M.M. Bradford, A rapid and sensitive method for the quantitation of microgram quantities of protein utilizing the principle of protein-dye binding, *Anal. Biochem.* 72 (1976) 248–254, <https://doi.org/10.1006/abio.1976.9999>.
- V. Ventrella, S. Nesci, F. Trombetti, P. Bandiera, M. Pirini, A.R. Borgatti, A. Pagliarani, Tributyltin inhibits the oligomycin-sensitive Mg-ATPase activity in Mytilus galloprovincialis digestive gland mitochondria, *Comp. Biochem. Physiol. C Toxicol. Pharmacol.* 153 (2011) 75–81, <https://doi.org/10.1016/j.cbpc.2010.08.007>.
- A. Cornish-Bowden, A simple graphical method for determining the inhibition constants of mixed, uncompetitive and non-competitive inhibitors, *Biochem. J.* 137 (1974) 143–144, <https://doi.org/10.1042/bj1370143>.
- T. Yonetani, The Yonetani-Theorell graphical method for examining overlapping subsites of enzyme active centers, *Methods Enzymol.* 87 (1982) 500–509, [https://doi.org/10.1016/S0076-6879\(82\)87028-6](https://doi.org/10.1016/S0076-6879(82)87028-6).
- S. Nesci, V. Ventrella, F. Trombetti, M. Pirini, A. Pagliarani, Thiol oxidation is crucial in the desensitization of the mitochondrial F1FO-ATPase to oligomycin and other macrolide antibiotics, *Biochim. Biophys. Acta* 1840 (2014) 1882–1891, <https://doi.org/10.1016/j.bbagen.2014.01.008>.
- S. Nesci, F. Trombetti, V. Ventrella, M. Pirini, A. Pagliarani, Kinetic properties of the mitochondrial F1FO-ATPase activity elicited by Ca<sup>2+</sup> in replacement of Mg<sup>2+</sup>, *Biochimie* 140 (2017) 73–81, <https://doi.org/10.1016/j.biochi.2017.06.013>.
- P. Bernardi, A. Rasola, M. Forte, G. Lippe, The mitochondrial permeability transition pore: channel formation by F-ATP synthase, integration in signal transduction, and role in pathophysiology, *Physiol. Rev.* 95 (2015) 1111–1155, <https://doi.org/10.1152/physrev.00001.2015>.
- D. Bald, T. Amano, E. Muneyuki, B. Pitarid, J.L. Rigaud, J. Kruij, T. Hisabori, M. Yoshida, M. Shibata, ATP synthesis by F<sub>0</sub>F<sub>1</sub>-ATP synthase independent of noncatalytic nucleotide binding sites and insensitive to azide inhibition, *J. Biol. Chem.* 273 (1998) 865–870, <https://doi.org/10.1074/jbc.273.2.865>.
- S. Nesci, F. Trombetti, V. Ventrella, A. Pagliarani, From the Ca<sup>2+</sup>-activated F1FO-ATPase to the mitochondrial permeability transition pore: an overview, *Biochimie* 152 (2018) 85–93, <https://doi.org/10.1016/j.biochi.2018.06.022>.
- S. Nesci, New insight in a new entity: the mitochondrial permeability transition pore arises from the Ca<sup>2+</sup>-activated F1FO-ATPases, *Sci. Bull.* 63 (2018) 143–145, <https://doi.org/10.1016/j.scib.2017.12.019>.
- V. Giorgio, V. Burchell, M. Schiavone, C. Bassot, G. Minervini, V. Petronilli, F. Argenton, M. Forte, S. Tosatto, G. Lippe, P. Bernardi, Ca<sup>2+</sup> binding to F-ATP synthase β subunit triggers the mitochondrial permeability transition, *EMBO Rep.* 18 (2017) 1065–1076, <https://doi.org/10.15252/embr.201643354>.
- S. Nesci, The mitochondrial permeability transition pore in cell death: a promising drug binding bioarchitecture, *Med. Res. Rev.* (2019) 1–7, <https://doi.org/10.1002/med.21635>.



# The mitochondrial F<sub>1</sub>F<sub>0</sub>-ATPase exploits the dithiol redox state to modulate the permeability transition pore

Cristina Algieri, Fabiana Trombetti, Alessandra Pagliarani, Vittoria Ventrella, Salvatore Nesci \*

Department of Veterinary Medical Sciences, University of Bologna, Via Tolara di Sopra, 50, Ozzano Emilia, Bologna, 40064, Italy

## ARTICLE INFO

### Keywords:

Mitochondria  
F<sub>1</sub>F<sub>0</sub>-ATPase  
mPTP  
Thiols  
Post-translational modification

## ABSTRACT

The dithiol reagents phenylarsine oxide (PAO) and dibromobimane (DBrB) have opposite effects on the F<sub>1</sub>F<sub>0</sub>-ATPase activity. PAO 20% increases ATP hydrolysis at 50 μM when the enzyme activity is activated by the natural cofactor Mg<sup>2+</sup> and at 150 μM when it is activated by Ca<sup>2+</sup>. The PAO-driven F<sub>1</sub>F<sub>0</sub>-ATPase activation is reverted to the basal activity by 50 μM dithiothreitol (DTE). Conversely, 300 μM DBrB decreases the F<sub>1</sub>F<sub>0</sub>-ATPase activity by 25% when activated by Mg<sup>2+</sup> and by 50% when activated by Ca<sup>2+</sup>. In both cases, the F<sub>1</sub>F<sub>0</sub>-ATPase inhibition by DBrB is insensitive to DTE. The mitochondrial permeability transition pore (mPTP) formation, related to the Ca<sup>2+</sup>-dependent F<sub>1</sub>F<sub>0</sub>-ATPase activity, is stimulated by PAO and desensitized by DBrB. Since PAO and DBrB apparently form adducts with different cysteine couples, the results highlight the crucial role of cross-linking of vicinal dithiols on the F<sub>1</sub>F<sub>0</sub>-ATPase, with (ir)reversible redox states, in the mPTP modulation.

## 1. Introduction

The F<sub>1</sub>F<sub>0</sub>-ATPase by triggering the mitochondrial permeability transition pore (mPTP) provides the molecular entity of this biological phenomenon [1,2]. The mPTP formation, which triggers lethal events in the cell, is involved in physiological and pathological functions and known to be affected by oxidative stress that oxidizes and/or cross-links the protein thiols. Consequently, the cysteine redox state can favor/hamper the “open” mPTP conformation, in turn promoted by Ca<sup>2+</sup> accumulation in the mitochondrial matrix. The mechanism(s) by which thiol oxidation promotes the mPTP formation was extensively investigated and may have biological implications in unravelling the mechanism of cell damage under oxidative stress [3]. Moreover, the recent observation of the different cryo-EM structure of the F<sub>1</sub>F<sub>0</sub>-ATPase in the presence of Mg<sup>2+</sup> or Ca<sup>2+</sup> as cation cofactor in the enzyme catalytic sites, highlighted the release of the lipid-plug from the c-ring in the “bent-pull” model [2,4]. In addition, Ca<sup>2+</sup>-interactions with the F<sub>1</sub>F<sub>0</sub>-ATPase were proven to modulate the mPTP activity [5]. The mPTP opens under an abrupt increase in Ca<sup>2+</sup> concentration in mitochondria. Under such conditions, the F<sub>1</sub>F<sub>0</sub>-ATPase replaces the natural cofactor Mg<sup>2+</sup> with Ca<sup>2+</sup>, which is probably only bound to the catalytic sites [6]. Ca<sup>2+</sup> insertion promotes a conformational change within the enzyme structure, which is transmitted from the F<sub>1</sub> domain to membrane-embedded

subunits of the F<sub>0</sub> domain, thus triggering the pore formation in the mitochondrial membrane [7,8]. Accordingly, Ca<sup>2+</sup> has higher atomic radius than Mg<sup>2+</sup> and can establish different interactions and coordination numbers within the catalytic sites of the enzyme. The Ca<sup>2+</sup> steric hindrance can modify the F<sub>1</sub> conformation and transmit a mechanical signal through the peripheral stalk to the membrane subunits of the F<sub>0</sub> domain. Indeed, the Ca<sup>2+</sup>-activated F<sub>1</sub>F<sub>0</sub>-ATPase assumes a disassembled conformation where F<sub>1</sub> is detached from F<sub>0</sub> driven by a twisted form of the peripheral stalk (Fig. 1a).

Dithiol reagents with different features are a precious tool to evaluate how (ir)reversible post-translational modifications of di-thiols on F<sub>1</sub>F<sub>0</sub>-ATPase [9] affect the formation and regulation of the mPTP. Phenylarsine oxide (PAO) and dibromobimane (DBrB) are sulphydryl (-SH) group modifiers that cause intramolecular cross-linking between two vicinal cysteine thiols [10]. PAO is a hydrophobic reagent and can directly react with functional -SH groups of the mPTP that are inaccessible to hydrophilic reagents in the absence of Ca<sup>2+</sup> [11]. Moreover, PAO selectively binds to vicinal thiols to form a stable dithioarsine ring and dramatically decreases the mPTP induction time in isolated mitochondria [12]. This abbreviation even occurs in the presence of excess EGTA (Ca<sup>2+</sup> chelator) in non-respiring mitochondria [11]. The threshold potential for mPTP opening is modulated by the mitochondrial redox state through both pyridine nucleotide pool (NADH/NAD<sup>+</sup> and

\* Corresponding author. Department of Veterinary Medical Sciences (DIMEVET), University of Bologna, Via Tolara di Sopra, 50, Ozzano Emilia, Bologna, 40064, Italy.

E-mail address: [salvatore.nesci@unibo.it](mailto:salvatore.nesci@unibo.it) (S. Nesci).

<https://doi.org/10.1016/j.abbi.2021.109027>

Received 4 August 2021; Received in revised form 6 September 2021; Accepted 7 September 2021

Available online 11 September 2021

0003-9861/© 2021 Elsevier Inc. All rights reserved.

NADPH/NADP<sup>+</sup>) and -SH groups (presumably by glutathione action) [13]. DBrB, which cross-links neighbouring cysteine residues, decreased the oligomycin-sensitive (OS)-ATPase to -35% of the control activity in beef heart mitochondria [14] by forming a protein-DBrB adduct. Conversely, DBrB cannot establish a thiol bridge when the protein already forms an intra protein disulfide [10]. Disulfides are featured by the thiol-thiol bond length, namely the distance between the two thiols (-S-S- distance). Disulfide bonds are usually about 2.05 Å in length, and 3.0 Å is taken as the cut-off for disulfides in the PDB database [15]. The capacity to join dithiols depends on the molecular structure of the cross-linked compound (X) which establishes sulfide bridges (-S-X-S-) of different lengths [16]. Indeed, DBrB can cover a broader distance between vicinal thiols than PAO (Fig. 1b).

The assessment of the dithiol reagents action mechanism on the F<sub>1</sub>F<sub>0</sub>-ATPase may be extremely useful to adequately exploit properties of the redox state of thiol groups for medical purposes.

## 2. Material and methods

### 2.1. Chemicals

Oligomycin (a mixture of oligomycins A, B and C), and Fura-FF were purchased from Vinci-Biochem (Vinci, Italy). Na<sub>2</sub>ATP, Phenylarsine oxide (PAO), Dibromobimane (DBrB), and 1,4-Dithioerythritol (DTE) were obtained from Sigma-Aldrich (Milan, Italy). Quartz double distilled water was used for all reagent solutions.

### 2.2. Preparation of the mitochondrial fractions

Swine hearts (*Sus scrofa domesticus*) were collected at a local abattoir and transported to the lab within 2 h in ice buckets at 0–4 °C. After removal of fat and blood clots as much as possible, approximately 30–40 g of heart tissue was rinsed in ice-cold washing Tris-HCl buffer (medium A) consisting of 0.25 M sucrose, 10 mM Tris (hydroxymethyl)-amino-methane (Tris), pH 7.4 and finely chopped into fine pieces with scissors. Each preparation was made from one heart. Once rinsed, tissues were gently dried on blotting paper and weighted. Then tissues were homogenized in medium B consisting of 0.25 M sucrose, 10 mM Tris, 1 mM

EDTA (free acid), 0.5 mg/ml BSA fatty acid-free, pH 7.4 with HCl at a ratio of 10 ml medium B per 1 g of fresh tissue. After a preliminary gentle break up by Ultraturrax T25, the tissue was carefully homogenized by a motor-driven Teflon pestle homogenizer (Braun Melsungen Type 853202) at 650 rpm with 3 up-and-down strokes. The mitochondrial fraction was then obtained by stepwise centrifugation (Sorvall RC2-B, rotor SS34). Briefly, the homogenate was centrifuged at 1000×g for 5 min, thus yielding a supernatant and a pellet. The pellet was re-homogenized under the same conditions of the first homogenization and re-centrifuged at 1000×g for 5 min. The gathered supernatants from these two centrifugations, filtered through four cotton gauze layers, were centrifuged at 10,500×g for 10 min to yield the raw mitochondrial pellet. The raw pellet was resuspended in medium A and further centrifuged at 10,500×g for 10 min to obtain the final mitochondrial pellet. The latter was resuspended by gentle stirring using a Teflon Potter Elvehjem homogenizer in a small volume of medium A, thus obtaining a protein concentration of 30 mg/ml [17]. All steps were carried out at 0–4 °C. The protein concentration was determined according to the colorimetric method of Bradford by Bio-Rad Protein Assay kit II with BSA as standard. The mitochondrial preparations were then stored in liquid nitrogen until the evaluation of F<sub>1</sub>F<sub>0</sub>-ATPase activities.

### 2.3. Mitochondrial F-ATPase activity assays

Thawed mitochondrial preparations were immediately used for F-ATPase activity assays. The capability of ATP hydrolysis was assayed in a reaction medium (1 ml). The optimal conditions to obtain the maximal activity of the F<sub>1</sub>F<sub>0</sub>-ATPase, which depend on substrates concentration and pH values, are at 0.15 mg mitochondrial protein and 75 mM ethanolamine-HCl buffer pH 9.0, 6.0 mM Na<sub>2</sub>ATP and 2.0 mM MgCl<sub>2</sub> for the Mg<sup>2+</sup>-activated F<sub>1</sub>F<sub>0</sub>-ATPase assay, and 75 mM ethanolamine-HCl buffer pH 8.8, 3.0 mM Na<sub>2</sub>ATP and 2.0 mM CaCl<sub>2</sub> for the Ca<sup>2+</sup>-activated F<sub>1</sub>F<sub>0</sub>-ATPase assay. These assay conditions were previously proven to elicit the maximal enzyme activities either stimulated by Mg<sup>2+</sup> or by Ca<sup>2+</sup> in swine heart mitochondria [5]. After 5 min preincubation at 37 °C, the reaction, carried out at the same temperature, was started by the addition of the substrate Na<sub>2</sub>ATP and stopped after 5 min by the addition of 1 ml of ice-cold 15% (w/w) trichloroacetic acid (TCA)

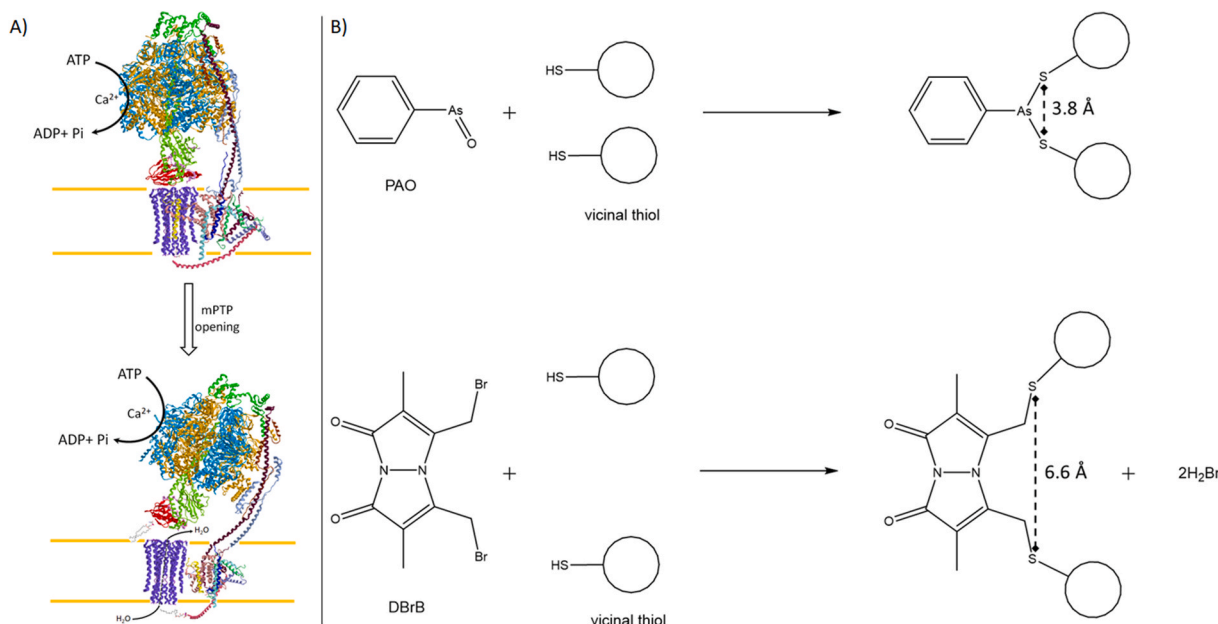


**Fig. 1.** Molecular mechanism. A) Model of F<sub>1</sub>F<sub>0</sub>-ATPase in the mPTP formation. The F<sub>1</sub>F<sub>0</sub>-ATPase activity sustained by the Ca<sup>2+</sup> as cofactor hydrolyzes ATP by causing disassembly/distortion of the entire enzyme complex. The structural modification of the Ca<sup>2+</sup>-activated F<sub>1</sub>F<sub>0</sub>-ATPase triggers the formation and opening of the mPTP [2,30]. B) Reactions involved in the dithiol bridge formation by phenylarsine oxide (PAO) and dibromobimane (DBrB). The distances between two thiol groups linked by the reagent X (-S-X-S-) were calculated by Chem3D.

aqueous solution. Once the reaction was stopped, vials were centrifuged for 15 min at 3500 rpm (Eppendorf Centrifuge 5202). In the supernatant, the concentration of inorganic phosphate (Pi) hydrolyzed by known amounts of mitochondrial protein, which is an indirect measure of F-ATPase activity, was spectrophotometrically evaluated [18]. According to the method employed, to detect the Pi release by the enzymatic reaction, the Pi released independently of the F<sub>1</sub>F<sub>0</sub>-ATPase activity should be quantified. To this aim, 1 µl from a stock solution of 3 mg/ml oligomycin in dimethylsulfoxide was directly added to the reaction mixture before starting the reaction. The total mitochondrial ATPase activity was calculated by detecting the Pi in control tubes run in parallel and containing 1 µl dimethylsulfoxide per ml reaction system. In each experimental set, control tubes were alternated to the condition to be tested. The employed dose of oligomycin, a specific inhibitor of F-ATPases which selectively blocks the F<sub>0</sub> subunit, ensured maximal enzyme activity inhibition and was currently used in F-ATPase assays [19].

In all experiments, the F<sub>1</sub>F<sub>0</sub>-ATPase activity was routinely measured by subtracting, from the Pi hydrolyzed by the total ATPase activity, the Pi hydrolyzed in the presence of oligomycin [20]. In all experiments the F-ATPase activity, either activated by Ca<sup>2+</sup> as a cofactor or by Mg<sup>2+</sup>, was expressed as µmol Pi·mg protein<sup>-1</sup> min<sup>-1</sup>.

#### 2.4. Evaluation of PTP

Immediately after the preparation of swine heart mitochondrial fractions, fresh mitochondrial suspensions (1 mg/ml) were energized in the assay buffer (130 mM KCl, 1 mM KH<sub>2</sub>PO<sub>4</sub>, 20 mM HEPES, pH 7.2 with Tris), incubated at 25 °C with 1 µg/ml rotenone and 5 mM succinate as respiratory substrate. To evaluate PAO or DBrB effect, selected di-thiol group cross-linking reagents concentrations, obtained by sampling small aliquots from standard PAO or DBrB aqueous solutions, as described in the Section "Mitochondrial F-ATPase activity assays", were added to the mitochondrial suspensions before mPTP evaluation. mPTP opening was induced by the addition of low concentrations of Ca<sup>2+</sup> (10 µM) as CaCl<sub>2</sub> aqueous solution at fixed time intervals (1 min). The Ca<sup>2+</sup> retention capacity (CRC), whose lowering indicates mPTP opening, was spectrofluorometrically evaluated in the presence of 0.8 µM Fura-FF. The probe has different spectral properties in the absence and in the presence of Ca<sup>2+</sup>, namely, it displays excitation/emission spectra of 365/514 nm in the absence of Ca<sup>2+</sup> (Fura-FF low Ca<sup>2+</sup>) and shifts to 339/507 nm in the presence of high Ca<sup>2+</sup> concentrations (Fura-FF high Ca<sup>2+</sup>). mPTP opening was evaluated by the increase in the fluorescence intensity ratio (Fura-FF high Ca<sup>2+</sup>)/(Fura-FF low Ca<sup>2+</sup>), which indicates a decrease in CRC [5]. All measurements were processed by LabSolutions RF software.

#### 2.5. Calculations and statistics

The data represent the mean ± SD (shown as vertical bars in the figures) of the number of experiments reported in the figure captions. In each experimental set, the analyses were carried out on different pools of animals. Statistical analyses were performed by SIGMASTAT software. The analysis of variance followed by Students–Newman–Keuls' test when *F* values indicated significance (*P* ≤ 0.05) was applied. Percentage data were arcsin-transformed before statistical analyses to ensure normality.

### 3. Results and discussion

In swine heart mitochondria the bifunctional thiol reagents PAO and DBrB show opposite effects on the F<sub>1</sub>F<sub>0</sub>-ATPase activity. PAO 20% increases the activity of the F<sub>1</sub>F<sub>0</sub>-ATPase either activated by Mg<sup>2+</sup> or by Ca<sup>2+</sup> at 50 µM and 150 µM, respectively (Fig. 2A). Conversely, DBrB shows a maximal 25% inhibition of the Mg<sup>2+</sup>-activated F<sub>1</sub>F<sub>0</sub>-ATPase at 150 µM DBrB, and a maximal 50% inhibition of the Ca<sup>2+</sup>-activated F<sub>1</sub>F<sub>0</sub>-ATPase at 300 µM DBrB (Fig. 2B). The opposite effect of the two dithiol reagents may be due to their interaction with different cysteine couples of the enzyme. Therefore, the post-translational cysteine modifications could alter the F<sub>1</sub>F<sub>0</sub>-ATPase structure independently of which cation activates the enzyme. Disulfide forms on the F<sub>1</sub>F<sub>0</sub>-ATPase by binding between Cys251 of two α subunits or Cys251 and Cys78 of α and γ subunit, respectively during holoenzyme assembly [21]. The disulfur cross-link between cysteines is associated with F<sub>1</sub>F<sub>0</sub>-ATPase dysfunction in heart failure patients [21]. Conversely, reversible dithiol bridges, established by mercury, increase the F<sub>1</sub>F<sub>0</sub>-ATPase activity when the MgATP substrate is bound in the catalytic sites [22].

To verify if the cysteine oxidation by PAO and DBrB was related to their opposite effects on the F<sub>1</sub>F<sub>0</sub>-ATPase the reducing thiol reagent DTE was tested. The Mg<sup>2+</sup>- or Ca<sup>2+</sup>-activated F<sub>1</sub>F<sub>0</sub>-ATPase activities were evaluated in the presence of 150 µM PAO (Fig. 3A and B) or 300 µM DBrB (Fig. 3C and D) with and without DTE to check if the modified cysteine thiols (-S-X-S-) of the protein adduct were reduction-sensitive. In the presence of 50 µM DTE the Mg<sup>2+</sup>- and Ca<sup>2+</sup>-activated F<sub>1</sub>F<sub>0</sub>-ATPase showed the same enzyme activity as the control in a PAO- and DTE-free reaction medium (Fig. 3A,C) or in a DBrB- and DTE-free reaction medium (Fig. 3B,D). The 50 µM DTE addition significantly lessened the 20% Mg<sup>2+</sup>- or Ca<sup>2+</sup>-activated F<sub>1</sub>F<sub>0</sub>-ATPase stimulation in the presence of PAO (Fig. 3A and B). Conversely, in the presence of DBrB, the Mg<sup>2+</sup>- or Ca<sup>2+</sup>-activated F<sub>1</sub>F<sub>0</sub>-ATPase inhibition by 25% and 50%, respectively were maintained irrespective of DTE (Fig. 3C and D). The respective reversible and irreversible redox behaviour of PAO- or DBrB-sensitive cysteine couples confirms that this regulation is irrespective of the cofactor bound to the catalytic sites. Oxidative stress causes a variety of post-translational modifications of thiol groups. The thiol-bearing cysteines are unique molecular switches which play structural and

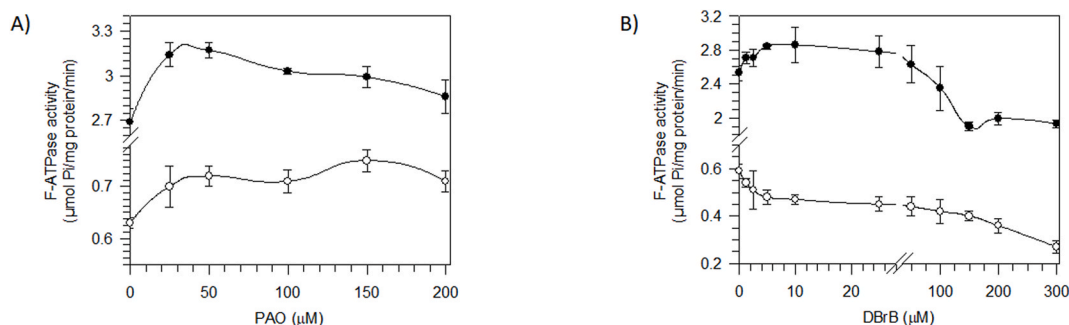
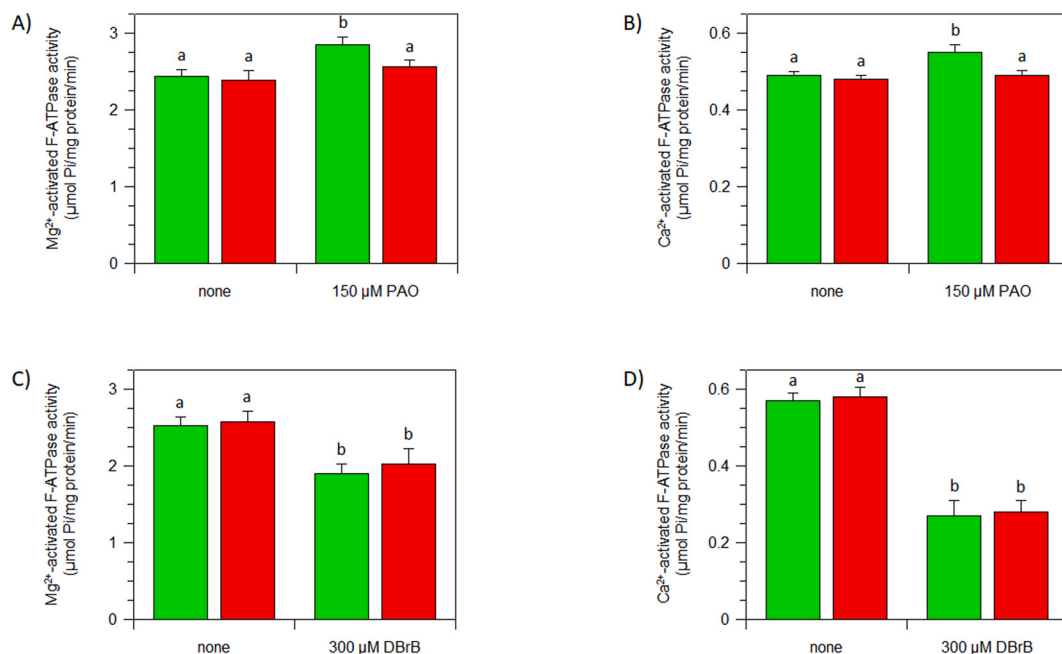


Fig. 2. Dose-response curve of di-thiol cross-linking reagents on the F<sub>1</sub>F<sub>0</sub>-ATPase activity. Effect of increasing PAO (A) or DBrB (B) concentrations on the F<sub>1</sub>F<sub>0</sub>-ATPase activated by Mg<sup>2+</sup> (Mg<sup>2+</sup>-activated F<sub>1</sub>F<sub>0</sub>-ATPase) (●) and by Ca<sup>2+</sup> (Ca<sup>2+</sup>-activated F<sub>1</sub>F<sub>0</sub>-ATPase) (○) activities. Data represent the mean ± SD from three independent experiments carried out on three different mitochondrial preparations.



**Fig. 3.** Mg<sup>2+</sup> and Ca<sup>2+</sup>-activated F<sub>1</sub>F<sub>0</sub>-ATPase activities in PAO or DBrB-treated mitochondria in the presence of thiol reducing (50 μM DTE) agent. The effect of 150 μM PAO (A and B) or 150 μM DBrB (C and D) was evaluated in the absence (green bars, ■) and in the presence (red bars, ■) of DTE. Data represent the mean ± SD from three independent experiments carried out on three different mitochondrial preparations. Different letters indicate significantly different values within each treatment ( $P \leq 0.05$ ). (For interpretation of the references to color in this figure legend, the reader is referred to the Web version of this article.)

regulatory roles in biology [23] and in mitochondria that are highly compartmentalized thiol-redox organelles [24]. The PAO and DBrB effects highlight how different dithiol modifiers act on the F<sub>1</sub>F<sub>0</sub>-ATPase catalytic activity and on the known redox state of vicinal cysteinyl residues in tuning the mPTP opening and the F<sub>1</sub>F<sub>0</sub>-ATPase, thus reinforcing their mutual link [25]. Indeed, the calcium retention capacity (CRC), by measuring the capability of intact mitochondria to accumulate Ca<sup>2+</sup> and to release it when the mPTP opens, showed opposite profiles in the presence of PAO and DBrB (Fig. 4), consistently with the F<sub>1</sub>F<sub>0</sub>-ATPase modulation by these reagents. In other words, in CRC assays the addition of Ca<sup>2+</sup> pulses make Ca<sup>2+</sup> accumulate in the mitochondrial matrix so as mitochondria take up Ca<sup>2+</sup>. The decreased Ca<sup>2+</sup> accumulation in mitochondria shown by CRC drop reflects the mPTP opening. Therefore, the CRC decrease in PAO-treated mitochondria, revealed by an increase in fluorescence intensity detected as Fura-FF ratio [(Fura-FF high Ca<sup>2+</sup>)/(Fura-FF low Ca<sup>2+</sup>)], points out that PAO sensitizes the mPTP formation to Ca<sup>2+</sup> and, consistently, stimulates the F<sub>1</sub>F<sub>0</sub>-ATPase activities. The PAO-driven increased mPTP sensitivity was counteracted by DTE, thus confirming the involvement of cross-linked critical dithiols in mPTP opening. The DBrB concentration tested (300 μM), selected on the basis of the 50% inhibition of the Ca<sup>2+</sup>-activated F<sub>1</sub>F<sub>0</sub>-ATPase whose activity is related to the mPTP opening [25–28], did not elicit any sudden increase in fluorescence intensity due to Ca<sup>2+</sup> release. Moreover, the mPTP inhibition by DBrB was insensitive to DTE (Fig. 4). The DBrB inhibition of mPTP formation was corroborated by the inhibition of the two F<sub>1</sub>F<sub>0</sub>-ATPase activities, especially of the Ca<sup>2+</sup>-activated F<sub>1</sub>F<sub>0</sub>-ATPase.

We can infer that two different cysteine couples specifically cross-linked with PAO and DBrB produce opposite effects on the F<sub>1</sub>F<sub>0</sub>-ATPase and on the mPTP. Moreover, apparently DTE only reduces the dithiols that react with PAO, whereas it can remove the irreversible inhibition caused by DBrB. It is tempting to speculate that the F<sub>1</sub>F<sub>0</sub>-ATPase has two distinct molecular strategies to regulate the mPTP opening: *i*) the reversible oxidation of vicinal dithiols (presumably not farther than 3.8 Å (Fig. 1B)); *ii*) the irreversible oxidation of dithiols far up to 6.6 Å from each other (Fig. 1B). Since, the mPTP participates in

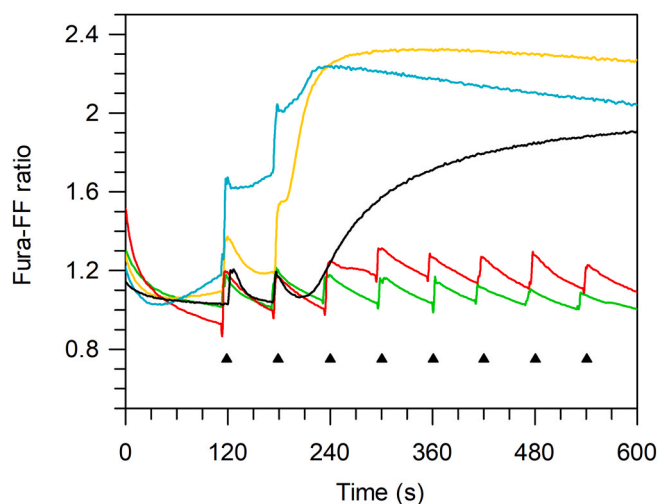


**Fig. 4.** Evaluation of PTP opening in intact mitochondrial preparations. CRC, detected as Fura-FF ratio, was monitored in response to subsequent 10 μM CaCl<sub>2</sub> pulses (shown by the arrows), as detailed in the Section Methods, in the absence (Control-black line, —) and in the presence of 150 μM PAO (light blue line, —), 150 μM DBrB (red line, —), 150 μM PAO + 50 μM DTE (gold line, —), and 150 μM DBrB + 50 μM DTE (green line, —). The PAO and DBrB concentrations were selected based on the maximal activation or inhibition of the Ca<sup>2+</sup>-activated F<sub>1</sub>F<sub>0</sub>-ATPase by PAO or DBrB, respectively. Three independent experiments were carried out on three different mitochondrial preparations. (For interpretation of the references to color in this figure legend, the reader is referred to the Web version of this article.)

both development and cell death [29], the dithiols by post-translational modification may act on the regulation of the transition from physiological to pathological mPTP opening in mitochondria. In this perspective, future studies could point out cysteine pairs on the F<sub>1</sub>F<sub>0</sub>-ATPase which may serve as drug targets to control pathological conditions due to mPTP dysregulation and, physiologically, are molecular keys to open

the mPTP.

### Author contributions

C.A. investigation and formal analysis; F.T. and V.V. validation; F.T. and A.P. resources and writing—review & editing; S.N. conceptualization, supervision and writing—original draft.

### Acknowledgments

This study was supported by a RFO grant from the University of Bologna, Italy.

Danilo Matteuzzi and Roberto Giusti (Department of Veterinary Medical Sciences, University of Bologna) are gratefully acknowledged for kindly conferring swine hearts from a local abattoir to Biochemistry laboratories.

### References

- [1] S. Nesci, A. Pagliarani, Emerging roles for the mitochondrial ATP synthase supercomplexes, *Trends Biochem. Sci.* 44 (2019) 821–823, <https://doi.org/10.1016/j.tibs.2019.07.002>.
- [2] G. Pinke, L. Zhou, L.A. Sazanov, Cryo-EM structure of the entire mammalian F-type ATP synthase, *Nat. Struct. Mol. Biol.* 27 (2020) 1077–1085, <https://doi.org/10.1038/s41594-020-0503-8>.
- [3] V. Petronilli, P. Costantini, L. Scorrano, R. Colonna, S. Passamonti, P. Bernardi, The voltage sensor of the mitochondrial permeability transition pore is tuned by the oxidation-reduction state of vicinal thiols. Increase of the gating potential by oxidants and its reversal by reducing agents, *J. Biol. Chem.* 269 (1994) 16638–16642.
- [4] N. Mnatsakanyan, E.A. Jonas, ATP synthase c-subunit ring as the channel of mitochondrial permeability transition: regulator of metabolism in development and degeneration, *J. Mol. Cell. Cardiol.* 144 (2020) 109–118, <https://doi.org/10.1016/j.yjmcc.2020.05.013>.
- [5] C. Algieri, F. Trombetti, A. Pagliarani, M. Fabbri, S. Nesci, The inhibition of gadolinium ion (Gd<sup>3+</sup>) on the mitochondrial F1FO-ATPase is linked to the modulation of the mitochondrial permeability transition pore, *Int. J. Biol. Macromol.* 184 (2021) 250–258, <https://doi.org/10.1016/j.ijbiomac.2021.06.065>.
- [6] M.J. Hubbard, N.J. McHugh, Mitochondrial ATP synthase F1-beta-subunit is a calcium-binding protein, *FEBS Lett.* 391 (1996) 323–329.
- [7] S. Nesci, F. Trombetti, V. Ventrella, A. Pagliarani, From the Ca<sup>2+</sup>-activated F1FO-ATPase to the mitochondrial permeability transition pore: an overview, *Biochimie* 152 (2018) 85–93, <https://doi.org/10.1016/j.biochi.2018.06.022>.
- [8] V. Giorgio, V. Burchell, M. Schiavone, C. Bassot, G. Minervini, V. Petronilli, F. Argenton, M. Forte, S. Tosatto, G. Lippe, P. Bernardi, Ca(2+) binding to F-ATP synthase  $\beta$  subunit triggers the mitochondrial permeability transition, *EMBO Rep.* 18 (2017) 1065–1076, <https://doi.org/10.15252/embr.201643354>.
- [9] S. Nesci, F. Trombetti, V. Ventrella, A. Pagliarani, Post-translational modifications of the mitochondrial F1FO-ATPase, *Biochim. Biophys. Acta* 1861 (2017) 2902–2912, <https://doi.org/10.1016/j.bbagen.2017.08.007>.
- [10] O. Rudyk, P. Eaton, Biochemical methods for monitoring protein thiol redox states in biological systems, *Redox Biol* 2 (2014) 803–813, <https://doi.org/10.1016/j.redox.2014.06.005>.
- [11] E. Lenartowicz, P. Bernardi, G.F. Azzone, Phenylarsine oxide induces the cyclosporin A-sensitive membrane permeability transition in rat liver mitochondria, *J. Bioenerg. Biomembr.* 23 (1991) 679–688, <https://doi.org/10.1007/BF00785817>.
- [12] P. Bernardi, S. Vassanelli, P. Veronese, R. Colonna, I. Szabó, M. Zoratti, Modulation of the mitochondrial permeability transition pore. Effect of protons and divalent cations, *J. Biol. Chem.* 267 (1992) 2934–2939.
- [13] P. Costantini, B.V. Chernyak, V. Petronilli, P. Bernardi, Modulation of the mitochondrial permeability transition pore by pyridine nucleotides and dithiol oxidation at two separate sites, *J. Biol. Chem.* 271 (1996) 6746–6751.
- [14] G. Zimmer, L. Mainka, B.M. Heil, Bromobimane crosslinking studies in oligomycin-sensitive ATPase from beef heart mitochondria. Mr 31 000 protein crosslinked, *FEBS Lett.* 150 (1982) 207–210, [https://doi.org/10.1016/0014-5793\(82\)81335-5](https://doi.org/10.1016/0014-5793(82)81335-5).
- [15] M.-A. Sun, Y. Wang, Q. Zhang, Y. Xia, W. Ge, D. Guo, Prediction of reversible disulfide based on features from local structural signatures, *BMC Genom.* 18 (2017) 279, <https://doi.org/10.1186/s12864-017-3668-8>.
- [16] A. Shvetsov, J.D. Stamm, M. Phillips, D. Warshaviak, C. Altenbach, P. A. Rubenstein, K. Hideg, W.L. Hubbell, E. Reisler, Conformational dynamics of loop 262–274 in G- and F-actin, *Biochemistry* 45 (2006) 6541–6549, <https://doi.org/10.1021/bi052558v>.
- [17] S. Nesci, V. Ventrella, F. Trombetti, M. Pirini, A. Pagliarani, Preferential nitrite inhibition of the mitochondrial F1FO-ATPase activities when activated by Ca(2+) in replacement of the natural cofactor Mg(2+), *Biochim. Biophys. Acta* 1860 (2016) 345–353, <https://doi.org/10.1016/j.bbagen.2015.11.004>.
- [18] V. Ventrella, S. Nesci, F. Trombetti, P. Bandiera, M. Pirini, A.R. Borgatti, A. Pagliarani, Tributyltin inhibits the oligomycin-sensitive Mg-ATPase activity in *Mytilus galloprovincialis* digestive gland mitochondria, *Comp. Biochem. Physiol. C Toxicol. Pharmacol.* 153 (2011) 75–81, <https://doi.org/10.1016/j.cbpc.2010.08.007>.
- [19] S. Nesci, V. Ventrella, F. Trombetti, M. Pirini, A. Pagliarani, The mitochondrial F1FO-ATPase desensitization to oligomycin by tributyltin is due to thiol oxidation, *Biochimie* 97 (2014) 128–137, <https://doi.org/10.1016/j.biochi.2013.10.002>.
- [20] S. Nesci, V. Ventrella, F. Trombetti, M. Pirini, A. Pagliarani, Tri-n-butyltin binding to a low-affinity site decreases the F1FO-ATPase sensitivity to oligomycin in mussel mitochondria, *Appl. Organomet. Chem.* 26 (2012) 593–599, <https://doi.org/10.1002/aoc.2904>.
- [21] S.-B. Wang, D.B. Foster, J. Rucker, B. O'Rourke, D.A. Kass, J.E. Van Eyk, Redox regulation of mitochondrial ATP synthase: implications for cardiac resynchronization therapy, *Circ. Res.* 109 (2011) 750–757, <https://doi.org/10.1161/CIRCRESAHA.111.246124>.
- [22] S. Nesci, F. Trombetti, M. Pirini, V. Ventrella, A. Pagliarani, Mercury and protein thiols: stimulation of mitochondrial F1FO-ATPase and inhibition of respiration, *Chem. Biol. Interact.* 260 (2016) 42–49, <https://doi.org/10.1016/j.cbi.2016.10.018>.
- [23] A. Fra, E.D. Yoboue, R. Sitia, Cysteines as redox molecular switches and targets of disease, *Front. Mol. Neurosci.* 10 (2017) 167, <https://doi.org/10.3389/fnmol.2017.00167>.
- [24] S. Dröse, U. Brandt, I. Wittig, Mitochondrial respiratory chain complexes as sources and targets of thiol-based redox-regulation, *Biochim. Biophys. Acta* 1844 (2014) 1344–1354, <https://doi.org/10.1016/j.bbapap.2014.02.006>.
- [25] C. Algieri, F. Trombetti, A. Pagliarani, V. Ventrella, C. Bernardini, M. Fabbri, M. Forni, S. Nesci, Mitochondrial Ca<sup>2+</sup>-activated F1 FO -ATPase hydrolyzes ATP and promotes the permeability transition pore, *Ann. N. Y. Acad. Sci.* 1457 (2019) 142–157, <https://doi.org/10.1111/nyas.14218>.
- [26] C. Algieri, F. Trombetti, A. Pagliarani, V. Ventrella, S. Nesci, Phenylglyoxal inhibition of the mitochondrial F1FO-ATPase activated by Mg<sup>2+</sup> or by Ca<sup>2+</sup> provides clues on the mitochondrial permeability transition pore, *Arch. Biochem. Biophys.* 681 (2020) 108258, <https://doi.org/10.1016/j.abb.2020.108258>.
- [27] S. Nesci, C. Algieri, F. Trombetti, V. Ventrella, M. Fabbri, A. Pagliarani, Sulfide affects the mitochondrial respiration, the Ca<sup>2+</sup>-activated F1FO-ATPase activity and the permeability transition pore but does not change the Mg<sup>2+</sup>-activated F1FO-ATPase activity in swine heart mitochondria, *Pharmacol. Res.* 166 (2021) 105495, <https://doi.org/10.1016/j.phrs.2021.105495>.
- [28] V. Algieri, C. Algieri, L. Maiuolo, A. De Nino, A. Pagliarani, M.A. Tallarida, F. Trombetti, S. Nesci, 1,5-Disubstituted-1,2,3-triazoles as inhibitors of the mitochondrial Ca<sup>2+</sup>-activated F1 FO -ATP(hydrol)ase and the permeability transition pore, *Ann. N. Y. Acad. Sci.* 1485 (2021) 43–55, <https://doi.org/10.1111/nyas.14474>.
- [29] M.J. Pérez, R.A. Quintanilla, Development or disease: duality of the mitochondrial permeability transition pore, *Dev. Biol.* 426 (2017) 1–7, <https://doi.org/10.1016/j.ydbio.2017.04.018>.
- [30] S. Nesci, A. Pagliarani, Incoming news on the F-type ATPase structure and functions in mammalian mitochondria, *BBA Advances* 1 (2021) 100001, <https://doi.org/10.1016/j.bbadv.2020.100001>.

*Note: The following work is part of the research article “C. Algieri, C. Bernardini, F. Oppedisano, D. La Mantia, F. Trombetti, E. Palma, M. Forni, V. Mollace, G. Romeo, S. Nesci (2022). The mitochondria bioenergetic functions and cell metabolism are modulated by bergamot polyphenolic fraction. Cells, 11: 1401 ”<https://doi.org/10.3390/cells11091401>” accepted after the thesis review.*

### **The effect of polyphenolic fraction of bergamot (BPF) on isolate mitochondria**

BPF was tested at concentrations increasing from 0 to 100  $\mu\text{g/ml}$  on the activity of  $\text{F}_1\text{F}_0$ -ATPase of mitochondria isolated from swine heart, activated by the natural cofactor  $\text{Mg}^{2+}$  and  $\text{Ca}^{2+}$ . Data show a slight inhibitory effect of 10% on the  $\text{Ca}^{2+}$ -activated  $\text{F}_1\text{F}_0$ -ATPase as opposed to when it binds the natural cofactor  $\text{Mg}^{2+}$ , in which an activation of 15% is shown (figure 10).

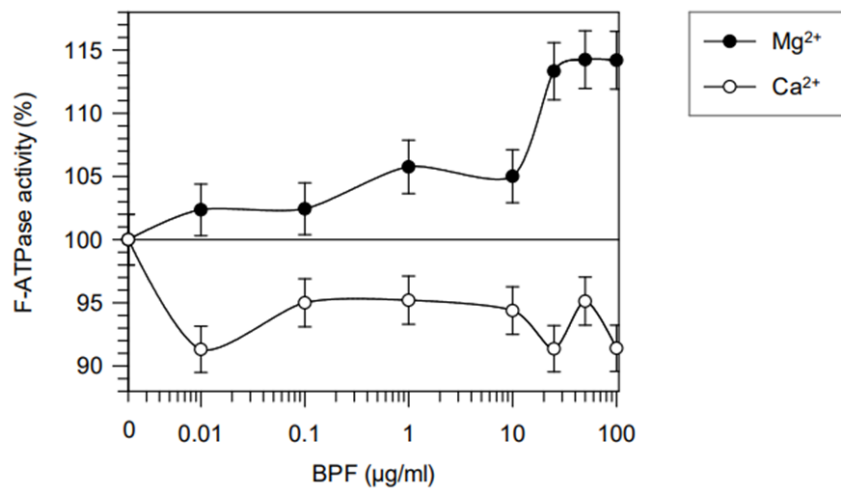


**Figure 10.** Effect of increasing concentrations of BPF on the  $\text{Ca}^{2+}$ -activated  $\text{F}_1\text{F}_0$ -ATPase ( $\circ$ ) and  $\text{Mg}^{2+}$ -activated  $\text{F}_1\text{F}_0$ -ATPase ( $\bullet$ ). Data represent the mean  $\pm$  SD from three independent experiments carried out on distinct mitochondrial preparations.

The inhibitory effect on  $\text{Ca}^{2+}$ -activated  $\text{F}_1\text{F}_0$ -ATPase was related to subsequent studies on the CRC of a suspension of isolated mitochondria. According to the fluorimetric method employed, the decrease in CRC from the mitochondria attributed to the opening of mPTP is revealed by an increase in the fluorescence intensity ratio ( $\text{Fura-FF high Ca}^{2+}$ )/( $\text{Fura-FF low Ca}^{2+}$ ). Compared to the control condition, the presence of BPF at 50  $\mu\text{g/ml}$  and 100  $\mu\text{g/ml}$  shows a desensitization of the opening of the mPTP, causing a concentration-dependent reduction of the pore size (*figure 11*).

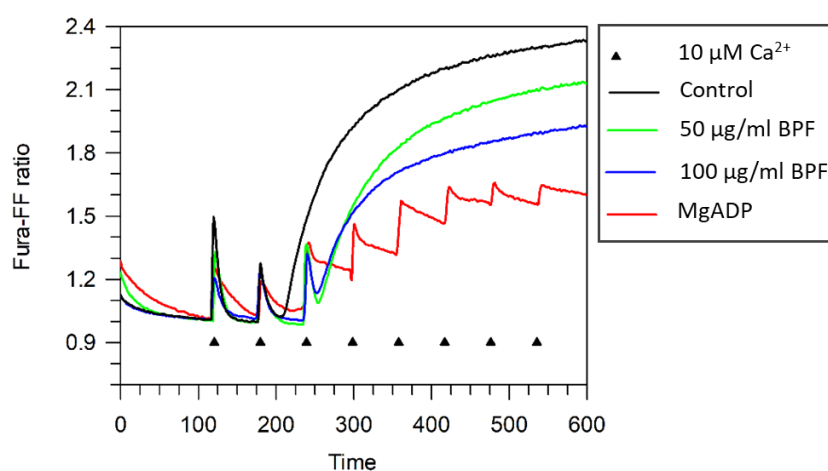


**Figure 11. Evaluation of mPTP opening.** CRC was monitored in response to subsequent 10  $\mu\text{M}$   $\text{CaCl}_2$  pulses (shown by the arrows), with MgADP (red line), in the absence (Control-black line) and in the presence of 50  $\mu\text{g/ml}$  (green line) and 100  $\mu\text{g/ml}$  (blue line) of BPF. Data represent the mean  $\pm$  SD from three independent experiments carried out on distinct mitochondrial preparations.

By evaluating the effect of BPF on the OXPHOS we detected a coupling efficiency improvement. Indeed, the RCR, determined by the rate of oxygen consumption while ADP is being phosphorylated divided by the rate after the ADP is used up, is improved by BPF in the presence of the glutamate/malate substrates, therefore, starting from CI (*figure 12A*), and succinate substrate, therefore, starting from CII (*figure 12B*). The BPF at 50  $\mu\text{g/ml}$  and 100  $\mu\text{g/ml}$  with glutamate/malate substrates and at 100  $\mu\text{g/ml}$  with succinate reduced mitochondrial decoupling

activity. In other words, the capacity for phosphorylating respiration relative to the respiration required to offset the proton leak was increased in mitochondria by BPF.

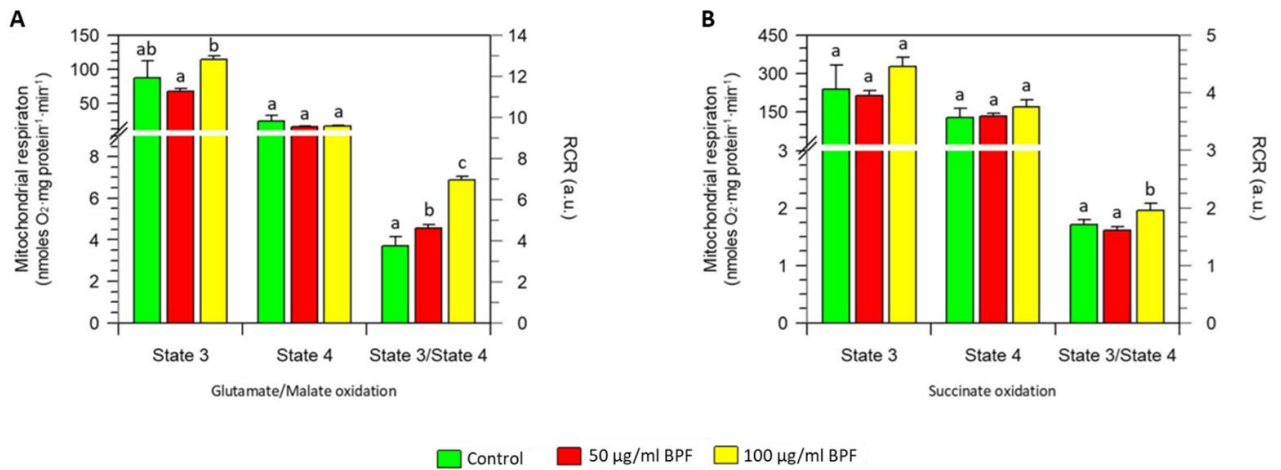


**Figure 12.** Evaluation of Glutamate/Malate oxidation (A) and Succinate oxidation (B) without and with 50 µg/mL BPF or 100 µg/mL BPF. Data represent the mean  $\pm$  SD from three independent experiments carried out on distinct mitochondrial preparations. Different letters indicate significant differences ( $P \leq 0.05$ ) among treatments within the same parameter.

## The effect of melatonin on the mitochondrial $F_1F_0$ -ATPase activity, mPTP formation and ROS production

Apparently, melatonin does not inhibit  $Mg^{2+}$ -activated  $F_1F_0$ -ATPase at  $37^\circ\text{C}$ , the temperature at which all experimental tests carried out on swine heart mitochondria are usually conducted, but data show an inhibitory effect which increases with decreasing temperature (*figure 13*). However, its effect does not depend on the change of state at the various temperatures of the membrane in which  $F_1F_0$ -ATPase is located because the Melting Temperature ( $T_m$ ), at which the membrane changes its state, remains unchanged with and without melatonin, as demonstrated by the Arrhenius plots (*figure 14*).

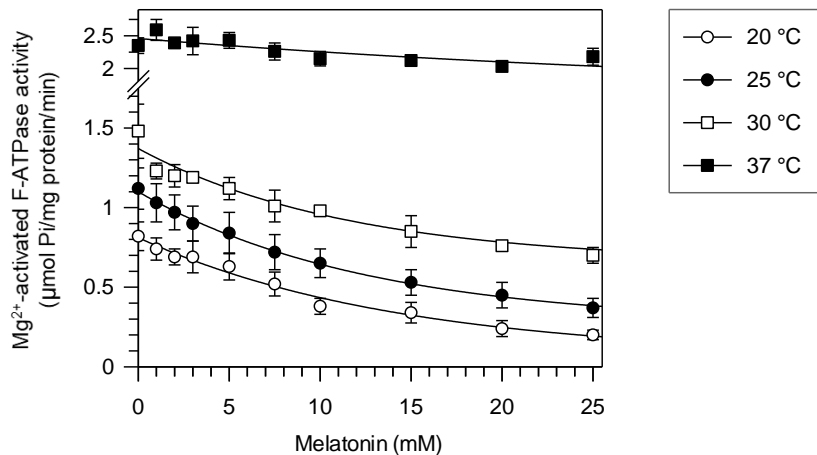


**Figure 13.** Dose-response curve of melatonin on the  $Mg^{2+}$ -activated  $F_1F_0$ -ATPase activity at  $20^\circ\text{C}$  ( $\circ$ ),  $25^\circ\text{C}$  ( $\bullet$ ),  $30^\circ\text{C}$  ( $\square$ ),  $37^\circ\text{C}$  ( $\blacksquare$ ). Data represent the mean  $\pm$  SD from three independent experiments carried out on distinct mitochondrial preparations.

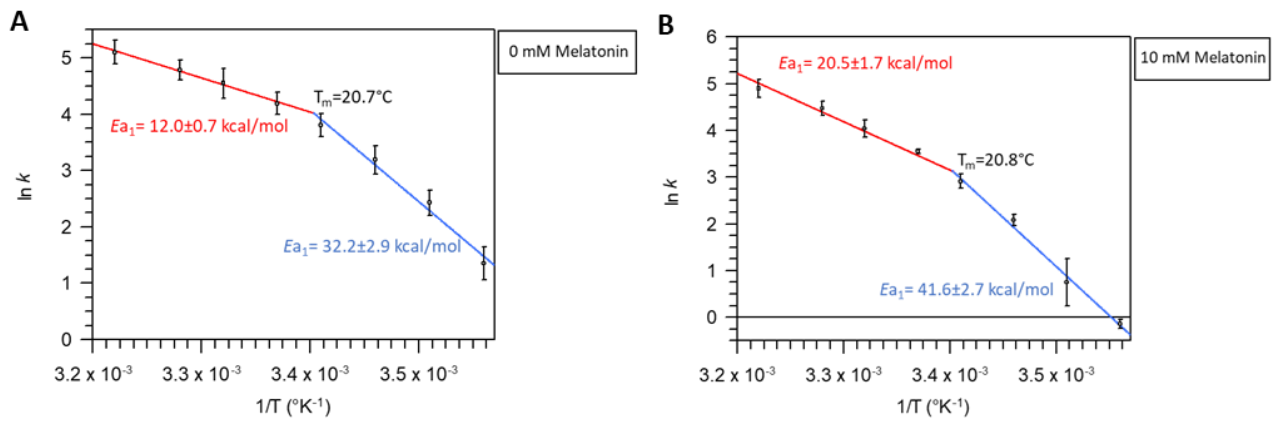


**Figure 14.** Arrhenius plots of the  $Mg^{2+}$ -activated  $F_1F_0$ -ATPase activity without (A) and with 10mM of melatonin (B). Data represent the mean  $\pm$  SD from three independent experiments carried out on distinct mitochondrial preparations.

Conversely, a strong inhibitory effect of melatonin on the  $Ca^{2+}$ -activated  $F_1F_0$ -ATPase is shown by the titration curve with an  $IC_{50}$  value equal to 6.625  $\mu$ M (figure 15).

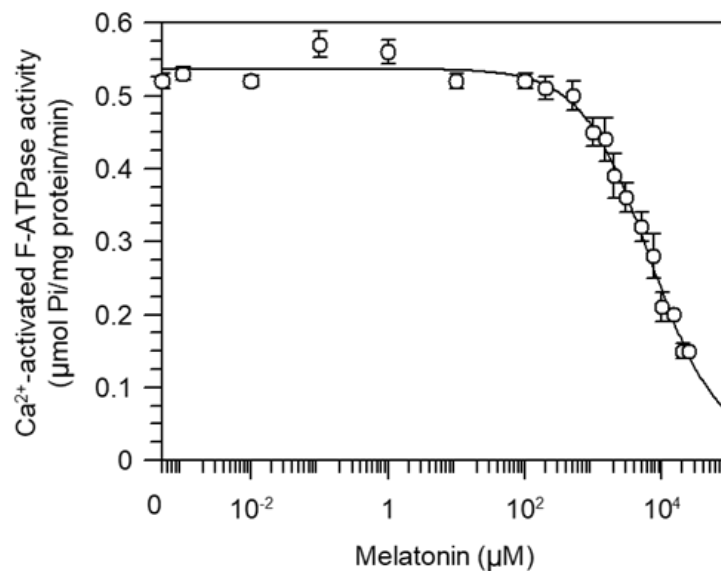


**Figure 15.** Dose-response curve of melatonin on the  $Ca^{2+}$ -activated  $F_1F_0$ -ATPase activity. Enzyme assays were carried out in the presence of increasing melatonin concentrations. Data represent the mean  $\pm$  SD from three independent experiments carried out on distinct mitochondrial preparations.

The inhibition mechanism of melatonin, shown by the Dixon and Cornish-Bowden plots, on the  $\text{Ca}^{2+}$ -activated  $F_1F_0$ -ATPase is uncompetitive with respect to the ATP substrate (*figure 16*), i.e. melatonin can only bind to the enzyme complex-ATP ( $ES$ ), forming the tertiary complex ( $ESI$ ) with a dissociation constant of the  $ESI$  complex ( $K'_i$ ) of  $4.4 \pm 0.5$  mM (*diagram 1*).

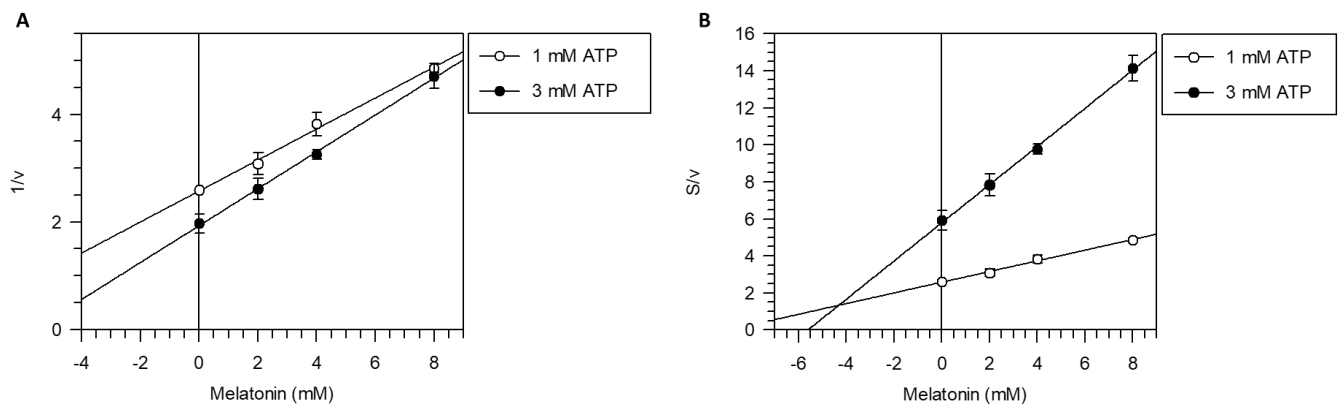


**Figure 16.** Mitochondrial  $\text{Ca}^{2+}$ -activated  $F_1F_0$ -ATPase inhibition mechanism by melatonin. Dixon (A) and Cornish-Bowden (B) plots were obtained at 1 mM ( $\circ$ ) or 3 mM ( $\bullet$ ) ATP. All points represent the mean  $\pm$  SD of distinct experiments carried out on three distinct mitochondrial preparations.

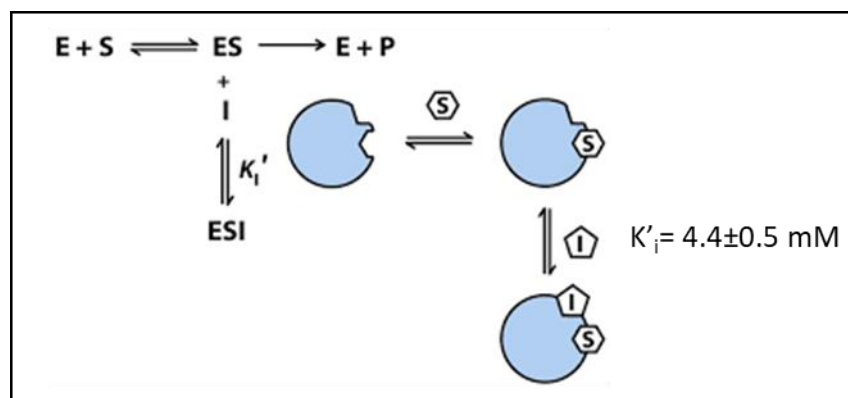


**Diagram 1.** Schematization of the uncompetitive inhibition mechanism of melatonin on  $\text{Ca}^{2+}$ -activated  $F_1F_0$ -ATPase.

Mutual exclusion analysis by incorporating binaries mixtures of  $F_1$  and  $F_0$  inhibitors in the reaction medium, aimed at verifying the possible interaction of melatonin with the catalytic sites of the  $F_1$  hydrophilic domain (NDB plus melatonin) or with the transmembrane portion  $F_0$  (DCCD plus melatonin) were performed. These experiments clarify whether melatonin can combine with the ternary complex  $ESI_1$  to form the quaternary complex  $ESI_1I_2$  or whether the binding of the first inhibitor ( $I_1$ ) prevents the binding of the other inhibitor ( $I_2$ ), *i.e.* if the two inhibitors are mutually exclusive.

The reciprocal of  $Ca^{2+}$ -activated  $F_1F_0$ -ATPase activity in the presence and absence of fixed NBD-Cl or DCCD was plotted as a function of increasing melatonin concentrations. In the mutual exclusion study between 0  $\mu$ M or 0.25  $\mu$ M DCCD and increasing concentrations of melatonin, two lines intersecting above the  $x$ -axis were obtained. This result describes a simultaneous interaction of DCCD and melatonin with the enzyme. The graphically obtained  $\alpha K'_{i2}$  value is the dissociation constant of melatonin from the enzyme-substrate-DCCD complex ( $ES$ -DCCD). The interaction constant ( $\alpha$ ) between two different compounds bound to the enzyme obtained from  $\alpha K'_i$  to  $K'_i$ , indicates whether the binding of an inhibitor (DCCD) influences ( $\alpha \neq 1$ ) or not ( $\alpha = 1$ ) the binding of melatonin with  $ES$ . Since  $\alpha < 1$  is obtained from the mutual exclusion between DCCD and melatonin, the two inhibitors bind independently of each other to give the  $ESI_1I_2$  complex and the binding of one facilitates the binding of the other (*figure 17B*). Similarly, the exclusion between melatonin and NBD-Cl, specifically by increasing the concentration of melatonin and keeping the concentration of 0  $\mu$ M or 7  $\mu$ M NBD-Cl, two parallel lines were obtained, demonstrating that the quaternary complex is not formed, *i.e.* the two inhibitors,  $I_1$  and  $I_2$ , bind to overlapping binding sites so they are mutually exclusive (*figure 17A*).

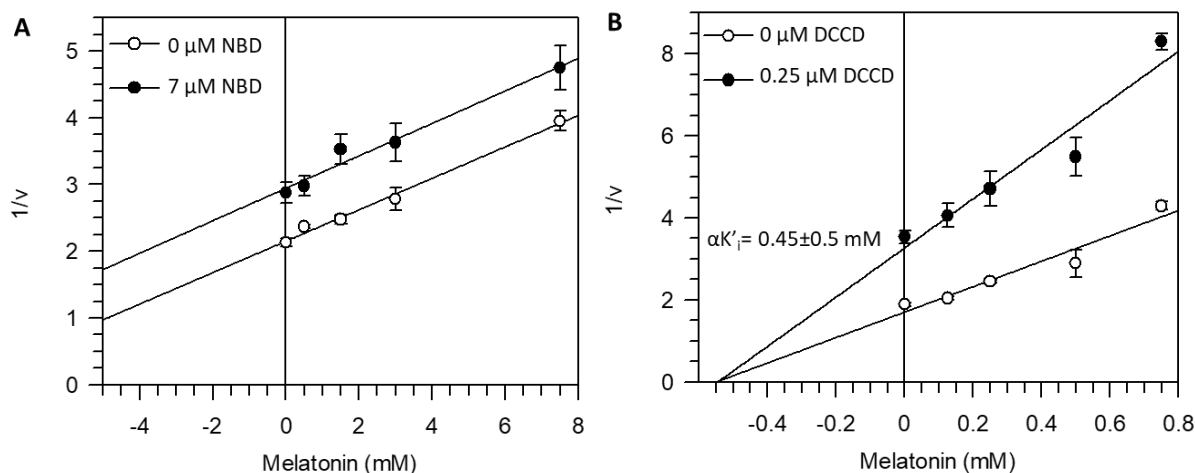


**Figure 17. Mutual exclusion analysis by Dixon plots for the mitochondrial  $\text{Ca}^{2+}$ -activated  $\text{F}_1\text{F}_0$ -ATPase inhibition by melatonin.** Assays were carried out in the absence ( $\circ$ ) or in the presence of  $7 \mu\text{M}$  NBD-Cl ( $\bullet$ ) (A) and in the absence ( $\circ$ ) or in the presence of  $0.25 \mu\text{M}$  DCCD ( $\bullet$ ) (B).

On the purified  $\text{F}_1$  domain of the enzyme, the hydrolytic activity was evaluated in the presence of the two cations  $\text{Ca}^{2+}$  (figure 18A) and  $\text{Mg}^{2+}$  (figure 18B). The success of the purification was confirmed by Western blot analysis (figure 19) and the lack of inhibitory effect of oligomycin, known to interact with the  $\text{F}_0$  portion of the enzyme. As for the NBD-Cl, which inhibits the hydrolytic activity by interacting with the  $\text{F}_1$  portion, melatonin exerts its inhibitory effect on the purified hydrophilic portion, confirming its binding on this enzymatic portion only in presence of  $\text{Ca}^{2+}$  (figure 18A).

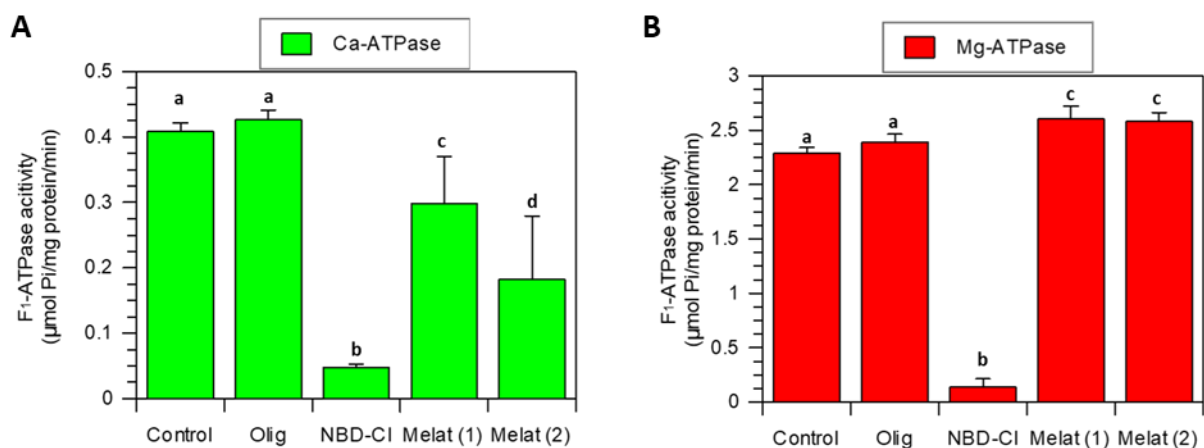


**Figure 18. Melatonin effect on purified  $F_1$ -ATPase.** The  $Ca^{2+}$ -activated  $F_1$ -ATPase activity was evaluated in the presence and in the absence of oligomycin, NBD-Cl and 7 mM and 10mM melatonin (A). The  $Mg^{2+}$ -activated  $F_1$ -ATPase activity assay was carried out in the absence and in the presence of oligomycin, NBD-Cl and 7 mM and 10mM melatonin (B). Each point represents the mean value  $\pm$  SD (vertical bars) of at least three experiments carried out on distinct mitochondrial preparations. Different letters indicate significant differences ( $P \leq 0.05$ ) among treatments within the same parameter.



**Figure 19. Identification of subunits of the partially purified  $F_1$  domain.** In the right lane, the bands of marker proteins with known molecular weight are visible. The bands of the catalytic  $\beta$  subunit identified by Western blot are shown on the left side. Lanes I and II are replicates of the partially purified  $F_1$  domain.

The effect of melatonin on mitochondrial respiration was evaluated on NADH and succinate energized mitochondria. Melatonin inhibited NADH- $O_2$  oxidase activity with  $IC_{50}$  value of  $4.47 \pm 0.21$  mM (figure 20A) but did not significantly affect succinate- $O_2$  oxidase activity (figure 20B).

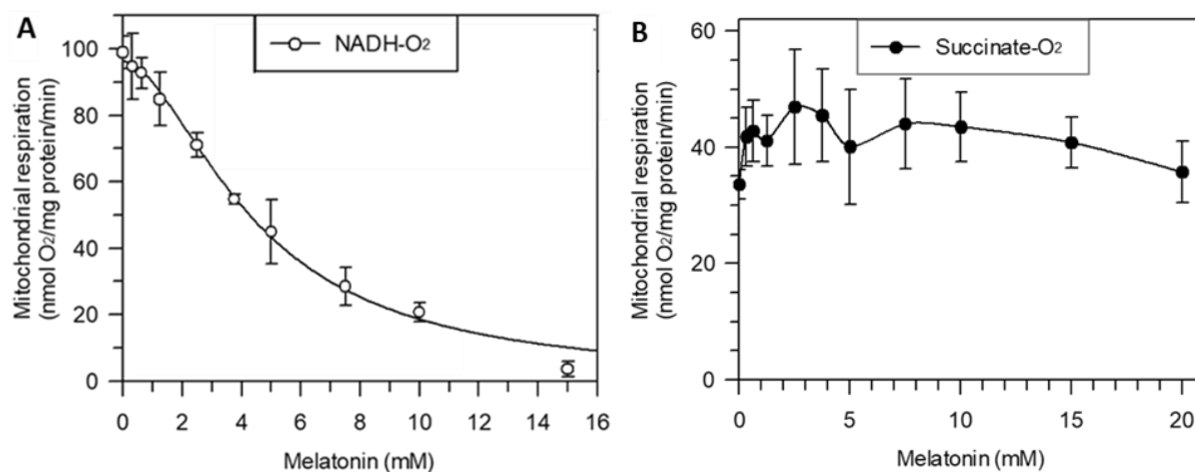


**Figure 20. Melatonin on mitochondrial respiration.** Melatonin titration curve on NADH- $O_2$  oxidase (A) and succinate- $O_2$  oxidase (B) activity. Each point represents the mean value  $\pm$  SD (vertical bars) of at least three experiments carried out on distinct mitochondrial preparations.

However, the RCR values calculated on fresh mitochondria energized at the first and second phosphorylation sites in the presence of glutamate/malate and succinate, respectively were not altered by melatonin (figure 21).

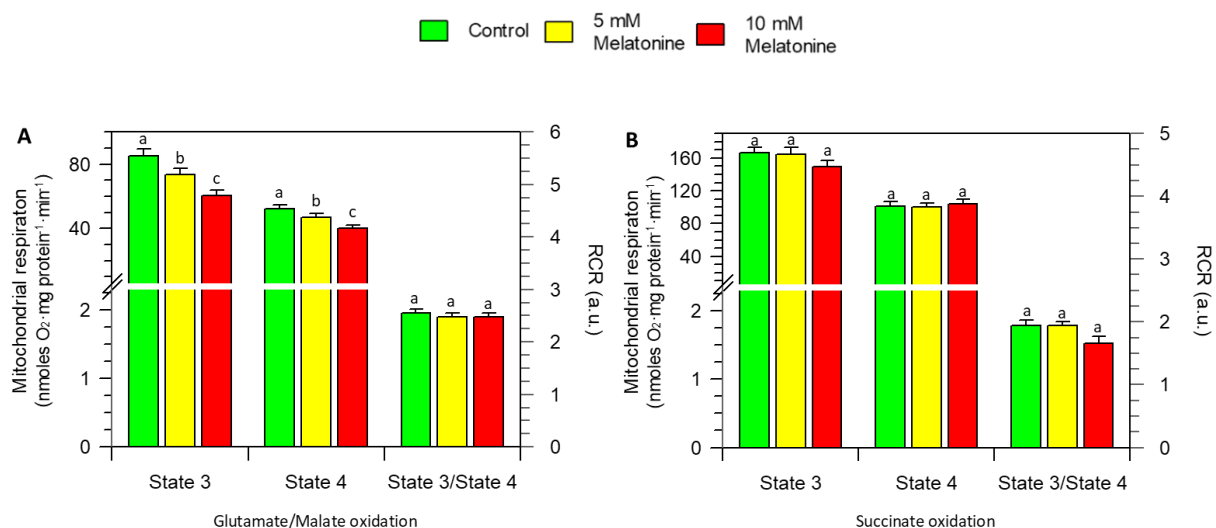


**Figure 21. Melatonin effects on OXPHOS.** Evaluation of glutamate/malate oxidation (A) and succinate oxidation (B) in the absence (control) and in the presence of 5 mM or 10mM melatonin. Data represent the mean  $\pm$  SD from three independent experiments carried out on distinct mitochondrial preparations. Different letters indicate significant differences ( $P \leq 0.05$ ) among treatments within the same parameter.

According to the selective inhibition of  $\text{Ca}^{2+}$ -activated  $\text{F}_1\text{F}_0$ -ATPase by melatonin (figure 15), the formation of mPTP, detected with the CRC measurement, in melatonin treated mitochondria was inhibited (figure 22), and more  $\text{Ca}^{2+}$  additions were needed to promote mPTP opening.

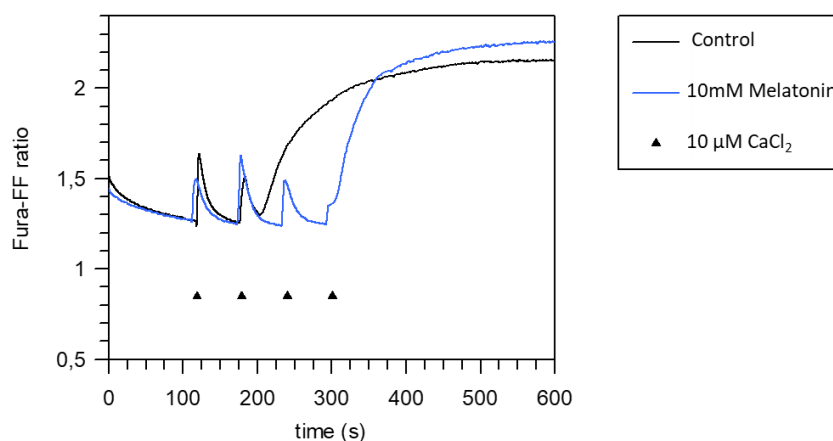


**Figure 22. Evaluation of mPTP opening.** CRC was monitored in response to subsequent  $10 \mu\text{M}$   $\text{CaCl}_2$  pulses (shown by the arrows), in the absence (Control-black line) and in the presence of 10 mM of melatonin (blu line). Data represent the mean  $\pm$  SD from three independent experiments carried out on distinct mitochondrial preparations.

Furthermore, from the spectrofluorimetric studies carried out using the MitoSox probe to detect the production of mitochondrial ROS, melatonin inhibited the production of ROS, both when the mitochondria were energized starting from CI (pyruvate/malate) (*figure 23A*) and from CII (succinate) (*figure 23B*).

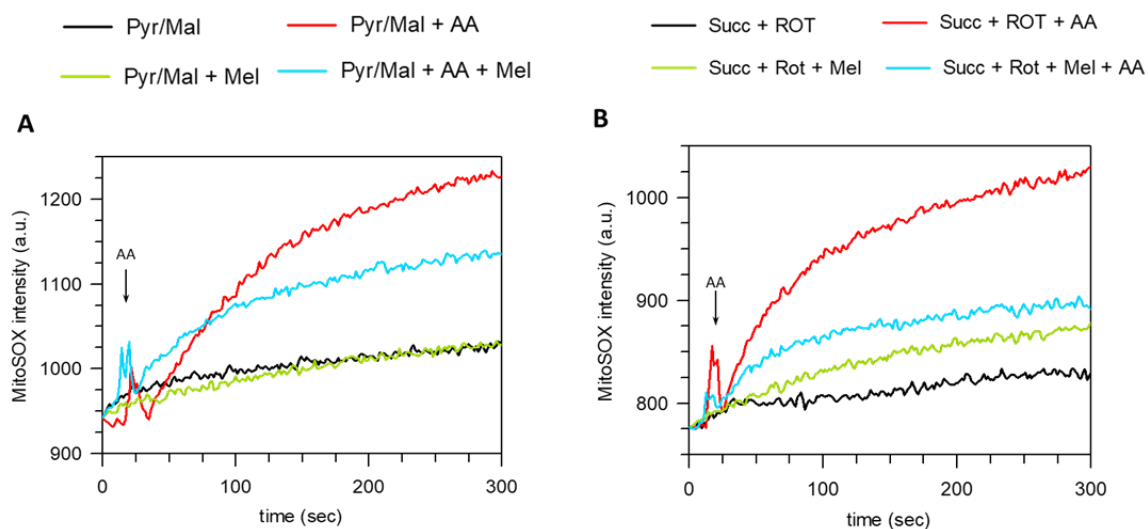


**Figure 23. Evaluation of ROS production.** ROS production was monitored in response to Antimycin A (shown by the arrow-red line) and in the absence (Control-black line), in the presence of 10 mM of melatonin (blu line) and with melatonin plus Antimycin A (green line), energizing the mitochondria with pyruvate/malate (A) and succinate (B). Data represent the mean  $\pm$  SD from three independent experiments carried out on distinct mitochondrial preparations.



# Sulfide affects the mitochondrial respiration, the Ca<sup>2+</sup>-activated F<sub>1</sub>F<sub>0</sub>-ATPase activity and the permeability transition pore but does not change the Mg<sup>2+</sup>-activated F<sub>1</sub>F<sub>0</sub>-ATPase activity in swine heart mitochondria

Salvatore Nesci<sup>\*</sup>, Cristina Algieri, Fabiana Trombetti, Vittoria Ventrella, Micaela Fabbri, Alessandra Pagliarani

Department of Veterinary Medical Sciences (DIMEVET), University of Bologna, Via Tolara di Sopra, 50, Ozzano Emilia, 40064 Bologna, Italy

## ARTICLE INFO

### Keywords:

H<sub>2</sub>S  
Mitochondria  
Mitochondrial respiration  
F<sub>1</sub>F<sub>0</sub>-ATPase  
Permeability transition pore  
Cofactors

## ABSTRACT

In mammalian cells enzymatic and non-enzymatic pathways produce H<sub>2</sub>S, a gaseous transmitter which recently emerged as promising therapeutic agent and modulator of mitochondrial bioenergetics. To explore this topic, the H<sub>2</sub>S donor NaHS, at micromolar concentrations, was tested on swine heart mitochondria. NaHS did not affect the F<sub>1</sub>F<sub>0</sub>-ATPase activated by the natural cofactor Mg<sup>2+</sup>, but, when Mg<sup>2+</sup> was replaced by Ca<sup>2+</sup>, a slight 15% enzyme inhibition at 100 μM NaHS was shown. Conversely, both the NADH-O<sub>2</sub> and succinate-O<sub>2</sub> oxidoreductase activities were totally inhibited by 200 μM NaHS with IC<sub>50</sub> values of 61.6 ± 4.1 and 16.5 ± 4.6 μM NaHS, respectively. Since the mitochondrial respiration was equally inhibited by NaHS at both first or second respiratory substrates sites, the H<sub>2</sub>S generation may prevent the electron transfer from complexes I and II to downhill respiratory chain complexes, probably because H<sub>2</sub>S competes with O<sub>2</sub> in complex IV, thus reducing membrane potential as a consequence of the cytochrome *c* oxidase activity inhibition. The Complex IV blockage by H<sub>2</sub>S was consistent with the linear concentration-dependent NADH-O<sub>2</sub> oxidoreductase inhibition and exponential succinate-O<sub>2</sub> oxidoreductase inhibition by NaHS, whereas the coupling between substrate oxidation and phosphorylation was unaffected by NaHS. Even if H<sub>2</sub>S is known to cause sulfhydration of cysteine residues, thiol oxidizing (GSSG) or reducing (DTE) agents, did not affect the F<sub>1</sub>F<sub>0</sub>-ATPase activities and mitochondrial respiration, thus ruling out any involvement of post-translational modifications of thiols. The permeability transition pore, the lethal channel which forms when the F<sub>1</sub>F<sub>0</sub>-ATPase is stimulated by Ca<sup>2+</sup>, did not open in the presence of NaHS, which showed a similar effect to ruthenium red, thus suggesting a putative Ca<sup>2+</sup> transport cycle inhibition.

## 1. Introduction

Mitochondrial bioenergetics relies on substrate oxidation during mitochondrial respiration to generate a transmembrane electrochemical gradient of H<sup>+</sup> (Δμ<sub>H+</sub>) that drives ADP phosphorylation to produce ATP [1]. The oxidative phosphorylation (OXPHOS) system in the inner mitochondrial membrane (IMM) basically consists of respiratory chain complexes that transfer reducing equivalents from NADH or FADH<sub>2</sub> ultimately to oxygen. According to the chemiosmotic hypothesis, the downhill electron flow through these enzyme complexes allows H<sup>+</sup> pumping by complex (C) I, III and IV in the intermembrane space, while the CII cannot pump H<sup>+</sup>. Finally, the OXPHOS coupling between the

transmembrane H<sup>+</sup> gradient formation and ATP synthesis is provided by the ATP synthase or F<sub>1</sub>F<sub>0</sub>-ATPase, which exploits the Δμ<sub>H+</sub> to synthesize ATP [2]. The respiratory complexes (RC) transfer electrons from NADH to O<sub>2</sub> by CI, CIII and finally CIV. FADH<sub>2</sub>, which receives electrons from succinate, follows a shorter route, namely CII, CIII and CIV [3]. RC can function separately or assemble in supercomplexes of defined stoichiometry [4], without involving CII. Recent studies on mammalian heart mitochondria showed that the individual complexes form the so-called respirasome [5,6] whose stoichiometry varies from the respiratory supercomplex (CI<sub>1</sub> + CIII<sub>2</sub> + CIV<sub>1</sub>) to the megacomplex (CI<sub>2</sub> + CIII<sub>2</sub> + CIV<sub>2</sub>) [7]. In addition, the CIII dimer may assemble with CIV (CIII<sub>2</sub> + CIV<sub>1</sub>) or CI (CI<sub>1</sub> + CIII<sub>2</sub>) [8]. The (CI<sub>1</sub> + CIII<sub>2</sub>) assembly may decrease the

<sup>\*</sup> Corresponding author.

E-mail address: [salvatore.nesci@unibo.it](mailto:salvatore.nesci@unibo.it) (S. Nesci).

<https://doi.org/10.1016/j.phrs.2021.105495>

Received 18 November 2020; Received in revised form 12 February 2021; Accepted 12 February 2021

Available online 15 February 2021

1043-6618/© 2021 Elsevier Ltd. All rights reserved.

production of reactive oxygen species [9] and favor respirasome formation [10]. Moreover, the dimerization of CV (the  $F_1F_0$ -ATPase) intervenes in membrane bending and in the formation of the *cristae* [11, 12]. The main role of the  $F_1F_0$ -ATPase in mitochondria is to produce ATP in  $F_1$  [13], driven by  $H^+$  flow through the membrane-embedded  $F_0$  domain [14]. The two functionally and structurally coupled domains allow the  $\Delta\mu_{H^+}$  transduction into ATP formation and vice versa [15,16]. The ubiquitous  $F_1F_0$ -ATPase occurs in bacteria, chloroplasts and mitochondria [17]. In mitochondria supernumerary subunits (SNS) [18], would confer to the  $F_1F_0$ -ATPase dimer the capability of arranging in rows and of opening the permeability transition pore (PTP) [19]. Accordingly, the  $F_0$  domain of the  $F_1F_0$ -ATPase, and particularly its core or c-ring, contains a lipid plug whose expulsion forms the hole, namely the main conductance channel known as PTP [18]. This molecular event is triggered by conformational changes driven by the replacement of the natural cofactor  $Mg^{2+}$  bound to the  $F_1$  domain by  $Ca^{2+}$ , when  $Ca^{2+}$  concentration increases in the matrix under patho(physio)logical conditions [20]. On these bases, most likely the  $Ca^{2+}$ -activated  $F_1F_0$ -ATPase inhibition can counteract the PTP formation and prevent or delay cell death [21]. Since the mPTP dysregulation is involved in the pathogenesis of various diseases [22], PTP rulers, which are an emerging topic to be investigated, may play the role of drugs.

Hydrogen sulphide ( $H_2S$ ) is an endogenous gaseous transmitter, which shares some of the signaling pathways with other endogenously produced gases [23], to mediate vascular remodeling and angiogenesis. By involving cyclic nucleotides as second messengers, the cardiovascular system and inflammation mechanisms are modulated by  $H_2S$  [24]. Due to its lipophilicity and low molecular weight,  $H_2S$  can easily cross biomembranes and chemically modify cell proteins by inducing post-translational modifications which affect their structure and function. The sulphydration by  $H_2S$  is a post-translational modifications of cysteine residues: the cysteine thiol (-SH) binds sulfur to yield hydroper sulfide (-SSH). The  $F_1F_0$ -ATPase can undergo persulfidation to modulate cell bioenergetics [25,26]. As many exogenous and endogenous compounds,  $H_2S$  is a Janus molecule that can show both beneficial and toxic effects: beneficial effects predominate at micro and nanomolar concentrations while at high concentrations,  $H_2S$  is a known mitochondrial poison [27]. In the present work, the effects of the widely used  $H_2S$  donor NaHS on the whole mitochondrial energy-converting enzymes are explored. The results can contribute to highlight the multiple and still partially unknown action mechanisms of this inorganic modulator in mammalian mitochondria and help to understand the molecular basis of its therapeutic potential.

## 2. Experimental procedures

### 2.1. Chemicals

NaHS, oligomycin (a mixture of oligomycins A, B and C), antimycin A, Ruthenium Red, Fura-FF, and JC-10 were purchased from Vinci-Biochem (Vinci, Italy). Cytochrome *c*, rotenone, NADH, succinate,  $Na_2ATP$ , 1,4-dithioerythritol (DTE), dithiotreitol (DTT) and oxidized L-glutathione (GSSG) were obtained from Sigma-Aldrich (Milan, Italy). Quartz double distilled water was used for all reagent solutions.

### 2.2. Preparation of mitochondrial fractions

Swine hearts (*Sus scrofa domestica*) were collected at a local abattoir and transported to the lab within 2 h in ice buckets at 0–4 °C. After removal of fat and blood clots as much as possible, approximately 30–40 g of heart tissue were rinsed in ice-cold washing Tris-HCl buffer (medium A) consisting of 0.25 M sucrose, 10 mM Tris(hydroxymethyl)aminomethane (Tris), pH 7.4 and finely chopped into fine pieces with scissors. Each preparation was made from one heart. Once rinsed, tissues were gently dried on blotting paper and weighted. Then tissues were homogenized in medium B consisting of 0.25 M sucrose, 10 mM Tris, 1

mM EDTA (free acid), 0.5 mg/mL BSA fatty acid free, pH 7.4 with HCl at a ratio of 10 mL medium B per 1 g of fresh tissue. After a preliminary gentle break up by Ultraturax T25, the tissue was carefully homogenized by a motor-driven teflon pestle homogenizer (Braun Melsungen Type 853202) at 650 rpm with 3 up-and-down strokes. The mitochondrial fraction was then obtained by stepwise centrifugation (Sorvall RC2-B, rotor SS34). Briefly, the homogenate was centrifuged at 1,000xg for 5 min, thus yielding a supernatant and a pellet. The pellet was re-homogenized under the same conditions of the first homogenization and re-centrifuged at 1,000xg for 5 min. The gathered supernatants from these two centrifugations, filtered through four cotton gauze layers, were centrifuged at 10,500xg for 10 min to yield the raw mitochondrial pellet. The raw pellet was resuspended in medium A and further centrifuged at 10,500xg for 10 min to obtain the final mitochondrial pellet. The latter was resuspended by gentle stirring using a Teflon Potter Elvehjem homogenizer in a small volume of medium A, thus obtaining a protein concentration of 30 mg/mL [28]. All steps were carried out at 0–4 °C. The protein concentration was determined according to the colorimetric method of Bradford [29] by Bio-Rad Protein Assay kit II with BSA as standard. The mitochondrial preparations were then stored in liquid nitrogen until the evaluation of F-ATPase activities.

### 2.3. Mitochondrial F-ATPase activity assays

Thawed mitochondrial preparations were immediately used for F-ATPase activity assays. The capability of ATP hydrolysis was assayed in a reaction medium (1 mL) containing 0.15 mg mitochondrial protein and 75 mM ethanolamine-HCl buffer pH 9.0, 6.0 mM  $Na_2ATP$  and 2.0 mM  $MgCl_2$  for the  $Mg^{2+}$ -activated  $F_1F_0$ -ATPase assay, and 75 mM ethanolamine-HCl buffer pH 8.8, 3.0 mM  $Na_2ATP$  and 2.0 mM  $CaCl_2$  for the  $Ca^{2+}$ -activated  $F_1F_0$ -ATPase assay. These assay conditions were previously proven to elicit the maximal enzyme activities either stimulated by  $Mg^{2+}$  or by  $Ca^{2+}$  in swine heart mitochondria [30]. After 5 min preincubation at 37 °C, the reaction, carried out at the same temperature, was started by the addition of the substrate  $Na_2ATP$  and stopped after 5 min by the addition of 1 mL of ice-cold 15% (w/w) trichloroacetic acid aqueous solution. Once the reaction was stopped, vials were centrifuged for 15 min at 3500 rpm (Eppendorf Centrifuge 5202). In the supernatant, the concentration of inorganic phosphate (Pi) hydrolyzed by known amounts of mitochondrial protein, which is an indirect measure of F-ATPase activity, was spectrophotometrically evaluated [31]. To this aim, 1  $\mu$ L from a mother solution of 3 mg/mL oligomycin in dimethylsulfoxide (DMSO) was directly added to the reaction mixture before starting the reaction. The total ATPase activity was calculated by detecting the Pi in control tubes run in parallel and containing 1  $\mu$ L DMSO per mL reaction system. In each experimental set, control tubes were alternated to the condition to be tested. The employed concentration of oligomycin, specific inhibitor of F-ATPases which selectively blocks the  $F_0$  subunit ensured maximal enzyme activity inhibition and was currently used in F-ATPase assays [20]. The  $F_1F_0$ -ATPase activity was routinely measured by subtracting, from the Pi hydrolyzed by total ATPase activity, the Pi hydrolyzed in the presence of oligomycin [28]. In all experiments the F-ATPase activity was expressed as  $\mu$ mol Pi  $\cdot$  mg protein<sup>-1</sup>  $\cdot$  min<sup>-1</sup>. The effects of the NaHS were tested by adding 10  $\mu$ L aliquots of standard NaHS solutions in DMSO to the reaction mixture immediately prior to the addition of the mitochondrial suspensions. The reaction system containing NaHS and mitochondria were preincubated at 37 °C for 5 min before starting the ATPase reaction by ATP addition. To this aim, aliquots of DMSO solutions of appropriate NaHS concentrations, obtained by dilution from the mother 50 mM NaHS solution in DMSO, were added to the reaction mixture to obtain the final NaHS concentrations in the range 0.1–100  $\mu$ M NaHS in the reaction system. Preliminary assays showed that, under the conditions adopted, DMSO had no effect on the ATPase activities under study. The effects of 50  $\mu$ M DTE and 1 mM GSSG were tested by adding 10  $\mu$ L aliquots of thiol reagent solutions in  $H_2O$  to the reaction mixture at the time of the

preincubation before starting the ATPase reaction.

#### 2.4. Mitochondrial respiration assays

Immediately after thawing, the mitochondrial fractions were used to evaluate the mitochondrial respiration. The experimental conditions adopted ruled out any potential concomitant effect of changes in the transmembrane electrochemical gradient of  $H^+$ . To detect mitochondrial respiratory activities, the oxygen consumption rates were polarographically evaluated by Clark-type electrode using a thermostated Oxytherm System (Hansatech Instruments) equipped with a 1 mL polarographic chamber. The reaction mixture (120 mM KCl, 10 mM Tris-HCl buffer pH 7.2), maintained under Peltier thermostataion at 37 °C and continuous stirring, contained 0.25 mg mitochondrial protein [32].

To evaluate the NADH- $O_2$  oxidoreductase activity, the mitochondrial oxidation was run under saturating substrate conditions (75  $\mu$ M NADH) after 2 min of stabilization of the oxygen signal. Preliminary tests assessed that under these conditions  $O_2$  consumption was suppressed by 2.5  $\mu$ M rotenone, known inhibitor of CI. [3] The succinate- $O_2$  oxidoreductase activity by CII was evaluated by detecting the succinate oxidation in the presence of 2.5  $\mu$ M rotenone. The reaction was started by the addition of 10 mM succinate after 2 min of stabilization of oxygen signal. Also in this case preliminary tests assessed that, under the conditions applied, succinate oxidation was suppressed by of 1  $\mu$ g/mL antimycin A, selective inhibitor of CIII [3].

To evaluate the effects of NaHS, the reaction was started by the addition of the mitochondrial suspensions to the polarographic chamber at 37 °C. Aliquots from mother solutions in DMSO and DTE in  $H_2O$ , prepared immediately before the experiments, were added to the polarographic chamber at the reaction start, sequentially or in reverse order when required, to obtain the final NaHS and DTE concentrations to be tested. The mitochondrial respiratory rate was automatically evaluated by  $O_2$ view software and expressed as nmoles  $O_2$ ·mg protein<sup>-1</sup>·min<sup>-1</sup>. Polarographic assays were run at least in triplicate on mitochondrial preparations obtained from different animals.

#### 2.5. Evaluation of oxidative phosphorylation

Immediately after the preparation of the mitochondrial fraction, the mitochondrial respiratory activity was polarographically evaluated by Clark-type electrode using a thermostated Oxytherm System (Hansatech Instruments) in terms of oxygen consumption at 37 °C in a 1 mL polarographic chamber. The reaction mixture, maintained under thermostataion and continuous stirring, contained 0.25 mg/mL mitochondrial suspension, 40 mM KCl, 0,2 mg/mL fatty acid-free BSA, 75 mM sucrose, 0,5 mM EDTA, 30 mM Tris-HCl, pH 7.4, 5 mM  $KH_2PO_4$  plus 3 mM  $MgCl_2$ . In detail, the rate of oxygen consumption was evaluated in the presence of specific substrates, namely glutamate/malate (1:1), for CI, succinate for CII, and in the presence of 1  $\mu$ g/mL rotenone, to inhibit CI, and 1  $\mu$ M antimycin A to inhibit CIII. Glutamate/malate oxidation was taken as a measure of the activity of NADH: ubiquinone oxidoreductase; succinate oxidation mirrored the multi-component succinoxidase pathway, which accounts for the electron flux in the respiratory chain through CII. To evaluate mitochondrial integrity, since intact mitochondrial membranes are not permeable to NADH, during the polarographic assay in the presence of glutamate/malate as substrate, 75  $\mu$ M NADH were added to the reaction mixture. Coupling of respiratory activity to phosphorylation was evaluated by adding 150 nmol ADP to state 2 respiring mitochondria [33,34]. The NaHS mother solution (50 mM NaHS) was prepared immediately before the experiments by dissolving NaHS in DMSO. This solution was used to obtain by further dilutions NaHS solutions of adequate concentrations, in order to minimize DMSO input in the reaction system. Preliminary experiments showed that addition of small DMSO aliquots (up to 5  $\mu$ L) to the reaction system (1 mL) did not affect the respiratory rates. Micromolar

concentrations of NaHS in the reaction system were tested. Respiratory activities were evaluated as nmoles  $O_2$ ·mg protein<sup>-1</sup>·min<sup>-1</sup>. In routine experimental protocol, reagents were injected by a syringe into the polarographic cell containing the mitochondrial protein suspensions in the presence and in the absence of NaHS in the following order: inhibitors of the previous respiratory chain steps, when required, substrate (s), ADP, inhibitor (rotenone for glutamate/malate stimulated respiration and antimycin A for succinate-stimulated respiration). State 3 and 4 respiratory activities, the respiratory control ratio (RCR), namely the ratio between State 3 and 4 activities, were determined as defined by Chance and Williams [33–35]. The rate of oxygen consumption was assessed in the presence of the specific substrates glutamate/malate for CI, succinate for CII. Polarographic assays were run at least in triplicate on three mitochondrial preparations from different animals.

#### 2.6. Evaluation of cytochrome c oxidase activity

The polarographic assay of the cytochrome *c*-oxidase activity, even if currently employed, may cause interference due to the possible concomitant oxidation of the substrate ascorbate + *N,N,N',N'*-Tetramethyl-*p*-phenylenediamine dihydrochloride (TMPD) in the presence of NaHS, known to exhibit reducing properties [36,37]. Therefore, the evaluation of the cytochrome *c* oxidase activity was carried out according to the colorimetric method detailed below.

The colorimetric assay, based on the detection of the decrease in absorbance at 550 nm of ferrocytochrome *c*, caused by its oxidation by the cytochrome *c* oxidase, was carried out on the basis of Sigma cytochrome *c* oxidase assay kit (Product Code: CYTOC-OX1) and adequately adapted. In order to obtain a reduced cytochrome *c* (cyt *c*) solution, the reducing agent dithiothreitol (DTT) was added to a 0.22 mM cyt *c* aqueous solution to yield a final concentration of 0.5 mM DTT, gently mixed and let to react for 15 min at room temperature. The cyt *c* reduction state was evaluated by 1:20 diluting the reduced cyt *c* solution with the assay buffer solution (10 mM Tris/HCl, pH 7.0, 120 mM KCl) and by recording the absorbance (A) at 550 and 565 nm by Perkin-Elmer lambda 45 spectrophotometer (Perkin-Elmer, Massachusetts, USA); a  $A_{550}/A_{565}$  ratio in the range 10–20 was taken as indicative of an adequately reduced cyt *c*. Both solutions of reduced cyt *c* and NaHS were prepared just before the enzyme activity analysis. Preliminary experiments showed that up to 10  $\mu$ L DMSO added to the reaction mixture (2 mL) did not affect the enzyme activity. To evaluate the cytochrome *c* oxidase activity, 0.4 mg mitochondrial protein were added to the assay buffer to a final volume of 2 mL in a 25 °C thermostated cuvette under continuous stirring. The reaction was started by adding aliquots of the reduced cyt *c* solution to yield a 10  $\mu$ M cyt *c* in the reaction mixture. The initial rate of cyt *c* oxidation, measured by following the  $A_{550}$  nm decrease up to 45' from cyt *c* addition, was evaluated by Perkin-Elmer UV KinLab Software [38]. Increasing NaHS concentrations, directly added to the reaction mixture before starting the enzymatic reaction, were tested. Control tests, in which the reaction was carried out in a NaHS free medium under the same assay conditions, were alternated to assays in NaHS containing samples. Each experiment was run in triplicate. The cytochrome *c* oxidase activity was expressed as oxidized cyt *c* units (U)/mL, where 1 U corresponds to 1  $\mu$ mol cyt *c* oxidized per min.

#### 2.7. Evaluation of PTP and membrane potential

Immediately after the preparation of swine heart mitochondrial fractions, fresh mitochondrial suspensions (1 mg/mL) were energized in the assay buffer (130 mM KCl, 1 mM  $KH_2PO_4$ , 20 mM HEPES, pH 7.2 with TRIS), incubated at 25 °C with 1  $\mu$ g/mL rotenone and 5 mM succinate as respiratory substrate. To evaluate NaHS effect, selected NaHS concentrations were added to the mitochondrial suspensions before PTP evaluation. PTP opening was induced by the addition of low concentrations of  $Ca^{2+}$  (10  $\mu$ M) as  $CaCl_2$  aqueous solution at fixed time intervals (1 min). The calcium retention capacity (CRC), whose lowering

indicates mPTP opening, was spectrofluorometrically evaluated in the presence of 0.8  $\mu\text{M}$  Fura-FF. The probe has different spectral properties in the absence and in the presence of  $\text{Ca}^{2+}$ , namely it displays excitation/emission spectra of 365/514 nm in the absence of  $\text{Ca}^{2+}$  (Fura-FF low  $\text{Ca}^{2+}$ ) and shifts to 339/507 nm in the presence of high  $\text{Ca}^{2+}$  concentrations (Fura-FF high  $\text{Ca}^{2+}$ ). PTP opening, was evaluated by the increase in the fluorescence intensity ratio (Fura-FF high  $\text{Ca}^{2+}$ )/(Fura-FF low  $\text{Ca}^{2+}$ ), which indicates a decrease in CRC. The membrane potential ( $\Delta\psi$ ) was evaluated in presence of 0.5  $\mu\text{M}$  JC-10. In polarized mitochondrial membranes, this probe selectively generates an orange JC-10 aggregate (excitation/emission spectra of 540/590 nm). The JC-10 monomers, generated when  $\Delta\psi$  decreases, cause a green shift (excitation/emission spectra of 490/525 nm). Accordingly, the membrane depolarization (decrease in  $\Delta\psi$ ) ascribed to PTP formation was detected by the increase in the fluorescence intensity ratio which corresponds to an increased JC-10 aggregate/JC-10 monomers ratio. [20,39]. All measurements were processed by LabSolutions RF software.

## 2.8. Calculations and statistics

The data represent the mean  $\pm$  SD (shown as vertical bars in the figures) of the number of experiments reported in the figure captions. In each experimental set, the analyzes were carried out on different pools of animals. Statistical analyzes were performed by SIGMASTAT software. The analysis of variance followed by Student's–Newman–Keuls' test when F values indicated significance ( $P \leq 0.05$ ) was applied. Percentage data were arcsin-transformed before statistical analyzes to ensure normality.

## 3. Results

### 3.1. NaHS effects on the $F_1F_0$ -ATPase and thiol redox state

In order to evaluate the effect of NaHS on the  $F_1F_0$ -ATPase activated by  $\text{Mg}^{2+}$  or by  $\text{Ca}^{2+}$ , the enzyme activities were evaluated in the range of 0.1 – 100  $\mu\text{M}$  NaHS (Fig. 1). The  $\text{Mg}^{2+}$ -dependent  $F_1F_0$ -ATPase was refractory to all NaHS concentrations tested (Fig. 1A). In contrast, the  $\text{Ca}^{2+}$ -dependent  $F_1F_0$ -ATPase was inhibited about 15% by 100  $\mu\text{M}$  NaHS (Fig. 1B). The same effect on the  $\text{Mg}^{2+}$ - and  $\text{Ca}^{2+}$ -dependent  $F_1F_0$ -ATPases was observed with freshly extracted mitochondria, which were not stored in liquid nitrogen (Fig. S1). Since NaHS was reported to form persulfide (–SSH) groups by modifying cysteine thiols, this possibility was verified by testing the NaHS effect in presence of thiol reducing/oxidizing agents, i.e. DTE and GSSG, on the  $F_1F_0$ -ATPase activity either activated by  $\text{Ca}^{2+}$  or by  $\text{Mg}^{2+}$  (Fig. 2). In the presence of 50  $\mu\text{M}$  DTE or 1 mM GSSG the  $\text{Mg}^{2+}$ -dependent  $F_1F_0$ -ATPase (Fig. 2A,C) was unaffected.

Similarly, the  $\text{Ca}^{2+}$ -dependent  $F_1F_0$ -ATPase in presence of 50  $\mu\text{M}$  DTE and 1 mM GSSG (Fig. 2B,D) showed a similar enzyme activity to the control (without DTE and NaHS). The significant  $\text{Ca}^{2+}$ -dependent  $F_1F_0$ -ATPase inhibition by 100  $\mu\text{M}$  NaHS, even if around 15%, was reduced by DTE but remained detectable with respect to the control (Fig. 2B). Conversely, 1 mM GSSG did not significantly change the  $\text{Ca}^{2+}$ -dependent  $F_1F_0$ -ATPase activity either in the presence or in the absence of 100  $\mu\text{M}$  NaHS (Fig. 2D).

### 3.2. NaHS effects on mitochondrial respiratory complexes

The effects of NaHS on mitochondrial respiration were evaluated in NADH- and succinate-energized mitochondria (Fig. 3). The effects of micromolar NaHS concentrations up to 100  $\mu\text{M}$ , were tested by detecting the oxygen consumption in uncoupled (freeze-thawed) mitochondria in the presence of either NADH or succinate as substrates, which stimulate the activity of CI (NADH) and CII (succinate). The substrate-dependent inhibition potency of NaHS, estimated as  $\text{IC}_{50}$  values, was calculated as  $15.4 \pm 3.7 \mu\text{M}$  for the NADH- $\text{O}_2$  oxidoreductase activity (Fig. 3A) and  $16.3 \pm 6.2 \mu\text{M}$  for the Succinate- $\text{O}_2$  oxidoreductase activity (Fig. 3B). The Succinate- $\text{O}_2$  oxidoreductase activity was also strongly reduced by a sigmoidal concentration-response profile. In order to understand whether NaHS inhibition on mitochondrial respiration mirrors a putative –SSH post-translational modification of enzyme cysteines, known as susceptible to oxidation, the thiol-reagent DTE, which maintains thiols reduced and prevents their oxidation, was tested (Fig. 4). However DTE had no significant effect on the NADH- $\text{O}_2$  and Succinate- $\text{O}_2$  oxidoreductase activities (Fig. 4A and C) and did not remove the inhibition by NaHS. To rule out a direct reaction between DTE and NaHS, the NADH- $\text{O}_2$  and succinate- $\text{O}_2$  oxidoreductase activities were evaluated by adding DTE before and after NaHS. In all cases the NaHS-driven inhibition on mitochondrial respiration was not reverted by DTE (Fig. 4B and D).

Since the respiration inhibition by NaHS was downstream maintained from CI to CII, the cytochrome c oxidase activity, which mirrors the activity of CIV was evaluated. Also in this case, NaHS concentration-dependently inhibited cytochrome c oxidation (Fig. 5), showing an  $\text{IC}_{50}$  value of  $65.8 \pm 6.6 \mu\text{M}$  NaHS, namely similar to that of the NADH- $\text{O}_2$  oxidoreductase. In order to understand the relationship between substrate oxidation by mitochondrial complexes and NaHS inhibition on the individual complexes, threshold plots were built. To this aim, the residual activity of NADH- $\text{O}_2$  (Fig. 6A) and succinate- $\text{O}_2$  oxidoreductases (Fig. 6B) detected at fixed NaHS concentrations were plotted as a function of the corresponding cytochrome c oxidase inhibition percentage (Fig. 6). These plots highlighted that the cytochrome c oxidase inhibition by NaHS was exponentially linked to the inhibition of the

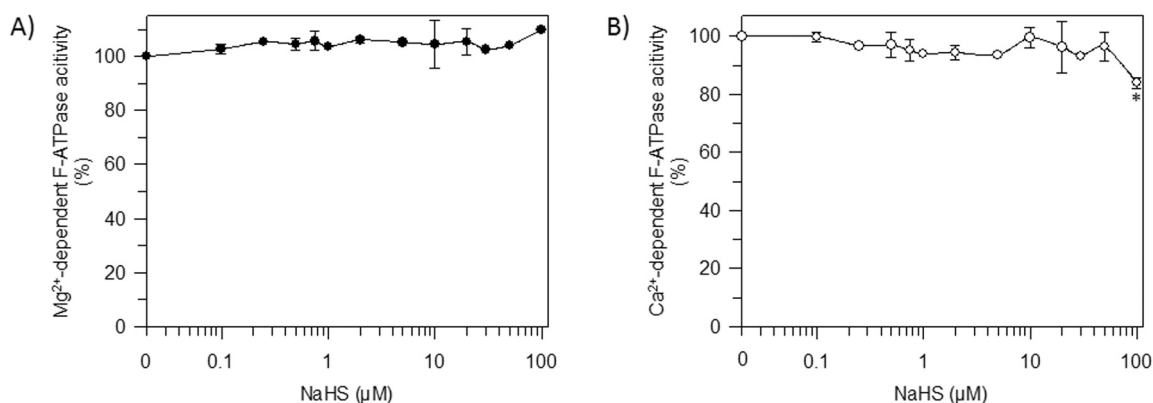


**Fig. 1.** Response of the mitochondrial  $\text{Mg}^{2+}$  and  $\text{Ca}^{2+}$ -dependent  $F_1F_0$ -ATPase activities to increasing NaHS concentrations. Data, expressed as percentage of the  $\text{Mg}^{2+}$ -dependent  $F_1F_0$ -ATPase (A) and  $\text{Ca}^{2+}$ -dependent  $F_1F_0$ -ATPase (B) in absence of NaHS, represent the mean  $\pm$  SD from three independent experiments carried out on different mitochondrial preparations. \* indicates significant differences with respect to the control ( $P \leq 0.05$ ).

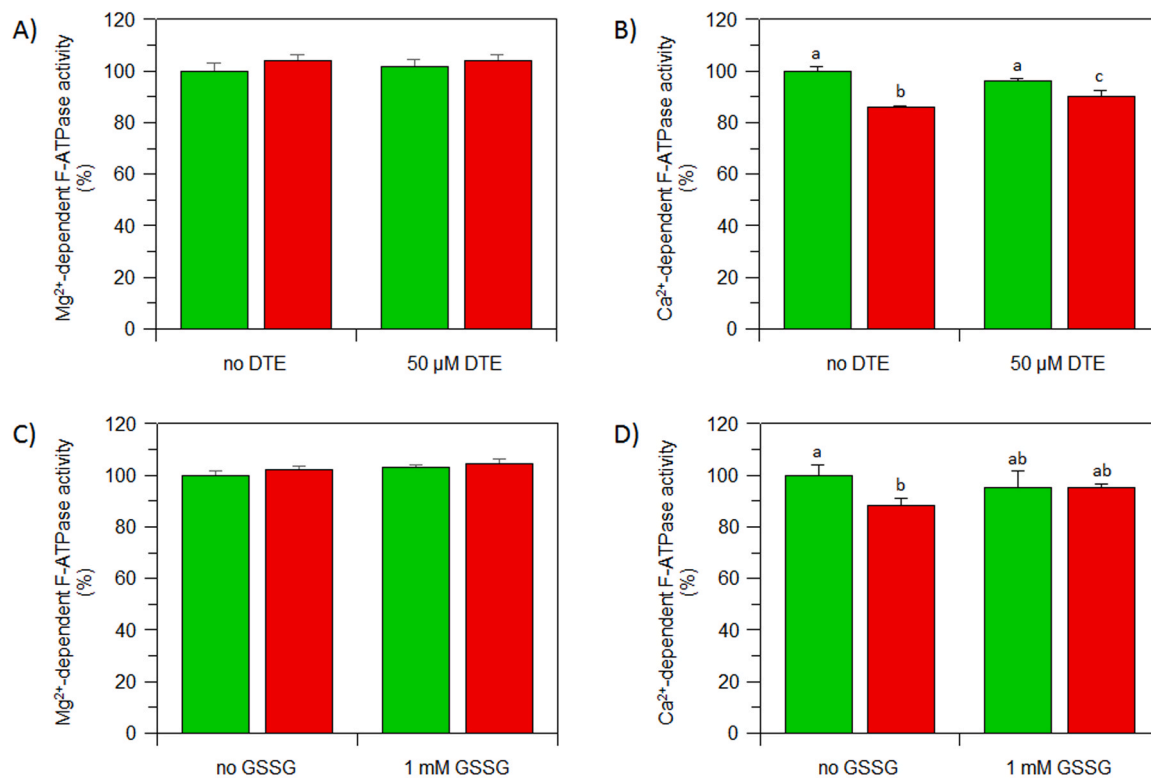


**Fig. 2.** Mg<sup>2+</sup> and Ca<sup>2+</sup>-dependent F<sub>1</sub>F<sub>0</sub>-ATPase activities of NaHS treated mitochondria in the presence of thiol-reagents. The effect of 50 μM DTE (A and B) or 1 mM GSSG were evaluated in the absence (green) and in the presence of 100 μM NaHS (red). Data, expressed as percentage of the Mg<sup>2+</sup>-dependent F<sub>1</sub>F<sub>0</sub>-ATPase and Ca<sup>2+</sup>-dependent F<sub>1</sub>F<sub>0</sub>-ATPase in absence of NaHS, represent the mean ± SD from three independent experiments carried out on different pools. Different letters indicate significantly different values within each treatment ( $P \leq 0.05$ ).

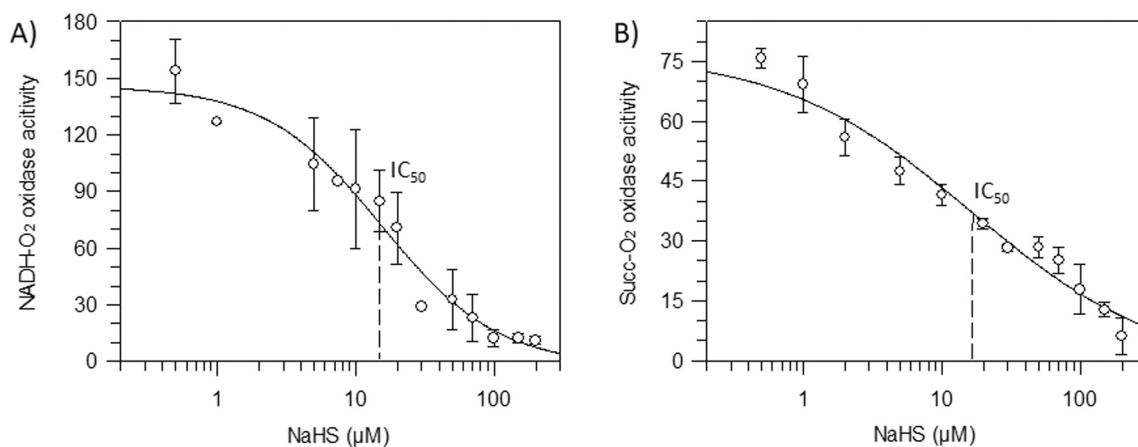


**Fig. 3.** NaHS effects on mitochondrial respiration. NADH-O<sub>2</sub> oxidoreductase activity (A) and Succinate-O<sub>2</sub> oxidoreductase activity (B) in the presence of increasing NaHS concentrations. All points represent the mean ± SD from three independent experiments carried out on different mitochondrial preparations.

NADH-O<sub>2</sub> oxidoreductase activity (Fig. 6A) or to the succinate-O<sub>2</sub> oxidoreductase inhibition (Fig. 6B).

The results obtained when 30 μM NaHS was added to state 3 respiring (ADP-stimulated) mitochondria showed a prompt decrease in oxygen consumption, both in the presence of NAD-dependent substrates (Fig. 7A) and in the presence of succinate (Fig. 7B). A significantly lower respiration occurred in state 4 respiratory activity, which mirrors the slowdown in oxygen consumption when added ATP is consumed, being phosphorylated to ATP. However, the coupling between substrate oxidation (glutamate/malate or succinate) and ADP phosphorylation, evaluated as State 3/State 4 ratio, was unaffected by NaHS (Fig. 7).

### 3.3. PTP opening and membrane potential sensitivity to the NaHS

The IMM integrity implies that mitochondria retain calcium and do not form the PTP. Ca<sup>2+</sup> concentration increase in mitochondria stimulates PTP formation and opening. On these bases, the CRC was evaluated by adding 10 μM Ca<sup>2+</sup> at subsequent steps of 1 min to succinate-energized freshly-prepared mitochondrial suspensions. According to the method applied, a detectable increase in fluorescence intensity, detected as Fura-FF ratio [(Fura-FF high Ca<sup>2+</sup>)/(Fura-FF low Ca<sup>2+</sup>)], was shown when a threshold matrix Ca<sup>2+</sup> concentration load was attained as a result of PTP opening. In control mitochondria the CRC decrease was

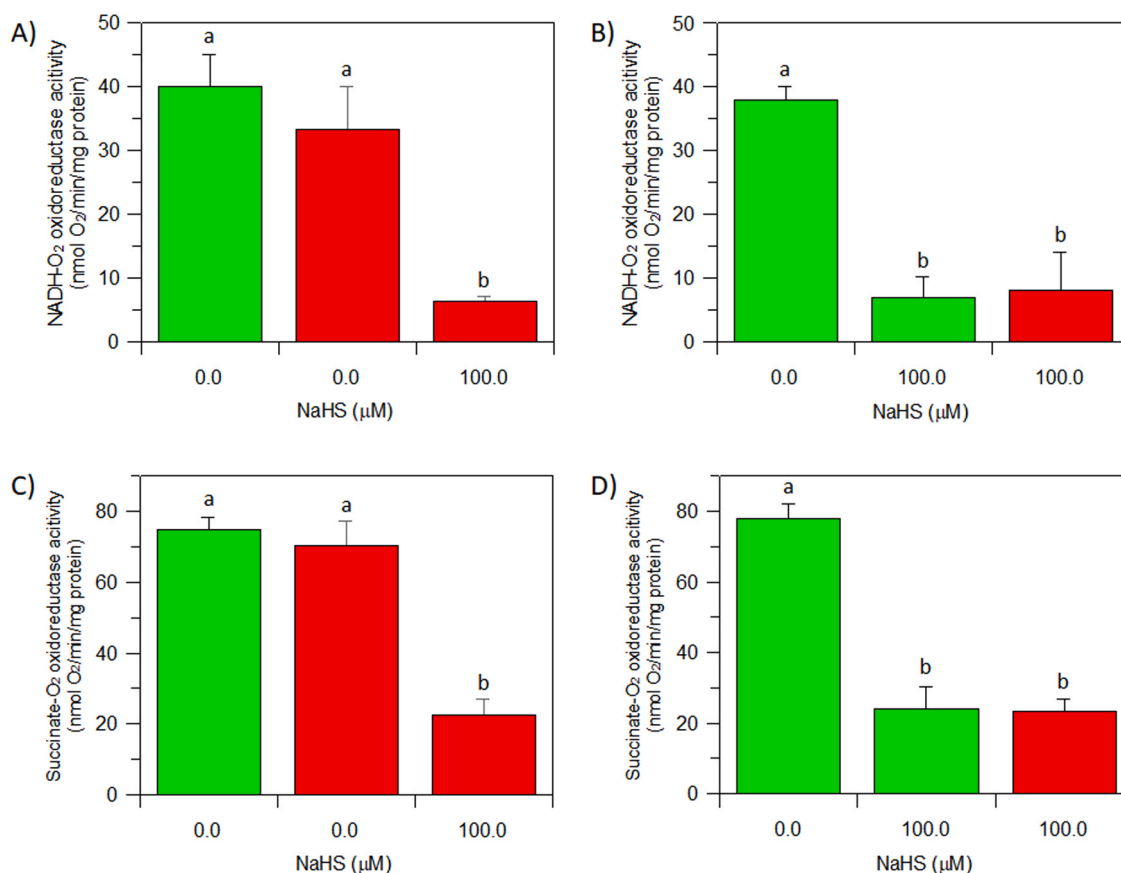


**Fig. 4.** Evaluation of the putative sulfhydrylation involvement in the inhibition of the mitochondrial respiration by NaHS. The NADH-O<sub>2</sub> oxidoreductase activity (A,B) and the Succinate-O<sub>2</sub> oxidoreductase activity (C,D) were assayed in the absence (green) (■) or in presence of 50 μM DTE (red) (■). 100 μM NaHS was added to reaction system containing mitochondrial suspensions energized with either 75 μM NADH or 10 mM succinate as substrates. The NaHS solution was added sequentially before or after DTE. Data represent the mean ± SD of three different experiments. Different letters indicate significantly different values ( $P \leq 0.05$ ).

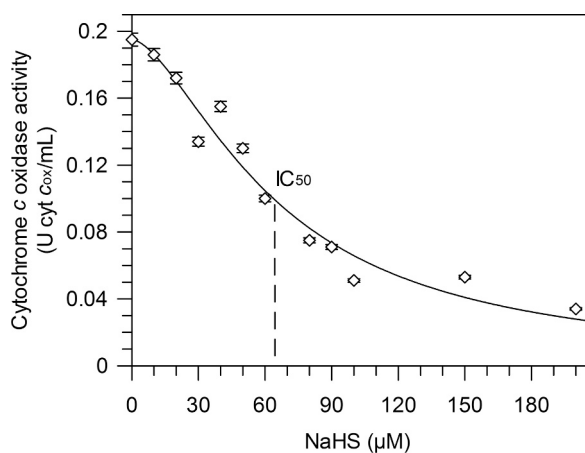


**Fig. 5.** Response of the cytochrome c oxidase activity to NaHS. The enzyme activity was spectrophotometrically assayed in the presence of 10 μM reduced cytochrome c as substrate at different NaHS concentrations. Data represent the mean ± SD (vertical bars) from three independent experiments carried out on different mitochondrial preparations.

revealed after 200' upon a two-train Ca<sup>2+</sup> pulses. In the presence of the polycationic dye ruthenium red (RR), the PTP is known to be desensitized, due to the failed Ca<sup>2+</sup> accumulation in the matrix caused by the selective RR inhibition of the mitochondrial calcium uniporter [40]. The

two NaHS concentrations tested (50 and 100 μM), selected on the basis of IC<sub>50</sub> values obtained on mitochondrial respiration and on the Ca<sup>2+</sup>-activated F<sub>1</sub>F<sub>0</sub>-ATPase, did not elicit any sudden increase in fluorescence intensity due to Ca<sup>2+</sup> release. Indeed, the rate of Ca<sup>2+</sup> uptake could be altered, as the time required to regain the basal [Ca<sup>2+</sup>] after each Ca<sup>2+</sup> pulse was different from that of the control and a gradual baseline increase was shown. Quite unexpectedly, NaHS and RR resulted in the similar trend, thus suggesting a common target, namely the inhibition of the mitochondrial calcium uniporter (Fig. 8A).

In order to improve clarity on the NaHS effects on PTP formation, Δφ, namely the transmembrane potential, which is abruptly dissipated by PTP opening, was evaluated. As shown in Fig. 6A, in control mitochondria, the CRC decrease at the second Ca<sup>2+</sup> pulse corresponded to the Δφ collapse, shown by the JC-10 ratio increase (Fig. 8B). To verify that the PTP formation depolarizes the mitochondria, 0.1 μM FCCP were added after the JC-10 ratio increase produced by Ca<sup>2+</sup> shots, but no increase in mitochondrial depolarization was recorded (data not shown). NaHS both at 50 and 100 μM only caused a gradual Δφ decrease, which most likely could be related to the inhibition of mitochondrial respiration and its related H<sup>+</sup> pumping activities, rather than to PTP opening.

#### 4. Discussion

The effects of H<sub>2</sub>S on mitochondrial bioenergetics has been extensively investigated and reviewed (see reviews and references therein [27,41,42]). The present work may represent an attempt to deepen the

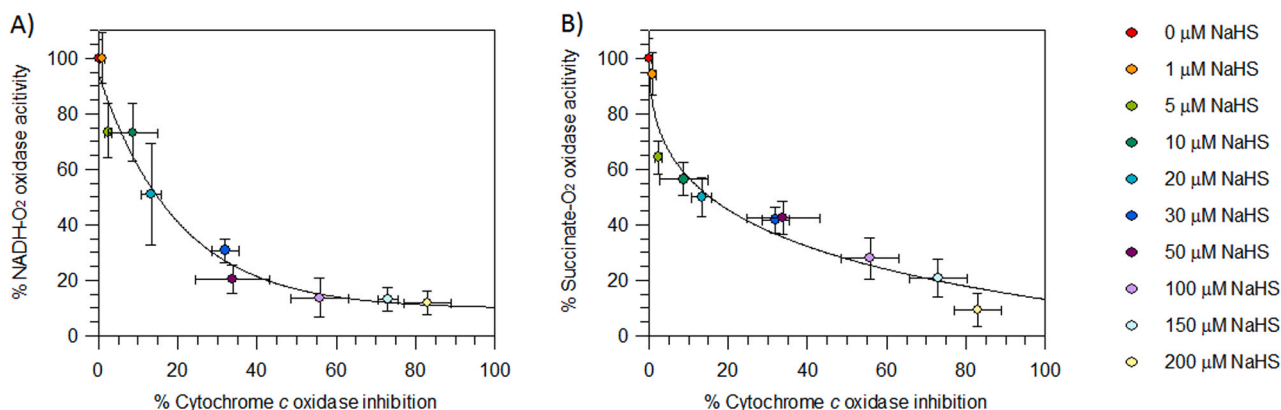


**Fig. 6.** Threshold plots of mitochondrial respiration. Each point represents the NADH-O<sub>2</sub> oxidoreductase (A) and the succinate-O<sub>2</sub> oxidoreductase (B) percentage of residual activity as a function of percent inhibition of cytochrome c oxidase by the NaHS concentrations shown at the right side of the plot. All points represent the mean ± SD (horizontal bars) from three independent experiments carried out on different mitochondrial preparations.

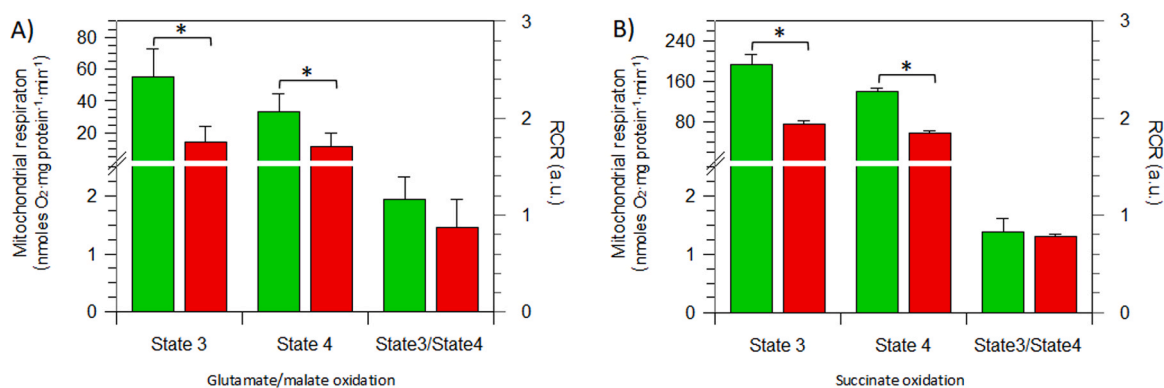


**Fig. 7.** NaHS effects on selected oxidative phosphorylation parameters: state 3 and 4 respiration and their ratio. Glutamate/malate- (A) and Succinate- (B) stimulated mitochondrial respiration in the presence (red) and in the absence (green) of 30 μM NaHS. All bars represent the mean ± SD from three independent experiments carried out on different mitochondrial preparations. \* indicates significantly different values ( $P \leq 0.05$ ).

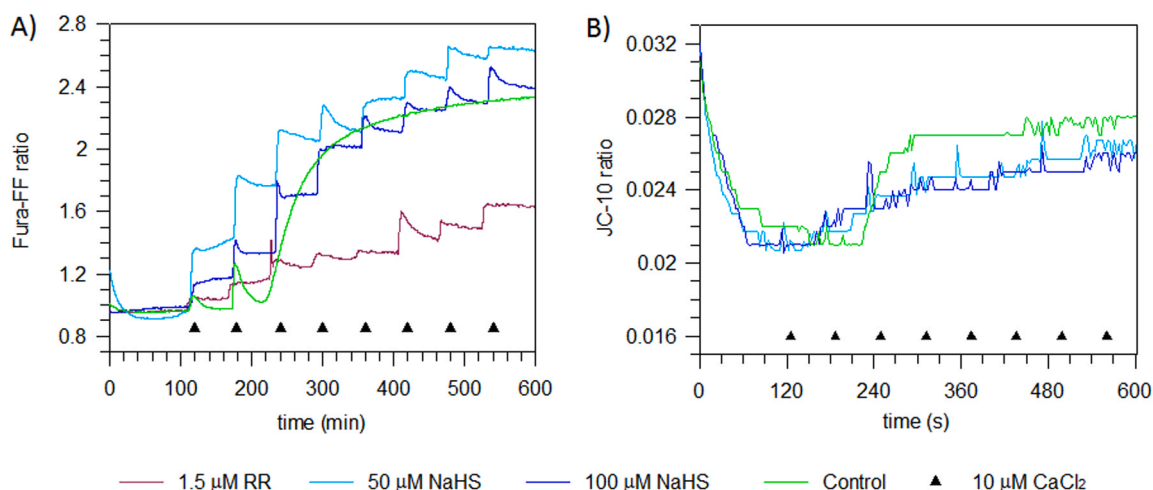


**Fig. 8.** Evaluation of PTP opening in intact mitochondrial preparations. Representative curves (A) of the calcium retention capacity (CRC) detected as Fura-FF ratio and (B) and the membrane potential ( $\Delta\psi$ ) detected as JC-10 ratio. CRC and  $\Delta\psi$  were monitored in response to subsequent 10 μM CaCl<sub>2</sub> pulses (shown by the triangles), as detailed in the 2.5 section. The NaHS concentrations were selected on the basis of IC<sub>50</sub> values obtained on mitochondrial respiration and on the Ca<sup>2+</sup>-activated F<sub>1</sub>F<sub>0</sub>-ATPase. RR, Ruthenium Red. Three independent experiments were carried out on three different mitochondrial preparations.

effects of NaHS concentrations, assumed to generate H<sub>2</sub>S, on the various components of the bioenergetic machinery in mitochondria isolated from swine heart, an excellent model to investigate drug effects in translational medicine, especially in the perspective of counteracting cardiovascular diseases. Of the three sulfide forms, which coexist in aqueous solution in an interconverting pH dependent-equilibrium, namely HS<sup>-</sup>, S<sup>2-</sup> and H<sub>2</sub>S, at physiological pH, H<sub>2</sub>S is the most likely candidate to directly affect mitochondrial proteins, since it can easily cross biomembranes due to its lipophilicity and lack of electric charge. The F<sub>1</sub>F<sub>0</sub>-ATPase was reported to be sulfhydrated or S-sulfurated, by using the correct term [43], by the H<sub>2</sub>S donor NaHS. The H<sub>2</sub>S target was identified on  $\alpha$  subunit at Cys244 and Cys294 in HepG2 and HEK293 cell lysates incubated with 100  $\mu$ M NaHS for 30 min at 37 °C. Moreover, the F<sub>1</sub>F<sub>0</sub>-ATPase activity showed a bell-shaped concentration-response curve in the range of 0.01 – 100  $\mu$ M NaHS [25]. Post-translational modifications on the F<sub>1</sub>F<sub>0</sub>-ATPase are well known to modulate the enzyme function [26]. However, in swine heart mitochondria NaHS, at the same concentrations proven to be effective on the F<sub>1</sub>F<sub>0</sub>-ATPase in HepG2 and HEK293 cells, has not effect on the ATP hydrolytic activity of the Mg<sup>2+</sup>-activated F<sub>1</sub>F<sub>0</sub>-ATPase. Conversely, the Ca<sup>2+</sup>-activated F<sub>1</sub>F<sub>0</sub>-ATPase, whose enzymatic function is linked to PTP opening [20, 39], is slightly inhibited by 100  $\mu$ M NaHS (Fig. 1). Most likely metabolic and signaling pathways might explain the F<sub>1</sub>F<sub>0</sub>-ATPase responsiveness to H<sub>2</sub>S in intact cells. Moreover, in swine heart mitochondria the weak even if significant Ca<sup>2+</sup>-activated F<sub>1</sub>F<sub>0</sub>-ATPase inhibition by 100  $\mu$ M NaHS is not due to any post-translational modification of cysteine thiols. Accordingly, the addition of thiol reagents, namely oxidizing (GSSG) and reducing (DTE) low molecular weight thiols maintains the Mg<sup>2+</sup>-activated F<sub>1</sub>F<sub>0</sub>-ATPase refractoriness to NaHS and the slight inhibition of the Ca<sup>2+</sup>-activated F<sub>1</sub>F<sub>0</sub>-ATPase activity (Fig. 2), thus ruling out the possibility of any direct sulfide reaction with F<sub>1</sub>F<sub>0</sub>-ATPase thiols.

On considering the F<sub>1</sub>F<sub>0</sub>-ATPase insensitivity to NaHS, sulfide effects were investigated on respiratory complexes. Freeze-thawed uncoupled mitochondria, insensitive to the uncoupler FCCP (data not shown) were used to evaluate mitochondrial respiration by adding CI (NADH) and CII (succinate) respiratory substrates. Even if both CI and CII were inhibited by NaHS, the inhibition extent is about three-fold higher on CII, as shown by the decreased succinate-O<sub>2</sub> oxidoreductase activity (Fig. 3). Since in both cases the inhibition is not reversed by DTE, which can reduce the persulfide groups (Fig. 4), post-translational modifications of protein thiols cannot be responsible for the inhibition of the enzyme activities. The electron transfer from both substrates (NADH and succinate) to O<sub>2</sub> in the respiratory chain is blocked downstream. Accordingly, the well known H<sub>2</sub>S inhibition of CIV [44] is confirmed by present data on the cytochrome *c* oxidase inhibition (Fig. 5). Moreover, at low concentrations H<sub>2</sub>S is known as the first inorganic electron donor to the mitochondrial electron transport chain through sulfide:quinone oxidoreductase (SQR) and CII, thereby stimulating mitochondrial respiration [45,46]. For this reason, the more pronounced H<sub>2</sub>S inhibition on the succinate-O<sub>2</sub> oxidoreductase, which shows an exponential enzyme activity decrease at increasing NaHS concentrations, than on the NADH-O<sub>2</sub> oxidoreductase may be due to a competitive coenzyme Q<sub>10</sub> reduction between SQR and succinate dehydrogenase activities. As CII do not participate in the respirasome assembly, whose supramolecular organization ensures a homogeneous distribution and a functionally relevant interaction between complexes in the membrane [10,47], H<sub>2</sub>S and succinate may mutually exclude as electron donors to the respiratory chain. This mechanism may add to CIV inhibition in slowing down the respiratory chain (Fig. 6). The insensitivity of the Mg<sup>2+</sup>-activated F<sub>1</sub>F<sub>0</sub>-ATPase to NaHS and the evidentiating of CIV as direct target of NaHS among mitochondrial respiration complexes are complemented and integrated by the NaHS inhibition of state 3 and state 4 respiration, whose ratio is unaffected by NaHS irrespective of CI or CII substrates. To sum up, NaHS reduces the electron flow in the OXPHOS system without affecting ATP synthesis (Fig. 7).

Isolated adult cardiac myocytes exposed to 100  $\mu$ M NaHS for 30 min

showed a delayed cardioprotection [48]. Ischemia/reperfusion injury is known to be attenuated by blocking the formation and opening of the PTP [49]. Present data show that NaHS-treated swine heart mitochondria can avoid an uncontrolled Ca<sup>2+</sup> release from mitochondria, associated with the collapse of the membrane potential (Fig. 7). Indeed, the CRC has a stepped course in the presence of NaHS, as well as RR trend, and does not show the typical profile where Ca<sup>2+</sup> addition causes a sharp increase in fluorescence followed by a gradual decline as mitochondria take up Ca<sup>2+</sup> (Fig. 7A). Finally, as repeated Ca<sup>2+</sup> pulses trigger PTP opening, a large increase in fluorescence corresponds to the complete release of mitochondrial calcium. The PTP desensitization by NaHS seems to be related to the concomitant hindrance of mitochondrial Ca<sup>2+</sup> uptake. In control mitochondria PTP opening is responsible for an abrupt IMM depolarization, as shown by the steep JC-10 fluorescence ratio increase upon Ca<sup>2+</sup> addition (Fig. 7B). Conversely, in NaHS treated mitochondria the gradual increase of JC-10 ratio is probably due to the inhibition of mitochondrial respiration that reduces membrane potential. Moreover, the Ca<sup>2+</sup> leak prior to Ca<sup>2+</sup> pulse would suggest that control and NaHS-treated mitochondria differ in their conformation/structure. Most likely, the different structural properties are not necessarily related to mPTP opening, but to the inhibition of the mitochondrial Ca<sup>2+</sup> uptake or, more generally, of Ca<sup>2+</sup> cycle [39,50,51]. Consistently, the inhibition of mitochondrial respiration by NaHS may decrease the transmembrane proton motive force, thus impairing the ion cycles, which involve the Ca<sup>2+</sup> uniport and the Ca<sup>2+</sup> efflux by a Na<sup>+</sup>-dependent pathway of Na<sup>+</sup>/Ca<sup>2+</sup> antiport and a Na<sup>+</sup>/H<sup>+</sup> antiport or Na<sup>+</sup>-independent pathway that has been suggested to occur via a Ca<sup>2+</sup>/H<sup>+</sup> exchanger and are all linked to the proton and calcium circuits [52].

Since H<sub>2</sub>S can behave as the good, the bad and the ugly depending on the cell environment and the concentration, the present findings lead us to think that a negative effect on mitochondrial respiration may have at the same time the positive effect of preventing or delaying PTP opening.

## 5. Conclusion

The present work points out that all shown the sulfide effects on mitochondrial bioenergetics are not dependent on post-translational modifications of protein thiols that, even if chemically possible and well documented, under the conditions adopted are not operative in swine heart mitochondria. Most likely, the multiple H<sub>2</sub>S action mechanisms are differently exerted according to the cell microenvironment and assay conditions.

The pharmacological interest of sulfide and of sulfide donors is strengthened, since micromolar concentrations are proven to delay PTP opening even if at the cost of a decreased mitochondrial respiration, which mirrors an inhibited electron transfer to CIV. So, further studies are required to deepen wanted and unwanted concentration-dependent effects of H<sub>2</sub>S, which being gaseous at physiological temperatures necessarily requires H<sub>2</sub>S donors, in the perspective of the use of these compounds in therapy.

## CRedit authorship contribution statement

**Salvatore Nesci:** Conceptualization, Writing - original draft, Supervision. **Cristina Algieri:** Investigation. **Fabiana Trombetti:** Validation, Writing - review & editing. **Vittoria Ventrella:** Writing - review & editing. **Micaela Fabbri:** Resources. **Alessandra Pagliarani:** Writing - review & editing, Funding acquisition.

## Declaration of Competing Interest

The authors declare that they have no competing interests in this work.

## Acknowledgements

Daniilo Matteuzzi and Roberto Giusti (Department of Veterinary Medical Sciences, University of Bologna) are gratefully acknowledged for kindly conferring swine hearts from a local abattoir to Biochemistry laboratories.

## Role of the funding source

This work was financed by the University of Bologna, Italy (Almaidea senior grant to AP).

## Appendix A. Supporting information

Supplementary data associated with this article can be found in the online version at [doi:10.1016/j.phrs.2021.105495](https://doi.org/10.1016/j.phrs.2021.105495).

## References

- [1] P. Mitchell, Keilin's respiratory chain concept and its chemiosmotic consequences, *Science* 206 (1979) 1148–1159.
- [2] P. Mitchell, Coupling of phosphorylation to electron and hydrogen transfer by a chemi-osmotic type of mechanism, *Nature* 191 (1961) 144–148.
- [3] D.G. Nicholls, S.J. Ferguson, 5 - Respiratory chains, in: D.G. Nicholls, S.J. Ferguson (Eds.), *Bioenergetics*, fourth ed., Academic Press, Boston, 2013, pp. 91–157, <https://doi.org/10.1016/B978-0-12-388425-1.00005-1>.
- [4] J.A. Enriquez, Supramolecular organization of respiratory complexes, *Annu. Rev. Physiol.* 78 (2016) 533–561, <https://doi.org/10.1146/annurev-physiol-021115-105031>.
- [5] J. Gu, M. Wu, R. Guo, K. Yan, J. Lei, N. Gao, M. Yang, The architecture of the mammalian respirasome, *Nature* 537 (2016) 639–643, <https://doi.org/10.1038/nature19359>.
- [6] J.A. Letts, K. Fiedorczuk, L.A. Sazanov, The architecture of respiratory supercomplexes, *Nature* 537 (2016) 644–648, <https://doi.org/10.1038/nature19774>.
- [7] R. Guo, S. Zong, M. Wu, J. Gu, M. Yang, Architecture of human mitochondrial respiratory megacomplex I2III2IV2, *Cell* 170 (2017) 1247–1257.e12, <https://doi.org/10.1016/j.cell.2017.07.050>.
- [8] K.M. Davies, T.B. Blum, W. Kühlbrandt, Conserved in situ arrangement of complex I and III2 in mitochondrial respiratory chain supercomplexes of mammals, yeast, and plants, *Proc. Natl. Acad. Sci. U.S.A.* 115 (2018) 3024–3029, <https://doi.org/10.1073/pnas.1720702115>.
- [9] E. Maranzana, G. Barbero, A.I. Falasca, G. Lenaz, M.L. Genova, Mitochondrial respiratory supercomplex association limits production of reactive oxygen species from complex I, *Antioxid. Redox Signal.* 19 (2013) 1469–1480, <https://doi.org/10.1089/ars.2012.4845>.
- [10] J.A. Letts, K. Fiedorczuk, G. Degliesposti, M. Skehel, L.A. Sazanov, Structures of respiratory supercomplex I+III2 reveal functional and conformational crosstalk, *Mol. Cell* 75 (2019) 1131–1146.e6, <https://doi.org/10.1016/j.molcel.2019.07.022>.
- [11] H. Guo, S.A. Bueler, J.L. Rubinstein, Atomic model for the dimeric FO region of mitochondrial ATP synthase, *Science* 358 (2017) 936–940, <https://doi.org/10.1126/science.aao4815>.
- [12] P. Paumard, J. Vaillier, B. Coulary, J. Schaeffer, V. Soubannier, D.M. Mueller, D. Brèthes, J.-P. di Rago, J. Velours, The ATP synthase is involved in generating mitochondrial cristae morphology, *EMBO J.* 21 (2002) 221–230, <https://doi.org/10.1093/emboj/21.3.221>.
- [13] H. Itoh, A. Takahashi, K. Adachi, H. Noji, R. Yasuda, M. Yoshida, K. Kinoshita, Mechanically driven ATP synthesis by F1-ATPase, *Nature* 427 (2004) 465–468, <https://doi.org/10.1038/nature02212>.
- [14] S. Nesci, A. Pagliarani, C. Algieri, F. Trombetti, Mitochondrial F-type ATP synthase: multiple enzyme functions revealed by the membrane-embedded FO structure, *Crit. Rev. Biochem. Mol. Biol.* 55 (2020) 309–321, <https://doi.org/10.1080/10409238.2020.1784084>.
- [15] W. Junge, H. Sialaff, S. Engelbrecht, Torque generation and elastic power transmission in the rotary F<sub>0</sub>(F<sub>1</sub>)-ATPase, *Nature* 459 (2009) 364–370, <https://doi.org/10.1038/nature08145>.
- [16] M. Yoshida, E. Muneyuki, T. Hisabori, ATP synthase—a marvellous rotary engine of the cell, *Nat. Rev. Mol. Cell Biol.* 2 (2001) 669–677, <https://doi.org/10.1038/35089509>.
- [17] W. Junge, N. Nelson, ATP synthase, *Annu. Rev. Biochem.* 84 (2015) 631–657, <https://doi.org/10.1146/annurev-biochem-060614-034124>.
- [18] G. Pinke, L. Zhou, L.A. Sazanov, Cryo-EM structure of the entire mammalian F-type ATP synthase, *Nat. Struct. Mol. Biol.* 27 (2020) 1077–1085, <https://doi.org/10.1038/s41594-020-0503-8>.
- [19] S. Nesci, A. Pagliarani, Emerging roles for the mitochondrial ATP synthase supercomplexes, *Trends Biochem. Sci.* 44 (2019) 821–823, <https://doi.org/10.1016/j.tibs.2019.07.002>.
- [20] C. Algieri, F. Trombetti, A. Pagliarani, V. Ventrella, C. Bernardini, M. Fabbri, M. Forni, S. Nesci, Mitochondrial Ca<sup>2+</sup>-activated F<sub>1</sub>FO<sub>1</sub>-ATPase hydrolyzes ATP and promotes the permeability transition pore, *Ann. N. Y. Acad. Sci.* 1457 (2019) 142–157, <https://doi.org/10.1111/nyas.14218>.
- [21] S. Nesci, The mitochondrial permeability transition pore in cell death: a promising drug binding bioarchitecture, *Med. Res. Rev.* 40 (2020) 811–817, <https://doi.org/10.1002/med.21635>.
- [22] P. Bernardi, A. Rasola, M. Forte, G. Lippe, The mitochondrial permeability transition pore: channel formation by F-ATP synthase, integration in signal transduction, and role in pathophysiology, *Physiol. Rev.* 95 (2015) 1111–1155, <https://doi.org/10.1152/physrev.00001.2015>.
- [23] G.K. Kolluru, X. Shen, C.G. Kevil, A tale of two gases: NO and H<sub>2</sub>S, foes or friends for life? *Redox Biol.* 1 (2013) 313–318, <https://doi.org/10.1016/j.redox.2013.05.001>.
- [24] L. Li, P. Rose, P.K. Moore, Hydrogen sulfide and cell signaling, *Annu. Rev. Pharmacol. Toxicol.* 51 (2011) 169–187, <https://doi.org/10.1146/annurev-pharmtox-010510-100505>.
- [25] K. Módis, Y. Ju, A. Ahmad, A.A. Untereiner, Z. Altaany, L. Wu, C. Szabo, R. Wang, S-Sulphydration of ATP synthase by hydrogen sulfide stimulates mitochondrial bioenergetics, *Pharmacol. Res.* 113 (2016) 116–124, <https://doi.org/10.1016/j.phrs.2016.08.023>.
- [26] S. Nesci, F. Trombetti, V. Ventrella, A. Pagliarani, Post-translational modifications of the mitochondrial F<sub>1</sub>FO<sub>1</sub>-ATPase, *Biochim. Biophys. Acta* 1861 (2017) 2902–2912, <https://doi.org/10.1016/j.bbagen.2017.08.007>.
- [27] C. Szabo, C. Ransy, K. Módis, M. Andriamihaja, B. Murghes, C. Coletta, G. Olah, K. Yanagi, F. Bouillaud, Regulation of mitochondrial bioenergetic function by hydrogen sulfide. Part I. Biochemical and physiological mechanisms, *Br. J. Pharmacol.* 171 (2014) 2099–2122, <https://doi.org/10.1111/bph.12369>.
- [28] S. Nesci, V. Ventrella, F. Trombetti, M. Pirini, A. Pagliarani, The mitochondrial F<sub>1</sub>FO<sub>1</sub>-ATPase desensitization to oligomycin by tributyltin is due to thiol oxidation, *Biochimie* 97 (2014) 128–137, <https://doi.org/10.1016/j.biochi.2013.10.002>.
- [29] M.M. Bradford, A rapid and sensitive method for the quantitation of microgram quantities of protein utilizing the principle of protein-dye binding, *Anal. Biochem.* 72 (1976) 248–254, <https://doi.org/10.1006/abio.1976.9999>.
- [30] C. Algieri, F. Trombetti, A. Pagliarani, V. Ventrella, S. Nesci, Phenylglyoxal inhibition of the mitochondrial F<sub>1</sub>FO<sub>1</sub>-ATPase activated by Mg<sup>2+</sup> or by Ca<sup>2+</sup> provides clues on the mitochondrial permeability transition pore, *Arch. Biochem. Biophys.* 681 (2020), 108258, <https://doi.org/10.1016/j.abb.2020.108258>.
- [31] V. Ventrella, S. Nesci, F. Trombetti, P. Bandiera, M. Pirini, A.R. Borgatti, A. Pagliarani, Tributyltin inhibits the oligomycin-sensitive Mg-ATPase activity in Mytilus galloprovincialis digestive gland mitochondria, *Comp. Biochem. Physiol. C Toxicol. Pharmacol.* 153 (2011) 75–81, <https://doi.org/10.1016/j.cbpc.2010.08.007>.
- [32] S. Nesci, F. Trombetti, M. Pirini, V. Ventrella, A. Pagliarani, Mercury and protein thiols: stimulation of mitochondrial F<sub>1</sub>FO<sub>1</sub>-ATPase and inhibition of respiration, *Chem. Biol. Interact.* 260 (2016) 42–49, <https://doi.org/10.1016/j.cbi.2016.10.018>.
- [33] B. Chance, G.R. Williams, Respiratory enzymes in oxidative phosphorylation. III. The steady state, *J. Biol. Chem.* 217 (1955) 409–427.
- [34] B. Chance, G.R. Williams, W.F. Holmes, J. Higgins, Respiratory enzymes in oxidative phosphorylation. V. A mechanism for oxidative phosphorylation, *J. Biol. Chem.* 217 (1955) 439–451.
- [35] R.W. Estabrook, [7] Mitochondrial respiratory control and the polarographic measurement of ADP: O ratios, in: *Methods in Enzymology*, Academic Press, 1967, pp. 41–47, [https://doi.org/10.1016/0076-6879\(67\)10010-4](https://doi.org/10.1016/0076-6879(67)10010-4).
- [36] O. Kabil, R. Banerjee, Redox biochemistry of hydrogen sulfide, *J. Biol. Chem.* 285 (2010) 21903–21907, <https://doi.org/10.1074/jbc.R110.128363>.
- [37] V. Vitvitskiy, J.L. Miljkovic, T. Bostelaar, B. Adhikari, P.K. Yadav, A.K. Steiger, R. Torregrossa, M.D. Pluth, M. Whiteman, R. Banerjee, M.R. Filipovic, Cytochrome c Reduction by H<sub>2</sub>S Potentiates Sulfide Signaling, *ACS Chem. Biol.* 13 (2018) 2300–2307, <https://doi.org/10.1021/acscchembio.8b00463>.
- [38] S. Nesci, V. Ventrella, F. Trombetti, M. Pirini, A. Pagliarani, Tributyltin (TBT) and mitochondrial respiration in mussel digestive gland, *Toxicol. Vitro* 25 (2011) 951–959, <https://doi.org/10.1016/j.tiv.2011.03.004>.
- [39] V. Algieri, C. Algieri, L. Maiuolo, A. De Nino, A. Pagliarani, M.A. Tallarida, F. Trombetti, S. Nesci, 1,5-Disubstituted-1,2,3-triazoles as inhibitors of the mitochondrial Ca<sup>2+</sup>-activated F<sub>1</sub>FO<sub>1</sub>-ATPase (hydrolyase) and the permeability transition pore, *Ann. N. Y. Acad. Sci.* (2020), <https://doi.org/10.1111/nyas.14474>.
- [40] M. Bragadin, T. Pozzan, G.F. Azzone, Kinetics of Ca<sup>2+</sup> carrier in rat liver mitochondria, *Biochemistry* 18 (1979) 5972–5978.
- [41] K. Módis, E.M. Bos, E. Calzia, H. van Goor, C. Coletta, A. Papapetropoulos, M. R. Hellmich, P. Radermacher, F. Bouillaud, C. Szabo, Regulation of mitochondrial bioenergetic function by hydrogen sulfide. Part II. Pathophysiol. Ther. *Asp. Br. J. Pharm.* 171 (2014) 2123–2146, <https://doi.org/10.1111/bph.12368>.
- [42] B.D. Paul, S.H. Snyder, K. Kashfi, Effects of hydrogen sulfide on mitochondrial function and cellular bioenergetics, *Redox Biol.* 38 (2021), 101772, <https://doi.org/10.1016/j.redox.2020.101772>.
- [43] A.K. Mustafa, M.M. Gadalla, N. Sen, S. Kim, W. Mu, S.K. Gazi, R.K. Barrow, G. Yang, R. Wang, S.H. Snyder, H<sub>2</sub>S signals through protein S-sulphydration, *Sci. Signal.* 2 (2009), ra72, <https://doi.org/10.1126/scisignal.2000464>.
- [44] P. Nicholls, J.K. Kim, Sulphide as an inhibitor and electron donor for the cytochrome c oxidase system, *Can. J. Biochem.* 60 (1982) 613–623, <https://doi.org/10.1139/o82-076>.
- [45] M. Gubern, M. Andriamihaja, T. Nübel, F. Blachier, F. Bouillaud, Sulfide, the first inorganic substrate for human cells, *FASEB J.* 21 (2007) 1699–1706, <https://doi.org/10.1096/fj.06-7407com>.

- [46] M.A. Powell, G.N. Somero, Hydrogen sulfide oxidation is coupled to oxidative phosphorylation in mitochondria of *Solemya reidi*, *Science* 233 (1986) 563–566, <https://doi.org/10.1126/science.233.4763.563>.
- [47] J.G. Fedor, J. Hirst, Mitochondrial supercomplexes do not enhance catalysis by quinone channeling, *Cell Metab.* 28 (2018) 525–531.e4, <https://doi.org/10.1016/j.cmet.2018.05.024>.
- [48] J.W. Calvert, W.A. Coetzee, D.J. Lefer, Novel insights into hydrogen sulfide-mediated cytoprotection, *Antioxid. Redox Signal* 12 (2010) 1203–1217, <https://doi.org/10.1089/ars.2009.2882>.
- [49] G. Morciano, C. Giorgi, M. Bonora, S. Punzetti, R. Pavasini, M.R. Wieckowski, G. Campo, P. Pinton, Molecular identity of the mitochondrial permeability transition pore and its role in ischemia-reperfusion injury, *J. Mol. Cell. Cardiol.* 78 (2015) 142–153, <https://doi.org/10.1016/j.yjmcc.2014.08.015>.
- [50] S. Marchi, V.A.M. Vitto, S. Patergnani, P. Pinton, High mitochondrial Ca<sup>2+</sup> content increases cancer cell proliferation upon inhibition of mitochondrial permeability transition pore (mPTP), *Cell Cycle* 18 (2019) 914–916, <https://doi.org/10.1080/15384101.2019.1598729>.
- [51] D.G. Nicholls, S.J. Ferguson, 9 - Cellular bioenergetics, in: D.G. Nicholls, S. J. Ferguson (Eds.), *Bioenergetics*, fourth ed., Academic Press, Boston, 2013, pp. 255–302, <https://doi.org/10.1016/B978-0-12-388425-1.00009-9>.
- [52] E. Murphy, C. Steenbergen, Regulation of mitochondrial Ca<sup>2+</sup> uptake, *Annu Rev. Physiol.* (2020), <https://doi.org/10.1146/annurev-physiol-031920-092419>.



## Mitochondrial $F_1F_0$ -ATPase and permeability transition pore response to sulfide in the midgut gland of *Mytilus galloprovincialis*

Cristina Algieri, Salvatore Nesci\*, Fabiana Trombetti, Micaela Fabbri, Vittoria Ventrella, Alessandra Pagliarani

Department of Veterinary Medical Sciences (DIMEVET), University of Bologna, via Tolara di Sopra, 50, 40064, Ozzano Emilia, Bologna, Italy



### ARTICLE INFO

#### Article history:

Received 3 September 2020

Received in revised form

10 November 2020

Accepted 12 November 2020

Available online 17 November 2020

#### Keywords:

$F_1F_0$ -ATPase

Mitochondria

Midgut gland

*Mytilus galloprovincialis*

Permeability transition pore

Sulfide

### ABSTRACT

The molecular mechanisms which rule the formation and opening of the mitochondrial permeability transition pore (mPTP), the lethal mechanism which permeabilizes mitochondria to water and solutes and drives the cell to death, are still unclear and particularly little investigated in invertebrates. Since  $Ca^{2+}$  increase in mitochondria is accompanied by mPTP opening and the participation of the mitochondrial  $F_1F_0$ -ATPase in the mPTP is increasingly sustained, the substitution of the natural cofactor  $Mg^{2+}$  by  $Ca^{2+}$  in the  $F_1F_0$ -ATPase activation has been involved in the mPTP mechanism. In mussel midgut gland mitochondria the similar kinetic properties of the  $Mg^{2+}$ - or  $Ca^{2+}$ -dependent  $F_1F_0$ -ATPase activities, namely the same affinity for ATP and bi-site activation kinetics by the ATP substrate, in spite of the higher enzyme activity and coupling efficiency of the  $Mg^{2+}$ -dependent  $F_1F_0$ -ATPase, suggest that both enzyme activities are involved in the bioenergetic machinery. Other than being a mitochondrial poison and environmental contaminant, sulfide at low concentrations acts as gaseous mediator and can induce post-translational modifications of proteins. The sulfide donor NaHS, at micromolar concentrations, does not alter the two  $F_1F_0$ -ATPase activities, but desensitizes the mPTP to  $Ca^{2+}$  input. Unexpectedly, NaHS, under the conditions tested, points out a chemical refractoriness of both  $F_1F_0$ -ATPase activities and a failed relationship between the  $Ca^{2+}$ -dependent  $F_1F_0$ -ATPase and the mPTP in mussels. The findings suggest that mPTP role and regulation may be different in different taxa and that the  $F_1F_0$ -ATPase insensitivity to NaHS may allow mussels to cope with environmental sulfide.

© 2020 Elsevier B.V. and Société Française de Biochimie et Biologie Moléculaire (SFBBM). All rights reserved.

## 1. Introduction

Sulfide is an important environmental agent for a variety of aquatic and terrestrial organisms. In recent years studies on sulfide effects have been mainly focused on mammals, due to the emerging sulfide role as physiological gaseous modulator and its involvement in cardiovascular [1] and liver [2] protection. Marine habitats have received most attention for the occurrence of hydrothermal vents and hypoxic habitats, where high sulfide concentrations impose biological adaptations to allow survival [3]. However, sulfide is a

naturally produced compound which affects and drives biochemical events from bacteria to mammals, and, depending on the dose and the available targets, may be a respiratory and neurological poison, a signaling molecule [4], and also have therapeutic potential [1]. In aquatic biota sulfide toxicology has common features, especially at the biochemical level, which affect health, survival, productivity and distribution of aquatic species [5].

In aqueous solutions,  $H_2S$  reversibly dissociates into the hydrosulfide ( $HS^-$ ) and bisulfide ( $S^{2-}$ ) anions, whose proportion is pH and temperature dependent. At physiological pH (7.4) and temperature (37 °C), the most abundant forms are  $HS^-$  (nearly 70%) and  $H_2S$  (about 30%). The latter is moderately lipophilic and can cross biological membranes. At increasing pHs, as in seawater, the  $H_2S$  level decreases, while  $HS^-$  and  $S^{2-}$  concentrations increase and may somehow contribute to sulfide bioactivity, even if the negative charges most likely prevent membrane crossing. However, the quantification of the actual concentration of these three species is

Abbreviations: CRC, calcium retention capacity; EDTA, ethylenediamine tetraacetic acid; DMSO, Dimethylsulphoxide; HEPES, (4-(2-hydroxyethyl)-1-piperazinethanesulfonic acid); mPTP, mitochondrial permeability transition pore; Tris, Tris(hydroxymethyl)-aminomethane.

\* Corresponding author.

E-mail address: [salvatore.nesci@unibo.it](mailto:salvatore.nesci@unibo.it) (S. Nesci).

not easy and often controversial [6,7], so the term sulfide is currently used to embrace the three interconverting forms [8].

Mitochondria provide the main defense against environmental sulfide [5] and also constitute one of its preferred targets [9]. Sulfide can affect mitochondrial proteins by directly producing post translational modifications of amino acid residues such as cysteine, and/or by indirectly affecting redox homeostasis [10]. Controversial effects were reported on the pro-oxidant and anti-oxidant effects of H<sub>2</sub>S and on its modulation of mitochondrial bioenergetics [11].

As far as we are aware no study has dealt with a direct effect of sulfide on the mitochondrial F<sub>1</sub>F<sub>0</sub>-ATPase, which plays a central role in the production of ATP under aerobic conditions and, as recently emerged, in the cell lifespan [12]. The mitochondrial F<sub>1</sub>F<sub>0</sub>-ATPase has been increasingly involved in the formation of the permeability transition pore (mPTP), which dramatically increases the inner mitochondrial membrane permeability and drives the cell to death. This lethal task, triggered by an increase in Ca<sup>2+</sup> concentration in the mitochondrial matrix which activates the hydrolytic activity of the F<sub>1</sub>F<sub>0</sub>-ATPase [13,14], is established in mammals [15,16], but still uncertain in invertebrates where it could depend on the so called lipidome, namely the lipid composition of the inner mitochondrial membrane [17,18], which may affect the membrane flexibility required to form the pore. Accordingly, the formation of the mPTP was only described in sea urchin gametes [19], hypothesized in the opisthobranch mollusk *Aplysia* [20] and undetected in crustaceans [21]. Clues of pore forming properties of F<sub>1</sub>F<sub>0</sub>-ATPase dimers were found in model organisms, namely *Drosophila* and yeast [22]. To our knowledge, there are no reports in bivalve mollusks, whose mitochondrial F<sub>1</sub>F<sub>0</sub>-ATPase mechanism exhibits some astonishing similarities to mammals [23]. Sulfide accumulates below mussel farms [24] and has a great impact on benthic populations [5].

The present work aims at casting light in a quite unexplored field, by testing sulfide effects on the mitochondrial F<sub>1</sub>F<sub>0</sub>-ATPase activated either by the natural cofactor Mg<sup>2+</sup> or by Ca<sup>2+</sup> in the midgut gland of *Mytilus galloprovincialis*, a widely cultivated species in the Mediterranean Sea. Interestingly, bivalve mollusks constitute emerging animal models to study molecular mechanisms, such as those involved in cancer [25], muscle contraction [26], inflammation [27] and aging [28], other than having a recognized role in ecotoxicology [29]. The results may also contribute to improve the knowledge of sulfide physio-pathological roles and of the mitochondrial responsiveness to sulfide in invertebrates under aerobic conditions.

## 2. Materials and Methods

### 2.1. Chemicals

NaHS, oligomycin (a mixture of oligomycins A, B and C) and Fura-FF were purchased from Vinci-Biochem (Vinci, Italy). Na<sub>2</sub>ATP was obtained from Sigma–Aldrich (Milan, Italy). Quartz double distilled water was used for all reagent solutions.

### 2.2. Animals

Adult specimen of commercial size (mean average weight 20 g, >25 mm shell length) of mussels *Mytilus galloprovincialis* Lamark were obtained from coastal culture plants in the Northern Adriatic Sea and transported alive in aerated seawater tanks to the laboratory. Approximately 60 mussels were used, divided into pools of 10–15 animals each. According to the Italian law, the use of commercially available bivalve shellfish for research purpose does not require any approval.

### 2.3. Preparation of mitochondrial fractions

From dissected mussels, the digestive glands (hepatopancreas) were quickly removed, pooled (10–15 animals for each pool), repeatedly rinsed in ice-cold medium A (0.25 M sucrose, 5 mM Tris(hydroxymethyl)-aminomethane (Tris), 5 mM ethylenediamine tetraacetic acid (EDTA), pH 7.4) and gently dried on blotting paper. Whenever detected, the crystalline stylus was promptly removed. Then tissues were weighted and stored in small vials in small amounts of medium A in liquid nitrogen until use. Immediately after thawing, excess medium was decanted and the digestive glands were homogenized in medium B (0.25 mM sucrose, 0.5 g/L fatty acid-free bovine serum albumin (BSA), Tris 24 mM, pH 7.4), in the proportion 11 mL medium B for each g (wet mass) of tissue, by Braun homogenizer Type 853202 at 450 rpm for 1 min. The mitochondrial fraction was obtained by stepwise centrifugation (Sorvall RC2-B, rotor SS34). The homogenate was centrifuged at 1,100×g for 8 min; the obtained supernatant was filtered through four gauze layers and further centrifuged at 16,800×g for 10 min to yield the raw mitochondrial pellet. The latter was resuspended in medium B and further centrifuged at the same speed for 10 min to obtain the final mitochondrial pellet which was resuspended by gentle stirring using a Teflon Potter Elvehjem homogenizer in a small volume of medium B, thus obtaining a protein concentration of 10–12 mg/mL. All steps were carried out at 0–4 °C. Protein concentration was determined by Bio-Rad Protein Assay kit II with BSA as standard according to the colorimetric method of Bradford [30]. Mitochondrial preparations were then stored in liquid nitrogen until use. The stability of mitochondrial preparations in liquid nitrogen was previously evaluated as a function of storage time. Results indicated that the mitochondrial Mg-ATPase activity was unaffected even after a year [31].

Prior to storage, the respiratory activities were polarographically evaluated [32] on freshly prepared mitochondrial membranes as previously described [33], to check their functionality. These tests, combined with the failed detection of the Na,K-ATPase activity, a known marker of plasma membranes [34], witnessed the quality and the virtual absence of contamination of mitochondrial preparations [35].

### 2.4. Mitochondrial F<sub>1</sub>F<sub>0</sub>-ATPase activity assays

Immediately after thawing, mitochondrial preparations were used to evaluate the F<sub>1</sub>F<sub>0</sub>-ATPase activity. The ATP hydrolysis capability was assayed in a reaction medium (1 mL) containing 0.15 mg mitochondrial protein and 75 mM ethanolamine–HCl buffer pH 8.9, 5.0 mM Na<sub>2</sub>ATP and 2.0 mM MgCl<sub>2</sub> for the Mg<sup>2+</sup>-activated F<sub>1</sub>F<sub>0</sub>-ATPase assay, and in the same buffer at pH 8.9 plus 5.0 mM Na<sub>2</sub>ATP and 2.0 mM CaCl<sub>2</sub> to evaluate the Ca<sup>2+</sup>-activated F<sub>1</sub>F<sub>0</sub>-ATPase activity. After 5 min preincubation at 30 °C, the reaction, carried out at the same temperature, was started by adding the substrate Na<sub>2</sub>ATP and stopped after 5 min by adding 1 mL of ice-cold 15% (w/w) trichloroacetic acid aqueous solution. Once the reaction was blocked, vials were centrifuged for 15 min at 3500 rpm (Eppendorf Centrifuge 5202). The concentration of inorganic phosphate (Pi) hydrolyzed by known amounts of mitochondrial protein in the supernatant, which indirectly detects the F<sub>1</sub>F<sub>0</sub>-ATPase activity, was spectrophotometrically evaluated [36]. To this aim, 1.0 µL from a stock solution of 4.0 mg/mL oligomycin in dimethylsulfoxide (DMSO) was directly added to the reaction mixture before starting the reaction. The total F<sub>1</sub>F<sub>0</sub>-ATPase activity was calculated by the Pi evaluation in control tubes run in parallel and containing 1.0 µL DMSO per mL reaction system. Control tubes were alternated to the condition to be tested in each set of

experiments. The dose of 4.0 mg/mL oligomycin, specific inhibitor of  $F_1F_0$ -ATPase, which selectively blocks the  $F_0$  subunit, which is currently used in  $F_1F_0$ -ATPase assays [37], ensured maximal  $F_1F_0$ -ATPase inhibition. The  $F_1F_0$ -ATPase activity, also defined as mitochondrial oligomycin-sensitive ATPase activity, was routinely measured by subtracting, from the Pi hydrolyzed by total mitochondrial ATPase activity, the Pi hydrolyzed in the presence of oligomycin (mitochondrial oligomycin-insensitive ATPase), and expressed as  $\mu\text{mol Pi} \cdot \text{mg protein}^{-1} \cdot \text{min}^{-1}$  in all experiments. Even if the mitochondrial ATPase activity in mussels referred to  $F_1F_0$ -ATPase could be only confirmed by SDS-gel and Western Blot analyses, the ways to confirm enzyme purity and integrity as done in *E. coli*  $F_1F_0$ -ATP synthase by other lab [38], at present we could not do it, due to the lack of adequate protocol and reagents.

The effects of the NaHS were tested by adding 4  $\mu\text{l}$  aliquots of NaHS in DMSO (control in NaHS-free medium with 4  $\mu\text{l}$  DMSO) to the reaction mixture immediately prior to the addition of the mitochondrial suspensions. To this aim, NaHS concentrations, obtained by dilution from the 25 mM NaHS DMSO stock solution, were added to the reaction mixture to obtain final NaHS concentrations in the range 0.1–100  $\mu\text{M}$  NaHS in the reaction system.

## 2.5. Kinetic analyses

In all plots the specific enzyme activity, evaluated as  $\mu\text{moles Pi} \cdot \text{mg protein}^{-1} \cdot \text{min}^{-1}$  was taken as the expression of the initial reaction rate  $v$ . To evaluate the enzyme activation kinetics by the ATP substrate, Hill plots were built [39]. To this aim  $\text{Mg}^{2+}$  and  $\text{Ca}^{2+}$ -ATPase assays were carried out at various stated ATP millimolar concentrations in the reaction medium, by keeping constant all other assay conditions. The linear transformation of Hill equation was used:

$$\log \frac{v_0}{V_{\max} - v_0} = -n_{\text{Hi}} \log[\text{ATP}] + \log K'$$

where  $V_{\max}$  and  $v_0$  represent the enzyme reaction rates, respectively in the presence of substrate concentration which gives the maximal rate and in the presence of a stated substrate concentration [ATP],  $K'$  is a constant value. By plotting  $\log v_0/(V_{\max}-v_0)$  versus  $\log[\text{ATP}]$  a straight line is obtained, whose slope is Hill coefficient ( $-n_{\text{Hi}}$ ). In case  $|n_{\text{Hi}}| \neq 1$  multiple binding sites for the substrate can be involved [39] even if the  $n_{\text{Hi}}$  value cannot stoichiometrically correspond to the binding sites.

To calculate the kinetic parameters ( $V_{\max}$  and  $K_m$ ) in the presence of different concentrations of ATP substrate, enzyme activity data were fitted to the Lineweaver-Burk equation in which the reciprocal of the reaction rate ( $1/v$ ) was plotted as a function of the reciprocal concentration of ATP, raised to a power ( $n_{\text{Hi}}$ ) which corresponds to Hill coefficient. This corrective procedure allows the building of a linear Lineweaver-Burk plot, and consequently the calculation of  $V_{\max}$  and  $K_m$  values from the intercept with y and x axis, respectively, even when  $n_{\text{Hi}}$  is  $\neq 1$ .

Correlation coefficients were never lower than 0.96 thus confirming the linearity of all plots.

## 2.6. mPTP assay

Immediately after the preparation of mussel midgut gland mitochondrial fractions, fresh mitochondrial suspensions (1 mg/mL) were energized in the assay buffer (130 mM KCl, 1 mM  $\text{KH}_2\text{PO}_4$ , 20 mM HEPES, pH 7.2 with TRIS), incubated at 30 °C with 1  $\mu\text{g}/\text{mL}$  rotenone and 5 mM succinate. To evaluate NaHS effect, selected NaHS doses were added to the mitochondrial suspensions before mPTP evaluation. mPTP opening was induced by the addition of

low concentrations of  $\text{Ca}^{2+}$  (10  $\mu\text{M}$ ) as  $\text{CaCl}_2$  solution at fixed time intervals (1 min). The calcium retention capacity (CRC), whose lowering indicates mPTP opening, was spectrofluorometrically evaluated in the presence of 0.8  $\mu\text{M}$  Fura-FF. The probe has different spectral properties in the absence and in the presence of  $\text{Ca}^{2+}$ , namely it displays excitation/emission spectra of 365/514 nm in the absence of  $\text{Ca}^{2+}$  (Fura-FF low  $\text{Ca}^{2+}$ ) and shifts to 339/507 nm in the presence of high  $\text{Ca}^{2+}$  concentrations (Fura-FF high  $\text{Ca}^{2+}$ ). mPTP opening, was evaluated by the increase in the fluorescence intensity ratio (Fura-FF high  $\text{Ca}^{2+}$ )/(Fura-FF low  $\text{Ca}^{2+}$ ), which indicates a decrease in CRC [40]. All measurements were processed by LabSolutions RF software.

## 2.7. Calculations and statistics

Statistical analyses were performed by SIGMASTAT software. The analysis of variance followed by Students–Newman–Keuls' test when F values indicated significance ( $P \leq 0.05$ ) was applied. Percentage data were arcsin-transformed before statistical analyses to ensure normality.

## 3. Results and discussion

### 3.1. $\text{Ca}^{2+}$ - and $\text{Mg}^{2+}$ -dependent $F_1F_0$ -ATPase kinetic parameters

As first approach, experiments aimed at pointing out the kinetic properties of the  $F_1F_0$ -ATPase in mussel digestive gland mitochondria either activated by the natural cofactor  $\text{Mg}^{2+}$  or by  $\text{Ca}^{2+}$ , being the latter involved in the lethal task of triggering the mPTP formation [14,40,41]. The  $F_1F_0$ -ATPase energy transduction mechanism converts the electrochemical gradient of a transmembrane proton motive force ( $\Delta p$ ) by torque generation into ATP chemical energy during ATP synthesis and *vice versa* by ATP hydrolysis [42]. Both enzyme tasks of ATP synthesis/hydrolysis are sustained by the natural cofactor  $\text{Mg}^{2+}$  or by other metal divalent cations [14,43,44]. However,  $\text{Ca}^{2+}$  only sustains ATP synthesis and in this case, the rotor rotation was reported to be not coupled to  $\Delta p$  generation in beef heart submitochondrial particles [43], in *Rhodospirillum rubrum* [45], in chloroplast thylakoids [46] and in pea stem mitochondria [47]. Conversely, ATP complexed with  $\text{Ca}^{2+}$  can drive the pH gradient formation with nearly the same effectiveness as MgATP in *Escherichia coli* [48]. Moreover, in swine heart submitochondrial particles the  $\text{Ca}^{2+}$ -dependent  $F_1F_0$ -ATPase is inhibited by succinate- $\text{O}_2$  oxidoreductase activity, which generating the  $\Delta p$  contrast the  $\text{H}^+$ -pumping  $F_1F_0$ -ATPase. On the other hand, dinitrophenol makes the submitochondrial particles membrane permeable to  $\text{H}^+$  and increases the hydrolytic activity of the  $\text{Ca}^{2+}$ -dependent  $F_1F_0$ -ATPase coupled to  $\text{H}^+$  pumping [13]. The  $\text{Ca}^{2+}$ -dependent  $F_1F_0$ -ATPase of swine heart [13] and pea stem mitochondria [47] are fully sensitive to oligomycin, a specific inhibitor of  $F_0$  domain [49]. In mussel midgut gland mitochondria ATP hydrolysis can be sustained by  $\text{Ca}^{2+}$ , other than by  $\text{Mg}^{2+}$ , even if the oligomycin-sensitive ATPase activity only represents the 40% of total ATPase activity, while in presence of  $\text{Mg}^{2+}$  the oligomycin sensitive ATPase is as much as 85% of the total ATPase activity (Fig. 1). Moreover, the coupling index calculated as mitochondrial oligomycin-sensitive ATPase activity on the total mitochondrial ATPase activity ratio of the  $\text{Mg}^{2+}$ -dependent  $F_1F_0$ -ATPase shows a better value than the  $\text{Ca}^{2+}$ -dependent  $F_1F_0$ -ATPase ( $0.85 \pm 0.13$  vs  $0.37 \pm 0.08$ ). Since we do not have the protocol for  $F_1F_0$ -ATPase isolation and purification from mussel mitochondria, the results obtained refer to the  $F_1F_0$  ATPase activity in isolated mitochondria.

Further experiments aimed at casting light on the enzyme kinetics, a quite unexplored field in mussel mitochondria. The binding change mechanism for the  $F_1$ -ATPase [50] is known to be

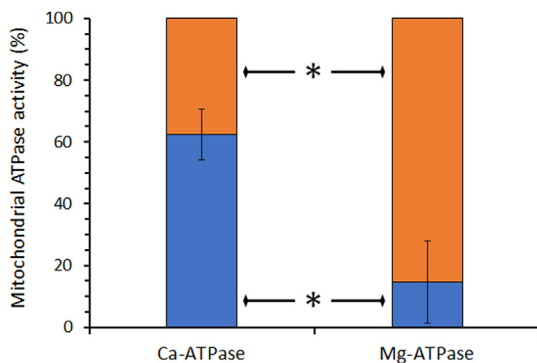


**Fig. 1.** Mitochondrial ATPase activity sustained by  $\text{Ca}^{2+}$  or by  $\text{Mg}^{2+}$ . The oligomycin-sensitive ATPase activity ■ and the oligomycin-insensitive ATPase activity ■ are expressed as percentages of the total mitochondrial ATPase activity sustained by  $\text{Ca}^{2+}$  or  $\text{Mg}^{2+}$ , respectively. Data expressed as column chart represent the mean  $\pm$  SD (vertical bars) from three experiments carried out on different mitochondrial preparations. \* indicates significantly different values ( $P \leq 0.05$ ).

sustained by positive cooperativity of three catalytic sites. The ATP substrate can simultaneously fill from one to three sites during the catalysis denoting it as uni-site, bi-site, or tri-site catalysis, respectively. The rate of ATP hydrolysis is ATP concentration dependent. Steady-state catalysis studies provide evidence that the main kinetic enhancement occurs by bi-site activation inducing strong positive cooperativity [51]. The mussel midgut gland  $\text{F}_1\text{F}_0$ -ATPase activated by  $\text{Mg}^{2+}$  or  $\text{Ca}^{2+}$  show similar Hill coefficients, namely  $1.72 \pm 0.20$  and  $1.71 \pm 0.22$  respectively (Fig. 2A and B), thus suggesting that, in both cases, ATP can also bind to a two catalytic sites to yield high rates of catalysis. However,  $\text{Mg}^{2+}$  and  $\text{Ca}^{2+}$  do not

sustain ATP hydrolysis by the  $\text{F}_1\text{F}_0$ -ATPase with the same efficiency. Accordingly, even if the  $K_m$  values are similar for the two differently activated ATPases, the  $\text{Mg}^{2+}$ -activated  $\text{F}_1\text{F}_0$ -ATPase shows a 57% higher  $V_{\text{max}}$  value than the  $\text{Ca}^{2+}$ -activated enzyme (Fig. 2C and D), which indicates that, when activated by  $\text{Mg}^{2+}$ , the enzyme hydrolytic activity is more efficient, as in mammals [13,14]. On this basis, the mussel oligomycin-sensitive  $\text{Ca}^{2+}$ -dependent  $\text{F}_1\text{F}_0$ -ATP(hydroly)ase could be enlisted in the mitochondrial bioenergetic regulation machinery, since its affinity for ATP is the same as the companion  $\text{Mg}^{2+}$ -activated enzyme.

### 3.2. NaHS effect on the mitochondrial $\text{F}_1\text{F}_0$ -ATPases and permeability transition pore

Since mussel midgut gland mitochondria contain an ATPase activity that can be activated by both  $\text{Mg}^{2+}$  and  $\text{Ca}^{2+}$  with different kinetic properties, it seemed interesting to evaluate the effect of the sulfide donor NaHS on these enzyme activities and to search for a putative connection with the mPTP. NaHS is widely used to generate  $\text{H}_2\text{S}$ , which, once only known as mitochondrial poison, in recent years has raised increasing interest in cell biology as endogenous gaseous neurotransmitter [52] that acts on cardiovascular system and inflammation as well as on nervous systems, pain appreciation, gastrointestinal and urogenital functions, and endocrine system [53]. The effect, deleterious or on the contrary beneficial, apparently depends on the dose and on the microenvironmental conditions, which in turn include a number of variables. Accordingly, NaHS and related compounds  $\text{H}_2\text{S}$ ,  $\text{HS}^-$  and  $\text{S}^{2-}$ , can also alter the function of cellular proteins and enzymes by inducing post-translational modifications especially on “redox sensor” cysteines [54]. In mammalian mitochondria the  $\alpha$  subunits of  $\text{F}_1\text{F}_0$ -

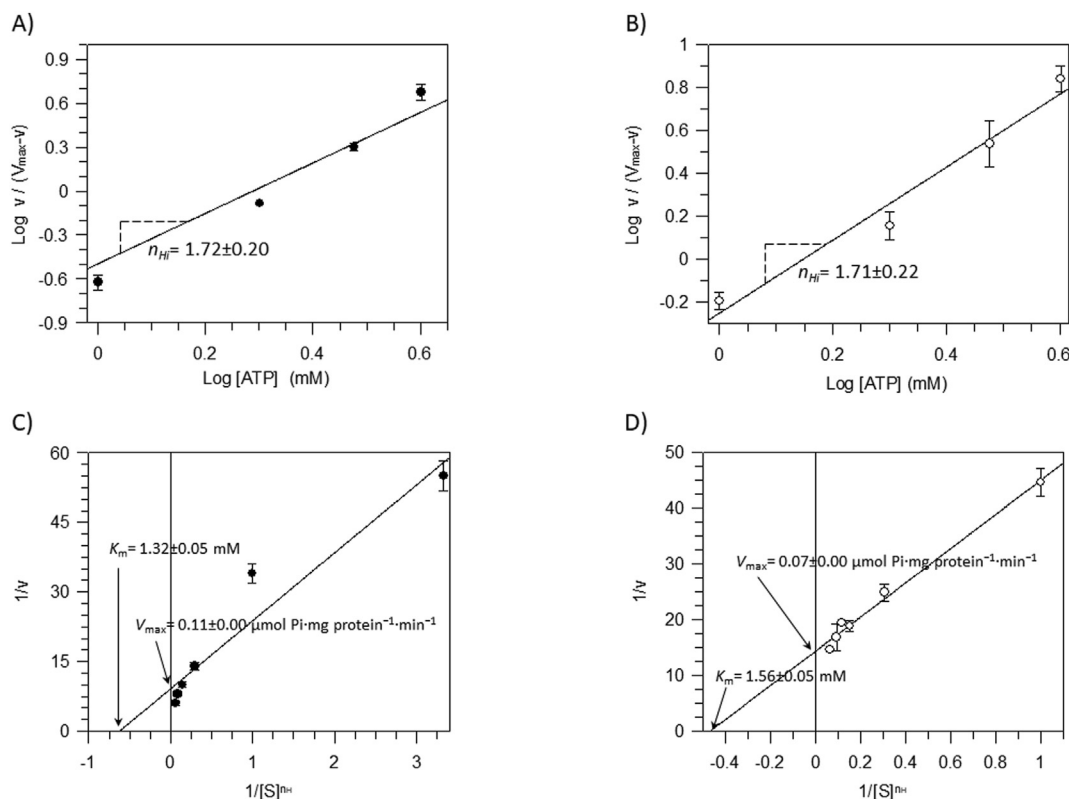


**Fig. 2.** Plots to obtain the kinetic parameters of the mitochondrial  $\text{Mg}^{2+}$ - and  $\text{Ca}^{2+}$ -dependent  $\text{F}_1\text{F}_0$ -ATPases. A and B) Hill plots of the  $\text{Mg}^{2+}$ -ATPase (●) and the  $\text{Ca}^{2+}$ -ATPase (○). C and D) Lineweaver-Burk plots of the  $\text{Mg}^{2+}$ -ATPase (●) and  $\text{Ca}^{2+}$ -ATPase (○). Data represent the mean  $\pm$  SD from three independent experiments carried out on distinct mitochondrial preparations.

ATPase, involved in the catalytic and non-catalytic sites of  $F_1$  domain [55], show cysteine residues at positions 244 and 294 prone to reversible  $S$ -sulfhydration [56]. Modification of thiol ( $-SH$ ) group of cysteines by covalent bond to  $H_2S$  forms persulfide ( $-SSH$ ) group [11]. Other than acting as a mitochondrial poison when blocks complex IV, sulfide can stimulate the ATP synthase by inducing  $S$ -sulfhydration of  $\alpha$  subunits in a concentration-dependent manner [56]. The increase in the enzyme catalytic mechanism when the  $\alpha$ Cys244 and  $\alpha$ Cys294 are  $S$ -sulfhydrized under (patho)physiological conditions prevents the disulfide bond formation under oxidative stress conditions, which forms before the individual subunits (e.g.  $\alpha$  and  $\gamma$  subunits) assemble into the ATP synthase complex [57] and alters the  $F_1$ -ATPase chemo-mechanical mechanism [58]. However, quite surprisingly, when increasing NaHS concentrations are tested on mussel midgut gland mitochondria, no effect on the  $Ca^{2+}$ - and  $Mg^{2+}$ -activated  $F_1F_0$ -ATPases is shown (Fig. 3). Although in eukaryotes there is a high similarity of amino acid sequences in the  $F_1F_0$ -ATPase subunits [59], the mussel  $F_1F_0$ -ATPase cysteines may be refractory to covalently bind to sulfide. Both mPTP and oxidative stress are known to be inhibited by exogenous  $H_2S$  that acts as a cell death modulator [60]. The role of  $Ca^{2+}$  in the PTP opening has also been associated with the interaction with phospholipids of the inner mitochondrial membranes where it appears to induce changes in cardiolipin (CL) packing and to increase CL susceptibility to oxidation [61]. On these bases, the peculiar CL molecular species of mussel, dominated by an extraordinary high level of 22:6n-3 exceeding 70% of total fatty acids [62] and identified as predominantly in a form with four docosahexaenoyl chains and thus easily exposed to oxidation, can help to explain the different regulation mechanisms in different taxa. The  $F_1F_0$ -ATPase is the molecular architecture proposed to coincide with the mPTP [63–65]. Recently two conformations with low and high ion-conductance have been attributed to the monomeric or dimeric form of the  $F_1F_0$ -ATPase [15,16] in presence of  $Ca^{2+}$ . Other membrane-embedded protein of IMM as adenine nucleotide translocase, could only sustain the low ion-conductance that is  $Ca^{2+}$ -dependent and bongkreic acid sensitive [16,66]. Even if the existence of mPTP is still elusive in mussels, the detection of the  $Ca^{2+}$ -activated  $F_1F_0$ -ATPase (hydrolyase), which was shown to most likely coincide with the mPTP [14,41], strongly suggests that mussel midgut gland mitochondria possess mPTP activity whose responsiveness to sulfide was tested. Accordingly, in mussel midgut gland

mitochondria the CRC decreases at increasing  $Ca^{2+}$  concentrations (Fig. 4). The NaHS treatment desensitizes the mPTP activity, even if it is ineffective on the  $Ca^{2+}$ -activated  $F_1F_0$ -ATPase (Fig. 3). Experiments carried out by adding to mitochondria the mitochondrial calcium uniporter inhibitor Ruthenium Red result in similar CRC profiles in response to subsequent 10  $\mu$ M  $CaCl_2$  pulses in the presence of 50 and 100  $\mu$ M NaHS and of 1  $\mu$ M Ruthenium Red. Regulatory role of CL can extend to adenine nucleotide translocase which constitute regulatory component of mPTP [16]. So, the  $Ca^{2+}$  uptake by mitochondria is clearly affected by NaHS (Fig. 4) and, as a consequence the mPTP, is desensitized, namely it requires higher  $Ca^{2+}$  load to open and release the cation.

#### 4. Conclusions

Some main observations can be drawn from the results of the present study. First, mussel midgut gland mitochondria contain an oligomycin-sensitive  $F_1F_0$ -ATPase activity that can be activated either by  $Mg^{2+}$  or by  $Ca^{2+}$ , as in mammals. Both  $F_1F_0$ -ATPase activity are coupled, as revealed by the extent of oligomycin sensitivity. However, some differences exist between molluscan and mammalian  $F_1F_0$ -ATPases revealed by the sulfide responsiveness. Second, mussel mitochondria are able to form the mPTP. However, the connection between the  $Ca^{2+}$ -dependent  $F_1F_0$ -ATPase and the mPTP is weakened in these invertebrates, since NaHS, at least under the experimental conditions adopted, has no effect on the enzyme activity even if it inhibits the mPTP. Moreover, if, on the one hand, the “mussel model” to deepen studies on mitochondria is strengthened, due to some kinetic similarities with mammals and the easy-to-use biological material, on the other hand the hypothesis that the mPTP regulation, and perhaps the same mPTP role, may be different in different taxa, is somehow shouldered. The mPTP responsiveness to sulfide in the mussel opens a new scenario to be investigated. Among the still unsolved questions, it remains unclear if sulfide can interact with other proteins involved in  $Ca^{2+}$  homeostasis and if the  $F_1F_0$ -ATPase refractoriness can physiologically play a protective role in sulfide-rich environments. Accordingly, some sulfide-driven post-translational modifications of proteins are irreversible and can produce permanent damage to the biostructures. In this perspective the chemical un-reactivity of the bioenergetic mechanisms can be even advantageous for mussels.

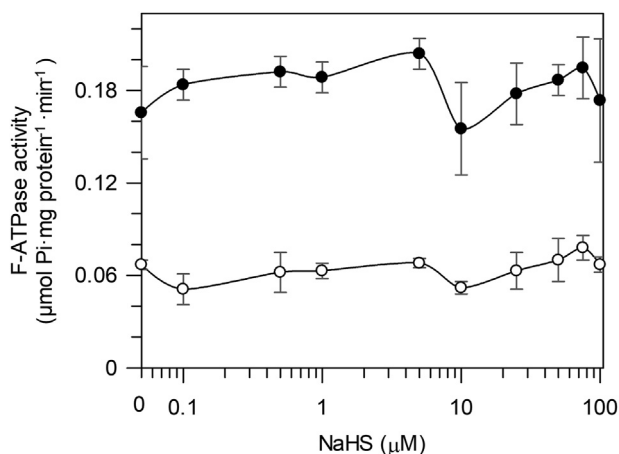


**Fig. 3.** *In vitro* response of the mitochondrial  $Mg^{2+}$ - and  $Ca^{2+}$ -dependent  $F_1F_0$ -ATPase activities to NaHS. The  $F_1F_0$ -ATPase activities of the mitochondrial  $Mg^{2+}$ -ATPase (●) and  $Ca^{2+}$ -ATPase (○) are plotted against NaHS concentrations (logarithmic scale). Each point represents the mean  $\pm$  SD from three experiments on distinct mitochondrial preparations.

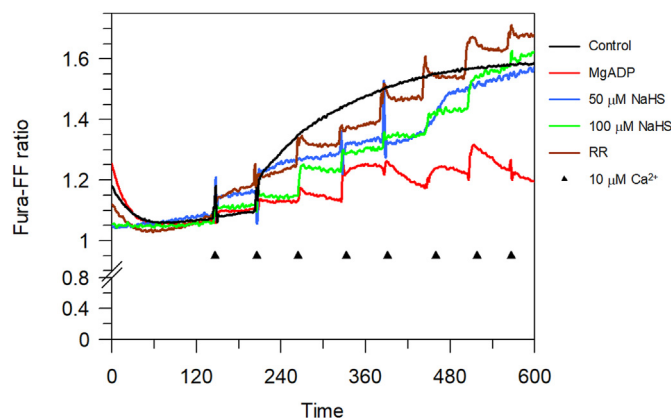


**Fig. 4.** Evaluation of mPTP opening. Representative curves of the calcium retention capacity (CRC) in mitochondrial preparations. CRC was monitored in response to subsequent 10  $\mu$ M  $CaCl_2$  pulses (shown by the arrows), as detailed in the Materials and Methods section, in the absence (control) and presence of 50 or 100  $\mu$ M NaHS, and in the presence of the mPTP inhibitors 2 mM MgADP or 1  $\mu$ M Ruthenium Red (RR). The experiments were carried out in triplicate on three distinct mitochondrial preparations.

## Funding

This work was financed by the University of Bologna, Italy (Almaidea senior grant to AP).

## Author contributions

CA, SN and MF carried out the experiments; SN planned the experimental design and supervised the experiments, SN and AP wrote the manuscript; AP VV and FT revised the text; AP funding acquisition; all authors read and approved the final text.

## Declaration of interest

None.

## References

- [1] R. Wang, Physiological implications of hydrogen sulfide: a whiff exploration that blossomed, *Physiol. Rev.* 92 (2012) 791–896, <https://doi.org/10.1152/physrev.00017.2011>.
- [2] D.-D. Wu, D.-Y. Wang, H.-M. Li, J.-C. Guo, S.-F. Duan, X.-Y. Ji, Hydrogen sulfide as a novel regulatory factor in liver health and disease, *Oxid Med Cell Longev* (2019) 3831713, <https://doi.org/10.1155/2019/3831713>, 2019.
- [3] D.W. Kraus, J.E. Doeller, Sulfide consumption by mussel gill mitochondria is not strictly tied to oxygen reduction: measurements using a novel polarographic sulfide sensor, *J. Exp. Biol.* 207 (2004) 3667–3679, <https://doi.org/10.1242/jeb.01212>.
- [4] J. Beltowski, Synthesis, metabolism, and signaling mechanisms of hydrogen sulfide: an overview, *Methods Mol. Biol.* (2007) 1–8, [https://doi.org/10.1007/978-1-4939-9528-8\\_1](https://doi.org/10.1007/978-1-4939-9528-8_1), 2019.
- [5] T. Bagarinao, Sulfide as an environmental factor and toxicant: tolerance and adaptations in aquatic organisms, *Aquat. Toxicol.* 24 (1992) 21–62, [https://doi.org/10.1016/0166-445X\(92\)90015-F](https://doi.org/10.1016/0166-445X(92)90015-F).
- [6] G.K. Kolluru, X. Shen, S.C. Bir, C.G. Kevil, Hydrogen sulfide chemical biology: pathophysiological roles and detection, *Nitric Oxide* 35 (2013) 5–20, <https://doi.org/10.1016/j.niox.2013.07.002>.
- [7] R. Wedmann, S. Bertlein, I. Macinkovic, S. Böltz, J.L. Miljkovic, L.E. Muñoz, M. Herrmann, M.R. Filipovic, Working with “H<sub>2</sub>S”: facts and apparent artifacts, *Nitric Oxide* 41 (2014) 85–96, <https://doi.org/10.1016/j.niox.2014.06.003>.
- [8] S.L. Malone Rubright, L.L. Pearce, J. Peterson, Environmental toxicology of hydrogen sulfide, *Nitric Oxide* 71 (2017) 1–13, <https://doi.org/10.1016/j.niox.2017.09.011>.
- [9] B. Murphy, R. Bhattacharya, P. Mukherjee, Hydrogen sulfide signaling in mitochondria and disease, *Faseb. J.* 33 (2019) 13098–13125, <https://doi.org/10.1096/fj.201901304R>.
- [10] T.V. Mishanina, M. Libiad, R. Banerjee, Biogenesis of reactive sulfur species for signaling by hydrogen sulfide oxidation pathways, *Nat. Chem. Biol.* 11 (2015) 457–464, <https://doi.org/10.1038/nchembio.1834>.
- [11] E. Cuevasanta, M.N. Möller, B. Alvarez, Biological chemistry of hydrogen sulfide and persulfides, *Arch. Biochem. Biophys.* 617 (2017) 9–25, <https://doi.org/10.1016/j.abb.2016.09.018>.
- [12] S. Nesci, Mitochondrial permeability transition, F<sub>1</sub>F<sub>0</sub>-ATPase and calcium: an enigmatic triangle, *EMBO Rep.* 18 (2017) 1265–1267, <https://doi.org/10.15252/embr.201744570>.
- [13] S. Nesci, F. Trombetti, V. Ventrella, M. Pirini, A. Pagliarani, Kinetic properties of the mitochondrial F<sub>1</sub>F<sub>0</sub>-ATPase activity elicited by Ca(2+) in replacement of Mg(2+), *Biochimie* 140 (2017) 73–81, <https://doi.org/10.1016/j.biochi.2017.06.013>.
- [14] C. Algieri, F. Trombetti, A. Pagliarani, V. Ventrella, C. Bernardini, M. Fabbri, M. Forni, S. Nesci, Mitochondrial Ca<sup>2+</sup>-activated F<sub>1</sub>F<sub>0</sub>-ATPase hydrolyzes ATP and promotes the permeability transition pore, *Ann. N. Y. Acad. Sci.* 1457 (2019) 142–157, <https://doi.org/10.1111/nyas.14218>.
- [15] A. Urbani, V. Giorgio, A. Carrer, C. Franchin, G. Arrigoni, C. Jiko, K. Abe, S. Maeda, K. Shinzawa-Ittoh, J.F.M. Bogers, D.G.G. McMillan, C. Gerle, I. Szabó, P. Bernardi, Purified F-ATP synthase forms a Ca<sup>2+</sup>-dependent high-conductance channel matching the mitochondrial permeability transition pore, *Nat. Commun.* 10 (2019) 4341, <https://doi.org/10.1038/s41467-019-12331-1>.
- [16] N. Mnatsakanyan, M.C. Llaguno, Y. Yang, Y. Yan, J. Weber, F.J. Sigworth, E.A. Jonas, A mitochondrial megachannel resides in monomeric F<sub>1</sub>F<sub>0</sub> ATP synthase, *Nat. Commun.* 10 (2019) 5823, <https://doi.org/10.1038/s41467-019-13766-2>.
- [17] C. Konrad, G. Kiss, B. Töröcsik, J.L. Lábár, A.A. Gerencser, M. Mándi, V. Adam-Vizi, C. Chinopoulos, A distinct sequence in the adenine nucleotide translocase from *Artemia franciscana* embryos is associated with insensitivity to bongkrekate and atypical effects of adenine nucleotides on Ca<sup>2+</sup> uptake and sequestration, *FEBS J.* 278 (2011) 822–836, <https://doi.org/10.1111/j.1742-4658.2010.08001.x>.
- [18] C. Chinopoulos, Mitochondrial permeability transition pore: back to the drawing board, *Neurochem. Int.* 117 (2018) 49–54, <https://doi.org/10.1016/j.neuint.2017.06.010>.
- [19] E. Torrezan-Nitao, R.C.B.Q. Figueiredo, L.F. Marques-Santos, Mitochondrial permeability transition pore in sea urchin female gametes, *Mech. Dev.* 154 (2018) 208–218, <https://doi.org/10.1016/j.mod.2018.07.008>.
- [20] C.M. Hickey, J.E. Geiger, C.J. Groten, N.S. Magoski, Mitochondrial Ca<sup>2+</sup> activates a cation current in *Aplysia* bag cell neurons, *J. Neurophysiol.* 103 (2010) 1543–1556, <https://doi.org/10.1152/jn.01121.2009>.
- [21] C. Konrad, G. Kiss, B. Töröcsik, V. Adam-Vizi, C. Chinopoulos, Absence of Ca<sup>2+</sup>-induced mitochondrial permeability transition but presence of bongkrekate-sensitive nucleotide exchange in *C. crangon* and *P. serratus*, *PLoS One* 7 (2012), e39839, <https://doi.org/10.1371/journal.pone.0039839>.
- [22] P. Bernardi, A. Rasola, M. Forte, G. Lippe, The mitochondrial permeability transition pore: channel formation by F-ATP synthase, integration in signal transduction, and role in pathophysiology, *Physiol. Rev.* 95 (2015) 1111–1155, <https://doi.org/10.1152/physrev.00001.2015>.
- [23] S. Nesci, V. Ventrella, F. Trombetti, M. Pirini, A. Pagliarani, Mussel and mammalian ATP synthase share the same bioenergetic cost of ATP, *J. Bioenerg. Biomembr.* 45 (2013) 289–300, <https://doi.org/10.1007/s10863-013-9504-1>.
- [24] P.S. Wilson, K. Vopel, Assessing the sulfide footprint of mussel farms with sediment profile imagery: a New Zealand trial, *PLoS One* 10 (2015), e0129894, <https://doi.org/10.1371/journal.pone.0129894>.
- [25] C. Walker, S.A. Böttger, J. Mulkern, E. Jerszyk, M. Litvaitis, M. Lesser, Mass culture and characterization of tumor cells from a naturally occurring invertebrate cancer model: applications for human and animal disease and environmental health, *Biol. Bull.* 216 (2009) 23–39, <https://doi.org/10.1086/BBLv216n1p23>.
- [26] X. Sun, Z. Liu, B. Wu, L. Zhou, Q. Wang, W. Wu, A. Yang, Differences between fast and slow muscles in scallops revealed through proteomics and transcriptomics, *BMC Genom.* 19 (2018) 377, <https://doi.org/10.1186/s12864-018-4770-2>.
- [27] S. Kapoor, N. Nailwal, M. Kumar, K. Barve, Recent patents and discovery of anti-inflammatory agents from marine source, recent pat inflamm allergy, *Drug Discov* 13 (2019) 105–114, <https://doi.org/10.2174/1872213X13666190426164717>.
- [28] D. Munro, P.U. Blier, The extreme longevity of Arctic islandica is associated with increased peroxidation resistance in mitochondrial membranes, *Aging Cell* 11 (2012) 845–855, <https://doi.org/10.1111/j.1474-9726.2012.00847.x>.
- [29] N.E. Moyer, G.N. Somero, M.W. Denny, Impact of heating rate on cardiac thermal tolerance in the California mussel, *Mytilus californianus*, *J. Exp. Biol.* 222 (2019), <https://doi.org/10.1016/j.jeb.203166>.
- [30] M.M. Bradford, A rapid and sensitive method for the quantitation of microgram quantities of protein utilizing the principle of protein-dye binding, *Anal. Biochem.* 72 (1976) 248–254.
- [31] A. Pagliarani, P. Bandiera, V. Ventrella, F. Trombetti, M. Pirini, S. Nesci, A.R. Borgatti, Tributyltin (TBT) inhibition of oligomycin-sensitive Mg-ATPase activity in mussel mitochondria, *Toxicol. Vitro* 22 (2008) 827–836, <https://doi.org/10.1016/j.tiv.2007.12.015>.
- [32] B. Chance, G.R. Williams, The respiratory chain and oxidative phosphorylation, *Adv. Enzymol. Relat. Subj. Biochem.* 17 (1956) 65–134, <https://doi.org/10.1002/9780470122624.ch2>.
- [33] S. Nesci, V. Ventrella, F. Trombetti, M. Pirini, A. Pagliarani, Tri-n-butyltin binding to a low-affinity site decreases the F<sub>1</sub>F<sub>0</sub>-ATPase sensitivity to oligomycin in mussel mitochondria, *Appl. Organomet. Chem.* 26 (2012) 593–599, <https://doi.org/10.1002/aoc.2904>.
- [34] A. Pagliarani, P. Bandiera, V. Ventrella, F. Trombetti, M.P. Manuzzi, M. Pirini, A.R. Borgatti, Response of Na(+)-dependent ATPase activities to the contaminant ammonia nitrogen in *Tapes philippinarum*: possible atpase involvement in ammonium transport, *Arch. Environ. Contam. Toxicol.* 55 (2008) 49–56, <https://doi.org/10.1007/s00244-007-9102-5>.
- [35] V. Ventrella, S. Nesci, F. Trombetti, P. Bandiera, M. Pirini, A.R. Borgatti, A. Pagliarani, Tributyltin inhibits the oligomycin-sensitive Mg-ATPase activity in *Mytilus galloprovincialis* digestive gland mitochondria, *Comp. Biochem. Physiol. C Toxicol. Pharmacol.* 153 (2011) 75–81, <https://doi.org/10.1016/j.cbpc.2010.08.007>.
- [36] S. Nesci, F. Trombetti, M. Pirini, V. Ventrella, A. Pagliarani, Mercury and protein thiols: stimulation of mitochondrial F<sub>1</sub>F<sub>0</sub>-ATPase and inhibition of respiration, *Chem. Biol. Interact.* 260 (2016) 42–49, <https://doi.org/10.1016/j.cbi.2016.10.018>.
- [37] S. Nesci, V. Ventrella, F. Trombetti, M. Pirini, A. Pagliarani, Multi-site TBT binding skews the inhibition of oligomycin on the mitochondrial Mg-ATPase in *Mytilus galloprovincialis*, *Biochimie* 93 (2011) 1157–1164, <https://doi.org/10.1016/j.biochi.2011.04.008>.
- [38] S. Raheem, A. Steiner, Z. Ahmad, Functional importance of αAsp-350 in the catalytic sites of *Escherichia coli* ATP synthase, *Arch. Biochem. Biophys.* 672 (2019) 108050, <https://doi.org/10.1016/j.abb.2019.07.015>.
- [39] I.H. Segel, Enzyme kinetics, in: W.J. Lennarz, M.D. Lane (Eds.), *Encyclopedia of Biological Chemistry*, Academic Press, Waltham, 2013, pp. 216–220, <https://doi.org/10.1016/B978-0-12-378630-2.00012-8>.
- [40] C. Algieri, F. Trombetti, A. Pagliarani, V. Ventrella, S. Nesci, Phenylglyoxal inhibition of the mitochondrial F<sub>1</sub>F<sub>0</sub>-ATPase activated by Mg<sup>2+</sup> or by Ca<sup>2+</sup> provides clues on the mitochondrial permeability transition pore, *Arch. Biochem. Biophys.* 681 (2020) 108258, <https://doi.org/10.1016/j.abb.2020.108258>.
- [41] Vincenzo Algieri, Cristina Algieri, Loredana Maiuolo, Antonio De Nino,

- Alessandra Pagliarani, A. Matteo, Tallarida, Fabiana Trombetti, Salvatore Nesci, 1,5-Disubstituted-1,2,3-triazoles as inhibitors of the mitochondrial Ca<sup>2+</sup>-activated F1FO-ATP(hydroly)ase and of the permeability transition pore, *Ann. N. Y. Acad. Sci.* (2020), <https://doi.org/10.1111/nyas.14474>.
- [42] S. Nesci, A. Pagliarani, C. Algieri, F. Trombetti, Mitochondrial F-type ATP synthase: multiple enzyme functions revealed by the membrane-embedded FO structure, *Crit. Rev. Biochem. Mol. Biol.* 55 (2020) 309–321, <https://doi.org/10.1080/10409238.2020.1784084>.
- [43] S. Papageorgiou, A.B. Melandri, G. Solaini, Relevance of divalent cations to ATP-driven proton pumping in beef heart mitochondrial FOF1-ATPase, *J. Bioenerg. Biomembr.* 30 (1998) 533–541.
- [44] Z. Gromet-Elhanan, S. Weiss, Regulation of  $\Delta$ DELTA- $\mu$ H + -coupled ATP synthesis and hydrolysis: role of divalent cations and of the FOF1- $\beta$  subunit, *Biochemistry* 28 (1989) 3645–3650, <https://doi.org/10.1021/bi00435a004>.
- [45] L. Nathanson, Z. Gromet-Elhanan, Mutations in the  $\beta$ -subunit Thr159 and Glu184 of the Rhodospirillum rubrum FOF1 ATP synthase reveal differences in ligands for the coupled Mg<sup>2+</sup>- and decoupled Ca<sup>2+</sup>-dependent FOF1 activities, *J. Biol. Chem.* 275 (2000) 901–905, <https://doi.org/10.1074/jbc.275.2.901>.
- [46] U. Pick, M. Weiss, A light-dependent dicyclohexylcarbodiimide-sensitive Ca-ATPase activity in chloroplasts which is not coupled to proton translocation, *Eur. J. Biochem.* 173 (1988) 623–628.
- [47] V. De Col, E. Petrusa, V. Casolo, E. Braidot, G. Lippe, A. Filippi, C. Peresson, S. Patui, A. Bertolini, V. Giorgio, V. Checchetto, A. Vianello, P. Bernardi, M. Zancani, Properties of the permeability transition of pea stem mitochondria, *Front. Physiol.* 9 (2018) 1626, <https://doi.org/10.3389/fphys.2018.01626>.
- [48] D.S. Perlin, L.R. Latchney, J.G. Wise, A.E. Senior, Specificity of the proton adenosinetriphosphatase of *Escherichia coli* for adenine, guanine, and inosine nucleotides in catalysis and binding, *Biochemistry* 23 (1984) 4998–5003.
- [49] D.G. Nicholls, S.J. Ferguson, 7 - ATP synthases and bacterial flagella rotary motors. *Bioenergetics*, fourth ed., Academic Press, Boston, 2013, pp. 197–220, <https://doi.org/10.1016/B978-0-12-388425-1.00007-5>.
- [50] P.D. Boyer, Catalytic site occupancy during ATP synthase catalysis, *FEBS Lett.* 512 (2002) 29–32, [https://doi.org/10.1016/S0014-5793\(02\)02293-7](https://doi.org/10.1016/S0014-5793(02)02293-7).
- [51] Y.M. Milgrom, R.L. Cross, Rapid hydrolysis of ATP by mitochondrial F1-ATPase correlates with the filling of the second of three catalytic sites, *Proc. Natl. Acad. Sci. U.S.A.* 102 (2005) 13831–13836, <https://doi.org/10.1073/pnas.0507139102>.
- [52] L. Li, P. Rose, P.K. Moore, Hydrogen sulfide and cell signaling, *Annu. Rev. Pharmacol. Toxicol.* 51 (2011) 169–187, <https://doi.org/10.1146/annurev-pharmtox-010510-100505>.
- [53] L. Li, P.K. Moore, Putative biological roles of hydrogen sulfide in health and disease: a breath of not so fresh air? *Trends Pharmacol. Sci.* 29 (2008) 84–90, <https://doi.org/10.1016/j.tips.2007.11.003>.
- [54] A.K. Mustafa, M.M. Gadalla, N. Sen, S. Kim, W. Mu, S.K. Gazi, R.K. Barrow, G. Yang, R. Wang, S.H. Snyder, HS signals through protein S-Sulfhydration, *Sci. Signal.* 2 (2009), <https://doi.org/10.1126/scisignal.2000464>.
- [55] H. Itoh, A. Takahashi, K. Adachi, H. Noji, R. Yasuda, M. Yoshida, K. Kinoshita, Mechanically driven ATP synthesis by F1-ATPase, *Nature* 427 (2004) 465–468, <https://doi.org/10.1038/nature02212>.
- [56] K. Módos, Y. Ju, A. Ahmad, A.A. Untereiner, Z. Altaany, L. Wu, C. Szabo, R. Wang, S-Sulfhydration of ATP synthase by hydrogen sulfide stimulates mitochondrial bioenergetics, *Pharmacol. Res.* 113 (2016) 116–124, <https://doi.org/10.1016/j.phrs.2016.08.023>.
- [57] S.-B. Wang, C.I. Murray, H.S. Chung, J.E. Van Eyk, Redox regulation of mitochondrial ATP synthase, *Trends Cardiovasc. Med.* 23 (2013) 14–18, <https://doi.org/10.1016/j.tcm.2012.08.005>.
- [58] S. Nesci, F. Trombetti, V. Ventrella, A. Pagliarani, Post-translational modifications of the mitochondrial F1FO-ATPase, *Biochim. Biophys. Acta* 1861 (2017) 2902–2912, <https://doi.org/10.1016/j.bbagen.2017.08.007>.
- [59] A. Pagliarani, S. Nesci, F. Trombetti, V. Ventrella, Thiol-related regulation of the mitochondrial F1FO-ATPase activity, in: S. Chakraborti, N.S. Dhalla (Eds.), *Regulation of Ca<sup>2+</sup>-ATPases, V-ATPases and F-ATPases*, Springer International Publishing, 2016, pp. 441–458, [https://doi.org/10.1007/978-3-319-24780-9\\_21](https://doi.org/10.1007/978-3-319-24780-9_21).
- [60] A.S. Papu John, S. Kundu, S. Pushpakumar, M. Amin, S.C. Tyagi, U. Sen, Hydrogen sulfide inhibits Ca<sup>2+</sup>-induced mitochondrial permeability transition pore opening in type-1 diabetes, *Am. J. Physiol. Endocrinol. Metab.* 317 (2019) E269–E283, <https://doi.org/10.1152/ajpendo.00251.2018>.
- [61] É.G.A. Miranda, J.C. Araujo-Chaves, C. Kawai, A.M.M. Brito, I.W.R. Dias, J.T. Arantes, I.L. Nantes-Cardoso, Cardiolipin structure and oxidation are affected by Ca<sup>2+</sup> at the interface of lipid bilayers, *Front. Chem.* 7 (2020), <https://doi.org/10.3389/fchem.2019.00930>.
- [62] R. Fiorini, A. Pagliarani, S. Nesci, M. Pirini, E. Tucci, V. Ventrella, Structural and functional changes in gill mitochondrial membranes from the Mediterranean mussel *Mytilus galloprovincialis* exposed to tri-n-butyltin, *Environ. Toxicol. Chem.* 31 (2012) 877–884, <https://doi.org/10.1002/etc.1764>.
- [63] K.N. Alavian, G. Beutner, E. Lazrove, S. Sacchetti, H.-A. Park, P. Licznarski, H. Li, P. Nabili, K. Hockensmith, M. Graham, G.A. Porter, E.A. Jonas, An uncoupling channel within the c-subunit ring of the F1FO ATP synthase is the mitochondrial permeability transition pore, *Proc. Natl. Acad. Sci. U.S.A.* 111 (2014) 10580–10585, <https://doi.org/10.1073/pnas.1401591111>.
- [64] V. Giorgio, S. von Stockum, M. Antoniel, A. Fabbro, F. Fogolari, M. Forte, G.D. Glick, V. Petronilli, M. Zoratti, I. Szabó, G. Lippe, P. Bernardi, Dimers of mitochondrial ATP synthase form the permeability transition pore, *Proc. Natl. Acad. Sci. U.S.A.* 110 (2013) 5887–5892, <https://doi.org/10.1073/pnas.1217823110>.
- [65] M. Bonora, A. Bononi, E. De Marchi, C. Giorgi, M. Lebedzinska, S. Marchi, S. Patergnani, A. Rimessi, J.M. Suski, A. Wojtala, M.R. Wieckowski, G. Kroemer, L. Galluzzi, P. Pinton, Role of the c subunit of the FO ATP synthase in mitochondrial permeability transition, *Cell Cycle* 12 (2013) 674–683, <https://doi.org/10.4161/cc.23599>.
- [66] J. Karch, M.J. Bround, H. Khalil, M.A. Sargent, N. Latchman, N. Terada, P.M. Peixoto, J.D. Molkenin, Inhibition of mitochondrial permeability transition by deletion of the ANT family and CypD, *Sci Adv* 5 (2019) eaaw4597, <https://doi.org/10.1126/sciadv.aaw4597>.

## Original Article

# 1,5-Disubstituted-1,2,3-triazoles as inhibitors of the mitochondrial $\text{Ca}^{2+}$ -activated $\text{F}_1\text{F}_0$ -ATP(hydrol)ase and the permeability transition pore

Vincenzo Algieri,<sup>1,a</sup>  Cristina Algieri,<sup>2,a</sup>  Loredana Maiuolo,<sup>1</sup> Antonio De Nino,<sup>1</sup> Alessandra Pagliarani,<sup>2</sup>  Matteo Antonio Tallarida,<sup>1</sup>  Fabiana Trombetti,<sup>2</sup>  and Salvatore Nesci<sup>2</sup> 

<sup>1</sup>Department of Chemistry and Chemical Technologies, University of Calabria, Cosenza, Italy. <sup>2</sup>Department of Veterinary Medical Sciences, University of Bologna, Ozzano Emilia, Italy

Addresses for correspondence: Loredana Maiuolo and Antonio De Nino, Department of Chemistry and Chemical Technologies, University of Calabria, Cosenza, 87036, Italy. [loredana.maiuolo@unical.it](mailto:loredana.maiuolo@unical.it) and [antonio.denino@unical.it](mailto:antonio.denino@unical.it); and Salvatore Nesci, Department of Veterinary Medical Sciences, University of Bologna, Ozzano Emilia, 40064, Italy. [salvatore.nesci@unibo.it](mailto:salvatore.nesci@unibo.it)

The mitochondrial permeability transition pore (mPTP), a high-conductance channel triggered by a sudden  $\text{Ca}^{2+}$  concentration increase, is composed of the  $\text{F}_1\text{F}_0$ -ATPase. Since mPTP opening leads to mitochondrial dysfunction, which is a feature of many diseases, a great pharmacological challenge is to find mPTP modulators. In our study, the effects of two 1,5-disubstituted 1,2,3-triazole derivatives, five-membered heterocycles with three nitrogen atoms in the ring and capable of forming secondary interactions with proteins, were investigated. Compounds 3a and 3b were selected among a wide range of structurally related compounds because of their chemical properties and effectiveness in preliminary studies. In swine heart mitochondria, both compounds inhibit  $\text{Ca}^{2+}$ -activated  $\text{F}_1\text{F}_0$ -ATPase without affecting F-ATPase activity sustained by the natural cofactor  $\text{Mg}^{2+}$ . The inhibition is mutually exclusive, probably because of their shared enzyme site, and uncompetitive with respect to the ATP substrate, since they only bind to the enzyme-ATP complex. Both compounds show the same inhibition constant ( $K_i$ ), but compound 3a has a doubled inactivation rate constant compared with compound 3b. Moreover, both compounds desensitize mPTP opening without altering mitochondrial respiration. The results strengthen the link between  $\text{Ca}^{2+}$ -activated  $\text{F}_1\text{F}_0$ -ATPase and mPTP and suggest that these inhibitors can be pharmacologically exploited to counteract mPTP-related diseases.

**Keywords:** triazole derivatives; mitochondria;  $\text{F}_1\text{F}_0$ -ATPase; permeability transition pore; calcium

## Introduction

The mitochondrial permeability transition pore (mPTP) is a channel of the inner mitochondrial membrane (IMM), whose persistent formation induces abnormalities in mitochondrial bioenergetics (membrane depolarization, ion homeostasis loss, and cessation of oxidative phosphorylation).<sup>1</sup>

Lastly, mitochondrial swelling and rupture of the outer mitochondrial membrane cause different forms of cellular death.<sup>2</sup> Since mPTP is increasingly involved in a variety of pathologies associated with mitochondrial dysfunctions, the molecular bioarchitecture that participates in mPTP formation represents a potential drug target to treat diseases featuring  $\text{Ca}^{2+}$  increase and cell death, including ischemia-reperfusion injury, childhood neuromuscular diseases, and age-related neurodegenerative

<sup>a</sup>These authors contributed equally to this work.

diseases.<sup>3</sup> mPTP has been suggested to stem from the  $F_1F_0$ -ATPase(s), even if it is still controversial if the monomeric or the dimeric  $F_1F_0$ -ATPase form opens the pore.<sup>4,5</sup> The  $F_1F_0$ -ATPase is a bipowered enzymatic engine that by means of the membrane-embedded  $F_0$  domain uses the electrochemical gradient of  $H^+$  obtained by mitochondrial respiration to synthesize ATP from ADP and  $P_i$  on the hydrophilic  $F_1$  domain.<sup>6</sup> The  $F_1F_0$ -ATPase can also work in reverse as  $H^+$  pump and exploit the phosphoanhydride bond energy released by ATP hydrolysis to polarize the IMM.<sup>7</sup> The torque generation of the  $F_1F_0$ -ATPase rotor couples ATP synthesis/hydrolysis in the  $F_1$  domain to  $H^+$  translocation in the  $F_0$  domain.<sup>8</sup> However, this bifunctional activity, unique in nature, is only sustained by the natural cofactor  $Mg^{2+}$ ,<sup>9</sup> while the substitution of  $Mg^{2+}$  by  $Ca^{2+}$  only allows oligomycin-sensitive ATP hydrolysis, namely, the coupling between  $F_1$  and  $F_0$ .<sup>10</sup> The abrupt increase in matrix  $Ca^{2+}$  concentration associated with oxidative stress under physio-pathological conditions activates the  $F_1F_0$ -ATPase catalytic site, hydrolyzes CaATP, and triggers mPTP formation.<sup>11,12</sup> These features make the  $Ca^{2+}$ -activated  $F_1F_0$ -ATPase an intriguing therapeutic target.<sup>13</sup> Any compound that inhibits mPTP can address drug design and also provide new insights into mPTP structure. Nowadays, the only accepted positive regulator of mPTP opening is cyclophilin D (CyPD), a *cis-trans* peptidyl-prolyl isomerase in the mitochondrial matrix.<sup>14</sup> Cyclosporine A (CsA) and analogs that bind CyPD are CyPD-dependent mPTP inhibitors,<sup>3</sup> which act by inhibiting CyPD and consequently mPTP. However, in CyPD gene knockout cells, the CsA-mediated mPTP inhibition is abolished, and the  $Ca^{2+}$  threshold required for mPTP opening is greatly increased.<sup>14</sup> Thus, the CsA effect is limited by its target availability, which determines its efficacy. The failed clinical success of CsA and derivatives is also due to their physicochemical properties, that is, poor water solubility and high molecular weight, which is associated with cytotoxicity, undesirable biological targets, and poor blood-brain barrier permeability.<sup>3,13</sup>

The 1,2,3-triazoles are a class of five-membered N-heterocycles with intriguing biological activities, including antibacterial, anticancer, and antiviral efficacy.<sup>15</sup> Their chemical structure with three vicinal nitrogen atoms in the ring and their aromatic

nature make this class of compounds resistant to many reactions, such as to oxidation, reduction, and acid or basic hydrolysis.<sup>16</sup> Moreover, triazoles have the same capability of forming hydrogen bonds as well as dipole-dipole and  $\pi$ -stacking interactions with various biological targets. These interactions can become even more relevant when several substituents are present on the backbone of these molecules.<sup>17</sup> For the synthesis of substituted 1,2,3-triazoles, the classical 1,3-dipolar cycloaddition of Huisgen between terminal alkynes and azides provides a mixture of 1,4- and 1,5-disubstituted triazoles.<sup>18</sup> This reaction was improved by the introduction of copper or ruthenium salts as catalysts, producing the 1,4- or 1,5-regioisomer, respectively.<sup>19,20</sup> More recently, new synthetic procedures were realized by eliminative azide-olefin 1,3-dipolar cycloaddition (EAO) between substituted azides as the dipole and electron-deficient alkenes as the dipolarophile, bypassing the problems that result from the use of only terminal alkynes.<sup>21,22</sup> In particular, nitroolefins received a good deal of attention for their ability to furnish triazoline intermediates in high yields that readily decompose to triazoles,<sup>23,24</sup> while enamines are a very good starting material to synthesize 1,4,5-trisubstituted triazoles, improving the properties deriving from multiple substituents on a triazole ring.<sup>25</sup>

Recently, triazole derivatives obtained by replacing the isoxazole core in analog compound have been considered as second-generation inhibitors of mPTP. Accordingly, this chemical modification was proven to improve plasma stability.<sup>26</sup> Indeed, drugs with a short half-life ( $t_{1/2}$ ) in plasma risk being degraded prior to being able to exert any biological effect. Thus, small molecules such as substituted 1,2,3-triazoles represent interesting compounds to evaluate the structure-activity relationship of  $F_1F_0$ -ATPase activity, the major playmaker of mPTP formation, and to clarify their effect on mPTP via the CyPD-independent mechanism. Among a wide variety of structurally related compounds, compounds **3a** and **3b** were selected for their chemical properties, which make them prone to interact with proteins and produce biological effects, and for their promising effectiveness on the  $F_1F_0$ -ATPase activity shown in our preliminary studies. The aim is to establish if these compounds, by interacting with the  $F_1F_0$ -ATPase complex, can block

mPTP formation and preserve the Mg<sup>2+</sup>-activated F<sub>1</sub>F<sub>0</sub>-ATPase functionality, namely, the ATP generating capability, without causing mitochondrial toxicity.

## Materials and methods

### Chemicals and reagents

Fura-FF and oligomycin were purchased from Vinci-Biochem (Vinci, Italy). Na<sub>2</sub>ATP was obtained from Sigma–Aldrich (Milan, Italy). All other chemicals were reagent grade and used without purification. Quartz double-distilled water was used for all reagent solutions, except when differently stated. Reactions were monitored by TLC using silica plates 60-F264 commercially available from Merck. <sup>1</sup>H and <sup>13</sup>C NMR spectra were recorded at 300 and 75 MHz, respectively, in CDCl<sub>3</sub> using tetramethylsilane as the internal standard (Bruker (Billerica, MA) ACP 300 MHz). Chemical shifts are given in parts per million and coupling constants in Hertz. LC-MS analyses were carried using an Agilent 6540 UHD Accurate—Mass Q-TOFLC-MS fitted with an electrospray ionization source (DualA)SESI) operating in positive ion mode. Chromatographic separation was achieved using a C18 RP analytical column (Poroshell 120, SB-C18, 50 × 2.1 mm, 2.7 mm) at 30 °C with an elution gradient from 5% to 95% of B over 13 min, A being H<sub>2</sub>O (0.1%FA) and B CH<sub>3</sub>CN (0.1% FA). Flow rate was 0.4 mL/min.

### Synthesis of 1-methyl pyridinium trifluoromethanesulfonate

1-Methyl pyridinium trifluoromethanesulfonate ([mpy]OTf) was prepared by halide-free direct synthesis as reported in the literature.<sup>27–29</sup>

### General procedure for the synthesis of 1,5-disubstituted-1,2,3-triazoles

In a two-necked round bottom flask, equipped with bubble condenser and magnetic stir bar, [mpy]OTf (5 mL), FeCl<sub>3</sub> (20 mol %), (*E*)-nitrostyrene derivative (**1a–1b**) (1 eq) and benzyl azide **2** (2 eq) were placed. The reaction was conducted at 100 °C. The crude was extracted with dichloromethane (3 × 5 mL) and the combined organic layer was evaporated under vacuum. The crude product was purified on a flash silica gel column by using hexane/ethyl acetate (9:1 v/v) to obtain the desired product. Complete characterization of products **3a** and **3b** is reported in the Supplementary Materials (online only).

**1-Benzyl-5-phenyl-1,2,3-triazole (3a).** White solid (mp. 69.7–70.2 °C), *y* = 95%.

<sup>1</sup>H-NMR (CDCl<sub>3</sub>, 300 MHz):  $\delta$  (ppm) 5.55 (s, 2H, CH<sub>2</sub>), 7.03–7.13 (m, 2H, Ar), 7.22–7.32 (m, 5H, Ar), 7.37–7.46 (m, 3H, Ar), 7.75 (s, 1H, CH). <sup>13</sup>C-APT NMR (CDCl<sub>3</sub>, 75 MHz):  $\delta$  (ppm) 51.83, 126.95, 127.17, 128.16, 128.84, 128.91, 128.97, 129.52, 133.30, 135.53, 138.17. ESI(+)-MS: *m/z* [M + H] calcd for C<sub>15</sub>H<sub>14</sub>N<sub>3</sub> 236.1182, found: 236.0952

**1-Benzyl-5-(2-nitrophenyl)-1,2,3-triazole (3b).** Pale yellow solid (mp. 82.5–83.4 °C), *y* = 91%.

<sup>1</sup>H-NMR (CDCl<sub>3</sub>, 300 MHz):  $\delta$  (ppm) 5.42 (s, 2H, CH<sub>2</sub>), 6.90–6.97 (m, 2H, Ar), 7.00 (d, 1H, *J* = 7.67Hz, Ar), 7.14–7.29 (m, 3H, Ar), 7.55 (t, 1H, *J* = 7.50Hz, Ar), 7.60–7.64 (m, 1H, Ar), 7.66 (s, 1H, CH), 8.12 (d, 1H, *J* = 8.15Hz, Ar). <sup>13</sup>C-APT NMR (CDCl<sub>3</sub>, 75 MHz):  $\delta$  (ppm) 52.76, 122.14, 124.83, 127.68, 128.34, 128.64, 130.96, 132.99, 133.02, 133.17, 133.84, 134.30, 148.45. ESI(+)-MS: *m/z* [M + H] calcd for C<sub>15</sub>H<sub>13</sub>N<sub>4</sub>O<sub>2</sub> 281.1033, found: 281.1016.

### Preparation of the mitochondrial fractions

Immediately after slaughter, hearts from adult swine (*Sus scrofa domestica*) were collected at a local abattoir and transported to the laboratory within 2 h in ice buckets at 0–4 °C. After the removal of fat and blood clots as much as possible, approximately 30–40 g of heart tissue was rinsed in ice-cold washing Tris-HCl buffer (medium A) that consists of 0.25 M sucrose, 10 mM Tris(hydroxymethyl)-aminomethane (Tris), pH 7.4. The tissue was finely chopped into fine pieces with scissors, gently dried on blotting paper, and weighed. Each preparation was made from one heart. The chopped tissue was homogenized in a buffer (medium B) consisting of 0.25 M sucrose, 10 mM Tris (pH 7.4 with HCl), 1.0 mM EDTA (free acid), 0.5 mg/mL bovine serum albumin (BSA), at a ratio of 10 mL medium B per 1 g of fresh tissue. After a preliminary gentle breakup by Ultraturrax T25, the tissue was carefully homogenized by a motor-driven Teflon pestle homogenizer (Braun Melsungen Type 853202) at 650 rpm with three up-and-down strokes. To obtain the mitochondrial fraction by stepwise centrifugation (Sorvall RC2-B, rotor SS34), the homogenate was centrifuged at 1000 × *g* for 5 min, thus yielding a supernatant and a pellet. The latter was rehomogenized under the same conditions of the first homogenization and recentrifuged at

1000 × g for 5 minutes. The supernatants from these two centrifugations were gathered and filtered through four cotton gauze layers and then centrifuged at 10,500 × g for 10 min to yield the raw mitochondrial pellet that was resuspended in medium A and further centrifuged at 10,500 × g for 10 min to obtain the final mitochondrial pellet. The latter was resuspended by gentle stirring using a Teflon Potter Elvehjem homogenizer in a small volume of medium A, thus obtaining a protein concentration of 30 mg/mL.<sup>30</sup> All steps were carried out at 0–4 °C. The protein concentration was determined according to the colorimetric method of Bradford<sup>31</sup> by the Bio-Rad Protein Assay kit II, using BSA as standard. The mitochondrial preparations were then stored in liquid nitrogen until the evaluation of F-ATPase activities.

### Mitochondrial F-ATPase activity assays

Immediately after thawing, mitochondrial preparations were used to evaluate the F-ATPase activity. The ATP hydrolysis capability was assayed in a reaction medium (1 mL) containing 0.15 mg mitochondrial protein and 75 mM ethanolamine-HCl buffer (pH 9.0), 6.0 mM Na<sub>2</sub>ATP, and 2.0 mM MgCl<sub>2</sub> for the Mg<sup>2+</sup>-activated F<sub>1</sub>F<sub>0</sub>-ATPase assay, and in the same buffer at pH 8.8 plus 3.0 mM Na<sub>2</sub>ATP and 2.0 mM CaCl<sub>2</sub> to evaluate the Ca<sup>2+</sup>-activated F<sub>1</sub>F<sub>0</sub>-ATPase activity. After 5 min preincubation at 37 °C, the reaction, carried out at the same temperature, was started by adding the substrate Na<sub>2</sub>ATP and stopped after 5 min by adding 1 mL of ice-cold 15% (w/w) trichloroacetic acid (TCA) aqueous solution. Once the reaction was blocked, vials were centrifuged for 15 min at 3500 rpm (Eppendorf Centrifuge 5202). The concentration of inorganic phosphate (Pi) hydrolyzed by known amounts of mitochondrial protein in the supernatant, which indirectly detects the F-ATPase activity, was spectrophotometrically evaluated.<sup>32</sup> For this purpose, 1.0 μL of 3.0 mg/mL oligomycin in dimethylsulfoxide (DMSO) was directly added to the reaction mixture before starting the reaction. The total ATPase activity was calculated by Pi evaluation in control tubes run in parallel and containing 1.0 μL DMSO per mL reaction system. Control tubes were alternated with the condition to be tested in each set of experiments. The dose of 3.0 mg/mL oligomycin, a specific inhibitor of F-ATPase that selectively blocks the F<sub>0</sub> subunit, which is cur-

rently used in F-ATPase assays,<sup>33</sup> ensured maximal F-ATPase inhibition. The F<sub>1</sub>F<sub>0</sub>-ATPase activity, measured by subtracting the Pi hydrolyzed in the presence of oligomycin from the Pi hydrolyzed by total ATPase activity,<sup>34</sup> was expressed as μmol Pi·mg protein<sup>-1</sup>·min<sup>-1</sup> in all experiments.

### Kinetic analyses

The inhibition mechanisms of the **3a** and **3b** triazole derivatives on the Ca<sup>2+</sup>- or Mg<sup>2+</sup>-activated F<sub>1</sub>F<sub>0</sub>-ATPases was explored by using Dixon and Cornish-Bowden plots, which complement one another.<sup>35</sup> For this purpose, the 1/*v* (reciprocal of the enzyme activity) in the Dixon plot or the S/*v* ratio in the Cornish-Bowden plot was plotted as a function of **3a** or **3b** concentration. In all plots, the enzyme-specific activity was taken as the expression of *v*. To build these plots, different experimental sets were designed in which the F-ATPase activity was evaluated in the presence of increasing triazole derivative concentrations at two ATP concentrations, keeping the metal cofactor (Mg<sup>2+</sup> or Ca<sup>2+</sup>) concentration constant. The values of *K*'<sub>i</sub>, which represent the dissociation constant of the ternary enzyme-substrate-inhibitor (ESI) complex, were calculated as the abscissa (changed to positive) of the intercept of the straight lines obtained in the Cornish-Bowden plots.

To obtain time course plots, the F-ATPase reaction was carried out in the presence of 1 mM **3a** or **3b** triazole derivative, previously solubilized in DMSO (directly added with the ATP substrate), in the reaction system and stopped after different time intervals (1–5 min) by TCA. Enzyme activity data were then plotted as percentages of the residual F-ATPase activity in the presence of 1 mM triazole derivative (**3a** or **3b**) (θ) versus the incubation time of the same compound. In this plot, 100% F-ATPase activity corresponded to the initial enzyme activity (θ<sub>i</sub>), assuming that the compound under study is not bound to the enzyme. By fitting the data in a semilogarithmic plot, straight lines were obtained according to the equation:

$$\log \theta = -\frac{k_{inact}}{2.3}t + \log \theta_i$$

In these plots, the slope of each straight line corresponds to  $-k_{inact}/2.3$  (angular coefficient) and the y-axis intercept to  $\log \theta_i$ . Thus, the inactivation first-order rate constant (*k*<sub>inact</sub>) for each triazole

derivative was calculated from the slope ( $k_{\text{inact}} = \text{slope} \cdot 2.3 \cdot 60^{-1}$ ) and expressed as  $\text{s}^{-1}$ .<sup>36,37</sup>

Kinetic studies on the mutual exclusion of different inhibitors on the same F-ATPase activity were carried out in order to cast light on the possible interaction on F<sub>1</sub>F<sub>0</sub>-ATPase between triazole derivatives **3a** and **3b**. To build Dixon-like plots, the reciprocal of enzyme activity data ( $1/v$ ) ( $y$  axis) was plotted versus the concentration of triazole **3b** ( $x$  axis) at a constant ATP substrate concentration and in the absence and in the presence of fixed concentrations of triazole **3a**.<sup>33</sup> According to the graphical method employed,<sup>38</sup> when the straight lines are parallel, namely, they have the same slopes, the enzyme inhibition mirrors the binding of either **3a** or **3b** to the enzyme, and the two compounds mutually exclude each other.

### Mitochondrial respiration assay

Immediately after thawing, the mitochondrial fractions were used to evaluate the mitochondrial respiration. The experiments on freeze-thawed mitochondria primarily aimed at clarifying the effects of the selected triazole compound effects on mitochondrial respiratory chain enzyme activities and the F<sub>1</sub>F<sub>0</sub>-ATPase. The experimental conditions adopted ruled out any potential concomitant effect of changes in the transmembrane electrochemical gradient of H<sup>+</sup>. To measure mitochondrial respiratory activities, the oxygen consumption rates were polarographically evaluated by Clark-type electrode using a thermostated Oxytherm System (Hansatech Instruments) equipped with a 1 mL polarographic chamber. The reaction mixture (120 mM KCl, 10 mM Tris-HCl buffer, pH 7.2), maintained under Peltier thermostat control at 37 °C and continuous stirring, contained 0.25 mg mitochondrial protein.<sup>34</sup>

To evaluate the NADH-O<sub>2</sub> oxidase activity, the mitochondrial oxidation was run under saturating substrate conditions (75 μM NADH) after 2 min of stabilization of oxygen signal. Preliminary tests showed that, under these conditions, O<sub>2</sub> consumption was suppressed by 2.5 μM rotenone, a known inhibitor of complex I.<sup>39</sup> The succinate-O<sub>2</sub> oxidase activity by complex II was determined by the succinate oxidation in the presence of 2.5 μM rotenone. The reaction was started by the addition of 10 mM succinate after 2 min of stabilization of oxygen signal. Also, in this case, preliminary tests showed that,

under the conditions applied, succinate oxidation was suppressed by 1 μg/mL antimycin A, a selective inhibitor of complex III.<sup>39</sup>

To evaluate the effects of the compounds under study, the mitochondrial suspensions were added at the same time as the triazole **3a** or **3b** solutions of adequate concentrations to the polarographic chamber before starting the reaction at 37 °C. Triazole solutions of adequate concentrations were prepared immediately before the experiments by dissolving the compounds in DMSO. The mitochondrial respiratory rate was automatically evaluated by O<sub>2</sub>view software and expressed as nmoles O<sub>2</sub>·mg protein<sup>-1</sup>·min<sup>-1</sup>. Polarographic assays were run at least in triplicate on mitochondrial preparations obtained from distinct animals.

### mPTP evaluation

Immediately after the preparation of swine heart mitochondrial fractions, fresh mitochondrial suspensions (1 mg/mL) were energized in the assay buffer (130 mM KCl, 1 mM KH<sub>2</sub>PO<sub>4</sub>, 20 mM HEPES, pH 7.2 with TRIS), incubated at 37 °C with 1 μg/mL rotenone and 5 mM succinate. To evaluate the triazole effect, selected doses of **3a** or **3b** were added to the mitochondrial suspensions before mPTP evaluation. mPTP opening was induced by the addition of low concentrations of Ca<sup>2+</sup> (10 μM) as CaCl<sub>2</sub> solution at fixed time intervals (1 min). The calcium retention capacity (CRC), whose lowering indicates mPTP opening, was spectrofluorometrically evaluated in the presence of 0.8 μM Fura-FF. The probe has different spectral properties in the absence and presence of Ca<sup>2+</sup>; namely, it displays an excitation/emission spectra of 365/514 nm in the absence of Ca<sup>2+</sup> (Fura-FF low Ca<sup>2+</sup>) and shifts to 339/507 nm in the presence of high Ca<sup>2+</sup> concentrations (Fura-FF high Ca<sup>2+</sup>). mPTP opening was evaluated by the increase in the fluorescence intensity ratio (Fura-FF high Ca<sup>2+</sup>)/(Fura-FF low Ca<sup>2+</sup>), which indicates a decrease in CRC. All measurements were processed by LabSolutions RF software.<sup>40</sup>

### Statistical analysis

The data represent the mean ± SD (shown as vertical bars in the figures) of the number of experiments reported in the figure captions and Table 1. In each set of biochemical experiments, the analyses were carried out on at least three distinct mitochondrial preparations. The differences between the

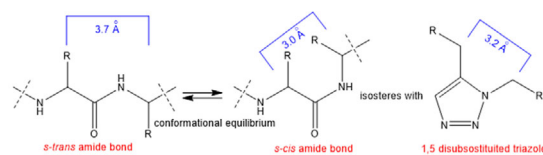


**Figure 1.** Peptide conformational equilibrium *s-trans/s-cis* and 1,5-disubstituted triazole isosteres.

enzyme activity data in differently treated mitochondria were evaluated by one-way ANOVA followed by Dunnett's test when *F* values indicated significance ( $P \leq 0.05$ ).

## Results and discussion

### Synthesis of triazole compounds

1,2,3-Triazole derivatives have good stability and high aqueous solubility in biological systems. In addition, they have structural similarity (i.e., planarity, size, hydrogen bond properties, and dipole moment) with the amide bond of enzymes,<sup>41</sup> which makes them isosteres with the *s-trans* and *s-cis* rotamers in the conformational equilibrium of the peptide bond (Fig. 1).

Although various synthetic procedures to regioselectively produce 1,4- and 1,5-disubstituted triazoles are described in the literature,<sup>42–44</sup> in this paper, we chose to prepare 1,5-disubstituted-1,2,3-triazoles because of their larger dipolar moment than 1,4-disubstituted triazoles (5.06 versus 4.31 debyes, respectively). Accordingly, most likely the inhibition of an enzyme may be affected by dipole-dipole interactions and strong hydrogen bonds with the employed substrate (Fig. 2).

More specifically, these compounds can act as hydrogen bond acceptors by exploiting the N2 and N3 nitrogen atoms of the aromatic ring and also as hydrogen bond donors via a CH bond. More-

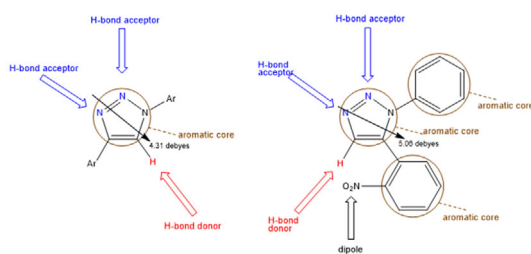


**Figure 2.** Summary of potential binding interactions for 1,4- and 1,5-disubstituted-1,2,3-triazoles.

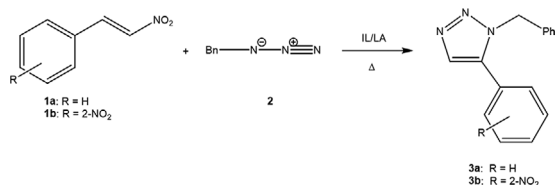


**Figure 3.** Pattern of r 1,5-disubstituted-1,2,3-triazole **3a** and **3b** synthesis.

over, the triazole aromatic core may be responsible for  $\pi$ -stacking interactions with aromatic side chains of amino acids in the active site of the enzyme target. These interactions may also be amplified by the presence of aromatic substituents on the triazole backbone.

For this reason, considering our experience with the synthesis of heterocycles by the 1,3-dipolar cycloaddition reaction and with the chemical interactions involved in substrate/enzyme processes,<sup>45–47</sup> we chose to synthesize two specific triazole derivatives, 1-benzyl-5-phenyl-1,2,3-triazole (**3a**) and 1-benzyl-5-(2-nitrophenyl)-1,2,3-triazole (**3b**), aiming at increasing the  $\pi$ -stacking and dipole-dipole interactions by molecular moieties different from the triazole aromatic core. Accordingly, phenyl rings and nitro group are especially suitable for forming  $\pi$ - $\pi$  and dipole-dipole interactions, respectively. In addition, the presence of the methylene group of N1-benzyl increases the degrees of freedom, allowing several interactions with the enzyme substrate.

In detail, the synthesis of the 1,5-disubstituted triazoles **3a** and **3b** consists of an EAOE between nitroolefins **1a–1b** as electron-deficient dipolarophile and benzylazide **2** as dipole in the presence of the ionic liquid 1-methyl pyridinium trifluoromethanesulfonate ([mpy]OTf) as solvent and FeCl<sub>3</sub> as Lewis acid catalyst (Fig. 3).<sup>44</sup>

In detail, we selected the reusable [mpy]OTf/FeCl<sub>3</sub> system because the strong coordination of the NO<sub>2</sub> group to the Fe-catalyst has a large impact on the regiocontrol of the reaction, by only yielding the 1,5-regioisomer. Furthermore, the strong stabilization of reaction intermediates due to the use of the [mpy]OTf allows the formation of the unstable triazolone intermediate and favors its transformation into more stable triazole compounds by the eliminative mechanism. The compounds **3a** and **3b**, recovered by simple extraction in dichloromethane

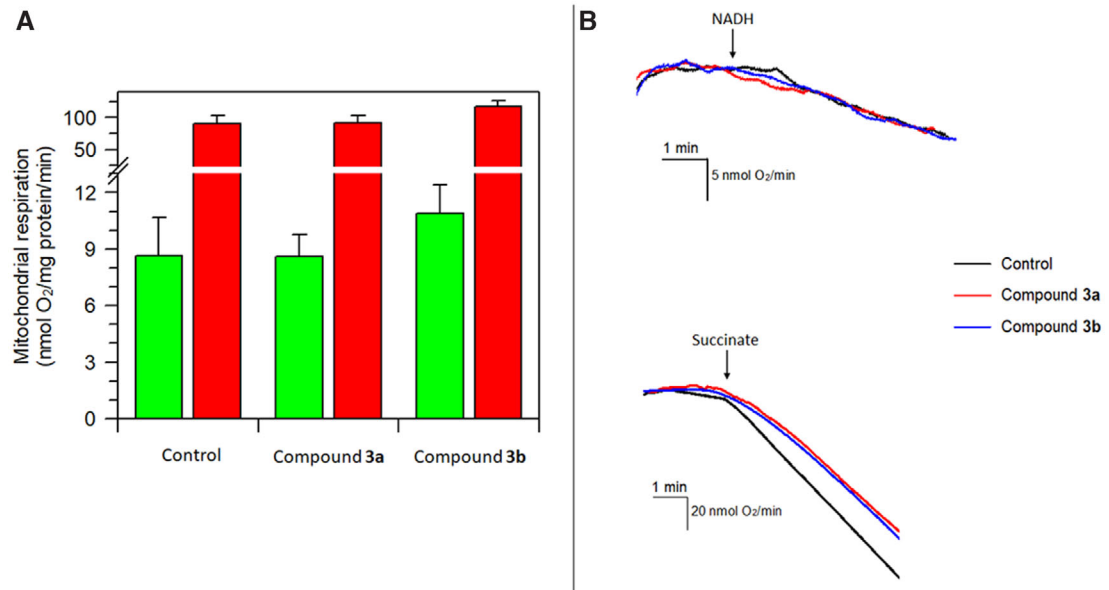


**Figure 4.** 1,5-Disubstituted-1,2,3-triazole effect on mitochondrial respiration. (A) NADH-O<sub>2</sub> (green vertical bars) and succinate-O<sub>2</sub> (red vertical bars) oxidase activity were evaluated without and with 1 mM of triazole derivatives **3a** and **3b**. Data expressed as column chart represent the mean  $\pm$  SD from three experiments carried out on different mitochondrial preparations. (B) Representative traces of the respiration recordings by NADH (upper traces) and succinate addition (lower traces). The arrows indicate the addition of the substrates.

and purified by flash chromatography and obtained in 95% and 91% yield, respectively, were used as model compounds for subsequent biological investigations.

#### 1,5-Disubstituted-1,2,3-triazole effects on mitochondrial bioenergetics

Energy production in mitochondria in the form of ATP depends on the respiratory chain activity and ADP phosphorylation efficiency by the  $F_1F_0$ -ATPase.<sup>48</sup> The effects of the compounds under study on these two matched potential targets were evaluated in parallel. The effect of triazole derivatives **3a** and **3b** on mitochondrial respiration was evaluated in NADH- and succinate-energized mitochondria. Triazoles **3a** and **3b** did not significantly affect the NADH-O<sub>2</sub>/succinate-O<sub>2</sub> oxidase activity (Fig. 4).

The titration curve of the triazole derivatives on the  $Ca^{2+}$ - and  $Mg^{2+}$ -activated  $F_1F_0$ -ATPase(s) shows that both the compounds tested did not affect the  $Mg^{2+}$ -activated enzyme (Fig. 5B and D). Conversely, when the effect of the same compounds was tested on the  $Ca^{2+}$ -activated  $F_1F_0$ -ATPase

activity, a significant enzyme inhibition was shown by 0.25 mM compound **3a** and 0.2 mM compound **3b** onward (Fig. 5A and C). Most likely, the different effect on the two differently activated  $F_1F_0$ -ATPases depends on the enzyme conformations promoted by the cofactor(s) bound to the catalytic and/or noncatalytic sites of the  $F_1$  domain.<sup>10,12,30</sup> The capability of different divalent cations to drive the  $F_1$ -ATPase mechanochemical coupling in mitochondria from different biological sources remains to be ascertained. However, in mammals,  $Ca^{2+}$ -binding to the catalytic  $\beta$  subunit has been proposed as the chemical event that triggers mPTP.<sup>11</sup> In the  $F_1$  catalytic site,  $Mg^{2+}$  is directly linked by  $\beta$ Thr-163 of the P-loop and the phosphate oxygens of ATP or ADP and coordinated with three water molecules to the  $\beta$ Arg-189,  $\beta$ Glu-192, and  $\beta$ Asp-256 residues.<sup>49</sup> The larger  $Ca^{2+}$  radius than  $Mg^{2+}$  implies a more flexible coordination geometry characterized by irregular bond distances and angles in the  $\beta$  subunit catalytic sites, and the coordination geometry changes to accommodate eight ligands.<sup>50</sup> On these bases, the modified catalytic structure, which alters the  $Ca^{2+}$ -driven catalytic mechanism of ATP

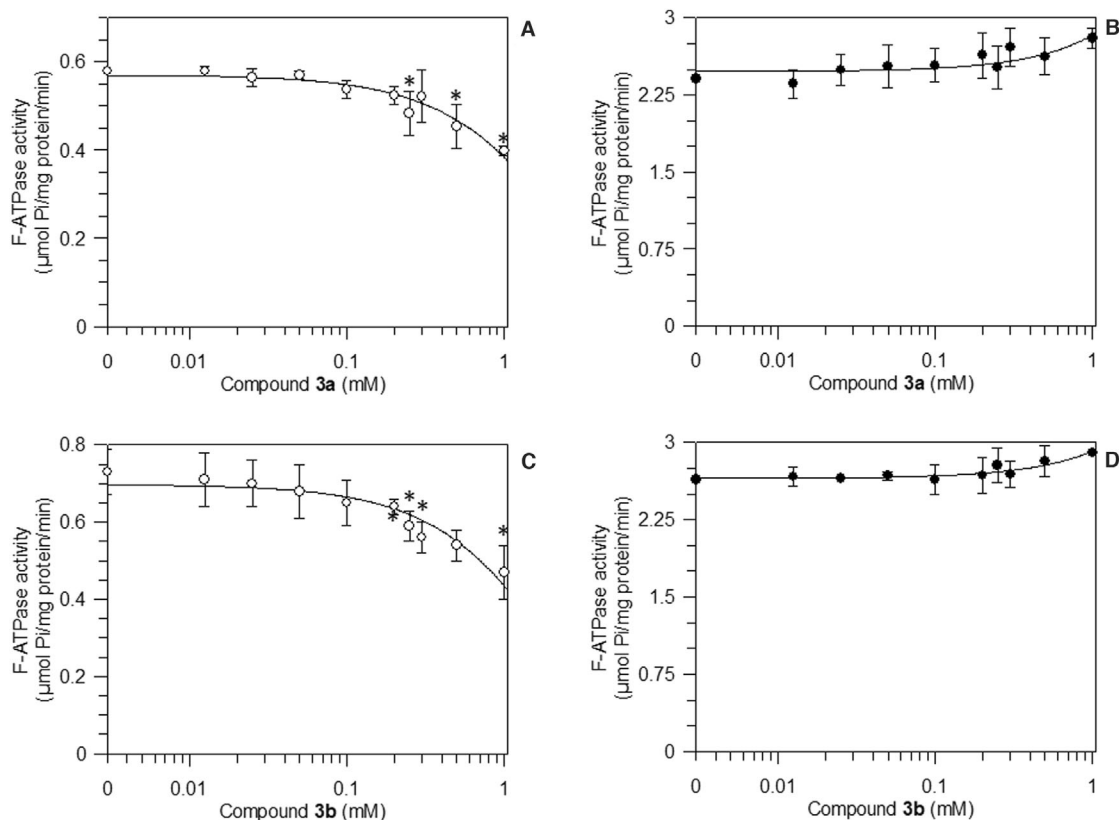


**Figure 5.** Effect of triazole derivatives **3a** and **3b** on activity of mitochondrial  $Ca^{2+}$  and  $Mg^{2+}$ -activated  $F_1F_0$ -ATPase.  $Ca^{2+}$ -activated  $F_1F_0$ -ATPase ( $\circ$ ) and  $Mg^{2+}$ -activated  $F_1F_0$ -ATPase activities ( $\bullet$ ) in the presence of increasing concentrations of compound **3a** (A and B) and compound **3b** (C and D). Data represent the mean  $\pm$  SD from three independent experiments carried out on distinct mitochondrial preparations. \*indicates significant differences with respect to the control without triazoles ( $P \leq 0.05$ ).

hydrolysis, makes the  $Ca^{2+}$ -activated  $F_1F_0$ -ATPase susceptible to triazole inhibition.

#### *Mechanism of 1,5-disubstituted-1,2,3-triazole inhibition of the mitochondrial $F_1F_0$ -ATPase*

To understand the mechanism of inhibition by the triazole derivatives **3a** and **3b** of the  $Ca^{2+}$ -activated  $F_1F_0$ -ATPase, further information can be obtained by kinetic studies, which can lead to define the features of the enzyme-inhibitor complex in the presence or in the absence of the ATP substrate. As far as we are aware, up to now, no study has considered triazole derivative effects on the  $F_1F_0$ -ATPase activity independently of potential perturbations of IMM potential and structure. Therefore, to detect triazole effects on these enzyme activities, uncoupled mitochondria obtained by freeze-thawing were used for kinetic analysis. Both of the 1,5-disubstituted-1,2,3-triazoles (**3a** and **3b**) tested

exert an uncompetitive inhibition (Fig. 6) by binding to the enzyme-ATP complex and forming the ESI tertiary complex. This inhibition type cannot be overcome by increasing ATP concentration. Thus, both compounds do not affect the ATP binding site, but they may interfere with a binding region that modifies the  $Ca^{2+}$ -dependent catalytic mechanism of ATP hydrolysis. Moreover, the Cornish-Bowden plots (Fig. 6B and D) show that the dissociation constant of the ESI complex ( $K'_i$ ) of the  $Ca^{2+}$ -activated  $F_1F_0$ -ATPase is  $1.09 \pm 0.04$  mM for compound **3a** and  $1.07 \pm 0.05$  mM for compound **3b** (Table 1). These similar values indicate that the ESI complex formation is independent of the triazole structure. However, since the inactivation rate constant is  $1.93 \times 10^{-3} \pm 0.26 \times 10^{-3} s^{-1}$  for **3a** and  $0.86 \times 10^{-3} \pm 0.14 \times 10^{-3} s^{-1}$  for **3b** (Fig. 7A), the former inhibitor shows a higher propensity to react than the latter,

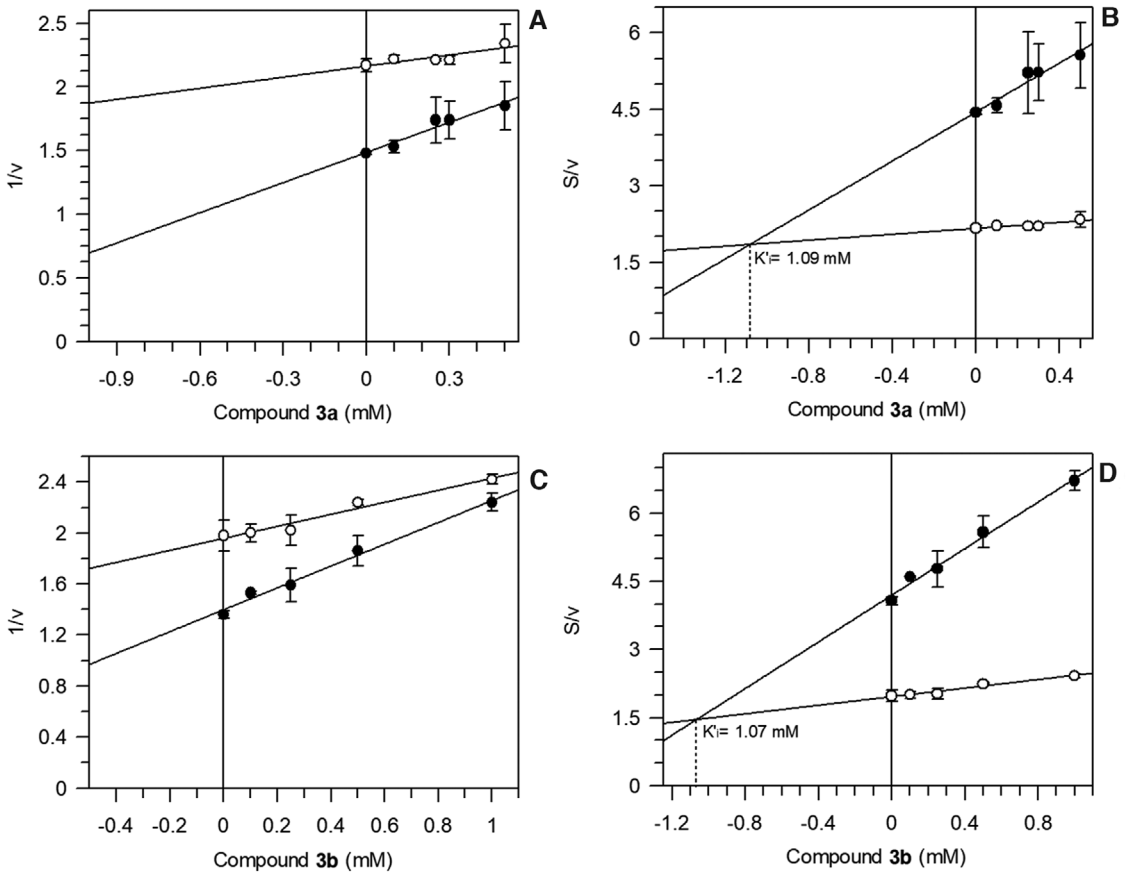


**Figure 6.** Ca<sup>2+</sup>-activated F<sub>1</sub>F<sub>0</sub>-ATPase inhibition by triazole derivatives 3a and 3b. Dixon (A and C) and Cornish-Bowden (B and D) plots obtained at 1 mM (○) or 3 mM (●) ATP for the Ca<sup>2+</sup>-activated F<sub>1</sub>F<sub>0</sub>-ATPase (A and B); 3 mM (□) or 6 mM (■) ATP for the Mg<sup>2+</sup>-F<sub>1</sub>F<sub>0</sub>-activated ATPase (C and D) and designing the experiments as detailed in Materials and methods. All points represent the mean ± SD (vertical bars) of four distinct experiments carried out on distinct mitochondrial preparations.

which implies a more rapid bond with the enzyme. The potency of a mechanism-based inhibitor, taken as the  $k_{inact}/K'_i$  ratio, is a measure of the inhibitor efficiency on the Ca<sup>2+</sup>-activated F<sub>1</sub>F<sub>0</sub>-ATPase.

Since triazole derivative 3a shows a  $k_{inact}/K'_i$  ratio that is 2.2 orders of magnitude higher than triazole derivative 3b (Table 1), the former inhibitor is much more powerful than the latter. Consistently, even

**Table 1.** Inhibition kinetic parameters of the Ca<sup>2+</sup>-activated F<sub>1</sub>F<sub>0</sub>-ATPase activity by triazole compounds

	Compound 3a	Compound 3b
$K'_i$ (mM)	1.09 ± 0.04	1.07 ± 0.05
$k_{inact}$ (s <sup>-1</sup> )	1.93 × 10 <sup>-3</sup> ± 0.26 × 10 <sup>-3</sup>	0.86 × 10 <sup>-3</sup> ± 0.14 × 10 <sup>-3</sup>
$k_{inact}/K'_i$ (mM <sup>-1</sup> ·s <sup>-1</sup> )	1.77 × 10 <sup>-3</sup>	0.80 × 10 <sup>-3</sup>

NOTE: The  $K'_i$  values (dissociation constant of the ESI complex) were graphically obtained from the Cornish plots drawn in Figure 6B and D as detailed in Materials and methods. The  $k_{inact}$  values (inactivation rate constant) were graphically obtained from the plots in Figure 7A as detailed in Materials and methods. Data are the mean values obtained from three sets of experiments carried out on distinct mitochondrial preparations.

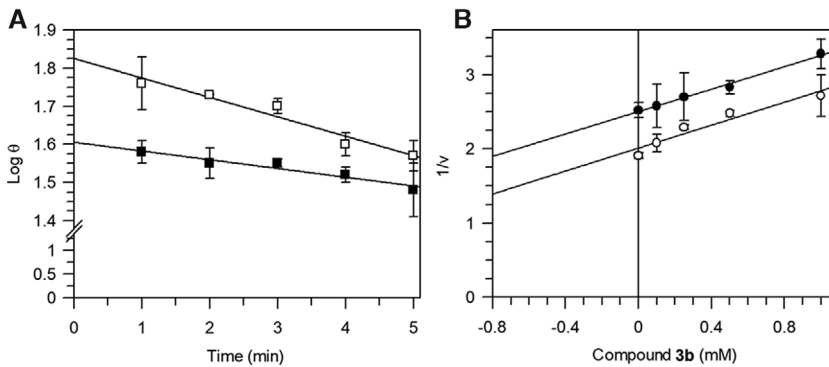


**Figure 7.** Kinetics of the Ca<sup>2+</sup>-activated F<sub>1</sub>F<sub>0</sub>-ATPase inhibition by triazole derivatives **3a** and **3b**. (A) Time course plot of Ca<sup>2+</sup>-activated F<sub>1</sub>F<sub>0</sub>-ATPase to obtain the inactivation rate constant ( $k_{\text{inact}}$ ) as detailed in Materials and methods with 1 mM of compound **3a** (□) and 1 mM of compound **3b** (■). (B) Multiple inhibitor analysis by Dixon plots for the Ca<sup>2+</sup>-activated F<sub>1</sub>F<sub>0</sub>-ATPase inhibition by compound **3b**. The F-ATPase assays were carried out in the absence (○) or presence of 0.5 mM compound **3a** (●). Each point represents the mean value  $\pm$  SD (vertical bars) of at least three experiments carried out on distinct mitochondrial preparations.

if the two compounds show the same propensity to form the ternary complex as reported by the  $K'_1$  values, **3a** reacts with the enzyme more quickly, resulting in a more efficient inhibition of Ca<sup>2+</sup>-activated F<sub>1</sub>F<sub>0</sub>-ATPase, probably because the two compounds establish different interactions with the enzyme even if they bind to the same site on the F<sub>1</sub>F<sub>0</sub>-ATPase. Indeed, the inhibition by binary mixtures of triazole derivatives **3a** and **3b**, tested by the diagnostic plot for mutual exclusion, suggests that the F<sub>1</sub>F<sub>0</sub>-ATPase can combine with either **3a** or **3b**, but not with both compounds simultaneously (Fig. 7B). The different chemical structure of the triazole derivatives resides in a nitro group in compound **3b**, which apparently does not affect the affinity for the F<sub>1</sub>F<sub>0</sub>-ATPase but may require some more time to establish interactions with the enzyme.

#### *mPTP sensitivity to the **3a** and **3b** triazole derivatives*

Recent advances strongly indicate that the Ca<sup>2+</sup>-activated F<sub>1</sub>F<sub>0</sub>-ATPase is the lethal functional mode of the mitochondrial enzyme that triggers mPTP.<sup>12</sup> The formation of this nonselective channel in functional and intact mitochondria, which normally accumulate Ca<sup>2+</sup> when Ca<sup>2+</sup> is stepwise provided, can be evaluated as CRC, which decreases when the mPTP opens. According to the fluorimetric method employed, the Ca<sup>2+</sup> release from mitochondria ascribed to mPTP opening is revealed

by an increase in the fluorescence intensity ratio (Fura-FF high Ca<sup>2+</sup>)/(Fura-FF low Ca<sup>2+</sup>). Consistent with the selective F<sub>1</sub>F<sub>0</sub>-ATPase inhibition by compounds **3a** and **3b** when the natural cofactor Mg<sup>2+</sup> is replaced by Ca<sup>2+</sup> (Fig. 5), mPTP formation in triazole-treated mitochondria is inhibited (Fig. 8). Accordingly, the increase in CRC upon subsequent 10  $\mu$ M Ca<sup>2+</sup> additions at fixed time intervals, shown by the rise in the (Fura-FF high Ca<sup>2+</sup>)/(Fura-FF low Ca<sup>2+</sup>) ratio, indicates that in the presence of the compounds tested, mitochondria attain a higher threshold value of Ca<sup>2+</sup> concentration to trigger mPTP formation (Fig. 8A); in other words, more Ca<sup>2+</sup> additions are required to promote mPTP opening (Fig. 8B). Noteworthy, the two compounds behave differently as mPTP inhibitors. Accordingly, triazole **3a** attains a lower CRC value (high Fura-FF ratio) than triazole **3b** when mPTP opens. We can speculate that the different effects on mPTP of the two compounds under study are due to the onset of different kinds of interactions in the same binding region on the Ca<sup>2+</sup>-activated F<sub>1</sub>F<sub>0</sub>-ATPase, which affect the mPTP size<sup>51</sup> (Fig. 7B). On these bases, a lower CRC value would mirror a larger mPTP size. Moreover, the sharp increase in fluorescence followed by a less sharp decline as mitochondria take up calcium in the presence of triazole **3a** has a gradual increase of baseline with each Ca<sup>2+</sup> pulse. We could assert that the trend could be due to an inhibitory effect of the mitochondrial calcium uniporter uptake.<sup>52</sup>

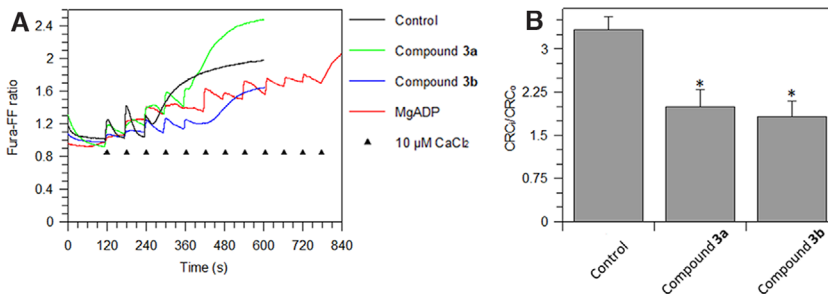


**Figure 8.** Evaluation of mPTP opening. Representative curves (A) of the CRC expressed as the Fura-FF ratio (Fura-FF high  $Ca^{2+}$ )/(Fura-FF low  $Ca^{2+}$ ), evaluated in response to subsequent  $10 \mu M$   $CaCl_2$  pulses (shown by the triangles), as detailed in Materials and methods, in untreated mitochondria (control), and in the presence of  $2 mM$  MgADP,  $1.0 mM$  compound 3a,  $1.0 mM$  compound 3b. (B) Quantitation of the mPTP is expressed as the ratio of the number of calcium pulses required to induce mPTP in MgADP-inhibited ( $CRC_i$ ) and untreated ( $CRC_o$ ) mitochondria. Data represent the mean  $\pm$  SD from three independent experiments carried out on distinct mitochondrial preparations. \*Indicates significant differences with respect to the control ( $P \leq 0.05$ ).

## Conclusions

The link between the inhibition power of the bioactive triazoles and their chemical structure could provide a road map to address further developments in pharmacology, which can be helpful in medical chemistry to treat mPTP-related human pathologies.  $F_1F_0$ -ATPase, as the main candidate component of mPTP, should be a mitochondrial target of these compounds to lessen or block mPTP formation. Since the different selectivity and interaction rate of structurally different compounds on the  $Ca^{2+}$ -activated  $F_1F_0$ -ATPase is not directly related to their mPTP inhibition efficiency, most likely the 1,5-disubstituted-1,2,3-triazoles tested mainly act on the subunits of  $F_1F_0$ -ATPase(s) involved in the mechanism of mPTP formation. On balance, the slowdown of mPTP formation (desensitization) could be indirectly due to changes in the conformational transmission mechanism from  $F_1$  to  $F_0$  that opens mPTP.

## Acknowledgments

Danilo Matteuzzi (Department of Veterinary Medical Sciences, University of Bologna) is gratefully acknowledged for kindly supplying swine hearts from a local abattoir to the Biochemistry laboratories. This work was financed by an RFO Grant from the University of Bologna, from the Carisbo Foundation (Grant No. 2018/0375), and by a research Grant from Calabria Region (PAC CALABRIA 2014–2020 - Asse Prioritario 12, Azione B) 10.5.12

CUP: H28D19000040006) and the University of Calabria.

## Supporting information

Additional supporting information may be found in the online version of this article.

## Competing interests

The authors declare no competing interests.

## References

- Zoratti, M. & I. Szabò. 1995. The mitochondrial permeability transition. *Biochim. Biophys. Acta* **1241**: 139–176.
- Bernardi, P., A. Rasola, M. Forte, et al. 2015. The mitochondrial permeability transition pore: channel formation by F-ATP synthase, integration in signal transduction, and role in pathophysiology. *Physiol. Rev.* **95**: 1111–1155.
- Briston, T., D.L. Selwood, G. Szabadkai, et al. 2019. Mitochondrial permeability transition: a molecular lesion with multiple drug targets. *Trends Pharmacol. Sci.* **40**: 50–70.
- Urbani, A., V. Giorgio, A. Carrer, et al. 2019. Purified F-ATP synthase forms a  $Ca^{2+}$ -dependent high-conductance channel matching the mitochondrial permeability transition pore. *Nat. Commun.* **10**: 4341.
- Mnatsakanyan, N., M.C. Llaguno, Y. Yang, et al. 2019. A mitochondrial megachannel resides in monomeric F<sub>1</sub>F<sub>0</sub> ATP synthase. *Nat. Commun.* **10**: 5823.
- Kühlbrandt, W. 2019. Structure and mechanisms of F-type ATP synthases. *Annu. Rev. Biochem.* **88**: 515–549.
- Nesci, S., F. Trombetti, V. Ventrella, et al. 2015. Opposite rotation directions in the synthesis and hydrolysis of ATP by the ATP synthase: hints from a subunit asymmetry. *J. Membr. Biol.* **248**: 163–169.
- Junge, W., H. Sielaff & S. Engelbrecht. 2009. Torque generation and elastic power transmission in the rotary F(O)F(1)-ATPase. *Nature* **459**: 364–370.

9. Frasch, W.D. 2000. The participation of metals in the mechanism of the F(1)-ATPase. *Biochim. Biophys. Acta* **1458**: 310–325.
10. Nesci, S., F. Trombetti, V. Ventrella, *et al.* 2017. Kinetic properties of the mitochondrial F<sub>1</sub>F<sub>0</sub>-ATPase activity elicited by Ca(2<sup>+</sup>) in replacement of Mg(2<sup>+</sup>). *Biochimie* **140**: 73–81.
11. Giorgio, V., V. Burchell, M. Schiavone, *et al.* 2017. Ca(2<sup>+</sup>) binding to F-ATP synthase β subunit triggers the mitochondrial permeability transition. *EMBO Rep.* **18**: 1065–1076.
12. Algieri, C., F. Trombetti, A. Pagliarani, *et al.* 2019. Mitochondrial Ca<sup>2+</sup>-activated F<sub>1</sub> F<sub>0</sub>-ATPase hydrolyzes ATP and promotes the permeability transition pore. *Ann. N.Y. Acad. Sci.* **1457**: 142–157.
13. Nesci, S. 2020. The mitochondrial permeability transition pore in cell death: a promising drug binding bioarchitecture. *Med. Res. Rev.* **40**: 811–817.
14. Baines, C.P., R.A. Kaiser, N.H. Purcell, *et al.* 2005. Loss of cyclophilin D reveals a critical role for mitochondrial permeability transition in cell death. *Nature* **434**: 658–662.
15. Thirumurugan, P., D. Matosiuk & K. Jozwiak. 2013. Click chemistry for drug development and diverse chemical-biology applications. *Chem. Rev.* **113**: 4905–4979.
16. Angell, Y.L. & K. Burgess. 2007. Peptidomimetics via copper-catalyzed azide-alkyne cycloadditions. *Chem. Soc. Rev.* **36**: 1674–1689.
17. Singhal, N., P.K. Sharma, R. Dudhe, *et al.* 2011. Recent advancement of triazole derivatives and their biological significance. *J. Chem. Pharm. Res.* **3**: 126–133.
18. Huisgen, R. 1963. 1,3-Dipolar cycloadditions. Past and future. *Angew. Chem. Int. Ed. Engl.* **2**: 565–598.
19. Tornøe, C.W., C. Christensen & M. Meldal. 2002. Peptidotriazoles on solid phase: [1,2,3]-triazoles by regioselective copper(i)-catalyzed 1,3-dipolar cycloadditions of terminal alkynes to azides. *J. Org. Chem.* **67**: 3057–3064.
20. Boren, B.C., S. Narayan, L.K. Rasmussen, *et al.* 2008. Ruthenium-catalyzed azide-alkyne cycloaddition: scope and mechanism. *J. Am. Chem. Soc.* **130**: 8923–8930.
21. Huisgen, R., G. Szeimies & L. Möbius. 1966. 1,3-Dipolare cycloadditionen, XXIV. Triazolone aus organischen Aziden und α,β-ungesättigten Carbonylverbindungen oder Nitrilen. *Chem. Ber.* **99**: 475–490.
22. Broeckx, W., N. Overbergh, C. Samyn, *et al.* 1971. Cycloaddition reactions of azides with electron-poor olefins: isomerization and thermolysis of the resulting Δ<sup>2</sup>-triazolines. *Tetrahedron* **27**: 3527–3534.
23. Wang, Y.-C., Y.-Y. Xie, H.-E. Qu, *et al.* 2014. Ce(OTf)<sub>3</sub>-catalyzed [3 + 2] cycloaddition of azides with nitroolefins: regioselective synthesis of 1,5-disubstituted 1,2,3-triazoles. *J. Org. Chem.* **79**: 4463–4469.
24. Maiuolo, L., B. Russo, V. Algieri, *et al.* 2019. Regioselective synthesis of 1,5-disubstituted 1,2,3-triazoles by 1,3-dipolar cycloaddition: role of Er(OTf)<sub>3</sub>, ionic liquid and water. *Tetrahedron Lett.* **60**: 672–674.
25. Nino, A.D., V. Algieri, M.A. Tallarida, *et al.* 2019. Regioselective synthesis of 1,4,5-trisubstituted-1,2,3-triazoles from aryl azides and enamines. *Eur. J. Org. Chem.* **2019**: 5725–5731.
26. Šileikytė, J., J. Devereaux, J. de Jong, *et al.* 2019. Second-generation inhibitors of the mitochondrial permeability transition pore with improved plasma stability. *ChemMedChem* **14**: 1771–1782.
27. Bortolini, O., A.D. Nino, A. Garofalo, *et al.* 2010. Mild oxidative conversion of nitroalkanes into carbonyl compounds in ionic liquids. *Syn. Commun.* **40**: 2483–2487.
28. De Nino, A., L. Maiuolo, P. Merino, *et al.* 2015. Efficient organocatalyst supported on a simple ionic liquid as a recoverable system for the asymmetric Diels-Alder reaction in the presence of water. *ChemCatChem* **7**: 830–835.
29. Bortolini, O., A. De Nino, A. Garofalo, *et al.* 2010. Erbium triflate in ionic liquids: a recyclable system of improving selectivity in Diels-Alder reactions. *Appl. Cat. A Gen.* **372**: 124–129.
30. Nesci, S., V. Ventrella, F. Trombetti, *et al.* 2016. Preferential nitrite inhibition of the mitochondrial F<sub>1</sub>F<sub>0</sub>-ATPase activities when activated by Ca(2<sup>+</sup>) in replacement of the natural cofactor Mg(2<sup>+</sup>). *Biochim. Biophys. Acta* **1860**: 345–353.
31. Bradford, M.M. 1976. A rapid and sensitive method for the quantitation of microgram quantities of protein utilizing the principle of protein-dye binding. *Anal. Biochem.* **72**: 248–254.
32. Nesci, S., V. Ventrella, F. Trombetti, *et al.* 2014. The mitochondrial F<sub>1</sub>F<sub>0</sub>-ATPase desensitization to oligomycin by tributyltin is due to thiol oxidation. *Biochimie* **97**: 128–137.
33. Nesci, S., V. Ventrella, F. Trombetti, *et al.* 2014. Thiol oxidation is crucial in the desensitization of the mitochondrial F<sub>1</sub>F<sub>0</sub>-ATPase to oligomycin and other macrolide antibiotics. *Biochim. Biophys. Acta* **1840**: 1882–1891.
34. Nesci, S., F. Trombetti, M. Pirini, *et al.* 2016. Mercury and protein thiols: stimulation of mitochondrial F<sub>1</sub>F<sub>0</sub>-ATPase and inhibition of respiration. *Chem. Biol. Interact.* **260**: 42–49.
35. Cornish-Bowden, A. 1974. A simple graphical method for determining the inhibition constants of mixed, uncompetitive and non-competitive inhibitors. *Biochem. J.* **137**: 143–144.
36. Mizutani, K., M. Yamamoto, K. Suzuki, *et al.* 2011. Structure of the rotor ring modified with N,N'-dicyclohexylcarbodiimide of the Na<sup>+</sup>-transporting vacuolar ATPase. *Proc. Natl. Acad. Sci. USA* **108**: 13474–13479.
37. Nesci, S., V. Ventrella, F. Trombetti, *et al.* 2013. Mussel and mammalian ATP synthase share the same bioenergetic cost of ATP. *J. Bioenerg. Biomembr.* **45**: 289–300.
38. Yonetani, T. 1982. The Yonetani-Theorell graphical method for examining overlapping subsites of enzyme active centers. *Meth. Enzymol.* **87**: 500–509.
39. Nicholls, D.G. & S.J. Ferguson. 2013. 5 - Respiratory chains. In *Bioenergetics*. 4th ed. D.G. Nicholls & S.J. Ferguson, Eds.: 91–157. Boston, MA: Academic Press.
40. Algieri, C., F. Trombetti, A. Pagliarani, *et al.* 2020. Phenylglyoxal inhibition of the mitochondrial F<sub>1</sub>F<sub>0</sub>-ATPase activated by Mg<sup>2+</sup> or by Ca<sup>2+</sup> provides clues on the mitochondrial permeability transition pore. *Arch. Biochem. Biophys.* **681**: 108258.

41. Corredor, M., J.S. Jordi Solà, & I.A. Alfonso. Disubstituted 1,2,3-triazoles as amide bond mimetics. *Targets Heterocyclic Syst.* **21**: 1–22.
42. Rostovtsev, V.V., L.G. Green, V.V. Fokin, *et al.* 2002. A stepwise Huisgen cycloaddition process: copper(I)-catalyzed regioselective “ligation” of azides and terminal alkynes. *Angew. Chem. Int. Ed.* **41**: 2596–2599.
43. Gangaprasad, D., J. Paul Raj, T. Kiranmye, *et al.* 2016. A tunable route to oxidative and eliminative [3+2] cycloadditions of organic azides with nitroolefins: CuO nanoparticles catalyzed synthesis of 1,2,3-triazoles under solvent-free condition. *Tetrahedron Lett.* **57**: 3105–3108.
44. De Nino, A., P. Merino, V. Algieri, *et al.* 2018. Synthesis of 1,5-functionalized 1,2,3-triazoles using ionic liquid/iron(III) chloride as an efficient and reusable homogeneous catalyst. *Catalysts* **8**. <https://doi.org/10.20944/preprints201807.0620.v1>.
45. Maiuolo, L., V. Algieri, F. Olivito, *et al.* 2020. Recent developments on 1,3-dipolar cycloaddition reactions by catalysis in green solvents. *Catalysts* **10**: 65–91.
46. Maiuolo, L., A. De Nino, V. Algieri, *et al.* 2017. Microwave-assisted 1,3-dipolar cyclo-addition: recent advances in synthesis of isoxazolidines. *Mini Rev. Org. Chem.* **14**: 136–142.
47. Merino, P., L. Maiuolo, I. Delso, *et al.* 2017. Chemical approaches to inhibitors of isoprenoid biosynthesis: targeting farnesyl and geranylgeranyl pyrophosphate synthases. *RSC Adv.* **7**: 10947–10967.
48. Nicholls, D. 1984. Chapter 2: Mechanisms of energy transduction. In *New Comprehensive Biochemistry*. L. Ernster, Ed.: 29–48. Elsevier.
49. Rees, D.M., M.G. Montgomery, A.G.W. Leslie, *et al.* 2012. Structural evidence of a new catalytic intermediate in the pathway of ATP hydrolysis by F<sub>1</sub>-ATPase from bovine heart mitochondria. *Proc. Natl. Acad. Sci. USA* **109**: 11139–11143.
50. Casadio, R. & B.A. Melandri. 1996. CaATP inhibition of the MgATP-dependent proton pump (H<sup>+</sup>-ATPase) in bacterial photosynthetic membranes with a mechanism of alternative substrate inhibition. *J. Biol. Inorg. Chem.* **1**: 284–291.
51. Neginskaya, M.A., M.E. Solesio, E.V. Berezhnaya, *et al.* 2019. ATP synthase C-subunit-deficient mitochondria have a small cyclosporine A-sensitive channel, but lack the permeability transition pore. *Cell Rep.* **26**: 11–17.e2.
52. Marchi, S., V.A.M. Vitto, S. Patergnani, *et al.* 2019. High mitochondrial Ca<sup>2+</sup> content increases cancer cell proliferation upon inhibition of mitochondrial permeability transition pore (mPTP). *Cell Cycle* **18**: 914–916.

## 9. Characterization of cell metabolism (section II)

Cell culture is a laboratory method that allows the growth of eukaryotic or prokaryotic cells under physiological and non-physiological conditions. One of the advantages of using cell culture to test the effect of drugs and other compounds is the homogeneity of clonal cell populations or specific cell types and well-defined culture systems to remove interfering genetic or environmental variables and thus allow for data generation of high reproducibility that cannot be otherwise guaranteed<sup>202</sup>. On these bases, cultured cells are often selected as *in vitro* models to study the effects of various compounds and culture conditions.

Cellular metabolism is a flexible network that allows tissues to meet demands for homeostasis and growth. The correct cellular functionality mainly depends on mitochondrial activity since these organelles are the main producer of energy necessary for multiple cellular functions. Mitochondria are crucial for excitable cells, such as neurons, heart and skeletal muscle, due to their characteristic of producing ATP mainly through OXPHOS, even though cells use different metabolic substrates to generate energy for their different functions<sup>203</sup>.

The study of the metabolic profile allows us to obtain specific information on cellular metabolism, such as the amount of ATP produced by the mitochondrial pathway (OXPHOS) in comparison with that produced by the glycolytic pathway, the metabolic potential under conditions of energy demand by the cell and other metabolic parameters. Such information is obtained by the addition in specific sequence, of metabolic selective modulators<sup>204</sup>. In this thesis, the energy metabolism of different cell lines has been characterized for three main purposes:

- A. To investigate the metabolic efficiency and flexibility of boar spermatozoa and the time-dependent trend of energy parameters.
- B. To select the most suitable mesenchymal stem cells for transplantation studies in regenerative medicine (UC-MSCs and AT-MSCs).

C. To test the effect of various compounds and culture conditions at the intestinal level (IPEC-J2).

A) For fertilization to be successful, mammalian spermatozoa should travel through the female genital tract and be morphologically and functionally intact<sup>205</sup>. Mammalian spermatozoa are known to use different metabolic substrates to generate energy for different cellular functions such as motility and ability<sup>206–208</sup>. Various studies have focused on the metabolic strategy of spermatozoa and the involvement of mitochondria in the energy supply system<sup>209–211</sup>. It seems that some mammalian species, such as humans, mice and pigs, preferentially use glycolysis, while equines mainly use mitochondrial OXPHOS; others, particularly bovine exploit an intermediate strategy to feed energy pathways<sup>212–214</sup>. To date, comprehensive studies have been conducted on wild boar and stallion sperm as representatives of metabolic strategies in mammalian sperm. However, it is still not very clear whether boar spermatozoa depend specifically on glycolysis for their energy supply; the same is true for the role of mitochondria in the sperm function of boars. In this regard, bioenergetic analyzes were carried out on boar sperm mitochondria aimed at defining how energy production is obtained with the aim of understanding whether their metabolism depends exclusively on glycolysis and a further study was carried out on their energy metabolism and its variability after one day from the collection of the semen, to improve knowledge on the still controversial role of mitochondria in spermatid function of boars;

B) non-specialized cells with the ability to renew themselves over long periods are termed stem cells<sup>215</sup>. Mesenchymal stem cells (MSCs) originate from the mesoderm<sup>216,217</sup> and have the capacity for multilinear differentiation<sup>218,219</sup>. Thanks to their properties, they are applied in cell therapy and tissue engineering in veterinary medicine, in particular for companion dogs which often suffer from age-related diseases. Therefore, they require new treatments and preventive strategies. Dog-derived MSCs have been isolated from a variety of adult tissues, such as adipose tissue (AT) which contains a high number of MSCs, making it a viable source of stem cells for heterologous use<sup>220</sup>.

In canine species, the clinical use of AT-MSCs is versatile due to their differentiation potential and the secretion of numerous immunomodulatory factors<sup>221</sup>. MSCs derived from fetal adnexa, such as umbilical cord matrix (UC), which is discarded at delivery, could overcome many of the limitations of adult tissue-derived MSCs, such as the invasive procedure required for sample retrieval<sup>222,223</sup>. Due to their out-of-body nature, these cells are easy to obtain non-invasively<sup>224,225</sup>. The study of metabolic and bioenergetic profiles carried out in this thesis work allows us to better understand the selected biological characteristics, such as cell proliferation, differentiation potential, molecular profile, to provide a general model of the characteristics of these cells as a first step for their potential future use in therapy;

C) the most physiologically representative cell line of the human intestinal barrier is the IPEC-J2 cell line, isolated from porcine small intestine. IPEC-J2 cells grow as a polarized monolayer made compact by the lateral expression of tight junction proteins<sup>226</sup>, their apical side is endowed with microvilli and produces mucin by recreating the protective mucous layer *in vivo*<sup>227</sup>. Furthermore, IPEC-J2 express several members of the Toll-like receptor family important molecules for the recognition of pathogenic components<sup>228</sup>; all typical characteristics of an epithelial phenotype. IPEC-J2 cell line was selected as an *in vitro* model to investigate the mechanisms of action at the biochemical and molecular level of a variety of compounds in the mammalian intestine. Overall, IPEC-J2 cells represent a favourable *in vitro* model for research applications, being an ideal tool for studying epithelial transport, interaction with enteric pathogens, as well as the effects of probiotics and nutrients. The IPEC-J2 cells were successfully cultured by adding primarily fetal bovine serum (FBS), to provide a wide variety of nutrients, transport proteins, hormone attachment and growth factors. However, the amount and type of serum added to the culture medium of IPEC-J2 cells induce a spontaneous differentiation process that modifies the functional parameters involved in the formation of a polarized monolayer with low or high transepithelial electrical resistance (TEER)<sup>229</sup>. To date, the energy metabolism of these cells has been little explored,

therefore, the effect of different serum concentrations on the energy metabolism of IPEC-J2 has been studied, as well as changes in functional properties, to better understand the physiological changes in the enterocytes during nutrient absorption. Thanks to their characteristics, IPEC-J2 cells provide an excellent *in vitro* model for studying the effects of VKs on cellular bioenergetics. Enterocytes are not only directly involved in the absorption of VKs but are also in proximity to the intestinal microbiota that supplies VK2. The mitochondrial function of enterocytes is essential for intestinal permeability therefore it is important to study their bioenergetics. Mitochondrial uncoupling increases intestinal permeability generating local and systemic inflammation that is associated with the development of inflammatory bowel disease<sup>176</sup>.



## Sperm function and mitochondrial activity: An insight on boar sperm metabolism

Salvatore Nesci, Marcella Spinaci, Giovanna Galeati, Chiara Nerozzi, Alessandra Pagliarani, Cristina Algieri, Carlo Tamanini, Diego Bucci\*

Department of Veterinary Medical Sciences, Alma Mater Studiorum – University of Bologna, Via Tolara di Sopra 50, 40064, Ozzano dell'Emilia, BO, Italy

### ARTICLE INFO

#### Article history:

Received 17 September 2019

Received in revised form

6 December 2019

Accepted 4 January 2020

Available online 7 January 2020

### ABSTRACT

In this study boar sperm mitochondrial activity was studied and deepened in order to delineate the main metabolic strategies used by boar sperm to obtain energy and to link them to sperm function.

Boar spermatozoa were collected, diluted at  $30 \times 10^6$  spz/mL and incubated for 1 h with: Rotenone (ROT), complex I inhibitor, Dimethyl-malonate (DMM), complex II inhibitor, antimycin A (ANTI), complex III inhibitor, oligomycin (OLIGO), ATP synthase inhibitor, Carbonyl cyanide m-chlorophenyl hydrazone (CCCP), uncoupling agent, 2-deoxy-glucose (2DG), glucose agonist, and Dimethyl sulphoxide (DMSO) as control vehicle. Viability and mitochondrial membrane potential (Sybr14/PI/JC1 staining) and sperm motility (using CASA system) were assayed after incubation.

ROT, ANTI, OLIGO and CCCP significantly reduced total and progressive motility as well as cell velocities; ANTI and CCCP depressed mitochondrial membrane potential but did not affect cell viability. Cluster analysis of kinematic parameters showed some interesting features of sperm subpopulations: ANTI and CCCP caused a shift in sperm subpopulation towards “slow non progressive” cells, OLIGO and ROT caused a shift towards “average” and “slow non progressive” cells, while DMM and 2DG increased the “fast progressive” cells subpopulation.

Sperm mitochondrial respiration and substrate oxidation, assayed polarographically and spectrofluorimetrically, respectively pointed out a high ATP turnover and a low spare respiratory capacity, mainly linked to the NADH-O<sub>2</sub> oxidase activity. Therefore, boar spermatozoa heavily rely on mitochondrial oxidative phosphorylation, and especially on Complex I activity, to produce ATP and fuel motility.

© 2020 Elsevier Inc. All rights reserved.

### 1. Introduction

Mammalian sperm cells have the central role to deliver the haploid male genome to the egg. To do this, sperm cells should go along the female genital tract and be integer from a morphological and a functional point of view [1].

It is well-known that sperm cells use different metabolic substrates to generate energy for the different cell functions such as motility, capacitation and sperm-oocyte interactions [2–4]. Various studies focused on the metabolic strategy of sperm cells and on the involvement of mitochondria in energy supplying system [5–7]. Some mammalian species, such as humans, mice and pigs, are reported to preferentially use glycolysis, while equine mainly uses mitochondrial oxidative phosphorylation (OXPHOS); others,

namely bovine, exploit an intermediate strategy to fuel energy pathways [1,3,4,8–10].

Interestingly, mitochondria are known to rule different sperm functions [4,11–14] and to physiologically produce reactive oxygen species (ROS), which address cell signaling pathways [15]. However, any impairment of the mitochondrial electron transport chain increases ROS level, causing oxidative damage to biomolecules [16] and detrimental effects on sperm quality (DNA integrity, membrane stability) and functions (energy production, motility, capacitation).

To explore the relevance of mitochondria in sperm bioenergetics, previous studies aimed at identifying the specific function of each respiratory complex both by testing selective inhibitors of each complex or by fueling the respiratory chain by substrates entering specific steps [5,7,17].

To date, the most complete studies were performed in boar and stallion spermatozoa as representatives of the most diversified

\* Corresponding author.

E-mail address: [diego.bucci3@unibo.it](mailto:diego.bucci3@unibo.it) (D. Bucci).

metabolic strategies in mammalian spermatozoa. Accordingly, boar spermatozoa have been suggested to use almost 95% glycolysis to fulfil energy requirements [2,3,18], while horse spermatozoa are more strictly dependent on mitochondrial oxidative phosphorylation [5,6,9].

Studies on mitochondrial functions in stallion and boar spermatozoa also demonstrated oxygen consumption coupled to ATP synthesis [5,17]. Mitochondrial respiration coupled to OXPHOS is the main ATP production system [19] and, under aerobic conditions, it is preferred to cellular acidification due to glycolysis. Sperm motility and fertilizing ability rely on the availability of ATP, the energy currency of the cell, in turn dependent on the mitochondrial status [20]. Finally, mitochondrial activity was associated to sperm capacitation in “*in vitro*” studies [5,17,21–23].

However, mitochondrial activities are not the unique bioenergetic source for sperm motility in many species and glycolysis can also be exploited to maintain sperm functions.

Whether boar spermatozoa are specifically dependent on glycolysis for their energy supply still remain to be defined; the same is true for the role of mitochondria in boar sperm function. The present study, which focuses on boar sperm mitochondria, combines two distinct approaches, namely functional investigations (motility and mitochondrial membrane potential linked to cell viability) and bioenergetic analyses, addressed to define how energy production is obtained. The aim is to understand if boar spermatozoa depend exclusively on glycolysis for their functionality and to improve the knowledge on the still controversial role of mitochondria in boar sperm function.

## 2. Materials and methods

Unless otherwise specified, all chemicals were purchased from Sigma-Aldrich (Saint-Louis, MO, USA).

Boar semen was purchased from a commercial company (Inseme S.P.A., Modena, Italy). Sperm samples were sent to the laboratory within 2 h from collection, washed and resuspended in Androhep [24] at a final concentration of  $30 \times 10^6$  spz/mL unless otherwise specified. Minimum requirement for inclusion of sperm sample in the study was viability above 80% at the arrival at the laboratory.

**Experiment 1.** Assessment of functional activity of spermatozoa using different specific inhibitors.

Twenty-four ejaculates from 10 boars were used in this experiment. Sperm cells were incubated for 1 h at 37 °C with Rotenone 5 μM (ROT) complex I inhibitor, Dimethyl-malonate 10 mM (DMM), complex II inhibitor, Carbonyl cyanide *m*-chlorophenyl hydrazone 5 μM (CCCP), uncoupling agent, 2-deoxy-glucose 10 mM (2DG) glucose agonist, antimycin A 1 μg/mL (ANTI), complex III inhibitor, oligomycin 4 μg/mL (OLIGO), ATP synthase inhibitor, and 2 μL Dimethyl sulphoxide (DMSO), control vehicle. At the end of the incubation period mitochondrial respiration, sperm motility, sperm viability and mitochondrial activity were evaluated as described below.

**Experiment 2.** Influence of complex I and II activity on sperm parameters.

Eight ejaculates from 5 boars were used in this experiment. This experiment was performed to focus on complex I and II activity and to evaluate the effects of ROT, DMM and of their combination incubating sperm cells for 1 h at 37 °C. Sperm motility, viability and mitochondrial activity were assayed.

**Experiment 3.** Mitochondrial respiration.

Five ejaculates from 3 different boars were used in this experiment. The experiment was conducted to focus on sperm ability to produce energy by mitochondrial oxidative phosphorylation by means of the methods described in section 2.1.3.

**Experiment 4.** Mitochondrial substrates oxidation.

Seven ejaculates from 3 different boars were used in this experiment. The experiment was conducted to focus on activity of complex I and II and their capability to oxidate different substrates, as reported in section 2.1.4.

### 2.1. Motility assessment

Sperm motility was measured by a computer-assisted sperm analysis system, using the open source Image J BGM plugin as described by Giaretta et al. [25]. Briefly, a Leitz diaphan microscope (Wild Leitz GmbH, D6330, Wetzlar, Germany) with a 10x plan objective with positive phase-contrast was used. The microscope was equipped with a Z31A Ascon technologic heated stage (Ascon technologic, PV – IT). The video camera, 3.1-megapixel CMOS USB 2.0 Infinity1-3 Camera (Lumenera corporation, Ottawa, ON, Canada), was coupled to the microscope by a c-mount adapter and videos were registered for 3 s at a resolution of 800x600 pixel and 60 frames/sec (fps). Images were recorded on a hard drive using the Infinity analyzing and capture software 6.4 (Lumenera corporation) and converted to avi format for subsequent analysis using the BGM Image J plugin.

Prior to any observation, spermatozoa ( $30 \times 10^6$  sperm/mL) were loaded onto a fixed height Leja Chamber SC 20-01-04-B (Leja, CIUDAD; The Netherlands). Five videos of separate fields and lasting 3 s each were recorded per sperm sample. Sperm motility endpoints assessed were: percent of total motile spermatozoa (TM), percent of progressive spermatozoa (PM), curvilinear velocity (VCL) and mean velocity (VAP), straight-line velocity (VSL), straightness (STR), linearity (LIN), beat cross frequency (BCF), lateral head displacement (ALH) and wobble (WOB). The setting parameters of the program were the followings: frames per second 60, number of frames 45, threshold path minimum VSL for motile sperm 10 μm/s; min VAP for motile 15 μm/s; min VCL for motile 25 μm/s; VAP cutoff for Progressive cells 25 μm/s; STR cutoff for Progressive cells 75%.

### 2.2. Sperm viability and mitochondrial membrane potential

For each sample, an aliquot (30 μL) of semen ( $30 \times 10^6$  spz/mL) was incubated with 2 μL of a 300 μM propidium iodide (PI) stock solution (final concentration 16.7 μM), 2 μL of a 10 μM SYBR green-14 stock solution (final concentration 0.56 μM), both obtained from the live/dead sperm viability kit (Molecular Probes, Inc.) and 2 μL of a 150 μM JC-1 solution (final concentration 8.3 μM) for 20 min at 37 °C in the dark. Ten μL of the sperm suspension were then placed on a slide and at least 200 spermatozoa per sample were scored using the above described fluorescence microscope. Spermatozoa stained with SYBR-14 but not with PI were considered as viable (SYBR-14+/PI-), whereas SYBR-14+/PI+ and SYBR-14-/PI+ spermatozoa were considered as non-viable. JC-1 monomers emit green fluorescence in mitochondria with low membrane potential (JC-1-) and form aggregates in mitochondria with high membrane potential (JC-1+), then emitting a bright red-orange fluorescence. Therefore, those viable sperm showing orange-red fluorescence in the mid piece (JC-1+) were considered as viable sperm with high mitochondrial membrane potential (SYBR-14+/PI-/JC-1+).

### 2.3. Mitochondrial respiration

The mitochondrial respiration was polarographically evaluated as oxygen consumption rate (OCR) was polarographically evaluated by Clark-type electrode using the Oxytherm System (Hansatech Instruments) at 38 °C in a reaction medium (1 mL) containing  $10^6$  cells in Androhep.

OCR values expressed as nmol O<sub>2</sub>/min/10<sup>6</sup> cells were recorded after sequential addition of selective inhibitors. The ATP synthase inhibitor OLIGO was used to prevent mitochondrial ATP production by OXPHOS and address spermatozoa to glycolysis. The ionophore FCCP, which makes the mitochondrial membrane permeable to H<sup>+</sup>, was employed to uncouple mitochondria and prevent ATP synthesis. Inhibition of the respiratory chain was obtained by the myxothiazol (Complex III inhibitor) plus ROT (Complex I inhibitor) mixture.

The OCR values before and after sequential addition of these inhibitors were used to calculate the bioenergetics parameters currently used to characterize mitochondrial respiration [26].

Basal respiration was detected as baseline OCR before OLIGO addition. Minimal respiration was measured as OCR in the presence of 4 µg/mL OLIGO, while maximal respiration was measured as OCR after addition of 0.5 µM FCCP. Non-mitochondrial respiration was evaluated as OCR in the presence of 1 µg/mL myxothiazol plus 4 µM ROT. The ATP turnover or oligomycin-sensitive respiration was obtained from the difference between the basal respiration and the minimal respiration (OCR in presence of OLIGO). Finally, the difference between the maximal and the basal respiration provided the spare capacity, which represents the ability to respond to an increased energy demand and can be considered as a measure of the flexibility of the OXPHOS machinery [26].

### 2.4. Mitochondrial substrate oxidation

The capability of substrate oxidation was assayed in a reaction medium (2 mL) containing  $10^6$  cells in Androhep at 38 °C. The oxidation of NADH and FADH<sub>2</sub>, which transfer electrons to Complex I and II, respectively was detected by exploiting the auto-fluorescence of the reduced form of these coenzymes [27]. Auto-fluorescence intensity of NADH (excitation 360 nm, emission 455 nm) and FADH<sub>2</sub> (excitation 450 nm, emission 520 nm) were monitored by Shimadzu RF-6000 spectrofluorophotometer. NADH and FADH<sub>2</sub> oxidation were measured as decrease in the auto-fluorescence intensity after addition of the following inhibitors: 2 µM ROT, 5 mM DDM (only in FADH<sub>2</sub> autofluorescence) in order to inhibit complexes I and II, respectively; 1 µg/mL OLIGO, which blocks proton flux across the F1FO-ATP synthase and ATP generation, to verify the coupling between substrate oxidation and ATP synthesis and 0.5 µM FCCP, which makes the mitochondrial membrane permeable to protons, to maximize NADH or FADH<sub>2</sub> oxidation at minimal concentration of these substrates intensity, expressed as NADH or FADH<sub>2</sub> arbitrary units/min/10<sup>6</sup> cells, was evaluated by LabSolutions RF software.

## 3. Results

### 3.1. Sperm motility and mitochondrial activity (Experiments 1 and 2)

Sperm motility parameters and mitochondrial activity assessed by JC1 are reported in Table 1.

The total and progressive motility, as well as the three velocity parameters (VCL, VAP, VSL) and lateral head displacement (ALH) are negatively affected by the mitochondrial inhibitors ROT, ANTI, OLIGO and CCCP, that equally depress motility kinematics. Beat

cross frequency (BCF) is significantly diminished (in comparison with control) only in CCCP group, while wobble (WOB) is negatively affected only by ROT.

Mitochondrial membrane potential significantly drops due to CCCP and ANTI treatment while sperm viability (JC1 positive and negative cells) is unaffected.

Table 2 shows the results obtained in sperm treated with complex I and II inhibitors namely ROT, DMM and their combination. Apparently, the Complex I inhibitor ROT is the main responsible for the observed effects, since the treatment with a binary mixture of ROT plus the Complex II inhibitor DMM shows the same inhibition extent as the ROT treatment on all the parameters under study, apart from STR, LIN, BCF and mitochondrial activity, unaffected by all treatments.

Principal component analysis results used to determine clusters are reported in the supplementary file 1.

Cluster analysis reveals some important features of motile sperm subpopulations: four different clusters emerged from the analysis that, on the basis of mean kinematic parameters values, were named as: rapid progressive, rapid non progressive, average; slow non progressive. Data are presented in Table 3. Spermatozoa were assigned to the different clusters and, as reported in Table 3, significant differences in the percentages of spermatozoa belonging to each subpopulation were found between treatments. It is evident that DMM and 2DG induce a shift in sperm subpopulation and an increase in rapid progressive cell subpopulation. ANTI and CCCP determine an increase in slow non progressive cells subpopulation, while OLIGO and ROT determine an increase in both average and slow non progressive sperm subpopulations. Finally, ROT + DMM determine a strong shift towards slow non progressive and average sperm subpopulation.

### 3.2. Sperm mitochondrial respiration and substrate oxidation (Experiments 3 and 4)

The OCR evaluation in absence or presence of the mitochondrial inhibitors allows the bioenergetics characterization of boar sperm mitochondria. The basal respiration attains 65% of the maximal respiration detected in the presence of FCCP (0.167 nmol O<sub>2</sub>/min/10<sup>6</sup> cells) and is inhibited by 90% with OLIGO. The calculated ATP turnover is 0.097 nmol O<sub>2</sub>/min/10<sup>6</sup> cells. The strong inhibition of respiration by OLIGO is the result of a good coupling efficiency (0.914 A.U.), close to the unit, which is the maximum attainable. The mitochondrial ATP production rate (486.85 pmol ATP/min), indirectly obtained from ATP turnover, provides how fast cells work to produce ATP. Moreover, sperm mitochondria are characterized by a high phosphorylation efficiency as shown by the high respiratory control ratio (7.56 A.U.). The ratio of the FCCP-stimulated respiration to the respiration in the presence of OLIGO, that is the ability of the cell to convert into ATP the activities of respiratory complexes, and low spare respiratory capacity (0.083 nmol O<sub>2</sub>/min/10<sup>6</sup> cells) is a good diagnostic tool in bioenergetics because, by indicating the ability of mitochondria to respond to an increased energy demand, it can show how close to its bioenergetic limit a cell is working (Fig. 1A). These data show that sperm mitochondria work slightly below this limit.

The fluorimetric detection of the mitochondrial oxidation of NADH and FADH<sub>2</sub>, which transfer electrons to Complex I and II, respectively, provides information on the respiratory complexes in sperm mitochondria preferentially used to feed the electron transport chain. ROT induces a striking decrease in NADH auto-fluorescence intensity (Fig. 1B), which suggests that NADH is oxidized through activation of mitochondrial respiration. The inhibition of ADP phosphorylation by OLIGO in coupled sperm mitochondria blocks the respiration and maintains the NADH level.

**Table 1**  
Motility parameters and mitochondrial activity of differently treated spermatozoa.

Treat	TM	PM	VCL	VAP	VSL	STR	LIN	ALH	BCF	WOB	JC1+live	JC1-live
CTR	52.32 ± 13.49 <sup>a</sup>	28.23 ± 8.04 <sup>a</sup>	153.98 ± 36.12 <sup>a</sup>	73.23 ± 17.02 <sup>a</sup>	56.28 ± 13.84 <sup>a</sup>	75.87 ± 4.43	39.52 ± 6.74	6.03 ± 1.36 <sup>a</sup>	25.22 ± 2.18 <sup>a</sup>	48.43 ± 7.72 <sup>ab</sup>	83.90 ± 7.67 <sup>a</sup>	0.18 ± 0.27 <sup>a</sup>
ROT	16.48 ± 7.79 <sup>b</sup>	6.00 ± 4.24 <sup>b</sup>	100.69 ± 32.89 <sup>b</sup>	34.78 ± 6.79 <sup>b</sup>	25.47 ± 5.11 <sup>b</sup>	75.26 ± 7.08	36.68 ± 11.67	3.81 ± 1.02 <sup>b</sup>	24.49 ± 2.07 <sup>ab</sup>	38.11 ± 9.31 <sup>b</sup>	81.24 ± 8.77 <sup>a</sup>	0.52 ± 1.35 <sup>a</sup>
DMM	55.15 ± 13.96 <sup>a</sup>	28.54 ± 10.55 <sup>a</sup>	166.36 ± 30.08 <sup>a</sup>	81.96 ± 15.72 <sup>a</sup>	60.69 ± 13.71 <sup>a</sup>	74.05 ± 6.86	39.16 ± 7.88	6.54 ± 1.00 <sup>a</sup>	24.27 ± 2.17 <sup>ab</sup>	50.37 ± 9.65 <sup>a</sup>	84.22 ± 6.20 <sup>a</sup>	0.05 ± 0.13 <sup>a</sup>
ANTI	10.46 ± 8.94 <sup>b</sup>	3.92 ± 3.91 <sup>b</sup>	97.42 ± 58.13 <sup>b</sup>	36.14 ± 14.08 <sup>b</sup>	26.72 ± 9.16 <sup>b</sup>	75.79 ± 11.02	44.43 ± 16.54	4.02 ± 2.13 <sup>b</sup>	22.69 ± 2.86 <sup>ab</sup>	46.86 ± 16.45 <sup>ab</sup>	0.10 ± 0.30 <sup>b</sup>	81.87 ± 5.81 <sup>b</sup>
OLIGO	12.56 ± 9.16 <sup>b</sup>	4.76 ± 4.13 <sup>b</sup>	109.46 ± 54.83 <sup>b</sup>	37.35 ± 12.20 <sup>b</sup>	26.79 ± 8.46 <sup>b</sup>	73.79 ± 6.93	39.57 ± 15.71	4.26 ± 1.98 <sup>b</sup>	24.44 ± 3.61 <sup>ab</sup>	42.00 ± 18.08 <sup>ab</sup>	83.62 ± 4.75 <sup>a</sup>	0.07 ± 0.19 <sup>a</sup>
CCCP	14.52 ± 8.04 <sup>b</sup>	5.60 ± 5.08 <sup>b</sup>	86.11 ± 30.13 <sup>b</sup>	33.32 ± 10.44 <sup>b</sup>	25.26 ± 8.46 <sup>b</sup>	77.15 ± 6.80	40.00 ± 10.85	3.52 ± 1.41 <sup>b</sup>	22.27 ± 2.48 <sup>b</sup>	43.23 ± 8.15 <sup>ab</sup>	0.03 ± 0.11 <sup>b</sup>	78.15 ± 7.48 <sup>b</sup>
2DG	54.25 ± 10.71 <sup>a</sup>	28.47 ± 6.48 <sup>a</sup>	163.70 ± 30.70 <sup>a</sup>	75.81 ± 14.82 <sup>a</sup>	56.96 ± 12.60 <sup>a</sup>	74.18 ± 4.92	37.64 ± 5.75	6.36 ± 1.14 <sup>a</sup>	25.31 ± 2.43 <sup>ab</sup>	46.91 ± 7.53 <sup>ab</sup>	82.66 ± 9.69 <sup>a</sup>	0.08 ± 0.19 <sup>a</sup>

Sperm motility parameters are: total motility (TM), progressive motility (PM), ALH amplitude of lateral head displacement ( $\mu\text{M}$ ); BCF beat cross frequency (Hz); LIN linearity (%); STR straightness (%); VCL curvilinear velocity ( $\mu\text{m}/\text{sec}$ ); VAP average path velocity ( $\mu\text{m}/\text{sec}$ ); VSL straight line velocity ( $\mu\text{m}/\text{sec}$ ), wobble (%) WOB; JC1+ live: living cells % with high mitochondrial membrane potential; JC1 - live: living cells % with low mitochondrial membrane potential. 24 ejaculates from 10 boars were used in this experiment; different superscripts within a column indicate a significant difference for  $p < 0.05$ .

CTR: control; ROT: rotenone; DMM dimetil-malonate; ANTI: antimycin; OLIGO: oligomycin; CCCP: carbonyl cyanide m-chlorophenyl hydrazine; 2DG: 2-desoxy-glucose.

**Table 2**  
Mean values for motility parameters and mitochondrial activity in differently treated spermatozoa.

Treatment	TM	PM	VCL	VAP	VSL	STR	LIN	ALH	BCF	WOB	JC1+live	JC1-live
CTR	42.93 ± 9.68 <sup>a</sup>	24.88 ± 3.96 <sup>a</sup>	142.56 ± 36.14 <sup>a</sup>	75.67 ± 18.39 <sup>a</sup>	59.44 ± 13.72 <sup>a</sup>	78.13 ± 3.52	43.88 ± 7.86	5.88 ± 1.38 <sup>a</sup>	25.30 ± 2.72 <sup>ab</sup>	54.00 ± 8.4 <sup>a</sup>	85.89 ± 3.65	0.00 ± 0.00
ROT	16.65 ± 8.77 <sup>b</sup>	7.08 ± 4.61 <sup>b</sup>	86.18 ± 25.65 <sup>b</sup>	34.23 ± 6.01 <sup>b</sup>	26.40 ± 5.45 <sup>b</sup>	78.25 ± 7.65	41.63 ± 13.88	3.46 ± 0.83 <sup>b</sup>	24.96 ± 1.71 <sup>ab</sup>	42.88 ± 10.74 <sup>b</sup>	79.41 ± 11.49	0.28 ± 0.61
DMM	49.75 ± 18.02 <sup>a</sup>	29.24 ± 12.01 <sup>a</sup>	154.79 ± 33.79 <sup>a</sup>	83.79 ± 18.02 <sup>a</sup>	64.92 ± 15.67 <sup>a</sup>	78.0 ± 4.14	44.12 ± 7.66	6.30 ± 1.21 <sup>a</sup>	24.32 ± 2.15 <sup>a</sup>	55.25 ± 11.54 <sup>a</sup>	84.36 ± 4.50	0.00 ± 0.00
DMM + ROT	8.77 ± 3.73 <sup>b</sup>	2.74 ± 2.11 <sup>b</sup>	79.24 ± 15.21 <sup>b</sup>	29.81 ± 6.38 <sup>b</sup>	23.03 ± 4.94 <sup>b</sup>	79.88 ± 5.64	38.62 ± 8.14	3.01 ± 0.57 <sup>b</sup>	27.74 ± 2.59 <sup>b</sup>	41.00 ± 5.50 <sup>b</sup>	84.30 ± 4.33	0.19 ± 0.27

Sperm motility parameters are: TM total motility, PM progressive motility, VCL curvilinear velocity ( $\mu\text{m}/\text{sec}$ ), VAP average path velocity ( $\mu\text{m}/\text{sec}$ ), VSL straight line velocity ( $\mu\text{m}/\text{sec}$ ), STR straightness (%), LIN linearity (%), ALH amplitude of lateral head displacement ( $\mu\text{m}$ ); BCF beat cross frequency (Hz), WOB wobble (%). 8 ejaculates from 5 boars were used in this experiment. Different superscripts within a column indicate a significant difference for  $p < 0.05$ .

CTR: control; ROT: rotenone; DMM Dimetil-malonate.

**Table 3**  
Cluster analysis results. Different distribution of spermatozoa subpopulation % depending on cluster and treatment.

Treatment	Rapid non progressive	Rapid progressive	Average	Slow non progressive
2DG	13.7 <sup>a</sup>	47 <sup>c</sup>	24.9 <sup>a</sup>	14.4 <sup>c</sup>
ANTI	20.7 <sup>b</sup>	7.8 <sup>b</sup>	25.4 <sup>a</sup>	46.1 <sup>b</sup>
CCCP	11.8 <sup>a</sup>	9.3 <sup>b</sup>	29.3 <sup>a</sup>	49.6 <sup>b</sup>
CTR	11.7 <sup>a</sup>	38.1 <sup>a</sup>	28.8 <sup>a</sup>	21.4 <sup>a</sup>
DMM	11.5 <sup>a</sup>	47.2 <sup>c</sup>	24.8 <sup>a</sup>	16.5 <sup>c</sup>
DMM + ROT	6.4 <sup>c</sup>	2.9 <sup>b</sup>	36.4 <sup>b</sup>	54.3 <sup>b</sup>
OLIGO	17.1 <sup>b</sup>	8.3 <sup>b</sup>	41.4 <sup>b</sup>	33.3 <sup>b</sup>
ROT	11.6 <sup>a</sup>	7.4 <sup>b</sup>	36.3 <sup>b</sup>	44.7 <sup>b</sup>

Each row represents the percentage of cells belonging to the different cluster (considering 100% the sum of percentage for each treatment). Different superscripts within a column indicate significant differences between treatments (chi square test,  $p < 0.001$ ).

A total of 10658 sperm cells were analysed, respectively: CTR 3403 cells; 2DG 1499 cells; 3412 cells; DMM + ROT 140 cells; ANTI 421 cells; OLIGO 532 cells; ROT 768 cells.

Interesting, the FCCP-dependent NADH oxidation, which mirrors the maximal respiration, attains the same value as the basal respiration (control) (Fig. 1B). FADH<sub>2</sub> oxidation is inhibited by DMM, and by OLIGO, thus confirming that mitochondrial respiration is stimulated by complex II substrates and coupled to ATP synthesis. However, FADH<sub>2</sub> autofluorescence intensity does not increase in the presence of mitochondrial uncoupler FCCP (Fig. 1C). Thus, the NADH and FADH<sub>2</sub> autofluorescence intensity drop clearly shows that ROT, by blocking Complex I, prevents any transfer of reducing equivalents in the oxidation-reduction reactions during sperm mitochondrial respiration (Fig. 1B and C).

#### 4. Discussion

In this study bioenergetic analyses clearly show that boar sperm mitochondria exploit OXPHOS and are susceptible to OLIGO, to the uncoupler FCCP and to the classical inhibitors of respiratory complexes. Interestingly, since the basal respiration is close to the FCCP-stimulated maximal respiration, the spare respiratory capacity, which indicates the capability of producing extra ATP by OXPHOS to respond to an increased energy demand, is low. Therefore, under physiological conditions, sperm mitochondria work at their maximal capacity to produce energy. Accordingly, the close-to-unit respiratory control ratio, which indicates a good coupling efficiency, shows that sperm mitochondria efficiently exploit the electrochemical gradient generated by mitochondrial respiration to phosphorylate ADP (Fig. 1A). Noteworthy, NADH oxidation is preferred to FADH<sub>2</sub> one. Since neither NADH nor FADH<sub>2</sub> autofluorescence is stimulated by FCCP, both oxidases (Complexes I and II) attain the maximal activities. Moreover, the high ROT inhibition suggests that mitochondrial respiration mainly depends on complex I (Fig. 1B and C). Consistently, the data from the Experiment 2 (Table 2) show that sperm motility and mitochondrial potential are apparently unaffected by DMM treatment, while the inhibition of motility (total and progressive motility as well as the other main kinematic parameters) by ROT is maintained when spermatozoa are incubated with ROT and DMM in combination.

In mammals the number of ATP molecules synthesized by OXPHOS for each electron pair transferred via the respiratory chain (known as P/O ratio) from NADH to O<sub>2</sub> is 2.7, while for FADH<sub>2</sub> oxidation is 1.6 [28]. Most likely, boar sperm mitochondria require an efficient OXPHOS and possess an adequate bioenergetics machinery to preferentially exploit Complex I, which is more advantageous in terms of ATP production, to supply the electron transport pathway.

Motility is the prominent ATP-consuming activity of sperm cells. Interestingly, motility (total and progressive) is reduced by OLIGO, which blocks the ATP synthase (Complex V), and by ROT, which inhibits Complex I. Similarly, ANTI, complex III inhibitor, prevents the inner mitochondrial membrane polarization required for ATP

synthesis and, as a consequence, it depresses total and progressive motility like OLIGO, ROT and CCCP. On the contrary DMM, inhibitor of complex II, does not affect total and progressive motility, as well as other sperm kinematic parameters. To sum up, sperm motility is reduced under two conditions: insufficient ATP availability, if complex V cannot synthesize ATP, and inhibition of Complex I and III, which cannot energize the mitochondrial membrane. Indeed, CCCP, by dissipating the transmembrane electrochemical gradient, prevents ATP synthesis by complex V and decreases sperm motility.

Regarding other kinematic parameters, the three velocity parameters (VCL, VAP and VSL) are decreased by ROT, OLIGO, ANTI and CCCP; this fact is interesting as not only the molecules decrease the number of motile sperm, but they even depress their speed, thus making them move more slowly than controls. The same is registered for lateral head displacement; this confirms that the strength of spermatozoa movement is limited by the above-mentioned inhibitors and so they move slowly and with less displacement from the mean trajectory. Interestingly, straightness and linearity are not compromised by the inhibitors and maintain the same levels of the control group; this could mean that the trajectory of sperm cells is not that different when using the inhibitors, but they only move slowly.

The strict relation between motility and mitochondrial activity was demonstrated in horse spermatozoa [7,29] and the activity of OLIGO is also confirmed in the study by Ramió-Lluch [17] in boar sperm cells.

Noteworthy, the mitochondrial membrane potential persists in the presence of OLIGO and ROT, but it is decreased by ANTI and CCCP treatments. Probably other pathways, which do not involve the respiratory complexes I and II, can fuel the respiratory chain via ubiquinone by starting electron transfer from ubiquinol to O<sub>2</sub> directly from complex III (Table 1). Even if mitochondria do not produce ATP, a low ATP level, produced by glycolysis, can maintain a polarized inner mitochondrial membrane to ensure ionic homeostasis. This is confirmed by data from ANTI and CCCP treatments: even if the mitochondrial membrane potential is depressed, sperm cells do not die, since they can sustain membrane integrity.

The addition of 2DG to the incubation medium does not affect sperm motility or the mitochondrial membrane potential. Conversely Davila and colleagues [5], demonstrated that 2DG was able to depress some motility kinematic parameters as well as total motility. Most likely, under our experimental conditions, the presence of glucose in the medium may fuel the glycolytic pathway so as to produce sufficient ATP to avoid the 2DG negative effect on sperm motility.

Some interesting features of sperm subpopulation composition and change after incubation with the different inhibitors are revealed by cluster analysis. As stated above this statistical technique permitted to delineate four different sperm subpopulations. The average sperm subpopulation in control sample showed a high

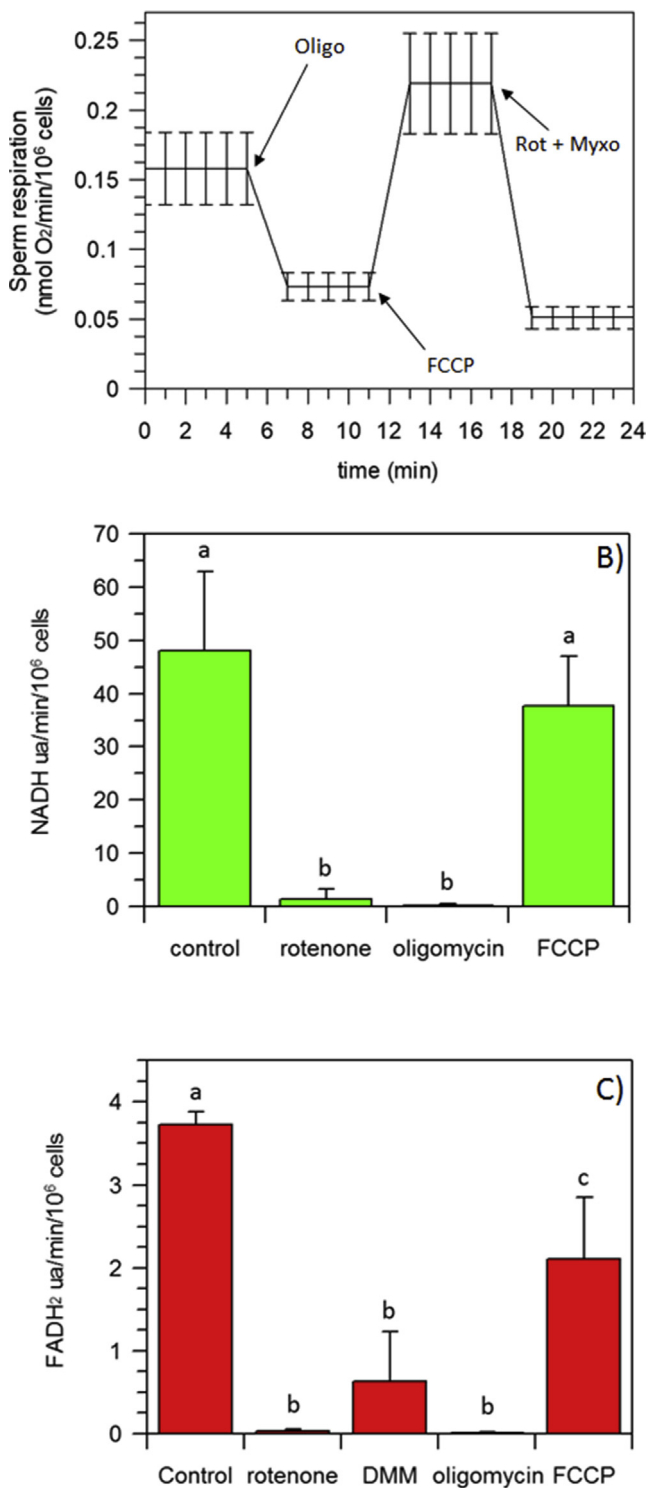


**Fig. 1.** Sperm mitochondria activities. A) Oxygen consumption rates (OCR) before and after sequential additions of oligomycin (OLIGO), carbonyl cyanide-4-(trifluoromethoxy)phenylhydrazone (FCCP), and a mixture of rotenone and Myxothiazol (Rot + Myxo), at the times indicated; B) NADH autofluorescence intensity in spermatozoa exposed to rotenone, oligomycin and FCCP; C) FADH<sub>2</sub> autofluorescence intensity in spermatozoa exposed to rotenone, dimethylmalonate (DMM), oligomycin and FCCP. The data are the mean values  $\pm$  SD (n = 7). Different letters indicate significantly different values within each treatment ( $P \leq 0.05$ ).

amount of rapid progressive cells (around 40%) and “average” cells, with the rapid non progressive cluster [30], not highly represented. It is noteworthy that both 2DG and DMM induced an increase in rapid progressive subpopulation. Rapid progressive cells increase when the mitochondrial oxidation is preferred to the glycolytic pathway in presence of 2DG. Moreover, in mitochondria the NADH-O<sub>2</sub> oxidase produces more ATP than succinate-O<sub>2</sub> oxidase and the rapid progressive subpopulation needs a lot of ATP for motility. Interestingly, succinate oxidation produces ubiquinol (the reduced form of coenzyme Q<sub>10</sub>) that, instead of transferring electrons to Complex III, in energized mitochondria can also drive the energy-dependent NAD<sup>+</sup> reduction by the complex I through the reverse electron transfer mechanism [31]. Conversely, in presence of DMM, which blocks Complex II, Complex I can only work in the forward mode and oxidize NADH. Moreover, “rapid progressive” spermatozoa subpopulation is deeply depressed by OLIGO, ROT, ANTI and CCCP, and an increase of the “slow non progressive” spermatozoa subpopulation is concomitant when ATP synthesis and/or NADH oxidation are inhibited. These data point out the important role of mitochondrial ATP production in boar sperm motility (Table 3).

These features of the different subpopulations were also visible in kinematics parameters resumed in Table 1, but the cluster analysis permitted to better delineate the motility features of these different subpopulation and it is interesting to note that this “unsupervised” statistical technique evidenced a biological feature of sperm cells.

In the present study, the mitochondrial activity characterization reveals that boar sperm total motility and the rate of rapid progressive sperm are markedly dependent on OXPHOS, namely mitochondrial ATP production. Indeed, mitochondria provide sperm with energy in form of ATP produced by the ATP synthase, while respiratory complexes (NADH-O<sub>2</sub> oxidase) indirectly impact ATP synthesis by producing the mitochondrial electrochemical gradient. Accordingly, 2DG has no effect on motility parameters. Consistently, a similar inhibitory effect on sperm motility by ROT and ANTI was observed in stallion sperm [7].

The overall data suggest that boar spermatozoa, even if commonly considered to preferentially exploit glycolysis to obtain energy, heavily rely on mitochondrial OXPHOS for ATP production to fuel motility. Therefore, an impaired mitochondrial activity should be considered as a possible cause of defective boar sperm functions.

#### Authors contributions

All the Authors contributed equally to the writing of this article. DB and SN performed experiments, effected the statistical analysis and organized the experimental design; all the other authors performed the experiments and contributed to experimental design adjustment.

#### Appendix A. Supplementary data

Supplementary data to this article can be found online at <https://doi.org/10.1016/j.theriogenology.2020.01.004>.

#### References

- [1] Storey BT. Mammalian sperm metabolism: oxygen and sugar, friend and foe. *Int J Dev Biol* 2008;52:427–37. <https://doi.org/10.1387/ijdb.072522bs>.
- [2] Rodríguez-Gil J. Mammalian sperm energy resources management and survival during conservation in refrigeration. *Reprod Domest Anim* 2006;41:11–20.
- [3] Rodríguez-Gil JE, Bonet S. Current knowledge on boar sperm metabolism: comparison with other mammalian species. *Theriogenology* 2016;85:4–11. <https://doi.org/10.1016/j.theriogenology.2015.05.005>.
- [4] Moraes CR, Meyers S. The sperm mitochondrion : organelle of many functions.

- Anim Reprod Sci 2018;194:71–80. <https://doi.org/10.1016/j.anireprosci.2018.03.024>.
- [5] Davila MP, Muñoz PM, Bolaños JMG, Stout TAE, Gadella BM, Tapia JA, et al. Mitochondrial ATP is required for the maintenance of membrane integrity in stallion spermatozoa, whereas motility requires both glycolysis and oxidative phosphorylation. *Reproduction* 2016. <https://doi.org/10.1530/REP-16-0409>.
- [6] Peña FJ, Plaza Davila M, Ball B, Squires EL, Martín Muñoz P, Ortega Ferrusola C, et al. The impact of reproductive technologies on stallion mitochondrial function. *Reprod Domest Anim* 2015. <https://doi.org/10.1111/rda.12551>.
- [7] Davila MP, Muñoz PM, Tapia JA, Ferrusola CO, Da Silva CCB, Peña FJ. Inhibition of mitochondrial complex I leads to decreased motility and membrane integrity related to increased hydrogen peroxide and reduced ATP production, while the inhibition of glycolysis has less impact on sperm motility. *PLoS One* 2015. <https://doi.org/10.1371/journal.pone.0138777>.
- [8] Gibb Z, Aitken RJ. The impact of sperm metabolism during in vitro Storage : the stallion as a model. *BioMed Res Int* 2016;2016:8.
- [9] Varner DD, Gibb Z, Aitken RJ. Stallion fertility: a focus on the spermatozoon. *Equine Vet J* 2015;47:16–24. <https://doi.org/10.1111/evj.12308>.
- [10] Bucci D, Rodríguez-Gil JE, Vallorani C, Spinaci M, Galeati G, Tamanini C. GLUTs and mammalian sperm metabolism. *J Androl* 2011;32:348–55. <https://doi.org/10.2164/jandrol.110.011197>.
- [11] Gibb Z, Lambourne SR, Aitken RJ. The paradoxical relationship between stallion fertility and oxidative stress. *Biol Reprod* 2014;91:1–10. <https://doi.org/10.1095/biolreprod.114.118539>.
- [12] Guthrie HD, Welch GR. Effects of reactive oxygen species on sperm function. *Theriogenology* 2012;78:1700–8. <https://doi.org/10.1016/j.theriogenology.2012.05.002>.
- [13] Guthrie HD, Welch GR, Long JA. Mitochondrial function and reactive oxygen species action in relation to boar motility. *Theriogenology* 2008;70:1209–15. <https://doi.org/10.1016/j.theriogenology.2008.06.017>.
- [14] Koppers AJ, De Luliis GN, Finnie JM, McLaughlin EA, Aitken RJ. Significance of mitochondrial reactive oxygen species in the generation of oxidative stress in spermatozoa. *J Clin Endocrinol Metab* 2008;93:3199–207. <https://doi.org/10.1210/jc.2007-2616>.
- [15] Zorov DB, Juhaszova M, Sollott SJ. Mitochondrial reactive oxygen species (ROS) and ROS-induced ROS release. 2019. p. 909–50. <https://doi.org/10.1152/physrev.00026.2013>.
- [16] Murphy MP. Understanding and preventing mitochondrial oxidative damage. *Biochem Soc Trans* 2016;1219–26. <https://doi.org/10.1042/BST20160108>. 0.
- [17] Ramió-Lluch L, Yeste M, Fernández-Novell JM, Estrada E, Rocha L, Cebrían-Pérez JA, et al. Oligomycin A-induced inhibition of mitochondrial ATP-synthase activity suppresses boar sperm motility and in vitro capacitation achievement without modifying overall sperm energy levels. *Reprod Fertil Dev* 2014. <https://doi.org/10.1071/RD13145>.
- [18] Marin S, Chiang K, Bassilian S, Lee W-NP, Boros LG, Fernández-Novell JM, et al. Metabolic strategy of boar spermatozoa revealed by a metabolomic characterization. *FEBS Lett* 2003;554:342–6. [https://doi.org/10.1016/S0014-5793\(03\)01185-2](https://doi.org/10.1016/S0014-5793(03)01185-2).
- [19] Papa S, Capitano G, Papa F. The mechanism of coupling between oxidation-reduction and proton translocation in respiratory chain. *Enzymes* 2018;1:322–49. <https://doi.org/10.1111/brv.12347>.
- [20] Piomboni P, Focarelli R, Stendardi A, Ferramosca A, Zara V. The role of mitochondria in energy production for human sperm motility, vols. 109–24; 2012. <https://doi.org/10.1111/j.1365-2605.2011.01218.x>.
- [21] Ramió-Lluch L, Fernández-Novell J, Peña A, Ramírez A, Concha I, Rodríguez-Gil J. “In vitro” capacitation and further “in vitro” progesterone-induced acrosome exocytosis are linked to specific changes in the expression and acrosome location of protein phosphorylation in serine residues of boar spermatozoa. *Reprod Domest Anim* 2011. <https://doi.org/10.1111/j.1439-0531.2011.01965.x>.
- [22] Ramió-Lluch L, Fernández-Novell JM, Peña A, Bucci D, Rigau T, Rodríguez-Gil JE. “In vitro” capacitation and subsequent acrosome reaction are related to changes in the expression and location of midpiece actin and mitofusin-2 in boar spermatozoa. *Theriogenology* 2012;77:979–88. <https://doi.org/10.1016/j.theriogenology.2011.10.004>.
- [23] Medrano A, Peña A, Rigau T, Rodríguez-Gil JE. Variations in the proportion of glycolytic/non-glycolytic energy substrates modulate sperm membrane integrity and function in diluted boar samples stored at 15–17 degrees C. *Reprod Domest Anim* 2005;40:448–53. <https://doi.org/10.1111/j.1439-0531.2005.00599.x>.
- [24] Johnson LA, Weitze KF, Fiser P, Maxwell WM. Storage of boar semen. *Anim Reprod Sci* 2000;62:143–72.
- [25] Giaretta E, Munerato M, Yeste M, Galeati G, Spinaci M, Tamanini C, et al. Implementing an open-access CASA software for the assessment of stallion sperm motility: relationship with other sperm quality parameters. *Anim Reprod Sci* 2017;176:11–9. <https://doi.org/10.1016/j.anireprosci.2016.11.003>.
- [26] Brand MD, Nicholls DG. Assessing mitochondrial dysfunction in cells. *Biochem J* 2011;435:297–312. <https://doi.org/10.1042/BJ20110162>.
- [27] Bartolomé F, Abramov AY. Measurement of mitochondrial NADH and FAD autofluorescence in live cells. *Methods Mol Biol* 2015. [https://doi.org/10.1007/978-1-4939-2257-4\\_23](https://doi.org/10.1007/978-1-4939-2257-4_23).
- [28] Ferguson SJ. ATP synthase : from sequence to ring size to the Poverkhnost/O ratio 2010;107:16755–6. <https://doi.org/10.1073/pnas.1012260107>.
- [29] Giaretta E, Bucci D, Mari G, Galeati G, Love CC, Tamanini C, et al. Is resveratrol effective in protecting stallion cooled semen? *J Equine Vet Sci* 2014;34:1307–12. <https://doi.org/10.1016/j.jevs.2014.09.011>.
- [30] Bucci D, Spinaci M, Yeste M, Mislei B, Gadani B, Prieto N, et al. Combined effects of resveratrol and epigallocatechin-3-gallate on post thaw boar sperm and IVF parameters. *Theriogenology* 2018;117:16–25. <https://doi.org/10.1016/j.theriogenology.2018.05.016>.
- [31] Gladyshev GV, Grivennikova VG, Vinogradov AD. FMN site-independent energy-linked reverse electron transfer in mitochondrial respiratory complex I. *FEBS Lett* 2018;592:2213–9. <https://doi.org/10.1002/1873-3468.13117>.

## Studies on sperm energy metabolism and time dependance after collection

The production of ATP obtained from mitochondrial OXPHOS and from the glycolytic pathway were quantified by the Seahorse analyzer on freshly collected (0 days) swine spermatozoa. The same was performed on spermatozoa one day after sperm collection (1 day) (*figure 24A*). Total ATP production was greater at 0 days than at 1 day, although the mitochondrial contribution in its synthesis remains always greater (*figure 24B*). What happens after 1 day is a drastic reduction in ATP produced by the mitochondrial pathway (*figure 24A*).

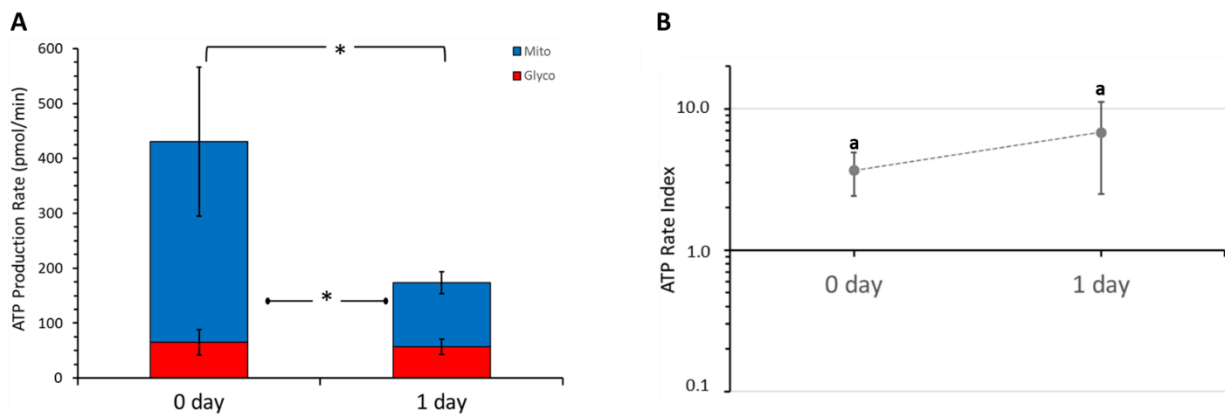


**Figure 24.** Evaluation of ATP production rate by mitochondrial OXPHOS (blue) or by glycolysis (red) on swine spermatozoa at 0 day and 1 day (A). The ATP rate index, calculated as the ratio between the mitochondrial ATP production rate and the glycolytic ATP production rate, is shown on the y-axis (logarithmic scale) in swine spermatozoa at 0 day and 1 day (B). Data represent the mean  $\pm$  SD (vertical bars) from three experiments carried out on distinct cell preparations.

Data relating to mitochondrial respiration were obtained from the sequential use of mitochondrial modulators (*figure 25A*). The results show that the OCR values at 0 days were not different from those after 1 day. In fact, the passage of time did not change any mitochondrial parameters such as: basal respiration, proton leak, maximal respiration, respiratory capacity, non-mitochondrial

oxygen consumption and ATP production (*figure 25B*). Treatment with oligomycin and FCCP mixture, known as mitochondrial stressor, provided the phenogram illustrating the relative baseline and stressed phenotype and metabolic potential response (expressed as baseline%) of the spermatozoa at 0 and 1 day (*figures 25C*) that indicated the cell's ability to meet an energy demand by mitochondrial respiration and glycolysis. Cells showed a greater utilization of mitochondrial respiration (*figure 25D*) when there was an increased demand for ATP (stress condition), in fact the mitochondrial metabolic potential increased approximately 3 times in the same way at 0 and 1 day. On the contrary the potential metabolic glycolytic remained at baseline in both cases (*figure 25C*).

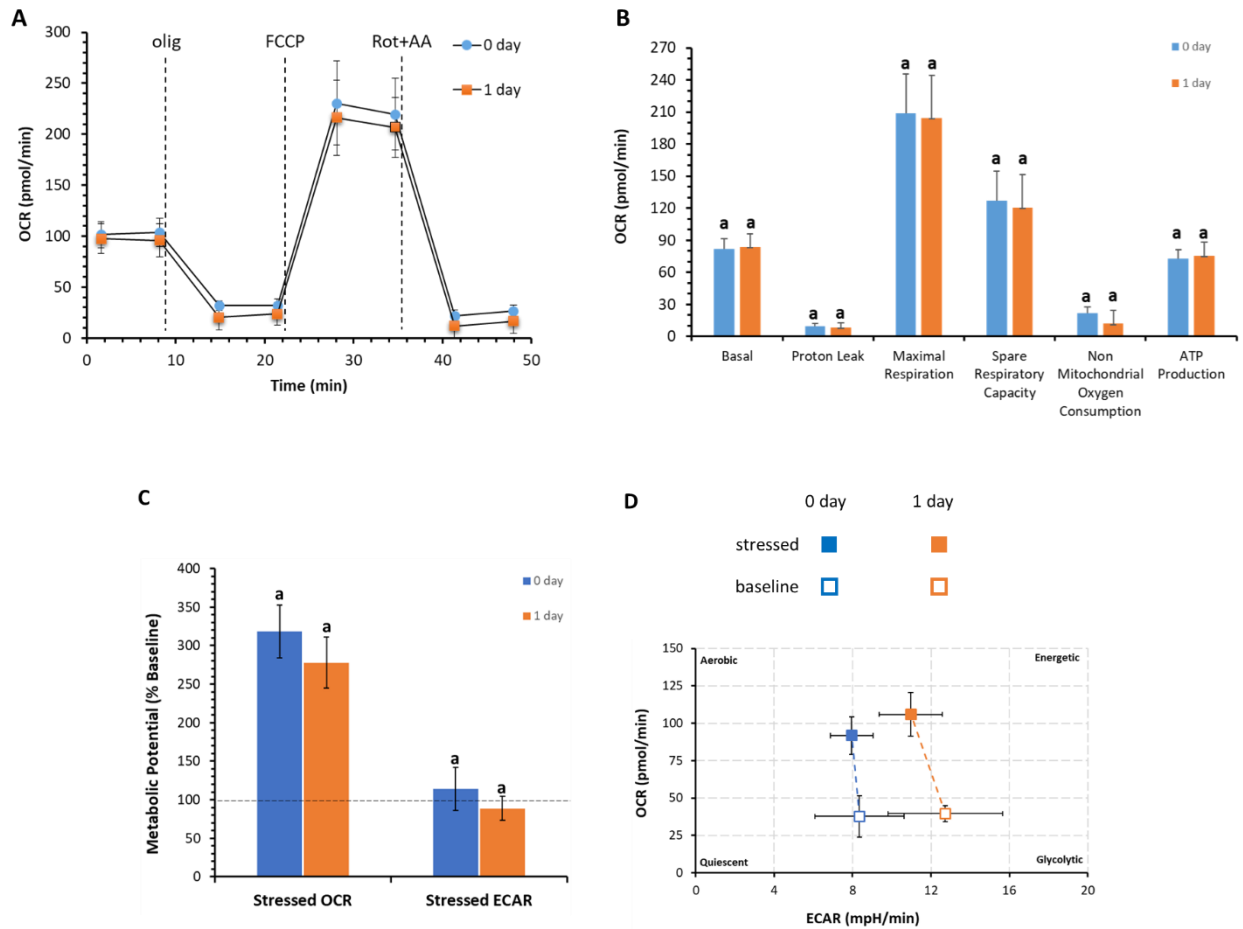


**Figure 25.** Oxygen consumption rate (OCR) at 0 and 1 day under basal respiration conditions and after the addition of  $1.5 \mu\text{M}$  oligomycin (olig),  $1.0 \mu\text{M}$  FCCP and a mixture of  $0.5 \mu\text{M}$  rotenone plus antimycin A (rot+AA) (A) Mitochondrial parameters (basal respiration, ATP production, proton leak, maximal respiration, spare respiratory capacity, non-mitochondrial oxygen consumption, ATP turnover) of spermatozoa at 0 (blue) and 1 day (orange) (B). The Metabolic potential in “Stressed OCR” and “Stressed ECAR” is expressed as % “Baseline OCR” and “Baseline ECAR” (dashed horizontal line) (C) and baseline (empty squares) and stressed (full squares) phenotypes (D) at 0 and 1 day. Data represent the mean  $\pm$  SD (vertical and where present also horizontal bars) from three experiments carried out on distinct cell preparations.

The oxidation rate of the substrates glucose (Glu) (figure 26A), fatty acids (FA) (figure 26B) and glutamine (Gln) (figure 26C) was also evaluated, which does not vary with time. The dependence of spermatozoa on the Glu oxidative pathway to maintain basal respiration was higher than AF or Gln. However, independently of the substrate, the metabolism of the spermatozoa had a lower parameter of “capacity” than “dependency” (figure 26). Furthermore, the inability of spermatozoa

to increase oxidation of a particular fuel to compensate for the inhibition of the alternative fuel path was demonstrated by the negative value of “flexibility” (figure 26).

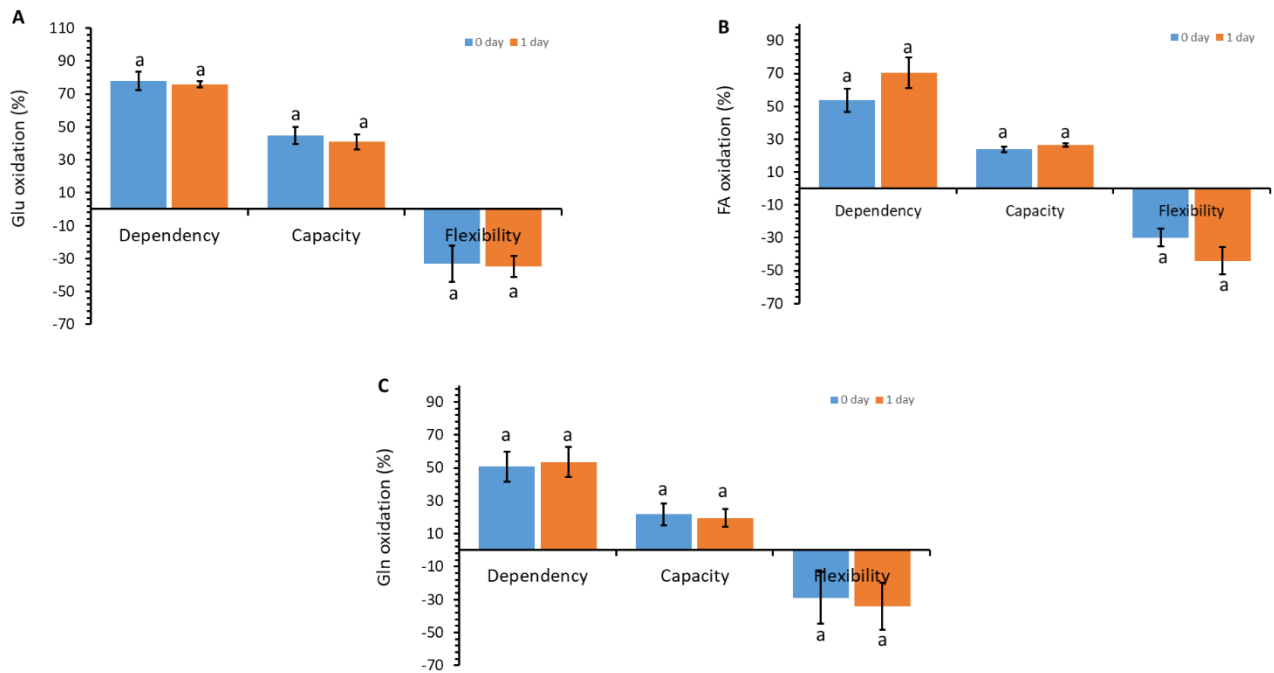


**Figure 26. Determination of the oxidation rate of fuels.** Fuel dependency, capacity and flexibility are calculated on the oxidation of glucose (A), fatty acids (B) and glutamine (C). The histogram represents the mean  $\pm$  SD (vertical bars) of three experiments conducted on different cell preparations.

## RESEARCH ARTICLE

# Biological characteristics and metabolic profile of canine mesenchymal stem cells isolated from adipose tissue and umbilical cord matrix

Romina Marcoccia<sup>1,2</sup>, Salvatore Nesci<sup>1</sup>, Barbara Merlo<sup>1,2\*</sup>, Giulia Ballotta<sup>1</sup>, Cristina Algieri<sup>1</sup>, Alessandra Pagliarani<sup>1</sup>, Eleonora Iacono<sup>1,2</sup>

**1** Department of Veterinary Medical Sciences, University of Bologna, Ozzano Emilia, Bologna, Italy, **2** Health Science and Technologies Interdepartmental Center for Industrial Research (HST-ICIR), University of Bologna, Bologna, Italy

\* [barbara.merlo@unibo.it](mailto:barbara.merlo@unibo.it)



## OPEN ACCESS

**Citation:** Marcoccia R, Nesci S, Merlo B, Ballotta G, Algieri C, Pagliarani A, et al. (2021) Biological characteristics and metabolic profile of canine mesenchymal stem cells isolated from adipose tissue and umbilical cord matrix. *PLoS ONE* 16(3): e0247567. <https://doi.org/10.1371/journal.pone.0247567>

**Editor:** Carlos E. Ambrósio, Faculty of Animal Sciences and Food Engineering, University of São Paulo, BRAZIL

**Received:** June 15, 2020

**Accepted:** February 9, 2021

**Published:** March 4, 2021

**Copyright:** © 2021 Marcoccia et al. This is an open access article distributed under the terms of the [Creative Commons Attribution License](https://creativecommons.org/licenses/by/4.0/), which permits unrestricted use, distribution, and reproduction in any medium, provided the original author and source are credited.

**Data Availability Statement:** All relevant data are within the manuscript and its [Supporting Information](#) files.

**Funding:** Metabolic analysis were supported by CARISBO Foundation grant n° 2018/0375 (Scientific Manager Prof. Pagliarani).

**Competing interests:** The authors have declared that no competing interests exist.

## Abstract

Despite the increasing demand of cellular therapies for dogs, little is known on the differences between adult and fetal adnexa canine mesenchymal stem cells (MSCs), and data on their metabolic features are lacking. The present study aimed at comparing the characteristics of canine adipose tissue (AT) and umbilical cord matrix (UC) MSCs. Moreover, for the first time in the dog, the cellular bioenergetics were investigated by evaluating the two main metabolic pathways (oxidative phosphorylation and glycolysis) of ATP production. Frozen-thawed samples were used for this study. No differences in mean cell proliferation were found ( $P>0.05$ ). However, while AT-MSCs showed a progressive increase in doubling time over passages, UC-MSCs showed an initial post freezing-thawing latency. No differences in migration, spheroid formation ability, and differentiation potential were found ( $P>0.05$ ). RT-PCR analysis confirmed the expression of CD90 and CD44, the lack of CD14 and weak expression of CD34, mostly by AT-MSCs. DLA-DRA1 and DLA-DQA1 were weakly expressed only at passage 0 by UC-MSCs, while they were expressed at different passages for AT-MSCs. There was no difference ( $P>0.05$ ) in total ATP production between cell cultures, but the ratio between the “mitochondrial ATP Production Rate” and the “glycolytic ATP Production Rate” was higher ( $P<0.05$ ) in AT- than in UC-MSCs. However, in both MSCs types the mitochondrial respiration was the main pathway of ATP production. Mitochondrial respiration and ATP turnover in UC-MSCs were higher ( $P<0.05$ ) than in AT-MSCs, but both had a 100% coupling efficiency. These features and the possibility of increasing the oxygen consumption by a spare respiratory capacity of four (AT-MSCs) and two (UC-MSCs) order of magnitude greater than basal respiration, can be taken as indicative of the cell propensity to differentiate. The findings may efficiently contribute to select the most appropriate MSCs, culture and experimental conditions for transplantation experiments in mesenchymal stem cell therapy for companion animals.

## Introduction

Stem cells are unspecialized cells with the ability to renew themselves for long periods without changes in their properties [1]. Mesenchymal stem cells (MSCs) are one type of non-hemopoietic stem cells, originating from mesoderm and present in different types of tissues [2, 3]. Furthermore, MSCs possess multi lineage differentiation capacity into chondrocytes, osteocytes, adipocytes and other cell types like myoblasts, bone marrow stromal cells, fibroblasts, cells co creating connective tissue of the body, as well as ligaments and tendons [4, 5]. Mesenchymal stem cells are characterized by the expression of typical mesenchymal surface Cluster Designation (CD), such as CD105, CD73 and CD90 and lack of hematopoietic ones, CD45, CD34, CD14 or CD11b, CD79 $\alpha$  or CD19 and HLA-DR [2].

Due to their properties, MSCs offer a great chance for cell-based therapies and tissue engineering applications in veterinary medicine, especially for canines (*Canis familiaris*). The effective management of companion animals, which often suffer from age-related diseases such as arthrosis and degenerative diseases due to their increased longevity, requires sophisticated new treatments and preventive strategies. Moreover, dogs could be employed as a model for human genetic and acquired diseases, helping to define the potential therapeutic efficiency and safety of stem cell therapy [6, 7].

To date, canine derived MSCs have been isolated from different adult tissues, such as liver, bone marrow [8], and adipose tissue [9, 10]. Adipose tissue (AT) is easily available and contains a high number of MSCs, especially in the perivascular region, which makes it a valid source of stem cells for autologous or heterologous use [11]. In canine species, the clinical use of AT-MSCs is versatile thanks to their differentiation potential and secretion of numerous immunomodulatory factors [12]. Nevertheless, MSCs derived from fetal adnexa, such as umbilical cord (UC) matrix, which are discarded at parturition, could overcome many of the limitations of adult tissues-derived MSCs, such as the invasive procedure required for sample recovery [13, 14]. Thanks to its extracorporeal nature, these cells are therefore easy to obtain non-invasively and without pain or stress for the donor [15, 16].

The metabolism gathers tuned biochemical pathways for maintenance of cellular homeostasis and cellular self-renewal capability [17]. To adequately select and address MSC therapeutic applications, a first task is to understand the biochemical and metabolic features of these cells. Data on MSCs metabolism are still controversial: stem cells prefer glycolysis to mitochondrial respiration when located in the niche because the environment could be hypoxic [17] and glycolysis is required by macromolecule and biostructure synthesis [18]. Despite some studies comparing canine adult and fetal adnexa derived MSC growth and differentiation capacity [19, 20], as far as we are aware no data on the metabolic profile are available. The aim of this study was to compare, for the first time, the metabolic profile of canine MSCs derived from adipose and umbilical cord tissues. The metabolic and bioenergetic profiles complement to selected biological features, such as cellular proliferation, differentiation potential, molecular profile, migration and spheroid formation ability, to provide an overall pattern of the characteristics of these cells as first step for their potential future use in therapy.

## Materials and methods

Chemicals were obtained from Sigma Aldrich (Merck); type I collagenase, DMEM (Dulbecco's Modified Eagle's Medium) high glucose medium with Glutamax, MEM (Modified Eagle's Medium) with Glutamax, and Fetal Bovine Serum (FBS) are branded GIBCO (ThermoFisher Scientific).

Laboratory plastic ware was from Falcon (VWR), unless otherwise stated.

## Animals

Intra-abdominal fat tissue from healthy one-year old dogs ( $n = 4$ ) was recovered at castration, while umbilical cord samples ( $n = 4$ ) were recovered at ovary-hysterectomy of a 30 days pregnant bitch. All animals were referred to the Department of Veterinary Medical Sciences (University of Bologna), and the written consent was given by the owners to allow the use of removed tissue for research purposes. Experimental procedures were approved by the Ethics Committee on animal use of the University of Bologna (Prot. 55948-X/10), and by the Italian Ministry of Health.

## Sample collection and cell isolation

Immediately after removal, AT and UC samples were stored in DPBS (Dulbecco's Phosphate Buffered Saline) supplemented with antibiotics (100 IU/mL penicillin, 100  $\mu$ g/mL streptomycin) at 4°C until the transfer to the lab. The whole portion of placental UC, freed from blood vessels, was used. MSCs were isolated as previously described by Iacono et al. [10]. Briefly, under a laminar flow hood, tissue was rinsed by repeated immersion in DPBS, weighed and finely minced (0.5 cm) using sterile scissors. Minced tissue was transferred into a 50 mL polypropylene tube and a digestion solution, containing 0.1% collagenase type I dissolved in DPBS, was added (1 mL solution/1 g tissue) mixing thoroughly. This mix was kept in a 37°C water bath for 30 min and mixed vigorously every 10 min. After incubation the collagenase was inactivated, diluting 1:1 with DPBS supplemented with 10% FBS and the resulting solution was filtered in order to discard the undigested tissue. Nucleated cells were pelleted at 470 g for 10 min at 25°C. The obtained pellet was suspended in culture medium composed of DMEM/MEM 1:1, plus 10% FBS added with antibiotics (100 IU/mL penicillin, 100  $\mu$ g/mL streptomycin). Cells were plated in a 25 cm<sup>2</sup> flask in 5 mL of culture medium and the flask was marked as "Passage 0" (P0). Cells were cultured in humidified air with 5% CO<sub>2</sub> at 38.5°C. After 48h of *in vitro* culture, the medium was completely re-placed and non-adherent cells removed. Medium was then changed twice a week until 80 to 90% confluence was reached.

## Cell freezing and thawing

Since samples were recovered in different moments, isolated P0 cells were frozen and stored in liquid nitrogen in order to perform all tests at the same time. AT- and UC-MSCs were deep-frozen as previously described by Merlo et al. [21]. Briefly, cells were allowed to proliferate until 80 to 90% confluence, thereafter they were dissociated by 0.25% trypsin for 10 min. Trypsin was then inactivated diluting 1:2 with DPBS+10% FBS. MSCs were centrifuged at 470g for 10 min at 25°C. The pellet was suspended in 0.5 mL of FBS, transferred in a 1.5 mL cryogenic tube (Sarstedt Inc.) and put at 5 to 8°C for 10 min. At the end of this period, the cells were diluted 1:1 with FBS+16% DMSO (dimethyl sulfoxide) for a final concentration of 8% DMSO. After other 10 min at 5 to 8°C, the cryogenic tube was put at -80°C for 24h in Mr Frosty (Nalgene) and finally stored in liquid nitrogen. AT- and UC-MSCs were thawed at 37°C and diluted with 20 mL culture medium, then centrifuged at 470 g for 10 min at 25°C. The pellet was suspended in 1 mL culture medium and the cells concentration was evaluated by using a haemocytometer. Cells were plated in a 25 cm<sup>2</sup> flask (5000 cells/cm<sup>2</sup>) as "Passage 1" (P1). Cells were allowed to proliferate until 80 to 90% confluence before trypsinization and successive passage.

## Cell culture and population doublings

Calculation of cell-doubling time (DT) and cell-doubling number (CDN), that is the approximate number of doublings that the cell population has undergone since isolation, was carried

out according to the following formulae [22]:

$$\text{CDN} = \ln(N_f/N_i)/\ln \quad (1)$$

where  $N_f$  and  $N_i$  are the final and the initial number of cells, respectively;

$$\text{DT} = \text{CT}/\text{CDN}$$

where CT is the cell culture time.

The experiment was done in three replicates.

### CFU (Colony forming unit) assay

To assess colony formation ability,  $1 \times 10^4$  cells at P1 were seeded in a 90 mm petri dish and cultured for 13 days [23]. For each sample three replicates were carried out. Colonies were fixed in 4% paraformaldehyde at room temperature (RT) and stained for 15 min with Giemsa 0,1% stain. Colonies formed by at least 16–20 nucleate cells were counted using an inverted light microscope (Eclipse TE 2000u, Nikon).

### Spheroid formation and migration assays

To define differences between AT- and UC-MSCs, spheroid formation and migration tests were performed. Each test was replicated 3 times for all samples.

For spheroid formation assay, P3 cells were cultured in multiwell Corning 96-well Black/Clear Round Bottom Ultra- Low Attachment Spheroid Microplate (5000 cells/25  $\mu\text{L}$  drop) for 24 h. This method provides information about the direct cell-cell adhesion architecture found in normal tissues, differently from the cell-substratum adhesion, performed on monolayer cultures adherent to rigid substrates. Images were acquired by a CCD camera (DS-Fi2, Nikon) mounted on a light inverted microscope. Starting from the binary masks obtained by ImageJ software ([imagej.nih.gov/ij/](http://imagej.nih.gov/ij/)), the volume of each spheroid was computed using ReViSP ([sourceforge.net/projects/revisp](https://sourceforge.net/projects/revisp)) [24], a software specifically designed to accurately estimate the volume of spheroids and to render an image of their 3D surface.

To assess cell migration potential, wound-healing assay was carried out, as previously described by Liang et al. [25]. Briefly, P3 cells were plated (5000 cell/ $\text{cm}^2$ ) in a 35 mm petri dish. At 80 to 90% confluence the cell monolayer was scraped using a 1000  $\mu\text{L}$  pipet tip. After washing twice with DPBS, the dish was incubated for 24 h. Images were acquired both immediately after the tip-scratch (time 0 = T0) and after the incubation period (time 1 = T1), and the distances of each scratch closure were calculated by ImageJ software ([imagej.nih.gov/ij/](http://imagej.nih.gov/ij/)). The migration percentages were calculated using the following formula [26]:

$$[(\text{distance at T0} - \text{distance at T1}) * 100]/\text{distance at T0}$$

### Multi lineage differentiation

*In vitro* differentiation potential toward osteogenic, adipogenic and chondrogenic lineages of AT- and UC-MSCs were studied. Cells (5000 cells/ $\text{cm}^2$ ) were cultured for three weeks under specific induction media (Table 1) [27]. As negative control, an equal number of cells was cultured in expansion medium. The specific induction media and expansion medium were replaced twice a week. The *in vitro* differentiation potential was assessed at P3 of the *in vitro* culture. Three replicates for each sample were carried out. For the cytological evaluation of the differentiation, cells were fixed with 4% paraformaldehyde at RT for 1 h and then stained with Oil Red O, Alcian Blue and Alizarin Red for adipogenic, chondrogenic and osteogenic induction, respectively. Stained cells were observed under an inverted light microscope and

**Table 1. Specific induction media compositions.**

Adipogenic medium	Chondrogenic Medium	Osteogenic Medium
• DMEM/MEM	• DMEM/MEM	• DMEM/MEM
• 10% FBS	• 1% FBS	• 10% FBS
• 0.5 mM IBMX (removed after 3 days)	• 6.25 µg/mL insulin • 50 nM AA2P	• 50 µM AA2P • 0.1 µM DXM
• 1 µM DXM (removed after 6 days)	• 0.1 µM DXM • 10 ng/mL hTGF-β1	• 10 mM BGP
• 10 µg/mL insulin		
• 0.1 mM indomethacin		

IBMX: isobutylmethylxanthine, DXM: Dexamethasone, hTGF: human Transforming Growth Factor, AA2P: Ascorbic Acid 2-Phosphate, BGP: Beta-Glycerophosphate

<https://doi.org/10.1371/journal.pone.0247567.t001>

photographed. Images obtained after chondrogenic and osteogenic differentiation were analysed for colour intensity using Image J software [28]. The intensity of adipogenic differentiation was assessed using a scoring system based on Oil Red O staining (Table 2) [29].

## Molecular characterization

Expression of specific mesenchymal (CD44, CD90), hematopoietic (CD34, CD14), and major histocompatibility complex (DLA-DQA1, DLA-DRA1) markers was investigated by RT-PCR analysis in undifferentiated canine AT- and UC-MSCs. The specific set of primers used are listed in Table 3. All tests were performed at each passage of *in vitro* culture on  $10^5$  cells, previously snap-frozen at  $-80^{\circ}\text{C}$ . The RNA was extracted using Nucleo Spin RNA kit (Macherey-Nagel, Düren, Germany) following the manufacturer's instructions. cDNAs were synthesized by RevertAid RT Kit (ThermoFisher Scientific, Waltham, Massachusetts, USA) and used directly in PCR reactions, following the instructions of Maxima Hot Start PCR Master Mix (2X) (ThermoFisher Scientific, Waltham, Massachusetts, USA). Canine glyceraldehyde-3-phosphate dehydrogenase (GAPDH) was employed as reference gene for each sample in order to standardize the results and to assess RNA purity. For all primers, in order to assess sample purity, a negative RT and a mix without primer were analyzed. PCR products were visualized (Benchtop 2UV/PhotoDoc-It 65, UVP International PBI) on an ethidium bromide stained 2% agarose gel.

## Cellular bioenergetics

The Seahorse XFp analyzer (Agilent) was used to simultaneously measure oxygen consumption rate (OCR), an index of cell respiration (pmol/min), and extracellular acidification rate (ECAR), an index of glycolysis (mpH/min). AT- and UC-MSCs were trypsinized and grown in XFp cell culture miniplates (Agilent) at  $10^4$  cells per well one day prior to the assay. On the day of an experiment, MSCs were switched to freshly made Seahorse XF DMEM medium pH 7.4 supplied with 10 mM glucose, 1 mM sodium pyruvate, and 2 mM L-glutamine. The plates

**Table 2. Semi-quantitative scoring system used in the evaluation of adipogenic differentiation.**

Score	% of differentiated cells	Size and arrangement of lipid droplets
0	0–5	No droplets
1	>5–50	Predominantly isolated and small
2	>50–80	Predominantly medium-sized
3	>80–100	Predominantly large

<https://doi.org/10.1371/journal.pone.0247567.t002>

Table 3. Sequences of primers used for RT-PCR analysis.

Gene	Primer sequences (5' → 3')	Amplicon (bp)	Reference
<b>Reference gene</b>			
<b>GAPDH</b>	FW: GGTCAACCAGGGCTGCTTT RV: ATTTGATGTTGGCGGGAT	209	[30]
<b>Mesenchymal markers</b>			
<b>CD90</b>	FW: CAGCATGACCCGGGAGAAAAAG RV: TGGTGGTGAAGCCGGATAAGTAGA	134	[31]
<b>CD44</b>	FW: GCCCTGAGCGTGGGCTTTGA RV: TCTGGCTGTAGCGGGTGCCA	268	[15]
<b>Hematopoietic markers</b>			
<b>CD14</b>	FW: CCCGGCGCTCACACCTTAGAC RV: CCTGGAGGGCCGGAACTTTTG	98	[31]
<b>CD34</b>	FW: GCCTGCTCAGTCTGCTGCC RV: TGGTCCCAGGCGTTAGGGTGA	255	[15]
<b>Major histocompatibility complex markers</b>			
<b>DLA-DRA1</b>	FW: CGCTCCAACCACACCCCGAA RV: GGCTGAGGGCAGGAAGGGGA	246	[15]
<b>DLA-DQA1</b>	FW: GCACTGGGGCCTGGATGAGC RV: ACCTGAGCGCAGGCCTTGA	163	[15]

<https://doi.org/10.1371/journal.pone.0247567.t003>

were incubated at 37°C in air for 45 minutes before measuring OCR and ECAR by the adequate programs (ATP Rate Assay or Cell Mito Stress Test). The injection ports of XFp sensor cartridges, which were hydrated overnight with XF calibrant at 37°C, were loaded with 10x concentration of inhibitors according to the instructions provided by Seahorse XFp ATP Rate Assay and CellMito Stress Test. The final concentration used for ATP Rate Assay were 1.5 μM oligomycin (port A) and 0.5 μM rotenone plus antimycin A (port B), while for Cell Mito Stress Test the final concentrations were 1.5 μM oligomycin (port A), 2.0 μM and 0.5 μM FCCP (port B) with AT- and UC-MSCs, respectively and 0.5 μM rotenone plus antimycin A (port C). All the analysis were run at 37°C. All data were analyzed by WAVE software version 2.6.1; OCR and ECAR values were normalized to the total number of cells for each well. All parameter values were calculated per well according to the manufacturer's instructions. Both ATP Rate Assay and Mito Stress Test were carried out three times on different days for each cell type.

The ATP Rate Assay provides the bioenergetic parameters currently used to characterize cellular ATP production, namely ATP production rate, related to the conversion of glucose to lactate in the glycolytic pathway (glycoATP Production Rate) and to mitochondrial oxidative phosphorylation (mitoATP Production Rate). Accordingly, the ratio between mitoATP Production Rate and glycoATP Production Rate (ATP Production Rate Index) is currently considered as a valuable parameter to detect changes and/or differences in the metabolic phenotype (ratio > 1 mainly OXPHOS pathway; ratio < 1 mainly glycolytic pathway). The Mito Stress Test enables to characterize cell respiration by the following parameters: basal respiration, detected as baseline OCR before oligomycin addition; minimal respiration measured as OCR in the presence of oligomycin; maximal respiration evaluated as OCR after FCCP addition. The non-mitochondrial respiration, evaluated as OCR in the presence of rotenone plus antimycin A, was subtracted from all the above parameters. The ATP turnover or oligomycin-sensitive respiration was obtained from the difference between the basal respiration and the minimal respiration (OCR in presence of oligomycin). Finally, the difference between the maximal and the basal respiration provided the spare capacity, which represents the ability

to respond to an increased energy demand and can be considered as a measure of the flexibility of the oxidative phosphorylation (OXPHOS) machinery.

### Statistical analysis

Cell-doubling number, cell-doubling time, percentages of migration and metabolic data are expressed as mean  $\pm$  SD. Statistical analyses were performed using IBM SPSS Statistics 25 (IBM Corporation). Data were analyzed for normal distribution, using a Shapiro Wilk test. Mean DTs, CDs, number of colonies and migration rate were analyzed using Student's T Test for unpaired variables, while the 3D spheroid volumes were compared using Mann-Whitney U-test. Metabolic data were analyzed by One-way ANOVA, followed by Students-Newman-Keuls' test when *F* values indicated significance. Significance was assessed for  $P < 0.05$ .

## Results

### Cell proliferation

Adherent cells with the characteristic spindle-shaped morphology were isolated from all samples of adipose tissue and umbilical cord matrix. For all samples of both tissues, undifferentiated cells were cultured until P4 after freezing-thawing, without changes in cell morphology. No statistically significant differences were observed in mean CDN (AT-MSCs  $10.3 \pm 1.9$  vs UC-MSCs  $11.5 \pm 0.8$ ;  $P > 0.05$ ). Furthermore, mean DTs were similar ( $P > 0.05$ ) (AT-MSCs  $85.1 \pm 43.8$  h vs UC-MSCs  $83.2 \pm 18.5$ h).

Comparing data among passages of the same cell culture, AT-MSCs showed a progressive increase in DTs over time. DT at P4 ( $134.9 \pm 53.7$  h) was significantly higher ( $P < 0.05$ ) than at P1 ( $59.4 \pm 28.2$  h) and P2 ( $58.7 \pm 10.5$  h) (Fig 1). On the other hand, UC-MSCs showed a slightly different trend (Fig 1). DT of UC-MSCs at P1 ( $85.7 \pm 15$  h) was significantly higher ( $P < 0.05$ ) than DT at P2 ( $64.0 \pm 12.8$  h) and similar ( $P > 0.05$ ) to DT at P3 ( $83.3 \pm 6.0$  h) and P4 ( $99.7 \pm 20.8$  h), while DT at P2 ( $64.0 \pm 12.8$  h) was the one significantly lower ( $P < 0.05$ ) than those registered at subsequent passages.

The mean number of colonies formed at P1 by AT-MSCs ( $87,8 \pm 51,8$ ) and UC-MSCs ( $41,0 \pm 35,4$ ) was not significantly different ( $P > 0.05$ ).

### Spheroid formation and migration assays

All samples of AT- and UC-MSCs, cultured in specific multi-well plate, were able to form spheroids. The volume of formed spheroids was similar between AT- and UC-MSCs ( $P > 0.05$ ) (Fig 2A–2B), confirming a comparable cell-cell adhesion ability. Furthermore, no differences were registered in the migration ability between the two groups (AT-MSCs  $53.5 \pm 11.8\%$  vs UC-MSCs  $49.0 \pm 24.2\%$ ;  $P > 0.05$ ), as demonstrated by the cell distribution (Fig 2C–2D).

### Multilineage differentiation

After adipogenic differentiation, the changes in the two types of MSCs were similar, and the original typical fibrous cell shape changed in shortened and rounded ones. Lipid droplets were observed in the cytoplasm of AT- and UC-MSCs. After Oil red O staining, the lipid droplets were stained red (Fig 3). The two groups reached a score of 2 (showing  $> 50$ – $80\%$  positive cells with medium-size droplets).

After three weeks of osteogenic induction, cell morphology changed from fibers to polygons and scales. Calcium nodules appeared in both AT- and UC-MSCs. All MSCs showed red mineralized deposits. Observing cells at low magnification (4X) (Fig 3) AT-MSCs formed less numerous

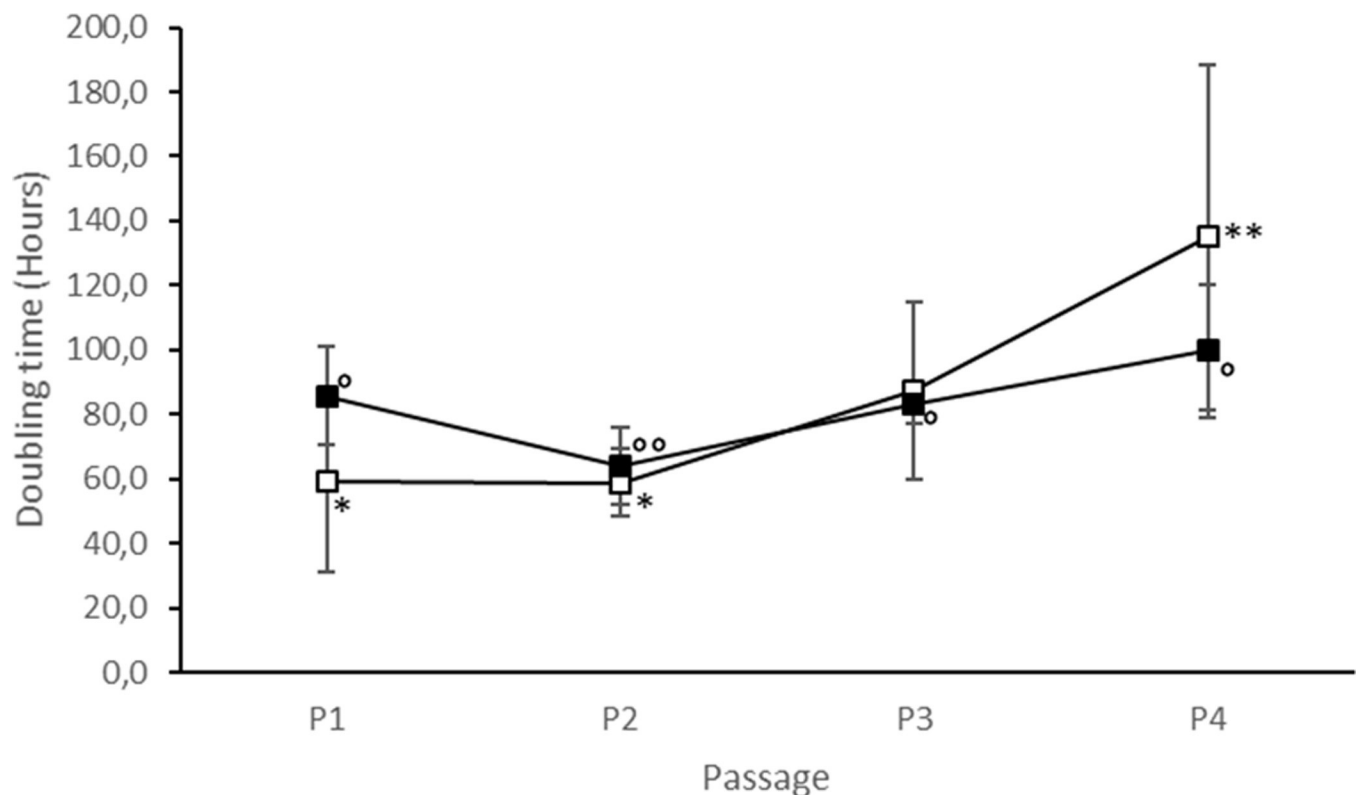


**Fig 1. Cell growth of canine AT- and UC-MSCs.** Doubling times of frozen-thawed AT-MSCs ( $\square$ ) and UC-MSCs ( $\blacksquare$ ) over four passages of *in vitro* culture. Data represent the mean  $\pm$  SD. Different symbols indicates significant differences: \* and \*\* for AT-MSCs, \* and \*\* for UC-MSCs ( $P < 0.05$ ).

<https://doi.org/10.1371/journal.pone.0247567.g001>

but larger deposits, while UC-MSCs tended to form more numerous but smaller deposits. These different features lead to a similar colour intensity between the two cell types ( $P > 0.05$ ).

Chondrogenic differentiation was observed after 21 days in MSCs from both groups (AT and UC); the cell shape changed and matrix secretion was observed. Chondrogenic potential was confirmed by Alcian Blue (Fig 3), which enabled the identification of an extracellular matrix rich in proteoglycans. Also for chondrogenic differentiation, the colour intensity was similar for the two MSC cultures ( $P > 0.05$ ).

### Molecular characterization by RT-PCR

Data is shown in Fig 4. All samples of AT- and UC-MSCs expressed typical mesenchymal markers, CD90 and CD44, at every passage of the *in vitro* culture. No samples expressed the typical hematopoietic marker CD14. The hematopoietic marker CD34 was expressed in different manner by AT- and UC-MSCs. In fact, an individual variability between AT samples was observed, since CD34 was poorly expressed at passage P3 by one adipose tissue sample, while it was weakly expressed at all passages (P0-P4) by the other two samples. The same marker, instead, was weakly expressed only at P0 by UC-MSCs in all samples. As for CD34, an individual variability among adipose tissue samples was observed in the expression of DLA-DQA1 and DLA-DRA1, while they were weakly expressed only at P0 by UC-MSCs.

### Cellular ATP production

The  $O_2$  consumption rate (OCR) and the extracellular acidification rate (ECAR) by lactate production were simultaneously measured in AT-MSCs (Fig 5A) and UC-MSCs under basal

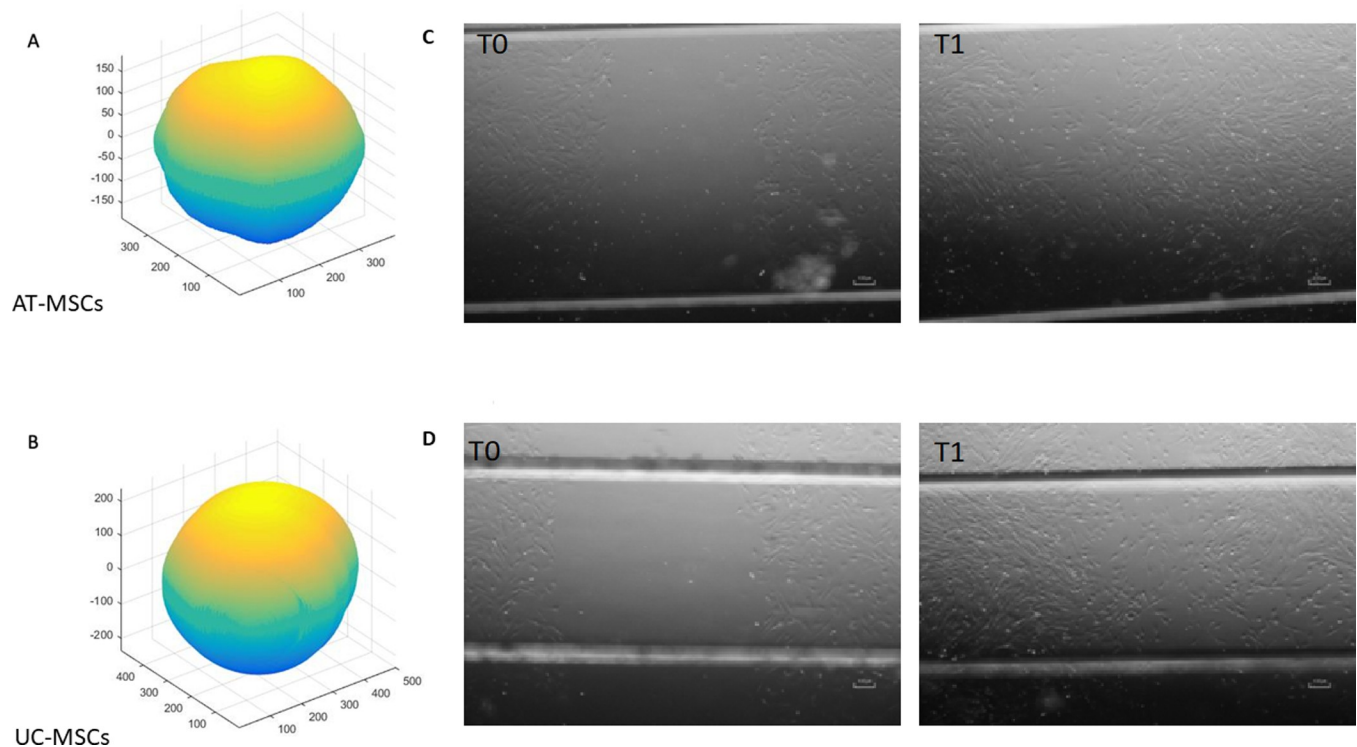


**Fig 2. Spheroid formation and scratch assays of canine AT- and UC-MSCs.** A-B) Volume reconstruction of an AT-MSC (A) and UC-MSCs (B) spheroid, obtained after 24 h of hanging drop culture. C-D) Scratch assay on AT-MSCs (C) and UC-MSCs (D) at T0 and after 24 h (T1) of cell growth (Magnification 4X).

<https://doi.org/10.1371/journal.pone.0247567.g002>

conditions (Fig 5B). In order to detect the total ATP production rates in living MSCs, serial additions of oligomycin (olig), a specific inhibitor of the mitochondrial ATP synthase, and of rotenone plus antimycin A (Rot+AA), inhibitors of mitochondrial complex I and III, respectively, were automatically and stepwise performed. This metabolic assay carried out according to Seahorse XFp technology, allowed us to evaluate the amount of ATP produced by OXPHOS and glycolysis, which represent the two main metabolic pathways responsible for ATP production in mammalian cells. The plots of Fig 5A and 5B highlight the OCR decrease due to the ADP phosphorylation inhibition by oligomycin and the block of electron transport chain by Rot+AA coupled to an increase in ECAR, which mirrors glycolytic rate. From the flux of  $O_2$  consumption and  $H^+$  production, the ATP production rates by OXPHOS and glycolysis were calculated (Fig 5C). AT- and UC-MSCs showed a different total ATP production rate, since OXPHOS and glycolytic pathways in UC-MSCs provided a higher amount ( $P < 0.05$ ) of cellular ATP than in AT-MSCs (Fig 5C). The energy map of both MSC types corroborates an aerobic energy metabolism with more active OXPHOS and glycolytic pathways in UC-MSCs than AT-MSCs (Fig 5D) ( $P < 0.05$ ). However, AT-MSCs showed a higher mitoATP/glycoATP ratio than UC-MSCs, which highlights a prevailing oxidative phenotype (Fig 5E) ( $P < 0.05$ ).

### Mitochondrial respiration

The key parameters of mitochondrial function, directly measured by the cell respiration profile of MSCs, are shown in Fig 6A. Both basal respiration and ATP turnover show significantly higher values in UC-MSCs than in AT-MSCs (Fig 6B) ( $P < 0.05$ ). Noteworthy, oligomycin inhibition completely blocks the mitochondrial oxygen consumption without any proton leak

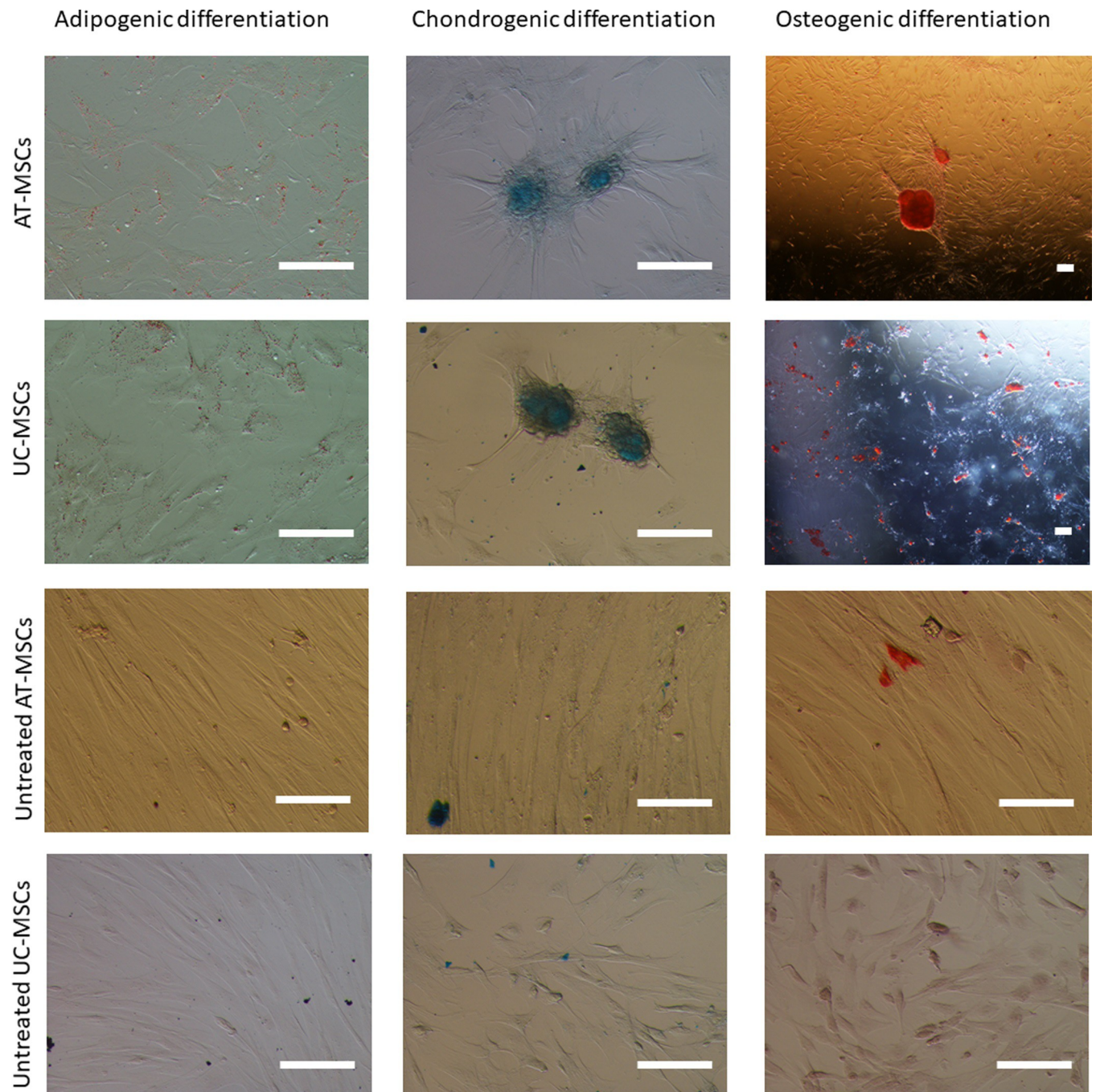


**Fig 3. Differentiation potential of AT- and UC-MSCs.** Canine AT- and UC-MSCs cultured toward adipogenic, chondrogenic and osteogenic differentiation. Magnification: 20X for all pictures except for 4X of osteogenic differentiated cells (bars = 100  $\mu$ m).

<https://doi.org/10.1371/journal.pone.0247567.g003>

detection. The same OCR values of basal respiration and ATP turnover confirm an almost 100% coupling efficiency. The cellular ATP demand in MSCs, when OXPHOS is inhibited by oligomycin, is fulfilled by the activation of glycolytic pathway (Fig 6C). AT- and UC-MSCs increase the maximal respiration by four and two orders of magnitude, respectively after FCCP addition. Consequently, the spare respiratory capacity, currently taken as a parameter

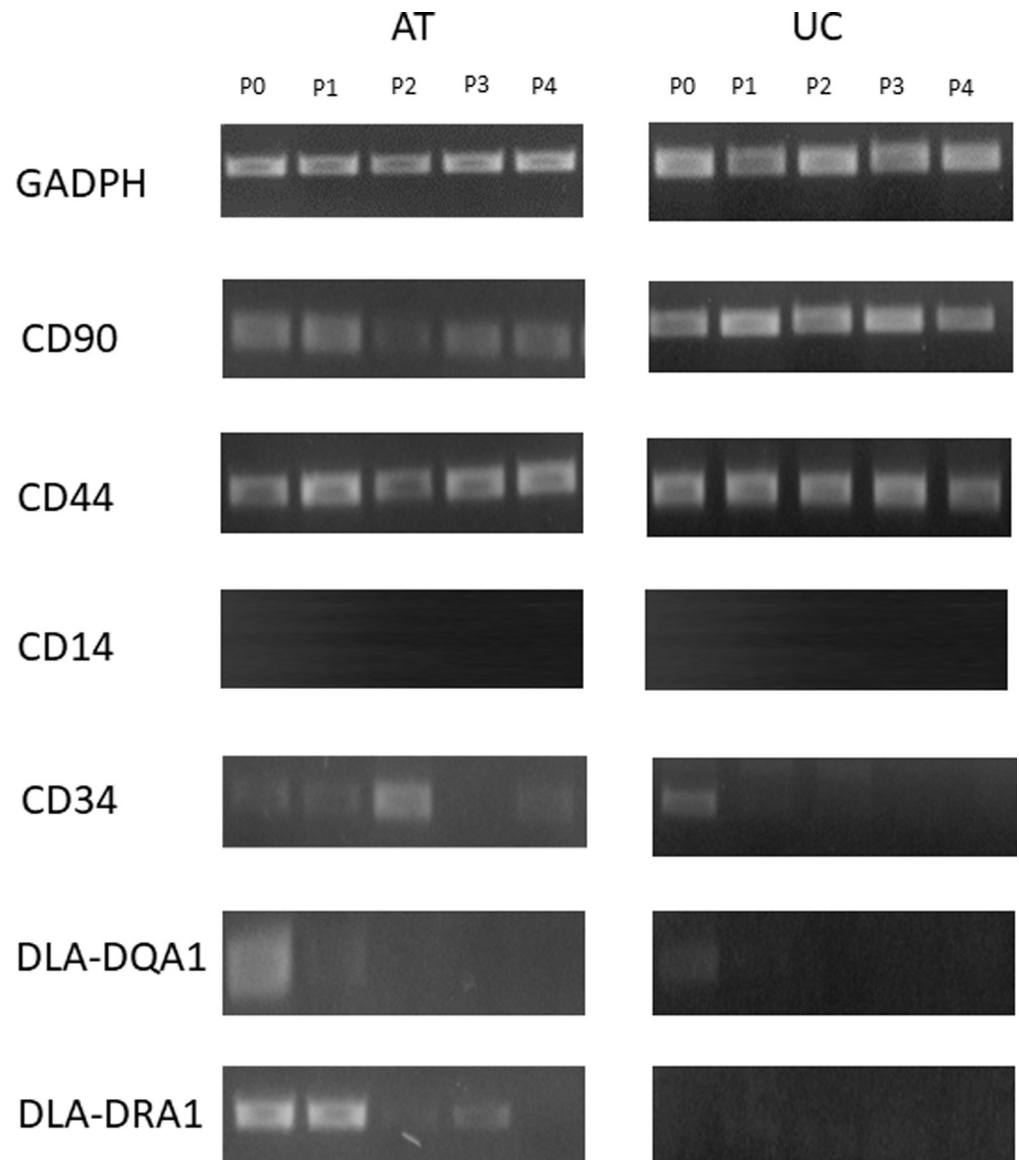


**Fig 4. RT-PCR analysis of gene expression in canine AT- and UC-MSCs.** Products from AT- and UC-MSCs samples are visualized over time, from passage 0 (P0) to passage 4 (P4) of *in vitro* culture.

<https://doi.org/10.1371/journal.pone.0247567.g004>

which defines the cell propensity to differentiate [32, 33], represents 79% and 59% maximal respiration for AT- and UC-MSCs, respectively.

## Discussion

In the present study, MSCs from canine umbilical cord and adipose tissue were isolated and several features were evaluated: *in vitro* proliferation, migration ability, spheroid formation capacity, differentiation potential, expression of stem markers and, for the first time in the dog, cell bioenergetics. Usually, for clinical application, cells are used during the first *in vitro* passages, to avoid any side effects due to senescence and cell transformation following a long culture period. Thus, only the first four culture passages were considered in this study. UC samples were collected from fetuses of a single female dog, so there could be a lack of

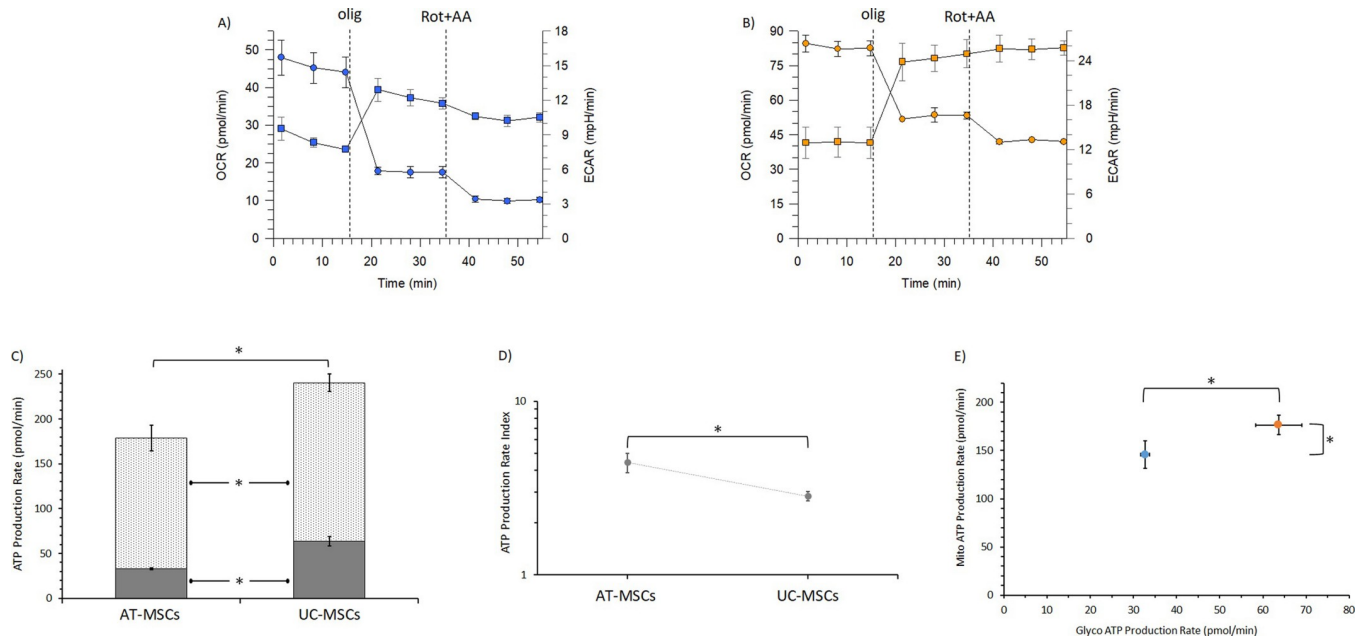


**Fig 5.** Real-Time ATP Production Rate Assay of basal OCR (blue spheres) and ECAR (blue squares) rates of AT-MSCs (A) and OCR (orange spheres) and ECAR (orange squares) rates of UC-MSCs (B). After detection of OCR and ECAR rates, oligomycin (1.5  $\mu$ M) and rotenone plus antimycin A (0.5  $\mu$ M) were serially injected at fixed times in order to allow to detect the mitochondrial and glycolytic ATP production rates. C) AT- and UC-MSCs quantification of ATP production by mitochondrial oxidative phosphorylation (dashed rectangle) or by the glycolytic pathway (glucose conversion to lactate) (filled rectangle). D) Energy map of AT-MSCs and UC-MSCs with OCR vs ECAR of AT- (blue spheres) and UC-MSCs (orange spheres) are plotted. E) The plot shows the ratio between the mitochondrial ATP production rate and the glycolytic ATP production rate (logarithmic scale). Data expressed as points (A, B, D, E plots) and column chart (C plot) represent the mean  $\pm$  SD (vertical bars) from three experiments carried out on different cell preparations. \* indicates significant differences ( $P < 0.05$ ).

<https://doi.org/10.1371/journal.pone.0247567.g005>

individual variation for the fetal-adnexa derived MSCs, while AT sample were obtained from different animals, so the individual variation exists, but the animals were all young, therefore age influence should be minimal. Nevertheless, it is likely that in the present study there was more variability for adult derived MSCs than for fetal adnexa derived ones.

Cell proliferation was similar for canine AT- and UC-MSCs, in accordance with the results observed in our laboratory for horse MSCs using the same protocol for DT calculation [34], but in contrast with data obtained in the dog [19], where AT-MSCs had a lower DT than UC-MSCs. The DTs for both MSCs lineages reported in that research [19] were shorter than those observed in the present study. These differences can be ascribed to different factors or to their combination, such as the different cell growth curve production method used to calculate DT, the different culture conditions, and also the different variability of MSC sources, since tissues were collected from the same animals. Indeed, when the same DT calculation method adopted in our research was applied, DTs of canine UC-MSCs from other studies [15, 35–37] were similar to our present results.

As previously observed [10], canine AT-MSCs presented a progressive increase in DT length over time, but with a slightly different trend for UC-MSCs. In fact, UC-MSCs showed a longer DT at first passage after thawing, and a progressive increase in DT over time starting from the second passage. This behaviour, never observed in other studies using non cryopreserved canine UC-MSCs [15, 35], may be explained as a freezing-thawing consequence, and could be related to a higher UC-MSCs sensitivity to the cryopreservation protocol used.

Colony formation was similar in both canine cell cultures. However, the mean number of colonies obtained in this study for AT and UC-MSCs is lower when compared with what

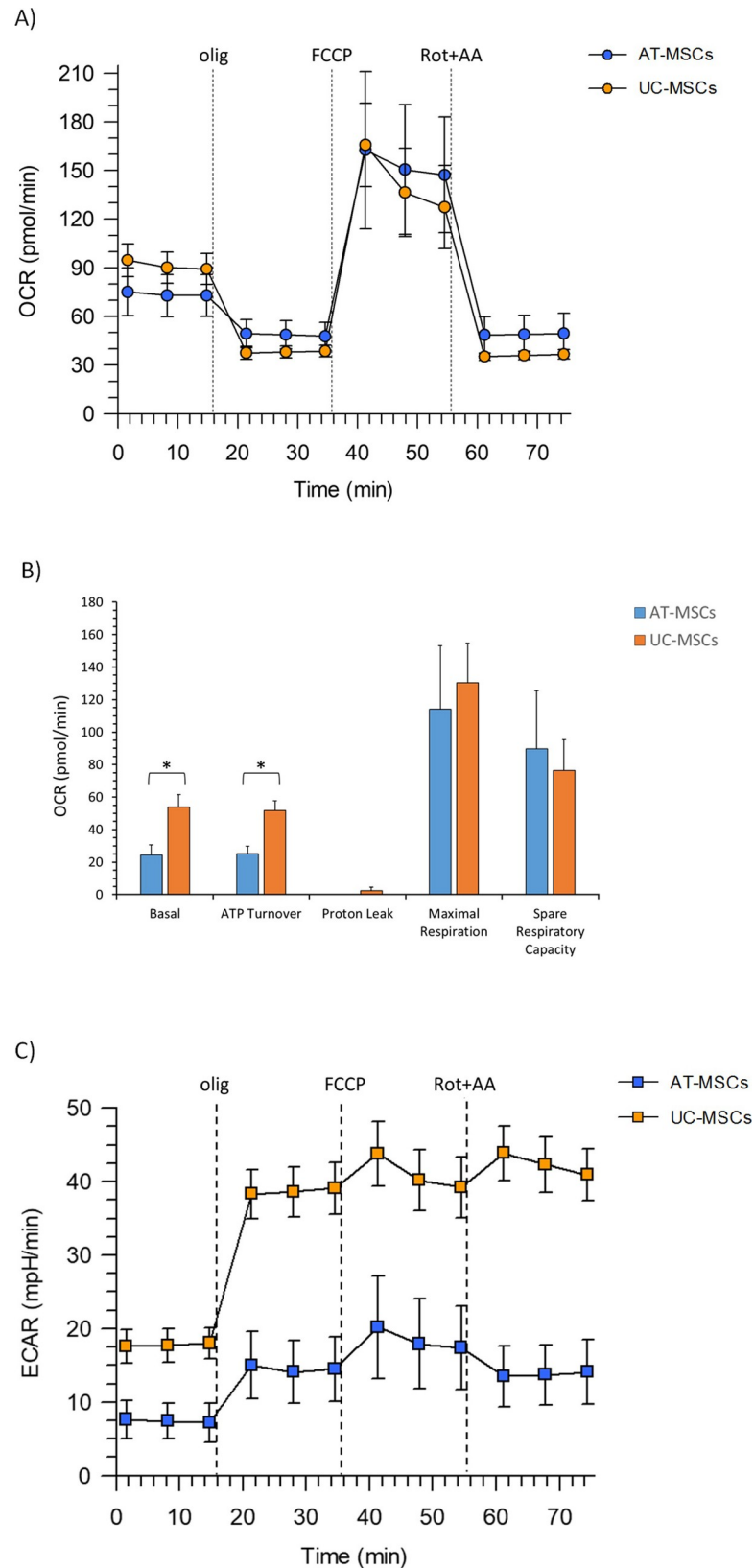


**Fig 6. Metabolic measurements in MSCs.** A) Mitochondrial respiration profile (OCR) of AT- and UC-MSCs under basal conditions and after the addition of 1.5  $\mu$ M oligomycin, 2.0  $\mu$ M and 0.5  $\mu$ M FCCP and a mixture of rotenone plus

antimycin A (0.5  $\mu$ M) injections where indicated by the dotted lines. B) Mitochondrial parameters (basal respiration, ATP production, proton leak, maximal respiration, spare respiratory capacity) in AT- and UC-MSCs. C) Basal ECAR and ECAR changes after addition of the mitochondrial inhibitors: 1.5  $\mu$ M oligomycin, 2.0  $\mu$ M and 0.5  $\mu$ M FCCP and a mixture of rotenone plus antimycin A (0.5  $\mu$ M) addition on AT- and UC-MSCs. Data expressed as points (A, C) and column chart (B) represent the mean  $\pm$  SD (vertical bars) from three experiments carried out on different cell preparations. \* indicates significant differences ( $P < 0.05$ ).

<https://doi.org/10.1371/journal.pone.0247567.g006>

found for canine amniotic membrane derived MSCs using the same protocol [23]. It is likely that different cells and culture medium influenced the results.

Migration potential of MSCs, also known as wound healing ability, is considered an important feature for their integration into the host tissue during therapeutic applications [38]. In the present study, the migration ability of canine AT- and UC-MSCs were similar. Nevertheless, the migration capacity of AT-MSCs observed in the present study was lower than that previously obtained [10], probably due to an individual variability and a different culture medium used.

Self-assembly of MSCs into aggregates has significant implication in their applications in cell therapy and tissue regeneration [39]. For example, the 3D spheroid culture system contributes to an optimization for efficient *in vitro* differentiation of MSCs [40], and *in vivo* MSC 3D transplantation of synovial MSC aggregates promoted cartilage tissue regeneration in a rabbit model [41]. Therefore, since the incidence in several breeds of osteoarticular pathologies in the dog, such as dysplasia or arthrosis, and the possibility of improving cellular treatments, the canine MSCs ability to form spheroids was investigated. This is the first report evaluating canine adult and fetal adnexa MSCs ability to form spheroids *in vitro*, and for this purpose, a specific multi-well plate was used. In this culture conditions, both cell cultures were able to form spheroids of similar volume, differently from what observed between adult and fetal adnexa derived cells in the horse [34]. This finding for canine MSC lineages is then supported by their similar ability to differentiate toward chondrogenic lineage. Accordingly, the *in vitro* MSC self-assembly as 3D aggregates has been suggested to recapitulate the *in vivo* mesenchymal condensation events that influence MSC properties beyond chondrogenic lineage [39]. Indeed, no difference was also observed in the differentiation ability of the studied cultured cells, in neither adipogenic nor osteogenic sense, confirming what already demonstrated for canine MSCs from different tissues [19].

On considering the molecular characteristics of studied cells, both lineages were positive for the mesenchymal markers CD90 and CD44, and negative for the hematopoietic marker CD14, as postulated by the International Society for Cellular Therapy [2]. On the other hand, differently from Zhan et al. [19], we observed the expression of CD34 by canine AT-MSCs, while UC-MSCs expressed this marker only at P0, as also recently observed for canine MSCs from UC perivascular tissue [42]. Nonetheless, nowadays the negative expression of CD34 is not considered an essential feature of MSCs, because it was demonstrated that the expression of this marker could be influenced by the environment, the cellular type and by the passage of *in vitro* culture [43]. As previously demonstrated [35, 44], a weak expression of DLA-DRA1 and DLA-DQA1 markers was observed in UC-MSCs only at passage 0. The weak detection of these markers can be attributed to contamination with other cells present in the cord matrix (endothelial cells, blood cells, etc.). Conversely, in the present study all AT-MSCs showed a weak expression of the above markers in almost all the passages. These data confirm that also in the dog mesenchymal stem cells isolated from the umbilical cord would seem less immunogenic and therefore safer for heterologous transplantation compared with adipose tissue derived counterparts [45].

The results show that both AT- and UC-MSCs mainly rely on OXPHOS to produce ATP, but they can increase the anaerobic glycolytic pathway when the mitochondrial respiration is

inhibited to fulfil the ATP demand. Therefore, the elevated dependence on the glycolytic flux, which is a common metabolic feature of stem and cancer cells, is maintained even if temporarily latent and may also represent an environmental adaptation strategy to maintain stem cell identity. Even if MSCs are the most commonly tested stem cells in experimental cell therapy [46–48], the mechanisms underpinning phenotypic and functional properties, which underlie the bioenergetic changes during differentiation, are not well understood. Apparently, the MSC metabolic plasticity and versatility respond to the cellular demands and the related energy requirements [46, 47]. Therefore, MSC fate in animal species can be addressed by energy metabolism, which in turn can be affected by many variables such as stemness [48], culture conditions [47] and even the individual physiological state [49]. In general, proliferating stem cells do not use OXPHOS [47], even if they maintain the ability to shift to OXPHOS when a more efficient ATP production is required, as shown by the results. Accordingly, mitochondrial dynamics significantly impacts cell function and fate [50] and metabolic reconfiguration is strictly associated to a different mitochondrial function [48]. Since stem cells can drive the plasticity in energy metabolism to satisfy their proliferative, differentiation and reprogramming state [51], we found that the canine MSCs studied not necessarily use the energy-consuming anabolic metabolism to synthesize the building blocks for macromolecules and biostructures [52], but they prefer to mainly exploit substrate catabolism to produce ATP. Although UC-MSCs showed higher ATP production than AT-MSCs, the latter synthesize more ATP by mitochondrial activity. However, in both cell cultures mitochondria have a high coupling efficiency, namely they efficiently match electron transport to ADP phosphorylation to yield ATP. To summarize, these cells are both able to address the whole energy obtained from substrate oxidation to ATP production, a feature found in non-specialized cell cultures. Importantly, AT- and UC-MSCs do not work at the limit of their bioenergetic capacity. They possess a spare respiratory capacity that exceeds by several orders of magnitude their basal OCR. This feature can guarantee the increase in aerobic metabolism required to satisfy the increased ATP demand during cell differentiation [53].

## Conclusions

In mammalian cells, the cellular ATP is provided by OXPHOS and glycolytic pathways. The proportion between these two distinct metabolic strategies mainly depends on the cell type, the physiological state and the related energy requirements. The two types of canine MSCs under study apparently share the same bioenergetic strategy, namely a OXPHOS prevalence, and possess other shared biological features, even if some differences exist in the expression of some molecular markers, such as CD34 and DLA-DQA1, and bioenergetic parameters. Further studies will help to elucidate the impact of cell passages and of the individual variability on cell metabolism and bioenergetics. The integration between histological, biological and bioenergetic studies can depict an innovative pattern of the cellular phenotype and of the metabolic strategies required to modulate control of stem cell progression and differentiation. Accordingly, the information obtained may efficiently contribute to select the most appropriate MSCs, culture and experimental conditions to carry out transplantation experiments in mesenchymal stem cell therapy for companion animals and strengthen the emerging hopes in regenerative and preventive medicine. The present data indicate that, between the two canine MSC types under study, most likely, due to the lower immunogenic properties and higher efficiency of ATP production, UC-MSCs may be more appropriate for transplantation studies, even if studies on the biological and metabolic properties of canine MSCs are still at the beginning. Undoubtedly, both MSC types, easy to obtain and endowed with an intriguing metabolic versatility, represent a very interesting matter of investigation and a putative potential tool in

regenerative medicine. Present data not only stimulate further studies to substantiate this intriguing hypothesis, but also strengthen the relevance of an increased knowledge of stem cell bioenergetics to address actions to improve the quality of *in vitro* cultures. Accordingly, the knowledge of the mitochondrial status and especially of some bioenergetics parameters such as the spare respiratory capacity, which guarantees a metabolic flexibility, may help to select the better candidates for transplantation studies [54].

## Supporting information

**S1 Raw images.**  
(PDF)

## Acknowledgments

The Authors thank Prof. Daniele Zambelli and Dr. Marco Cunto, Department of Veterinary Medical Sciences, University of Bologna, for accessing to samples.

## Author Contributions

**Conceptualization:** Eleonora Iacono.

**Data curation:** Romina Marcocchia, Salvatore Nesci.

**Formal analysis:** Salvatore Nesci, Barbara Merlo.

**Funding acquisition:** Alessandra Pagliarani.

**Investigation:** Romina Marcocchia, Salvatore Nesci, Cristina Algieri, Eleonora Iacono.

**Project administration:** Eleonora Iacono.

**Resources:** Giulia Ballotta.

**Validation:** Salvatore Nesci.

**Writing – original draft:** Romina Marcocchia, Salvatore Nesci.

**Writing – review & editing:** Barbara Merlo, Alessandra Pagliarani, Eleonora Iacono.

## References

1. Wei X, Yang X, Han Z, Qu F, Shao L, Shi Y. Mesenchymal stem cells: a new trend for cell therapy. *APS*. 2013; 34: 747–54. <https://doi.org/10.1038/aps.2013.50> PMID: 23736003
2. Dominici M, Le Blanc K, Mueller I, Slaper-Cortenbach I, Marini FC, Krause DS, et al. Minimal criteria for defining multipotent mesenchymal stromal cells. The International Society for Cellular Therapy Position Statement. *Cytotherapy*. 2006; 8: 315–7. <https://doi.org/10.1080/14653240600855905> PMID: 16923606
3. Sun M, Sun L, Huang C, Chen B, Zhou Z. Induction of macrophage M2b/c polarization by adipose tissue-derived mesenchymal stem cells. *J Immunol Re*. 2019. Available from: <https://www.hindawi.com/journals/jir/2019/7059680/> <https://doi.org/10.1155/2019/7059680> PMID: 31321244
4. Ullah I, Subbarao RB, Rho GJ. Human mesenchymal stem cells—Current trends and future prospective. *Biosci Rep*. 2015; 35: e00191. Available from: <https://portlandpress.com/bioscirep/article/doi/10.1042/BSR20150025/56141> PMID: 25797907
5. Caplan AI, Dennis JE. Mesenchymal stem cells as trophic mediators. *J Cell Biochem*. 2006; 98: 1076–84. <https://doi.org/10.1002/jcb.20886> PMID: 16619257
6. Hayes B, Fagerlie SR, Ramakrishnan A, Baran S, Harkey M, Graf L, et al. Derivation, characterization, and *in vitro* differentiation of canine embryonic stem cells. *Stem Cells*. 2018; 26: 465–73.
7. Schneider MR, Wolf E, Braun J, Kolb HJ, Adler H. Canine embryo-derived stem cells and models for human diseases. *Hum Mol Genet*. 2008; 17: R42–7. <https://doi.org/10.1093/hmg/ddn078> PMID: 18632696

8. Wenceslau CV, Miglino MA, Martins DS, Ambrosio CE, Lizier NF, Pignatari GC, et al. Mesenchymal progenitor cells from canine fetal tissues: yolk sac, liver, and bone marrow. *Tissue Eng Part A*. 2011; 17: 2165–76. <https://doi.org/10.1089/ten.TEA.2010.0678> PMID: 21529262
9. Black LL, Gaynor J, Gahring D, Adams C, Aron D, Harman S, et al. Effect of adipose-derived mesenchymal stem and regenerative cells on lameness in dogs with chronic osteoarthritis of the coxofemoral joints: a randomized, double-blinded, multicenter, controlled trial. *Vet Ther*. 2007; 8: 272–84. PMID: 18183546
10. Iacono E, Pascucci L, Bazzucchi C, Cunto M, Ricci F, Rossi B, et al. Could hypoxia influence basic biological properties and ultrastructural features of adult canine mesenchymal stem/stromal cells? *Vet Res Commun*. 2018; 42: 297–308. <https://doi.org/10.1007/s11259-018-9738-9> PMID: 30238341
11. Bateman ME, Strong AL, Gimble JM, Bunnell BA. Concise review: using fat to fight disease: a systematic review of nonhomologous adipose-derived stromal/stem cell therapies. *Stem Cells*. 2018; 36: 1311–28. <https://doi.org/10.1002/stem.2847> PMID: 29761573
12. Arnhold S, Wenisch S. Adipose tissue derived mesenchymal stem cells for musculoskeletal repair in veterinary medicine. *Am J Stem Cells*. 2015; 4: 1–12. PMID: 25973326
13. Cremonesi F, Corradetti B, Lange Consiglio A. Fetal adnexa derived stem cells from domestic animal: progress and perspectives. *Theriogenology*. 2011; 75: 1400–15. <https://doi.org/10.1016/j.theriogenology.2010.12.032> PMID: 21463720
14. Iacono E, Rossi B, Merlo B. Stem cells from foetal adnexa and fluid in domestic animals: an update on their features and clinical application. *Reprod Domest Anim*. 2015; 50: 353–64. <https://doi.org/10.1111/rda.12499> PMID: 25703812
15. Filioli Uranio M, Valentini L, Lange-Consiglio A, Caira M, Guaricci AC, L'Abbate A, et al. Isolation, proliferation, cytogenetic, and molecular characterization and in vitro differentiation potency of canine stem cells from foetal adnexa: a comparative study of amniotic fluid, amnion, and umbilical cord matrix. *Mol Reprod Dev*. 2011; 78: 361–73. <https://doi.org/10.1002/mrd.21311> PMID: 21491540
16. Marcus AJ, Woodbury D. Fetal stem cells from extra-embryonic tissues: do not discard. *J Cell Mol Med*. 2008; 12: 730–42. <https://doi.org/10.1111/j.1582-4934.2008.00221.x> PMID: 18194447
17. Nesci S, Bernardini C, Salaroli R, Zannoni A, Trombetti F, Ventrella V, et al. Characterization of metabolic profiles and lipopolysaccharide effects on porcine vascular wall mesenchymal stem cells. *J Cell Physiol*. 2019; 234: 16685–91. <https://doi.org/10.1002/jcp.28429> PMID: 30825197
18. Tsogtbaatar E, Landin C, Minter-Dykhouse K, Folmes CDL. Energy metabolism regulates stem cell pluripotency. *Front Cell Dev Biol*. 2020; 8: 87. Available from: <https://www.frontiersin.org/articles/10.3389/fcell.2020.00087/full> <https://doi.org/10.3389/fcell.2020.00087> PMID: 32181250
19. Zhan XS, El-Ashram S, Luo DZ, Luo HN, Wang BY, Chen SF, et al. A comparative study of biological characteristics and transcriptome profiles of mesenchymal stem cells from different canine tissues. *Int J Mol Sci*. 2019; 20: 1485. Available from: <https://www.mdpi.com/1422-0067/20/6/1485> <https://doi.org/10.3390/ijms20061485> PMID: 30934541
20. Ryu HH, Kang BJ, Park SS, Kim Y, Sung GJ, Woo HM, et al. Comparison of mesenchymal stem cells derived from fat, bone marrow, Wharton's jelly, and umbilical cord blood for treating spinal cord injuries in dogs. *J Vet Med Sci*. 2012; 74: 1617–30. <https://doi.org/10.1292/jvms.12-0065> PMID: 22878503
21. Merlo B, Pirondi S, Iacono E, Rossi B, Ricci F, Mari G. Viability, in vitro differentiation and molecular characterization of equine adipose tissue-derived mesenchymal stem cells cryopreserved in serum and serum-free medium. *Cryo Letters*. 2016; 37: 243–52. PMID: 27925007
22. Rainaldi G, Pinto B, Piras A, Vatteroni L, Simi S, Citti L. Reduction of proliferative heterogeneity of CHEF18 Chinese hamster cell line during the progression toward tumorigenicity. *In Vitro Cell Dev Biol—Animal*. 1991; 27: 949–52. <https://doi.org/10.1007/BF02631122> PMID: 1757399
23. Pinheiro AO, Lara VM, Souza AF, Casals JB, Bressan FF, Neto PF, et al. Characterization and immunomodulation of canine amniotic membrane stem cells. *Stem Cells Cloning*. 2020; 13: 43–55. <https://doi.org/10.2147/SCCAA.S237686> PMID: 32440160
24. Bellotti C, Duchi S, Bevilacqua A, Lucarelli E, Piccinini F. Long term morphological characterization of mesenchymal stromal cells 3D spheroids built with a rapid method based on entry-level equipment. *Cytotechnology*. 2016; 68: 2479–90. <https://doi.org/10.1007/s10616-016-9969-y> PMID: 27023795
25. Liang CC, Park AY, Guan JL. In vitro scratch assay: a convenient and inexpensive method for analysis of cell migration in vitro. *Nature Protocols*. 2007; 2: 329–33. <https://doi.org/10.1038/nprot.2007.30> PMID: 17406593
26. Rossi B, Merlo B, Colleoni S, Iacono E, Tazzari PL, Ricci F, et al. Isolation and in vitro characterization of bovine amniotic fluid derived stem cells at different trimesters of pregnancy. *Stem Cell Rev Rep*. 2014; 10: 712–24. <https://doi.org/10.1007/s12015-014-9525-0> PMID: 24906426
27. Mizuno H, Hyakusoku H. Mesengenic potential and future clinical perspective of human processed liposarcoma cells. *J Nippon Med Sch*. 2003; 70: 300–06. <https://doi.org/10.1272/jnms.70.300> PMID: 12928709

28. Merlo B, Teti G, Mazzotti E, Ingrà L, Salvatore V, Buzzi M, et al. Wharton's jelly derived mesenchymal stem cells: comparing human and horse. *Stem Cell Rev Rep*. 2018; 14: 574–84. <https://doi.org/10.1007/s12015-018-9803-3> PMID: 29508214
29. Burk J, Ribitsch I, Gittel C, Juelke H, Kasper C, Staszuk C, et al. Growth and differentiation characteristics of equine mesenchymal stroma cells derived from different sources. *Vet J*. 2013; 195: 98–106. <https://doi.org/10.1016/j.tvjl.2012.06.004> PMID: 22841420
30. Jung DI, Ha J, Kang BT, Kim JW, Quan FS, Lee JH, et al. A comparison of autologous and allogenic bone marrow-derived mesenchymal stem cell transplantation in canine spinal cord injury. *J Neurol Sci*. 2009; 285: 67–77. <https://doi.org/10.1016/j.jns.2009.05.027> PMID: 19555980
31. Malagola E, Teunissen M, van der Laan LJ, Verstegen MM, Schotanus BA, van Steenbeek FG, et al. Characterization and comparison of canine multipotent stromal cells derived from liver and bone marrow. *Stem Cells Dev*. 2016; 25: 139–50. <https://doi.org/10.1089/scd.2015.0125> PMID: 26462417
32. Marchetti P, Fovez Q, Germain N, Khamari R, Kluzka J. Mitochondrial spare respiratory capacity: mechanisms, regulation, and significance in non transformed and cancer cells. *The FASEB J*. 2020; 34: 13106–13124. <https://doi.org/10.1096/fj.202000767R> PMID: 32808332
33. Keuper M, Jastroch M, Yi C, Fisher-Pozowski F, Wabitsch M, Tschop M H, et al. Spare mitochondrial respiratory capacity permits human adipocytes to maintain ATP homeostasis under hypoglycemic conditions. *The FASEB J*. 2013; 28: 761–770. <https://doi.org/10.1096/fj.13-238725> PMID: 24200885
34. Merlo B, Teti G, Lanci A, Burk J, Mazzotti E, Falconi M, et al. Comparison between adult and foetal adnexa derived equine post-natal mesenchymal stem cells. *BMC Vet Res*. 2019; 15: 277. Available from: <https://bmcvetres.biomedcentral.com/articles/10.1186/s12917-019-2023-5> <https://doi.org/10.1186/s12917-019-2023-5> PMID: 31375144
35. Filioli Uranio M, Dell'Aquila ME, Caira M, Guaricci AC, Ventura M, Catacchio CR, et al. Characterization and *in vitro* differentiation potency of early-passage canine amnion- and umbilical cord-derived mesenchymal stem cells as related to gestational age. *Mol Reprod Dev*. 2014; 81: 539–51. <https://doi.org/10.1002/mrd.22322> PMID: 24659564
36. Lee KS, Cha SH, Kang HW, Song JY, Lee KW, Ko KB, et al. Effects of serial passage on the characteristics and chondrogenic differentiation of canine umbilical cord matrix derived mesenchymal stem cells. *Asian-Australas J Anim Sci*. 2013; 26: 588–95. <https://doi.org/10.5713/ajas.2012.12488> PMID: 25049827
37. Rutigliano L, Valentini L, Martino NA, Pizzi F, Zanghi A, Dell'Aquila ME, et al. Ochratoxin A at low concentrations inhibits *in vitro* growth of canine umbilical cord matrix mesenchymal stem cells through oxidative chromatin and DNA damage. *Reprod Toxicol*. 2015; 57: 121–29. <https://doi.org/10.1016/j.reprotox.2015.05.017> PMID: 26055943
38. Li G, Zhang X, Wang H, Wang X, Meng C, Chan C, et al. Comparative proteomic analysis of mesenchymal stem cells derived from human bone marrow, umbilical cord, and placenta: implication in the migration. *J Proteome Res*. 2009; 9: 20–30.
39. Sart S, Tsai AC, Li Y, Ma T. Three-dimensional aggregates of mesenchymal stem cells: cellular mechanism, biological properties, and applications. *Tissue Eng Part B Rev*. 2014; 20: 365–80. <https://doi.org/10.1089/ten.TEB.2013.0537> PMID: 24168395
40. Wang W, Itaka K, Ohba S, Nishiyama N, Chung UI, Yamasaki Y, et al. 3D spheroid culture system on micropatterned substrates for improved differentiation efficiency of multipotent mesenchymal stem cells. *Biomaterials*. 2009; 30: 2705–15. <https://doi.org/10.1016/j.biomaterials.2009.01.030> PMID: 19215979
41. Suzuki S, Muneta T, Tsuji K, Ichinose S, Makino H, Umezawa A, et al. Properties and usefulness of aggregates of synovial mesenchymal stem cells as a source for cartilage regeneration. *Arthritis Res Ther*. 2012; 14: R136. Available from: <https://arthritis-research.biomedcentral.com/articles/10.1186/ar3869> <https://doi.org/10.1186/ar3869> PMID: 22676383
42. Sepúlveda RV, Eleotério In Memoriam RB, Valente FL, Araújo FR, Sabino AP, Evangelista FCG, et al. Canine umbilical cord perivascular tissue: a source of stem cells for therapy and research. *Res Vet Sci*. 2020; 129: 193–202. <https://doi.org/10.1016/j.rvsc.2020.02.006> PMID: 32087438
43. Lin C, Ning H, Lin G, Lue T. Is CD34 truly a negative marker for mesenchymal stromal cells?. *Cytotherapy* 2012; 14: 1159–63. <https://doi.org/10.3109/14653249.2012.729817> PMID: 23066784
44. Seo MS, Jeong YH, Park JR, Park SB, Rho KH, Kim HS, et al. Isolation and characterization of canine umbilical cord blood-derived mesenchymal stem cells. *J Vet Sci*. 2009; 10: 181–7. <https://doi.org/10.4142/jvs.2009.10.3.181> PMID: 19687617
45. Kim JH, Jo CH, Kim HR, Hwang YI. Comparison of immunological characteristics of mesenchymal stem cells from the periodontal ligament, umbilical cord, and adipose tissue. *Stem Cells Int*. 2018; 2018:8429042. Available from: <https://www.hindawi.com/journals/sci/2018/8429042/>. <https://doi.org/10.1155/2018/8429042> PMID: 29760736

46. Shum LC, White NS, Mills BN, Bentley KL, Eliseev RA. Energy metabolism in mesenchymal stem cells during osteogenic differentiation. *Stem Cells Dev.* 2016; 25: 114–122. <https://doi.org/10.1089/scd.2015.0193> PMID: 26487485
47. Yuan X, Logan TM, Ma T. Metabolism in human mesenchymal stromal cells: a missing link between hMSC biomanufacturing and therapy?. *Front Immunol.* 2019; 10: 977. Available from: <https://www.frontiersin.org/articles/10.3389/fimmu.2019.00977/full> <https://doi.org/10.3389/fimmu.2019.00977> PMID: 31139179
48. Barilani M, Palorini R, Votta G, Piras R, Buono G, Grassi M, et al. Central metabolism of functionally heterogeneous mesenchymal stromal cells. *Sci Rep.* 2019; 9: 15420. Available from: <https://www.nature.com/articles/s41598-019-51937-9> <https://doi.org/10.1038/s41598-019-51937-9> PMID: 31659213
49. Iaffaldano L, Nardelli C, D'Alessio F, D'Argenio V, Nunziato M, Mauriello L, et al. Altered bioenergetic profile in umbilical cord and amniotic mesenchymal stem cells from newborns of obese women. *Stem Cells Dev.* 2018; 27: 199–206. <https://doi.org/10.1089/scd.2017.0198> PMID: 29205089
50. Khacho M, Clark A, Svoboda DS, Azzi J, MacLaurin JG, Meghaizel C, et al. Mitochondrial dynamics impacts stem cell identity and fate decisions by regulating a nuclear transcriptional program. *Cell Stem Cell.* 2016; 19: 232–47. <https://doi.org/10.1016/j.stem.2016.04.015> PMID: 27237737
51. Folmes CD, Dzeja PP, Nelson TJ, Terzic A. Metabolic plasticity in stem cell homeostasis and differentiation. *Cell Stem Cell.* 2012; 11: 596–606. <https://doi.org/10.1016/j.stem.2012.10.002> PMID: 23122287
52. Nesci S. Glucose and glutamine in the mitochondrial oxidative metabolism of stem cells. *Mitochondrion.* 2017; 35: 11–2. <https://doi.org/10.1016/j.mito.2017.04.004> PMID: 28438612
53. Lonergan T, Brenner C, Bavister B. Differentiation-related changes in mitochondrial properties as indicators of stem cell competence. *J Cell Physiol.* 2006; 208: 149–53. <https://doi.org/10.1002/jcp.20641> PMID: 16575916
54. Bertolo A, Capossela S, Fränkl G, Baur M, Pötzel T, Stoyanov J. Oxidative status predicts quality in human mesenchymal stem cells. *Stem Cell Res Ther.* 2017; 8: 3. <https://doi.org/10.1186/s13287-016-0452-7> PMID: 28061861



# Relationship between serum concentration, functional parameters and cell bioenergetics in IPEC-J2 cell line

Chiara Bernardini<sup>1</sup> · Cristina Algieri<sup>1</sup> · La Debora Mantia<sup>1</sup> · Augusta Zannoni<sup>1,2</sup> · Roberta Salaroli<sup>1</sup> · Fabiana Trombetti<sup>1</sup> · Monica Forni<sup>1,2</sup> · Alessandra Pagliarani<sup>1</sup> · Salvatore Nesci<sup>1</sup>

Accepted: 3 March 2021 / Published online: 16 March 2021  
© The Author(s), under exclusive licence to Springer-Verlag GmbH Germany, part of Springer Nature 2021

## Abstract

The foetal bovine serum (FBS) concentration could influence functional parameters of IPEC-J2 cells. IPEC-J2 is a non-transformed continuous epithelial cell line that represents an established in vitro model to study porcine gut inflammation and alterations of intestinal integrity. This cell line also represents a good translational model thanks to the high similitudes between pig and human gastrointestinal tract. With the aim to assess if the FBS-dependent functional variations are linked to the bioenergetic aspects, the addition of 5% and 10% FBS in the IPEC-J2 culture medium were tested. Doubling time and TEER measurement indicated that cells cultured at higher FBS dose grow faster and as a more compact monolayer. 10% FBS increases ATP production and mitochondrial oxidative phosphorylation (OxPhos) and does not affect glycolysis. Both at 5% and 10% FBS ATP production mainly comes from OxPhos and FBS concentration does not affect the cell respiration bioenergetic parameters. Noteworthy, IPEC-J2 treated with 5% and 10% FBS have a metabolic potential since both OxPhos and glycolysis increase by > 100% and < 50%, respectively in comparison with baseline metabolism. Moreover, glucose, fatty acids and glutamine constitute the preferred metabolic fuel for mitochondrial respiration at both FBS conditions tested. Accordingly, the cells flexibility to oxidize these substrates shows that IPEC-J2 mitochondria cannot maintain the basal ATP production without oxidizing all the substrates available irrespective of FBS concentration. To sum up, in IPEC-J2 cells OxPhos increases with the FBS-stimulated functional physiological parameters to fulfil ATP requirements.

**Keywords** IPEC-J2 · Cell metabolism · Oxidative phosphorylation · Mitochondria · Glycolysis · Foetal bovine serum

## Introduction

The IPEC-J2 cell lines, isolated from pig small intestine, are neither tumourigenic nor transformed and show morphological and functional similarity to the porcine enterocyte. This cell line represents a well-established model to simulate the human intestinal barrier by mimicking the human physiology more closely than any other cell line

of non-human origin (Vergauwen 2015). IPEC-J2 show epithelial phenotypic characteristic: they grow as polarized monolayer made compact by the lateral expression of tight junction's proteins as occludin and claudin (Mariani et al. 2009). Their apical side is equipped with microvilli and they produce mucin recreating the in vivo protective mucous layer (Vergauwen 2015). Moreover, IPEC-J2 express several members of the Toll-like receptor family important molecules for the recognition of pathogen components and, if stimulated, they can produce cytokines and chemokines (Schierack et al. 2006). Overall IPEC-J2 cells, represent a favourable in vitro model for research applications, being an ideal tool to study epithelial transport, interaction with enteric pathogens, as well as the effects of probiotics and nutrients. IPEC-J2 has been successfully cultured using many different protocols (Vergauwen 2015), in which serum, mostly foetal bovine serum (FBS), has been added to provide a wide variety of nutrients, carrier proteins, hormones attachment and

---

Monica Forni and Alessandra Pagliarani are senior authors.

---

✉ Monica Forni  
monica.forni@unibo.it

<sup>1</sup> Department of Veterinary Medical Science, University of Bologna, Via Tolara di Sopra, 50, 40064 Ozzano Emilia, BO, Italy

<sup>2</sup> Health Sciences and Technologies—Interdepartmental Center for Industrial Research (CIRI-SDV), Alma Mater Studiorum, University of Bologna, Bologna, Italy

growth factors. Moreover, it has been demonstrated that the amount and the type of serum added to the culture medium of IPEC-J2 cells induces a process of spontaneous differentiation that modifies the functional parameters involved in the formation of a polarized monolayer with low or high transepithelial electrical resistance (TEER) (Zakrzewski et al. 2013). While IPEC-J2 cells have been largely studied for their nutrient requirements and membrane transport features (Mao et al. 2018; Zuo et al. 2019), as far as we are aware the energy metabolism of these cells has been poorly explored. Cellular metabolism is a flexible network that allows tissues to meet demands for homeostasis and growth. The metabolic shift from oxidative phosphorylation (OxPhos) to glycolysis under oxygen availability is known as Warburg effect (DeBerardinis and Chandel 2020). Cells with a glycolytic phenotype exhibit significantly higher rates of proton production by glucose fermentation to lactate (detected as extracellular acidification rate, ECAR) than cells using OxPhos (detected as oxygen consumption rate, OCR). Bioenergetic profiling is currently used to assess the amount of energy in the form of ATP produced by mitochondrial versus non-mitochondrial respiration; namely, respiration (oxygen consumption) which yields ATP synthesis, and uncoupled respiration, which does not produce ATP, by adding to the chamber containing cells a series of metabolic inhibitors (Shum et al. 2016). Shifts in substrate utilization and energy metabolism can be conveniently and simultaneously detected by evaluating the OCR, to quantify mitochondrial respiration and the ECAR, an indicator of glycolysis. In general, glycolytic dependence, which is a common metabolic feature of stem and cancer cells, may also represent an environmental adaptation strategy to maintain the cell identity during proliferation (Yuan et al. 2019). Conversely, during differentiation a phenotypic and functional change in bioenergetics due to the related cell energy requirements is featured by an increase in mitochondrial OxPhos (Nesci 2017). It is essential to consider the epithelial cell biology in the light of the two metabolic pathways of ATP production in the cells; namely, glycolysis and oxidative phosphorylation (OxPhos), being the latter, in terms of energy, much more efficient. Accordingly, the energy-consuming transport processes along the epithelial barrier of the gastrointestinal tract requires an efficient oxygen turnover whose extent depends on the nutrient availability (Vaugelade et al. 1994). In intestinal cells, in general oxygen consumption stimulates cellular activity, but the physiological activation depends on nutrient absorption. Since information on IPEC-J2 bioenergetics is scanty; in this work, we aim at ascertaining if different concentrations of foetal bovine serum (FBS), which provides nutrients to the cultured IPEC-J2, can modify the IPEC-J2 functional properties and energy metabolism. The

results, obtained in a well-established cell model, can contribute to cast light on the physiological metabolic changes in enterocytes during nutrient absorption.

## Materials and methods

### Cell culture

The non-transformed cell line IPEC-J2 (intestinal porcine epithelial cells from jejunum) was purchased from the “Deutsche Sammlung von Mikroorganismen und Zellkulturen GmbH” (DSMZ). Cells were cultured in Dulbecco’s Modified Eagle Medium (DMEM) (4.5 g/L glucose) added with 10% or 5% of foetal bovine serum (FBS, Life Technologies) and 1 × antibiotic–antimycotic solution (Life Technologies) in a 5% CO<sub>2</sub> atmosphere at 37 °C. Cultures were split weekly in 25 or 75 cm<sup>2</sup> culture flasks (Corning-Becton Dickinson and Company Becton Drive, Franklin Lakes, NJ, USA). The doubling time (DT) was calculated as indicated previously (Zaniboni et al. 2014), briefly  $DT = h/CD$ , where  $h$  was the culture time in hours between two passages and  $CD$  was the cell doubling calculated as  $CD = (\log_{10}N - \log_{10}N_0)/\log_{10}2$ ,  $N$  is the number of cells at 80–90% confluency and  $N_0$  is the number of cells seeded. The monolayer formation and integrity were assessed through the measurement of trans-epithelial electrical resistance (TEER). Briefly, the cells were seeded into transparent PET membrane (0.4 μm pore size) inserts in 24 well plates at a density of  $1 \times 10^5$  cells/well. TEER measurements were conducted daily, using a Millicell ERS-2 VoltOhmmeter® (Millipore, Billerica, MA) and the values were expressed as  $\text{Ohm} \times \text{cm}^2$  ( $\Omega\text{cm}^2$ ).

### Cellular bioenergetics

The Seahorse XFp analyzer (Agilent) was used to simultaneously measure oxygen consumption rate (OCR), an index of cell respiration (pmol/min), and extracellular acidification rate (ECAR), an index of glycolysis (mpH/min). IPEC-J2 cells (10 k/well) were grown in XFp cell culture miniplates (Agilent) for 24 h. On the experiment day, IPEC-J2 were switched to freshly made Seahorse XF DMEM medium pH 7.4 supplied with 10 mM glucose, 1 mM sodium pyruvate and 2 mM L-glutamine. The plates were incubated at 37 °C in air for 45’ before measuring OCR and ECAR by the adequate programs (ATP Rate Assay, Cell Mito Stress Test and Cell Energy Phenotype Test). The injection ports of XFp sensor cartridges, which were hydrated overnight with XF calibrant at 37 °C, were loaded with 10 × concentration of inhibitors according to the instructions provided by Seahorse XFp ATP Rate Assay, Cell Mito Stress Test and Cell Energy Phenotype Test. The final concentration

used for ATP Rate Assay were 1.5  $\mu\text{M}$  oligomycin (port A) and 0.5  $\mu\text{M}$  rotenone (Rot) plus antimycin A (AA) (port B). For Cell Mito Stress Test the final concentrations were 1.5  $\mu\text{M}$  oligomycin (olig) (port A), 1.0  $\mu\text{M}$  carbonyl-cyanide-4-(trifluoromethoxy) phenylhydrazone (FCCP) (port B) and 0.5  $\mu\text{M}$  rotenone plus antimycin A (port C), while for the Cell Energy Phenotype Test the final concentrations were 1.5  $\mu\text{M}$  oligomycin plus 1.0  $\mu\text{M}$  FCCP (port A). All the analysis were run at 37 °C. All data were analyzed by WAVE software version 2.6.1; OCR and ECAR values were normalized to the total number of cells per each well. All parameter values were calculated per well according to the manufacturer's instructions. Both ATP Rate Assay, Mito Stress Test and Cell Energy Phenotype Test were carried out three times on different days.

The ATP Rate Assay provides the bioenergetic parameters currently used to characterize the cellular ATP production, namely ATP production rate, related to the conversion of glucose to lactate in the glycolytic pathway (glycoATP Production Rate) and to mitochondrial OxPhos (mitoATP Production Rate). Accordingly, the ratio between mitoATP Production Rate and glycoATP Production Rate (ATP Rate Index) is currently considered as a valuable parameter to detect changes and/or differences in the metabolic phenotype (a ratio > 1 means mainly OxPhos pathway; ratio < 1 means mainly glycolytic pathway).

The Mito Stress Test enables to characterize cell respiration by the following parameters: basal respiration, detected as baseline OCR before oligomycin addition; minimal respiration measured as OCR in the presence of oligomycin; maximal respiration evaluated as OCR after FCCP addition. The so-called proton leak which corresponds to the difference between the basal respiration and the respiration in the presence of oligomycin (minimal respiration), indicates the re-entry of  $\text{H}^+$  in the intermembrane space independently of the  $\text{F}_1\text{F}_0$ -ATP synthase. The non-mitochondrial respiration, evaluated as OCR in the presence of rotenone plus antimycin A (respiratory chain inhibitors), was subtracted from all the above parameters. The ATP turnover or oligomycin-sensitive respiration was obtained from the difference between the basal respiration and the minimal respiration (OCR in presence of oligomycin). Finally, the difference between the maximal and the basal respiration provided the spare capacity, which represents the ability to respond to an increased energy demand and can be considered as a measure of the flexibility of the OxPhos machinery.

The simultaneous measurement of mitochondrial respiration and glycolysis was carried out by the Cell Energy Phenotype Test under baseline and stressed conditions, the latter after simultaneous addition of oligomycin and FCCP. Oligomycin inhibits the mitochondrial ATP production by the  $\text{F}_1\text{F}_0$ -ATP synthase and the cell compensates the failed OxPhos by increasing the glycolysis rate, while

the dissipation of electrochemical gradient of  $\text{H}^+$  in mitochondria by the ionophore FCCP drives the highest oxygen consumption (uncoupled respiration). The assay allows to evaluate two main parameters of cell energy metabolism known as metabolic phenotypes (baseline and stressed phenotype) and metabolic potential. The baseline phenotype is featured by the OCR and ECAR values in cells under the starting condition in the presence of substrates. The stressed phenotype is shown by the OCR and ECAR values in cells after the addition of stressor compounds (oligomycin plus FCCP). The metabolic potential is the ability to increase energy production via respiration and glycolysis and it is defined as the % increase of stressed phenotype over baseline phenotype of OCR and ECAR.

The Fuel Flex Test determines the rate of oxidation of glucose (Glu), fatty acids (FA) and glutamine (Gln) by measuring OCR. Accordingly, the decline in oxygen consumption mirrors the decrease in fuel oxidation. The parameters cell dependency, capacity and flexibility to oxidize the three mitochondrial fuels was evaluated according to the protocol of the Fuel Flex Test kit, by blocking the nutrient oxidation pathways by specific inhibitors. By sequentially inhibiting the pathway of interest, followed by the two alternative pathways, this method allows to calculate how the cells exploit the pathway of interest to fulfil their energy demand. According to the protocol adopted, the wells contained the final concentrations of 3.0  $\mu\text{M}$  BPTES (bis-2-(5-phenylacetamido-1,3,4-thiadiazol-2-yl)ethyl sulphide), allosteric inhibitor of glutamine oxidase, which blocks glutamine oxidation pathway, 4.0  $\mu\text{M}$  etomoxir, the long chain fatty acid pathway inhibitor, which inhibits the carnitine palmitoyl-transferase 1A coding gene or 2.0  $\mu\text{M}$  UK5099, which inhibits glucose oxidation by blocking the mitochondrial pyruvate carrier. The fuel dependency represents the cell reliance on a stated oxidative pathway to maintain baseline respiration. It is calculated by adding the specific inhibitor to block the pathway of interest followed by the inhibitors of two alternative pathways. Conversely, the fuel capacity is shown by the OCR driven by a specific substrate oxidation, obtained by blocking the other fuel pathways. The fuel flexibility was obtained by subtracting the fuel dependency from the fuel capacity, for each pathway under study; this parameter describes the mitochondrial ability to switch from one oxidative pathway to another to allow OCR maintenance when a specific pathway is inhibited.

## Statistical analysis

Statistical analyses were performed by SIGMASTAT software. Each treatment was replicated three or eight times (viability test) in three independent experiments. The data were analyzed by the Student's *t* test or by one-way analysis of variance (ANOVA) followed by Students–Newman–Keuls'

test when  $F$  values indicated significance ( $P \leq 0.05$ ) was applied. The percentage data were arcsin-transformed before statistical analyses to ensure normality.

## Results

### Functional parameters: doubling time and TEER measurement

IPEC-J2 grew adherently as epithelial monolayer both cultured at 5% or 10% of FBS (Fig. 1a). The different percentage of serum determined differences in the doubling time, in fact the mean of DT calculated for ten generations showed

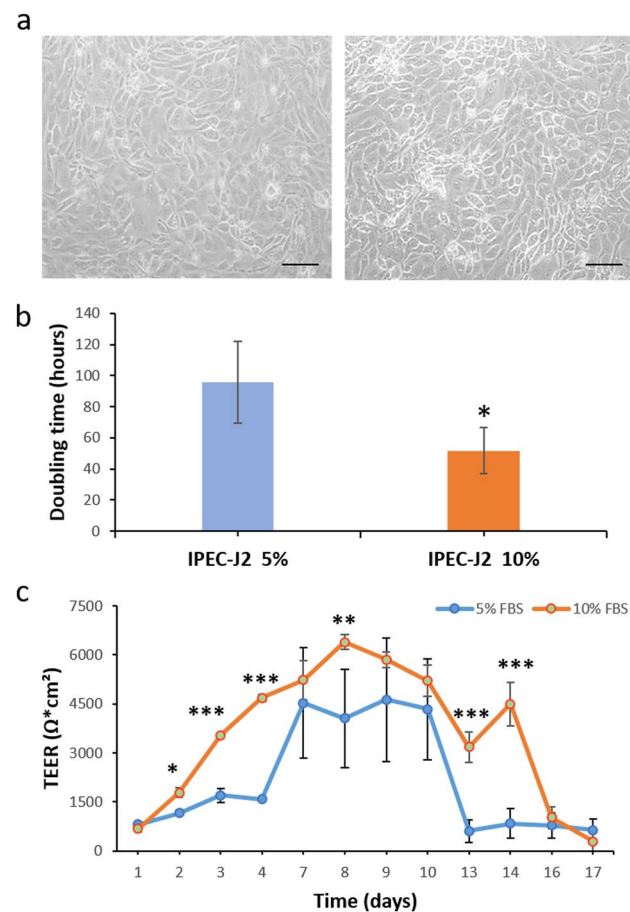


**Fig. 1** Effect of different FBS concentrations on IPEC-J2 functional parameters. **a** Representative images of IPEC-J2 cultured at 5 or 10% of FBS: no evident morphology differences were detected. Scale bar 100  $\mu\text{m}$ . **b** Doubling time of IPEC-J2 cultured at different % of FBS: cells cultured at 10% FBS showed significant decrease in the duplication time. The data represent the mean  $\pm$  SD,  $*P \leq 0.05$ . **c** Time course of transepithelial electrical resistance (TEER) measurement of IPEC-J2 cultured at different FBS percentages: cells cultured at the higher dose showed higher TEER value as compared to cells cultured at the lower dose. The data represent the mean  $\pm$  SD.  $*P \leq 0.05$   $**P \leq 0.01$   $***P \leq 0.001$

that 10% of serum determined a significant decrease of the IPEC-J2 duplication time (Fig. 1b). IPEC-J2 cells were seeded at a high density for TEER measurements and formed a compact monolayer 24 h after cell seeding, so no cell proliferation was required before starting TEER measurements. The different percentage of serum impacted also on TEER. The measurement of TEER began to rise already two days after the cells seeding on transwell, reaching the maximum at about 7 days post-seeding. Then, TEER remained stable for 3 days before to decline. Even if the trend of TEER is the same both for cells cultured at 5 or 10% FBS, TEER values reached with the highest serum concentration were always higher than those obtained with the lowest one. Furthermore, the downward trend of TEER in IPEC-J2 cultured at 5% respect to 10% was faster.

### Intracellular ATP levels

The ATP rate production is obtained from OCR and ECAR values under basal conditions. Injection of oligomycin inhibits mitochondrial ATP synthesis, while the subsequent addition of rotenone plus antimycin A causes strong inhibition of mitochondrial respiration. Thus, the depicted kinetic profile of OCR and ECAR measurement data allows the calculation of the mitoATP and glycoATP production rate (Fig. 2a). IPEC-J2 cultured for 24 h at 5% and 10% FBS concentration shows a different total ATP production rate; the 10% FBS promotes a higher amount of cellular ATP than the 5% FBS due to the OxPhos increase while glycolysis is unaffected (Fig. 2a). On considering the total ATP production, IPEC-J2 cells at 5% and 10% FBS show an ATP rate index greater than 1, which points out in both cases a prevailing mitochondrial oxidative metabolism with respect to the glycolytic pathway (Fig. 2b). The doubling time results show an increased cell growth rate in the presence of high FBS concentrations, which are consistent with the increased ATP production (Fig. 2c). However, glycolysis does not increase ATP production when cell doubling time is lower at 10% FBS than 5% FBS (Fig. 2d). Since the slope ( $\sigma$ ) of the straight line obtained (Fig. 2c) is of the same magnitude order as that of the total ATP production (Fig. 2e); namely, 1.585 vs 1.452, the mitochondrial ATP synthesis is the main responsible for the energy production required by cell proliferation. Moreover, the energy metabolism detected in IPEC-J2 cultured for 96 h shows a different profile with a decreased ATP production with respect to that detected after 24 h from cell seeding. Moreover, 5% FBS IPEC-J2 shows a higher ATP production than the 10% FBS ones, even if this difference cannot be ascribed to a preferential higher contribution of OxPhos or glycolysis (Fig. S1a). Irrespective of FBS concentration, the ATP rate index is lower than 1, thus pointing out that, under these experimental conditions, IPEC-J2 cells mainly rely on the glycolytic pathway (Fig.

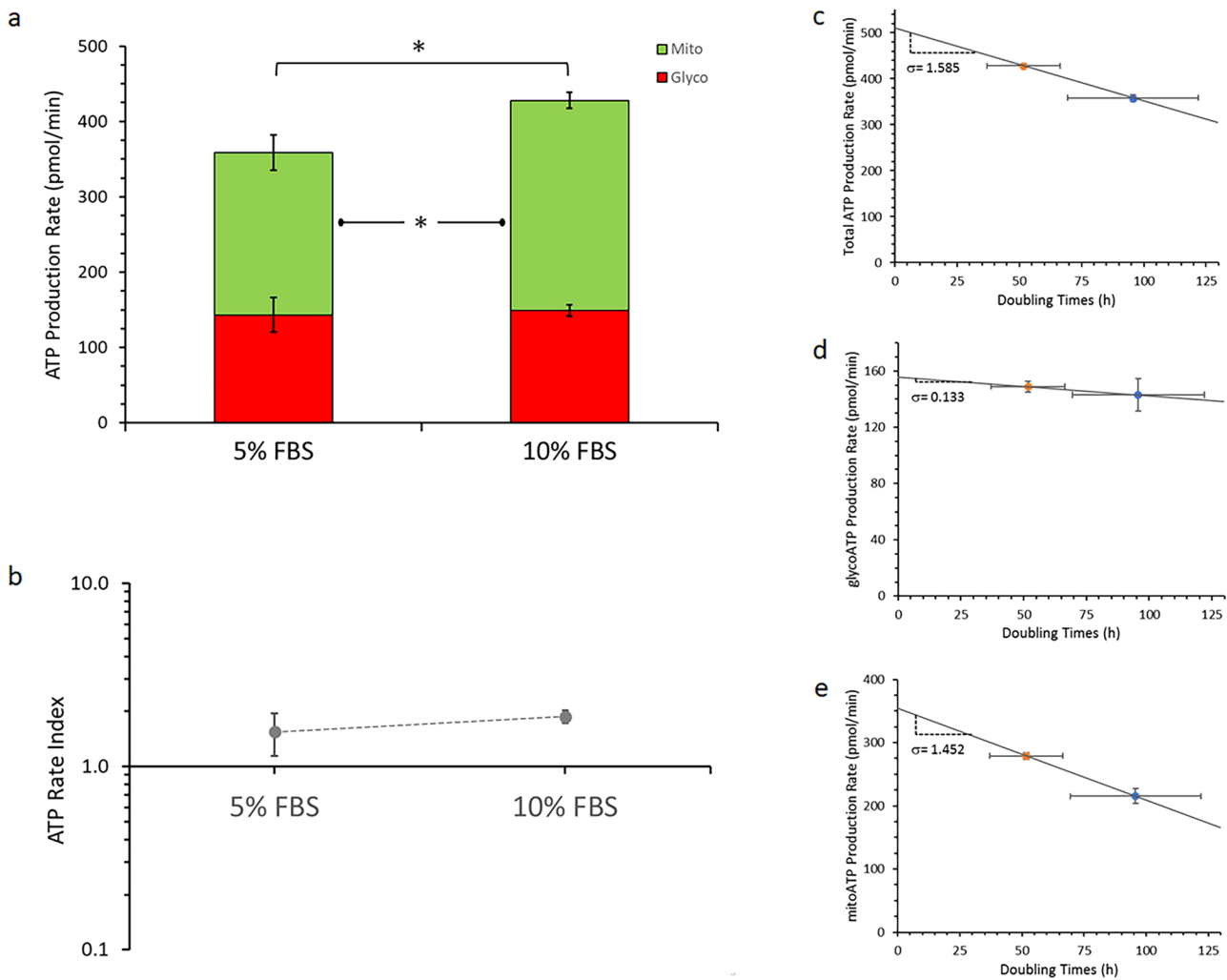


**Fig. 2** ATP production in IPEC-J2 cells. **a** Quantification of ATP production by mitochondrial oxidative phosphorylation (green box) or by the glycolytic pathway (glucose conversion to lactate) (red box). **b** The plot shows the ratio between the mitochondrial ATP production rate and glycolytic ATP production rate (logarithmic scale). **c** total ATP production rate, **d** glycoATP production rate and **e** mitoATP

production rate linked to the doubling times of IPEC-J2 at 5% (blue circle) and 10% (orange circle) FBS. The data are expressed as column chart (**a** plot) and points (**b**, **c**, **d** and **e** plots) which represent the mean  $\pm$  SD (vertical bars) from three experiments carried out on different cell preparations. “Asterisk” indicates significant differences ( $P \leq 0.05$ )

S1b). Mitochondrial ATP production of IPEC-J2 cells cultured in 5% and 10% FBS 96 h after seeding, is significantly decreased and energy metabolism mainly rely on glycolysis, an effect ascribed to the confluence of the cell culture and irrespective of FBS concentration.

**Cell respiration**

The mitochondrial respiration expressed as OCR of IPEC-J2 cells grown at different concentrations of FBS is shown in Fig. 3a. The kinetic profile obtained using serially injected mitochondrial inhibitors (olig, FCCP, Rot + AA) is not substantially different at the two FBS concentrations tested. Indeed, bioenergetic parameters do not show any significant

change at the two FBS concentrations (Fig. 3b). However, the OCR values of basal respiration and ATP turnover confirm a satisfactory coupling efficiency with  $0.73 \pm 0.03$  a.u. at 5% FBS and  $0.69 \pm 0.05$  a.u. at 10% FBS. The spare respiratory capacity, which defines the cell propensity to adjust cell bioenergetics to fulfil the increased energy demand required by proliferation, represents 63.1% and 56.4% of the maximal respiration at 5% and 10% FBS, respectively. These results are consistent with the striking increase in the maximal respiration, evaluated after FCCP addition, which attains more than twofold higher values than basal respiration.

On considering the energy production mode, namely mitochondrial OxPhos and glycolysis, the metabolic switch

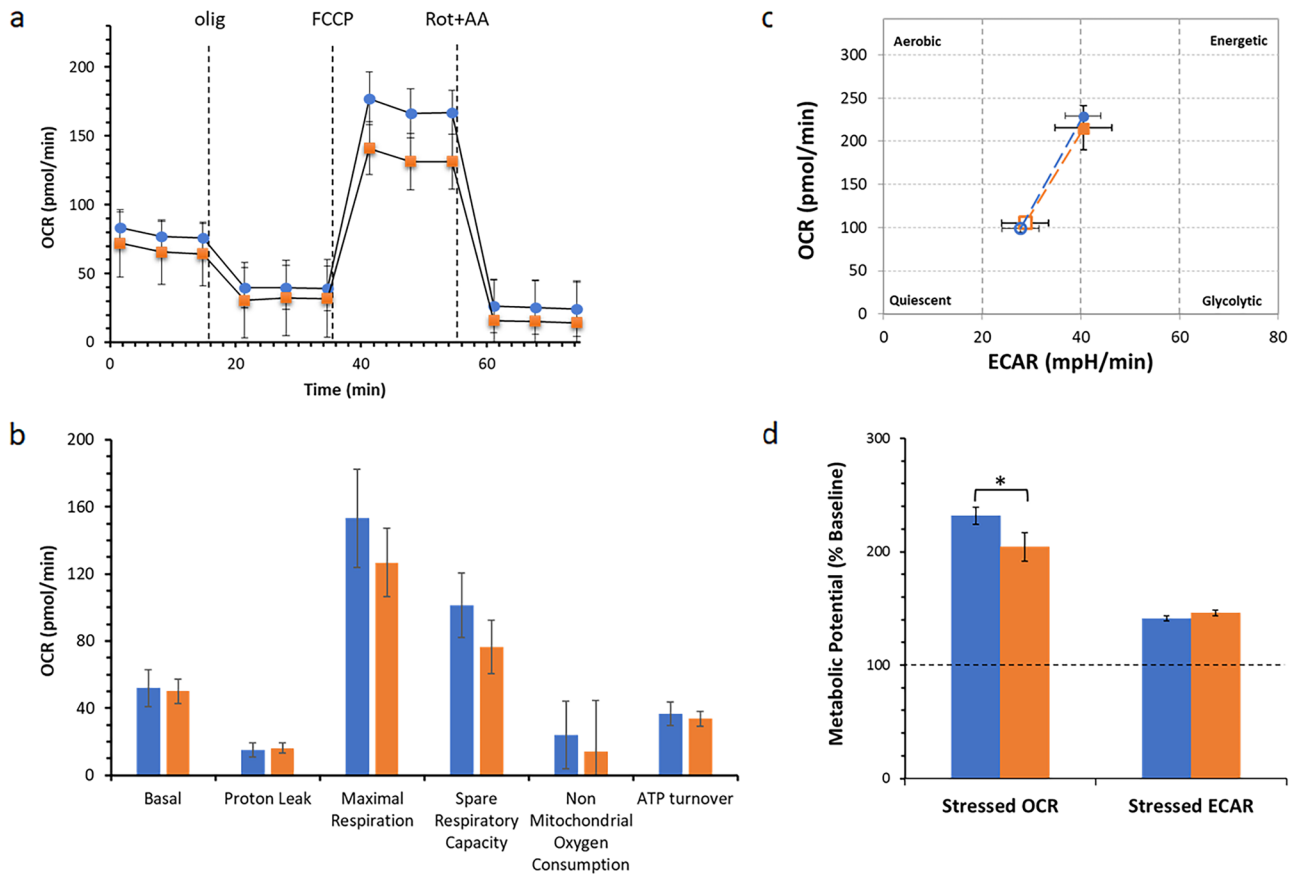


**Fig. 3** Energy profile of IPEC-J2 cells cultured at 5% and 10% FBS. **a** Oxygen consumption rate (OCR) at 5% (blue circle) and 10% (orange circle) FBS under basal conditions and after the addition of 1.5  $\mu\text{M}$  oligomycin (olig), 1.0  $\mu\text{M}$  FCCP and a mixture of 0.5  $\mu\text{M}$  rotenone plus antimycin A (rot+AA) by injections indicated by the dotted lines. **b** Mitochondrial parameters (basal respiration, ATP production, proton leak, maximal respiration, spare respiratory capacity, non-mitochondrial oxygen consumption, ATP turnover) in 5% (blue box) and 10% (orange box) FBS-treated IPEC-J2. **c** Metabolic phenotype of IPEC-J2. Baseline phenotype of 5% FBS (open blue circle) and

10% FBS-treated IPEC-J2 (open orange square) and stressed phenotype of 5% FBS (closed blue circle) and 10% FBS-treated IPEC-J2 (closed orange square). **d** Metabolic potential in “Stressed OCR” and “Stressed ECAR”, expressed as % “Baseline OCR” and “Baseline ECAR” (dashed horizontal line), in 5% (blue box) and 10% (orange box) FBS treated IPEC-J2. The data expressed as points (**a**, **c**) and column chart (**b**, **d**) represents the mean  $\pm$  SD (vertical and where present also horizontal bars) from three experiments carried out on different cell preparations. “Asterisk” indicates significant differences ( $P \leq 0.05$ )

between these two modes can be detected in a single pairwise experiment under the two FBS conditions to point out the metabolic phenotype of IPEC-J2 (Fig. 3c). IPEC-J2 at starting assay condition (baseline phenotype) in the presence of substrates and without stressor compounds (oligomycin plus FCCP) do not show any difference in the metabolic pathways at the two FBS concentrations tested. Conversely, the stressed metabolic phenotype evaluated in the presence of stressor compounds, only shows a slightly higher mitochondrial respiration in 5% FBS treated cells than in 10% FBS treated ones (Fig. 3c). There is no difference in stressed ECAR between 5% and 10% FBS treated IPEC-J2. However, the metabolic potential of IPEC-J2, which are able to increase ATP production in response to the cell energy demand, primarily lies in the efficient mitochondrial energy metabolism under both FBS conditions tested. Indeed,

the metabolic potential of OxPhos increases by 131.7% at 5% FBS and by 104.3% at 10% FBS, while glycolysis only increases by 46.0% and 41.3% at 5% and 10% FBS, respectively, as compared to baseline metabolism. Moreover, 5% FBS-treated IPEC-J2 are able to increase their aerobic potential more than 10% FBS treated IPEC-J2 when cellular ATP production is required, while no difference in ECAR between the two differently FBS-treated cells under stressed conditions is detectable (Fig. 3d).

To evaluate if the different FBS concentration (5% and 10% FBS) may affect the preferred substrate utilization for mitochondrial respiration in 24 h culture IPEC-J2, as we proved that confluent cells mainly rely on glycolysis for ATP production (Fig. S1). The parameters fuel dependency, capacity and flexibility of IPEC-J2 cells for the oxidation of glucose, glutamine and fatty acids

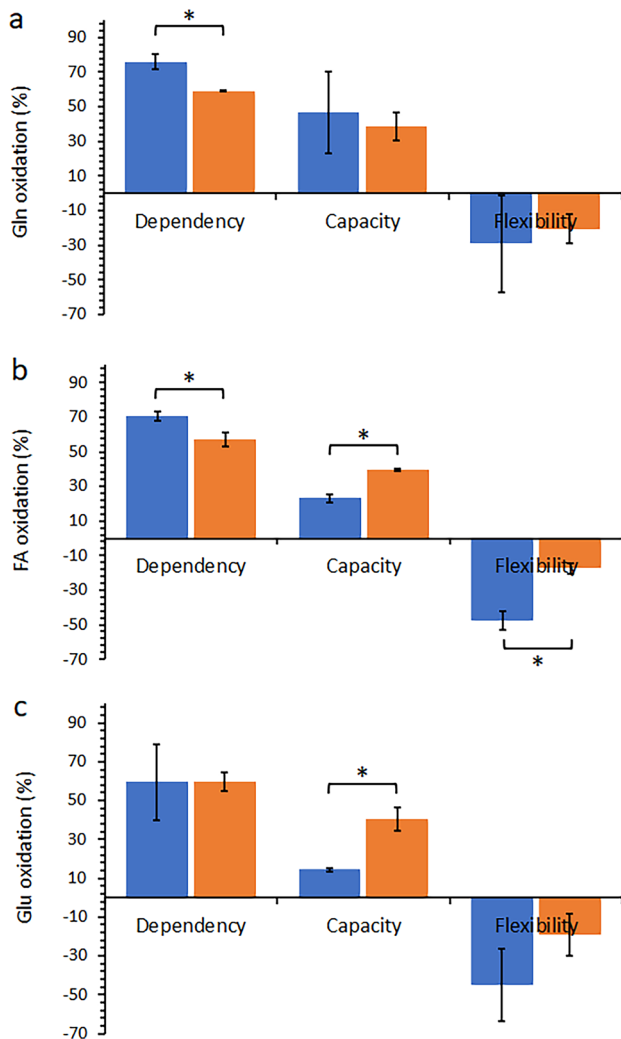


**Fig. 4** Determination of the rate of fuels oxidation by measuring IPEC-J2 respiration. Fuel dependency, capacity and flexibility are calculated on oxidation of glucose (a), fatty acids (b) and glutamine (c). All three fuel parameters (dependency, capacity and flexibility) are displayed as a bar chart for 5% (blue box) and 10% (orange box) FBS treated IPEC-J2. *Gln* glutamine, *FA* fatty acids, *Glu* glucose. The column chart represents the mean  $\pm$  SD (vertical bars) from three experiments carried out on different cell preparations. “Asterisk” indicates significant differences ( $P \leq 0.05$ )

were evaluated by sequential injections of the inhibitors of each oxidative pathway, as described in Sect. *Cellular Bioenergetics* (Fig. 4). IPEC-J2 cells show a higher dependency for glutamine oxidation at 5% FBS than at 10% FBS (Fig. 4a), whereas the capacity and flexibility do not show any difference between the two differently FBS treated IPEC-J2. On considering the oxidation of FAs, 5% FBS IPEC-J2 show higher dependency and flexibility and a lower capacity than 10% FBS IPEC-J2 cells (Fig. 4b). Finally, the only difference in glucose oxidation between

the two differently FBS-treated IPEC-J2 consists in the higher capacity at 10% FBS than at 5% FBS (Fig. 4c).

## Discussion

IPEC-J2 cells represent a unique tool for investigating porcine intestinal barrier function and an excellent translational model, in fact they mimic human intestinal barrier more closely than other tumour cell lines and non-human cell lines (Vergauwen 2015; van der Hee et al. 2020). Many different culture conditions have been tested since their first isolation in 1989 and it has been demonstrated that the percentage of serum used has an impact on functional parameters (Vergauwen 2015). In the present research, we confirmed that higher percentage of serum determined a decrease of the time of duplication, cells grew faster. Furthermore, even if in both culture condition cell grew as an epithelial monolayer (Geens and Niewold 2011), IPEC-J2 at 10% FBS created a more compact junctions as indicated by the TEER measurement conducted for seventeen days.

The two FBS concentrations tested affect the IPEC-J2 cell functional parameters and the energy metabolism adapts to satisfy the physiological demands of the cell (Kaelin and McKnight 2013). Indeed, the IPEC-J2 cells cultured at the higher FBS concentration increase ATP production by enhancing the mitochondrial OxPhos without changing the glycolytic ATP synthesis, which remains constant under the two conditions tested (Fig. 2a). Thus, IPEC-J2 cells mainly rely on mitochondrial oxidation that accounts for the production of more than 50% of cellular ATP (Fig. 2b). These results are consistent with the stimulation of cell growth by 10% FBS (Fig. 1b). Indeed, MitoATP and total ATP production rates, but not glycoATP production rate, are increased by the 10% FBS treatment which also stimulates IPEC-J2 proliferation as shown by the decrease in the doubling time (Fig. 2c–e). The relationship between cell growth and bioenergetics allows to better understand the role of energy metabolism in IPEC-J2 proliferation and represents a metabolic index which indicates how much these cells rely on mitoATP production, in other words on OxPhos. Therefore, the results strengthen the role of mitochondrial OxPhos as main energy supplier for IPEC-J2 cell growth, even if a change in the metabolic profile occurs when the cells are confluent and prefer glycolysis to mitochondrial respiration (Fig. S1). However, the increased ATP production provided by mitochondria in the 10% FBS treated IPEC-J2 is not associated with changes in the mitochondrial bioenergetic parameters (Fig. 3a, b) (Zhou et al. 2017). A possible key role in the modification of cellular metabolism, in response to the adaptation of the IPEC-J2 physiology

to the change in FBS concentrations, is probably played by changes in biosignalling and/or gene expression (Hüttemann et al. 2007; Villena 2015). Moreover, if IPEC-J2 cells are under stressed conditions and cells require a higher energy supply, mitochondria are the main source of cellular ATP production (Fig. 3c). Moreover, the OxPhos stimulation, which is more evident in 5% FBS treated cells (Fig. 3d) and has the meaning to supply energy to the cell, while glycolysis is apparently unaffected, mirrors the cell ability to synthesize more ATP molecules at a lower bioenergetic cost (Balaban 1990; Kim and Dang 2005). Mitochondria can utilize three different nutrients, i.e. glucose, fatty acids and glutamine, to power the IPEC-J2 respiration. Each nutrient type is essential to maintain the basal OCR. When fuel Dependency overwhelms Capacity for a stated fuel, it is clear that the fuel under study is required and oxidized to maintain basal OCR (Fig. 4). Indeed, the inhibition of one substrate pathway cannot be offset by using alternative fuel pathway(s) as the Flexibility has a negative value irrespective of the substrate. Although no differences in Flexibility are detected between 5% and 10% FBS IPEC-J2 cells with both glutamine and glucose as substrates (Fig. 4a, c), apparently 5% FBS favours ATP production via mitochondrial FA oxidation. Accordingly, the contribution of mitochondrial FA oxidation to ATP production in IPEC-J2 cells is higher when cells are cultured in 5% FBS than in 10% FBS (Fig. 4b). Most likely, since FA oxidation is much more efficient than the other two pathways in terms of ATP production, the lower FBS concentration addresses IPEC-J2 cells to exploit this advantageous pathway.

On balance, the present findings, which point out the capability of IPEC-J2 cells to adapt their functional physiological parameters in response to different FBS concentrations, highlight that the oxidative energy metabolism can be remodelled to fulfil the energy demands of the cell without altering the mitochondrial bioenergetic parameters. Owing to the close similarity between swine and human intestinal function, research on IPEC-J2 cells may provide useful information not only on the physiology and energy metabolism of enterocytes, but also on the relevant role of environmental stimuli in addressing cell bioenergetics.

**Supplementary Information** The online version contains supplementary material available at <https://doi.org/10.1007/s00418-021-01981-2>.

**Acknowledgements** This work was supported by the CARISBO Foundation Grant no. 2019.0534 to S.N., Bologna, Italy.

## Declarations

**Conflict of interest** The authors declare that there is no conflict of interests.

**Authorship** C.B. and S.N. conceived and designed the experiments; C.A. and D.L.M. performed the experiments; A.Z., R.S. and F.T. resources and formal analysis; S.N. analyzed the data; C.B., M.F., A.P. and S.N. supervised the experiments; C.B., M.F., A.P. and S.N. wrote the manuscript; M.F. and A.P. revised the text; S.N. funding acquisition. All authors read and approved the manuscript.

## References

- Balaban RS (1990) Regulation of oxidative phosphorylation in the mammalian cell. *Am J Physiol* 258:C377–389. <https://doi.org/10.1152/ajpcell.1990.258.3.C377>
- DeBerardinis RJ, Chandel NS (2020) We need to talk about the Warburg effect. *Nat Metab*. <https://doi.org/10.1038/s42255-020-0172-2>
- Geens MM, Niewold TA (2011) Optimizing culture conditions of a porcine epithelial cell line IPEC-J2 through a histological and physiological characterization. *Cytotechnology* 63:415–423. <https://doi.org/10.1007/s10616-011-9362-9>
- Hüttemann M, Lee I, Samavati L et al (2007) Regulation of mitochondrial oxidative phosphorylation through cell signaling. *Biochim Biophys Acta Mol Cell Res* 1773:1701–1720. <https://doi.org/10.1016/j.bbamcr.2007.10.001>
- Kaelin WG, McKnight SL (2013) Influence of metabolism on epigenetics and disease. *Cell* 153:56–69. <https://doi.org/10.1016/j.cell.2013.03.004>
- Kim J, Dang CV (2005) Multifaceted roles of glycolytic enzymes. *Trends Biochem Sci* 30:142–150. <https://doi.org/10.1016/j.tibs.2005.01.005>
- Mao X, Ren M, Chen D et al (2018) Leucine modulates the IPEC-J2 cell proteome associated with cell proliferation, metabolism and phagocytosis. *Anim Nutr* 4:316–321. <https://doi.org/10.1016/j.aninu.2018.03.006>
- Mariani V, Palermo S, Fiorentini S et al (2009) Gene expression study of two widely used pig intestinal epithelial cell lines: IPEC-J2 and IPI-2I. *Vet Immunol Immunopathol* 131:278–284. <https://doi.org/10.1016/j.vetimm.2009.04.006>
- Nesci S (2017) Glucose and glutamine in the mitochondrial oxidative metabolism of stem cells. *Mitochondrion* 35:11–12. <https://doi.org/10.1016/j.mito.2017.04.004>
- Schierack P, Nordhoff M, Pollmann M et al (2006) Characterization of a porcine intestinal epithelial cell line for in vitro studies of microbial pathogenesis in swine. *Histochem Cell Biol* 125:293–305. <https://doi.org/10.1007/s00418-005-0067-z>
- Shum LC, White NS, Mills BN et al (2016) Energy metabolism in mesenchymal stem cells during osteogenic differentiation. *Stem Cells Dev* 25:114–122. <https://doi.org/10.1089/scd.2015.0193>
- van der Hee B, Madsen O, Vervoort J et al (2020) Congruence of transcription programs in adult stem cell-derived jejunum organoids and original tissue during long-term culture. *Front Cell Dev Biol* 8:375. <https://doi.org/10.3389/fcell.2020.00375>
- Vaugelade P, Posho L, Darcy-Vrillon B et al (1994) Intestinal oxygen uptake and glucose metabolism during nutrient absorption in the pig. *Proc Soc Exp Biol Med* 207:309–316. <https://doi.org/10.3181/00379727-207-43821>
- Vergauwen H (2015) The IPEC-J2 Cell Line. In: Verhoeckx K, Cotter P, López-Expósito I et al (eds) *The impact of food bioactives on health: in vitro and ex vivo models*. Springer, Cham
- Villena JA (2015) New insights into PGC-1 coactivators: redefining their role in the regulation of mitochondrial function and beyond. *FEBS J* 282:647–672. <https://doi.org/10.1111/febs.13175>
- Yuan X, Logan TM, Ma T (2019) Metabolism in human mesenchymal stromal cells: a missing link between hMSC biomaterial manufacturing and

- therapy? *Front Immunol* 10:977. <https://doi.org/10.3389/fimmu.2019.00977>
- Zakrzewski SS, Richter JF, Krug SM et al (2013) Improved cell line IPEC-J2, characterized as a model for porcine jejunal epithelium. *PLoS ONE* 8:e79643. <https://doi.org/10.1371/journal.pone.0079643>
- Zaniboni A, Bernardini C, Alessandri M et al (2014) Cells derived from porcine aorta tunica media show mesenchymal stromal-like cell properties in in vitro culture. *Am J Physiol Cell Physiol* 306:C322–333. <https://doi.org/10.1152/ajpcell.00112.2013>
- Zhou Y, Al-Saaidi RA, Fernandez-Guerra P et al (2017) Mitochondrial spare respiratory capacity is negatively correlated with nuclear reprogramming efficiency. *Stem Cells Dev* 26:166–176. <https://doi.org/10.1089/scd.2016.0162>
- Zuo F, Gu Q, Li S et al (2019) Effects of different methionine sources on methionine metabolism in the IPEC-J2 cells. *Biomed Res Int* 2019:5464906. <https://doi.org/10.1155/2019/5464906>

**Publisher's Note** Springer Nature remains neutral with regard to jurisdictional claims in published maps and institutional affiliations.



# Vitamin K Vitamers Differently Affect Energy Metabolism in IPEC-J2 Cells

Chiara Bernardini<sup>1</sup>, Cristina Algeri<sup>1</sup>, Debora La Mantia<sup>1</sup>, Fabiana Trombetti<sup>1</sup>,  
Alessandra Pagliarani<sup>1†‡</sup>, Monica Forni<sup>1,2†‡</sup> and Salvatore Nesci<sup>1\*†</sup>

<sup>1</sup> Department of Veterinary Medical Science, University of Bologna, Ozzano Emilia, Italy, <sup>2</sup> Health Sciences and Technologies—Interdepartmental Center for Industrial Research (CIRI-SDV), Alma Mater Studiorum—University of Bologna, Bologna, Italy

## OPEN ACCESS

### Edited by:

Cesare Indiveri,  
University of Calabria, Italy

### Reviewed by:

Annamaria Tonazzi,  
National Research Council (CNR), Italy  
Stefan Kahlert,  
Otto von Guericke University  
Magdeburg, Germany

### \*Correspondence:

Salvatore Nesci  
salvatore.nesci@unibo.it

†These authors share last authorship

‡These authors share senior  
authorship

### Specialty section:

This article was submitted to  
Cellular Biochemistry,  
a section of the journal  
Frontiers in Molecular Biosciences

**Received:** 17 March 2021

**Accepted:** 16 April 2021

**Published:** 24 May 2021

### Citation:

Bernardini C, Algeri C,  
La Mantia D, Trombetti F, Pagliarani A,  
Forni M and Nesci S (2021) Vitamin K  
Vitamers Differently Affect Energy  
Metabolism in IPEC-J2 Cells.  
Front. Mol. Biosci. 8:682191.  
doi: 10.3389/fmolb.2021.682191

The fat-soluble vitamin K (VK) has long been known as a requirement for blood coagulation, but like other vitamins, has been recently recognized to play further physiological roles, particularly in cell development and homeostasis. Vertebrates cannot *de novo* synthesize VK, which is essential, and it can only be obtained from the diet or by the activity of the gut microbiota. The IPEC-J2 cell line, obtained from porcine small intestine, which shows strong similarities to the human one, represents an excellent functional model to *in vitro* study the effect of compounds at the intestinal level. The acute VK treatments on the bioenergetic features of IPEC-J2 cells were evaluated by Seahorse XP Agilent technology. VK exists in different structurally related forms (vitamers), all featured by a naphthoquinone moiety, but with distinct effects on IPEC-J2 energy metabolism. The VK1, which has a long hydrocarbon chain, at both concentrations (5 and 10  $\mu\text{M}$ ), increases the cellular ATP production due to oxidative phosphorylation (OXPHOS) by 5% and by 30% through glycolysis. The VK2 at 5  $\mu\text{M}$  only stimulates ATP production by OXPHOS. Conversely, 10  $\mu\text{M}$  VK3, which lacks the long side chain, inhibits OXPHOS by 30% and glycolysis by 45%. However, even if IPEC-J2 cells mainly prefer OXPHOS to glycolysis to produce ATP, the OXPHOS/glycolysis ratio significantly decreases in VK1-treated cells, is unaffected by VK2, and only significantly increased by 10  $\mu\text{M}$  VK3. VK1, at the two concentrations tested, does not affect the mitochondrial bioenergetic parameters, while 5  $\mu\text{M}$  VK2 increases and 5  $\mu\text{M}$  VK3 reduces the mitochondrial respiration (i.e., maximal respiration and spare respiratory capacity). Moreover, 10  $\mu\text{M}$  VK3 impairs OXPHOS, as shown by the increase in the proton leak, namely the proton backward entry to the matrix space, thus pointing out mitochondrial toxicity. Furthermore, in the presence of both VK1 and VK2 concentrations, the glycolytic parameters, namely the glycolytic capacity and the glycolytic reserve, are unaltered. In contrast, the inhibition of glycoATP production by VK3 is linked to the 80% inhibition of glycolysis, resulting in a reduced glycolytic capacity and reserve. These data, which demonstrate the VK ability to differently modulate IPEC-J2 cell energy metabolism according to the different structural features of the vitamers, can mirror VK modulatory effects on the cell membrane features and, as a cascade, on the epithelial cell properties and gut functions: balance of salt and water, macromolecule cleavage, detoxification of harmful compounds, and nitrogen recycling.

**Keywords:** vitamin K, mitochondria, oxidative phosphorylation, glycolysis, IPEC-J2, ATP

## INTRODUCTION

Vitamin K (VK) was originally recognized as a component in blood clotting, being a cofactor for vitamin K-dependent carboxylase, which facilitates the post-translational modification of glutamic acid to  $\gamma$ -carboxy-glutamic acid residues in selected proteins (Suttie, 1985). The relevant recognized VK role in coagulation, hence the symbol K, from the German term “Koagulation,” promptly enrolled VK among micronutrients.

Even if partially provided by gut microbiota, VK requires dietary uptake, even if the required amounts are still undefined. The intestinal absorption of VKs follows the dietary lipid pattern (Shearer et al., 2012).

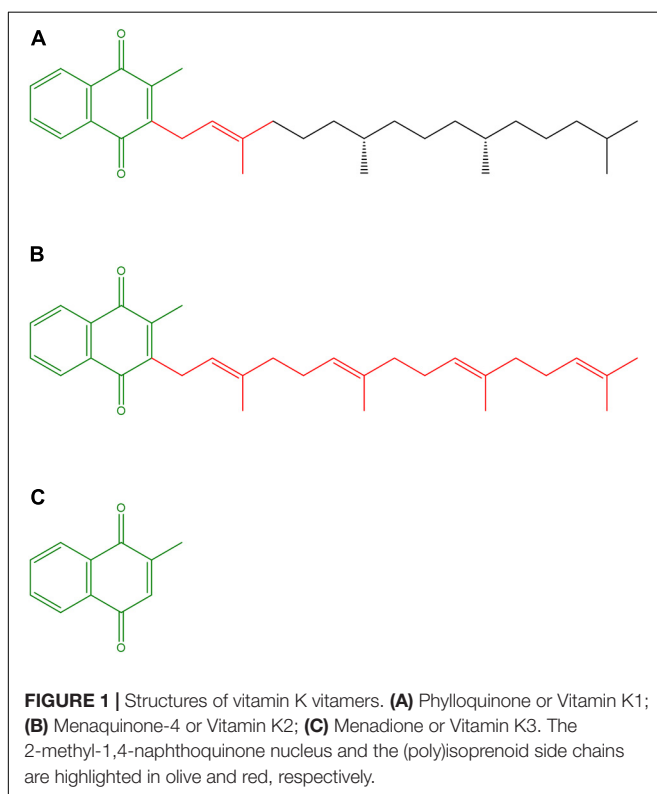
The VK family consists of structurally similar naphthoquinones (**Figure 1**), which, due to their lipophilicity, can easily cross cell membranes. VK naturally exists in two forms, namely, phyloquinone (VK1), which bears a phytyl side chain, mainly comes from vegetables and constitutes more than 90% of dietary VKs, and menaquinones (VK2), which exist in multiple structures, mainly come from bacterial synthesis in the gut, and occur in fermented foods (Schwalfenberg, 2017). The extent to which endogenous VK2 production contributes to the daily VK requirement is still unknown (Shearer et al., 2012). Accordingly, the VK2 form menaquinone-4 can be synthesized from VK1, which is absorbed in the small intestine, and represents the most abundant VK form in tissues (Okano et al., 2008). The VK homologs are characterized by a 2-methyl-1,4-naphthoquinone nucleus and a polyisoprenoid side chain at the 3-position (**Figure 1**). In VK2 vitamers the side chain varies

in both length and saturation degree (Tsugawa and Shiraki, 2020). The VK2 basic structure, which has a side chain with four double bonds, is similar to Coenzyme Q<sub>10</sub> (CoQ<sub>10</sub>), involved as an electron carrier in mitochondrial respiration, but has a shorter hydrophobic side chain whose four prenyl units confer higher hydrophilicity. Finally, menadione, or VK3, lacks the hydrocarbon side chain and is considered as a metabolite or a provitamin (Schwalfenberg, 2017).

Over the last two decades, roles and action mechanisms of VKs other than the involvement in  $\gamma$ -carboxylation, a post-translational modification which modulates the function of various proteins, have been discovered. Recently, VKs were found to play a relevant role in extrahepatic metabolism, such as in bone and blood vessels, in energy metabolism (Tsugawa and Shiraki, 2020), and in counteracting inflammation, as VK deficiency has been associated with human diseases with inflammatory background. Until very recently, VKs were considered capable of playing a role against colorectal cancer and other cancer types (Schwalfenberg, 2017) by inhibiting the cell proliferation, including an active induction of the cell cycle arrest, and to induce apoptosis in different human gastrointestinal cancer cells (Orlando et al., 2015). VKs also improve cognitive function in elderly patients and decrease the risk of diabetes (Schwalfenberg, 2017). At least some of these emerging roles may also be related to the VK involvement in signaling as modulators of selected nuclear receptors. Accordingly, VK2 (menaquinone-4) binds to the transcription factor SXR/PXR, thus acting like a hormone like other lipophilic vitamins. Therefore, its effects are widely spread in body systems, and it is recognized to increase longevity (Gordeladze, 2017). VK2 can also bind the 17 $\beta$ -Hydroxysteroid dehydrogenase type 4 (17 $\beta$ -HSD4) and activate protein kinase A (PKA), but the mechanisms of binding and enzyme regulation remain unknown (Azuma and Inoue, 2019).

The CoQ<sub>10</sub>-like structure of VK2 has raised hopes to exploit VK to treat some mitochondrial defects (Vos et al., 2012). However, the possible replacement of CoQ<sub>10</sub> by VK2 in the respiratory chain, as well as the putative role of vitamins K3 and C to improve ATP production by reducing cytochrome *c* through two coupled redox cycles (Ivanova et al., 2018), are still a matter of debate. Unexpectedly, VK2 was a poorly efficient respiratory substrate in human cells *in vitro* (Cerqua et al., 2019). VK3 is potentially toxic and able to counteract some cancer types (Schwalfenberg, 2017). Interestingly, VK3 affects the redox status of thiols, can induce oxidative stress in cancer cells, and seems the most efficient VK form in combination with vitamin C to restore oxidative phosphorylation (Ivanova et al., 2018).

Up to now, VK involvement in the bioenergetics of enterocytes, which are not only directly involved in VK absorption but also are in proximity with gut microbiota which provide VK2, has not been explored. The IPEC-J2 cell line (Vergauwen, 2015), initially established in 1989 and obtained from the small intestine of the pig, which shows anatomical and physiological similarities to humans, has been selected as *in vitro* model to investigate the action mechanisms at the biochemical and molecular level of a variety of compounds on mammalian intestine (Wu et al., 2019). Due to their features, IPEC-J2 cells provide an excellent *in vitro* model to



investigate the effects of VKs on cell bioenergetics. This cell line is neither transformed nor tumorigenic and reproduces the human physiology features more closely than any other cell line of non-human origin. Of note, this cell line guarantees the reproducibility of the results since it maintains the differentiated characteristics and exhibits strong similarities to primary cell cultures. As far as we are aware, only a few studies approached cell bioenergetics in this cell line under normal conditions (Tan et al., 2015; Bernardini et al., 2021), highlighting that these cells mirror the known behavior of intestinal cells, since they preferentially derive energy from glucose plus glutamine than from glucose alone. Enterocytes mainly use glycolysis to provide metabolic precursors to the liver, while mitochondrial respiration provides the main energy source (Nesci, 2017). IPEC-J2, as well as IPEC-J1, have the typical differentiation of an enterocyte, which is independent of the culture system. The aerobic environment can start the initial proliferation and sequential differentiation of intestinal epithelial cells and progeny loss (Nossol et al., 2011). Enterocyte mitochondrial function is important for gut permeability. Accordingly, mitochondrial uncoupling increases intestinal permeability, generating local and systemic inflammation, which is associated with the development of inflammatory bowel diseases (Bórquez et al., 2020).

This study, which focuses on VK effects on IPEC-J2 cells, aims at deepening the knowledge on the multiple VK roles and on the responses of the energy machinery to these quinone compounds. IPEC-J2 cells, which exhibit strong similarities to primary intestinal epithelial cells, may address studies on the most suitable VK form to modulate enterocyte bioenergetics. Accordingly, structural differences among VK vitamers may be relevant to produce different effects. Moreover, this study, by providing clues on the putative modulatory role of VKs on cell bioenergetics, may open further therapeutic perspectives of these fascinating micronutrients.

## MATERIALS AND METHODS

### Chemicals

$\alpha$ -Phylloquinone (Vitamin K1), Menaquinone-4 (Vitamin K2), and Menadiolone (Vitamin K3) were purchased from Cayman Chemical. Seahorse XF Assay Kits and Reagents were purchased from Agilent. All other chemicals were reagent grade and used without purification. Quartz double-distilled water was used for all reagent solutions, except when otherwise stated.

### Cell Culture

The non-transformed cell line IPEC-J2 was purchased from the "Deutsche Sammlung von Mikroorganismen und Zellkulturen GmbH" (DSMZ). Cells were cultured in Dulbecco's Modified Eagle Medium (DMEM) (4.5 g/l glucose) added with 10% of fetal bovine serum (FBS, Life Technologies) and 1 $\times$  antibiotic-antimycotic solution (Life Technologies) in a 5% CO<sub>2</sub> atmosphere at 37°C. Cultures were split weekly in T25 [0.5  $\times$  10<sup>6</sup> or T75 (1.5  $\times$  10<sup>6</sup>) culture flasks (Corning-Becton Dickinson and Company Becton Drive, Franklin Lakes, NJ, United States). For cryopreservation, 1.5  $\times$  10<sup>6</sup> were resuspended in 1 ml of

freezing medium (DMEM added with 20% FBS, 1 $\times$  antibiotic-antimycotic solution, and 10% DMSO). The cryovials were placed in a freezing box and stored at -80°C overnight. For long-term storage, the cryovials were transferred into a cryogenic biobank.

### Cellular Bioenergetics

The Seahorse XFp analyzer (Agilent) was used to simultaneously measure oxygen consumption rate (OCR), an index of cell respiration (pmol/min), and extracellular acidification rate (ECAR), an index of glycolysis (mpH/min). IPEC-J2 cells (1  $\times$  10<sup>4</sup> / well) were grown in XFp cell culture miniplates (Agilent) for 24 h. On the experiment day, IPEC-J2 cells were switched to freshly made Seahorse XF DMEM medium pH 7.4 supplemented with 10 mM glucose, 1 mM sodium pyruvate, and 2 mM L-glutamine, in the absence (Control) and in the presence of 5 or 10  $\mu$ M of each VK vitamer (VK1, VK2 or VK3) under study. The plates were incubated at 37°C in air for 45 min before measuring OCR and ECAR by the adequate programs (ATP Rate Assay, Cell Mito Stress Test and Cell Energy Phenotype Test). The injection ports of XFp sensor cartridges, which were hydrated overnight with XF calibrant at 37°C, were loaded with 10 $\times$  concentration of inhibitors according to the instructions provided by Seahorse XFp ATP Rate Assay, Cell Mito Stress Test, and Cell Energy Phenotype Test. The final concentration used for ATP Rate Assay were 1.5  $\mu$ M oligomycin (port A) and 0.5  $\mu$ M rotenone (Rot) plus 0.5  $\mu$ M antimycin A (AA) (port B). For Cell Mito Stress Test the final concentrations were 1.5  $\mu$ M oligomycin (olig) (port A), 1.0  $\mu$ M Carbonyl-cyanide-4-(trifluoromethoxy) phenylhydrazone (FCCP) (port B), and 0.5  $\mu$ M rotenone plus antimycin A (port C), while for the Cell Energy Phenotype Test the final concentrations were 1.5  $\mu$ M oligomycin plus 1.0  $\mu$ M FCCP (port A). All the analysis were run at 37°C. All data were analyzed by WAVE software; OCR and ECAR values were normalized to the total number of cells per well. All parameter values were calculated per well, according to the manufacturer's instructions. Both ATP Rate Assay, Mito Stress Test, and Cell Energy Phenotype Test were carried out three times in independent experiments (Marcocchia et al., 2021).

The ATP Rate Assay provides the bioenergetic parameters currently used to characterize the cellular ATP production, namely ATP production rate, related to the conversion of glucose to lactate in the glycolytic pathway (glycoATP Production Rate) and to the mitochondrial OXPHOS (mitoATP Production Rate). Accordingly, the ratio between mitoATP Production Rate and glycoATP Production Rate (ATP Rate Index) is currently considered as a valuable parameter to detect changes and/or differences in the metabolic phenotype (a ratio > 1 means mainly OXPHOS pathway; a ratio < 1 means mainly glycolytic pathway).

The Mito Stress Test enables the characterization of cell respiration by the following parameters: basal respiration, detected as baseline OCR before oligomycin addition; minimal respiration measured as OCR in the presence of oligomycin; and maximal respiration evaluated as OCR after FCCP addition. The so-called proton leak, which corresponds to the difference between the basal respiration and the respiration in the presence of oligomycin (minimal respiration), indicates the re-entry of H<sup>+</sup> in the intermembrane space independently of the F<sub>1</sub>F<sub>0</sub>-ATP

synthase. The non-mitochondrial respiration, evaluated as OCR in the presence of rotenone plus antimycin A (respiratory chain inhibitors), was subtracted from all the above parameters. The ATP turnover or oligomycin-sensitive respiration was obtained from the difference between the basal respiration and the minimal respiration (OCR in presence of oligomycin). Finally, the difference between the maximal and the basal respiration provided the spare capacity, which represents the ability to respond to an increased energy demand and can be considered as a measure of the flexibility of the OXPHOS machinery (Bernardini et al., 2021).

The simultaneous measurement of mitochondrial respiration and glycolysis was carried out by the Cell Energy Phenotype Test under baseline and stressed conditions, the latter after simultaneous addition of oligomycin and FCCP. Oligomycin inhibits the mitochondrial ATP production by the  $F_1F_0$ -ATP synthase and the cell compensates the failed OXPHOS by increasing the glycolysis rate, while the dissipation of the electrochemical gradient of  $H^+$  in mitochondria by the ionophore FCCP drives the highest oxygen consumption (uncoupled respiration). The assay allows to evaluate two main parameters of cell energy metabolism, known as metabolic phenotypes (baseline and stressed phenotype) and metabolic potential. The baseline phenotype is featured by the OCR and ECAR values in cells under the starting condition in the presence of substrates. The stressed phenotype is shown by the OCR and ECAR values in cells after addition of stressor compounds (oligomycin plus FCCP). The metabolic potential is the ability to increase energy production *via* respiration and glycolysis and it is defined as the % increase of stressed phenotype over baseline phenotype of OCR and ECAR (Bernardini et al., 2021).

## Statistical Analysis

Statistical analyses were performed by SIGMASTAT software. Each treatment was replicated three or eight times (viability test) in three independent experiments. Data were analyzed by the Student's *t*-test, or by one-way analysis of variance (ANOVA) followed by Students–Newman–Keuls test when *F* values indicated significance ( $P \leq 0.05$ ) was applied. Percentage data were *arcsin*-transformed before statistical analyses to ensure normality.

## RESULTS

### Intracellular ATP Production

The cellular ATP level produced by OXPHOS and glycolysis in the presence of the different VK vitamers are shown in **Figure 2** by OCR and ECAR values, respectively, under basal metabolic conditions. The calculation of the mitoATP and glycoATP production rate (**Figure 2**), obtained by injecting oligomycin to inhibit mitochondrial ATP synthesis and then rotenone plus antimycin A to block mitochondrial respiration, highlight that IPEC-J2 cells are characterized by an oxidative metabolism. VK1 induces an increase in total ATP production at both the concentrations tested (5 and 10  $\mu$ M). This increase is due to a significant glycoATP production activation, whereas

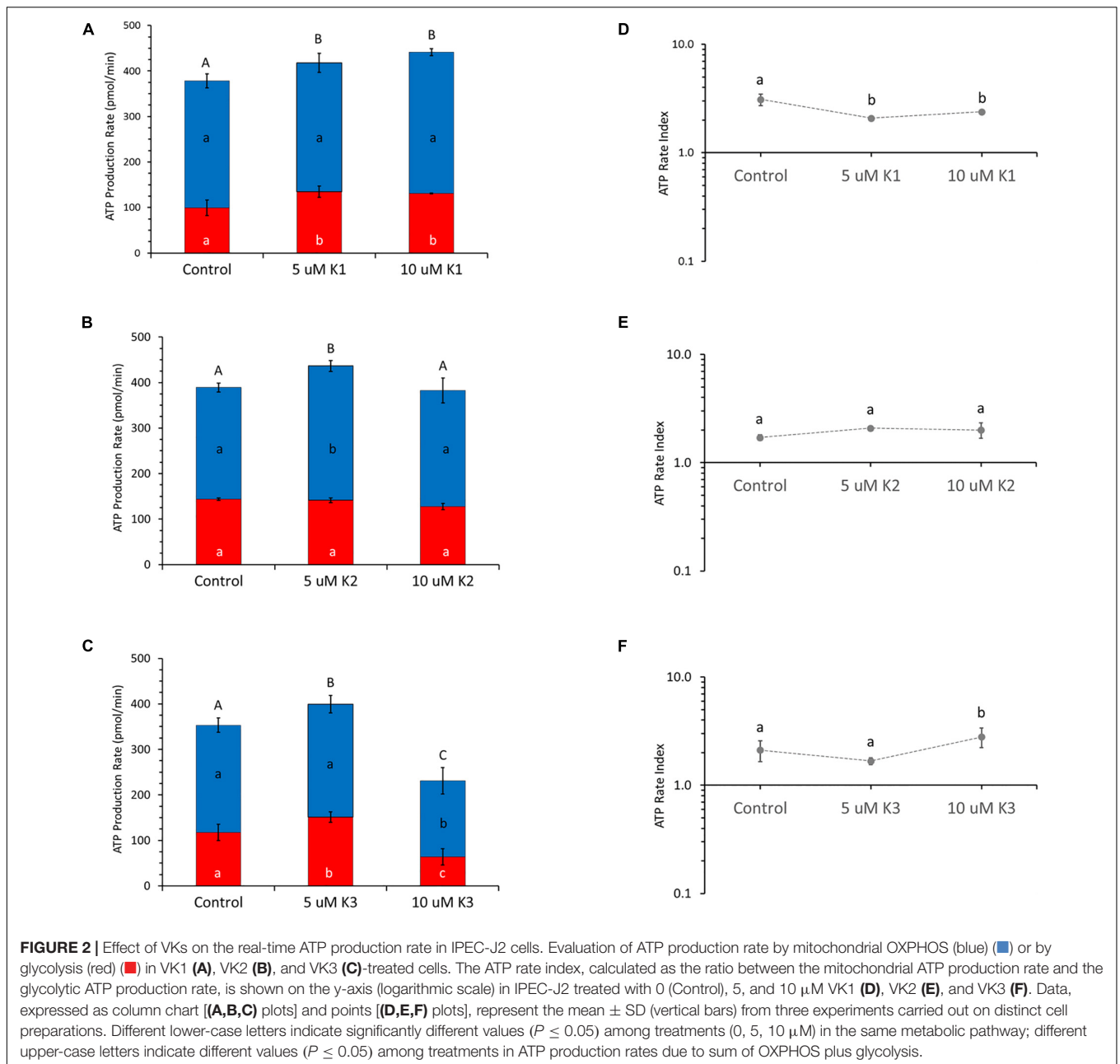
the mitoATP production is unaffected (**Figure 2A**). Conversely, VK2 does not affect the glycoATP production. The total ATP production is only 20% increased by 5  $\mu$ M VK2 with respect to the control, due to an enhanced mitochondrial ATP synthesis (**Figure 2B**). VK3 shows a concentration-dependent effect on intracellular ATP production by increasing the glycolysis by 30% without modifying the mitochondrial activity at 5  $\mu$ M, whereas at 10  $\mu$ M it reduces by 50% the glycoATP and the mitoATP synthesis by 30% (**Figure 2C**). Even if all the VK vitamers can modify ATP production, the results highlight that the ratio between mitoATP Production Rate and glycoATP Production Rate (ATP Rate Index) is always  $> 1$ . In detail, 5 and 10  $\mu$ M VK1 decrease the propensity to produce mitoATP with respect to the control (**Figure 2D**), whereas this effect is not shown by VK2 which does not modify the ATP rate index (**Figure 2E**). In IPEC-J2 cells treated with 10  $\mu$ MVK3, the residual ATP production mainly relies on mitochondrial oxidative metabolism (**Figure 2F**).

### Cellular Respiration

The profile and function of cell respiration of IPEC-J2 cells treated with VKs are shown in **Figure 3**. The key parameters of cell metabolism were obtained from functional metabolic data as detailed in the Materials and mMethods section. The results show that OCR values in the presence of both VK1 concentrations tested are not different from control ones (**Figures 3A,B**). VK1 does not modify the basal respiration and the proton leak; consequently, the calculated ATP turnover is not affected. Therefore, the coupling efficiency in the presence and in the absence of VK1 is about 0.80 a.u. (the maximal value of 1.0 a.u. is obtained when all the basal respiration is sensitive to oligomycin). The IPEC-J2 OCR in the presence of FCCP (maximal respiration) shows a twice higher value than basal OCR. The spare respiratory capacity, which defines the cell propensity to adjust cell bioenergetics to fulfill the increased energy demand, constantly attains a 50% OCR value of the FCCP-stimulated OCR, irrespective of the VK1 presence (**Figure 3B**).

VK2 has a concentration-dependent effect on the OCR (**Figure 3C**). Accordingly, 5  $\mu$ M VK2 increases the basal, maximal, and spare capacity OCR, as well as ATP turnover with respect to the control. Conversely, at 10  $\mu$ M VK2 the effect on the same parameters is inhibitory (**Figure 3D**). Even if the basal and ATP turnover is higher in presence of 5  $\mu$ M VK2 and lower at 10  $\mu$ M VK2, with respect to the control, the coupling efficiencies values in the presence of VK2 (0.77 a.u.) are not different from those of the control. Likewise, on comparing the maximal respiration and the spare respiratory capacity in the absence or in the presence of the two VK2 concentrations, significantly different OCR values are shown. However, the OCR values of the maximal respiration and spare respiratory capacity in all treatments (0.0, 5.0, and 10  $\mu$ M VK2) are of the same extent. In detail, the maximal respiration is always twice higher than the basal respiration, whereas for the latter the OCR activity is increased by 50% with FCCP (**Figure 3D**).

As shown in **Figure 3E**, the respiratory profile of IPEC-J2 cells decreases with increasing VK3 concentrations. Even if the basal respiration is apparently unaffected by VK3 (**Figure 3F**),



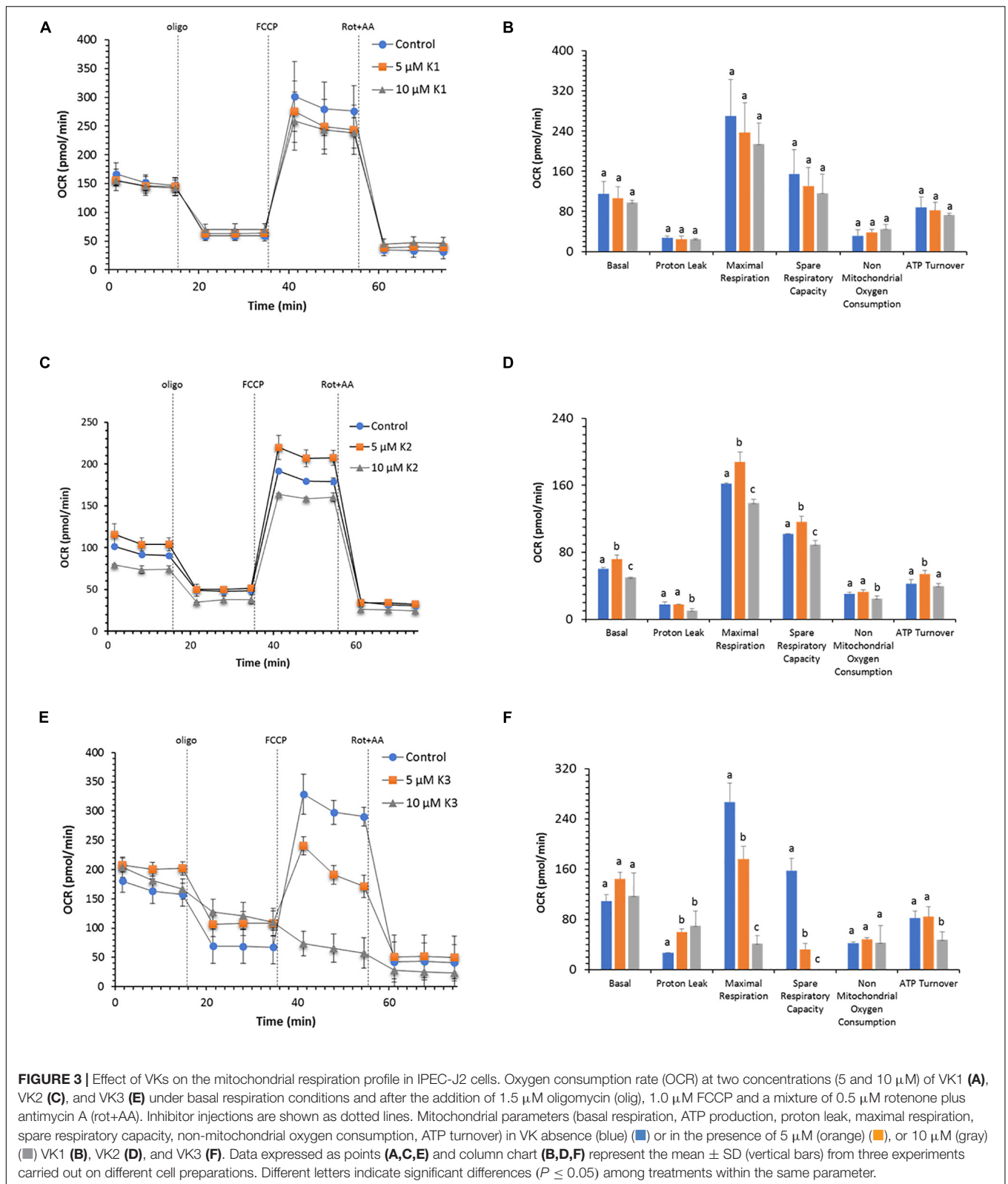
the coupling efficiency is halved by 10  $\mu\text{M}$  VK3 as a result of an increase in proton leak. In addition, IPEC-J2 cells treated with 5  $\mu\text{M}$  VK3 do not show any respiration stimulation by FCCP, while when these cells are treated with 10  $\mu\text{M}$  VK3, not only do they not show any increase in OCR in response to FCCP, but also the OCR after FCCP addition is lower than the basal OCR. Consistently, a strong inhibition of respiration with strongly decreased or even abolished spare respiratory capacity is detected in the presence of 5 and 10  $\mu\text{M}$  VK3, respectively.

### Extracellular Acidification

The glycolytic function in IPEC-J2 cells evaluated as extracellular acidification rate (ECAR) does not show any change in the

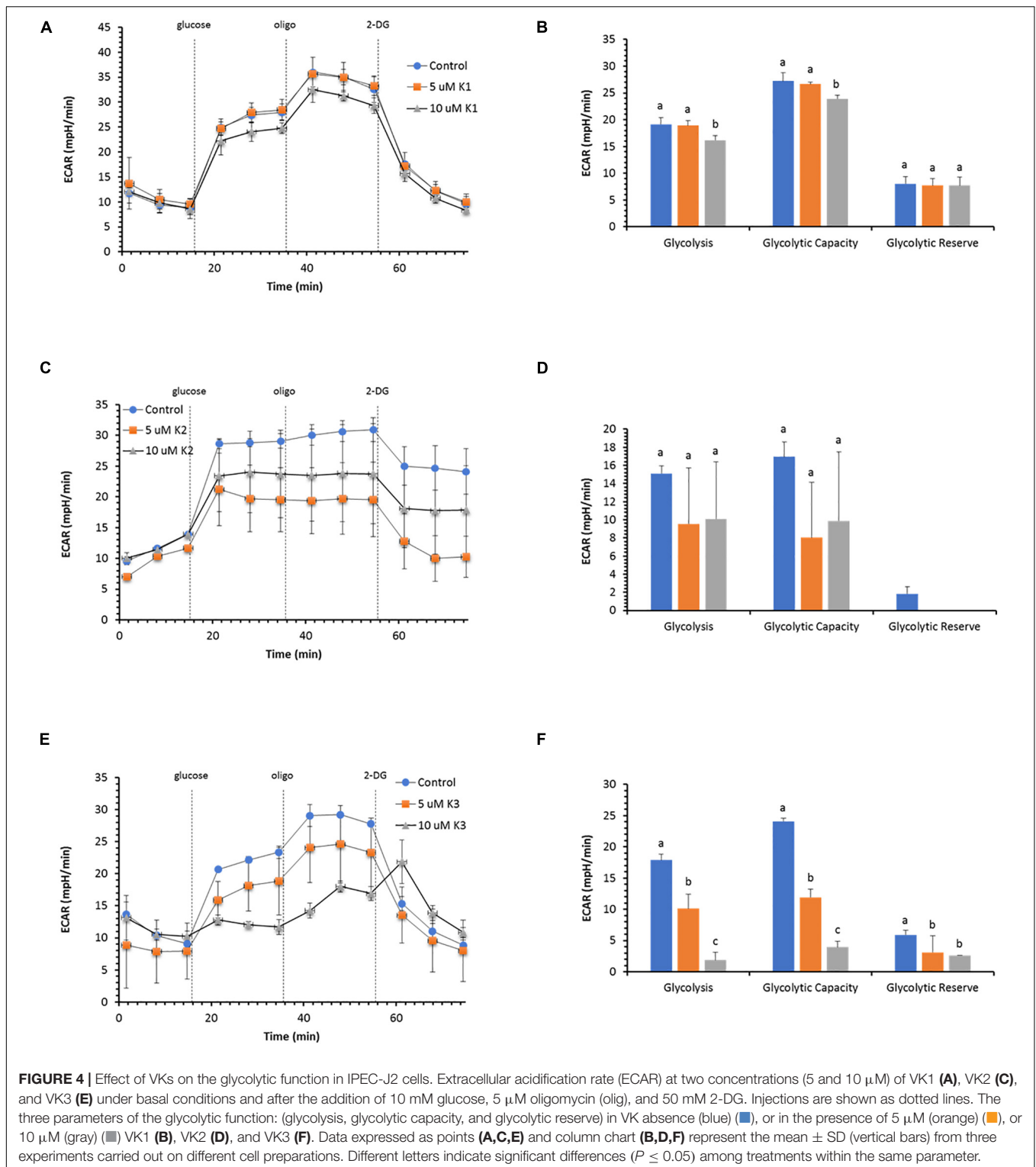
presence of the two VK1 concentrations tested (Figure 4A). The key parameters of glycolytic flux, i.e., Glycolysis and Glycolytic Capacity, attain the same value in the presence or in the absence of 5  $\mu\text{M}$  VK. Conversely, 10  $\mu\text{M}$  VK1 inhibits both parameters by 15% (Figure 4B). However, the Glycolytic Reserve, defined as the difference between Glycolytic Capacity and Glycolysis, is unaffected by 10  $\mu\text{M}$  VK1, since the two parameters show a proportional decrease in ECAR with respect to the control (Figure 3B).

Also, VK2 does not substantially modify the glycolytic profile of IPEC-J2 cells (Figure 4C), but in this case the glycolytic reserve disappears, since the Glycolysis rate has the same ECAR value as the Glycolytic Capacity (Figure 4D).



VK3 shows an inhibitory action on ECAR with a concentration-dependent effect (Figure 4E). The Glycolysis and the Glycolytic Capacity are inhibited by 50 and 13% with 5

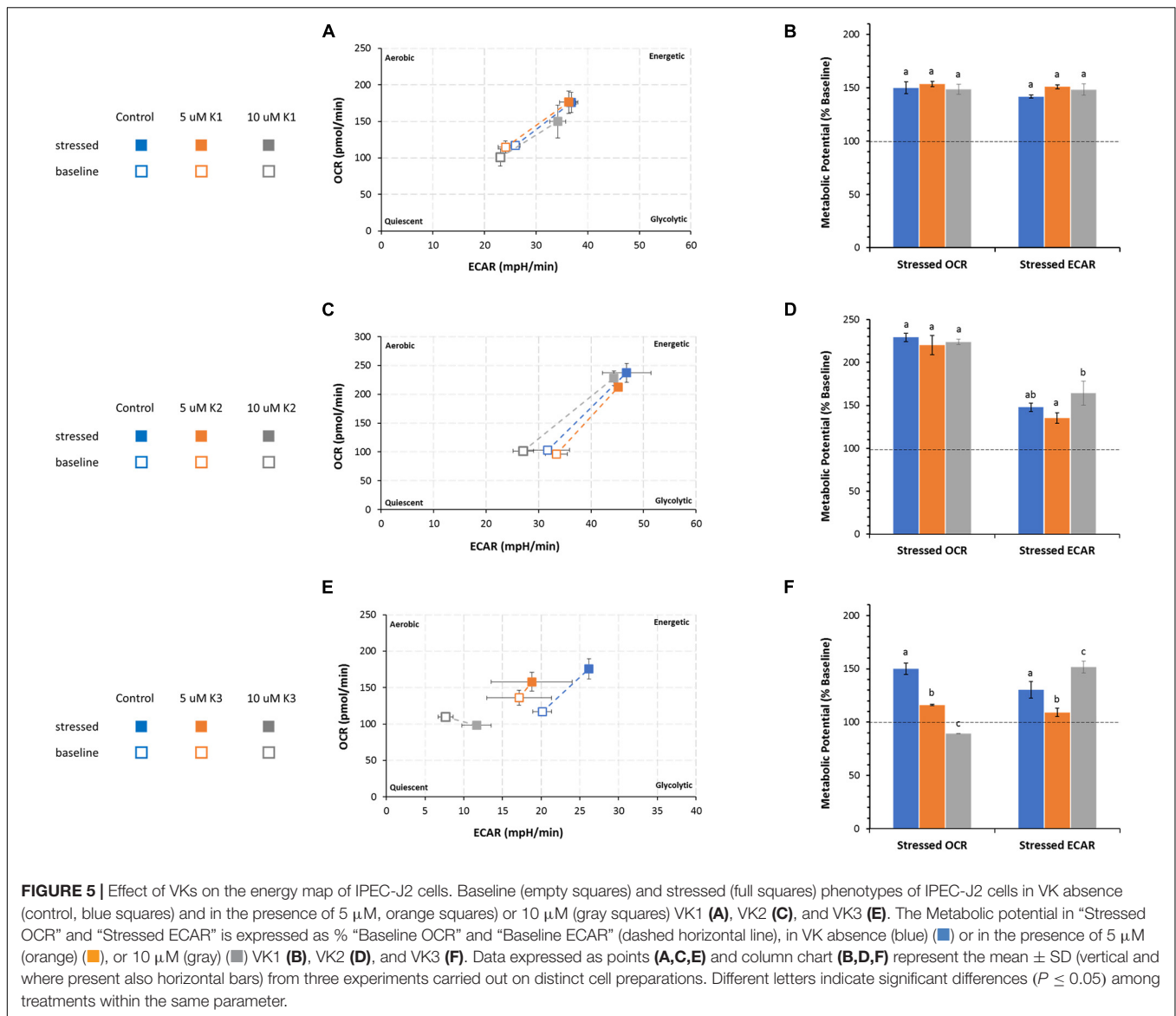
and 10  $\mu\text{M}$  VK3, respectively. Conversely, the decrease in the Glycolytic Reserve is independent of the VK3 concentration tested (Figure 4F).



## Bioenergetic Phenogram

The cell energy production of IPEC-J2 cells detected by OCR and ECAR in the presence or in the absence of VKs is shown as metabolic phenotype under normal (baseline) and stressed conditions (Figure 5). The treatment with

oligomycin and FCCP mixture, known as mitochondrial stressors, provides the phenogram which illustrates the relative baseline and stressed phenotype, and the response of the metabolic potential (expressed as % baseline) of IPEC-J2 cells after treatment with VKs.



According to the method adopted, the metabolic potential indicates the cell's ability to meet an energy demand by mitochondrial respiration and glycolysis.

Irrespective of the presence of VK1, IPEC-J2 cells show an increase in the utilization of both pathways (mitochondrial respiration and glycolysis) (Figure 5A) under stressed conditions without any significant difference in the metabolic potential in the presence or absence of VK1 (Figure 5B).

The IPEC-J2 phenogram under starting assay conditions (baseline phenotype) in the presence of substrates and without stressors (oligomycin plus FCCP) do not show any difference in the metabolic pathways between control and VK2 treated cells. The same results are detected under stressed conditions irrespective of the presence of VK2, even if in this case the cells undergo a metabolic switch toward an energetic phenotype (Figure 5C). The cell energy demand is satisfied by an increase in OCR. The metabolic potential primarily relies on an efficient

mitochondrial energy metabolism. No difference in OCR values between the VK2-treated IPEC-J2 cells and the control under stressed conditions is detectable (Figure 4D). The two VK2 concentrations tested do not modify the glycolytic activity stimulated by stressor compounds with respect to the control, even if the stressed ECAR, expressed as metabolic potential, in 5  $\mu$ M VK2-treated IPEC-J2 cells is lower than that in 10  $\mu$ M VK2-treated cells (Figure 5D).

VK3 affects the IPEC-J2 cells' energy production, highlighting an energy map which shows an inhibited aerobic metabolism (Figure 5E). Stressed OCR and ECAR in the 5  $\mu$ M VK3-treated IPEC-J2 cells are inhibited by 23 and 16%, respectively. The treatment with 10  $\mu$ M K3 makes IPEC-J2 cells shift their energy production mode from OXPHOS to glycolysis (Figure 5F). In these cells the stressed OCR is 11% lower than baseline OCR, whereas the metabolic potential of glycolysis (ECAR) increases by 50% when compared to baseline metabolism (Figure 5F).

However, the baseline OCR/ECAR ratio in VK3-treated IPEC-J2 cells is  $> 4$ . This means that, other than acidification from glycolysis, the ECAR values in VK3-treated IPEC-J2 cells include the contribution of the mitochondrial acidification by  $\text{CO}_2$  production by Krebs cycle. Accordingly, in aqueous media  $\text{CO}_2$  forms the weak acid  $\text{H}_2\text{CO}_3$ .

## DISCUSSION

As far as we are aware, up to now the effect of the three VK vitamers on the bioenergetic metabolism of enterocytes has been poorly investigated. The IPEC-J2 cell line provides an excellent model to evaluate in detail the mechanism(s) involved in cell energy production. These cells also represent a good translational model to study fat-soluble vitamin effects on cellular metabolism in the gut. IPEC-J2 cells rely on oxidative metabolisms to supply the energy required by the physiological functions (Vaugelade et al., 1994; Bernardini et al., 2021).

The enhancement of ATP production by IPEC-J2 cells is the most relevant bioenergetic effect of VK1, which primarily contributes to stimulate the glycolytic pathway at both the concentrations tested. Indeed, the modification of ATP rate index highlights that VK1-treated IPEC-J2 cells switch to a less aerobic metabolism, namely glycolysis vs OXPHOS, with respect to the control, but without affecting the mitochondrial respiration and the glycolysis parameters. The ATP production of VK2-treated IPEC-J2 cells is only increased at the lower VK2 concentration tested, namely  $5 \mu\text{M}$  VK2. Indeed, the effect is corroborated by the Mito Stress Test which shows that the mitochondrial parameters are improved at  $5 \mu\text{M}$  VK2 concentration tested. The VK2 structure resembles that of the  $\text{CoQ}_{10}$ , a membrane-embedded electron carrier of mitochondrial electron transfer system (mETS) (Lenaz et al., 1999), even if it cannot substitute  $\text{CoQ}_{10}$  (Cerqua et al., 2019). VK2 can mimic the two structural components of  $\text{CoQ}_{10}$  which are crucial in OXPHOS, namely in the naphthoquinone core, which transfer electrons during the redox-cycle, and in the isoprenoid tail, which allows diffusion into the lipid bilayer. Recently both VK1 and VK2 were found to decrease the order and to increase fluidity in model membranes (Ausili et al., 2020). Therefore, these VKs may also act indirectly by facilitating the function of respiratory complexes through the inner mitochondrial membrane.

Short-chain quinones are known to be toxic, especially those containing 0–3 isoprene units, whereas  $\text{CoQ}_4$  displays only minimal toxicity (Takahashi et al., 2018). During mitochondrial respiration the VK2 might transfer electrons from complex I or complex II directly or indirectly to cytochrome  $c$ , according to the diffusion mode of shuttling electrons along the respiratory chain (Nesci and Lenaz, 2021). This VK2 role as electron transporter in the respiratory chain (Colpa-Boonstra and Slater, 1958) is still controversial. Accordingly, in spite of reports which rule out this possibility (Cerqua et al., 2019), in an *in vitro* model VK2 enhanced respiratory chain efficiency and contributed to building the electrochemical proton gradient ( $\Delta\mu\text{H}^+$ ) by respiratory complexes that are exploited to generate ATP, similarly to  $\text{CoQ}_{10}$  (Vos et al., 2012). Our

findings show that the effect on mitochondrial respiration could depend on VK2 concentration, namely the positive effect shown at  $5 \mu\text{M}$  VK2 may become harmful at high concentrations. The VK2 structural properties are consistent with the stimulation of mitochondrial respiration without any effect on glycolysis. Consistently, low VK2 concentrations can favor an energy boost in IPEC-J2 cell activation, proliferation, and differentiation by increasing the OXPHOS capability to produce ATP.

Vitamer VK3 is the only one of the three forms of VK under study which exerts a negative effect on energy metabolism of IPEC-J2 cells. Accordingly, cell respiration is inhibited by both VK3 concentrations. The VK3-driven increase in  $\text{H}^+$  leakage through the inner mitochondrial membrane leads to the decrease in the ATP synthesis. However, uncoupling agents such as FCCP can stimulate the mitochondrial respiration of VK3-treated IPEC-J2 cells. The increase in non-phosphorylating substrate oxidation is typical of a decrease in  $\Delta\mu\text{H}^+$ , accompanied by production of reactive oxygen species and increase in oxygen consumption (Zorov et al., 2020). Conversely, we also detected in VK3-treated IPEC-J2 cells an inhibited mitochondrial respiration, as it happens in the presence of excess of uncouplers. Moreover, the negative effect on cell metabolism is underscored by VK3-driven enhancement of the ECAR-insensitive glycolytic activity in IPEC-J2 cells. However, VK3-treated IPEC-J2 cells can only rely on the glycolytic pathway to supply the energy required when their energy production mode shifts upon induction of signaling pathways of stress (Hung and Calkins, 2016).

The present study points out that the different VK vitamers tested promote different effects on IPEC-J2 cell bioenergetics. Accordingly, the chemical structure of the sidechain of VKs is confirmed to be crucial to produce the effects.

New roles for VKs in reducing risk of certain chronic diseases have been proposed in the last decades (Shearer et al., 2012). Consistently, the present work which shows for the first time how different VK forms and concentrations differently act on the bioenergetics of IPEC-J2 cell line contributes to deepening the knowledge on the varied roles of VKs in enterocytes, of which the IPEC-J2 cell line constitutes a fascinating model. The swine is increasingly used in translational research and drug development (Monticello and Haschek, 2016). Therefore, the benefits of a VK stimulation of ATP production in enterocytes underlines and confirms the relevance of gut microbiota, as VK producer, in maintaining a healthy gut and, as a cascade, in the prevention and/or treatment of diseases of the intestinal tract. Interestingly, since the last century (Krasinski et al., 1985) certain chronic gastrointestinal disorders were associated with VK deficiency. At present this connection is established with Crohn's disease (Schoon et al., 2001), celiac disease (Djuric et al., 2007), and inflammatory bowel disease (Nowak et al., 2014). Pathological conditions are often associated with impaired mitochondrial bioenergetics (Nesci et al., 2021). Moreover, VK antagonists used in clinical therapy to prevent thromboembolism together with coadministration of other drugs can induce drug-drug interaction effects with VK malabsorption (Takada et al., 2015). Infants cannot obtain VK from the breast milk and have poor

intestinal adsorption due to immature gut flora. Therefore, VK oral administration is the best way to prevent Vitamin K deficiency bleeding in infancy (Araki and Shirahata, 2020). It seems likely to postulate that an insufficient ATP production by enterocytes, related to a poor VK availability, also due to antibiotic treatments (Shirakawa et al., 1990), may represent, or contribute to, the biochemical bases of some gut pathologies.

## DATA AVAILABILITY STATEMENT

The raw data supporting the conclusions of this article will be made available by the authors, without undue reservation.

## REFERENCES

- Araki, S., and Shirahata, A. (2020). Vitamin K deficiency bleeding in infancy. *Nutrients* 12:780. doi: 10.3390/nu12030780
- Ausili, A., Clemente, J., Pons-Belda, ÓD., de Godos, A., Corbalán-García, S., Torrecillas, A., et al. (2020). Interaction of vitamin K1 and vitamin K2 with dimyristoylphosphatidylcholine and their location in the membrane. *Langmuir* 36, 1062–1073. doi: 10.1021/acs.langmuir.9b03552
- Azuma, K., and Inoue, S. (2019). Multiple modes of vitamin K actions in aging-related musculoskeletal disorders. *Int. J. Mol. Sci.* 20:2844. doi: 10.3390/ijms20112844
- Bernardini, C., Algieri, C., La Mantia, D., Zannoni, A., Salaroli, R., Trombetti, F., et al. (2021). Relationship between serum concentration, functional parameters and cell bioenergetics in IPEC-J2 cell line. *Histochem. Cell Biol.* (in press). doi: 10.1007/s00418-021-01981-2
- Bórquez, J. C., Hidalgo, M., Rodríguez, J. M., Montaña, A., Porras, O., Troncoso, R., et al. (2020). Sucralose stimulates mitochondrial bioenergetics in Caco-2 cells. *Front. Nutr.* 7:585484. doi: 10.3389/fnut.2020.585484
- Cerqua, C., Casarin, A., Pierrel, F., Vazquez Fonseca, L., Viola, G., Salviati, L., et al. (2019). Vitamin K2 cannot substitute Coenzyme Q10 as electron carrier in the mitochondrial respiratory chain of mammalian cells. *Sci. Rep.* 9:6553. doi: 10.1038/s41598-019-43014-y
- Colpa-Boonstra, J. P., and Slater, E. C. (1958). The possible role of vitamin K in the respiratory chain. *Biochim. Biophys. Acta* 27, 122–133. doi: 10.1016/0006-3002(58)90298-1
- Djuric, Z., Zivic, S., and Katic, V. (2007). Celiac disease with diffuse cutaneous vitamin K-deficiency bleeding. *Adv. Ther.* 24, 1286–1289. doi: 10.1007/BF02877775
- Gordeladze, J. O. (ed.) (2017). *Vitamin K2 - Vital for Health and Wellbeing*. London: InTech, doi: 10.5772/61430
- Hung, K.-M., and Calkins, M. J. (2016). Mitochondrial homeostatic disruptions are sensitive indicators of stress in neurons with defective mitochondrial DNA transactions. *Mitochondrion* 31, 9–19. doi: 10.1016/j.mito.2016.08.015
- Ivanova, D., Zhelev, Z., Getsov, P., Nikolova, B., Aoki, I., Higashi, T., et al. (2018). Vitamin K: Redox-modulation, prevention of mitochondrial dysfunction and anticancer effect. *Redox Biol.* 16, 352–358. doi: 10.1016/j.redox.2018.03.013
- Krasinski, S. D., Russell, R. M., Furie, B. C., Kruger, S. F., Jacques, P. F., and Furie, B. (1985). The prevalence of vitamin K deficiency in chronic gastrointestinal disorders. *Am. J. Clin. Nutr.* 41, 639–643. doi: 10.1093/ajcn/41.3.639
- Lenaz, G., Fato, R., Di Bernardo, S., Jarreta, D., Costa, A., Genova, M. L., et al. (1999). Localization and mobility of coenzyme Q in lipid bilayers and membranes. *Biofactors* 9, 87–93. doi: 10.1002/biof.5520090202
- Marcocchia, R., Nesci, S., Merlo, B., Ballotta, G., Algieri, C., Pagliarini, A., et al. (2021). Biological characteristics and metabolic profile of canine mesenchymal stem cells isolated from adipose tissue and umbilical cord matrix. *PLoS One* 16:e0247567. doi: 10.1371/journal.pone.0247567
- Monticello, T. M., and Haschek, W. M. (2016). Swine in translational research and drug development. *Toxicol. Pathol.* 44, 297–298. doi: 10.1177/1019262316630838

## AUTHOR CONTRIBUTIONS

CA and DLM performed the experiments. CA and CB analyzed the data. SN conceived the original idea. CB, MF, AP, and SN planned the experiments. SN supervised the project. AP and SN wrote the manuscript. CB, FT, and MF revised the text. MF acquired funding. All authors read and approved the manuscript.

## FUNDING

This work was supported by University of Bologna, grant BIR2019 to MF.

- Nesci, S. (2017). Glucose and glutamine in the mitochondrial oxidative metabolism of stem cells. *Mitochondrion* 35, 11–12. doi: 10.1016/j.mito.2017.04.004
- Nesci, S., and Lenaz, G. (2021). The mitochondrial energy conversion involves cytochrome c diffusion into the respiratory supercomplexes. *Biochim. Biophys. Acta Bioenerg.* 1862:148394. doi: 10.1016/j.bbabi.2021.148394
- Nesci, S., Trombetti, F., Pagliarini, A., Ventrella, V., Algieri, C., Tioli, G., et al. (2021). Molecular and supramolecular structure of the mitochondrial oxidative phosphorylation system: implications for pathology. *Life* 11:242. doi: 10.3390/life11030242
- Nossol, C., Diesing, A.-K., Walk, N., Faber-Zuschratter, H., Hartig, R., Post, A., et al. (2011). Air-liquid interface cultures enhance the oxygen supply and trigger the structural and functional differentiation of intestinal porcine epithelial cells (IPEC). *Histochem. Cell Biol.* 136, 103–115. doi: 10.1007/s00418-011-0826-y
- Nowak, J. K., Grzybowska-Chlebowczyk, U., Landowski, P., Szaflarska-Poplawska, A., Klineciewicz, B., Adamczak, D., et al. (2014). Prevalence and correlates of vitamin K deficiency in children with inflammatory bowel disease. *Sci. Rep.* 4:4768. doi: 10.1038/srep04768
- Okano, T., Shimomura, Y., Yamano, M., Sahara, Y., Kamao, M., Sugiura, M., et al. (2008). Conversion of phyloquinone (Vitamin K1) into menaquinone-4 (Vitamin K2) in mice: two possible routes for menaquinone-4 accumulation in cerebra of mice. *J. Biol. Chem.* 283, 11270–11279. doi: 10.1074/jbc.M702971200
- Orlando, A., Linsalata, M., Tutino, V., D'Attoma, B., Notarnicola, M., and Russo, F. (2015). Vitamin K1 exerts antiproliferative effects and induces apoptosis in three differently graded human colon cancer cell lines. *Biomed. Res. Int.* 2015:296721. doi: 10.1155/2015/296721
- Schoon, E. J., Müller, M. C., Vermeer, C., Schurgers, L. J., Brummer, R. J., and Stockbrügger, R. W. (2001). Low serum and bone vitamin K status in patients with longstanding Crohn's disease: another pathogenetic factor of osteoporosis in Crohn's disease? *Gut* 48, 473–477. doi: 10.1136/gut.48.4.473
- Schwalfenberg, G. K. (2017). Vitamins K1 and K2: the emerging group of vitamins required for human health. *J. Nutr. Metab.* 2017:6254836. doi: 10.1155/2017/6254836
- Shearer, M. J., Fu, X., and Booth, S. L. (2012). Vitamin K nutrition, metabolism, and requirements: current concepts and future research. *Adv. Nutr.* 3, 182–195. doi: 10.3945/an.111.001800
- Shirakawa, H., Komai, M., and Kimura, S. (1990). Antibiotic-induced vitamin K deficiency and the role of the presence of intestinal flora. *Int. J. Vitam. Nutr. Res.* 60, 245–251.
- Suttie, J. W. (1985). Vitamin K-Dependent Carboxylase. *Annu. Rev. Biochem.* 54, 459–477. doi: 10.1146/annurev.bi.54.070185.002331
- Takada, T., Yamanashi, Y., Konishi, K., Yamamoto, T., Toyoda, Y., Masuo, Y., et al. (2015). NPC1L1 is a key regulator of intestinal vitamin K absorption and a modulator of warfarin therapy. *Sci. Transl. Med.* 7:275ra23. doi: 10.1126/scitranslmed.3010329
- Takahashi, T., Mine, Y., and Okamoto, T. (2018). Intracellular reduction of coenzyme Q homologues with a short isoprenoid side chain induces apoptosis of HeLa cells. *J. Biochem.* 163, 329–339. doi: 10.1093/jb/mvy002

- Tan, B., Xiao, H., Li, F., Zeng, L., and Yin, Y. (2015). The profiles of mitochondrial respiration and glycolysis using extracellular flux analysis in porcine enterocyte IPEC-J2. *Anim. Nutr.* 1, 239–243. doi: 10.1016/j.aninu.2015.08.004
- Tsugawa, N., and Shiraki, M. (2020). Vitamin K Nutrition and Bone Health. *Nutrients* 12, 1909. doi: 10.3390/nu12071909
- Vaugelade, P., Posho, L., Darcy-Vrillon, B., Bernard, F., Morel, M. T., and Duée, P. H. (1994). Intestinal oxygen uptake and glucose metabolism during nutrient absorption in the pig. *Proc. Soc. Exp. Biol. Med.* 207, 309–316. doi: 10.3181/00379727-207-43821
- Vergauwen, H. (2015). “The IPEC-J2 Cell Line,” in *The Impact of Food Bioactives on Health*, eds K. Verhoeckx, P. Cotter, I. López-Expósito, C. Kleiveland, T. Lea, A. Mackie, et al. (Cham: Springer International Publishing), 125–134. doi: 10.1007/978-3-319-16104-4\_12
- Vos, M., Esposito, G., Edirisinghe, J. N., Vilain, S., Haddad, D. M., Slabbaert, J. R., et al. (2012). Vitamin K2 is a mitochondrial electron carrier that rescues pink1 deficiency. *Science* 336, 1306–1310. doi: 10.1126/science.1218632
- Wu, Z., Tan, B., Liu, Y., Dunn, J., Martorell Guerola, P., Tortajada, M., et al. (2019). Chemical composition and antioxidant properties of essential oils from peppermint, native spearmint and scotch spearmint. *Molecules* 24:2825. doi: 10.3390/molecules24152825
- Zorov, D. B., Andrianova, N. V., Babenko, V. A., Bakeeva, L. E., Zorov, S. D., Zorova, L. D., et al. (2020). Nonphosphorylating oxidation in mitochondria and related processes. *Biochemistry (Mosc)* 85, 1570–1577. doi: 10.1134/S0006297920120093

**Conflict of Interest:** The authors declare that the research was conducted in the absence of any commercial or financial relationships that could be construed as a potential conflict of interest.

Copyright © 2021 Bernardini, Algieri, La Mantia, Trombetti, Pagliarani, Forni and Nesci. This is an open-access article distributed under the terms of the Creative Commons Attribution License (CC BY). The use, distribution or reproduction in other forums is permitted, provided the original author(s) and the copyright owner(s) are credited and that the original publication in this journal is cited, in accordance with accepted academic practice. No use, distribution or reproduction is permitted which does not comply with these terms.

**Notice:** *In the results section some published works are reported in which the candidate name occurs in intermediate author position. In these works the candidate role was as follows:*

*- in the paper entitled “Sulfide affects the mitochondrial respiration, the Ca<sup>2+</sup>-activated F<sub>1</sub>F<sub>0</sub>-ATPase activity and the permeability transition pore but does not change the Mg<sup>2+</sup>-activated F<sub>1</sub>F<sub>0</sub>-ATPase activity in swine heart mitochondria” the candidate evaluated the mitochondrial activities in the presence and in the absence of NaHS;*

*-in the papers entitled “Sperm function and mitochondrial activity: An insight on boar sperm metabolism”, “Biological characteristics and metabolic profile of canine mesenchymal stem cells isolated from adipose tissue and umbilical cord matrix”, “Relationship between serum concentration, functional parameters and cell bioenergetics in IPEC-J2 cell line” and “Vitamin K vitamers differently affect energy metabolism in IPEC-J2 cells” the candidate carried out the experiments to investigate the cell bioenergetics.*

## *Discussion*

## Section I

The different experimental approaches used in this thesis have allowed us to obtain a model of the relationship between  $\text{Ca}^{2+}$ -activated  $\text{F}_1\text{F}_0$ -ATPase and mPTP formation. The different sizes of the cations  $\text{Mg}^{2+}$  (atomic radius 1.45Å) and  $\text{Ca}^{2+}$  (atomic radius 1.94 Å) would promote a different coordination chemistry in the catalytic sites of the  $\text{F}_1$  hexamer.  $\text{Ca}^{2+}$  forms irregular bond angles in the  $\beta$  subunits, while the  $\text{Mg}^{2+}$  forms hexacoordinate octahedral complexes<sup>230</sup>. The binding of the nucleotide to the catalytic and non-catalytic  $\text{F}_1\text{F}_0$ -ATPase subunits requires the coordination of the essential cofactor  $\text{Mg}^{2+}$  which contributes to the asymmetry of the binding site and the generation of the different affinities for nucleotides<sup>231</sup> therefore the presence of  $\text{Ca}^{2+}$  modifies the kinetic parameters of the enzyme<sup>62</sup>. The recent cryo-EM structure of  $\text{F}_1\text{F}_0$ -ATPase<sup>27</sup> shows a strong conformational change in the enzyme structure when  $\text{Ca}^{2+}$  is bound to it. This change in shape triggers the formation of mPTP according to the "bent-pull" model of the c-ring-gated channel<sup>50</sup>.

The catalytic sites of  $\text{F}_1\text{F}_0$ -ATPase have different conformational states promoted by the binding of different cofactor cations, for example, divalent cations of different sizes such as  $\text{Mg}^{2+}$ ,  $\text{Mn}^{2+}$  and  $\text{Ca}^{2+}$  which lead to a different modulation of the F-ATPase. The competitive activation of  $\text{Mn}^{2+}$  on the  $\text{F}_1\text{F}_0$ -ATPase activated by  $\text{Mg}^{2+}$  demonstrates the possibility of binding of  $\text{Mg}^{2+}$  or  $\text{Mn}^{2+}$  in the catalytic sites during catalysis. Noncompetitive inhibition of  $\text{Ca}^{2+}$  on  $\text{Mg}^{2+}$ -activated  $\text{F}_1\text{F}_0$ -ATPase suggests that  $\text{Ca}^{2+}$  and  $\text{Mg}^{2+}$  bind to distinct sites in the catalytic subunits of  $\text{F}_1$ .  $\text{Ca}^{2+}$  binds to the cofactor-free  $\text{F}_1\text{F}_0$ -ATPase or the  $\text{Mg}^{2+}$  bound  $\text{F}_1\text{F}_0$ -ATPase, while  $\text{Mg}^{2+}$  and  $\text{Mn}^{2+}$  compete for the same binding site. Therefore, the greater steric hindrance of  $\text{Ca}^{2+}$  compared to  $\text{Mg}^{2+}$  and  $\text{Mn}^{2+}$  prevents its insertion into the catalytic sites.

The use of  $\text{F}_1$ -ATPase inhibitors allows us to better understand the distinct mechanisms between  $\text{Ca}^{2+}$ -and  $\text{Mg}^{2+}$ -activated  $\text{F}_1\text{F}_0$ -ATPase. The  $\text{F}_1$  domain can bind covalent inhibitors that modify

amino acid residues near the substrate-binding site or non-covalent inhibitors, such as polyphenolic phytochemicals. NBD-Cl covalently binds to  $\beta$ -Tyr-311 and changes its phenolic oxygen only when the catalytic site is in the  $\beta_E$  conformation<sup>232</sup>. However, the NBD-Cl group can shift from Tyr to  $\beta$ -Lys-162 within the same  $\beta_E$  subunit at  $\text{pH} \geq 9.0$ <sup>233</sup>. The steric encumbrance of NBD-Cl prevents conversion to  $\beta_{TP}$  and blocks the hydrolysis of ATP<sup>234</sup>. The similar mechanism of NBD-Cl inhibition on  $\text{Ca}^{2+}$ - and  $\text{Mg}^{2+}$ -activated  $F_1F_0$ -ATPase with respect to cationic cofactors or substrate is consistent with the inhibitor's inability to occupy the nucleotide-binding site. The binding of  $\text{Ca}^{2+}$  to the  $F_1$  domain favors the interaction of the inhibitor with the enzyme in fact the inhibition of the enzyme by NBD-Cl is more effective on  $\text{Ca}^{2+}$ -activated  $F_1F_0$ -ATPase than  $\text{Mg}^{2+}$ -activated  $F_1F_0$ -ATPase; conformational changes promoted by  $\text{Ca}^{2+}$  can make the binding site more prone to accept the inhibitor.

Piceatannol, resveratrol and quercetin are phytochemical compounds known to inhibit the hydrolysis of ATP by binding  $F_1$  without interfering with the catalytic sites, they block the rotating mechanism by binding where the C-terminal tip of the  $\gamma$  subunit interacts with the “bearing”, a region of ring below the “crown region” of the  $\alpha$  and  $\beta$  subunits<sup>118</sup>. They exert different types of inhibition on  $\text{Ca}^{2+}$ - and  $\text{Mg}^{2+}$ -activated  $F_1F_0$ -ATPase but their inhibition mechanism is never competitive, each phytochemical binds to a distinct site with respect to ATP,  $\text{Mg}^{2+}$  and  $\text{Ca}^{2+}$ . The inhibitory efficiency of each phytochemical is higher on  $\text{Ca}^{2+}$ -activated  $F_1F_0$ -ATPase than  $\text{Mg}^{2+}$ -activated  $F_1F_0$ -ATPase, probably because the size of  $\text{Ca}^{2+}$  in the globular hexamer  $(\alpha\beta)_3$  implies a greater impact of the cation on the torsional mechanism of the rotor. The inhibitory effect of the inhibitors on partially purified  $F_1$  confirm their prevailing inhibition on the  $\text{Ca}^{2+}$ -activated  $F_1F_0$ -ATPase. Therefore, Is- $F_1$  selectively inhibit  $F_1$ -ATPase activity and, consequently, the  $\text{Ca}^{2+}$ -dependent hydrolysis of ATP.

NBD-Cl inhibits the  $\text{Ca}^{2+}$ -induced opening of mPTP like CsA, a known blocker of mPTP, while polyphenolic phytochemicals desensitize the opening, that is increase the threshold of  $\text{Ca}^{2+}$

required for its formation. Furthermore, polyphenolic phytochemicals block the sudden dissipation of the membrane potential due to the formation of mPTP, effects that could also be influenced by some concomitant changes in the activities of the mitochondrial respiratory chain complexes. The data demonstrate that the differences between  $Mg^{2+}$  and  $Ca^{2+}$  in their coordination properties and in inducing different conformational changes within  $F_1$ , even if they do not affect the catalytic mechanism of ATP hydrolysis, are functionally selective. Therefore, only  $Ca^{2+}$  can drive the conformational transmission mechanism that leads to the opening of the mPTP.

Another ion as  $Gd^{3+}$  was used to verify the effect on  $F_1F_0$ -ATPase, exploiting its inhibition mechanism, and explore its alleged connection with the mPTP.  $Gd^{3+}$  is known to induce mitochondrial dysfunction, probably due to the opening of the mPTP<sup>128</sup>. Moreover, in erythrocyte membranes it can interact with membrane phospholipids<sup>235</sup>, forming pores<sup>236</sup>. Furthermore,  $Gd^{3+}$  was shown to inhibit membrane permeabilization by physically modifying the membrane structure in a model system<sup>237</sup>. The effect of  $GdCl_3$  evaluated on  $Mg^{2+}$ - or  $Ca^{2+}$ -activated  $F_1F_0$ -ATPase shows an inhibition of the  $F_1F_0$ -ATPase activity independently of divalent cofactors at increasing  $GdCl_3$  concentrations. When  $F_1F_0$ -ATPase is activated by  $Mg^{2+}$  it only reaches a maximum inhibition of 40% at the maximum concentration tested, while activated by  $Ca^{2+}$  the enzyme is progressively inhibited until it reaches a value close to zero at maximum concentration. The inhibition exerted by  $Gd^{3+}$  on the  $Mg^{2+}$ -activated  $F_1F_0$ -ATPase shows a competitive mechanism with respect to the ATP substrate, indicating that the inhibitor binds only to the free enzyme, while it shows a uncompetitive mechanism with respect to the  $Mg^{2+}$  cofactor, that is  $Gd^{3+}$  only binds to the enzyme- $Mg^{2+}$  complex. A competitive inhibition mechanism is also exerted on the  $F_1F_0$ -ATPase activated by  $Ca^{2+}$  with respect to the ATP substrate;  $Gd^{3+}$  prevents the binding of ATP to the enzyme by inhibiting the activity of ATPase independently of the cationic cofactor. The inhibition constant ( $K_i$ ) of  $Ca^{2+}$ -activated  $F_1F_0$ -ATPase is about three times lower than that of  $Mg^{2+}$ -activated  $F_1F_0$ -ATPase activity demonstrating that  $Gd^{3+}$  competes in most efficiently with

ATP at the substrate-binding site to form the binary complex ( $EI$ ) when  $F_1F_0$ -ATPase is activated by  $Ca^{2+}$ . Furthermore, in the presence of  $Ca^{2+}$  the inhibition mechanism is of a mixed type towards the cofactor, that is  $Gd^{3+}$  can bind both to the free enzyme and to the enzyme- $Ca^{2+}$ . These results demonstrate that  $Gd^{3+}$  and  $Ca^{2+}$  bind to distinct enzymatic sites. Since the  $Gd^{3+}$  binding site does not overlap the  $Ca^{2+}$  binding site on the  $\beta$  subunits<sup>238</sup>, the  $Ca^{2+}$ -activated  $F_1F_0$ -ATPase can form a binary (enzyme- $Gd^{3+}$ ) or ternary ( $Ca^{2+}$ -enzyme- $Gd^{3+}$ ) complex with the inhibitor. However, the formation of the enzyme- $Gd^{3+}$  complex is preferred over that of the enzyme-cofactor-inhibitor complex, since the dissociation constant of the enzyme-inhibitor complex  $K_i$  is lower than that of the enzyme-substrate-inhibitor complex ( $K'_i$ ). Furthermore  $Gd^{3+}$  binds to the enzyme-cofactor complex to form the ternary complex with the same strength when the cofactor is  $Mg^{2+}$  or  $Ca^{2+}$ . The natural logarithm of the residual activity (uninhibited rate minus inhibited rate) respect to time provides the observed first order rate constants calculated from the slopes of the lines obtained at different concentrations of  $GdCl_3$  in the presence of  $Mg^{2+}$  or  $Ca^{2+}$ . In both cases, the time course of  $Gd^{3+}$  mediated inhibition is an exponential function. The greater propensity of  $Gd^{3+}$  to react with  $Ca^{2+}$ -activated  $F_1F_0$ -ATPase compared to  $Mg^{2+}$ -activated  $F_1F_0$ -ATPase is also confirmed by a significantly higher  $k_{inact}$  value for  $Ca^{2+}$ -activated  $F_1F_0$ -ATPase. The  $k_{inact}/K_I$  ratio shows the inhibition potency of  $Gd^{3+}$ , which indicates the inhibition efficiency. On the  $Ca^{2+}$ -activated  $F_1F_0$ -ATPase  $k_{inact}/K_I$  is higher than the ratio for the  $Mg^{2+}$ -activated  $F_1F_0$ -ATPase activity, therefore the  $Gd^{3+}$  reacts more rapidly with the enzyme in the presence of  $Ca^{2+}$ , resulting in a faster and stronger inhibition of  $Ca^{2+}$ -activated  $F_1F_0$ -ATPase activity. All data indicate that when  $Ca^{2+}$  replaces the natural cofactor  $Mg^{2+}$  at the binding site of the enzyme,  $F_1F_0$ -ATPase becomes more prone to inhibition by  $Gd^{3+}$ . The latter desensitizes the mPTP opening, *i. e.* is a higher concentration of  $Ca^{2+}$  in the mitochondrial matrix is needed to trigger the formation of mPTP compared to the control mitochondria. Consistently, the extent of mPTP formation, expressed as the ratio of the number of  $Ca^{2+}$  pulses needed to induce mPTP in  $MgADP$ -inhibited ( $CRC_i$ ) and untreated ( $CRC_o$ ) mitochondria, doubled in the presence of  $GdCl_3$ .

Amino acid residues are crucial for the structure and function of an enzyme. The role of arginine residues in the structure/function of  $F_1F_0$ -ATPase and the correlation with the mPTP formation were evaluated by using PGO, modulator of Arg residues. The results show that PGO more efficiently inhibits  $Ca^{2+}$ -activated  $F_1F_0$ -ATPase than  $Mg^{2+}$ -activated  $F_1F_0$ -ATPase. The uncompetitive inhibition mechanism of  $F_1F_0$ -ATPase with respect to the ATP substrate in the presence of  $Ca^{2+}$  or  $Mg^{2+}$  shows that PGO does not interact with the enzyme cofactor sites and binds to another site respect to ATP. Consequently, the *ES*-PGO complex is formed only when the *ES* complex has already been formed. Mutual inhibition studies between PGO and azide, the latter known to block ATP hydrolysis when  $P_i$  leaves the catalytic site<sup>239</sup>, indicate that PGO and azide are not mutually exclusive and can form the quaternary complex (*ES*-azide-PGO). From this, we deduce that PGO binds to another site than the azide binding site in the  $F_1$  domain. In coupled  $F_1F_0$ -ATPase, blockade of the  $H^+$  translocation inhibits the hydrolysis of ATP. Mutual exclusion studies with oligomycin and DCCD show that PGO does not prevent the flow of transmembrane  $H^+$  within  $F_0$ . While oligomycin and DCCD bind to the  $H^+$  binding sites of the *c*-ring and inhibit  $F_1F_0$ -ATPase, PGO binds to the  $F_1F_0$ -ATPase complex to form the *ESI*<sub>1</sub>-PGO complex, without interfering with the binding sites of  $F_0$  inhibitors. In mutual exclusion studies, however, considering the lower  $\alpha K'_i$  values of the  $Ca^{2+}$ -activated  $F_1F_0$ -ATPase compared to that of the  $Mg^{2+}$ -activated  $F_1F_0$ -ATPase, it is evident that PGO has a greater propensity to form the quaternary complex (*ESI*<sub>1</sub>*I*<sub>2</sub>) in the presence of  $Ca^{2+}$  than in the presence of  $Mg^{2+}$ . Furthermore, the  $\alpha > 1$  value obtained for  $Mg^{2+}$ -activated  $F_1F_0$ -ATPase with all inhibitors under study indicates that inhibitors of the  $F_1/F_0$  domain and PGO hinder each other. On the contrary, all the  $\alpha$  values obtained for the  $Ca^{2+}$ -activated  $F_1F_0$ -ATPase are around 1.0, which indicates no interference between the distinct binding sites of the inhibitor. The presence of  $Mg^{2+}$  or  $Ca^{2+}$  favors different conformational states on the  $F_1F_0$ -ATPase<sup>240</sup>, therefore the most evident inhibition of PGO on the  $Ca^{2+}$ -activated  $F_1F_0$ -ATPase could be explained by a modification of the enzymatic structure caused by the Arg adducts. In rat mitochondria 1 mM PGO has been reported to inhibit mPTP<sup>241</sup>.

The same treatment in porcine heart mitochondria activates mPTP.  $\text{Ca}^{2+}$ -activated  $\text{F}_1\text{F}_0$ -ATPase activity has been shown to be essential for triggering mPTP opening but, inhibition of  $\text{Ca}^{2+}$ -activated  $\text{F}_1\text{F}_0$ -ATPase by PGO contrasts with facilitating mPTP opening. Probably among the many Arg residues of  $\text{F}_1\text{F}_0$ -ATPase, located in the  $\alpha$ ,  $\beta$ ,  $\gamma$ ,  $\epsilon$  subunits of the  $\text{F}_1$  domain, and in the  $a$ ,  $c$  and  $g$  subunits of the  $\text{F}_0$  domain, the only Arg candidate to form an adduct with PGO responsible for the formation of mPTP is the conserved Arg-107 of the  $g$  subunit in yeast, which corresponds to Arg-96 in the human sequence<sup>242</sup>. This chemical change determines the inhibition of  $\text{F}_1\text{F}_0$ -ATPase but does not affect either the  $\text{F}_1$  catalytic mechanism or the  $\text{H}^+$  translocation within  $\text{F}_0$ . The  $g$  subunit is involved in one of the  $\text{F}_1\text{F}_0$ -ATPase dimerization sites and joins the  $e$  subunit and the N-terminal helix of the  $b$  subunits of each monomer<sup>42</sup>. Probably the PGO adduct on the  $g$  subunit favors a conformational rearrangement in the transmembrane portion of  $\text{F}_1\text{F}_0$ -ATPase that mimics the  $\text{Ca}^{2+}$ -activated  $\text{F}_1\text{F}_0$ -ATPase conformation that forms mPTP.

Since (ir)reversible post-translational modifications of di-thiols on  $\text{F}_1\text{F}_0$ -ATPase affect the mPTP formation and regulation, dithiol reagents have been used to learn about the role of cysteines in mPTP formation. The thiol reagents PAO and DBrB show opposite effects on  $\text{F}_1\text{F}_0$ -ATPase activity: PAO increases the  $\text{Mg}^{2+}$ - and  $\text{Ca}^{2+}$ -activated  $\text{F}_1\text{F}_0$ -ATPase activity while DBrB inhibits them. The opposite effect of the two dithiol reagents may be due to their interaction with different cysteine pairs of the enzyme. Post-translational modifications of cysteine could alter the  $\text{F}_1\text{F}_0$ -ATPase structure regardless of which cation activates the enzyme. Disulfide is formed on  $\text{F}_1\text{F}_0$ -ATPase by binding between Cys251 of two  $\alpha$  subunits or Cys251 and Cys78 of  $\alpha$  and  $\gamma$  subunits, respectively during the assembly of the holoenzyme. Cross-linking between cysteines is associated with  $\text{F}_1\text{F}_0$ -ATPase dysfunction in patients with heart failure<sup>243</sup>. Conversely, reversible dithiol bridges, established by mercury, increase  $\text{F}_1\text{F}_0$ -ATPase activity when the  $\text{Mg}$ -ATP substrate is bound at the catalytic sites<sup>192</sup>. To verify if the modified cysteine thiols (-S-X-S) of the protein adduct were sensitive to the reduction, the thiol reducing reagent DTE was tested. DTE does not

alter the basic  $Mg^{2+}$ - or  $Ca^{2+}$ -activated  $F_1F_0$ -ATPase activity. Rather, DTE significantly reduced PAO activation on  $Mg^{2+}$ - or  $Ca^{2+}$ -activated  $F_1F_0$ -ATPase. In contrast, the inhibition of  $Mg^{2+}$ - or  $Ca^{2+}$ -activated  $F_1F_0$ -ATPase caused by DBrB was maintained even in the presence of DTE. The respective reversible and (ir)reversible redox behavior of PAO or DBrB sensitive cysteine pairs confirms that this regulation is independent of the catalytic site bound cofactor. The PAO and DBrB effects show how different modifiers of dithiol act on the catalytic activity of  $F_1F_0$ -ATPase and on the known redox state of the vicinal cysteine residues by modulating the opening of mPTP and  $F_1F_0$ -ATPase. CRC, measuring the ability of intact mitochondria to accumulate  $Ca^{2+}$  and release it upon opening the mPTP, showed opposite effects in the presence of PAO and DBrB, consistent with the modulation of  $F_1F_0$ -ATPase. PAO sensitizes the formation of mPTP, consistent with the stimulation of  $Ca^{2+}$ -activated  $F_1F_0$ -ATPase activity. The PAO driven increase in mPTP sensitivity is neutralized by DTE, thus confirming the involvement of cross-linked critical dithiols in the opening of mPTP. On the contrary, the DBrB inhibition of mPTP formation, not modulated by the DTE, is corroborated by the inhibition of the two  $F_1F_0$ -ATPase activities. These results lead us to think that two different pairs of cysteines specifically crosslinked with PAO and DBrB produce opposite effects on  $F_1F_0$ -ATPase and mPTP. Furthermore, DTE apparently only reduces the dithiols that react with PAO and not those that interact with DBrB. It is possible to hypothesize that the  $F_1F_0$ -ATPase has two distinct molecular strategies to regulate the opening of mPTP, *i.e.* the reversible oxidation of vicinal dithiols (not more than 3.8 Å) or the irreversible oxidation of distant dithiols (up to 6.6 Å). Since the mPTP participates in both development and cell death<sup>78</sup>, the dithiols by post-translational modification can act on the regulation of the transition from physiological to pathological opening of mPTP in mitochondria. This allows us to hypothesize that cysteine pairs could be highlighted on the  $F_1F_0$ -ATPase that can act as pharmacological targets to control pathological conditions due to the dysregulation of mPTP and physiologically are molecular keys to open the mPTP.

BPF, rich in polyphenols, was tested on the mitochondrial activity, due to its beneficial features and especially for its antioxidant and anti-inflammatory effects found in recent times. Its positive effects are found on the  $F_1F_0$ -ATPase activity, in fact, data show that BPF stimulates  $F_1F_0$ -ATPase activity raised by the natural cofactor  $Mg^{2+}$  by 15%. Conversely, when the enzyme is activated by  $Ca^{2+}$ , the activity is inhibited by 10%. This latter inhibitory effect is also correlated in this case to the formation of mPTP, since 50  $\mu g/ml$  BPF and 100  $\mu g/ml$  BPF desensitize the pore opening, causing a concentration-dependent reduction of the pore size. BPF other than showing a protective effect on the mPTP formation also improves the RCR, which increases when the mitochondria are energized by CI or CII substrates.

Melatonin, selected for its antioxidant properties, was used to evaluate the role of ROS in the formation of mPTP. First, melatonin shows an inhibitory effect on  $Mg^{2+}$ -activated  $F_1F_0$ -ATPase but only at low temperatures. As demonstrated by the Arrhenius diagrams, melatonin does not affect the state of the membrane at low temperatures but probably, the stiffening of the membrane causes conformational changes to the enzymatic complex, leading to a better interaction with melatonin, allowing it to exert its inhibitory effect. However, this binding involves the inhibition of  $Ca^{2+}$ -activated  $F_1F_0$ -ATPase already at 37 °C, a temperature typical of mammalian mitochondria, with an uncompetitive mechanism, that is, it binds the complexed enzyme to the ATP substrate (*ESI*). Probably the conformational change implemented at low temperatures of the  $Mg^{2+}$ -activated  $F_1F_0$ -ATPase partly mimics, in  $F_1$ , the conformation of the enzyme activated by the  $Ca^{2+}$  cofactor at 37 °C, favoring the inhibitory effect of melatonin on the enzyme activated by the two different cations, to different temperatures. Mutual exclusion studies between known  $F_1$  (NBD-Cl) and  $F_0$  (DCCD) inhibitors further reinforce the idea that melatonin interacts on the  $F_1$  portion, mutually excluding with NBD-Cl, rather than interacting in the transmembrane portion, as also confirmed by its inhibitory effect on the hydrolytic activity of purified  $F_1$ -ATPase. Melatonin interacts with CI of the ETC with a consequent inhibitory effect on respiration. Exciting

the mitochondria with pyruvate/malate, therefore starting from CI, state 3 and state 4 are reduced to the same extent. Therefore, the ratio state 3/state 4, which indicates the coupling efficiency, is unaffected. So, it is possible to affirm that phosphorylation oxidative is not modified by melatonin. Furthermore, the production of ROS by CI is also reduced by the presence of melatonin, as demonstrated by fluorometric studies, probably due to its inhibitory effect on CI. However, despite not having altered the consumption of oxygen starting from the CII, ROS production in succinate-energized mitochondria is similarly inhibited. These data, therefore, support the beneficial effects of melatonin as it inhibits  $\text{Ca}^{2+}$ -activated  $\text{F}_1\text{F}_0$ -ATPase without altering the physiological condition in correlation with the desensitization of mPTP formation and the reduction of ROS production.

On considering the involvement of mitochondria and in particular of the mPTP formation in severe pathologies, including cardiovascular diseases and the link between the  $\text{F}_1\text{F}_0$ -ATPase and the mPTP, NaHS, as sulfide donor, was tested on mitochondria isolated from swine heart, to define its molecular mechanism in the perspective of using sulfides to combat cardiovascular pathologies<sup>244</sup>. The investigations carried out in parallel on mitochondrial preparations of the digestive gland of mussels, were instead aimed at verifying how well preserved, and therefore universal, the mitochondrial mechanisms of response to  $\text{H}_2\text{S}$  were.

Among the three forms  $\text{HS}^-$ ,  $\text{S}^{2-}$  and  $\text{H}_2\text{S}$ , at physiological pH,  $\text{H}_2\text{S}$  directly affects mitochondrial proteins, as it can easily cross biomembranes due to its lipophilicity and lack of electrical charge inducing post-translational modifications of the  $\text{F}_1\text{F}_0$ -ATPase, specifically S-sulfur<sup>245</sup>, interacting with Cys244 and Cys294 of the  $\alpha$  subunit, causing modulation of the enzymatic function. In contrast, in swine heart mitochondria, NaHS has no effect on the of  $\text{Mg}^{2+}$ - activated  $\text{F}_1\text{F}_0$ -ATP(hydrol)ase but slightly inhibits  $\text{Ca}^{2+}$ -activated  $\text{F}_1\text{F}_0$ -ATP(hydrol)ase. The addition of low molecular weight thiol reagents, oxidants (GSSG) and reducing agents (DTE), does not alter the effect of NaHS, allowing us to exclude the possibility that it can interact directly with the thiols of the  $\text{F}_1\text{F}_0$ -ATPase. The metabolic and signaling pathways could most likely explain the reactivity

of the  $F_1F_0$ -ATPase to  $H_2S$  in intact cells. On considering the insensitivity of  $F_1F_0$ -ATPase to NaHS, the effects of NaHS on respiratory complexes CI and CII were investigated. Both complexes are inhibited by NaHS but the inhibition is approximately three-fold greater on CII. In both cases the inhibition is not modulated by the DTE, which can reduce the persulfide groups, therefore the post-translational modifications of the thiols cannot be responsible for the inhibition of these enzymatic activities. The known inhibition of  $H_2S$  on CIV<sup>246</sup> is confirmed by our data on inhibition of cytochrome *c* oxidase. Therefore, the transfer of electrons starting from both the two complexes CI and CII to the  $O_2$  in the respiratory chain is blocked downstream. Furthermore, at low concentrations  $H_2S$  is known as the first inorganic electron donor to the mitochondrial electron transport chain via sulfide, thus stimulating mitochondrial respiration<sup>247,248</sup>. CII does not participate in the respirasome assembly<sup>249,250</sup>,  $H_2S$  and succinate can be mutually exclusive as electron donors to the respiratory chain. For this reason,  $H_2S$  inhibition is more pronounced on succinate- $O_2$  oxidoreductase than on NADH- $O_2$  oxidoreductase. Insensitivity of  $Mg^{2+}$ -activated  $F_1F_0$ -ATPase to NaHS and inhibition of CIV between mitochondrial respiratory complexes explain a respiration inhibition of state 3 and 4, the ratio of which is not affected by NaHS regardless of CI or CII substrates. Therefore, NaHS reduces the flow of electrons in the OXPHOS system without affecting the synthesis of ATP. Ischemic/reperfusion injury is known to be attenuated by blocking the formation and opening of mPTP<sup>251</sup>. Therefore, the swine heart mitochondria have been treated with NaHS and it seems that they can avoid an uncontrolled release of  $Ca^{2+}$  from mitochondria, associated with the collapse of the membrane potential. Accordingly, the CRC shows a gradual decrease in the presence of NaHS, comparable to the trend of red ruthenium (RR), a known inhibitor of the mitochondrial  $Ca^{2+}$  uniporter (MCU) and does not show the typical profile of  $Ca^{2+}$  uptake by mitochondria. Accordingly, the gradual increase in CRC demonstrates that added  $Ca^{2+}$  does not enter the mitochondrion but binds to the probe which is out of it. Therefore, the desensitization of the mPTP by NaHS appears to be related to the lack of mitochondrial absorption of  $Ca^{2+}$ . In the control mitochondria, the opening of the mPTP causes a strong depolarization of

the IMM, as shown by the large increase in the fluorescence ratio of JC-10 after the addition of  $\text{Ca}^{2+}$ . Conversely, in NaHS treated mitochondria the gradual increase in the JC-10 ratio is likely due to the inhibition of mitochondrial respiration which reduces membrane potential. Consistently, the inhibition of mitochondrial respiration by NaHS can decrease the transmembrane proton motive force, thus compromising ion cycles, which involve the  $\text{Ca}^{2+}$  uniport and  $\text{Ca}^{2+}$  efflux from a  $\text{Na}^+$  pathway<sup>252</sup>. Therefore, a negative effect on mitochondrial respiration can have the positive effect to prevent or delay the formation of the mPTP.

In the comparative study, at first, the kinetic properties of  $\text{F}_1\text{F}_0$ -ATPase in the mitochondria of the digestive glands of mussels activated by the natural cofactor  $\text{Mg}^{2+}$  or by  $\text{Ca}^{2+}$  were investigated. ATP hydrolysis can be supported by  $\text{Ca}^{2+}$  and  $\text{Mg}^{2+}$ , although the oligomycin-sensitive ATPase activity is lower in the presence of  $\text{Ca}^{2+}$  than in the presence of  $\text{Mg}^{2+}$ . In fact, the coupling index (oligomycin-sensitive mitochondrial ATPase activity on the ratio of total mitochondrial ATPase activity) of  $\text{Mg}^{2+}$ -activated  $\text{F}_1\text{F}_0$ -ATPase shows a better value than  $\text{Ca}^{2+}$ -activated  $\text{F}_1\text{F}_0$ -ATPase. It is known that the rate of ATP hydrolysis depends on the concentration of ATP. The binding change mechanism for  $\text{F}_1$ -ATPase<sup>35</sup> is supported by the positive cooperativity of three catalytic sites, in fact, the substrate can simultaneously fill from one to three sites during catalysis (uni-site, bi-site or tri-site). This mechanism also occurs in the midgut gland of mussels where  $\text{Mg}$ - or  $\text{Ca}^{2+}$ -activated  $\text{F}_1\text{F}_0$ -ATPase exhibits similar Hill coefficients so, in both cases, ATP can also bind to two site catalysts to produce high rates of catalysis.  $\text{Mg}^{2+}$  and  $\text{Ca}^{2+}$  do not support ATP hydrolysis with the same efficiency: the  $\text{Mg}^{2+}$ -activated  $\text{F}_1\text{F}_0$ -ATPase shows a higher  $V_{\text{max}}$  value than that of  $\text{Ca}^{2+}$ -activated  $\text{F}_1\text{F}_0$ -ATPase, which indicates that, when activated by  $\text{Mg}^{2+}$ , the hydrolytic activity of the enzyme is more efficient, as in mammals. Therefore, mussel  $\text{Ca}^{2+}$ -activated  $\text{F}_1\text{F}_0$ -ATPase(hydroly)ase could be employed as a mitochondrial bioenergetic regulatory mechanism since its affinity for ATP is the same as the associated enzyme activated by  $\text{Mg}^{2+}$ . In mitochondria extracted from the digestive glands of mussels, NaHS showed no effect on F-ATPase, regardless

of the activating cation. Although in eukaryotes the amino acid sequences of the  $F_1F_0$ -ATPase subunits are very conserved, it seems that in mussels the enzymatic complex is somewhat refractory to  $H_2S$ . Probably these invertebrates have adapted to living in environments that can become very rich in sulphides, developing molecular mechanisms that are not very sensitive to  $H_2S$  over the course of evolution. The detection of  $Ca^{2+}$ -activated  $F_1F_0$ -ATPase, which has been shown to most likely coincide with mPTP suggests that the mitochondria of the mussel gland probably possess the ability to form mPTP. This was evaluated and confirmed by studying the CRC which decreases with increasing concentrations of  $Ca^{2+}$ , an unequivocal sign of the opening of the pore. Treatment with NaHS desensitizes mPTP activity, although it is ineffective on  $Ca^{2+}$ -activated  $F_1F_0$ -ATPase. A similar trend was found by treating the mitochondria with RR, so the uptake of  $Ca^{2+}$  by the mitochondria is clearly influenced by NaHS and, as a result, the mPTP is desensitized. Most likely, even in these mitochondria, the effects of NaHS do not occur directly on mPTP, but on the mitochondrial uptake of  $Ca^{2+}$  or, more generally, of the  $Ca^{2+}$  cycle, which is altered following the inhibition of transporters<sup>253</sup>.

The numerous studies based on the consideration of  $F_1F_0$ -ATPase as a possible pharmacological target, also involved a new class of chemical compounds, the triazole derivatives, obtained by replacing the isoxazole core in analogous compounds, which were considered as second-generation inhibitors of mPTP. This chemical modification improves their stability in plasma<sup>254</sup>, in fact, drugs with a short half-life in plasma, risk being degraded before they can exert any biological effect.

Triazoles 3a and 3b under study do not significantly affect NADH- $O_2$ /succinate- $O_2$  oxidase activity. However, the titration curve on  $Mg^{2+}$ -activated  $F_1F_0$ -ATPase shows that 3a and 3b do not affect the enzyme. In contrast, significant enzymatic inhibition by both compounds on the  $Ca^{2+}$ -activated  $F_1F_0$ -ATPase is evident. The different effect on the two differently activated  $F_1F_0$ -ATPases depends on the enzymatic conformations promoted by the cofactors linked to the

catalytic and/or non-catalytic sites of the F<sub>1</sub> domain<sup>98</sup>. Enzyme kinetics studies show that 3a and 3b exert uncompetitive inhibition by binding to the enzyme-ATP complex and forming the tertiary *ESI* complex. Therefore, both compounds do not affect the ATP binding site, but can interfere with a binding region that modifies the Ca<sup>2+</sup>-dependent catalytic mechanism of ATP hydrolysis. The dissociation constants of the *ESI* complex ( $K'_i$ ) of Ca<sup>2+</sup>- and Mg<sup>2+</sup>-activated F<sub>1</sub>F<sub>0</sub>-ATPase are similar indicating that the formation of the *ESI* complex is independent of the compounds structure. Since the inactivation rate constant ( $k_{inact}$ ) is greater for 3a than 3b, 3a has a greater propensity to react than for the latter, which implies a faster binding to the enzyme.

The  $k_{inact}/K'_i$  ratio is a measure of the inhibitor's efficiency on Ca<sup>2+</sup>-activated F<sub>1</sub>F<sub>0</sub>-ATPase and 3a shows a  $k_{inact}/K'_i$  ratio higher than 3b, therefore the former inhibitor is much more potent than the latter, probably because the two compounds establish different interactions with the enzyme even if they bind to the same site on the F<sub>1</sub>F<sub>0</sub>-ATPase. In fact, the mutual exclusion studies between 3a and 3b show that F<sub>1</sub>F<sub>0</sub>-ATPase can combine with 3a or 3b, but not with both compounds at the same time. The different chemical structure of the triazole derivatives resides in a nitro group in compound 3b, which apparently does not affect the affinity for F<sub>1</sub>F<sub>0</sub>-ATPase but may take a little longer to establish interactions with the enzyme. Consistently with the inhibition exerted on Ca<sup>2+</sup>-activated F<sub>1</sub>F<sub>0</sub>-ATPase, the formation of mPTP is also desensitized by compounds 3a and 3b, but in a different way; triazole 3a allows to reach a lower CRC value (larger mPTP dimension) than triazole 3b. It is probable that the different effects on mPTP of the two compounds are due to the different types of interactions in the same binding region on Ca<sup>2+</sup>-activated F<sub>1</sub>F<sub>0</sub>-ATPase, influencing the size of mPTP<sup>69</sup>. Furthermore, the sharp increase in fluorescence followed by a less marked decline as the mitochondria absorb calcium, in the presence of triazole 3a has a gradual increase in the baseline with each pulse of Ca<sup>2+</sup>, probably due to an inhibitory effect of the mitochondrial absorption of MCU by triazole 3a<sup>253</sup>.

## Section II

Cellular metabolism controls and ensures biological functions and cellular health. Metabolic pathways are a powerful predictor of cellular performance in *in vitro* disease models. They can be used for drug discovery, by modulating metabolic targets towards restoring a healthy phenotype or to optimize and improve cell performance. For this reason, it is interesting to characterize the metabolism of a specific cell line to understand its physiological conditions to be able to discriminate them from the pathological ones or to exploit them for the study of possible therapeutic agents.

Bioenergetic analyses on boar sperm mitochondria, aimed at understanding the role of mitochondria in sperm function, show that OXPHOS is exploited with a basal respiration close to maximum respiration stimulated by FCCP, therefore these mitochondria have a low reserve respiratory capacity (the ability to produce extra ATP by OXPHOS in response to an increased energy demand). The RCR close to unity shows that sperm mitochondria effectively exploit the electrochemical gradient generated by mitochondrial respiration to phosphorylate ADP. Furthermore, the oxidation of NADH is preferred to that of FADH<sub>2</sub> and the high inhibition by ROT suggests that the mitochondrial respiration depends mainly on CI. Most likely the mitochondria of boar sperm preferentially exploit CI because it is more advantageous in terms of production of ATP, in fact in mammals starting from CI, for each pair of electrons, 2.7 molecules of ATP are synthesized compared to the 1.6 produced starting from CII<sup>255</sup>. Studies carried out on freshly collected spermatozoa and immediately after 1 day of collection show how the amount of total ATP produced decreases over time, mainly due to a drastic reduction in mitochondrial ATP synthesis which at 0 days is the major contributor. However, the mitochondrial parameters remain unchanged over time and the energy map shows an increase in mitochondrial activity when the cell requires more energy. Probably, after one day, the mitochondrial functionality is not altered,

on the contrary, the number of active mitochondria is reduced and therefore results in a drastic reduction in the amount of total ATP. Furthermore, these cells mainly oxidize glucose with respect to fatty acids and glutamine, without any variability over time and, as demonstrated by the negative value of “flexibility”, they are unable to use a single combustible substrate to produce energy but require all substrates at the same time.

Mesenchymal stem cells (MSCs) used for cell therapy and tissue engineering applications in veterinary medicine, particularly for companion dogs that often suffer from age-related diseases, require new treatments and preventive strategies, as well as being used as a model for human genetic diseases, helping to define the potential therapeutic efficiency and safety of stem cell therapy<sup>256,257</sup>. The mechanisms underlying the phenotypic and functional properties of MSCs, important for bioenergetic changes during differentiation, are not well understood. Energy metabolism, influenced by many variables, defines the fate of these cells. Bioenergetic analyzes of canine adipose tissue (AT) and umbilical cord matrix (UC) MSCs show that both produce ATP by exploiting OXPHOS but can implement the anaerobic glycolytic pathway when mitochondrial respiration is inhibited. Dependence on glycolytic flux, which is a common metabolic feature of stem cells, may represent an environmental adaptation strategy to maintain stem cell identity. UC-MSCs show higher ATP production than AT-MSCs, but the latter synthesize more ATP by mitochondrial activity; these cells can direct the entire energy obtained from the oxidation of the substrate to the production of ATP, a characteristic found in non-specialized cell cultures. In both cell cultures, mitochondria efficiently combine electron transport with ADP phosphorylation to produce ATP. Furthermore, AT and UC-MSCs do not function at the limit of their bioenergetic capacity but have a reserve respiratory capacity that exceeds their baseline OCR. This characteristic can guarantee the increase in aerobic metabolism, necessary to increase the production of ATP required during cell differentiation<sup>258</sup>.

The study of energy metabolism in the presence of 5% and 10% of FBS of IPEC-J2 cells aimed at evaluating how energy metabolism adapts to meet the physiological demands of the cell under different culture conditions<sup>259</sup>. Thanks to the similarity between the intestinal function of pigs and that of humans, the studies on IPEC-J2 cells provide information on the physiology and energy metabolism of enterocytes, but also on the impact of environmental stimuli on cellular bioenergetics. Consistently with the stimulation of cell growth in the presence of 10% of FBS, these cells increase the production of mitochondrial ATP, without changing its bioenergetics, while the production of glycolytic ATP remains constant under the two conditions tested. Therefore, mitochondrial OXPHOS appears to be the main energy source for the growth of IPEC-J2 cells, although, when cells are confluent, they rely primarily on the glycolytic pathway to produce ATP. Under stressful conditions, cells require a greater energy supply and mitochondria are the main source of ATP production for IPEC-J2, more evident in cells treated with 5% FBS, while glycolysis is unaffected. This reflects the cellular ability to synthesize more ATP molecules at a lower bioenergy cost<sup>260,261</sup>. Studies of the oxidation of glucose, fatty acids and glutamine have shown that each type of nutrient is essential to maintain basal OCR, in fact, by inhibiting the oxidation of a specific substrate, this cannot be compensated by using alternative substrate pathways since flexibility has a negative value regardless of the substrate, in the presence of 5% and 10% of FBS. However, 5% of FBS promotes the production of ATP through the oxidation of mitochondrial fatty acids, probably because it is much more efficient than the other two pathways in terms of ATP production. Probably, the changes in metabolism induced by the different concentrations of FBS are caused by changes in the biosignaling and/or gene expression<sup>262,263</sup>. The IPEC-J2 cell line shows many anatomical and physiological similarities to humans, reproduces human physiological characteristics, and is selected as a model to study the mechanisms of action at the molecular level of a variety of compounds on the mammalian intestine<sup>264</sup> such as the effects of fat-soluble vitamins. For this reason, the effects of K vitamers on the energy metabolism of IPEC-J2 were studied. Vitamer VK1 induces an increase in the production of ATP by cells by also

stimulating the glycolytic pathway. Indeed, the modification of the ATP rate index shows that the cells treated with VK1 switch to a more glycolytic metabolism than the control, without affecting mitochondrial respiration and glycolysis parameters. Vitamer VK2 increases ATP production only at the lowest concentration tested, which also improves mitochondrial parameters. Probably the structure of VK2, which resembles that of Q, an electron carrier incorporated in the inner mitochondrial membrane<sup>265</sup>, allows mimicking its function even though it cannot replace it<sup>266</sup>. Furthermore, VK1 and VK2 can have an indirect action on respiratory complexes by inducing an increase in membrane fluidity<sup>267</sup>. In fact, studies show that *in vitro* VK2 improved respiratory efficiency by also forming the proton electrochemical gradient mimicking Q<sup>173</sup>. Although the role of VK2 as an electron transporter along the respiratory chain<sup>268</sup> is unclear, our results show that the structural properties of VK2 are consistent with the stimulation of mitochondrial respiration with no effect on glycolysis. Consistently, low concentrations of VK2 induce an increase in energy in the activation, proliferation and differentiation of IPEC-J2 cells. Vitamer VK3 instead exerts a negative effect by inhibiting cellular respiration and glycolysis, favoring the loss of H<sup>+</sup> through the internal mitochondrial membrane and leading to a decrease in ATP synthesis. However, decoupling agents such as FCCPs can stimulate mitochondrial respiration of cells. Furthermore, under conditions of induced stress, VK3-treated IPEC-J2 cells can rely on the glycolytic pathway to provide the necessary energy.

The studies on mammalian cells from different sources, in addition to those on mitochondria, were designed to exploit the cell bioenergetics to test how cells respond to various exogenous and endogenous factors and to explore the cell capability to adapt the energy metabolism. In some cases, the modulation capability of cell bioenergetics may also somehow predict cell behaviour under experimental conditions. So, the two sections of the thesis complement each other as both can contribute to opening the way to a bioenergetic approach in pharmacological and physiological research.

## ***Conclusion***

## Section I

In this thesis work, the investigation of the effect of different ions and small molecules on mitochondria and cultured cells allowed us to confirm some molecular aspects of the mitochondrial  $\text{Ca}^{2+}$ -activated  $\text{F}_1\text{F}_0$ -ATPase. The latter promotes the hydrolysis of ATP with a different kinetic mechanism from that of the natural cofactor  $\text{Mg}^{2+}$ , probably due to its different chemical nature, which prevents the insertion of  $\text{Ca}^{2+}$  into the  $\text{Mg}^{2+}$  sites. As widely discussed, the binding of  $\text{Ca}^{2+}$  to catalytic sites of enzyme induces conformational changes that lead to the formation of mPTP. Data obtained from studies in the presence of  $\text{F}_1$ -ATPase inhibitors show inhibition of hydrolytic activity sustained by  $\text{Ca}^{2+}$  and of mPTP formation, suggesting that the two mutually dependent cellular events are linked by a molecular mechanism. The modulation of mPTP by exogenous compounds, investigated in the presence of  $\text{Gd}^{3+}$ , highlights how the two  $\text{Mg}^{2+}$ - and  $\text{Ca}^{2+}$ - activated  $\text{F}_1\text{F}_0$ -ATPase structures are different and therefore respond differently to modulators. In fact, the inhibition exerted by  $\text{Gd}^{3+}$  is more accentuated on  $\text{Ca}^{2+}$ -activated  $\text{F}_1\text{F}_0$ -ATPase than on  $\text{Mg}^{2+}$ -activated  $\text{F}_1\text{F}_0$ -ATPase, as well as inhibiting the opening of the mPTP, probably because the interactions of  $\text{Gd}^{3+}$  on  $\text{F}_1$  hinder positive conformational changes to the pore formation. Indeed, lanthanide ions have long been known as blockers of membrane permeabilization<sup>237</sup>. In the same way, also PGO, which induces post-translational modifications of the Arg residues, has a more pronounced inhibitory effect of the  $\text{F}_1\text{F}_0$ -ATPase in the presence of  $\text{Ca}^{2+}$ . However, PGO, unlike the other modulators, favors the opening of the mPTP, probably because it mimics the steric arrangement of the enzyme involved in mPTP. The cross-linking agent DBrB, which binds Cys approximately 6.6 Å distant, inhibits the hydrolytic activity of  $\text{F}_1\text{F}_0$ -ATPase in the presence of  $\text{Ca}^{2+}$  and  $\text{Mg}^{2+}$ , an effect not altered by the reducing agent DTE, and totally inhibits the formation of mPTP. These data, contrary to those obtained in the presence of less distant Cys cross-linking PAO, about 3.8 Å, show how differently distant and specifically

cross-linked Cys pairs produce opposite effects on F<sub>1</sub>F<sub>0</sub>-ATPase and mPTP. The results demonstrate that F<sub>1</sub>F<sub>0</sub>-ATPase uses two distinct molecular strategies to regulate the opening of mPTP involving the oxidation of near or distant dithiols. Therefore, the dithiols, by post-translational modification, can act on the regulation of the transition from the physiological to the pathological opening of mPTP in the mitochondria. The data obtained in the presence of BPF allow us to confirm its beneficial effects also at the mitochondrial level. Accordingly, BPF seems to protect against the regulated cell death induced by mPTP and improves the RCR. Studies carried out in the presence of melatonin allow us to hypothesize that it exerts a scavenger effect against ROS, reducing their production under all the experimental conditions tested. Furthermore, in accordance with the inhibition exerted on Ca<sup>2+</sup>-activated F<sub>1</sub>F<sub>0</sub>-ATPase, the opening of mPTP is also inhibited by melatonin, probably also in relation to its scavenger effect against ROS, known to induce the formation of mPTP<sup>269</sup>.

On considering the putative role of the F<sub>1</sub>F<sub>0</sub>-ATPase as innovative pharmacological target, the beneficial effects of H<sub>2</sub>S, known as a cardiovascular protector, do not directly affect the enzyme involved in the processes of mPTP formation that triggers the cell death in ischemia-reperfusion phenomena. Indeed, H<sub>2</sub>S shows a weak inhibition effect on the Ca<sup>2+</sup>-activated F<sub>1</sub>F<sub>0</sub>-ATPase, indirectly due to the inhibition of the mitochondrial uptake of Ca<sup>2+</sup>. This mechanism seems quite conserved, as even in mussel, as regards the effects of NaHS on mPTP, the results obtained are very similar. The pharmacological interest in sulphide is therefore strengthened, especially since no negative effects have been highlighted on the Mg<sup>2+</sup>-activated F<sub>1</sub>F<sub>0</sub>-ATPase. Triazole compounds inhibit Ca<sup>2+</sup>-activated F<sub>1</sub>F<sub>0</sub>-ATPase and reduce the formation of mPTP. Since the different selectivity and rate of interaction of these structurally different compounds on the Ca<sup>2+</sup>-activated F<sub>1</sub>F<sub>0</sub>-ATPase are not directly related to their mPTP inhibition efficiency, the tested triazoles most likely mainly act on the F<sub>1</sub>F<sub>0</sub>-ATPase subunits involved in the mPTP formation mechanism. Most likely, they induce changes in the F<sub>1</sub> to F<sub>0</sub> conformational transmission

mechanism that opens mPTP. The data obtained clarify molecular aspects useful for addressing further studies and developments in pharmacology, in particular for the treatment of pathologies related to mPTP.

## Section II

The characterization of cellular energy metabolism in the different lines under study made it possible to obtain valuable information on the specific bioenergetic characteristics of each cell and also in response to some exogenous factors, clarifying how the metabolic mechanisms vary and adapt to the different conditions tested in order to support cell viability. The characterization of the mitochondrial activity of wild boar spermatozoa revealed that the main spermatid activities are supported by the synthesis of ATP predominantly through OXPHOS. However, with the passage of time, the mitochondrial ATP production dramatically decreases, possibly due to a reduction in the number of active mitochondria 1 day after semen collection, since the mitochondrial parameters are not altered. The overall data suggest that wild boar sperm, although it is believed to preferentially harness glycolysis for energy, heavily relies on mitochondrial OXPHOS for ATP production to primarily support motility. Therefore, reduced mitochondrial activity or decreased number of active mitochondria over time could be considered a possible cause of sperm dysfunction.

The studies on the energy metabolism of MSCs, useful for selecting these cells and the best experimental conditions for conducting transplantation experiments in the therapy with mesenchymal stem cells of companion animals, reinforce the emerging hopes in regenerative and preventive medicine. The AT-MSCs and UC-MSCs under study share the same metabolic synthesis characteristics as ATP production relies on OXPHOS. However, UC-MSCs increased ATP production efficiency makes them more appropriate for transplant studies. Undoubtedly, both types of MSCs, easy to obtain and with metabolic versatility, represent a potential putative tool in regenerative medicine. The metabolic characterization carried out on IPEC-J2 cells highlighted the ability they must adapt their functional physiological parameters in response to different concentrations of fetal bovine serum (FBS), remodeling the oxidative energy metabolism to meet

the energy demands of the cell without altering the mitochondrial bioenergetic parameters. Due to the close similarity between the intestinal function of swine and humans, research on IPEC-J2 cells provides useful information not only on the physiology and energy metabolism of enterocytes, but also on the relevant role of environmental stimuli on cellular bioenergetics. The different VK vitamers tested have different modulatory effects on the bioenergetics of IPEC-J2 cells, due to their different chemical structure. Certain gastrointestinal disorders such as Crohn's disease<sup>270</sup> celiac disease<sup>271</sup> and inflammatory bowel disease<sup>272</sup> are linked to VK deficiency. Insufficient production of ATP by enterocytes, correlated to low availability of VK, also due to antibiotic treatments<sup>273</sup> can contribute to the biochemical basis of some intestinal pathologies. Therefore, the benefits of VK vitamers stimulation of ATP production in enterocytes underscore the importance of the intestinal microbiota, as a VK producer, in maintaining a healthy gut and in the prevention and/or treatment of intestinal tract diseases.

Taken as a whole, the data obtained from the experiments carried out and described in this thesis, strengthen the adequacy of the biostructures involved in cell bioenergetics to find new targets for drugs, and on the other hand, to test new compounds/drugs and select the most suitable conditions for research studies in Veterinary and Human Medicine. So, endowed with a potential (putative) applied exploitation from pharmacology to preventive and regenerative medicine, the present data can represent a basic preliminary attempt to improve health.

## ***Publication list***

1. **Algieri, C.**, Bernardini, C., Oppedisano, F., La Mantia, D., Trombetti, F., Palma, E., Forni, M., Mollace, V., Romeo, G., Nesci, S. Mitochondria Bioenergetic Functions and Cell Metabolism Are Modulated by the Bergamot Polyphenolic Fraction. *Cells*. 11, 1401 (2022).
2. **Algieri, C.**, Trombetti, F., Pagliarani, A., Ventrella, V. & Nesci, S. The mitochondrial F<sub>1</sub>F<sub>0</sub>-ATPase exploits the dithiol redox state to modulate the permeability transition pore. *Arch. Biochem. Biophys.* 712, 109027 (2021).
3. **Algieri, C.**, Trombetti, F., Pagliarani, A., Fabbri, M. & Nesci, S. The inhibition of gadolinium ion (Gd<sup>3+</sup>) on the mitochondrial F<sub>1</sub>F<sub>0</sub>-ATPase is linked to the modulation of the mitochondrial permeability transition pore. *Int. J. Biol. Macromol.* 184, 250–258 (2021).
4. Bernardini, C., **Algieri, C.**, La Mantia, D., Trombetti, F., Pagliarani, A., Forni, M. & Nesci, S. Vitamin K Vitamers Differently Affect Energy Metabolism in IPEC-J2 Cells. *Front. Mol. Biosci.* 8, 682191 (2021).
5. Bernardini, C., **Algieri, C.**, Mantia, LD., Zannoni, A., Salaroli, R., Trombetti, F., Forni, M., Pagliarani, A. & Nesci, S. Relationship between serum concentration, functional parameters and cell bioenergetics in IPEC-J2 cell line. *Histochem. Cell Biol.* 156, 59–67 (2021).
6. Nesci, S., Trombetti, F., Pagliarani, A., Ventrella, V., **Algieri, C.**, Tioli, G. & Lenaz, G. Molecular and Supramolecular Structure of the Mitochondrial Oxidative Phosphorylation System: Implications for Pathology. *Life Basel Switz.* 11, 242 (2021).
7. Marcocchia, R., Nesci, S., Merlo, B., Ballotta, G., **Algieri, C.**, Pagliarani, A. & Iacono, E. Biological characteristics and metabolic profile of canine mesenchymal stem cells isolated from adipose tissue and umbilical cord matrix. *PLoS One* 16, e0247567 (2021).
8. Nesci, S., **Algieri, C.**, Trombetti, F., Ventrella, V., Fabbri, M. & Pagliarani, A. Sulfide affects the mitochondrial respiration, the Ca<sup>2+</sup>-activated F<sub>1</sub>F<sub>0</sub>-ATPase activity and the permeability transition pore but does not change the Mg<sup>2+</sup>-activated F<sub>1</sub>F<sub>0</sub>-ATPase activity in swine heart mitochondria. *Pharmacol. Res.* 166, 105495 (2021).
9. **Algieri, C.**, Nesci, S., Trombetti, F., Fabbri, M., Ventrella, V. & Pagliarani, A. Mitochondrial F<sub>1</sub>F<sub>0</sub>-ATPase and permeability transition pore response to sulfide in the midgut gland of *Mytilus galloprovincialis*. *Biochimie* 180, 222–228 (2021).
10. Algieri, V.\*, **Algieri, C.\***, Maiuolo, L., De Nino, A., Pagliarani, A., Tallarida, M. A., Trombetti, F. & Nesci, S. 1,5-Disubstituted-1,2,3-triazoles as inhibitors of the mitochondrial Ca<sup>2+</sup>-activated F<sub>1</sub>F<sub>0</sub>-ATP(hydrol)ase and the permeability transition pore. *Ann. N. Y. Acad. Sci.* (2020).  
\* These authors contributed equally to this work

11. Bernardini, C., La Mantia, D., Nesci, S., Salaroli, R., **Algieri, C.**, Pagliarani, A., Zannoni, A. & Forni, M. Effects of Hydrogen Sulfide Donor NaHS on Porcine Vascular Wall-Mesenchymal Stem Cells. *Int. J. Mol. Sci.* 21, (2020).
12. Nesci, S., Pagliarani, A., **Algieri, C.** & Trombetti, F. Mitochondrial F-type ATP synthase: multiple enzyme functions revealed by the membrane-embedded F<sub>0</sub> structure. *Crit. Rev. Biochem. Mol. Biol.* 55, 309–321 (2020).
13. **Algieri, C.**, Trombetti, F., Pagliarani A., Ventrella, V. & Nesci, S. Phenylglyoxal inhibition of the mitochondrial F<sub>1</sub>F<sub>0</sub>-ATPase activated by Mg<sup>2+</sup> or by Ca<sup>2+</sup> provides clues on the mitochondrial permeability transition pore. *Arch. Biochem. Biophys.* 681, 108258 (2020).
14. Nesci, S., Spinaci, M., Galeati, G., Nerozzi, C., Pagliarani, A., **Algieri, C.**, Tamanini, C. & Bucci, D. Sperm function and mitochondrial activity: An insight on boar sperm metabolism. *Theriogenology* 144, 82–88 (2020).
15. **Algieri, C.**, Trombetti, F., Pagliarani, A., Ventrella, V., Bernardini, C., Fabbri, M., Forni, M. & Nesci, S. Mitochondrial Ca<sup>2+</sup>-activated F<sub>1</sub>F<sub>0</sub> -ATPase hydrolyzes ATP and promotes the permeability transition pore. *Ann. N. Y. Acad. Sci.* 1457, 142–157 (2019).
16. Nesci, S., Trombetti, F., **Algieri, C.** & Pagliarani, A. A Therapeutic Role for the F<sub>1</sub>F<sub>0</sub>-ATP Synthase. *SLAS Discov. Adv. Life Sci. R D* 24, 893–903 (2019).
17. Trombetti, F., Pagliarani, A., Ventrella, V., **Algieri, C.** & Nesci, S. Crucial aminoacids in the F<sub>0</sub> sector of the F<sub>1</sub>F<sub>0</sub>-ATP synthase address H<sup>+</sup> across the inner mitochondrial membrane: molecular implications in mitochondrial dysfunctions. *Amino Acids* 51, 579–587 (2019).

## References

1. Chimica Generale, Organica e Biologica. *PICCIN Nuova Libreria S.P.A.* <http://www.piccin.it/it/chimica-generale/223-chimica-generale-organica-e-biologica-788829912155.html>.
2. DeBerardinis, R. J. & Thompson, C. B. Cellular metabolism and disease: what do metabolic outliers teach us? *Cell* **148**, 1132–1144 (2012).
3. Xiao, W., Wang, R.-S., Handy, D. E. & Loscalzo, J. NAD(H) and NADP(H) Redox Couples and Cellular Energy Metabolism. *Antioxid. Redox Signal.* **28**, 251–272 (2018).
4. Martínez Cuesta, S., Rahman, S. A., Furnham, N. & Thornton, J. M. The Classification and Evolution of Enzyme Function. *Biophys. J.* **109**, 1082–1086 (2015).
5. Bioenergetics - 3rd Edition. <https://www.elsevier.com/books/bioenergetics/nicholls/978-0-12-518121-1>.
6. Judge, A. & Dodd, M. S. Metabolism. *Essays Biochem.* **64**, 607–647 (2020).
7. Hanson, R. W. The role of ATP in metabolism. *Biochem. Educ.* **17**, 86–92 (1989).
8. I principi di biochimica di Lehninger - Zanichelli. <https://www.zanichelli.it/ricerca/prodotti/principi-di-biochimica-di-lehninger>.
9. Guo, X. *et al.* Glycolysis in the control of blood glucose homeostasis. *Acta Pharm. Sin. B* **2**, 358–367 (2012).
10. Akram, M. Mini-review on glycolysis and cancer. *J. Cancer Educ. Off. J. Am. Assoc. Cancer Educ.* **28**, 454–457 (2013).
11. Houstěk, J., Cannon, B. & Lindberg, O. Glycerol-3-phosphate shuttle and its function in intermediary metabolism of hamster brown-adipose tissue. *Eur. J. Biochem.* **54**, 11–18 (1975).
12. Stefely, J. A. & Pagliarini, D. J. Biochemistry of Mitochondrial Coenzyme Q Biosynthesis. *Trends Biochem. Sci.* **42**, 824–843 (2017).
13. Bertini, I., Cavallaro, G. & Rosato, A. Cytochrome c: occurrence and functions. *Chem. Rev.* **106**, 90–115 (2006).
14. Beinert, H. Iron-sulfur proteins: ancient structures, still full of surprises. *J. Biol. Inorg. Chem. JBIC Publ. Soc. Biol. Inorg. Chem.* **5**, 2–15 (2000).
15. Parey, K., Wirth, C., Vonck, J. & Zickermann, V. Respiratory complex I - structure, mechanism and evolution. *Curr. Opin. Struct. Biol.* **63**, 1–9 (2020).
16. Kluckova, K., Bezawork-Geleta, A., Rohlena, J., Dong, L. & Neuzil, J. Mitochondrial complex II, a novel target for anti-cancer agents. *Biochim. Biophys. Acta* **1827**, 552–564 (2013).
17. Sun, F. *et al.* Crystal structure of mitochondrial respiratory membrane protein complex II. *Cell* **121**, 1043–1057 (2005).
18. Xia, D. *et al.* Structural analysis of cytochrome bc<sub>1</sub> complexes: implications to the mechanism of function. *Biochim. Biophys. Acta* **1827**, 1278–1294 (2013).
19. Cramer, W. A., Hasan, S. S. & Yamashita, E. The Q cycle of cytochrome bc complexes: a structure perspective. *Biochim. Biophys. Acta* **1807**, 788–802 (2011).
20. Mitchell, P. The protonmotive Q cycle: a general formulation. *FEBS Lett.* **59**, 137–139 (1975).

21. Zhang, Z. *et al.* Electron transfer by domain movement in cytochrome bc<sub>1</sub>. *Nature* **392**, 677–684 (1998).
22. Michel, H., Behr, J., Harrenga, A. & Kannt, A. Cytochrome c oxidase: structure and spectroscopy. *Annu. Rev. Biophys. Biomol. Struct.* **27**, 329–356 (1998).
23. Vercellino, I. & Sazanov, L. A. The assembly, regulation and function of the mitochondrial respiratory chain. *Nat. Rev. Mol. Cell Biol.* 1–21 (2021) doi:10.1038/s41580-021-00415-0.
24. Vonck, J. & Schäfer, E. Supramolecular organization of protein complexes in the mitochondrial inner membrane. *Biochim. Biophys. Acta* **1793**, 117–124 (2009).
25. Lenaz, G. & Genova, M. L. Structure and organization of mitochondrial respiratory complexes: a new understanding of an old subject. *Antioxid. Redox Signal.* **12**, 961–1008 (2010).
26. Mitchell, P. Coupling of phosphorylation to electron and hydrogen transfer by a chemi-osmotic type of mechanism. *Nature* **191**, 144–148 (1961).
27. Pinke, G., Zhou, L. & Sazanov, L. A. Cryo-EM structure of the entire mammalian F-type ATP synthase. *Nat. Struct. Mol. Biol.* **27**, 1077–1085 (2020).
28. Junge, W., Lill, H. & Engelbrecht, S. ATP synthase: an electrochemical transducer with rotatory mechanics. *Trends Biochem. Sci.* **22**, 420–423 (1997).
29. Nesci, S., Trombetti, F., Ventrella, V. & Pagliarani, A. Opposite rotation directions in the synthesis and hydrolysis of ATP by the ATP synthase: hints from a subunit asymmetry. *J. Membr. Biol.* **248**, 163–169 (2015).
30. Symersky, J., Osowski, D., Walters, D. E. & Mueller, D. M. Oligomycin frames a common drug-binding site in the ATP synthase. *Proc. Natl. Acad. Sci. U. S. A.* **109**, 13961–13965 (2012).
31. Okuno, D., Iino, R. & Noji, H. Rotation and structure of FoF<sub>1</sub>-ATP synthase. *J. Biochem. (Tokyo)* **149**, 655–664 (2011).
32. Allegretti, M. *et al.* Horizontal membrane-intrinsic  $\alpha$ -helices in the stator a<sub>0</sub>-subunit of an F-type ATP synthase. *Nature* **521**, 237–240 (2015).
33. Mitome, N. *et al.* Essential arginine residue of the F<sub>o</sub>(a)-subunit in F<sub>o</sub>(a)F<sub>1</sub>-ATP synthase has a role to prevent the proton shortcut without c-ring rotation in the F<sub>o</sub>(a) proton channel. *Biochem. J.* **430**, 171–177 (2010).
34. Hahn, A. *et al.* Structure of a Complete ATP Synthase Dimer Reveals the Molecular Basis of Inner Mitochondrial Membrane Morphology. *Mol. Cell* **63**, 445–456 (2016).
35. Boyer, P. D. Catalytic site occupancy during ATP synthase catalysis. *FEBS Lett.* **512**, 29–32 (2002).
36. Murataliev, M. B. & Boyer, P. D. The mechanism of stimulation of MgATPase activity of chloroplast F<sub>1</sub>-ATPase by non-catalytic adenine-nucleotide binding. Acceleration of the ATP-dependent release of inhibitory ADP from a catalytic site. *Eur. J. Biochem.* **209**, 681–687 (1992).
37. Lippe, G., Coluccino, G., Zancani, M., Baratta, W. & Crusiz, P. Mitochondrial F-ATP Synthase and Its Transition into an Energy-Dissipating Molecular Machine. *Oxid. Med. Cell. Longev.* **2019**, 8743257 (2019).
38. Spikes, T. E., Montgomery, M. G. & Walker, J. E. Structure of the dimeric ATP synthase from bovine mitochondria. *Proc. Natl. Acad. Sci.* **117**, 23519–23526 (2020).
39. Nesci, S., Pagliarani, A., Algieri, C. & Trombetti, F. Mitochondrial F-type ATP synthase: multiple enzyme functions revealed by the membrane-embedded FO structure. *Crit. Rev. Biochem. Mol. Biol.* **55**, 309–321 (2020).

40. Rampelt, H. & van der Laan, M. The Yin & Yang of Mitochondrial Architecture - Interplay of MICOS and F1Fo-ATP synthase in cristae formation. *Microb. Cell Graz Austria* **4**, 236–239 (2017).
41. García, J. J., Morales-Ríos, E., Cortés-Hernandez, P. & Rodríguez-Zavala, J. S. The inhibitor protein (IF1) promotes dimerization of the mitochondrial F1Fo-ATP synthase. *Biochemistry* **45**, 12695–12703 (2006).
42. Gu, J. *et al.* Cryo-EM structure of the mammalian ATP synthase tetramer bound with inhibitory protein IF1. *Science* **364**, 1068–1075 (2019).
43. Nakamura, J., Fujikawa, M. & Yoshida, M. IF1, a natural inhibitor of mitochondrial ATP synthase, is not essential for the normal growth and breeding of mice. *Biosci. Rep.* **33**, (2013).
44. Nesci, S. & Pagliarani, A. Emerging Roles for the Mitochondrial ATP Synthase Supercomplexes. *Trends Biochem. Sci.* **44**, 821–823 (2019).
45. Arselin, G. *et al.* The GxxxG motif of the transmembrane domain of subunit e is involved in the dimerization/oligomerization of the yeast ATP synthase complex in the mitochondrial membrane. *Eur. J. Biochem.* **270**, 1875–1884 (2003).
46. Bustos, D. M. & Velours, J. The modification of the conserved GXXXG motif of the membrane-spanning segment of subunit g destabilizes the supramolecular species of yeast ATP synthase. *J. Biol. Chem.* **280**, 29004–29010 (2005).
47. Guo, H., Bueler, S. A. & Rubinstein, J. L. Atomic model for the dimeric FO region of mitochondrial ATP synthase. *Science* **358**, 936–940 (2017).
48. Giorgio, V. *et al.* Dimers of mitochondrial ATP synthase form the permeability transition pore. *Proc. Natl. Acad. Sci. U. S. A.* **110**, 5887–5892 (2013).
49. Alavian, K. N. *et al.* An uncoupling channel within the c-subunit ring of the F1Fo ATP synthase is the mitochondrial permeability transition pore. *Proc. Natl. Acad. Sci. U. S. A.* **111**, 10580–10585 (2014).
50. Mnatsakanyan, N. & Jonas, E. A. ATP synthase c-subunit ring as the channel of mitochondrial permeability transition: Regulator of metabolism in development and degeneration. *J. Mol. Cell. Cardiol.* **144**, 109–118 (2020).
51. Torrezan-Nitao, E., Figueiredo, R. C. B. Q. & Marques-Santos, L. F. Mitochondrial permeability transition pore in sea urchin female gametes. *Mech. Dev.* **154**, 208–218 (2018).
52. Liu, Y. *et al.* Shengmai Formula suppressed over-activated Ras/MAPK pathway in *C. elegans* by opening mitochondrial permeability transition pore via regulating cyclophilin D. *Sci. Rep.* **6**, 38934 (2016).
53. Yuan, Z., Zhang, J., Tu, C., Wang, Z. & Xin, W. The protective effect of blueberry anthocyanins against perfluorooctanoic acid-induced disturbance in planarian (*Dugesia japonica*). *Ecotoxicol. Environ. Saf.* **127**, 170–174 (2016).
54. Ren, X., Zhang, L., Zhang, Y., Mao, L. & Jiang, H. Mitochondria response to camptothecin and hydroxycamptothecine-induced apoptosis in *Spodoptera exigua* cells. *Pestic. Biochem. Physiol.* **140**, 97–104 (2017).
55. Pan, C. *et al.* Effects of 10-hydroxycamptothecin on intrinsic mitochondrial pathway in silkworm BmN-SWU1 cells. *Pestic. Biochem. Physiol.* **127**, 15–20 (2016).
56. Konràd, C. *et al.* A distinct sequence in the adenine nucleotide translocase from *Artemia franciscana* embryos is associated with insensitivity to bongkrekate and atypical effects of adenine nucleotides on Ca<sup>2+</sup> uptake and sequestration. *FEBS J.* **278**, 822–836 (2011).

57. Konrad, C., Kiss, G., Torocsik, B., Adam-Vizi, V. & Chinopoulos, C. Absence of Ca<sup>2+</sup>-Induced Mitochondrial Permeability Transition but Presence of Bongkrekate-Sensitive Nucleotide Exchange in *C. crangon* and *P. serratus*. *PLOS ONE* **7**, e39839 (2012).
58. Bernardi, P., Rasola, A., Forte, M. & Lippe, G. The Mitochondrial Permeability Transition Pore: Channel Formation by F-ATP Synthase, Integration in Signal Transduction, and Role in Pathophysiology. *Physiol. Rev.* **95**, 1111–1155 (2015).
59. Bonora, M. *et al.* Role of the c subunit of the FO ATP synthase in mitochondrial permeability transition. *Cell Cycle Georget. Tex* **12**, 674–683 (2013).
60. Nesci, S. & Pagliarani, A. Incoming news on the F-type ATPase structure and functions in mammalian mitochondria. *BBA Adv.* **1**, 100001 (2020).
61. Nesci, S. & Pagliarani, A. Ca<sup>2+</sup> as cofactor of the mitochondrial H<sup>+</sup> -translocating F1 FO -ATP(hydrol)ase. *Proteins* (2020) doi:10.1002/prot.26040.
62. Nesci, S., Trombetti, F., Ventrella, V., Pirini, M. & Pagliarani, A. Kinetic properties of the mitochondrial F1FO-ATPase activity elicited by Ca<sup>2+</sup> in replacement of Mg<sup>2+</sup>. *Biochimie* **140**, 73–81 (2017).
63. Giorgio, V. *et al.* Ca<sup>2+</sup> binding to F-ATP synthase  $\beta$  subunit triggers the mitochondrial permeability transition. *EMBO Rep.* **18**, 1065–1076 (2017).
64. Daum, B., Walter, A., Horst, A., Osiewacz, H. D. & Kühlbrandt, W. Age-dependent dissociation of ATP synthase dimers and loss of inner-membrane cristae in mitochondria. *Proc. Natl. Acad. Sci. U. S. A.* **110**, 15301–15306 (2013).
65. Ader, N. R. *et al.* Molecular and topological reorganizations in mitochondrial architecture interplay during Bax-mediated steps of apoptosis. *eLife* **8**, e40712 (2019).
66. Bonora, M., Giorgi, C. & Pinton, P. Molecular mechanisms and consequences of mitochondrial permeability transition. *Nat. Rev. Mol. Cell Biol.* 1–20 (2021) doi:10.1038/s41580-021-00433-y.
67. Carraro, M., Carrer, A., Urbani, A. & Bernardi, P. Molecular nature and regulation of the mitochondrial permeability transition pore(s), drug target(s) in cardioprotection. *J. Mol. Cell. Cardiol.* **144**, 76–86 (2020).
68. Szabo, I. & Zoratti, M. Mitochondrial channels: ion fluxes and more. *Physiol. Rev.* **94**, 519–608 (2014).
69. Neginskaya, M. A. *et al.* ATP Synthase C-Subunit-Deficient Mitochondria Have a Small Cyclosporine A-Sensitive Channel, but Lack the Permeability Transition Pore. *Cell Rep.* **26**, 11-17.e2 (2019).
70. Karch, J. *et al.* Inhibition of mitochondrial permeability transition by deletion of the ANT family and CypD. *Sci. Adv.* **5**, eaaw4597 (2019).
71. Bonora, M. *et al.* Mitochondrial permeability transition involves dissociation of F1FO ATP synthase dimers and C-ring conformation. *EMBO Rep.* **18**, 1077–1089 (2017).
72. Morciano, G. *et al.* Discovery of Novel 1,3,8-Triazaspiro[4.5]decane Derivatives That Target the c Subunit of F1/FO-Adenosine Triphosphate (ATP) Synthase for the Treatment of Reperfusion Damage in Myocardial Infarction. *J. Med. Chem.* **61**, 7131–7143 (2018).
73. Mnatsakanyan, N. *et al.* A mitochondrial megachannel resides in monomeric F1FO ATP synthase. *Nat. Commun.* **10**, 5823 (2019).
74. Urbani, A. *et al.* Purified F-ATP synthase forms a Ca<sup>2+</sup>-dependent high-conductance channel matching the mitochondrial permeability transition pore. *Nat. Commun.* **10**, 4341 (2019).

75. Bernardi, P. & von Stockum, S. The permeability transition pore as a Ca<sup>2+</sup> release channel: new answers to an old question. *Cell Calcium* **52**, 22–27 (2012).
76. Hom, J. R. *et al.* The permeability transition pore controls cardiac mitochondrial maturation and myocyte differentiation. *Dev. Cell* **21**, 469–478 (2011).
77. Kwong, J. Q. & Molkenin, J. D. Physiological and pathological roles of the mitochondrial permeability transition pore in the heart. *Cell Metab.* **21**, 206–214 (2015).
78. Pérez, M. J. & Quintanilla, R. A. Development or disease: duality of the mitochondrial permeability transition pore. *Dev. Biol.* **426**, 1–7 (2017).
79. Papu John, A. S. *et al.* Hydrogen sulfide inhibits Ca<sup>2+</sup>-induced mitochondrial permeability transition pore opening in type-1 diabetes. *Am. J. Physiol. Endocrinol. Metab.* **317**, E269–E283 (2019).
80. Bonora, M. & Pinton, P. The Mitochondrial Permeability Transition Pore and Cancer: Molecular Mechanisms Involved in Cell Death. *Front. Oncol.* **4**, (2014).
81. Gan, X. *et al.* CypD-mPTP axis regulates mitochondrial functions contributing to osteogenic dysfunction of MC3T3-E1 cells in inflammation. *J. Physiol. Biochem.* **74**, 395–402 (2018).
82. Visalli, G. *et al.* Mitochondrial Impairment Induced by Sub-Chronic Exposure to Multi-Walled Carbon Nanotubes. *Int. J. Environ. Res. Public Health* **16**, (2019).
83. Zhou, B. *et al.* Mitochondrial Permeability Uncouples Elevated Autophagy and Lifespan Extension. *Cell* **177**, 299–314.e16 (2019).
84. Shares, B. H. *et al.* Inhibition of the mitochondrial permeability transition improves bone fracture repair. *Bone* **137**, 115391 (2020).
85. Ahmad, Z., Hassan, S. S. & Azim, S. A Therapeutic Connection between Dietary Phytochemicals and ATP Synthase. *Curr. Med. Chem.* **24**, 3894–3906 (2017).
86. Nesci, S., Trombetti, F., Ventrella, V. & Pagliarani, A. Post-translational modifications of the mitochondrial F1FO-ATPase. *Biochim. Biophys. Acta Gen. Subj.* **1861**, 2902–2912 (2017).
87. Chène, P. ATPases as drug targets: learning from their structure. *Nat. Rev. Drug Discov.* **1**, 665–673 (2002).
88. Salomon, A. R., Voehringer, D. W., Herzenberg, L. A. & Khosla, C. Apoptolidin, a selective cytotoxic agent, is an inhibitor of F<sub>0</sub>F<sub>1</sub>-ATPase. *Chem. Biol.* **8**, 71–80 (2001).
89. Rodríguez-Enríquez, S. *et al.* Canonical and new generation anticancer drugs also target energy metabolism. *Arch. Toxicol.* **88**, 1327–1350 (2014).
90. Syed, H., Tauseef, M. & Ahmad, Z. A connection between antimicrobial properties of venom peptides and microbial ATP synthase. *Int. J. Biol. Macromol.* **119**, 23–31 (2018).
91. Pagliarani, A., Nesci, S. & Ventrella, V. Novel Drugs Targeting the c-Ring of the F<sub>1</sub>FO-ATP Synthase. *Mini Rev. Med. Chem.* **16**, 815–824 (2016).
92. Nesci, S., Ventrella, V., Trombetti, F., Pirini, M. & Pagliarani, A. Thiol oxidation of mitochondrial F<sub>0</sub>-c subunits: a way to switch off antimicrobial drug targets of the mitochondrial ATP synthase. *Med. Hypotheses* **83**, 160–165 (2014).
93. Nesci, S., Trombetti, F., Ventrella, V. & Pagliarani, A. The c-Ring of the F<sub>1</sub>FO-ATP Synthase: Facts and Perspectives. *J. Membr. Biol.* **249**, 11–21 (2016).

94. Nesci, S., Ventrella, V., Trombetti, F., Pirini, M. & Pagliarani, A. Thiol oxidation is crucial in the desensitization of the mitochondrial F1FO-ATPase to oligomycin and other macrolide antibiotics. *Biochim. Biophys. Acta* **1840**, 1882–1891 (2014).
95. Dalle-Donne, I., Rossi, R., Colombo, G., Giustarini, D. & Milzani, A. Protein S-glutathionylation: a regulatory device from bacteria to humans. *Trends Biochem. Sci.* **34**, 85–96 (2009).
96. Nesci, S., Ventrella, V. & Pagliarani, A. Modulation of the F1FO-ATPase function by butyltin compounds. *Appl. Organomet. Chem.* **27**, 199–205 (2013).
97. Bragadin, M., Pozzan, T. & Azzone, G. F. Kinetics of Ca<sup>2+</sup> carrier in rat liver mitochondria. *Biochemistry* **18**, 5972–5978 (1979).
98. Nesci, S., Ventrella, V., Trombetti, F., Pirini, M. & Pagliarani, A. Preferential nitrite inhibition of the mitochondrial F1FO-ATPase activities when activated by Ca<sup>2+</sup> in replacement of the natural cofactor Mg<sup>2+</sup>. *Biochim. Biophys. Acta BBA - Gen. Subj.* **1860**, (2015).
99. Nesci, S., Ventrella, V., Trombetti, F., Pirini, M. & Pagliarani, A. Mini-review. Nitrite as novel pore-shutter: hints from the preferential inhibition of the mitochondrial ATP-ase when activated by Ca<sup>2+</sup>. *Sci. E Ric.* **44**, 57–63 (2017).
100. Preiss, L. *et al.* Structure of the mycobacterial ATP synthase Fo rotor ring in complex with the anti-TB drug bedaquiline. *Sci. Adv.* **1**, e1500106 (2015).
101. Guo, H. *et al.* Structure of mycobacterial ATP synthase bound to the tuberculosis drug bedaquiline. *Nature* **589**, 143–147 (2021).
102. Kundu, S., Biukovic, G., Grüber, G. & Dick, T. Bedaquiline Targets the  $\epsilon$  Subunit of Mycobacterial F-ATP Synthase. *Antimicrob. Agents Chemother.* **60**, 6977–6979 (2016).
103. Kumar, S. *et al.* Screening of antitubercular compound library identifies novel ATP synthase inhibitors of Mycobacterium tuberculosis. *Tuberc. Edinb. Scotl.* **108**, 56–63 (2018).
104. Zheng, J. & Ramirez, V. D. Inhibition of mitochondrial proton F0F1-ATPase/ATP synthase by polyphenolic phytochemicals. *Br. J. Pharmacol.* **130**, 1115–1123 (2000).
105. Ahmad, Z., Okafor, F., Azim, S. & Laughlin, T. F. ATP synthase: a molecular therapeutic drug target for antimicrobial and antitumor peptides. *Curr. Med. Chem.* **20**, 1956–1973 (2013).
106. Johnson, K. M. *et al.* Identification and validation of the mitochondrial F1FO-ATPase as the molecular target of the immunomodulatory benzodiazepine Bz-423. *Chem. Biol.* **12**, 485–496 (2005).
107. Szabó, I. & Zoratti, M. The giant channel of the inner mitochondrial membrane is inhibited by cyclosporin A. *J. Biol. Chem.* **266**, 3376–3379 (1991).
108. Kaufmann, T. *et al.* Characterization of the signal that directs Bcl-x(L), but not Bcl-2, to the mitochondrial outer membrane. *J. Cell Biol.* **160**, 53–64 (2003).
109. Gotow, T. *et al.* Selective localization of Bcl-2 to the inner mitochondrial and smooth endoplasmic reticulum membranes in mammalian cells. *Cell Death Differ.* **7**, 666–674 (2000).
110. Alavian, K. N. *et al.* Bcl-xL regulates metabolic efficiency of neurons through interaction with the mitochondrial F1FO ATP synthase. *Nat. Cell Biol.* **13**, 1224–1233 (2011).
111. Ngo, H. X. & Garneau-Tsodikova, S. What are the drugs of the future? *MedChemComm* **9**, 757–758 (2018).
112. Gurevich, E. V. & Gurevich, V. V. Therapeutic potential of small molecules and engineered proteins. *Handb. Exp. Pharmacol.* **219**, 1–12 (2014).

113. Metallotherapeutic Drugs and Metal-Based Diagnostic Agents: The Use of Metals in Medicine | Wiley. *Wiley.com* <https://www.wiley.com/en-us/Metallotherapeutic+Drugs+and+Metal+Based+Diagnostic+Agents%3A+The+Use+of+Metals+in+Medicine-p-9780470864036>.
114. Citron, M. Strategies for disease modification in Alzheimer's disease. *Nat. Rev. Neurosci.* **5**, 677–685 (2004).
115. Cherny, R. A. *et al.* Treatment with a copper-zinc chelator markedly and rapidly inhibits beta-amyloid accumulation in Alzheimer's disease transgenic mice. *Neuron* **30**, 665–676 (2001).
116. Biochimica della nutrizione - Zanichelli. <https://www.zanichelli.it/ricerca/prodotti/biochimica-della-nutrizione>.
117. de Oliveira, M. R. *et al.* Resveratrol and the mitochondria: From triggering the intrinsic apoptotic pathway to inducing mitochondrial biogenesis, a mechanistic view. *Biochim. Biophys. Acta* **1860**, 727–745 (2016).
118. Gledhill, J. R., Montgomery, M. G., Leslie, A. G. W. & Walker, J. E. Mechanism of inhibition of bovine F1-ATPase by resveratrol and related polyphenols. *Proc. Natl. Acad. Sci. U. S. A.* **104**, 13632–13637 (2007).
119. Carresi, C. *et al.* The Effect of Natural Antioxidants in the Development of Metabolic Syndrome: Focus on Bergamot Polyphenolic Fraction. *Nutrients* **12**, E1504 (2020).
120. Caravan, P., Ellison, J. J., McMurry, T. J. & Lauffer, R. B. Gadolinium(III) Chelates as MRI Contrast Agents: Structure, Dynamics, and Applications. *Chem. Rev.* **99**, 2293–2352 (1999).
121. Zhao, J. *et al.* High concentration of gadolinium ion modifying isolated rice mitochondrial biogenesis. *Biol. Trace Elem. Res.* **156**, 308–315 (2013).
122. Curtis, M. J. & Wolpert, T. J. The oat mitochondrial permeability transition and its implication in victorin binding and induced cell death. *Plant J. Cell Mol. Biol.* **29**, 295–312 (2002).
123. Kanda, T., Oba, H., Toyoda, K., Kitajima, K. & Furui, S. Brain gadolinium deposition after administration of gadolinium-based contrast agents. *Jpn. J. Radiol.* **34**, 3–9 (2016).
124. Sherry, A. D., Caravan, P. & Lenkinski, R. E. Primer on gadolinium chemistry. *J. Magn. Reson. Imaging JMRI* **30**, 1240–1248 (2009).
125. Hao, D. *et al.* MRI contrast agents: basic chemistry and safety. *J. Magn. Reson. Imaging JMRI* **36**, 1060–1071 (2012).
126. YE, L., SHI, Z., Liu, H., YANG, X. & WANG, K. Gadolinium induced apoptosis of human embryo liver LO2 cell line by ROS-mediated AIF pathway. *J. Rare Earths - J RARE EARTH* **29**, 178–184 (2011).
127. Halestrap, A. P. & Brenner, C. The adenine nucleotide translocase: a central component of the mitochondrial permeability transition pore and key player in cell death. *Curr. Med. Chem.* **10**, 1507–1525 (2003).
128. Zhao, J. *et al.* Mitochondrial dysfunction induced by different concentrations of gadolinium ion. *Chemosphere* **100**, 194–199 (2014).
129. Takahashi, K. The reaction of phenylglyoxal with arginine residues in proteins. *J. Biol. Chem.* **243**, 6171–6179 (1968).

130. Johans, M. *et al.* Modification of permeability transition pore arginine(s) by phenylglyoxal derivatives in isolated mitochondria and mammalian cells. Structure-function relationship of arginine ligands. *J. Biol. Chem.* **280**, 12130–12136 (2005).
131. Eriksson, O., Fontaine, E., Petronilli, V. & Bernardi, P. Inhibition of the mitochondrial cyclosporin A-sensitive permeability transition pore by the arginine reagent phenylglyoxal. *FEBS Lett.* **409**, 361–364 (1997).
132. Rudyk, O. & Eaton, P. Biochemical methods for monitoring protein thiol redox states in biological systems. *Redox Biol.* **2**, 803–813 (2014).
133. Redox regulation of mitochondrial ATP synthase: implications for cardiac resynchronization therapy - PubMed. <https://pubmed.ncbi.nlm.nih.gov/21817160/>.
134. Petronilli, V. *et al.* The voltage sensor of the mitochondrial permeability transition pore is tuned by the oxidation-reduction state of vicinal thiols. Increase of the gating potential by oxidants and its reversal by reducing agents. *J. Biol. Chem.* **269**, 16638–16642 (1994).
135. Bernardi, P. *et al.* Modulation of the mitochondrial permeability transition pore. Effect of protons and divalent cations. *J. Biol. Chem.* **267**, 2934–2939 (1992).
136. Lenartowicz, E., Bernardi, P. & Azzone, G. F. Phenylarsine oxide induces the cyclosporin A-sensitive membrane permeability transition in rat liver mitochondria. *J. Bioenerg. Biomembr.* **23**, 679–688 (1991).
137. Shvetsov, A. *et al.* Conformational dynamics of loop 262-274 in G- and F-actin. *Biochemistry* **45**, 6541–6549 (2006).
138. Reiter, R. J., Tan, D. X., Korkmaz, A. & Rosales-Corral, S. A. Melatonin and stable circadian rhythms optimize maternal, placental and fetal physiology. *Hum. Reprod. Update* **20**, 293–307 (2014).
139. Manchester, L. C., Poeggeler, B., Alvarez, F. L., Ogden, G. B. & Reiter, R. J. Melatonin immunoreactivity in the photosynthetic prokaryote *Rhodospirillum rubrum*: implications for an ancient antioxidant system. *Cell. Mol. Biol. Res.* **41**, 391–395 (1995).
140. Ma, Y. *et al.* Endophytic Bacterium *Pseudomonas fluorescens* RG11 May Transform Tryptophan to Melatonin and Promote Endogenous Melatonin Levels in the Roots of Four Grape Cultivars. *Front. Plant Sci.* **7**, 2068 (2016).
141. The changing biological roles of melatonin during evolution: from an antioxidant to signals of darkness, sexual selection and fitness - PubMed. <https://pubmed.ncbi.nlm.nih.gov/20039865/>.
142. Reiter, R. J., Tan, D. X. & Galano, A. Melatonin: exceeding expectations. *Physiol. Bethesda Md* **29**, 325–333 (2014).
143. Manchester, L. C. *et al.* Melatonin: an ancient molecule that makes oxygen metabolically tolerable. *J. Pineal Res.* **59**, 403–419 (2015).
144. Venegas, C. *et al.* Extrapineal melatonin: analysis of its subcellular distribution and daily fluctuations. *J. Pineal Res.* **52**, 217–227 (2012).
145. van der Bliek, A. M., Sedensky, M. M. & Morgan, P. G. Cell Biology of the Mitochondrion. *Genetics* **207**, 843–871 (2017).
146. Reiter, R. J. *et al.* Melatonin as an antioxidant: under promises but over delivers. *J. Pineal Res.* **61**, 253–278 (2016).
147. Galano, A., Tan, D. X. & Reiter, R. J. Melatonin as a natural ally against oxidative stress: a physicochemical examination. *J. Pineal Res.* **51**, 1–16 (2011).

148. Reiter, R. J. *et al.* Medical implications of melatonin: receptor-mediated and receptor-independent actions. *Adv. Med. Sci.* **52**, 11–28 (2007).
149. Barberino, R. S. *et al.* Melatonin protects against cisplatin-induced ovarian damage in mice via the MT1 receptor and antioxidant activity. *Biol. Reprod.* **96**, 1244–1255 (2017).
150. Deng, S.-L. *et al.* Melatonin reduces oxidative damage and upregulates heat shock protein 90 expression in cryopreserved human semen. *Free Radic. Biol. Med.* **113**, 347–354 (2017).
151. Stankov, B. & Reiter, R. J. Melatonin receptors: current status, facts, and hypotheses. *Life Sci.* **46**, 971–982 (1990).
152. Dubocovich, M. L. *et al.* International Union of Basic and Clinical Pharmacology. LXXV. Nomenclature, classification, and pharmacology of G protein-coupled melatonin receptors. *Pharmacol. Rev.* **62**, 343–380 (2010).
153. Andrabi, S. A., Sayeed, I., Siemen, D., Wolf, G. & Horn, T. F. W. Direct inhibition of the mitochondrial permeability transition pore: a possible mechanism responsible for anti-apoptotic effects of melatonin. *FASEB J. Off. Publ. Fed. Am. Soc. Exp. Biol.* **18**, 869–871 (2004).
154. Agil, A. *et al.* Melatonin Improves Mitochondrial Dynamics and Function in the Kidney of Zucker Diabetic Fatty Rats. *J. Clin. Med.* **9**, E2916 (2020).
155. Szabo, C. *et al.* Regulation of mitochondrial bioenergetic function by hydrogen sulfide. Part I. Biochemical and physiological mechanisms. *Br. J. Pharmacol.* **171**, 2099–2122 (2014).
156. Kolluru, G. K., Shen, X. & Kevil, C. G. A tale of two gases: NO and H<sub>2</sub>S, foes or friends for life? *Redox Biol.* **1**, 313–318 (2013).
157. Papapetropoulos, A. *et al.* Hydrogen sulfide is an endogenous stimulator of angiogenesis. *Proc. Natl. Acad. Sci. U. S. A.* **106**, 21972–21977 (2009).
158. Olson, K. R. & Straub, K. D. The Role of Hydrogen Sulfide in Evolution and the Evolution of Hydrogen Sulfide in Metabolism and Signaling. *Physiol. Bethesda Md* **31**, 60–72 (2016).
159. Wen, Y.-D., Wang, H. & Zhu, Y.-Z. The Drug Developments of Hydrogen Sulfide on Cardiovascular Disease. *Oxid. Med. Cell. Longev.* **2018**, 4010395 (2018).
160. Murphy, B., Bhattacharya, R. & Mukherjee, P. Hydrogen sulfide signaling in mitochondria and disease. *FASEB J. Off. Publ. Fed. Am. Soc. Exp. Biol.* **33**, 13098–13125 (2019).
161. Módis, K. *et al.* S-Sulfhydration of ATP synthase by hydrogen sulfide stimulates mitochondrial bioenergetics. *Pharmacol. Res.* **113**, 116–124 (2016).
162. Bagarinao, T. *Sulfide as an environmental factor and toxicant: tolerance and adaptations in aquatic organisms.* <http://www.sulfide-life.info/mtobler/images/stories/readings/bagarinao%201992%20aquat%20toxicol.pdf> (1992).
163. Nagesh, H. N. *et al.* Design, synthesis and evaluation of 6-(4-((substituted-1H-1,2,3-triazol-4-yl)methyl)piperazin-1-yl)phenanthridine analogues as antimycobacterial agents. *Bioorg. Med. Chem. Lett.* **23**, 6805–6810 (2013).
164. Thomas, K. D., Adhikari, A. V., Chowdhury, I. H., Sumesh, E. & Pal, N. K. New quinolin-4-yl-1,2,3-triazoles carrying amides, sulphonamides and amidopiperazines as potential antitubercular agents. *Eur. J. Med. Chem.* **46**, 2503–2512 (2011).
165. Mir, F. *et al.* Sulfur rich 2-mercaptobenzothiazole and 1,2,3-triazole conjugates as novel antitubercular agents. *Eur. J. Med. Chem.* **76**, 274–283 (2014).

166. Angell, Y. L. & Burgess, K. Peptidomimetics via copper-catalyzed azide-alkyne cycloadditions. *Chem. Soc. Rev.* **36**, 1674–1689 (2007).
167. Singhal, N., Sharma, P. K., Dudhe, R. & Kumar, N. Recent advancement of triazole derivatives and their biological significance. *J. Chem. Pharm. Res.* **3**, 126–133 (2011).
168. Stocco, A. *et al.* Treatment with a triazole inhibitor of the mitochondrial permeability transition pore fully corrects the pathology of sapje zebrafish lacking dystrophin. *Pharmacol. Res.* **165**, 105421 (2021).
169. Suttie, J. W. Vitamin K-dependent carboxylase. *Annu. Rev. Biochem.* **54**, 459–477 (1985).
170. Shearer, M. J., Fu, X. & Booth, S. L. Vitamin K nutrition, metabolism, and requirements: current concepts and future research. *Adv. Nutr. Bethesda Md* **3**, 182–195 (2012).
171. Okano, T. *et al.* Conversion of phyloquinone (Vitamin K1) into menaquinone-4 (Vitamin K2) in mice: two possible routes for menaquinone-4 accumulation in cerebra of mice. *J. Biol. Chem.* **283**, 11270–11279 (2008).
172. Tsugawa, N. & Shiraki, M. Vitamin K Nutrition and Bone Health. *Nutrients* **12**, E1909 (2020).
173. Vos, M. *et al.* Vitamin K2 is a mitochondrial electron carrier that rescues pink1 deficiency. *Science* **336**, 1306–1310 (2012).
174. Schwalfenberg, G. K. Vitamins K1 and K2: The Emerging Group of Vitamins Required for Human Health. *J. Nutr. Metab.* **2017**, 6254836 (2017).
175. Orlando, A. *et al.* Vitamin K1 exerts antiproliferative effects and induces apoptosis in three differently graded human colon cancer cell lines. *BioMed Res. Int.* **2015**, 296721 (2015).
176. Bórquez, J. C. *et al.* Sucralose Stimulates Mitochondrial Bioenergetics in Caco-2 Cells. *Front. Nutr.* **7**, 585484 (2020).
177. Barré-Sinoussi, F. & Montagutelli, X. Animal models are essential to biological research: issues and perspectives. *Future Sci. OA* **1**, FSO63 (2015).
178. Lunney, J. K. Advances in swine biomedical model genomics. *Int. J. Biol. Sci.* **3**, 179–184 (2007).
179. Wernersson, R. *et al.* Pigs in sequence space: a 0.66X coverage pig genome survey based on shotgun sequencing. *BMC Genomics* **6**, 70 (2005).
180. Kim, J., Lee, T., Kim, T.-H., Lee, K.-T. & Kim, H. An integrated approach of comparative genomics and heritability analysis of pig and human on obesity trait: evidence for candidate genes on human chromosome 2. *BMC Genomics* **13**, 711 (2012).
181. Pig animal model - Specipig. <https://www.specipig.com/pig-model>.
182. Ottaviani, E., Malagoli, D. & Franceschi, C. Common evolutionary origin of the immune and neuroendocrine systems: from morphological and functional evidence to in silico approaches. *Trends Immunol.* **28**, 497–502 (2007).
183. Ottaviani, E. *et al.* Epigenetic modification in neurons of the mollusc *Pomacea canaliculata* after immune challenge. *Brain Res.* **1537**, 18–26 (2013).
184. Harel, I. *et al.* A platform for rapid exploration of aging and diseases in a naturally short-lived vertebrate. *Cell* **160**, 1013–1026 (2015).
185. Vaughan, C., Pearsall, I., Yeudall, A., Deb, S. P. & Deb, S. p53: its mutations and their impact on transcription. *Subcell. Biochem.* **85**, 71–90 (2014).

186. Tascadda, F. *et al.* Molluscs as models for translational medicine. *Med. Sci. Monit. Basic Res.* **21**, 96–99 (2015).
187. Nesci, S., Ventrella, V., Trombetti, F., Pirini, M. & Pagliarani, A. The mitochondrial F1FO-ATPase desensitization to oligomycin by tributyltin is due to thiol oxidation. *Biochimie* **97**, 128–137 (2014).
188. Bradford, M. M. A rapid and sensitive method for the quantitation of microgram quantities of protein utilizing the principle of protein-dye binding. *Anal. Biochem.* **72**, 248–254 (1976).
189. Penin, F., Godinot, C. & Gautheron, D. C. Optimization of the purification of mitochondrial F1-adenosine triphosphatase. *Biochim. Biophys. Acta* **548**, 63–71 (1979).
190. Cornish-Bowden, A. A simple graphical method for determining the inhibition constants of mixed, uncompetitive and non-competitive inhibitors. *Biochem. J.* **137**, 143–144 (1974).
191. Yonetani, T. The Yonetani-Theorell graphical method for examining overlapping subsites of enzyme active centers. *Methods Enzymol.* **87**, 500–509 (1982).
192. Nesci, S., Trombetti, F., Pirini, M., Ventrella, V. & Pagliarani, A. Mercury and protein thiols: Stimulation of mitochondrial F1FO-ATPase and inhibition of respiration. *Chem. Biol. Interact.* **260**, 42–49 (2016).
193. Bioenergetics - 4th Edition. <https://www.elsevier.com/books/bioenergetics/nicholls/978-0-12-388425-1> (2020).
194. Chance, B. & Williams, G. R. Respiratory enzymes in oxidative phosphorylation. III. The steady state. *J. Biol. Chem.* **217**, 409–427 (1955).
195. Chance, B., Williams, G. R., Holmes, W. F. & Higgins, J. Respiratory enzymes in oxidative phosphorylation. V. A mechanism for oxidative phosphorylation. *J. Biol. Chem.* **217**, 439–451 (1955).
196. Bartolomé, F. & Abramov, A. Y. Measurement of mitochondrial NADH and FAD autofluorescence in live cells. *Methods Mol. Biol. Clifton NJ* **1264**, 263–270 (2015).
197. XFp Real-Time ATP Rate Assay Kit User Guide. 24.
198. Seahorse XFp Cell Mito Stress Test Kit User Guide. 18.
199. Seahorse XF Cell Energy Phenotype Test Kit User Guide. 20.
200. Seahorse XF Mito Fuel Flex Test Kit User Manual. 26.
201. Módis, K. *et al.* Regulation of mitochondrial bioenergetic function by hydrogen sulfide. Part II. Pathophysiological and therapeutic aspects. *Br. J. Pharmacol.* **171**, 2123–2146 (2014).
202. Segeritz, C.-P. & Vallier, L. Cell Culture. *Basic Sci. Methods Clin. Res.* 151–172 (2017) doi:10.1016/B978-0-12-803077-6.00009-6.
203. Rossi, A., Pizzo, P. & Filadi, R. Calcium, mitochondria and cell metabolism: A functional triangle in bioenergetics. *Biochim. Biophys. Acta Mol. Cell Res.* **1866**, 1068–1078 (2019).
204. Shum, L. C., White, N. S., Mills, B. N., Bentley, K. L. de M. & Eliseev, R. A. Energy Metabolism in Mesenchymal Stem Cells During Osteogenic Differentiation. *Stem Cells Dev.* **25**, 114–122 (2016).
205. Storey, B. T. Mammalian sperm metabolism: oxygen and sugar, friend and foe. *Int. J. Dev. Biol.* **52**, 427–437 (2008).
206. Rodriguez-Gil, J. E. Mammalian sperm energy resources management and survival during conservation in refrigeration. *Reprod. Domest. Anim. Zuchthyg.* **41 Suppl 2**, 11–20 (2006).

207. Rodríguez-Gil, J. E. & Bonet, S. Current knowledge on boar sperm metabolism: Comparison with other mammalian species. *Theriogenology* **85**, 4–11 (2016).
208. Moraes, C. R. & Meyers, S. The sperm mitochondrion: Organelle of many functions. *Anim. Reprod. Sci.* **194**, 71–80 (2018).
209. Davila, M. P. *et al.* Mitochondrial ATP is required for the maintenance of membrane integrity in stallion spermatozoa, whereas motility requires both glycolysis and oxidative phosphorylation. *Reprod. Camb. Engl.* **152**, 683–694 (2016).
210. Peña, F. J. *et al.* The Impact of Reproductive Technologies on Stallion Mitochondrial Function. *Reprod. Domest. Anim. Zuchthyg.* **50**, 529–537 (2015).
211. Plaza Davila, M. *et al.* Inhibition of Mitochondrial Complex I Leads to Decreased Motility and Membrane Integrity Related to Increased Hydrogen Peroxide and Reduced ATP Production, while the Inhibition of Glycolysis Has Less Impact on Sperm Motility. *PloS One* **10**, e0138777 (2015).
212. Gibb, Z. & Aitken, R. J. The Impact of Sperm Metabolism during In Vitro Storage: The Stallion as a Model. *BioMed Res. Int.* **2016**, 9380609 (2016).
213. Varner, D. D., Gibb, Z. & Aitken, R. J. Stallion fertility: a focus on the spermatozoon. *Equine Vet. J.* **47**, 16–24 (2015).
214. Bucci, D. *et al.* GLUTs and mammalian sperm metabolism. *J. Androl.* **32**, 348–355 (2011).
215. Wei, X. *et al.* Mesenchymal stem cells: a new trend for cell therapy. *Acta Pharmacol. Sin.* **34**, 747–754 (2013).
216. Dominici, M. *et al.* Minimal criteria for defining multipotent mesenchymal stromal cells. The International Society for Cellular Therapy position statement. *Cytotherapy* **8**, 315–317 (2006).
217. Sun, M., Sun, L., Huang, C., Chen, B.-C. & Zhou, Z. Induction of Macrophage M2b/c Polarization by Adipose Tissue-Derived Mesenchymal Stem Cells. *J. Immunol. Res.* **2019**, 7059680 (2019).
218. Ullah, I., Subbarao, R. B. & Rho, G. J. Human mesenchymal stem cells - current trends and future prospective. *Biosci. Rep.* **35**, e00191 (2015).
219. Caplan, A. I. & Dennis, J. E. Mesenchymal stem cells as trophic mediators. *J. Cell. Biochem.* **98**, 1076–1084 (2006).
220. Bateman, M. E., Strong, A. L., Gimble, J. M. & Bunnell, B. A. Concise Review: Using Fat to Fight Disease: A Systematic Review of Nonhomologous Adipose-Derived Stromal/Stem Cell Therapies. *Stem Cells Dayt. Ohio* **36**, 1311–1328 (2018).
221. Arnhold, S. & Wenisch, S. Adipose tissue derived mesenchymal stem cells for musculoskeletal repair in veterinary medicine. *Am. J. Stem Cells* **4**, 1–12 (2015).
222. Cremonesi, F., Corradetti, B. & Lange Consiglio, A. Fetal adnexa derived stem cells from domestic animal: progress and perspectives. *Theriogenology* **75**, 1400–1415 (2011).
223. Iacono, E., Rossi, B. & Merlo, B. Stem cells from foetal adnexa and fluid in domestic animals: an update on their features and clinical application. *Reprod. Domest. Anim. Zuchthyg.* **50**, 353–364 (2015).
224. Filioli Uranio, M. *et al.* Isolation, proliferation, cytogenetic, and molecular characterization and in vitro differentiation potency of canine stem cells from foetal adnexa: a comparative study of amniotic fluid, amnion, and umbilical cord matrix. *Mol. Reprod. Dev.* **78**, 361–373 (2011).
225. Marcus, A. J. & Woodbury, D. Fetal stem cells from extra-embryonic tissues: do not discard. *J. Cell. Mol. Med.* **12**, 730–742 (2008).

226. Mariani, V., Palermo, S., Fiorentini, S., Lanubile, A. & Giuffra, E. Gene expression study of two widely used pig intestinal epithelial cell lines: IPEC-J2 and IPI-2I. *Vet. Immunol. Immunopathol.* **131**, 278–284 (2009).
227. Vergauwen, H. The IPEC-J2 Cell Line. in *The Impact of Food Bioactives on Health: in vitro and ex vivo models* (eds. Verhoeckx, K. et al.) (Springer, 2015).
228. Schierack, P. *et al.* Characterization of a porcine intestinal epithelial cell line for in vitro studies of microbial pathogenesis in swine. *Histochem. Cell Biol.* **125**, 293–305 (2006).
229. Zakrzewski, S. S. *et al.* Improved cell line IPEC-J2, characterized as a model for porcine jejunal epithelium. *PLoS One* **8**, e79643 (2013).
230. Casadio, R. & Melandri, B. A. CaATP inhibition of the MgATP-dependent proton pump (H<sup>+</sup>-ATPase) in bacterial photosynthetic membranes with a mechanism of alternative substrate inhibition. *JBIC J. Biol. Inorg. Chem.* **1**, 284–291 (1996).
231. Frasch, W. D. The participation of metals in the mechanism of the F(1)-ATPase. *Biochim. Biophys. Acta* **1458**, 310–325 (2000).
232. Andrews, W. W., Hill, F. C. & Allison, W. S. Identification of the essential tyrosine residue in the beta subunit of bovine heart mitochondrial F1-ATPase that is modified by 7-chloro-4-nitro[14C]benzofurazan. *J. Biol. Chem.* **259**, 8219–8225 (1984).
233. Andrews, W. W., Hill, F. C. & Allison, W. S. Identification of the lysine residue to which the 4-nitrobenzofurazan group migrates after the bovine mitochondrial F1-ATPase is inactivated with 7-chloro-4-nitro[14C]benzofurazan. *J. Biol. Chem.* **259**, 14378–14382 (1984).
234. Orriss, G. L., Leslie, A. G., Braig, K. & Walker, J. E. Bovine F1-ATPase covalently inhibited with 4-chloro-7-nitrobenzofurazan: the structure provides further support for a rotary catalytic mechanism. *Struct. Lond. Engl.* **1993** **6**, 831–837 (1998).
235. Ermakov YuA, null, Averbakh, A. Z., Arbusova, A. B. & Sukharev, S. I. Lipid and cell membranes in the presence of gadolinium and other ions with high affinity to lipids. 2. A dipole component of the boundary potential on membranes with different surface charge. *Membr. Cell Biol.* **12**, 411–426 (1998).
236. Cheng, Y. *et al.* Gadolinium induces domain and pore formation of human erythrocyte membrane: an atomic force microscopic study. *Biochim. Biophys. Acta* **1421**, 249–260 (1999).
237. Gianulis, E. C. & Pakhomov, A. G. Gadolinium modifies the cell membrane to inhibit permeabilization by nanosecond electric pulses. *Arch. Biochem. Biophys.* **570**, 1–7 (2015).
238. Hubbard, M. J. & McHugh, N. J. Mitochondrial ATP synthase F1-beta-subunit is a calcium-binding protein. *FEBS Lett.* **391**, 323–329 (1996).
239. Bald, D. *et al.* ATP synthesis by F0F1-ATP synthase independent of noncatalytic nucleotide binding sites and insensitive to azide inhibition. *J. Biol. Chem.* **273**, 865–870 (1998).
240. Nesci, S., Trombetti, F., Ventrella, V. & Pagliarani, A. From the Ca<sup>2+</sup>-activated F1FO-ATPase to the mitochondrial permeability transition pore: an overview. *Biochimie* **152**, 85–93 (2018).
241. Eriksson, O., Fontaine, E. & Bernardi, P. Chemical modification of arginines by 2,3-butanedione and phenylglyoxal causes closure of the mitochondrial permeability transition pore. *J. Biol. Chem.* **273**, 12669–12674 (1998).
242. Guo, L. *et al.* Arginine 107 of yeast ATP synthase subunit g mediates sensitivity of the mitochondrial permeability transition to phenylglyoxal. *J. Biol. Chem.* **293**, 14632–14645 (2018).

243. Wang, S.-B. *et al.* Redox regulation of mitochondrial ATP synthase: implications for cardiac resynchronization therapy. *Circ. Res.* **109**, 750–757 (2011).
244. Ong, S.-B., Samangouei, P., Kalkhoran, S. B. & Hausenloy, D. J. The mitochondrial permeability transition pore and its role in myocardial ischemia reperfusion injury. *J. Mol. Cell. Cardiol.* **78**, 23–34 (2015).
245. Mustafa, A. K. *et al.* H<sub>2</sub>S signals through protein S-sulfhydration. *Sci. Signal.* **2**, ra72 (2009).
246. Nicholls, P. & Kim, J. K. Sulphide as an inhibitor and electron donor for the cytochrome c oxidase system. *Can. J. Biochem.* **60**, 613–623 (1982).
247. Goubern, M., Andriamihaja, M., Nübel, T., Blachier, F. & Bouillaud, F. Sulfide, the first inorganic substrate for human cells. *FASEB J. Off. Publ. Fed. Am. Soc. Exp. Biol.* **21**, 1699–1706 (2007).
248. Powell, M. A. & Somero, G. N. Hydrogen Sulfide Oxidation Is Coupled to Oxidative Phosphorylation in Mitochondria of *Solemya reidi*. *Science* **233**, 563–566 (1986).
249. Letts, J. A., Fiedorczuk, K., Degliesposti, G., Skehel, M. & Sazanov, L. A. Structures of Respiratory Supercomplex I+III<sub>2</sub> Reveal Functional and Conformational Crosstalk. *Mol. Cell* **75**, 1131-1146.e6 (2019).
250. Fedor, J. G. & Hirst, J. Mitochondrial Supercomplexes Do Not Enhance Catalysis by Quinone Channeling. *Cell Metab.* **28**, 525-531.e4 (2018).
251. Morciano, G. *et al.* Molecular identity of the mitochondrial permeability transition pore and its role in ischemia-reperfusion injury. *J. Mol. Cell. Cardiol.* **78**, 142–153 (2015).
252. Murphy, E. & Steenbergen, C. Regulation of Mitochondrial Ca<sup>2+</sup> Uptake. *Annu. Rev. Physiol.* **83**, 107–126 (2021).
253. Marchi, S., Vitto, V. A. M., Patergnani, S. & Pinton, P. High mitochondrial Ca<sup>2+</sup> content increases cancer cell proliferation upon inhibition of mitochondrial permeability transition pore (mPTP). *Cell Cycle Georget. Tex* **18**, 914–916 (2019).
254. Šileikytė, J. *et al.* Second-Generation Inhibitors of the Mitochondrial Permeability Transition Pore with Improved Plasma Stability. *ChemMedChem* **14**, 1771–1782 (2019).
255. Ferguson, S. J. ATP synthase: from sequence to ring size to the P/O ratio. *Proc. Natl. Acad. Sci. U. S. A.* **107**, 16755–16756 (2010).
256. Hayes, B. *et al.* Derivation, characterization, and in vitro differentiation of canine embryonic stem cells. *Stem Cells Dayt. Ohio* **26**, 465–473 (2008).
257. Schneider, M. R., Wolf, E., Braun, J., Kolb, H.-J. & Adler, H. Canine embryo-derived stem cells and models for human diseases. *Hum. Mol. Genet.* **17**, R42-47 (2008).
258. Lonergan, T., Brenner, C. & Bavister, B. Differentiation-related changes in mitochondrial properties as indicators of stem cell competence. *J. Cell. Physiol.* **208**, 149–153 (2006).
259. Kaelin, W. G. & McKnight, S. L. Influence of metabolism on epigenetics and disease. *Cell* **153**, 56–69 (2013).
260. Balaban, R. S. Regulation of oxidative phosphorylation in the mammalian cell. *Am. J. Physiol.* **258**, C377-389 (1990).
261. Kim, J.-W. & Dang, C. V. Multifaceted roles of glycolytic enzymes. *Trends Biochem. Sci.* **30**, 142–150 (2005).

262. Hüttemann, M., Lee, I., Samavati, L., Yu, H. & Doan, J. W. Regulation of mitochondrial oxidative phosphorylation through cell signaling. *Biochim. Biophys. Acta* **1773**, 1701–1720 (2007).
263. Villena, J. A. New insights into PGC-1 coactivators: redefining their role in the regulation of mitochondrial function and beyond. *FEBS J.* **282**, 647–672 (2015).
264. Wu, Z. *et al.* Chemical Composition and Antioxidant Properties of Essential Oils from Peppermint, Native Spearmint and Scotch Spearmint. *Mol. Basel Switz.* **24**, E2825 (2019).
265. Lenaz, G. *et al.* Localization and mobility of coenzyme Q in lipid bilayers and membranes. *BioFactors Oxf. Engl.* **9**, 87–93 (1999).
266. Cerqua, C. *et al.* Vitamin K2 cannot substitute Coenzyme Q10 as electron carrier in the mitochondrial respiratory chain of mammalian cells. *Sci. Rep.* **9**, 6553 (2019).
267. Ausili, A. *et al.* Interaction of Vitamin K1 and Vitamin K2 with Dimyristoylphosphatidylcholine and Their Location in the Membrane. *Langmuir ACS J. Surf. Colloids* **36**, 1062–1073 (2020).
268. Colpa-Boonstra, J. P. & Slater, E. C. The possible role of vitamin K in the respiratory chain. *Biochim. Biophys. Acta* **27**, 122–133 (1958).
269. Zorov, D. B., Filburn, C. R., Klotz, L. O., Zweier, J. L. & Sollott, S. J. Reactive oxygen species (ROS)-induced ROS release: a new phenomenon accompanying induction of the mitochondrial permeability transition in cardiac myocytes. *J. Exp. Med.* **192**, 1001–1014 (2000).
270. Schoon, E. J. *et al.* Low serum and bone vitamin K status in patients with longstanding Crohn's disease: another pathogenetic factor of osteoporosis in Crohn's disease? *Gut* **48**, 473–477 (2001).
271. Djuric, Z., Zivic, S. & Katic, V. Celiac disease with diffuse cutaneous vitamin K-deficiency bleeding. *Adv. Ther.* **24**, 1286–1289 (2007).
272. Nowak, J. K. *et al.* Prevalence and correlates of vitamin K deficiency in children with inflammatory bowel disease. *Sci. Rep.* **4**, 4768 (2014).
273. Shirakawa, H., Komai, M. & Kimura, S. Antibiotic-induced vitamin K deficiency and the role of the presence of intestinal flora. *Int. J. Vitam. Nutr. Res. Int. Z. Vitam.-Ernährungsforschung J. Int. Vitaminol. Nutr.* **60**, 245–251 (1990).